

# nature

## FAT CELL FATE

PP2A/MAT14-  
mediates  
metabolism to brown fat

Editorial  
Feedback on the issue

Editorial  
The role of adenosine

Editorial  
Dyslipidemia

Editorial  
Lipid metabolism

## Case not closed

The FBI says it has evidence showing that Bruce Ivins was behind the 2001 anthrax attacks — but with his death, this will not be tested in court. A full enquiry into the case is needed if justice is to be done.

Was Bruce Ivins a scientist-gone-wrong who single-handedly orchestrated the 2001 anthrax attacks in the United States? Or was the 62-year-old anthrax-vaccine researcher at Fort Detrick, Maryland, an emotionally unstable innocent whose profile made him a convenient fall guy for the FBI?

The jury is still out on those questions — or rather, it would be if one had ever had a chance to hear the evidence. Ivins's apparent suicide last month means there will not be a trial, which makes it all the more important that the government release the evidence it planned to use to accuse him. In full. Now.

On 6 August, the FBI's parent agency, the US Department of Justice, released what it described as hundreds of pages of evidence against Ivins, and declared it would close the case because it was satisfied it had its man. But Ivins's attorney, Paul Kemp, has described these documents as "heaps of innuendo and a staggering lack of real evidence". He has a point.

For example, many of the documents are just search warrants — a reminder that, despite extensive searches of Ivins's house and cars, the FBI failed to come up with any physical evidence directly implicating him in the attacks. Similarly, the bureau has no evidence to place Ivins at the postboxes in Princeton, New Jersey, from which the anthrax-laden letters were sent.

The core of the case against Ivins, as released so far, is contained in just a couple of dozen pages of affidavits — only four paragraphs of which discuss what the FBI says is the smoking gun: the genetic analysis of the anthrax powder from the letters. The FBI says it found four distinctive genetic mutations in the anthrax used in the attacks. It tested for these mutations in isolates of the Ames anthrax strain from 16 domestic, government and university laboratories, alongside ones from labs in Canada, Sweden and the United Kingdom.

In all, more than 1,000 samples were collected, only 8 of which had the 4 mutations, according to the affidavit. Each of these isolates, it says, was directly related to a strain batch named RMR-1029, which was created in 1997 and held in a flask at the US Army research facility in Fort Detrick. The affidavits describe Ivins as the "sole custodian" of that batch. Many other researchers had access to it, but

the FBI claims to have eliminated them as suspects.

The genetic analysis itself seems quite solid. The FBI has collaborated with some of the best outside scientists on anthrax, and on 18 August convened many of them to answer journalists' questions about the science. The researchers on the panel explained that none of the analysis techniques used in this case is new; just the application to anthrax forensics. Several peer-reviewed papers on the forensic work have already been published, and another dozen or so are anticipated (see page 928).

Although this openness about the techniques is commendable, neither the conclusions drawn from the scientific analysis, nor such crucial legal elements as the veracity of the provenance and handling of samples, have been tested in court. So far only one side of the story has been heard: that of the prosecution.

Certainly Ivins's behaviour in the crucial autumn months of 2001 raises questions about his emotional stability, but mental illness does not necessarily a murderer make.

The FBI should explain why it thinks the scientific evidence implicates Ivins himself, and not just the flask. As Kemp aptly puts it: "In this country, we prosecute people, not beakers." The absence of such a full disclosure can only feed suspicions that the FBI has again targeted an innocent man in this case — as it did with former Fort Detrick researcher Steven Hatfill.

This case is too important to be brushed under the carpet. The anthrax attacks killed five people, infected several others, paralysed the United States with fear and shaped the nation's bioterrorism policy. Science and law share a conviction that conclusions require evidence, and that the evidence be debated openly. The FBI says it regrets that Ivins's untimely death has denied it the chance to have its day in court. So presumably the bureau would welcome a full congressional or independent enquiry into this case, as has been called for by Senator Chuck Grassley (Republican, Iowa) and several other lawmakers. It is essential that such an enquiry takes place. ■

**"Only full disclosure can lift suspicions that the FBI has again targeted an innocent man."**

## Scandalous behaviour

Austria's most serious report of scientific misconduct in recent memory must be handled properly.

The academic community in Austria often seems to be a closed, elite set, especially in the sphere of medicine. The power and influence wielded by a professor are hard to understand from the outside, and the rigid hierarchy of the academic system has been

hard to dismantle from the inside, despite reformers' best efforts.

The upper echelons of that community also seem to know how to close ranks. Witness an example now threatening to emerge from the Medical University of Innsbruck, where there are worrying signs that investigations into a scandal of unprecedented dimensions in this small country may be thwarted.

According to a report from the Austrian Agency for Health and Food Safety, a urologist at the university, Hannes Strasser, has conducted a high-profile clinical trial so inappropriately that it must be considered entirely invalid (see page 922). Moreover, that trial

## Case not closed

The FBI says it has evidence showing that Bruce Ivins was behind the 2001 anthrax attacks — but with his death, this will not be tested in court. A full enquiry into the case is needed if justice is to be done.

Was Bruce Ivins a scientist-gone-wrong who single-handedly orchestrated the 2001 anthrax attacks in the United States? Or was the 62-year-old anthrax-vaccine researcher at Fort Detrick, Maryland, an emotionally unstable innocent whose profile made him a convenient fall guy for the FBI?

The jury is still out on those questions — or rather, it would be if one had ever had a chance to hear the evidence. Ivins's apparent suicide last month means there will not be a trial, which makes it all the more important that the government release the evidence it planned to use to accuse him. In full. Now.

On 6 August, the FBI's parent agency, the US Department of Justice, released what it described as hundreds of pages of evidence against Ivins, and declared it would close the case because it was satisfied it had its man. But Ivins's attorney, Paul Kemp, has described these documents as "heaps of innuendo and a staggering lack of real evidence". He has a point.

For example, many of the documents are just search warrants — a reminder that, despite extensive searches of Ivins's house and cars, the FBI failed to come up with any physical evidence directly implicating him in the attacks. Similarly, the bureau has no evidence to place Ivins at the postboxes in Princeton, New Jersey, from which the anthrax-laden letters were sent.

The core of the case against Ivins, as released so far, is contained in just a couple of dozen pages of affidavits — only four paragraphs of which discuss what the FBI says is the smoking gun: the genetic analysis of the anthrax powder from the letters. The FBI says it found four distinctive genetic mutations in the anthrax used in the attacks. It tested for these mutations in isolates of the Ames anthrax strain from 16 domestic, government and university laboratories, alongside ones from labs in Canada, Sweden and the United Kingdom.

In all, more than 1,000 samples were collected, only 8 of which had the 4 mutations, according to the affidavit. Each of these isolates, it says, was directly related to a strain batch named RMR-1029, which was created in 1997 and held in a flask at the US Army research facility in Fort Detrick. The affidavits describe Ivins as the "sole custodian" of that batch. Many other researchers had access to it, but

the FBI claims to have eliminated them as suspects.

The genetic analysis itself seems quite solid. The FBI has collaborated with some of the best outside scientists on anthrax, and on 18 August convened many of them to answer journalists' questions about the science. The researchers on the panel explained that none of the analysis techniques used in this case is new; just the application to anthrax forensics. Several peer-reviewed papers on the forensic work have already been published, and another dozen or so are anticipated (see page 928).

Although this openness about the techniques is commendable, neither the conclusions drawn from the scientific analysis, nor such crucial legal elements as the veracity of the provenance and handling of samples, have been tested in court. So far only one side of the story has been heard: that of the prosecution.

Certainly Ivins's behaviour in the crucial autumn months of 2001 raises questions about his emotional stability, but mental illness does not necessarily a murderer make.

The FBI should explain why it thinks the scientific evidence implicates Ivins himself, and not just the flask. As Kemp aptly puts it: "In this country, we prosecute people, not beakers." The absence of such a full disclosure can only feed suspicions that the FBI has again targeted an innocent man in this case — as it did with former Fort Detrick researcher Steven Hatfill.

This case is too important to be brushed under the carpet. The anthrax attacks killed five people, infected several others, paralysed the United States with fear and shaped the nation's bioterrorism policy. Science and law share a conviction that conclusions require evidence, and that the evidence be debated openly. The FBI says it regrets that Ivins's untimely death has denied it the chance to have its day in court. So presumably the bureau would welcome a full congressional or independent enquiry into this case, as has been called for by Senator Chuck Grassley (Republican, Iowa) and several other lawmakers. It is essential that such an enquiry takes place. ■

**"Only full disclosure can lift suspicions that the FBI has again targeted an innocent man."**

## Scandalous behaviour

Austria's most serious report of scientific misconduct in recent memory must be handled properly.

The academic community in Austria often seems to be a closed, elite set, especially in the sphere of medicine. The power and influence wielded by a professor are hard to understand from the outside, and the rigid hierarchy of the academic system has been

hard to dismantle from the inside, despite reformers' best efforts.

The upper echelons of that community also seem to know how to close ranks. Witness an example now threatening to emerge from the Medical University of Innsbruck, where there are worrying signs that investigations into a scandal of unprecedented dimensions in this small country may be thwarted.

According to a report from the Austrian Agency for Health and Food Safety, a urologist at the university, Hannes Strasser, has conducted a high-profile clinical trial so inappropriately that it must be considered entirely invalid (see page 922). Moreover, that trial

represents just a fraction of the total number of patients who paid handsomely for the stem-cell treatment for urinary incontinence without knowing it was experimental.

Strasser's department chair, Georg Bartsch, insists that he has no connection with, and no responsibility for, the scandal — despite having 'honorary authorship' on all the relevant papers, a practice that contravenes the university's code of practice. And Strasser himself has written an open letter to university authorities denying any wrongdoing.

At the beginning of July, a preliminary version of the report was circulated to those involved. Shortly afterwards, for reasons known only to itself, the university council announced plans to fire the university's respected rector, Clemens Sorg — who was going public with the problems — on grounds that many university and clinic officials believe to be invalid. Then the Austrian Academy of Sciences put its independent investigation, requested by Sorg, on hold. And on 13 August, the heads of the university hospital suddenly withdrew a letter of support for Sorg that they had sent out a few days earlier, saying they now realized it interfered with the university's internal affairs.

The council would be wise to think carefully before carrying out its threat to fire the rector under these conditions.

It seems clear that the academy of sciences is doing itself, and the community it represents, an inexcusable disservice by stepping back from helping to resolve a scandal of this magnitude. The academy

claims, remarkably, to believe that Sorg asked for its help as an individual, not as the university's representative, and now that he may be dismissed, his concerns may similarly be dismissed — apparently on the grounds that the academy is an independent body. It would display its independence better by carrying forward its investigation into this shameful affair whether the person of the rector changes or not.

The academy is right in pointing out one thing, though. It may be morally responsible, but it is not legally responsible for addressing issues of scientific misconduct.

There is no body in Austria with this remit. A few years ago, the ministry of research began discussions about creating a body similar to the US Office of Research Integrity or the Danish Committees on Scientific Dishonesty, but talks have so far come to nothing. Hopefully this affair will at least speed up this process.

It seems axiomatic that the chair of a university department must take responsibility for the goings-on in that department, and most certainly for any paper he or she co-authors. Any responses that the university makes to the report must take these factors into account — whatever steps Bartsch takes to disassociate himself from the affair.

Austria is a small country, and networks between power-brokers are small and tight. But something, it seems, is rotten in the state of Austria, and it needs to be faced and dealt with openly. ■

**"There is no official body in Austria responsible for addressing issues of scientific misconduct."**

## A case for nurture

**Innovation is a complex ecosystem that requires careful cultivation.**

Where does innovation come from? How can it best be nurtured and encouraged? These questions are taking on global significance as fast-developing nations such as China, India and Brazil increasingly see leadership in innovation as key to their economic competitiveness. Although the link between innovation and economic strength is a matter for debate, the power of innovation to shape and transform society makes it worth studying. Earlier this summer, *Nature* began a monthly series of Commentaries to explore the origins of innovation and how it can be nurtured (see [www.nature.com/nature/focus/innovation](http://www.nature.com/nature/focus/innovation)).

One common theme in the series is that the standard, linear model of innovation is too simplistic. That model, extant since at least the 1940s, posits that new ideas and technologies originate in the nursery of basic research. And, like growing children moving through school and university to full-time employment, these innovations progress through applied research to development and, finally, to the marketplace.

This linear sequence contains an element of truth. But it misses the fact that many innovative ideas come the other direction: from users, consumers and efforts to solve practical problems. The linear model also tends to overstate the contribution that basic research makes to the final outcome, by neglecting the roles played by design,

manufacturing and business processes. And the model tends to give policy-makers the impression that innovation is considerably more predictable and controllable than it actually is.

A more accurate picture is that of a nonlinear 'ecosystem', in which innovation is driven by multiple players, forces and feedback loops working simultaneously. Such an ecosystem cannot be managed — at least, not in the conventional sense of top-down control. But it can be cultivated, in the way that a gardener can try to create the right conditions for plants to grow, while accepting that unforeseen elements ultimately dictate the outcome.

Such unpredictability is discussed on page 940 by David Guston, co-director of the Consortium for Science, Policy and Outcomes at Arizona State University in Tempe. The disruptive force of innovations, such as those edging their way towards fruition in stem-cell therapy, often seems at odds with a public policy that must consider the societal impacts of innovation and the social mores of the times. Scientists and engineers often feel hamstrung by the impositions of policy and regulation. Nevertheless, policies that nurture and guide innovation in socially acceptable frameworks could vastly increase public support and understanding of research goals.

The unpredictable nature of innovation means that this investment may not always turn out as expected. But with careful forethought, policy can usefully prepare the soil. This series of Commentaries will continue to explore the origin and nature of innovation — and, we hope, will provide powerful new ideas for culturing its growth. ■

**"Scientists and engineers often feel hamstrung by the impositions of policy and regulation."**

represents just a fraction of the total number of patients who paid handsomely for the stem-cell treatment for urinary incontinence without knowing it was experimental.

Strasser's department chair, Georg Bartsch, insists that he has no connection with, and no responsibility for, the scandal — despite having 'honorary authorship' on all the relevant papers, a practice that contravenes the university's code of practice. And Strasser himself has written an open letter to university authorities denying any wrongdoing.

At the beginning of July, a preliminary version of the report was circulated to those involved. Shortly afterwards, for reasons known only to itself, the university council announced plans to fire the university's respected rector, Clemens Sorg — who was going public with the problems — on grounds that many university and clinic officials believe to be invalid. Then the Austrian Academy of Sciences put its independent investigation, requested by Sorg, on hold. And on 13 August, the heads of the university hospital suddenly withdrew a letter of support for Sorg that they had sent out a few days earlier, saying they now realized it interfered with the university's internal affairs.

The council would be wise to think carefully before carrying out its threat to fire the rector under these conditions.

It seems clear that the academy of sciences is doing itself, and the community it represents, an inexcusable disservice by stepping back from helping to resolve a scandal of this magnitude. The academy

claims, remarkably, to believe that Sorg asked for its help as an individual, not as the university's representative, and now that he may be dismissed, his concerns may similarly be dismissed — apparently on the grounds that the academy is an independent body. It would display its independence better by carrying forward its investigation into this shameful affair whether the person of the rector changes or not.

The academy is right in pointing out one thing, though. It may be morally responsible, but it is not legally responsible for addressing issues of scientific misconduct.

There is no body in Austria with this remit. A few years ago, the ministry of research began discussions about creating a body similar to the US Office of Research Integrity or the Danish Committees on Scientific Dishonesty, but talks have so far come to nothing. Hopefully this affair will at least speed up this process.

It seems axiomatic that the chair of a university department must take responsibility for the goings-on in that department, and most certainly for any paper he or she co-authors. Any responses that the university makes to the report must take these factors into account — whatever steps Bartsch takes to disassociate himself from the affair.

Austria is a small country, and networks between power-brokers are small and tight. But something, it seems, is rotten in the state of Austria, and it needs to be faced and dealt with openly. ■

**"There is no official body in Austria responsible for addressing issues of scientific misconduct."**

## A case for nurture

**Innovation is a complex ecosystem that requires careful cultivation.**

Where does innovation come from? How can it best be nurtured and encouraged? These questions are taking on global significance as fast-developing nations such as China, India and Brazil increasingly see leadership in innovation as key to their economic competitiveness. Although the link between innovation and economic strength is a matter for debate, the power of innovation to shape and transform society makes it worth studying. Earlier this summer, *Nature* began a monthly series of Commentaries to explore the origins of innovation and how it can be nurtured (see [www.nature.com/nature/focus/innovation](http://www.nature.com/nature/focus/innovation)).

One common theme in the series is that the standard, linear model of innovation is too simplistic. That model, extant since at least the 1940s, posits that new ideas and technologies originate in the nursery of basic research. And, like growing children moving through school and university to full-time employment, these innovations progress through applied research to development and, finally, to the marketplace.

This linear sequence contains an element of truth. But it misses the fact that many innovative ideas come the other direction: from users, consumers and efforts to solve practical problems. The linear model also tends to overstate the contribution that basic research makes to the final outcome, by neglecting the roles played by design,

manufacturing and business processes. And the model tends to give policy-makers the impression that innovation is considerably more predictable and controllable than it actually is.

A more accurate picture is that of a nonlinear 'ecosystem', in which innovation is driven by multiple players, forces and feedback loops working simultaneously. Such an ecosystem cannot be managed — at least, not in the conventional sense of top-down control. But it can be cultivated, in the way that a gardener can try to create the right conditions for plants to grow, while accepting that unforeseen elements ultimately dictate the outcome.

Such unpredictability is discussed on page 940 by David Guston, co-director of the Consortium for Science, Policy and Outcomes at Arizona State University in Tempe. The disruptive force of innovations, such as those edging their way towards fruition in stem-cell therapy, often seems at odds with a public policy that must consider the societal impacts of innovation and the social mores of the times. Scientists and engineers often feel hamstrung by the impositions of policy and regulation. Nevertheless, policies that nurture and guide innovation in socially acceptable frameworks could vastly increase public support and understanding of research goals.

The unpredictable nature of innovation means that this investment may not always turn out as expected. But with careful forethought, policy can usefully prepare the soil. This series of Commentaries will continue to explore the origin and nature of innovation — and, we hope, will provide powerful new ideas for culturing its growth. ■

**"Scientists and engineers often feel hamstrung by the impositions of policy and regulation."**

# RESEARCH HIGHLIGHTS

## Don't you step on my...

*Behav. Ecol. Sociobiol.* doi:10.1007/s00265-008-0620-6 (2008)

Among blue-footed boobies, bright blue feet are known to be important for courtship, but it seems that's not all they're good for. Researchers now find that if male feet lose colour after a first egg is laid, females reduce their reproductive efforts.

Roxana Torres at the National Autonomous University of Mexico in Mexico City and her colleagues monitored pairs of the birds (*Sula nebouxii*) on Isla Isabel, off the coast of Mexico. In general, boobies lay two eggs of similar weight each year, with an average delay of four days between the two. The team captured males within 24 hours of the first egg being laid and used crayons to make the foot colour of half the males duller and so less healthy looking.

The researchers found that females paired with males that returned with unsavoury feet delayed laying their second eggs and, when they did lay them, produced smaller eggs than did females with untampered mates.



C. COURTEAU/NATURE PL

## ELECTROPHYSIOLOGY

### On the pulse

*Appl. Phys. Lett.* 93, 033906 (2008)

They're a staple of every hospital television show: to get the beeping signal of an electrocardiograph, medics hurriedly attach electrodes to a patient's skin. Now Robert Prance and his colleagues at the University of Sussex in Brighton, UK, have found a way to measure the electrical signals of a person's breathing and heartbeat remotely.

Their sensor detected clear signals from both the front and back of a seated subject, up to 40 centimetres away, in a laboratory full of distracting electrical noise. Other techniques exist that can remotely discern the tiny movements of the heart and lungs, but those systems actively irradiate their subject with laser light or microwaves.

The researchers note that their passive system could be used for security and healthcare, and perhaps even to detect driver drowsiness.

## MICROBIOLOGY

### Running on arsenic

*Science* 321, 967-970 (2008)

Arsenic-fuelled photosynthetic bacteria may have helped shape the arsenic cycle on ancient Earth.

The newly discovered bacteria use electrons from arsenite to drive photosynthesis in the absence of oxygen, producing arsenate in the process. Ronald Orem and of the US Geological Survey in Menlo Park, California, and his co-workers found the microbes growing in red and green mats in arsenite-rich brine pools (pictured right) at Mono

Lake, California. A pure culture of one purple bacterium isolated from the red mats required both light and arsenite to thrive.

Although other bacteria are known to rely on arsenic, this is the first example of the photosynthetic use of arsenite in the absence of oxygen. The process could have been important on Earth before oxygenic photosynthesis reshaped the atmosphere.

## FLUID DYNAMICS

### Slip and slide

*Phys. Rev. Lett.* 101, 064501 (2008)

A principle of fluid flow is that the bottom-most molecules of a liquid stick to the surface of the solid they are sliding past — creating friction that, for instance, slows down water flowing through a pipe.

Choongyeop Lee at the University of California, Los Angeles, and his colleagues created textured surfaces with micrometre-scale grooves and posts. On these, fluids can slip past friction-free for tiny distances, coasting on the pockets of air between the

grooves or posts. They report a slip length for water almost ten times longer than previously achieved — long enough, they suggest, to show that engineered surfaces can significantly reduce drag in fluid systems.

## ATMOSPHERIC CHEMISTRY

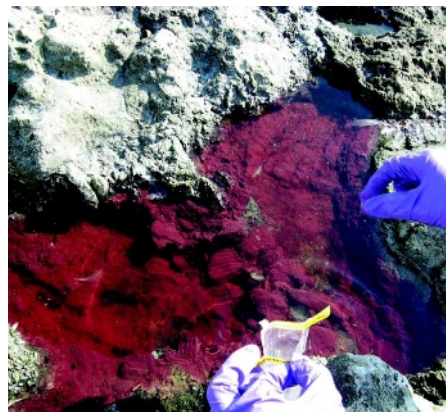
### Attacked from within

*J. Am. Chem. Soc.* doi:10.1021/ja8041965 (2008)

Organic compounds in the lower atmosphere can be attacked by the particles they are sitting on, according to researchers at the University of California, Irvine.

Lab-based experiments by Barbara Finlayson-Pitts and her colleagues show that airborne sea-salt particles containing nitrate or nitrite ions can produce reactive hydroxyl radicals that attack the organic compounds adsorbed onto the particles' surfaces. It was previously thought that oxidation of these organics occurred through attack from outside by ozone or hydroxyl radicals.

Nitrate and nitrite ions are known to be present in many atmospheric particles and in the polar snowpacks. On the basis of the group's experiments, Finlayson-Pitts says it is highly likely that this bottom-up oxidation is happening in air, and could be contributing to atmospheric chemistry.



## CLIMATE INDICATORS

### Early birds

*Global Change Biol.* 14, 1959-1972 (2008)

The first robin sighting of spring may not be the best indicator of climate warming.

Abraham Miller-Rushing at Boston University and his colleagues analysed 33 years' worth of data on 32 bird species in

# RESEARCH HIGHLIGHTS

## Don't you step on my...

*Behav. Ecol. Sociobiol.* doi:10.1007/s00265-008-0620-6 (2008)

Among blue-footed boobies, bright blue feet are known to be important for courtship, but it seems that's not all they're good for. Researchers now find that if male feet lose colour after a first egg is laid, females reduce their reproductive efforts.

Roxana Torres at the National Autonomous University of Mexico in Mexico City and her colleagues monitored pairs of the birds (*Sula nebouxii*) on Isla Isabel, off the coast of Mexico. In general, boobies lay two eggs of similar weight each year, with an average delay of four days between the two. The team captured males within 24 hours of the first egg being laid and used crayons to make the foot colour of half the males duller and so less healthy looking.

The researchers found that females paired with males that returned with unsavoury feet delayed laying their second eggs and, when they did lay them, produced smaller eggs than did females with untampered mates.



C. COURTEAU/NATURE PL

## ELECTROPHYSIOLOGY

### On the pulse

*Appl. Phys. Lett.* 93, 033906 (2008)

They're a staple of every hospital television show: to get the beeping signal of an electrocardiograph, medics hurriedly attach electrodes to a patient's skin. Now Robert Prance and his colleagues at the University of Sussex in Brighton, UK, have found a way to measure the electrical signals of a person's breathing and heartbeat remotely.

Their sensor detected clear signals from both the front and back of a seated subject, up to 40 centimetres away, in a laboratory full of distracting electrical noise. Other techniques exist that can remotely discern the tiny movements of the heart and lungs, but those systems actively irradiate their subject with laser light or microwaves.

The researchers note that their passive system could be used for security and healthcare, and perhaps even to detect driver drowsiness.

## MICROBIOLOGY

### Running on arsenic

*Science* 321, 967-970 (2008)

Arsenic-fuelled photosynthetic bacteria may have helped shape the arsenic cycle on ancient Earth.

The newly discovered bacteria use electrons from arsenite to drive photosynthesis in the absence of oxygen, producing arsenate in the process. Ronald Orem and of the US Geological Survey in Menlo Park, California, and his co-workers found the microbes growing in red and green mats in arsenite-rich brine pools (pictured right) at Mono

Lake, California. A pure culture of one purple bacterium isolated from the red mats required both light and arsenite to thrive.

Although other bacteria are known to rely on arsenic, this is the first example of the photosynthetic use of arsenite in the absence of oxygen. The process could have been important on Earth before oxygenic photosynthesis reshaped the atmosphere.

## FLUID DYNAMICS

### Slip and slide

*Phys. Rev. Lett.* 101, 064501 (2008)

A principle of fluid flow is that the bottom-most molecules of a liquid stick to the surface of the solid they are sliding past — creating friction that, for instance, slows down water flowing through a pipe.

Choongyeop Lee at the University of California, Los Angeles, and his colleagues created textured surfaces with micrometre-scale grooves and posts. On these, fluids can slip past friction-free for tiny distances, coasting on the pockets of air between the

grooves or posts. They report a slip length for water almost ten times longer than previously achieved — long enough, they suggest, to show that engineered surfaces can significantly reduce drag in fluid systems.

## ATMOSPHERIC CHEMISTRY

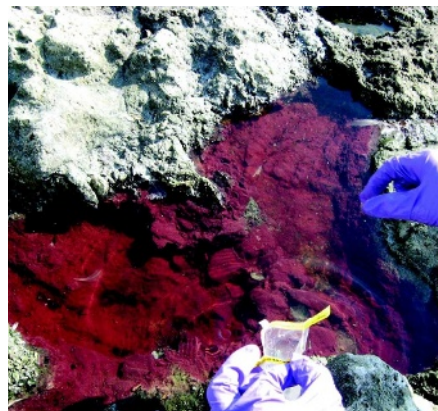
### Attacked from within

*J. Am. Chem. Soc.* doi:10.1021/ja8041965 (2008)

Organic compounds in the lower atmosphere can be attacked by the particles they are sitting on, according to researchers at the University of California, Irvine.

Lab-based experiments by Barbara Finlayson-Pitts and her colleagues show that airborne sea-salt particles containing nitrate or nitrite ions can produce reactive hydroxyl radicals that attack the organic compounds adsorbed onto the particles' surfaces. It was previously thought that oxidation of these organics occurred through attack from outside by ozone or hydroxyl radicals.

Nitrate and nitrite ions are known to be present in many atmospheric particles and in the polar snowpacks. On the basis of the group's experiments, Finlayson-Pitts says it is highly likely that this bottom-up oxidation is happening in air, and could be contributing to atmospheric chemistry.



## CLIMATE INDICATORS

### Early birds

*Global Change Biol.* 14, 1959-1972 (2008)

The first robin sighting of spring may not be the best indicator of climate warming.

Abraham Miller-Rushing at Boston University and his colleagues analysed 33 years' worth of data on 32 bird species in

## JOURNAL CLUB

**Michelle D. Wang**  
Howard Hughes Medical Institute, Cornell University, Ithaca, New York

**A biophysicist marvels at the idea of grabbing microscopic particles with light by tweaking its phase.**

Light carries energy and momentum. Have you ever gazed at a comet on a hot summer night? The dust tail seen streaming out from a comet is caused by sunlight bombarding dust particles from its surface and pushing them away from the Sun. The same radiation pressure can be used to 'trap', or hold, microscopic particles. And if an item of interest — for example, a biological molecule — is attached to a particle subject to trapping, it can then be manipulated as the trap is moved.

So how does one generate optical traps? Conventionally, a laser beam is directed through the objective lens of a microscope and focused to a small spot very close to the specimen. The trapping force relies on the gradient of the laser's intensity — the tighter the focus, the greater the intensity change within the focused beam, and the greater the trapping force.

For a long time, this has been the only type of trap available. But not any more! David Grier and his colleagues have created a new type of trap that relies on the gradient of the 'phase' of a laser's light as well as its intensity (Y. Roichman *et al.* *Phys. Rev. Lett.* **100**, 013602; 2008). Light waves, like ocean waves, have crests and troughs. The phase of a light wave specifies what position within the wave, from crest to trough, the light is in at a given moment. By tweaking the phase of the laser in the trap, the researchers are able not only to hold a particle steady, but also to move it in a line or spin it around in a circle. It is now possible to design optical traps that are more flexible and versatile, and that can generate as much trapping force as before, but with less light.

I would not be surprised if these traps soon become one of the must-have tools in single-molecule biophysics, cell biology and colloidal physics.

Discuss this paper at <http://blogs.nature.com/nature/journalclub>

Massachusetts. They found that the first sighting of a migratory bird, although one of the most commonly used statistics, can be confounded by population size. As bird numbers decline, there are fewer early outliers, making the first birds harder to spot. By extension, growing populations are expected to distort results in the opposite direction.

Instead, the team used the mean arrival date, which did not change with population size. Overall, the birds' mean arrival was two and a half days earlier by the end of the period covered by the data set than at the start.

## ANIMAL BEHAVIOUR

## Crowd control

*Am. J. Primatol.* doi:10.1002/ajp.20601 (2008)  
Many researchers would expect parasitic infection rates to increase as groups of animals get bigger and more hosts are available. Contrary to this, researchers reveal that as groups of red colobus monkeys (*Procolobus rufomitratus*) get larger, they have fewer parasites.

Tamaini Snaith at McGill University in Montreal, Canada, and her colleagues made the discovery while studying the monkeys in Uganda. They tested faeces for parasites and monitored group dynamics. The researchers noticed that large groups tended to spread out more than smaller ones, and suggest that this could lower infection rates.

They add that although the monkeys may be spreading out in response to the parasites, feeding competition could also be driving the spread, making the parasite reduction a happy accident.

## IMMUNOLOGY

## The power of tick spit

*J. Exp. Med.* doi:10.1084/jem.20072689 (2008)  
Proteins used by ticks to evade their hosts' immune systems may one day provide a new way to fight inflammation, researchers say.

Compounds in tick saliva block inflammation and allow the bloodsucking parasites to feed off a host for long time periods without alerting its immune system. Amanda Proudfoot and Christine Power of Merck Serono Geneva Research Centre in Switzerland and their team isolated a family of tick saliva proteins that very selectively bind specific pro-inflammatory members of a protein family called chemokines.

Two of these proteins, which have been named evasins, produced no obvious allergic reaction and reduced inflammation when given to mice suffering from several conditions, including skin or joint inflammation and lung injury.

## BOTANY

## Biofuel heir apparent?

*Global Change Biol.* **14**, 2000–2014 (2008)  
The perennial grass *Miscanthus × giganteus* (pictured below) is photosynthetic royalty. In field tests conducted by Stephen Long and his co-workers at the University of Illinois in Urbana, this sterile hybrid converted 1% of solar energy into biomass that could be harvested to make cellulosic ethanol. That's ten times the standard 0.1% efficiency cited for plants in general.

The team compared *Miscanthus* with switchgrass (*Panicum virgatum*), a current US favourite for the cellulosic fuel of the future. *Miscanthus* produced an average of 30 tonnes of harvestable biomass per hectare; switchgrass produced just 10 tonnes.



S. LONG, UNIV. ILLINOIS

## BIOPHYSICS

## Mob rule

*Proc. Natl Acad. Sci. USA* **105**, 11754–11759 (2008)  
The crowding inherent within cells may affect not only protein movement and folding, but also shape, according to Pernilla Wittung-Stafshede at Rice University in Houston, Texas, and her colleagues.

They focused on the VlsE protein, a proposed virulence factor in *Borrelia burgdorferi*, the bacterium that causes Lyme disease. VlsE is usually rugby-ball shaped, but the team found that it adopts different equilibrium shapes *in vitro* in the presence of varying levels of a polymeric 'crowding agent' that mimics cytoplasmic macromolecules. When the native protein is loosened up by a denaturing agent or by heat, two new structures — a 'bean' shape and a roughly spherical conformation — intervene between the rugby ball and the denatured protein as soon as the crowding agent is added.

If crowding can be 'tuned', it might be possible to expose different sites in proteins and alter their behaviour.



## NEWS

## Report finds grave flaws in urology trial

A clinical trial of a stem-cell procedure for urinary incontinence by urologists at the Medical University of Innsbruck, Austria, was full of serious procedural and ethical problems, finds a report by the government's Agency for Health and Food Safety.

The study by Hannes Strasser and his colleagues, to determine the experimental therapy's efficacy, was published last year (H. Strasser *et al.* *Lancet* **369**, 2179–2186; 2007). A partial study was published a few months after (H. Strasser *et al.* *World J. Urol.* **25**, 385–392; 2007).

The agency's report says that the urologists failed to get appropriate approval for the trial from authorities, including an ethics committee, and failed to adequately inform patients about the nature of the procedures and to insure them. Other problems outlined in the report include poor study design, inconsistent handling of patients and failure to randomize patients properly.

The report also says that many of the documents relating to the trials that were presented for inspection may have been forged, including

supposed insurance certificates and e-mail correspondence with *The Lancet*.

The therapy involves removing tissue from a patient's arm to create muscle stem cells, then

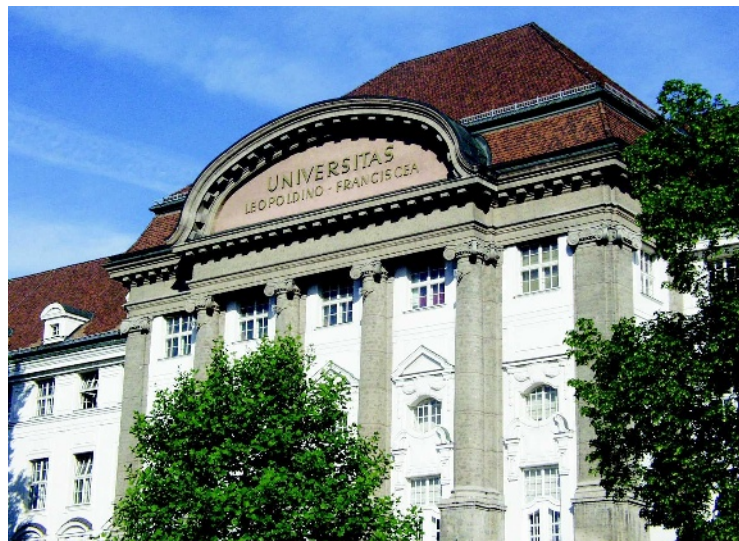
out the report. The university hospital has now forbidden him from treating patients. But, controversially, the report exonerates the head of the urology department, Georg Bartsch, even though he signed many of the documents related to the therapies and is listed as a co-author on the publications.

Meanwhile, the university rector, Clemens Sorg — who has been outspoken about his intention to act on any scientific misconduct exposed by the inspection, and who asked the Austrian Academy of Sciences to investigate the situation — has been threatened with the sack.

Strasser declined to comment on the case. But he has written an open letter to university authorities denying wrong-doing.

Bartsch, an oncologist, dissociates himself from all parts of the trial, saying that

he was unaware of the problems developing until the rector informed him of concerns in November 2007. Although the *Lancet* paper lists him as one of five co-authors who did "all investigations and treatments", and includes



Staff at the Medical University of Innsbruck have been accused of misconduct.

injecting these cells into the same person's urinary sphincter muscle.

Strasser, who is head of the urology department's incontinence division, designed and led the stem-cell project and is implicated through-

## Europe gets centres of excellence for neuroscience

An ambitious 'Janelia Farm-style' neuroscience institute to lead international efforts in understanding the brain and behaviour at the level of basic neural circuits is being planned for London.

University College London (UCL) will host the new centre, after beating rival universities Oxford and Cambridge, *Nature* has learned. The £140-million (US\$261-million) institute will be funded by the Wellcome Trust, the largest UK research charity, and the Gatsby Charitable Foundation, founded by David Sainsbury, a British politician and businessman. The individuals involved declined to comment, but Richard Morris, head of neuroscience at the Wellcome Trust, says no decision has been made.

The aim of the centre will be to "elucidate how neural circuits carry out information processing that underpins behaviour", according to the charities' letter to the

universities competing for the project, sent earlier this year. The institute will take an interdisciplinary approach, combining state-of-the-art molecular and cellular biology with computational modelling.

UCL may have beaten competitors because its 400-strong neuroscience department is one of the most productive in the country. And it already has a world-class computational neuroscience centre, also funded by the Gatsby foundation.

The institute will reportedly work mainly with model organisms such as mice, fruitflies and nematodes. It will employ newly developed techniques such as optogenetics, which allows researchers to switch genetically modified neurons on and off using light. It is believed that the institute will eventually host some 12–15 research groups at a new £60-million building on Huntley Street in Bloomsbury, near both the

Wellcome Trust and UCL's central campus.

The research at the new institute will focus on topics "we're all interested in at the moment", says Wolf Singer, a director at the Max Planck Institute for Brain Research in Frankfurt, Germany. Last month, two German pharmaceutical entrepreneurs, Andreas and Thomas Strüngmann, donated €200 million (US\$295 million) for a new Max Planck cognitive neuroscience research centre in Frankfurt (see *Nature* 454, 381; 2008). European research institutes have primarily been government funded — the involvement of donors such as Sainsbury and the Strüngmanns will help Europe compete better with America, Singer says.

The size and approach of the London project has led many neuroscientists to compare it to Janelia Farm, a biological institute in Ashburn, Virginia, that is funded by the Howard Hughes Medical Institute.



## ANGSTROM OLYMPICS

Chemists vie to create  
shortest metal-metal bond  
[www.nature.com/news](http://www.nature.com/news)

his signature of agreement, Bartsch insists he did not request authorship but that Strasser included him "in honour of my seniority". On 31 July Bartsch asked *The Lancet* to withdraw his name, as "Strasser had not retracted the article as I had suggested". Bartsch adds that the agency's report "is not a legal document in any case".

Bartsch says that 'honorary authorship' is given on occasion within his department. He was a member of the university ethics committee until 1997 and, in 2001, he headed an ad hoc committee that oversaw the introduction of 'good scientific practice' in the faculty of medicine. Three years later the university's senate approved a ten-point protocol along these lines, including an explicit rejection of honorary authorship.

The loss-of-confidence motion against Sorg, an immunologist, was brought by the all-powerful university council on 7 July, shortly after the preliminary report was circulated to those involved. The council comprises seven 'high-standing representatives' of Austrian society and has the power to dismiss the rector. The council accuses Sorg of a 'serious breach of duty', in particular by exposing the university to 'the danger of serious economic damage'.

But on 28 July, the university senate voted unanimously that the specific concerns put forward by the council were too trivial to warrant dismissal. Sorg has also received a letter of support from top university officials expressing concern about the council's actions. The council will vote on Sorg's dismissal at a

special meeting on 21 August.

Meanwhile, Austria's science academy has put its investigation into whether the urologists had followed good scientific practice on hold. "We had the impression that the request came from Sorg as a person, not a university representative," says Peter Schuster, the academy's president. "When the problem of Sorg's possible impeachment came up, we put the case temporarily on ice."

Sorg, who says that his request was made in an official capacity as a representative of the university, is now under pressure to decide quickly on consequences for Strasser and Bartsch, given that the council may vote to dismiss him within days. As a first step, he asked Strasser to confirm by 18 August that he retracted all relevant papers. Further disciplinary actions are being considered by Sorg and the head of the university's hospital. Sorg has also asked the council to send its report to the public prosecutor.

In the meantime, several of the hundreds of patients who have undergone the procedure by Strasser's team — within and outside of the trial — claim that they have had serious side effects. Injuries such as sealing of the urinary sphincter and rupture of the bladder have been registered with authorities. Thomas Juen, the Innsbruck lawyer who is representing the patients, says: "This is a very grave scandal for the university, and the pressure on the public prosecutor to bring criminal charges will be very high." ■

Alison Abbott

See Editorial, page 917.

UCL



UCL: the nerve centre of neuroscience?

Since opening in 2006, the institute has taken an interdisciplinary approach to imaging and modelling neural circuits. The new UCL institute "sounds like Janelia East", says Karel Svoboda, a neuroscientist at Janelia. "That is not necessarily a bad thing," he adds.

Others are concerned that the London institute should distinguish itself from other interdisciplinary centres that are proliferating in this field. "It will be important for the new institute to choose its subject areas carefully to avoid duplication," says Colin Blakemore, a neurobiologist at the University of Oxford.

Svoboda agrees, but says that its central London location and affiliation with a major research university should give a distinctly different character from Janelia Farm. And a Janelia-style centre does not yet exist in Europe, he says. "If organized in the right way, it could really attract fantastic talent."

The institute could be built by 2011. ■

Geoff Brumfiel

## Unproven stem-cell therapy ban

The Bulgarian deputy minister for health has resigned over the country's decision to ban the use of a controversial stem-cell therapy to treat neurological disorders.

The therapy, which since 2005 has been carried out on around 250 patients at St Ivan Rilski Hospital in Sofia, contravenes European Union regulations and is of unproven value, the Bulgarian health ministry ruled on 8 August. Three days later the deputy minister, Matey Mateev, resigned in protest.

The therapy involves harvesting stem cells from a patient's bone marrow, concentrating and purifying them, then injecting them into the same patient's brain or spinal cord. It aims to regenerate nerves and stimulate metabolism after spinal-cord trauma, stroke or neurodegenerative disease, says Venceslav Bussarsky, who heads the hospital's neurosurgery department, and is also president of the Bulgarian Society of Neurosurgery. Each treatment costs €1,000–2,000 (US\$1,500–3,000).

Bussarsky, who claims that companies or individuals with competing financial interests are behind the actions of the health ministry, says that the treatment was successful in nearly half of the patients.

But such stem-cell transplantation is highly controversial. "No scientific evidence has been shown from clinical trials that this treatment would have any positive effect in humans," says Paolo Bianco, a stem-cell researcher at the Sapienza University of Rome.

When Bulgaria joined the European Union in 2007, the country had to comply with the existing European directives on the transplantation of human tissues and cells. The St Ivan therapies contravene these directives, says the health ministry, which is also concerned about the lack of proof that the therapy is effective.

The ministry says that close relatives of Mateev own the two private companies that took part in the St Ivan transplants — in violation of government ethics codes concerning conflicts of interest for leading officials. Mateev's "retirement" is connected to this violation, according to the ministry.

Mateev insists that the directives have been incorrectly translated into the Bulgarian language. "Also the committee did not talk to any of the medical people involved, they only inspected papers," he says. Mateev, a physician, was director at St Ivan from 2002 until 2006. ■

Maria Rossbauer



## ANGSTROM OLYMPICS

Chemists vie to create  
shortest metal-metal bond  
[www.nature.com/news](http://www.nature.com/news)

his signature of agreement, Bartsch insists he did not request authorship but that Strasser included him "in honour of my seniority". On 31 July Bartsch asked *The Lancet* to withdraw his name, as "Strasser had not retracted the article as I had suggested". Bartsch adds that the agency's report "is not a legal document in any case".

Bartsch says that 'honorary authorship' is given on occasion within his department. He was a member of the university ethics committee until 1997 and, in 2001, he headed an ad hoc committee that oversaw the introduction of 'good scientific practice' in the faculty of medicine. Three years later the university's senate approved a ten-point protocol along these lines, including an explicit rejection of honorary authorship.

The loss-of-confidence motion against Sorg, an immunologist, was brought by the all-powerful university council on 7 July, shortly after the preliminary report was circulated to those involved. The council comprises seven 'high-standing representatives' of Austrian society and has the power to dismiss the rector. The council accuses Sorg of a 'serious breach of duty', in particular by exposing the university to 'the danger of serious economic damage'.

But on 28 July, the university senate voted unanimously that the specific concerns put forward by the council were too trivial to warrant dismissal. Sorg has also received a letter of support from top university officials expressing concern about the council's actions. The council will vote on Sorg's dismissal at a

special meeting on 21 August.

Meanwhile, Austria's science academy has put its investigation into whether the urologists had followed good scientific practice on hold. "We had the impression that the request came from Sorg as a person, not a university representative," says Peter Schuster, the academy's president. "When the problem of Sorg's possible impeachment came up, we put the case temporarily on ice."

Sorg, who says that his request was made in an official capacity as a representative of the university, is now under pressure to decide quickly on consequences for Strasser and Bartsch, given that the council may vote to dismiss him within days. As a first step, he asked Strasser to confirm by 18 August that he retracted all relevant papers. Further disciplinary actions are being considered by Sorg and the head of the university's hospital. Sorg has also asked the council to send its report to the public prosecutor.

In the meantime, several of the hundreds of patients who have undergone the procedure by Strasser's team — within and outside of the trial — claim that they have had serious side effects. Injuries such as sealing of the urinary sphincter and rupture of the bladder have been registered with authorities. Thomas Juen, the Innsbruck lawyer who is representing the patients, says: "This is a very grave scandal for the university, and the pressure on the public prosecutor to bring criminal charges will be very high." ■

Alison Abbott

See Editorial, page 917.

## Unproven stem-cell therapy ban

The Bulgarian deputy minister for health has resigned over the country's decision to ban the use of a controversial stem-cell therapy to treat neurological disorders.

The therapy, which since 2005 has been carried out on around 250 patients at St Ivan Rilski Hospital in Sofia, contravenes European Union regulations and is of unproven value, the Bulgarian health ministry ruled on 8 August. Three days later the deputy minister, Matey Mateev, resigned in protest.

The therapy involves harvesting stem cells from a patient's bone marrow, concentrating and purifying them, then injecting them into the same patient's brain or spinal cord. It aims to regenerate nerves and stimulate metabolism after spinal-cord trauma, stroke or neurodegenerative disease, says Venceslav Bussarsky, who heads the hospital's neurosurgery department, and is also president of the Bulgarian Society of Neurosurgery. Each treatment costs €1,000–2,000 (US\$1,500–3,000).

Bussarsky, who claims that companies or individuals with competing financial interests are behind the actions of the health ministry, says that the treatment was successful in nearly half of the patients.

But such stem-cell transplantation is highly controversial. "No scientific evidence has been shown from clinical trials that this treatment would have any positive effect in humans," says Paolo Bianco, a stem-cell researcher at the Sapienza University of Rome.

When Bulgaria joined the European Union in 2007, the country had to comply with the existing European directives on the transplantation of human tissues and cells. The St Ivan therapies contravene these directives, says the health ministry, which is also concerned about the lack of proof that the therapy is effective.

The ministry says that close relatives of Mateev own the two private companies that took part in the St Ivan transplants — in violation of government ethics codes concerning conflicts of interest for leading officials. Mateev's "retirement" is connected to this violation, according to the ministry.

Mateev insists that the directives have been incorrectly translated into the Bulgarian language. "Also the committee did not talk to any of the medical people involved, they only inspected papers," he says. Mateev, a physician, was director at St Ivan from 2002 until 2006. ■

Maria Rossbauer

UCL



UCL: the nerve centre of neuroscience?

Since opening in 2006, the institute has taken an interdisciplinary approach to imaging and modelling neural circuits. The new UCL institute "sounds like Janelia East", says Karel Svoboda, a neuroscientist at Janelia. "That is not necessarily a bad thing," he adds.

Others are concerned that the London institute should distinguish itself from other interdisciplinary centres that are proliferating in this field. "It will be important for the new institute to choose its subject areas carefully to avoid duplication," says Colin Blakemore, a neurobiologist at the University of Oxford.

Svoboda agrees, but says that its central London location and affiliation with a major research university should give a distinctly different character from Janelia Farm. And a Janelia-style centre does not yet exist in Europe, he says. "If organized in the right way, it could really attract fantastic talent."

The institute could be built by 2011. ■

Geoff Brumfiel

# WHATEVER FLOATS YOUR BOAT

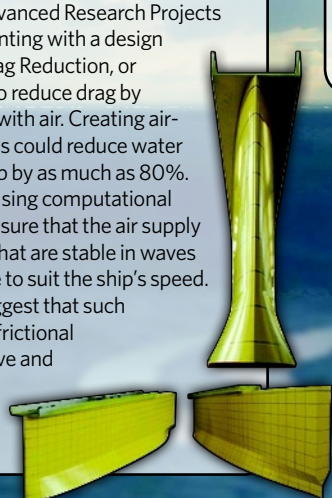
Shipping is one of the most fuel-efficient ways to move freight, but the industry still produces significant greenhouse-gas emissions, including more than a quarter of the world's nitrogen oxides emissions. And it also produces more sulphur dioxide emissions than all land transportation combined. In the latest of our Future Transport series, **Duncan Graham-Rowe** looks at the new wave in shipping.

## DRAG RACING

Reducing drag is likely to be the most effective way of mitigating environmental impact. Ships that slip faster and more easily through the water use less energy and produce fewer emissions.

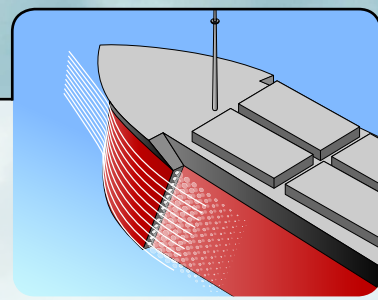
## CAVITY CUSHIONS

The US Defense Advanced Research Projects Agency is experimenting with a design called Air Cavity Drag Reduction, or AIRCAT, that aims to reduce drag by lubricating the ship with air. Creating air-filled cavities on hulls could reduce water contact with the ship by as much as 80%. Hulls are designed using computational fluid dynamics to ensure that the air supply creates air cavities that are stable in waves and vary their shape to suit the ship's speed. Tests on models suggest that such cavities can reduce frictional drag by a factor of five and possibly increase ships' speed by four times.



## MICROBUBBLES

One effort, being explored by Yoshiaki Kodama at Japan's National Maritime Research Institute in Tokyo, is to inject a blanket of tiny bubbles beneath a ship's hull. The idea is to reduce contact between the ship and the water. The bubbles, which are as small as 2 millimetres across, are designed to reduce drag by displacing water at the boundary layer, the centimetre or so closest to the hull where the interaction between ship and water is strongest. As air is 100 times less viscous than water, the bubbles should reduce drag considerably. They are blown out of holes at the bow, and forced along the hull by their own buoyancy; ribs running along



the ship's length prevent the bubbles from slipping sideways.

"We carried out a full-scale experiment earlier this year," says Kodama. A 120-metre-long ship was tested off the coast of Japan and found to achieve a 10% energy saving over a similar journey without the bubbles. However, energy has to be put into creating the bubbles, says Kodama, so the net saving was closer to about 5%.

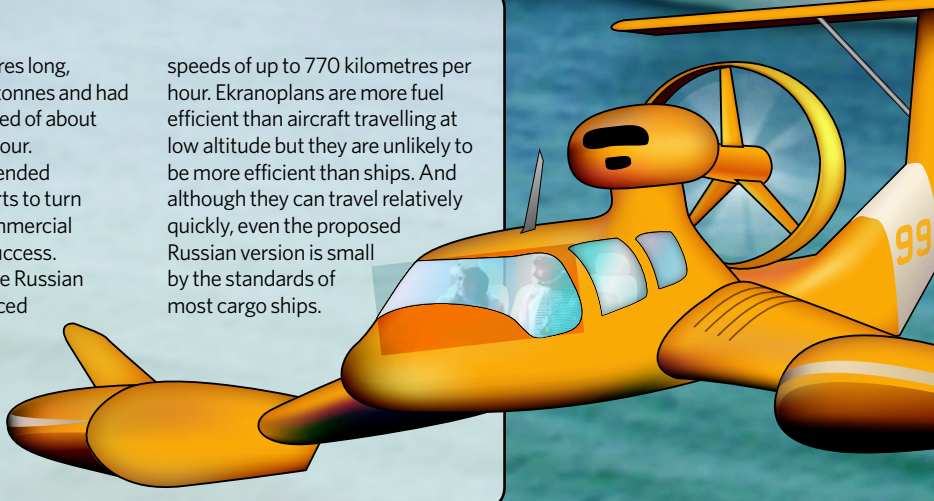
## FLOATING ON AIR

Not touching the water at all would considerably reduce drag. This is the principle of the ekranoplan, an unusual vehicle that can travel on a cushion of air just above the water. Ekranoplans often resemble aircraft, but they do not fly. Instead they use truncated wings to create the cushion of high-pressure air on which the craft moves. Developed in the Soviet Union, the most famous example was the Ekranoplan KM, a huge, fast-moving craft dubbed the Caspian Sea Monster by the US Central Intelligence Agency. Designed for military transportation,

the KM was 100 metres long, weighed nearly 500 tonnes and had a fully loaded top speed of about 400 kilometres per hour.

Since the cold war ended there have been efforts to turn ekranoplans into commercial vehicles, with little success. However, last year the Russian government announced plans to develop a fleet of 2,300-tonne ekranoplans for its navy that could carry 900-tonne payloads and reach

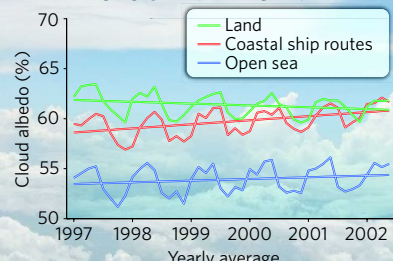
speeds of up to 770 kilometres per hour. Ekranoplans are more fuel efficient than aircraft travelling at low altitude but they are unlikely to be more efficient than ships. And although they can travel relatively quickly, even the proposed Russian version is small by the standards of most cargo ships.



## CLOUD COVER

Not all emissions warm Earth. According to work by remote-sensing specialist Abhay Devasthale and his colleagues at the University of Hamburg, Germany, ships' exhaust fumes are making clouds colder and bigger. The researchers studied six years' worth of satellite data to see how ships in coastal European waters affected cloud formation. Where shipping increased, the reflectivity of clouds increased by 1.5% (see chart). This is due to sulphur dioxide emissions, which form nuclei upon which cloud droplets can form. Devasthale says he is now analysing 20 years of shipping data covering the busier Atlantic, to see the effects there.

### OBSERVED CHANGES IN CLOUD REFLECTIVITY



Source: Devasthale, A. et al. *Geophys. Res. Lett.* **33**, LO2811 (2006).

## THE SHIP OF THINGS TO COME



## KITES

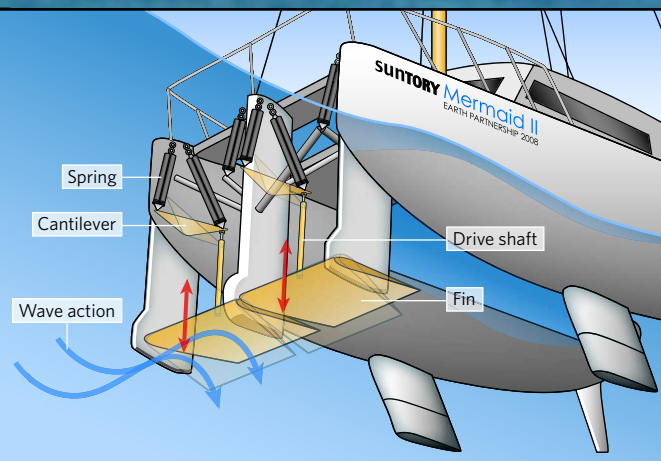
The idea of sticking a sail on a ship may not sound particularly high-tech, but it could be just what the shipping industry needs.

By fixing huge kite-like sails to the bows of ships, SkySails, a company based in Hamburg, Germany, says it can reduce annual fuel costs by up to 35%. The kite-sail is very different from the average spinnaker, and much more effective. For one thing, there are no bothersome masts to deal with. Instead, the wing-shaped sail is designed to fly as much as 300 metres above the ship, connected only by a tether. At such

heights the wind is much stronger and more stable. The sails are self-deploying and computer-controlled, so no sailing knowledge is required of the crew. Since December, SkySails has been testing the technology on two medium-sized cargo ships and found that its 160-square-metre sails can generate 8 tonnes of tractive force, the equivalent of the power produced by an Airbus A318 turbine engine. According to SkySails, under optimum wind conditions the sail has been able to reduce fuel consumption by as much as 50%. Currently there are more than 100,000 cargo ships and cruisers that could be fitted with this technology.

## WAVE POWER

An unusual way to reduce ships' fuel consumption is to make them wave-powered. In July this year, Japanese sailor Ken-Ichi Horie completed a 7,000-kilometre, 110-day voyage from Japan to Hawaii in a wave-powered catamaran. Propulsion was generated by two horizontal fins mounted beneath the bow, at the front of the ship. Incoming waves cause these fins to move up and down, producing dolphin-like kicks of thrust and driving the ship forward at speeds of up to 5 knots (9.25 kilometres per hour).



K. HAN



## BRAINY BIRDS

Smart songbirds have the best tunes — and the most pulling power.

[www.nature.com/news](http://www.nature.com/news)

CORBIS

# Bell Labs bottoms out

It generated six Nobel prizes in as many decades, but after a string of staff departures, physicists claim that the once iconic Bell Laboratories has finally pulled out of basic science.

Just four scientists are left working in Bell's fundamental physics department in Murray Hill, New Jersey, *Nature* has learned. Others have either left or been reassigned to other parts of the company, and a major materials-fabrication facility has been shut down.

"Four people can't be called a basic research group," says Ronen Rapaport, who left the laboratory last summer for a position at the Hebrew University of Jerusalem. "It's a single project."

But officials at Alcatel-Lucent, Bell's parent company, say that reports of the lab's death are greatly exaggerated. Fundamental science remains, but it has moved away from physics, says Gee Rittenhouse, vice-president of research at Bell Labs. "We've shifted the fundamental research over to include mathematics, computer science, networking and wireless," he says.

Founded in 1925, Bell Labs was once considered the world's pre-eminent industrial laboratory for physics (see 'Moving with the times'). Scientists working there regularly won Nobel prizes, including ones for the invention of the transistor and the laser. Much of the early work was funded by the enormous profits of Bell's then parent company, AT&T, which held a monopoly on US telecommunications for more than half a century. But deregulation forced AT&T to split off Bell and other parts of the company into Lucent Technologies in 1996. Lucent struggled to finance its new research arm and the situation rapidly deteriorated after demand for telecommunications equipment collapsed in 2001.

Faced with redundancies and cutbacks, the lab's reputation was dealt a further blow in 2002, when one of its star researchers, Jan Hendrik Schön, was found to have falsified data in more than a dozen papers (see *Nature* 419, 419–421; 2002). Some believed that the lab's fortunes could be reversed by Lucent's merger with French telecom firm Alcatel in 2006 (see *Nature* 440, 1111; 2006). But Alcatel-Lucent has faced six consecutive quarterly losses and its stock value has halved since the merger. On 29 July, Serge Tchuruk, the company's chairman, and Patricia Russo, its chief executive, both announced that they would step down.



The invention of the transistor earned researchers at Bell Labs a Nobel prize.

The latest troubles of the parent company have been mirrored at the lab. Alcatel-Lucent does not provide information about redundancies, but Bell's Murray Hill campus has been "heavily consolidated" since the merger, according to Bettina Tratz-Ryan, a telecoms analyst with Gartner, an IT market-research firm based in Stamford, Connecticut. Staff levels have been cut and some buildings have been sold to property speculators. In February, Bell shut down a top-of-the-line silicon fabrication facility once used by materials scientists. Rittenhouse confirmed that around 20 people were made redundant or reassigned as a result of the shutdown.

Given the grim outlook, many scientists started to look for other work to avoid redundancy, according to Vladimir Aksyuk, a visiting professor at the US National Institute of Standards and Technology in Gaithersburg, Maryland, who left Bell Labs in May. Throughout the turmoil, a small and talented group of roughly 30 physicists remained committed to basic research, but most have now left for more stable jobs. "The company just can't support research anymore," Aksyuk says. "Walk down the halls and there's a bunch of empty rooms."

"Almost everyone has gone away now," agrees Dick Slusher, a former Bell researcher now at the Georgia Institute of Technology in Atlanta. Slusher and others say that just Mike Manfra, Lauren Pfeiffer, Steve Simon and Robert Willett continue to conduct basic physics research at the laboratory.

Rittenhouse does not deny that the lab's focus has changed, but says Bell's research needs to be aligned with the company's needs. Lucent spun-off its semiconductor business in 2002 and its business needs have since moved away from materials science and towards networking, he says. "We've had to adjust our physics group's focus." In addition to quantum computing, he says, Alcatel-Lucent's 850 or so researchers continue to work on high-speed electronics and micromechanical electronic devices. "We can still do good research," he argues.

For physicists such as Rapaport, however, the halcyon days are over. The stock certificates he brought with him from Alcatel-Lucent are so diminished in value that he won't even bother to sell them, he says. Instead, "I can hang them on the wall as a memory of Bell Labs." ■

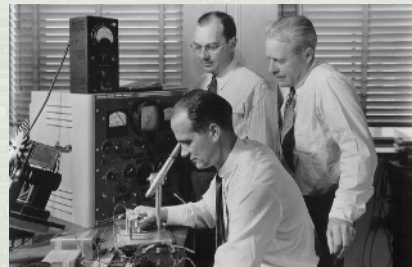
Geoff Brumfiel

## Moving with the times

**1925** Bell Labs founded as a merger between the Western Electric Company and AT&T.

**1927** Clinton Davisson demonstrates electron diffraction.

**1947** John Bardeen, Walter Brattain and William Shockley (below) invent the transistor.



ALCATEL-LUCENT/BELL LABS

**1958** Arthur Schawlow and Charles Townes describe the concept of the laser.



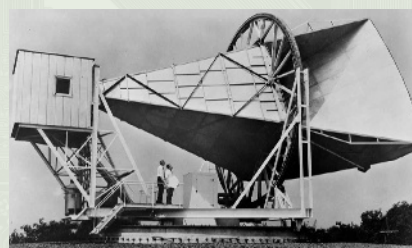
KEystone/GETTY IMAGES

**1962** Bell Labs builds Telstar I (below), the first orbiting communications satellite.



NASA

**1965** Arno Penzias and Bob Wilson identify cosmic background radiation leftover from the Big Bang using the Horn reflector antenna (below) in Holmdel, New Jersey.



**1969** Ken Thompson and Dennis Ritchie develop the UNIX operating system.

**1982** Horst Stormer, Robert Laughlin and Daniel Tsui demonstrate the fractional quantum Hall effect.

**1985** Steven Chu uses lasers to cool and trap atoms.

**1996** Lov Grover develops quantum algorithm for speedy searches of unsorted databases.

# FBI to reveal anthrax data

The US Federal Bureau of Investigation (FBI) plans to publish in peer-reviewed journals much of the scientific evidence it used to pin the 2001 anthrax attacks on microbiologist Bruce Ivins.

Ivins's suicide on 29 July means that the government's case against him will never be heard in court. The trickle of circumstantial evidence released in an investigation that had previously fingered the wrong man has lawmakers, scientists and others clamouring for more information.

In response, the FBI invited scientists and journal editors to a briefing in Washington DC on 18 August to discuss the science of the case and investigators' conclusion that a single man carried out the multiple, deadly mailings of anthrax spores. But FBI officials admit that some mysteries of the case may never be resolved. "I don't think we're ever going to put the suspicions to bed," said Vahid Majidi, assistant director of the division of weapons of mass destruction at the FBI. "There's always going to be a spore on a grassy knoll."

In lieu of expert witnesses and cross-examinations, the FBI plans to offer the evidence for peer review and will keep much of the data quiet until they are published. FBI laboratory director Chris Hassell anticipates a dozen or so papers related to the case, in addition to those that have already been published. However, Hassell says, some details of the investigation will remain confidential, so that potential bioterrorists won't know exactly what they're up against. "It's just what we have to do for national security," he says.

"Given that Ivins cannot stand trial, putting the data through the rigorous process of scientific review may be the best available alternative," says Alan Pearson, director of the biological and chemical weapons control programme at the Center for Arms Control and Non-Proliferation in Washington DC.

However, the scientific data are only part of the puzzle. In court, prosecutors would have outlined all pertinent elements of the investigation, and defence lawyers would have attacked that evidence. "I'd like to see it peer-reviewed by a couple of lawyers," says Abigail Salyers, a microbiologist at the University of Illinois at Urbana-Champaign.



K. LAMBERT/AP PHOTO

Letters laced with anthrax were posted to Congress staff.

DNA sequencing was the key to tracing the mailed spores to a particular mix of anthrax, if not to Ivins himself, FBI officials confirmed at the briefing. Several laboratories were involved in helping to trace the spores.

Paul Keim, a microbial geneticist at Northern Arizona University in Flagstaff, identified the anthrax from the letters as being the Ames strain, one of dozens of known strains of *Bacillus anthracis*. Within the sample were different variants of the Ames strain that characterized a signature mixture, the FBI said. Scientists at the Institute for Genomic Research in Rockville, Maryland, sequenced a dozen genomes from the letters and identified mutations specific to the bacteria used in the attacks.

**"Ivins cannot stand trial, so putting the data through the rigorous process of scientific review may be the best available alternative."**

The FBI selected four insertions and deletions to serve as markers for the attack cocktail. They obtained more than 1,000 samples of Ames bacteria from labs across the world. Of those samples, eight were a match. Those mixtures, the FBI said, were all linked to RMR-1029 — a flask in Ivins's lab. This analysis was completed in early 2007, Hassell said. Narrowing the focus from all individuals with access to RMR-1029 to Ivins was, apparently, a matter of non-scientific techniques.

Questions remain about the quality of the spores in the mailings — which was sufficiently high to allow the investigators to genetically reverse-engineer the spores — and about the possible presence of silica in the spores, which has been described as an attempt to 'weaponize' them by helping them to disperse. The FBI claims that nothing was added to help the spores disperse. ■

**Amber Dance**

**See Editorial, page 917.**

## Leak leaves Antarctic observatory blinded

A robotic observatory atop a plateau in eastern Antarctica has shut down after an exhaust leak caused its generator module to overheat. A Chinese expedition installed the PLATeau Observatory (PLATO) in January at Dome A, the highest point in eastern Antarctica at 4,100 metres altitude (see *Nature* 451, 752; 2008). The observatory had operated continuously for 204 days before the leak. It is hoped that solar power will revive some of PLATO's instruments by the end of August, as spring nears.

PLATO has four 14.5-centimetre telescopes and weather instruments to test conditions at the site, which is one of the coldest and driest places on Earth. The Polar Research Institute of China has plans to return to the site next year to add three 50-centimetre telescopes.

## US ocean agency upgrades its research fleet

The US National Oceanic and Atmospheric Administration (NOAA) has retired the last of its wooden-hulled ships on the same day it commissioned a modern research vessel.

On 13 August, the *John N. Cobb* was retired in Seattle, Washington, after 58 years of service. The ship conducted fishery studies off the coast of Alaska and was reportedly kept running with parts scavenged from nautical museums.

Joining the fleet is the *Okeanos Explorer*, which NOAA purchased from the US navy in 2004. The agency has upgraded the ship, adding two unmanned submersible vehicles, a satellite communications system for conducting experiments remotely and a fresh coat of white paint. The *Okeanos Explorer*

J. BORTNIAK/NOAA



The *John N. Cobb* has been retired after 58 years.

## New species of robin found in Gabon

Ornithologists from the US Smithsonian Institution have identified a tiny fiery breasted robin as a new species.

The olive-backed forest robin (*Stiphrornis pyrrholaemus*) was first found on an expedition to forests in southwest Gabon in 2001, but it was thought to be a juvenile of a known species. The researchers have now confirmed that the robin is a distinct species by comparing its vocalizations and genetic code with those of other specimens in the Smithsonian's collection.

The finding was published last week in the journal *Zootaxa*.



C. WARD

will specialize in mapping and basic exploration of interesting sites. After field testing, the vessel will head to the tropical Pacific.

## Computer experts blast ruling to gag students

Computer scientists in the United States have condemned a court order that blocks three undergraduates from the Massachusetts Institute of Technology in Cambridge from discussing aspects of their research on the security of Boston's transit system.

The Massachusetts Bay Transportation Authority sought the order to prevent the students from giving a talk entitled "Anatomy of a Subway Hack" at a major convention in Las Vegas, Nevada. The talk exposed flaws in the transit system's 'smart cards', which are used for electronic ticketing.

In a letter supporting the students, 11 leading computer scientists warn that such restraining orders "will stifle research efforts and weaken academic computing research programmes".

As *Nature* went to press, a decision on whether to lift or amend the order was pending.

## Plans for the largest ever solar-power plants

A utility company in the California has inked a deal for two massive solar-panel projects.

San Francisco-based Pacific Gas and Electric Company (PG&E) agreed last week to purchase power from two solar-panel manufacturers in the state. OptiSolar, based

in Hayward, will build a 550-megawatt plant, to be accompanied by a 250-megawatt plant from SunPower of San Jose.

To date, photovoltaics have been relegated to relatively small projects, measured in the tens of megawatts. PG&E's 800-megawatt scheme would exceed the largest solar panel project in operation today by a factor of more than 30, and its power capacity could rival that of a mid-sized coal-fired power plant.

The plants are scheduled to be fully operational by 2013, but are contingent on new transmission lines and the extension of federal tax credits for renewable energy.

## Science illustration course draws to an end

An award-winning science illustration programme at the University of California, Santa Cruz, is facing closure.

On 12 August, administrators announced that they would end the programme next spring because of mounting debt in the university's continuing-education system. The 27-year-old science illustration course, one of a handful in the nation to offer graduate training, failed to bring in enough tuition dollars to cover its costs. The announced closure is the latest in a series of cuts.

The university is still looking for alternative ways to finance the illustration curriculum, says Ann Caudle, the course's director. "There is a sliver of a chance we might continue the programme."

### Correction

The News Feature 'The green menace' (*Nature* 452, 148–150; 2008) failed to give the full name and affiliation of Jan Leach, a plant pathologist at Colorado State University in Fort Collins.

# FIRE AND LIFE

Recent eruptions and field expeditions may herald a return to glory for the Son of Krakatau. **Jerry Guo** explores what the 78-year-old island has to offer.

**S**prouting 300 metres above the sea, the cone of Anak Krakatau teases voyagers with anticipation. The volcano spews hot steam from an off-centre crater, as the surf crashes against the lava flows that have cooled around the base. In this contest between water and rock, the rock is winning. As the island gains a foothold in the vast Pacific, it provides scientists with a rare glimpse at how life takes hold in a newborn ecosystem.

Anak Krakatau — ‘child of Krakatau’ in Indonesian — is one of the most striking geological oddities of the modern era: an island that first rose up out of the sea in 1927 and receded and reappeared three times until it established itself permanently above sea level in 1930. It has arisen from the centre of the deep underwater caldera left by the original Krakatau volcano, which blew itself to pieces in 1883 in one of the most powerful and devastating eruptions in recorded history. The explosions and the tsunamis they created killed 36,000 people.

This patch of rock three kilometres square and sandwiched in the strait between Java and Sumatra has earned itself a reputation as a laboratory for observing how life arrives, endures and perishes on an island. In the 1980s and early 1990s, research conducted there on the 170 plant, 40 bird and dozens of bat and insect species, came to define much of what is known about island colonization, ecological disturbance

and community dynamics. Anak Krakatau became the testing ground — and flashpoint — for many textbook principles of island biogeography.

Then interest began to wane. Scientists packed their bags and turned to other hotspots — the Galapagos, Seychelles, another newborn island in Iceland. “The work that was easy was quickly done,” explains Richard Field, an ecologist at the University of Nottingham, UK. Research on Anak went through a ‘quiet phase’. Even volcanic activity eased up.

But a slew of research projects, led by teams from Britain, Germany, Japan and Indonesia, could mark the start of a second age for the island.



Tukirin Partomihardjo evaluates the flora of Anak Krakatau.

“Anak still has a lot to teach us,” says Field. “It’s one of the classic natural experiments.”

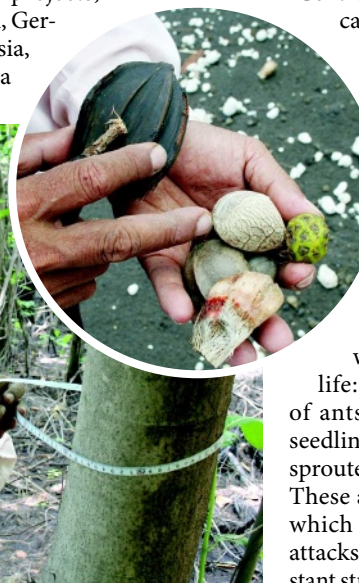
Eruptions throughout November — the most violent in more than a decade — captured the world’s attention with news that Anak was rattling windowpanes in western Java, some 40 kilometres away, and producing 3-kilometre-high ash plumes and spewing showers of lava bombs. The volcano has remained active ever since, with eruptions this January, April, June and July, according to Australia’s Darwin Volcanic Ash Advisory

Centre and Indonesia’s Center of Volcanology and Geological Hazard Mitigation. It is during a lull between eruptions that Tukirin Partomihardjo, a wiry botanist wearing a neatly pressed white-collared dress shirt and sporting a machete, wades onto the black-sand beach at Anak. The 56-year-old ‘King of Krakatau’ has arrived.

It’s hard to take a step on Anak without crushing some sort of life: blue-ish ghost crabs, armies of ants, fast-multiplying casuarina seedlings and even a coconut that has sprouted an impressive-looking stem. These are some of Anak’s colonizers, which every day continue to launch attacks on the island. “There is a constant struggle here,” says Partomihardjo, who works for Indonesia’s Bogor

T. PFEIFFER/WWW.VOLCANODISCOVERY.COM

J. GUO



Herbarium, referring to these pioneering species' battle with the elements.

Much of what biologists can say about the fate of such species came from data on Anak. The textbook case-study of this 'species succession' began just 9 months after the final 1930 eruption, when a single spider was found clinging to a rock. Fungi and other microbes soon followed and, in a decade, the lower slopes began to be covered with a grassland savannah that was dominated by sugarcane. Life brought more life. At some point, seed dispersal by animals — land crabs, monitor lizards and countless species of birds — outpaced that by sea. The emerging mixed forest, with its nooks and perches, attracted more birds and ultimately bats, explains Field. Wind-dispersed species, such as orchids, then moved farther inland. The rest is history. "Anak played a big part in helping people understand colonizing processes," says Field.

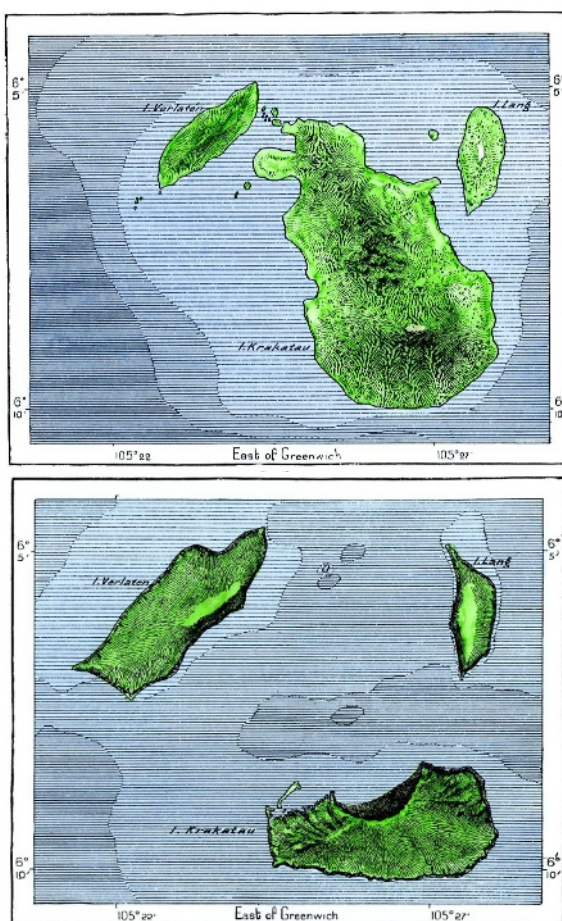
In the early 1990s, Partomihardjo showed that banks of seeds that had been buried by ash or by crabs on the shore for as long as six decades could contribute to the first waves of life on a barren landscape<sup>1</sup>. Now, one of his ongoing projects is to examine the diversity of the beach seed bank. In just one day, he finds some 30 species of seed of varying descriptions: green cactus-like, flat and pea-shaped, walnut-shaped. Blown or having floated in from the nearby 'stepping stone' islands as well as from Java and Sumatra, these specimens litter the beach. Not all will survive. Partomihardjo holds up a dark, oblong mangrove seed and shakes his head. "This can't survive here." The rocky, wave-dashed coast is just too inhospitable for the plant to take root and thrive.

### Death and rebirth

Heading into a modest jungle on the eastern side of the island, Partomihardjo walks through a panoply of dominant casuarinas, waist-high grasses, ferns and 30-metre-high fig trees. It's hard to imagine that this was all under water a mere 78 years ago. The forest has bald spots, though, where recent lava flows have wiped out the newly emergent vegetation. "What's unusual is that the island keeps getting disturbed by volcanic activity," says Field. These eruptions can reset the clock on the succession process, yielding valuable data on ecological disturbance and recovery. But the eruptions also make continuous monitoring difficult, if not life-threatening. One of Partomihardjo's colleagues died on the island during a monitoring expedition in the 1990s.

Last September, a team of 11 field biologists, led by Partomihardjo and Field, erected a network of 21 monitoring plots on Anak. They tagged and mapped every tree within the 20 × 20 metre plots to gather long-term data on the forest's health and succession dynamics. The eruptions have wreaked havoc on many parts of the island. "Many trees have died," he says, blaming the ash that has covered much of the forest. "But this place will recover."

consortium of Japanese research groups led by Kagoshima University completed a three-year study of insect communities on Anak, including wasps, bees, ants, termites and gall-gnawing arthropods. The team found 16 species of wasp and 18 species of ant that had not previously been documented on the island, and hopes to publish its findings soon. "Anak is still very interesting for us," says Suzuki Eizi. "We need to monitor it for a long period."



Maps of Krakatau before (top) and after (bottom) its 1883 eruption show how volcanic activity reshaped the landscape. Anak Krakatau rose in the centre of three islands that remained.

Partomihardjo is the world's leading expert on the Krakatau islands. He first visited them in 1981 during a training seminar, and has been back some 30 times since, leading almost all foreign research expeditions there. "He has spent longer working on Anak than any other biologist living or dead and knows it more intimately than anyone else," says Robert Whittaker, an ecologist at the University of Oxford, UK, who is himself an authority on the islands.

Research at Anak has been pushing ahead on numerous fronts. This March, a

### Step by step

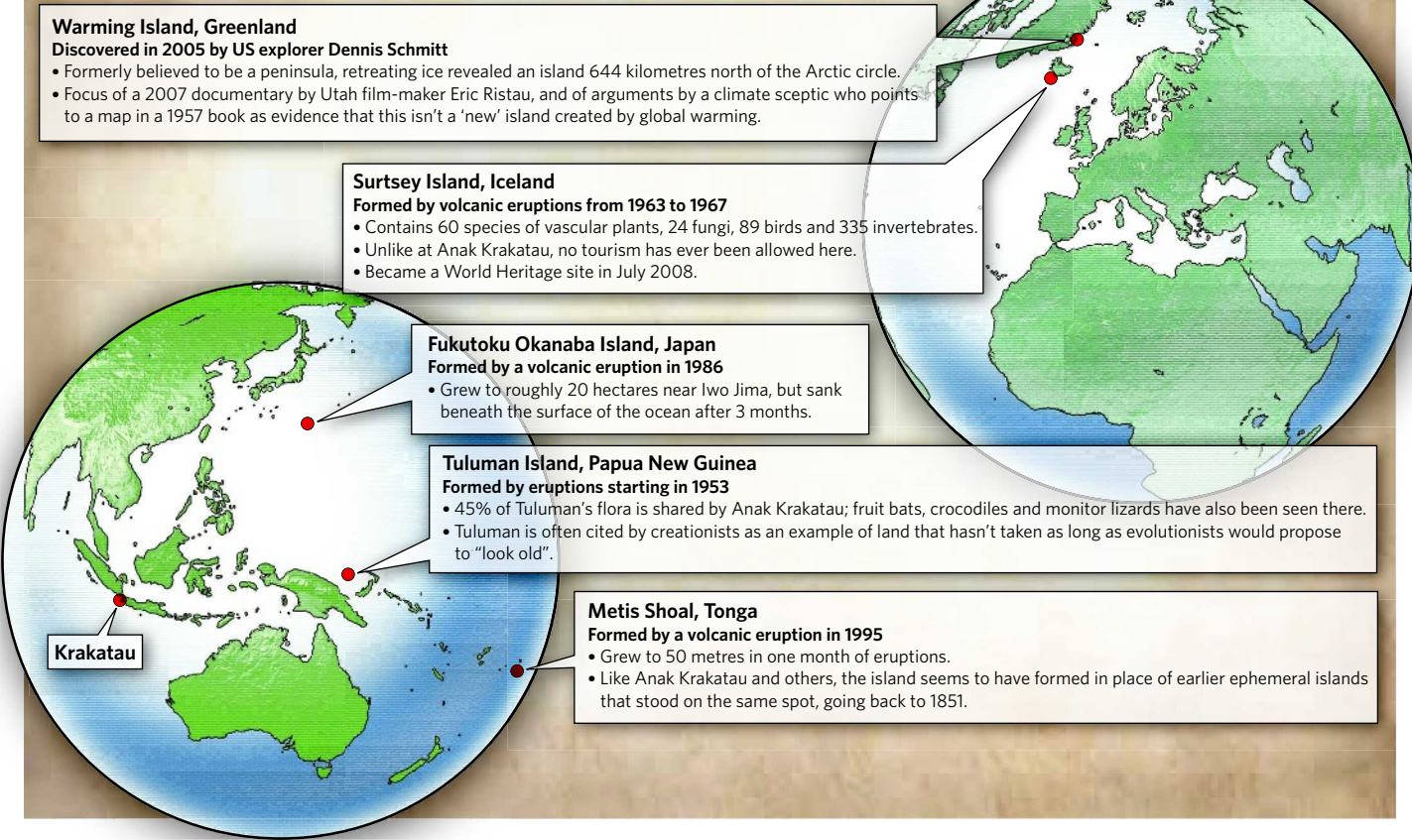
Field's team also started surveying trees, birds and ants last year, and have several papers in preparation. One important finding, for instance, is that colonization and extinction, at least in plants and birds, could be less random than previously thought. In 1967, Robert MacArthur and E. O. Wilson cited the randomness of bird colonization on Krakatau as a prime example for their classic theory of island biogeography — that species diversity grows along a smooth curve to ultimately reach equilibrium. Research conducted by Whittaker on Krakatau in the 1990s — and picking up again now — suggests that the equilibrium model may be too simplistic. "Overall, a complex picture of ecosystem assembly is emerging from the Krakatau islands, one that suggests that island colonization is essentially a special case of succession," explains Field, who subscribes to the emerging school of thought that island biogeography is in part a deterministic process<sup>2</sup>. Take Anak's fig trees. Each species depends on specific birds, bats and wasps for seed dispersal and reproduction. "You can't get figs without the wasps and you can't get the wasps without the figs. Our results don't fit with the MacArthur-Wilson idea that both colonization and extinction are equally likely for any species," says Field.

Furthermore, later research showed that colonization seemed not to follow another commonly accepted theory that terrestrial life comes from nearby 'stepping stone' islands, perhaps because the environments were so different. One study<sup>3</sup> revealed that Old World fruit bats can retain viable seeds in their guts long enough to transport them hundreds of kilometres, skipping over small nearby islands in the process.

Geologists, too, have been showing an interest in Anak's activity. In 2005, German and Indonesian volcanologists rigged the island with three remote monitoring stations. They hope to use sophisticated neural network programs<sup>4</sup> to analyse the dizzying array of

# Island uprising

New islands have popped up all over the globe. They are a centre for study, and sometimes controversy.



data — meteorological, chemical, seismic — recorded by the stations to predict future eruptions. The raw numbers are also broadcast online in real-time, including a video feed.

## Rewriting history

Meanwhile, Ken Wohletz, a volcanologist from Los Alamos National Laboratory in New Mexico, wants to restart a controversial project that claimed to have found a possible mega-eruption in Krakatau's past. He cites evidence from tree rings in Europe, ice cores in Greenland and ash deposits from the Sundra Straits that suggest a massive eruption in AD 535 — 20 times bigger than the 1883 event — precipitated the Dark Ages through "climate stabilization lasting years or perhaps decades". He theorizes that the AD 535 eruption could have dramatically altered the climate, affecting crops and the spread of disease, and triggering the collapse of several civilizations in Indonesia, South America and Persia, but concedes that the supporting data, for the moment, are sketchy. "It will be hard to find more evidence to date such an eruption," Wohletz says.

For one, his radiocarbon datings yielded a wide-open time window: from 6600 BC to AD 1215; critics also point to the Byzantine Empire, which went through a Golden Age during this time, as a counterexample of a global doomsday. "It will take years and years

to put together the full story," he says.

Such attention is a testament of the singular importance of the Krakatau islands to the scientific community, given that 'new islands' appear (and disappear) with some regularity. Since Anak Krakatau achieved permanent status in 1930, several new additions have been made to this geological family (see 'Island uprising'). The only new island to receive anywhere close to Anak's scientific scrutiny has been Surtsey, off the coast of Iceland, a volcano strikingly similar in shape, size and geology to Anak. Despite its inaccessible location, Surtsey has a leg up on Anak in one crucial aspect: it has an 18-year-old continuous data record based on 25 permanent plots, with monitoring trips every July. "The colonization on Anak has not been followed as frequently as here," says Borghor Magnusson, a plant ecologist from the Icelandic Institute of Natural History in Reykjavik and leader of biological research on the island.

Although colonization of Surtsey has followed the classic path taken by Anak in many respects, Icelandic biologists have, in the past two decades, picked up on a distinct difference: the importance of birds to the island's health and growth. "The gull colony [some 200 breeding pairs] has a big impact," says Magnusson, citing its role in seed transport, soil fertilization and habitat creation. "We're

still experiencing this phase of colonization."

Back at Anak, the Sun is about to set. Partomihardjo eyes the summit indecisively — a longstanding government directive warns people against going near the active cone. "Why not," he resolves. "Let's go."

As he climbs nimbly towards the top, he recounts one particularly close call back in the 1990s, when he got caught during an eruption. "Big stones were falling all around me," he says. Then he pauses and points to an old monitoring station nearby that was crushed by lava bombs the size of basketballs. "I thought I was going to die."

At dusk, he almost reaches the crater ridge (which he claims has grown 100 metres since his visit last October). But without a gas mask, he decides to turn back. Never mind the scorching ground. Still, even in this desolate landscape, with its crags and loose soil, he notices a rousing sight on the way down: a single pioneering shrub clinging bravely to life, its purple flowers in full bloom.

**Jerry Guo** is a freelance writer in New Haven, Connecticut, reporting from Indonesia.

1. Whittaker, R. J. *et al. Biotropica* **27**, 346–354 (1995).
2. Ward, S. A. & Thornton, I. W. B. *Glob. Ecol. Biogeogr.* **9**, 7–18 (2000).
3. Shilton, L. A., Altringham, J. D., Compton, S. G. & Whittaker, R. J. *Proc. R. Soc. B* **266**, 219–223 (1999).
4. Ibs-von Seht, M. & Kniess, R. *Geophys. Res. Abs.* **9**, 03440 (2007).

# THE GREAT SQUID HUNT

When jumbo Humboldt squid disappeared from Chilean waters, it led to the demise of a world-class electrophysiology laboratory. Now the creatures are back, finds **Tony Scully**, and so are the scientists.

It was three years ago that electrophysiologist Francisco Bezanilla heard that the squid were back. That summer he had already travelled from the University of California, Los Angeles, to the Woods Hole Marine Laboratory, Massachusetts, in pursuit of the creatures. Like other researchers, he spent two months there each year when the Atlantic or longfin inshore squid, *Loligo pealeii*, bred in local waters. He found their giant nerve cells the best biological preparation for studying the electrical signals that cross the cell membrane. But he still struggled to isolate the weak signal generated by the flow of potassium ions.

So when Bezanilla heard what fellow Chilean Miguel Holmgren had to say, his ears pricked up. Holmgren, a neuroscientist at the National Institutes of Health (NIH) in Bethesda, Maryland, had word from family back home that the jumbo Humboldt squid, *Dosidicus gigas*, were in plentiful supply at fish markets throughout Chile. Memories from more than 40 years ago came flooding back to Bezanilla: of his old mentor, Mario Luxoro; of the bustling Laboratory of Cell Physiology in Montemar, Chile, that lured scientists from all over the world; and of long summer days spent hunched over the squid's spaghetti-like nerve axons. Bezanilla and other researchers had been forced to leave Montemar when the Humboldt squid mysteriously disappeared from local waters in 1970. Bezanilla thought that the squid's return might allow him to resurrect the old laboratory, and that the squid's giant axons — on average twice the diameter of its Atlantic cousin and loaded with many more ion pumps — might generate the stronger potassium signal he sought.

In January this year, Bezanilla and Holmgren travelled to the small seaside town of Montemar. They found the old laboratory succumbing to the ravages of time: cracks ran through the walls and a layer of grime covered every



A chance to experiment on the axons of the Humboldt squid drew electrophysiologists to Chile.

surface. "It was so sad to see my old laboratory in this state," says Bezanilla, who now works at the University of Chicago, Illinois. "The place looked awful." The two men scrubbed down the benches and unpacked their equipment. They paid local fisherman to take a trip out in search of the squid. In anticipation, they rigged up their electronics, ready to dissect the Humboldt's axons and, in doing so, continue a quest to understand a neuron's electrical properties that began over a century ago.

## Nervous steps

In 1902, German physiologist Julius Bernstein was the first to measure the minute electrical charges on nerve axons. He proposed that the cell membrane somehow blocks the movement of ions and maintains a difference in voltage so that the inside of axons is negative relative to the outside. That changes when a signal propagates along the nerve. The

barrier opens, negatively charged potassium ions leak out and an 'action potential' — a wave of voltage he estimated to be 70 millivolts — whips along the length of the nerve. But at that time Bernstein was unable to directly measure the amplitude of the action potential because the frog nerves he was experimenting with were too small to allow him to insert an electrode inside the cell.

Researchers took to experimenting on the cells of marine life such as the common shore crab and algae. Both were in plentiful supply and considerably easier to handle than frogs — plus working with crabs provided an excellent working lunch during long days in the lab. Electrophysiologists attached themselves to marine laboratories, of which, by the 1930s, the two most prominent were at Woods Hole and Plymouth, UK. Kenneth Cole from Columbia University, New York, for example, would spend the summer at Woods Hole

experimenting with the large excitable cells of the sea algae *Nitella*.

It was British zoologist John Zachary Young who first proposed experimenting on *L. pealeii*. Squid are the one of the fastest swimmers in the ocean: giant axons that run the length of the body trigger muscular pulses that propel the creature forward. Young urged Cole to take advantage of these axons, which are up to 1 millimetre in diameter, 50 times the thickness of axons found in the common shore crab and 1,000 times that of human axons. Cole found that he could thread a wire electrode right into the cell without disrupting the electrical signal propagating down the axon. Using this 'voltage clamp' technique, with electrodes both inside and outside the cell, it was possible to measure the current as ions move across the membrane during a nerve impulse.

### Giant bandwagon

Others were quick to catch on. In 1938, Alan Hodgkin visited the lab in Woods Hole "because some scientists have been getting the most exciting results on the giant nerve fibres of the squid", he wrote at the time. "Cole has been getting results which make everyone else's look silly."

The Second World War interrupted work, but soon after it ended Hodgkin and his long-time collaborator Andrew Huxley sought a local supply of *L. pealeii* in Plymouth. There were a few barren years before fisherman finally delivered a major catch in 1949. In the late summer months they made discoveries using these axons that would overturn Bernstein's cellular membrane theory. Hodgkin and Huxley showed that during an action potential the voltage across the cell membrane changed by 110 millivolts (ranging from  $-70$  to  $+40$ ), not the 70 millivolts Bernstein had predicted, and that ions do not simply equilibrate across the membrane. The movement of ions is controlled by selective pores, or gates, and during an action potential the positive sodium ions rush inside the cell followed almost immediately by an outpouring of potassium ions. Hodgkin and Huxley shared the 1963 Nobel prize in Physiology or Medicine with Australian John Eccles for discovering how nerve signals travel. Hodgkin later joked that their prize should have gone to the squid.

*L. pealeii* was big, but for some it wasn't big enough. At the Massachusetts Institute of Technology in Cambridge, Francis Otto Schmitt wanted to identify the components of axoplasm, the fluid inside nerve



Humboldt squid axons can be the size of spaghetti.

cells. It could be squeezed out of the giant squid axon as simply as toothpaste from a tube — but even then it was problematic because the squid rarely grows longer than a metre and its axon is highly branched.

In a 1955 interview with the *New York Times*, Schmitt also bemoaned the limited supply: only 300 squid per week for the annual two month breeding season. As luck would have it, multimillionaire and champion sports-fisherman Lou Marron happened to read that report. As is the wont of fishermen, he knew of a catch twice as big. He wrote to Schmitt about a species of squid he had used to bait swordfish on expeditions in the Pacific Ocean off the coast of north Chile. He offered to take him there to prove it.

Two years later, the pair set off for Chile with a small team including Schmitt's Chilean PhD student, Mario Luxoro. "I told Schmitt we had huge squid in Chile," Luxoro says, but

**"When we had squid we would work from eight in the morning till two in the morning."**

— Mario Luxoro

Schmitt had been sceptical of their existence. "He thought I was just an exaggerating South American." Still, the prospect of a bountiful supply of squid during the winter months in Massachusetts was appealing to Schmitt. And Luxoro felt vindicated when the team landed the jumbo squid now known to be the Humboldt. Named after the Humboldt ocean current that runs the length of South America, this squid grows up to two metres in length, making it one of the largest squid species in the world and twice the size of their Atlantic cousins that had been the mainstay of electrophysiologists.

The University of Chile in Santiago ran a marine-biology laboratory in Montemar and Schmitt leased a small room there before returning to Massachusetts. Luxoro remained behind, hired by Schmitt to organize the dissection, preparation and packaging of the squid axons for transport to the United States. The proteins inside degrade quickly, so the preparations of squid axoplasm were packaged into boxes with dry-ice for transport back to the United States by air. Even so, few of the packages arrived in a suitable condition for analysis. Both men were unhappy with the arrangement. The lab "was only a factory for axoplasm", recalls Luxoro, who was frustrated at spending December to February packing squid. "They were not interested in us doing pure research."

### Birth of a lab

Luxoro felt that it was time for Chileans to do their own experiments on the valuable asset swimming nearby. With other Chilean researchers, he persuaded the chancellor of the University of Chile to buy a separate house for scientists wishing to study electrophysiology. They were given a former brothel that had a water supply in every room. In 1962, the Laboratory of Cell Physiology was born.

By now, scientists were trying to understand how different channels mediate ion transport across the axon membrane.

The team grew to a dozen or so scientists and went on to compete with laboratories around the world. With little money and relatively crude equipment, the researchers could nevertheless ask sophisticated questions because they had an abundance of the best experimental material: the large surface area of the giant axons generated electrical signals strong enough to measure accurately. Luxoro and his student Eduardo Rojas, for example, were the first to provide experimental evidence that proteins within the lipid membrane, rather than the lipid



molecules themselves, actively transport ions across the membrane<sup>1</sup>. It was also in Montemar that Rojas and Clay Armstrong demonstrated that movement of sodium and potassium ions during an action potential occurs via different membrane channels<sup>2</sup> rather than a single protein, as some had argued. The new laboratory, loosely led by Luxoro, enjoyed much independence. "It was a great time, when we had squid we would work from eight in the morning till two in the morning," he says.

Electrophysiologists flocked to Montemar during the Southern Hemisphere summer. "I loved it there," says Armstrong, a physiologist recently retired from the University of Pennsylvania, Philadelphia. "They were ingenious at setting up experiments using old parts. It was great fun to watch." During this time, a young and impressionable Bezanilla began to dissect the squid and later complete a PhD.

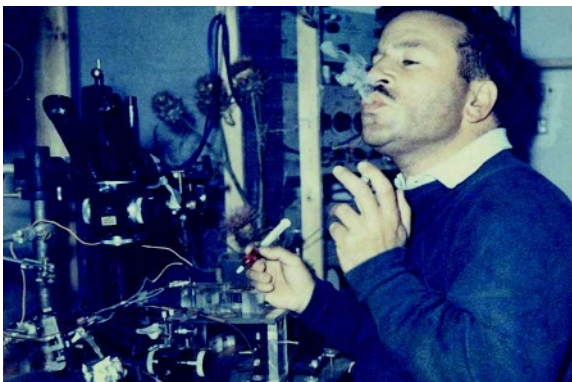
Then, in the summer of 1970, the fishermen returned empty handed day after day. Just over a decade after Schmitt and Luxoro made their expedition to Chile, the Humboldt squid migrated out of range of local fishermen, and beyond the reach of scientists in Montemar. The squid probably followed small fish, krill and other prey, which are sensitive to environmental events such as El Niño.

### Gradual decline

It was the beginning of the end for Montemar as an international research station. Many left to fill posts elsewhere: Bezanilla was offered a postdoc at the NIH. The dictatorship of Augusto Pinochet from 1973 further deprived Chilean science of investment. "It was a horrible time," says Luxoro, who remained in Montemar, using barnacles (*Megabalanus psittacus*) to study muscle physiology. "A lot of people went away and science practically disappeared."

By the end of the 1970s, the invention of the 'patch-clamp' method by Bert Sakmann and Erwin Neher had removed much of the need for large axons. The technique involves pressing a glass tube one thousandth of a millimetre in diameter against the cell membrane, isolating a small patch from the surrounding extracellular fluid. An ultrasensitive amplifier can be used to measure the flow of ions across the membrane. In 1990, Luxoro reluctantly accepted a teaching position at the main campus in Santiago and the laboratory was abandoned.

But for some purposes, squid remains irreplaceable. David Gadsby, a membrane physiologist at Rockefeller University in New York,



Mario Luxoro in the Montemar lab, 1960 (top); Francisco Bezanilla in 2008 (below); and the lab's seaside location, 1960s (bottom).



works alongside Bezanilla and Holmgren at Woods Hole every summer to study the action of ion channels in the North Atlantic squid. "We now have three-dimensional static images of the protein pumps and ion channels, but to understand how the conformation of these proteins change in response to varying voltages we need to use the squid," says Gadsby. Much has been learned about how a sodium-potassium pump actively transports sodium ions across the membrane to maintain the resting potential, but the movement of potassium ions is harder to measure. Bezanilla and Holmgren want to study the conformational changes in the pump as potassium ions are transported, and hoped that this would be clearer from variations in the Humboldt axon's strong potassium signal.

It was for this reason, and a wish to revive his old laboratory, that Bezanilla returned early this year to Montemar with Holmgren and paid the fishermen to bring in a catch. "We normally pay US\$1,700 for a delivery in Woods Hole but here we only had to pay \$100," says Holmgren. Their trip and the investment were rewarded: to their great relief the first consignment of squid in nearly four decades arrived at the laboratory.

In their first experiments, the scientists tried to wash away the sodium ions in order

to measure the weaker potassium ion signal alone. "We found that the signal-to-noise-ratio of the ion is improved by a factor of five or six with the Humboldt squid compared with the squid we normally use," says Holmgren. One explanation may be that the thicker membrane contains a higher concentration of ion channels and pumps per unit area.

### Rebuilding the dream

After spending two weeks working at the laboratory, the scientists returned to the United States bolstered by their preliminary results — and determined to return. They are now applying for funding to go back to Montemar in December. Meanwhile, Ramón Latorre, a neuroscientist who also began his career in Montemar and is now with the University of Valparaíso, is in negotiations with the University of Chile to renovate the lab for visiting scientists. Latorre is applying for a half-million-dollar grant from the local government, which would fit out a conference room and three laboratories.

Gadsby hopes to make his first trip to Montemar later this year. Humboldt squid are now found as far north as California, but the return of the squid to the waters near Montemar has a special significance for electrophysiologists. "I've seen old photographs of the lab

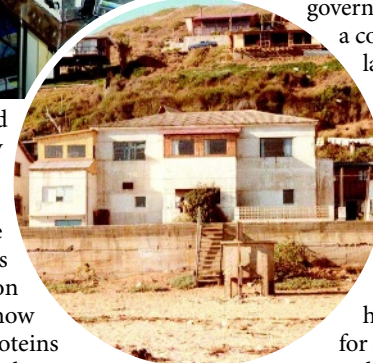
and I can't wait to see it for real," Gadsby says. Whether the squid will be there to greet them, though, is beyond the scientists' control. "We're dependent on the migratory patterns of the squid," Gadsby says. The researchers are well aware that the creatures could vanish as mysteriously as they appeared — taking with them the hopes for their experiments and the lab's revival.

As long as the creatures stick around, Bezanilla is hopeful that the lab will return to its glory days as an international research hub. "It was a great feeling to see the place come alive again," he says. "I hope that in the future people will realize the importance of this laboratory, and that the Humboldt squid will once again attract researchers back to Chile's shore." ■

**Tony Scully has just finished an internship in Nature's Munich office.**

I. LATWATER

M. HOLMGREN



1. Rojas, E. & Luxoro, M. *Nature* **199**, 78-79 (1963).
2. Armstrong, C. M., Bezanilla, F. & Rojas, E. *J. Gen. Physiol.* **62**, 375-391 (1973).

# CORRESPONDENCE

## IVF: stars may have to consider the risk of stolen parenthood

SIR — Your Editorial 'Life after SuperBabe' (*Nature* **454**, 253; 2008) and Special Report 'Making babies: the next 30 years' (*Nature* **454**, 260–262; 2008) summarize the far-reaching social and ethical implications that arise from progress in *in vitro* fertilization (IVF) and stem-cell research. One aspect that has so far received scant attention is likely to have a substantial impact on both legal practice and everyday behaviour, at least for the rich and famous.

Scientific progress should eventually enable us to derive both sperm and egg from differentiated cells, using a combination of induced pluripotency (iPS) and directed differentiation (see 'New sources of sex cells' *Nature* **452**, 913; 2008). Before too long, it may be possible to collect a few hundred skin cells secretly from a used towel, a toothbrush or even an empty glass of water, then reprogram and differentiate these cells into sperm or egg. IVF could then be used to produce a child whose genetic parents are the involuntary tissue donors.

Such 'stolen' parenthood might be viewed as a dubious and expensive practical joke, if a child were to be conceived whose genetic parents were, say, Nicolas Sarkozy and Angela Merkel, derived from laundry at a G8 summit. But the widespread use of genetic evidence in paternity suits could provide a serious financial incentive for a woman to bear an iPS-derived IVF child whose genetic parents are herself and, say, Paul McCartney or Mick Jagger, presenting a lucrative opportunity to sue the genetic father for support for his 'illegitimate' child. And even if such financial incentives were to be removed through changes in legal practice, the problem of stolen parenthood is likely to



persist, given the significance that many people assign to kinship with famous people.

Two societal reactions might follow. First, abuse of human biological material in a wide sense is likely to become a statutory offence, generalizing the prohibition of secret genetic testing that has already been enacted in many countries. Second, persons who perceive themselves as potential victims of stolen parenthood might sterilize whatever waste they dispose of, unless of course they see their status soaring by allowing their parenthood to be stolen by as many groupies as possible.

**Christoph Bock** Department of Computational Biology, Max-Planck-Institut für Informatik, 66123 Saarbrücken, Germany  
e-mail: cbock@mpi-inf.mpg.de

## IVF: tight regulation may not be suitable for all cultures

SIR — In her Essay '30 years: from IVF to stem cells' (*Nature* **454**, 280–281; 2008), Ruth Deech reminds us of the role that the Human Fertilisation and Embryology Authority

(HFEA) has played through regulation in guiding the practice and scientific investigation of assisted-reproduction technology in the United Kingdom. But I disagree with her opinion that assisted reproduction in the United States is "nearly an unregulated black market". The medical aspects of assisted reproduction are in fact regulated extensively.

It is true that individuals and their physicians in the United States have the freedom to make decisions regarding who can reproduce and under what circumstances without the type of regulation provided by the HFEA. But it is against federal law to perform an *in vitro* fertilization (IVF) cycle without reporting that cycle and its results to the federal government; federal regulations require registration of clinics and extensive screening of potential gamete donors; all drugs and devices must be approved by the federal government; and health-care providers must be licensed by state governments.

In addition to complying with codified regulations, more than 90% of IVF clinics in the United States subscribe to unannounced on-site inspections and adhere voluntarily to guidelines developed jointly by the American

Society for Reproductive Medicine and the Society for Assisted Reproductive Technology. Publications in the scientific literature attest to the positive impact of these guidelines on patient outcomes.

The HFEA has had an important impact on assisted-reproduction technology and is an excellent example of extensive regulation. We cannot guess whether this degree of regulation in other countries would either be necessary or have comparable impact. Regulation can assume different forms, each dependent on individual cultures.

**David Adamson** American Society for Reproductive Medicine, and Fertility Physicians of Northern California, 540 University Avenue, Suite 200, Palo Alto, California 94301, USA  
e-mail: enicoll@asrm-dc.org

## A possible way out of the impact-factor game

SIR — Your Editorial 'Unbalanced portfolio' (*Nature* **453**, 1144; 2008) defends the scientific autonomy of researchers against pressure from bureaucrats seeking maximum economic returns. Although this position is admirable and likely to be popular among researchers, it might also be worth reflecting on our current situation.

Few scientists nowadays can afford to pursue research for science's sake, as suggested in the Editorial. Rather, most of us are trapped in a game of numbers, in which all our research output can be reduced to one or more of the following metrics: impact factors, average citations per article, total number of articles published, and the h-index.

This reductionist attitude towards scientific research has fostered an unhealthy research environment, evident in the copious examples of 'salami slicing' that litter scientific journals. Furthermore, the rules and significance of the game are

# CORRESPONDENCE

## IVF: stars may have to consider the risk of stolen parenthood

SIR — Your Editorial 'Life after SuperBabe' (*Nature* **454**, 253; 2008) and Special Report 'Making babies: the next 30 years' (*Nature* **454**, 260–262; 2008) summarize the far-reaching social and ethical implications that arise from progress in *in vitro* fertilization (IVF) and stem-cell research. One aspect that has so far received scant attention is likely to have a substantial impact on both legal practice and everyday behaviour, at least for the rich and famous.

Scientific progress should eventually enable us to derive both sperm and egg from differentiated cells, using a combination of induced pluripotency (iPS) and directed differentiation (see 'New sources of sex cells' *Nature* **452**, 913; 2008). Before too long, it may be possible to collect a few hundred skin cells secretly from a used towel, a toothbrush or even an empty glass of water, then reprogram and differentiate these cells into sperm or egg. IVF could then be used to produce a child whose genetic parents are the involuntary tissue donors.

Such 'stolen' parenthood might be viewed as a dubious and expensive practical joke, if a child were to be conceived whose genetic parents were, say, Nicolas Sarkozy and Angela Merkel, derived from laundry at a G8 summit. But the widespread use of genetic evidence in paternity suits could provide a serious financial incentive for a woman to bear an iPS-derived IVF child whose genetic parents are herself and, say, Paul McCartney or Mick Jagger, presenting a lucrative opportunity to sue the genetic father for support for his 'illegitimate' child. And even if such financial incentives were to be removed through changes in legal practice, the problem of stolen parenthood is likely to



persist, given the significance that many people assign to kinship with famous people.

Two societal reactions might follow. First, abuse of human biological material in a wide sense is likely to become a statutory offence, generalizing the prohibition of secret genetic testing that has already been enacted in many countries. Second, persons who perceive themselves as potential victims of stolen parenthood might sterilize whatever waste they dispose of, unless of course they see their status soaring by allowing their parenthood to be stolen by as many groupies as possible.

**Christoph Bock** Department of Computational Biology, Max-Planck-Institut für Informatik, 66123 Saarbrücken, Germany  
e-mail: cbock@mpi-inf.mpg.de

## IVF: tight regulation may not be suitable for all cultures

SIR — In her Essay '30 years: from IVF to stem cells' (*Nature* **454**, 280–281; 2008), Ruth Deech reminds us of the role that the Human Fertilisation and Embryology Authority

(HFEA) has played through regulation in guiding the practice and scientific investigation of assisted-reproduction technology in the United Kingdom. But I disagree with her opinion that assisted reproduction in the United States is "nearly an unregulated black market". The medical aspects of assisted reproduction are in fact regulated extensively.

It is true that individuals and their physicians in the United States have the freedom to make decisions regarding who can reproduce and under what circumstances without the type of regulation provided by the HFEA. But it is against federal law to perform an *in vitro* fertilization (IVF) cycle without reporting that cycle and its results to the federal government; federal regulations require registration of clinics and extensive screening of potential gamete donors; all drugs and devices must be approved by the federal government; and health-care providers must be licensed by state governments.

In addition to complying with codified regulations, more than 90% of IVF clinics in the United States subscribe to unannounced on-site inspections and adhere voluntarily to guidelines developed jointly by the American

Society for Reproductive Medicine and the Society for Assisted Reproductive Technology. Publications in the scientific literature attest to the positive impact of these guidelines on patient outcomes.

The HFEA has had an important impact on assisted-reproduction technology and is an excellent example of extensive regulation. We cannot guess whether this degree of regulation in other countries would either be necessary or have comparable impact. Regulation can assume different forms, each dependent on individual cultures.

**David Adamson** American Society for Reproductive Medicine, and Fertility Physicians of Northern California, 540 University Avenue, Suite 200, Palo Alto, California 94301, USA  
e-mail: enicoll@asrm-dc.org

## A possible way out of the impact-factor game

SIR — Your Editorial 'Unbalanced portfolio' (*Nature* **453**, 1144; 2008) defends the scientific autonomy of researchers against pressure from bureaucrats seeking maximum economic returns. Although this position is admirable and likely to be popular among researchers, it might also be worth reflecting on our current situation.

Few scientists nowadays can afford to pursue research for science's sake, as suggested in the Editorial. Rather, most of us are trapped in a game of numbers, in which all our research output can be reduced to one or more of the following metrics: impact factors, average citations per article, total number of articles published, and the h-index.

This reductionist attitude towards scientific research has fostered an unhealthy research environment, evident in the copious examples of 'salami slicing' that litter scientific journals. Furthermore, the rules and significance of the game are

**"A playboy mathematician with yarns about ice and reindeer was the toast of the town."** D. Graham Burnett, page 943

all but opaque to the lay public (and to some members of our own profession), which alienates their interest in our investigations.

But our research is more relevant for them if it can be measured by its economic return. It would be hard to argue that the pressure to publish is somehow better or more meaningful than the pressure to recoup economic returns. Done properly, research assessment based on a balance between publications and economic output may be a way out of the impact-factor game.

**Herman Tse** Department of Microbiology, The University of Hong Kong, Pokfulam, Hong Kong  
e-mail: htse@hkucc.hku.hk

## The human face of a difficult, heroic, passionate scientist

**SIR** — In his Book Review 'Making genetic history' (*Nature* **453**, 1181–1182; 2008) of James Schwartz's *In Pursuit of the Gene*, Jerry Coyne claims that the US geneticist Hermann Joseph Muller was "the perennial underdog: Jewish, short, bald and with a high voice". Bald and short he was, but his voice was more baritone than tenor. As for his Jewishness, Coyne is perpetuating a myth: Muller's father converted from Catholicism to become a Unitarian because of his liberal social and scientific views; his mother's side was of English ancestry, mixed Jewish and Anglican. Muller was raised Unitarian, became an atheist and took an interest later in his life in humanism.

Coyne casts me in the lago role for poisoning the outlook of Schwartz about Muller through my "worshipful" biography. I pointed out Muller's insecurity, his suicide attempt, his difficult confrontational personality, his naïve embrace of Soviet communism, his almost ideological passion for positive eugenics and the reasons for his so-called 'priority complex'.

But I also admired Muller for his

courage in the way he took on failed competing theories of the gene, and for his passion for what he believed to be scientific truth. How many scientists would have engaged in a public debate with Trofim Lysenko, calling him a charlatan, in the year of Stalin's purge trials?

I wish that all science was done in a friendly, cooperative and respectful manner. In the fly lab Muller shared with Thomas Hunt Morgan and his 'boys', this was not so. Any reading of the correspondence in many archives will reveal the discontent, rivalry and hard feelings that accompanied a genuine enthusiasm to share ideas. Science is very human. Both Schwartz and I tried to present it that way.

**Elof Axel Carlson** Department of Biochemistry and Cell Biology, Stony Brook University, Stony Brook, New York 11794-5215, USA  
e-mail: ecarlson31@netzero.com

## Micromanaging ideas risks impeding flow of potential benefits

**SIR** — In his Correspondence 'Translational research: don't neglect basic science' (*Nature* **454**, 274; 2008), Stephen Moss is concerned that fundamental research will wither at the expense of translational science. But it's the proponents of translational research who should be more worried about reductions in the funding of discovery science, because this is the wellspring from which all science's societal benefit flows.

The problem is that discoveries are hard to plan for and not obviously applicable before they happen. This inherent inefficiency must nevertheless be underpinned by substantial investment, much like miners sorting tons of earth to find a gemstone. Some might argue that we already know enough and should now put what we do understand into practice. But that

approach can have an enormous attrition rate — look at drug development.

Astute science policy-makers need to realize that monikers such as 'basic', 'translational' and 'clinical' applied to medical research are all part of a continuous spectrum that many researchers can successfully travel in both directions if necessary. The risk is that in our efforts to accelerate a useful outcome through top-down interventions and incentives, we may deplete the flow of quality discoveries for development and end up refining rubbish. The scientific process has served society well, generating enormous advances over the past 500 years.

It's simple: recognize and promote excellence in basic research, balance volume of discovery with selective development and throw in a dash of patience. This system isn't broken and doesn't need fixing. We are doing humanity a disservice by trying to micromanage inspiration.

**Jim Woodgett** Samuel Lunenfeld Research Institute, Joseph and Wolf Lebovic Health Complex, Mount Sinai Hospital, 600 University Avenue, Toronto, Ontario M5G 1X5, Canada  
e-mail: woodgett@lunenfeld.ca

## Open debate could slow flu vaccine production

**SIR** — In his Commentary 'The contents of the syringe' (*Nature* **454**, 160–161; 2008), Steven Salzberg is highly critical of the World Health Organization (WHO) process for selecting influenza strains to include in vaccines for the coming year. He suggests that predictions could be improved by using sophisticated informatic modelling techniques to interrogate the available sequence and antigenicity data. However, the WHO's expert group responsible for strain selection is now deploying

these routinely and its track record has generally been good.

Salzberg argues that the expert group's recommendations should then be opened up for external critique. This is impractical. Strain selection is carried out under huge time pressure, with manufacturers having just six months to deliver tens of millions of vaccine doses. Delays can have very serious economic and political consequences for vaccine producers and health authorities. Decisions are left until as late as possible, usually mid-February for Northern Hemisphere countries, in order to have the widest data set to inform the decision.

Unfortunately, epidemics are sometimes only just beginning at that time. As providers of reagents to standardize vaccine potency, we are acutely aware of pressures inherent in the system, with days making a difference to the delivery of vaccine on schedule. To allow time for critical input, the strain-selection process would need to be brought forward, which would defeat the object by reducing the amount of hard data available to inform the decision.

Salzberg believes that using cell culture, rather than eggs, for production could speed up vaccine production, thus allowing more time for strain selection. The effect, if any, would be small because the time to delivery of final vaccine lots depends primarily on a whole series of quality-control, formulation, filling and packaging steps that are essentially the same whatever the production system.

We must still, therefore, rely on an imperfect process in which a group of experts makes the choice quickly, and as best it can. No doubt there is scope for further improvement, but an open debate before each decision is made would be counter-productive.

**Stephen Inglis, John Wood, Philip Minor** National Institute for Biological Standards and Control, South Mimms, Potters Bar, Hertfordshire EN6 3QG, UK  
e-mail: singlis@nibsc.ac.uk

# CORRESPONDENCE

## IVF: stars may have to consider the risk of stolen parenthood

SIR — Your Editorial 'Life after SuperBabe' (*Nature* **454**, 253; 2008) and Special Report 'Making babies: the next 30 years' (*Nature* **454**, 260–262; 2008) summarize the far-reaching social and ethical implications that arise from progress in *in vitro* fertilization (IVF) and stem-cell research. One aspect that has so far received scant attention is likely to have a substantial impact on both legal practice and everyday behaviour, at least for the rich and famous.

Scientific progress should eventually enable us to derive both sperm and egg from differentiated cells, using a combination of induced pluripotency (iPS) and directed differentiation (see 'New sources of sex cells' *Nature* **452**, 913; 2008). Before too long, it may be possible to collect a few hundred skin cells secretly from a used towel, a toothbrush or even an empty glass of water, then reprogram and differentiate these cells into sperm or egg. IVF could then be used to produce a child whose genetic parents are the involuntary tissue donors.

Such 'stolen' parenthood might be viewed as a dubious and expensive practical joke, if a child were to be conceived whose genetic parents were, say, Nicolas Sarkozy and Angela Merkel, derived from laundry at a G8 summit. But the widespread use of genetic evidence in paternity suits could provide a serious financial incentive for a woman to bear an iPS-derived IVF child whose genetic parents are herself and, say, Paul McCartney or Mick Jagger, presenting a lucrative opportunity to sue the genetic father for support for his 'illegitimate' child. And even if such financial incentives were to be removed through changes in legal practice, the problem of stolen parenthood is likely to



persist, given the significance that many people assign to kinship with famous people.

Two societal reactions might follow. First, abuse of human biological material in a wide sense is likely to become a statutory offence, generalizing the prohibition of secret genetic testing that has already been enacted in many countries. Second, persons who perceive themselves as potential victims of stolen parenthood might sterilize whatever waste they dispose of, unless of course they see their status soaring by allowing their parenthood to be stolen by as many groupies as possible.

**Christoph Bock** Department of Computational Biology, Max-Planck-Institut für Informatik, 66123 Saarbrücken, Germany  
e-mail: cbock@mpi-inf.mpg.de

## IVF: tight regulation may not be suitable for all cultures

SIR — In her Essay '30 years: from IVF to stem cells' (*Nature* **454**, 280–281; 2008), Ruth Deech reminds us of the role that the Human Fertilisation and Embryology Authority

(HFEA) has played through regulation in guiding the practice and scientific investigation of assisted-reproduction technology in the United Kingdom. But I disagree with her opinion that assisted reproduction in the United States is "nearly an unregulated black market". The medical aspects of assisted reproduction are in fact regulated extensively.

It is true that individuals and their physicians in the United States have the freedom to make decisions regarding who can reproduce and under what circumstances without the type of regulation provided by the HFEA. But it is against federal law to perform an *in vitro* fertilization (IVF) cycle without reporting that cycle and its results to the federal government; federal regulations require registration of clinics and extensive screening of potential gamete donors; all drugs and devices must be approved by the federal government; and health-care providers must be licensed by state governments.

In addition to complying with codified regulations, more than 90% of IVF clinics in the United States subscribe to unannounced on-site inspections and adhere voluntarily to guidelines developed jointly by the American

Society for Reproductive Medicine and the Society for Assisted Reproductive Technology. Publications in the scientific literature attest to the positive impact of these guidelines on patient outcomes.

The HFEA has had an important impact on assisted-reproduction technology and is an excellent example of extensive regulation. We cannot guess whether this degree of regulation in other countries would either be necessary or have comparable impact. Regulation can assume different forms, each dependent on individual cultures.

**David Adamson** American Society for Reproductive Medicine, and Fertility Physicians of Northern California, 540 University Avenue, Suite 200, Palo Alto, California 94301, USA  
e-mail: enicoll@asrm-dc.org

## A possible way out of the impact-factor game

SIR — Your Editorial 'Unbalanced portfolio' (*Nature* **453**, 1144; 2008) defends the scientific autonomy of researchers against pressure from bureaucrats seeking maximum economic returns. Although this position is admirable and likely to be popular among researchers, it might also be worth reflecting on our current situation.

Few scientists nowadays can afford to pursue research for science's sake, as suggested in the Editorial. Rather, most of us are trapped in a game of numbers, in which all our research output can be reduced to one or more of the following metrics: impact factors, average citations per article, total number of articles published, and the h-index.

This reductionist attitude towards scientific research has fostered an unhealthy research environment, evident in the copious examples of 'salami slicing' that litter scientific journals. Furthermore, the rules and significance of the game are

**"A playboy mathematician with yarns about ice and reindeer was the toast of the town."** D. Graham Burnett, page 943

all but opaque to the lay public (and to some members of our own profession), which alienates their interest in our investigations.

But our research is more relevant for them if it can be measured by its economic return. It would be hard to argue that the pressure to publish is somehow better or more meaningful than the pressure to recoup economic returns. Done properly, research assessment based on a balance between publications and economic output may be a way out of the impact-factor game.

**Herman Tse** Department of Microbiology, The University of Hong Kong, Pokfulam, Hong Kong  
e-mail: htse@hkucc.hku.hk

## The human face of a difficult, heroic, passionate scientist

SIR — In his Book Review 'Making genetic history' (*Nature* **453**, 1181–1182; 2008) of James Schwartz's *In Pursuit of the Gene*, Jerry Coyne claims that the US geneticist Hermann Joseph Muller was "the perennial underdog: Jewish, short, bald and with a high voice". Bald and short he was, but his voice was more baritone than tenor. As for his Jewishness, Coyne is perpetuating a myth: Muller's father converted from Catholicism to become a Unitarian because of his liberal social and scientific views; his mother's side was of English ancestry, mixed Jewish and Anglican. Muller was raised Unitarian, became an atheist and took an interest later in his life in humanism.

Coyne casts me in the lago role for poisoning the outlook of Schwartz about Muller through my "worshipful" biography. I pointed out Muller's insecurity, his suicide attempt, his difficult confrontational personality, his naïve embrace of Soviet communism, his almost ideological passion for positive eugenics and the reasons for his so-called 'priority complex'.

But I also admired Muller for his

courage in the way he took on failed competing theories of the gene, and for his passion for what he believed to be scientific truth. How many scientists would have engaged in a public debate with Trofim Lysenko, calling him a charlatan, in the year of Stalin's purge trials?

I wish that all science was done in a friendly, cooperative and respectful manner. In the fly lab Muller shared with Thomas Hunt Morgan and his 'boys', this was not so. Any reading of the correspondence in many archives will reveal the discontent, rivalry and hard feelings that accompanied a genuine enthusiasm to share ideas. Science is very human. Both Schwartz and I tried to present it that way.

**Elof Axel Carlson** Department of Biochemistry and Cell Biology, Stony Brook University, Stony Brook, New York 11794-5215, USA  
e-mail: ecarlson31@netzero.com

## Micromanaging ideas risks impeding flow of potential benefits

SIR — In his Correspondence 'Translational research: don't neglect basic science' (*Nature* **454**, 274; 2008), Stephen Moss is concerned that fundamental research will wither at the expense of translational science. But it's the proponents of translational research who should be more worried about reductions in the funding of discovery science, because this is the wellspring from which all science's societal benefit flows.

The problem is that discoveries are hard to plan for and not obviously applicable before they happen. This inherent inefficiency must nevertheless be underpinned by substantial investment, much like miners sorting tons of earth to find a gemstone. Some might argue that we already know enough and should now put what we do understand into practice. But that

approach can have an enormous attrition rate — look at drug development.

Astute science policy-makers need to realize that monikers such as 'basic', 'translational' and 'clinical' applied to medical research are all part of a continuous spectrum that many researchers can successfully travel in both directions if necessary. The risk is that in our efforts to accelerate a useful outcome through top-down interventions and incentives, we may deplete the flow of quality discoveries for development and end up refining rubbish. The scientific process has served society well, generating enormous advances over the past 500 years.

It's simple: recognize and promote excellence in basic research, balance volume of discovery with selective development and throw in a dash of patience. This system isn't broken and doesn't need fixing. We are doing humanity a disservice by trying to micromanage inspiration.

**Jim Woodgett** Samuel Lunenfeld Research Institute, Joseph and Wolf Lebovic Health Complex, Mount Sinai Hospital, 600 University Avenue, Toronto, Ontario M5G 1X5, Canada  
e-mail: woodgett@lunenfeld.ca

## Open debate could slow flu vaccine production

SIR — In his Commentary 'The contents of the syringe' (*Nature* **454**, 160–161; 2008), Steven Salzberg is highly critical of the World Health Organization (WHO) process for selecting influenza strains to include in vaccines for the coming year. He suggests that predictions could be improved by using sophisticated informatic modelling techniques to interrogate the available sequence and antigenicity data. However, the WHO's expert group responsible for strain selection is now deploying

these routinely and its track record has generally been good.

Salzberg argues that the expert group's recommendations should then be opened up for external critique. This is impractical. Strain selection is carried out under huge time pressure, with manufacturers having just six months to deliver tens of millions of vaccine doses. Delays can have very serious economic and political consequences for vaccine producers and health authorities. Decisions are left until as late as possible, usually mid-February for Northern Hemisphere countries, in order to have the widest data set to inform the decision.

Unfortunately, epidemics are sometimes only just beginning at that time. As providers of reagents to standardize vaccine potency, we are acutely aware of pressures inherent in the system, with days making a difference to the delivery of vaccine on schedule. To allow time for critical input, the strain-selection process would need to be brought forward, which would defeat the object by reducing the amount of hard data available to inform the decision.

Salzberg believes that using cell culture, rather than eggs, for production could speed up vaccine production, thus allowing more time for strain selection. The effect, if any, would be small because the time to delivery of final vaccine lots depends primarily on a whole series of quality-control, formulation, filling and packaging steps that are essentially the same whatever the production system.

We must still, therefore, rely on an imperfect process in which a group of experts makes the choice quickly, and as best it can. No doubt there is scope for further improvement, but an open debate before each decision is made would be counter-productive.

**Stephen Inglis, John Wood, Philip Minor** National Institute for Biological Standards and Control, South Mimms, Potters Bar, Hertfordshire EN6 3QG, UK  
e-mail: singlis@nibsc.ac.uk

**"A playboy mathematician with yarns about ice and reindeer was the toast of the town."** D. Graham Burnett, page 943

all but opaque to the lay public (and to some members of our own profession), which alienates their interest in our investigations.

But our research is more relevant for them if it can be measured by its economic return. It would be hard to argue that the pressure to publish is somehow better or more meaningful than the pressure to recoup economic returns. Done properly, research assessment based on a balance between publications and economic output may be a way out of the impact-factor game.

**Herman Tse** Department of Microbiology, The University of Hong Kong, Pokfulam, Hong Kong  
e-mail: htse@hkucc.hku.hk

## The human face of a difficult, heroic, passionate scientist

**SIR** — In his Book Review 'Making genetic history' (*Nature* **453**, 1181–1182; 2008) of James Schwartz's *In Pursuit of the Gene*, Jerry Coyne claims that the US geneticist Hermann Joseph Muller was "the perennial underdog: Jewish, short, bald and with a high voice". Bald and short he was, but his voice was more baritone than tenor. As for his Jewishness, Coyne is perpetuating a myth: Muller's father converted from Catholicism to become a Unitarian because of his liberal social and scientific views; his mother's side was of English ancestry, mixed Jewish and Anglican. Muller was raised Unitarian, became an atheist and took an interest later in his life in humanism.

Coyne casts me in the lago role for poisoning the outlook of Schwartz about Muller through my "worshipful" biography. I pointed out Muller's insecurity, his suicide attempt, his difficult confrontational personality, his naïve embrace of Soviet communism, his almost ideological passion for positive eugenics and the reasons for his so-called 'priority complex'.

But I also admired Muller for his

courage in the way he took on failed competing theories of the gene, and for his passion for what he believed to be scientific truth. How many scientists would have engaged in a public debate with Trofim Lysenko, calling him a charlatan, in the year of Stalin's purge trials?

I wish that all science was done in a friendly, cooperative and respectful manner. In the fly lab Muller shared with Thomas Hunt Morgan and his 'boys', this was not so. Any reading of the correspondence in many archives will reveal the discontent, rivalry and hard feelings that accompanied a genuine enthusiasm to share ideas. Science is very human. Both Schwartz and I tried to present it that way.

**Elof Axel Carlson** Department of Biochemistry and Cell Biology, Stony Brook University, Stony Brook, New York 11794-5215, USA  
e-mail: ecarlson31@netzero.com

## Micromanaging ideas risks impeding flow of potential benefits

**SIR** — In his Correspondence 'Translational research: don't neglect basic science' (*Nature* **454**, 274; 2008), Stephen Moss is concerned that fundamental research will wither at the expense of translational science. But it's the proponents of translational research who should be more worried about reductions in the funding of discovery science, because this is the wellspring from which all science's societal benefit flows.

The problem is that discoveries are hard to plan for and not obviously applicable before they happen. This inherent inefficiency must nevertheless be underpinned by substantial investment, much like miners sorting tons of earth to find a gemstone. Some might argue that we already know enough and should now put what we do understand into practice. But that

approach can have an enormous attrition rate — look at drug development.

Astute science policy-makers need to realize that monikers such as 'basic', 'translational' and 'clinical' applied to medical research are all part of a continuous spectrum that many researchers can successfully travel in both directions if necessary. The risk is that in our efforts to accelerate a useful outcome through top-down interventions and incentives, we may deplete the flow of quality discoveries for development and end up refining rubbish. The scientific process has served society well, generating enormous advances over the past 500 years.

It's simple: recognize and promote excellence in basic research, balance volume of discovery with selective development and throw in a dash of patience. This system isn't broken and doesn't need fixing. We are doing humanity a disservice by trying to micromanage inspiration.

**Jim Woodgett** Samuel Lunenfeld Research Institute, Joseph and Wolf Lebovic Health Complex, Mount Sinai Hospital, 600 University Avenue, Toronto, Ontario M5G 1X5, Canada  
e-mail: woodgett@lunenfeld.ca

## Open debate could slow flu vaccine production

**SIR** — In his Commentary 'The contents of the syringe' (*Nature* **454**, 160–161; 2008), Steven Salzberg is highly critical of the World Health Organization (WHO) process for selecting influenza strains to include in vaccines for the coming year. He suggests that predictions could be improved by using sophisticated informatic modelling techniques to interrogate the available sequence and antigenicity data. However, the WHO's expert group responsible for strain selection is now deploying

these routinely and its track record has generally been good.

Salzberg argues that the expert group's recommendations should then be opened up for external critique. This is impractical. Strain selection is carried out under huge time pressure, with manufacturers having just six months to deliver tens of millions of vaccine doses. Delays can have very serious economic and political consequences for vaccine producers and health authorities. Decisions are left until as late as possible, usually mid-February for Northern Hemisphere countries, in order to have the widest data set to inform the decision.

Unfortunately, epidemics are sometimes only just beginning at that time. As providers of reagents to standardize vaccine potency, we are acutely aware of pressures inherent in the system, with days making a difference to the delivery of vaccine on schedule. To allow time for critical input, the strain-selection process would need to be brought forward, which would defeat the object by reducing the amount of hard data available to inform the decision.

Salzberg believes that using cell culture, rather than eggs, for production could speed up vaccine production, thus allowing more time for strain selection. The effect, if any, would be small because the time to delivery of final vaccine lots depends primarily on a whole series of quality-control, formulation, filling and packaging steps that are essentially the same whatever the production system.

We must still, therefore, rely on an imperfect process in which a group of experts makes the choice quickly, and as best it can. No doubt there is scope for further improvement, but an open debate before each decision is made would be counter-productive.

**Stephen Inglis, John Wood, Philip Minor** National Institute for Biological Standards and Control, South Mimms, Potters Bar, Hertfordshire EN6 3QG, UK  
e-mail: singlis@nibsc.ac.uk

# COMMENTARY

## Innovation policy: not just a jumbo shrimp

Policies that predict and direct innovative research might seem to be a practical impossibility, says **David H. Guston**, but social sciences point to a solution.

Innovation policy could be seen as an oxymoron. Like an 'open secret', or 'jumbo shrimp' — which the late comedian George Carlin compared to 'military intelligence' — the words just don't go together. Innovation policy evokes a tension. How does one predict and direct something that is by nature unpredictable and, by necessity, often undirected?

The tension in innovation policy runs deeper than word play, of course. Policies are made too late to change the past that necessitated them and too early to understand the future they are meant to shape. Innovation sparks the difference between that past and future. Policies are incremental, but the goals of innovation often tend toward the revolutionary. An explicit goal of recent initiatives in nanoscience, for example, has been to usher in "the next industrial revolution"<sup>1</sup>. That is about as non-incremental as one could imagine, given that the transformations associated with steam power and information technology affected both industrial organization, and every aspect of social and family life, language and art, politics, warfare and more.

Innovation policy should encourage a dynamic scientific enterprise to contribute to identifiable social outcomes, such as in areas of health, energy and the environment. But research occasionally generates radical changes that are unpredictable and often not associated with those pre-defined social goals. Nations invest in research for social purposes that are often thwarted by the nature of the research process itself. For example, investment in health research may return many high-quality scientific papers, but less in terms of affordable and accessible improvements in health care. Innovation policies for nanotechnology embody these contradictions.

### Research initiatives

The US National Nanotechnology Research and Development Act of 2003 authorizes a National Nanotechnology Initiative (NNI) to coordinate about US\$1.5 billion in research across some two dozen agencies. Currently in revision before Congress, the act emphasizes commercialization for international competitiveness as a driving rationale on one hand, while requiring research into societal impacts on the other<sup>2</sup>. Interestingly, the



societal research promoted by the NNI may provide ways to address the contradictions inherent to innovation policy.

The NNI has funded research to develop 'anticipatory governance'<sup>3</sup>, which works by correcting three unspoken and ill-formed premises that underpin these contradictions.

The first of these premises is that policy is supposed to have a clear cause-and-effect relationship in society. But limiting policies to being effective instruments misses the value-laden nature of political deliberation and choice. Policies are, and should rightly be, about articulating public values<sup>4</sup>.

Although many pieces of basic legislation contain clear articulations of public values, the NNI act announces none. A close reading of the law's text, however, reveals several guiding public values: nanoscience research should be performed with an interdisciplinary bent. It should be oriented toward improving the economic competitiveness of the United

States. It should be subject to suitable administrative oversight. And it should be done in close conjunction with public engagement and societal implications research. But in part because these values must be teased out of the text, they have remained controversial or even unrecognized among the communities that implement the law.

The second premise is that policy is supposed to be grounded on a clear understanding of the natural world. We must consider both the shortcomings of our understanding of the natural world and the strengths of our understanding of the social world. Among the former is that — as Danish physicist Niels Bohr reportedly said — "prediction is very difficult, especially about the future". At any given point in time, science provides both an incomplete and a changing portrayal of the natural world. In matters closely related to policy, such as climate change, it is often not the case that more data helps to make science more complete politically<sup>5</sup>. And even if scientists might have some monopoly over the technical knowledge in their chosen field, they have no similarly exclusive take on the vast bodies of knowledge and practice

implicated in turning their discoveries into actual innovations or policy decisions.

Luckily, discarding science-based prediction as an exclusive contributor to legislative action does not disarm policy-makers. Understanding from the social world — concepts such as precaution and anticipation — can help to remove unpredictability as a roadblock. Precaution, as seen in environmental risk management, connotes acting to avoid predicted but uncertain hazards. Anticipation, in contrast, denotes building the capacity to respond to unpredicted and unpredictable risks. Many of us frequent gyms to lift weights. But we do not predict that our lives will depend on our ability to perform a 'lat pull' or a curl, or to bench-press our weight. Instead, we rightly believe that these exercises will build in our bodies

a capacity to withstand whatever physical and emotional stresses we might confront. Giving up on prediction does not mean giving up on anticipation. We must exercise the various intellectual and imaginative capacities that will prepare us for the challenges that innovation will surely offer.

The third flawed premise is that ongoing and occasionally revolutionary change is inherent to the scientific enterprise. We vastly underestimate our ability to productively shape the scientific enterprise and effectively steer it. Policy-makers, their scientific advisers and their lab-bench constituents too often cling to Hungarian-British polymath Michael Polanyi's logic that "you can kill or mutilate the advance of science, [but] you cannot shape it"<sup>6</sup>. The scientific enterprise we have — its foci, productivity, contributions, strengths and shortcomings — is at least as attributable to the governing forces of personalities, policies, and institutions as it is to the autonomous play of researchers.

**"We vastly underestimate our ability to productively shape the scientific enterprise."**

### Simple solution

Anticipatory governance addresses these three shortcomings. It prescribes the explicit inclusion of values in deliberations, often through the direct engagement of various groups, including the lay public. Public engagement has been a major theme in nationally sponsored societal research programmes for nanotechnology, including the



Nanoscale Informal Science Education (NISE) Network in the United States. Funded by the National Science Foundation, NISE aims to transform the role of science museums from informal educators of the public to conveners of public deliberation. The Center for Nanotechnology in Society (CNS) at Arizona State University in Tempe recently conducted the first-ever National Citizens' Technology Forum held in the United States. Similar public-engagement activities have also been featured in the nanotechnology policies of the European Union, United Kingdom, France and Belgium, among other locales.

Next, anticipatory governance prescribes the creation of what one might call

**"Global society needs much of what knowledge-based innovation has to offer."**

'anticipatory knowledge', particularly through exercises such as scenario development, to build a broad-based capacity to recognize and understand social change and its relationship to scientific and technical change. Several roadmaps elaborate the technical visions of nanotechnological futures, such as the four stages of nanotechnological development<sup>7</sup>. But more integrated socio-technical scenario projects have flourished, including scenario development by the Project on Emerging Nanotechnology at the Woodrow Wilson International Center for

Scholars in Washington DC, the 'open-source' scenario development of the Nano-Futures project by the CNS, and scenarios of converging technologies developed by the University of Oxford's James Martin Institute, UK. Particularly when coupled with engagement activities, the creation of such anticipatory knowledge can help the public voice its concerns about looming socio-technical change.

Anticipatory governance further prescribes the integration of engagement and foresight with scientific and technical work. This informs social scientists' own perspectives with cutting-edge research. It also increases the capacity of natural scientists to understand the societal aspects of their own work, be more reflective about practices and choices within the laboratory and if necessary change their practices to align their research with public visions and values. Such activities have occurred in many small-scale trials. Social scientists

and humanists have 'embedded' themselves in research laboratories to become active participants in laboratory activities both to observe researchers and to prompt a more reflexive disposition among them, even modestly reorienting their work in more socially robust directions. The integrative activities at the CNS, for example, are beginning to catalogue concrete, positive consequences within laboratories. Our nanoscientist colleagues report helpful changes and desire more such interactions.

### Beyond nano

The engagement, foresight and integration activities listed here are still too few and too far between. The scale of the research enterprise and the scope of innovation policies dwarfs them. Their few demonstrated successes are not well-disseminated. And they are not linked together in a way that supports anticipatory governance. Yet these early steps offer a prudent approach for innovation policy for nanotechnology and other fields including synthetic biology and neuro-technologies.

Global society needs much of what knowledge-based innovation has to offer. Anticipatory governance is a necessary exercise. It defrays the inherent contradictions of innovation policy, while ensuring that public values and foresight accompany scientific practice, keeping the revolution from turning unproductively against itself and against us. ■

**David H. Guston** directs the Center for Nanotechnology in Society, co-directs the Consortium for Science, Policy and Outcomes and is Professor of Political Science at Arizona State University, Tempe, 85287, Arizona, USA. e-mail: [david.guston@asu.edu](mailto:david.guston@asu.edu)

1. National Science and Technology Council Interagency Working Group on Nanoscience, Engineering and Technology. *National Nanotechnology Initiative: Leading to the Next Industrial Revolution* (2000).
2. Fisher, E. & Mahajan, R. *L. Sci. Pub. Pol.* **33**, 5-16 (2006).
3. Barber, D., Fisher, E., Selin, C. & Guston, D. in *The Handbook of Science and Technology Studies* 3rd edn (eds Hackett, E. J., Amsterdamska, O., Lynch, M. E. & Wajcman, J.) 979-1000 (MIT Press, 2008).
4. Bozeman, B. *Public Values and Public Interest: Counterbalancing Economic Individualism* (Georgetown Univ. Press, 2007).
5. Sarewitz, D. *Environ. Sci. Pol.* **7**, 385-403 (2004).
6. Polanyi, M. *Minerva* **1**, 54-74 (1962).
7. Roco, M. *J. Nanopart. Res.* **6**, 1-10 (2004).

To comment on this article and others in our innovation series, visit <http://tinyurl.com/5uolx2>.

See Editorial, page 918.

# BOOKS & ARTS

## Flat Earth and Amazons

Charles-Marie de La Condamine's quest to Peru to calculate Earth's flattened shape included some adventures that didn't make it into the official records at the time, finds **D. Graham Burnett**.

### Measuring the New World: Enlightenment Science and South America

by Neil Safier

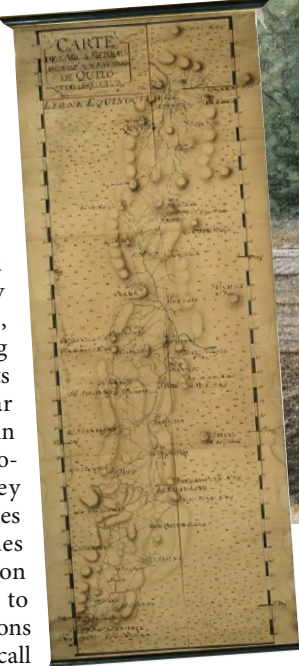
University of Chicago Press: 2008.

336 pp. \$45

European explorers, those sturdy peripatetics of reason in the age of empire, generally enjoyed lording it over the 'natives' — or at least they tended to write things up that way for the people back at home. What actually went on in the jungle, desert or Arctic has always been tough to sort out; and what the locals made of these transitory self-promoters dressed in puttees is unrecoverable.

Sometimes we catch a tantalizing glimpse, such as when the globe-trotting French nobleman and savant

Charles-Marie de La Condamine recorded an unexpected Peruvian comedy review in the Andean highlands in the eighteenth century. The butt of the show was La Condamine himself, and his coterie of snooty scientific Argonauts, who had been fussing with a set of instruments in the mountains near Quito for several years in the late 1730s. The Europeans knew that they were intrepid luminaries from the Académie des Sciences in Paris, sent on a geodetic expedition to resolve pressing questions in what we would now call geophysics. But the valley's inhabitants thought that they were goofballs, and worked up a skit to prove it. Dragging out a stage-set scientific observatory — giant graduated quadrants of wood and pasteboard, along with various accoutrements of the enlightened natural philosopher — the villagers of Tarqui launched into a spirited masquerade, dramatizing in *opera buffa* style the absurd attentions that the Frenchmen lavished on their instruments. From the eyepiece to the notebook to the eyepiece to the ... eek! Check the clock! Belly laughs all around.



L. C. CARMONTELLE, MUSÉE CONDÉ, CHANTILLY, FRANCE/LAUROS/GIRAUDON/BRIDGEMAN ART LIBRARY

La Condamine lost the race to map the meridian arc (left) and determine Earth's true shape.

Historian Neil Safier begins his book on science and South America in the mid-eighteenth century with this alluring scene of satirical inversion. He asks: "What if we were to follow the Tarquin mimics in looking at the gestures and practices of European science overseas?" This might mean that Safier intends to stage his own comic pantomime, an undertaking that would push the boundaries in the academic history of Latin America, but no such luck. Rather, he tells an unheroic story of science in the making, a story that uncovers the fibs, elisions and erasures that happen between the muddy field and publication back in Paris. This sort of 'aha, gotcha' history is not much

fun. Although Safier has admirable linguistic gifts, shows an impressive command of his sources and writes with verve, *Measuring the New World* is mostly a frustrating book.

This is despite the romance and fascination of its subject. La Condamine and his fellow explorers embarked on one of the great quests of the age: nearly a decade of South American wandering, collecting, surveying and astronomical observation, together with plenty of arguing, sex, madness and even some killing, all for the purpose of resolving a fundamental question: what is the shape of Earth? Round, you might say, but Isaac Newton's late-seventeenth-century work on the physical forces acting on the planet suggested that the

spinning globe would not be perfectly spherical, but would bulge around its equator, like a pumpkin. This contradicted theoretical work done by René Descartes earlier in the century. Descartes' champions contested Newton's prediction, as did measurements from surveyors working on the national map of France. Indeed, there seemed to be evidence that Earth might be pointed at its poles like an egg. National pride (France versus England), scientific approach (mathematicians versus cartographers) and bragging rights in physics (Newton versus Descartes) were all at stake — not to mention the accuracy of charts and maps, crucial in a world of expanding global trade.

Resolving the question demanded the careful measurement of the length on the ground of a degree of meridian arc — first in one place, ideally near the equator, and then in another, ideally near a pole. If each 360th of Earth's axial cross-sections was the same length, then we stood on a sphere; a difference in those lengths would indicate a spheroid, be it oblate like a pumpkin, or prolate, like an egg.

The fieldwork for these precise measurements was arduous. Highly accurate astronomical observations were needed to establish that the endpoints of the arc marked off a true degree. Working out the length of the degree on the ground required fanatically attentive techniques of land surveying: first pace off a baseline, then project this length through an array of triangles, sighted from promontories along the degree. With all the angles of the triangles known, it was mere trigonometry to work out the lengths of their sides, and thereby, the length of the degree itself. After several months of these exertions, most of the Frenchmen had stopped talking to each other, having fallen out over protocol and procedure. It looked as if each team was going to work up a separate set of results. So much for scientific universalism. Throw in hostile encounters with the locals, a shortage of cash, and larger political machinations — the Spanish crown and its officers had mixed feelings about a bunch of foreign scientific interlopers making maps in the heart of an Iberian colony — and you have all the ingredients for a fiasco.

This, in many ways, is how the La Condamine expedition has been remembered, not least because the explorers had barely set their telescopes up in the Andes when they learned they'd been beaten to the punch. The dashing polar explorer Pierre Louis Maupertuis had turned up in Paris in an unusual fur hat to announce that Earth was indeed flatter at the poles: Newton was right! Maupertuis and his crew had received the easier geodetic assignment from the Académie des Sciences. Instead

of going halfway around the world to the equator, they had simply zipped up to Lapland, where favourable conditions and organizational zeal led to a speedy set of measurements of the polar degree, which could be compared with measurements already done in France. Maupertuis — a playboy mathematician with a flawless sense of theatre and lots of yarns about ice and reindeer — was the toast of the town.

Not to be outdone, La Condamine broadened the scope of his investigations. He descended the Amazon River on the lookout for Amazons and El Dorado, throwing himself into botanical and zoological collection, writing extensively, if not very accurately, about Amerindians, and generally trying to rescue a more-or-less failed geodetic expedition by transforming it into a grand exploration of Spanish America, commemorated in texts and maps.

It is with these latter documents that Safier is, on the whole, concerned. He attempts to trace the paths by which the explorer's experience in the field — native informants, empirical observations, elements of fantasy — make their way into books, pictures and charts. But the yield is meagre. He repeatedly alerts the

reader to the "insidious effacement" of the role of indigenous peoples in the production of knowledge. Although this is an interesting topic, and one that has been pursued by a number of scholars in recent decades, Safier's examples are not persuasive. It is true that La Condamine doesn't say much about the porters who carried his equipment, but so what?

The conclusion of the book raises the interesting possibility that La Condamine used his ideas about native American women and runaway slaves to buttress his claims about the reality of Amazons, and there is a strong chapter on the French republishing of a Spanish history of the Incas. But on the whole, few readers will enjoy *Measuring the New World*. Freed from the straitened preoccupations of disciplinary history, the palpably smart Safier might yet give us a lovable and insightful work on Latin American exploration. Perhaps a satirical play? ■

**D. Graham Burnett** is an editor at *Cabinet* magazine in Brooklyn, New York, and teaches history of science at Princeton University, Princeton, New Jersey 08544, USA. His latest book is *Trying Leviathan*.

## Microbial fuels for the future

### Bioenergy

Edited by Judy D. Wall, Caroline S. Harwood and Arnold Demain  
ASM Press: 2008. 454 pp. \$149.95

An individual in the United States consumes the equivalent of 100 watts of continuous power from food, but it takes more than a hundred times this amount to sustain their lifestyle. Fossil fuels cannot provide this much power for every person on the planet, and we must reduce our dependence on these fuels to address global carbon dioxide emissions and climate change. To succeed, we need sustainable and carbon-neutral sources of energy. How can we find or make these fuels?

Microbes, according to the microbiologists and biochemists who contribute to *Bioenergy*, hold the answers. Editors Judy Wall, Caroline Harwood and Arnold Demain have assembled 31 impressive chapters that address the opportunities and challenges of using microbes to produce bioelectricity, to help in oil recovery or to make biofuels — including ethanol, methanol, methane and hydrogen.

*Bioenergy* supplies a wealth of technical information. Each chapter has an accessible

introduction and each author positions their favourite fuel within the larger context of energy production and utilization. Nancy Nichols and her colleagues note that in 2008, the United States will produce 30 billion litres of fuel ethanol, mainly from corn (maize). In 2006, around 20% of the US corn crop was used to make ethanol, which represented more than 2% of all liquid fuels used for transportation. Z. Lewis Liu and co-workers say that if all of the corn grown in the United States was used to make fuel, only 15% of current US fuel needs would be satisfied. These numbers show that we will need more than corn ethanol to fuel our cars.

Using any food source as a fuel is controversial. Perhaps reflecting this, only one of the twelve chapters on bioethanol directly addresses the use of food crops. Other chapters focus on the real challenge: how to turn cellulose, the main constituent of plant cell walls, into ethanol. Microbes can break down cellulose to produce sugar efficiently, but during the process they also consume the sugar. This loss can be avoided by using enzymes instead of microbes, but enzymes are expensive to make. After ethanol is formed by fermenting the sugar, another energy-intensive process is needed to remove the water by-product.

spinning globe would not be perfectly spherical, but would bulge around its equator, like a pumpkin. This contradicted theoretical work done by René Descartes earlier in the century. Descartes' champions contested Newton's prediction, as did measurements from surveyors working on the national map of France. Indeed, there seemed to be evidence that Earth might be pointed at its poles like an egg. National pride (France versus England), scientific approach (mathematicians versus cartographers) and bragging rights in physics (Newton versus Descartes) were all at stake — not to mention the accuracy of charts and maps, crucial in a world of expanding global trade.

Resolving the question demanded the careful measurement of the length on the ground of a degree of meridian arc — first in one place, ideally near the equator, and then in another, ideally near a pole. If each 360th of Earth's axial cross-sections was the same length, then we stood on a sphere; a difference in those lengths would indicate a spheroid, be it oblate like a pumpkin, or prolate, like an egg.

The fieldwork for these precise measurements was arduous. Highly accurate astronomical observations were needed to establish that the endpoints of the arc marked off a true degree. Working out the length of the degree on the ground required fanatically attentive techniques of land surveying: first pace off a baseline, then project this length through an array of triangles, sighted from promontories along the degree. With all the angles of the triangles known, it was mere trigonometry to work out the lengths of their sides, and thereby, the length of the degree itself. After several months of these exertions, most of the Frenchmen had stopped talking to each other, having fallen out over protocol and procedure. It looked as if each team was going to work up a separate set of results. So much for scientific universalism. Throw in hostile encounters with the locals, a shortage of cash, and larger political machinations — the Spanish crown and its officers had mixed feelings about a bunch of foreign scientific interlopers making maps in the heart of an Iberian colony — and you have all the ingredients for a fiasco.

This, in many ways, is how the La Condamine expedition has been remembered, not least because the explorers had barely set their telescopes up in the Andes when they learned they'd been beaten to the punch. The dashing polar explorer Pierre Louis Maupertuis had turned up in Paris in an unusual fur hat to announce that Earth was indeed flatter at the poles: Newton was right! Maupertuis and his crew had received the easier geodetic assignment from the Académie des Sciences. Instead

of going halfway around the world to the equator, they had simply zipped up to Lapland, where favourable conditions and organizational zeal led to a speedy set of measurements of the polar degree, which could be compared with measurements already done in France. Maupertuis — a playboy mathematician with a flawless sense of theatre and lots of yarns about ice and reindeer — was the toast of the town.

Not to be outdone, La Condamine broadened the scope of his investigations. He descended the Amazon River on the lookout for Amazons and El Dorado, throwing himself into botanical and zoological collection, writing extensively, if not very accurately, about Amerindians, and generally trying to rescue a more-or-less failed geodetic expedition by transforming it into a grand exploration of Spanish America, commemorated in texts and maps.

It is with these latter documents that Safier is, on the whole, concerned. He attempts to trace the paths by which the explorer's experience in the field — native informants, empirical observations, elements of fantasy — make their way into books, pictures and charts. But the yield is meagre. He repeatedly alerts the

reader to the "insidious effacement" of the role of indigenous peoples in the production of knowledge. Although this is an interesting topic, and one that has been pursued by a number of scholars in recent decades, Safier's examples are not persuasive. It is true that La Condamine doesn't say much about the porters who carried his equipment, but so what?

The conclusion of the book raises the interesting possibility that La Condamine used his ideas about native American women and runaway slaves to buttress his claims about the reality of Amazons, and there is a strong chapter on the French republishing of a Spanish history of the Incas. But on the whole, few readers will enjoy *Measuring the New World*. Freed from the straitened preoccupations of disciplinary history, the palpably smart Safier might yet give us a lovable and insightful work on Latin American exploration. Perhaps a satirical play? ■

**D. Graham Burnett** is an editor at *Cabinet* magazine in Brooklyn, New York, and teaches history of science at Princeton University, Princeton, New Jersey 08544, USA. His latest book is *Trying Leviathan*.

## Microbial fuels for the future

### Bioenergy

Edited by Judy D. Wall, Caroline S. Harwood and Arnold Demain  
ASM Press: 2008. 454 pp. \$149.95

An individual in the United States consumes the equivalent of 100 watts of continuous power from food, but it takes more than a hundred times this amount to sustain their lifestyle. Fossil fuels cannot provide this much power for every person on the planet, and we must reduce our dependence on these fuels to address global carbon dioxide emissions and climate change. To succeed, we need sustainable and carbon-neutral sources of energy. How can we find or make these fuels?

Microbes, according to the microbiologists and biochemists who contribute to *Bioenergy*, hold the answers. Editors Judy Wall, Caroline Harwood and Arnold Demain have assembled 31 impressive chapters that address the opportunities and challenges of using microbes to produce bioelectricity, to help in oil recovery or to make biofuels — including ethanol, methanol, methane and hydrogen.

*Bioenergy* supplies a wealth of technical information. Each chapter has an accessible

introduction and each author positions their favourite fuel within the larger context of energy production and utilization. Nancy Nichols and her colleagues note that in 2008, the United States will produce 30 billion litres of fuel ethanol, mainly from corn (maize). In 2006, around 20% of the US corn crop was used to make ethanol, which represented more than 2% of all liquid fuels used for transportation. Z. Lewis Liu and co-workers say that if all of the corn grown in the United States was used to make fuel, only 15% of current US fuel needs would be satisfied. These numbers show that we will need more than corn ethanol to fuel our cars.

Using any food source as a fuel is controversial. Perhaps reflecting this, only one of the twelve chapters on bioethanol directly addresses the use of food crops. Other chapters focus on the real challenge: how to turn cellulose, the main constituent of plant cell walls, into ethanol. Microbes can break down cellulose to produce sugar efficiently, but during the process they also consume the sugar. This loss can be avoided by using enzymes instead of microbes, but enzymes are expensive to make. After ethanol is formed by fermenting the sugar, another energy-intensive process is needed to remove the water by-product.



Finding new biofuel sources, such as algae that make hydrogen gas, might help solve the energy crisis.

Gaseous biofuels, such as hydrogen and methane, are made easily from many source materials using mature technologies. Hydrogen gas and volatile fatty acids, such as acetic acid, can be made from cellulose by fermentation. According to Ann Wilkie, most biomass sources can produce biomethane after limited preparation, such as drying or shredding. Certain microbes can convert acetic acid into methane gas, and methane or hydrogen can be converted to methanol. Hydrogen and methane are highly insoluble, so they can be recovered from water more easily than ethanol. In one of the seven chapters on methane and methanol, Bakul Dave reminds us that single-carbon fuels such as methanol lack carbon–carbon bonds, and therefore do not leave residues during combustion.

Combustion of hydrogen gas is better than methane as it produces only water. Three chapters are devoted to the production of hydrogen by photosynthesis in algae or bacteria, but none describes the use of fermentation or microbial electrolysis cells to make hydrogen. According to Marc Rousset and Laurent Cournac, hydrogenase enzymes that catalyse both the production and the consumption of hydrogen offer excellent opportunities to capture energy directly from sunlight, rather than through biomass, by splitting water into hydrogen and oxygen. But the sensitivity of these enzymes to oxygen needs to be decreased. Caroline Harwood describes using whole cells of purple non-sulphur bacteria to form hydrogen without splitting water. She notes that these cells can be immobilized in thin latex sheets to form panels. If perfected, this wonderful method could make hydrogen through the use of biosolar collectors.

My favourite bioenergy approach involves using bacteria to make electricity directly in microbial fuel cells. Certain strains of *Geobacter* might power these, but Peter Aelterman and his colleagues explain that many different types of bacteria release electrons to electrodes and can yield useful current. Why such a variety of bacteria can transfer electrons, in both directions, across their outer cell membranes remains a mystery worthy of further investigation. In the near future,

microbial fuel cells could harness energy from waste water by replacing the energy-consuming bioreactors used in conventional treatment systems with those that produce bioelectricity or biohydrogen.

What is missing from *Bioenergy* is a discussion of the social and political implications of a microbe-based, biofuel economy. For example, growing algae or certain crops for biofuel production requires enormous amounts of water. Nutrient releases from different crops into the environment also need to be critically evaluated. The possibility of extracting methane from gas hydrates in the ocean floor is addressed but, from a climate-change perspective, the release of stored carbon in this fuel could have disastrous consequences.

Solving the energy crisis using renewable biofuels will require microbiologists, electrochemists, engineers and politicians. This book is an excellent overview of the many possible methods for harnessing microbes to make energy, and I hope it will inspire researchers from fields outside microbiology to move into bioenergy production. ■

**Bruce Logan** is the Kappe Professor of Environmental Engineering at Pennsylvania State University, and director of the Penn State Hydrogen Energy Center, University Park, Pennsylvania 16802, USA. He is author of *Microbial Fuel Cells*.  
e-mail: bel3@engr.psu.edu

## A potter round Darwin's patch

### Darwin's Garden: Down House and The Origin of Species

by Michael Boulter

Constable & Robinson/Counterpoint:  
2008/2009. 320 pp/272 pp.  
\$16.99/£17.95

Writing of his discovery, with Francis Crick, of the structure of DNA in *The Double Helix*, James Watson remarks: "much of our success was due to the long uneventful periods when we walked among the colleges". Likewise, the influence of place on the intellectual processes of the scientist is one of the most engaging ideas in Michael Boulter's new book about Charles Darwin's garden.

Darwin bought Down House, 23 kilometres from the centre of London, in 1842. He lived there with his family until his death 40 years later, and almost all of his most significant books and papers, including *On the Origin of Species*,

published in 1859, were written in its study. The 7 hectares of land belonging to the house provided Darwin with a range of environments in which to formulate, develop and test his ideas. The long Sandwalk, a circular path through native trees, was Darwin's main thinking spot, and he would walk several laps every day. In the kitchen gardens and meadows, he investigated the effects of natural and artificial selection, and in the glasshouses he experimented with the cross pollination of exotic plant species.

Boulter sets out in the first half of *Darwin's Garden* the history of the purchase of Down House, the family's move there and the use of the garden in Darwin's scientific work. The ideas explored are thought-provoking, and there can be no doubt that the garden at Down had an extremely important role in Darwin's work.

However, Boulter moves too frequently between discussion of the importance of place and of time, making it hard for the reader to



Finding new biofuel sources, such as algae that make hydrogen gas, might help solve the energy crisis.

Gaseous biofuels, such as hydrogen and methane, are made easily from many source materials using mature technologies. Hydrogen gas and volatile fatty acids, such as acetic acid, can be made from cellulose by fermentation. According to Ann Wilkie, most biomass sources can produce biomethane after limited preparation, such as drying or shredding. Certain microbes can convert acetic acid into methane gas, and methane or hydrogen can be converted to methanol. Hydrogen and methane are highly insoluble, so they can be recovered from water more easily than ethanol. In one of the seven chapters on methane and methanol, Bakul Dave reminds us that single-carbon fuels such as methanol lack carbon–carbon bonds, and therefore do not leave residues during combustion.

Combustion of hydrogen gas is better than methane as it produces only water. Three chapters are devoted to the production of hydrogen by photosynthesis in algae or bacteria, but none describes the use of fermentation or microbial electrolysis cells to make hydrogen. According to Marc Rousset and Laurent Cournac, hydrogenase enzymes that catalyse both the production and the consumption of hydrogen offer excellent opportunities to capture energy directly from sunlight, rather than through biomass, by splitting water into hydrogen and oxygen. But the sensitivity of these enzymes to oxygen needs to be decreased. Caroline Harwood describes using whole cells of purple non-sulphur bacteria to form hydrogen without splitting water. She notes that these cells can be immobilized in thin latex sheets to form panels. If perfected, this wonderful method could make hydrogen through the use of biosolar collectors.

My favourite bioenergy approach involves using bacteria to make electricity directly in microbial fuel cells. Certain strains of *Geobacter* might power these, but Peter Aelterman and his colleagues explain that many different types of bacteria release electrons to electrodes and can yield useful current. Why such a variety of bacteria can transfer electrons, in both directions, across their outer cell membranes remains a mystery worthy of further investigation. In the near future,

microbial fuel cells could harness energy from waste water by replacing the energy-consuming bioreactors used in conventional treatment systems with those that produce bioelectricity or biohydrogen.

What is missing from *Bioenergy* is a discussion of the social and political implications of a microbe-based, biofuel economy. For example, growing algae or certain crops for biofuel production requires enormous amounts of water. Nutrient releases from different crops into the environment also need to be critically evaluated. The possibility of extracting methane from gas hydrates in the ocean floor is addressed but, from a climate-change perspective, the release of stored carbon in this fuel could have disastrous consequences.

Solving the energy crisis using renewable biofuels will require microbiologists, electrochemists, engineers and politicians. This book is an excellent overview of the many possible methods for harnessing microbes to make energy, and I hope it will inspire researchers from fields outside microbiology to move into bioenergy production. ■

**Bruce Logan** is the Kappe Professor of Environmental Engineering at Pennsylvania State University, and director of the Penn State Hydrogen Energy Center, University Park, Pennsylvania 16802, USA. He is author of *Microbial Fuel Cells*.  
e-mail: bel3@engr.psu.edu

## A potter round Darwin's patch

### Darwin's Garden: Down House and The Origin of Species

by Michael Boulter

Constable & Robinson/Counterpoint:  
2008/2009. 320 pp/272 pp.  
\$16.99/£17.95

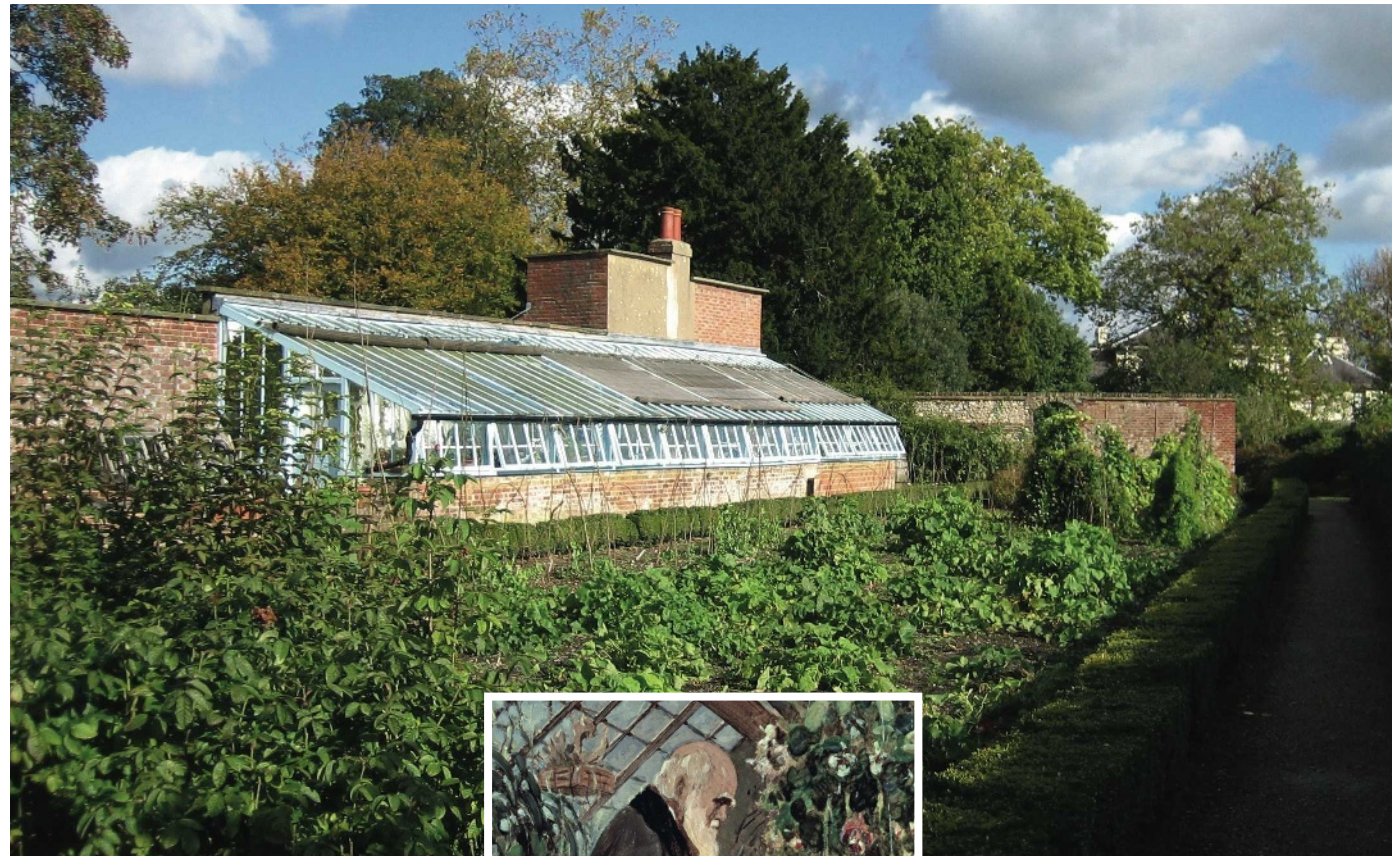
Writing of his discovery, with Francis Crick, of the structure of DNA in *The Double Helix*, James Watson remarks: "much of our success was due to the long uneventful periods when we walked among the colleges". Likewise, the influence of place on the intellectual processes of the scientist is one of the most engaging ideas in Michael Boulter's new book about Charles Darwin's garden.

Darwin bought Down House, 23 kilometres from the centre of London, in 1842. He lived there with his family until his death 40 years later, and almost all of his most significant books and papers, including *On the Origin of Species*,

published in 1859, were written in its study. The 7 hectares of land belonging to the house provided Darwin with a range of environments in which to formulate, develop and test his ideas. The long Sandwalk, a circular path through native trees, was Darwin's main thinking spot, and he would walk several laps every day. In the kitchen gardens and meadows, he investigated the effects of natural and artificial selection, and in the glasshouses he experimented with the cross pollination of exotic plant species.

Boulter sets out in the first half of *Darwin's Garden* the history of the purchase of Down House, the family's move there and the use of the garden in Darwin's scientific work. The ideas explored are thought-provoking, and there can be no doubt that the garden at Down had an extremely important role in Darwin's work.

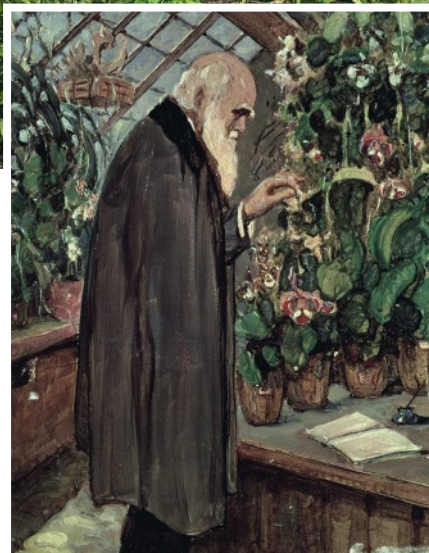
However, Boulter moves too frequently between discussion of the importance of place and of time, making it hard for the reader to



J. COLLIER, DOWN HOUSE, KENT/BRIDGEMAN ART LIBRARY

disentangle Darwin's influences. Darwin's work at the time was constrained by the lack of an explanation for the inheritance of characteristics, by the controversy surrounding the age of the Earth — at that stage few geologists, including Charles Lyell, advocated an Earth that was sufficiently old for the evolution of so many complex organisms — and by the prevailing views of society on the roles of mankind and religion in the world. These issues apply to all Victorian scientists, whereas the influence of Down House is specific to Darwin. Separate chapters on each topic might have made for a clearer analysis.

The book suggests that many of Darwin's breakthroughs came in single flashes of inspiration in the garden, rather than after years of painstaking work. Although it gives due credit to the years that Darwin spent investigating the morphology and taxonomy of barnacles, it gives much less weight to his similarly detailed work on orchids and other plants, work that made essential contributions to the development of his ideas about reproductive isolation and speciation. Boulter ascribes Darwin's explanation of how species become reproductively isolated from one another to his noticing a single hedge parsley plant in an unusual location. Boulter alleges that, from seeing a single plant in the wrong place, Darwin



apparently became convinced that migration and subsequent geographically isolated speciation could explain the origins of all new species. Yet it is highly unlikely that so simple a sight could provide all the answers. Evolutionary biologists still debate the issues surrounding speciation today.

Boulter next explores how Darwin's thoughts and experiments have contributed to modern science. He describes recent research on the mutant forms of orchid, which Darwin studied in the greenhouse at Down, and recent explanations for the rapid spread and diversification of flowering plants, which Darwin described as "an abominable mystery". This readable section provides insights into how a changing

**Darwin's scientific ideas were influenced by observations he made in the gardens and greenhouse at his home, Down House in Kent.**

scientific and social perspective can influence our interpretation of the living world. Yet here, in an understandable attempt to make difficult concepts clear to a broad audience, Boulter sacrifices scientific accuracy to an extent that undermines the specialist reader's confidence in the book as a whole. Contradictory statements about the ages of certain groups of organisms, a long section that gives the impression that *hox* genes controlling animal body segmentation are present in plants and a misleading definition of a gene are just some examples of the book's numerous errors.

*Darwin's Garden* is an enjoyable read that introduces some thought-provoking ideas about the roles of place, time and perception in the scientific process. If the science and the history are taken with a pinch of salt, it makes for a very good story. ■

**Beverley Glover** is senior lecturer in plant molecular genetics at the University of Cambridge, Department of Plant Sciences, Downing Street, Cambridge CB2 3EA, UK, and author of *Understanding Flowers and Flowering: An Integrated Approach*.  
e-mail: [bjg26@cam.ac.uk](mailto:bjg26@cam.ac.uk)



Agriculture in Niger's Sahel region has depleted the soil's nutrients.

D. ROSE/PANOS PICTURES

## Exhibition digs deep to save our soils

### Dig It! The Secrets of Soil

Smithsonian National Museum of Natural History, Washington DC  
Until 3 January 2010

Soil is more than mere dirt beneath our feet. It holds the nutrients that produce our food. More carbon is sequestered in soil than in all the plants on Earth, and its role as a carbon sink is becoming increasingly important as atmospheric carbon dioxide levels rise. A shovelful of soil can house more creatures, including earthworms, insects and microbes, than there are humans on Earth.

*Dig It! The Secrets of Soil*, a new exhibition showing at the Smithsonian Institution's National Museum of Natural History in Washington DC until January 2010, explores the science of Earth's skin with dioramas, videos and hands-on demonstrations.

Visitors can admire samples of the rocky black land of Texas, the chunky red soil of North Carolina, and earth from 52 other US states and territories. Red or yellow often indicates iron compounds, and black can signify manganese. Also offered are 'mystery soils' for sleuths to identify from a series of clues.

Most fun are the videos that put a soil spin on hit television series. In the animation *Chef's Challenge*, two soil cooks battle to make a pleasing ecosystem from the secret

ingredient — sand. One chef offers up a forest; another a bog. Judging between the two recipes are a turtle, a bird and a methane bubble called Gassy Gallagher. Naturally, Gallagher votes for the bog.

On another screen, the Soil Science Investigators look into the disappearance of a 45-kilogram blue ribbon pumpkin called Linus. Soil microbes in the pumpkin remains found at the crime scene help to estimate Linus's time of death, and wheelbarrow tracks reveal that the barrow passed through a forest. "Soil. It's the greatest. Tells us how things grow, how things die," intones Detective Clay. Oddly, though, the clue that finally cracks the caper isn't found in soil, but flour.

These fun skits hold serious messages. Soils take millennia to form, and their recipes are far from simple. But soils can be destroyed in decades.

Most life resides in the top few centimetres, and the majority of soil organisms remain unknown to science. Those that have been identified provide services as diverse as transferring nutrients between the air and plant roots, recycling dead creatures and making antibiotics such as penicillin.

Soil requires a delicately balanced chemistry to support its complex ecosystem of plants, animals, bacteria and fungi. Agriculture, in particular, strips nutrients from the topsoil and plants struggle when those nutrients are

not replenished. Adding fertilizer and leaving fields fallow can help revitalize them, but that isn't an option for poor farmers. In south Asia, people rely on manure and plant matter for fuel, so those nutrients are not recycled back into the soil. Pollution from irrigation water damages the land further.

More than two-thirds of Africa's soils are depleted, notably in Niger's Sahel region. People, animals and agriculture have destroyed native plants that held the soil in place. Water now flushes the soil away, and with it the nutrients for the farmer's crop.

The globe has faced thinning soils before; civilizations have fallen because their agriculture degraded the land. Ancient Mesopotamian city-dwellers diverted river water to irrigate fields. As it evaporated, mineral salts were left behind, making the land too salty for crops. Some suggest that California's San Joaquin Valley, which faces its own irrigation problems, is headed for a similar fate.

A deeper understanding of soil and its management, as explained in this exhibition, could lead to solutions for these global problems. As Franklin D. Roosevelt said, "The nation that destroys its soil, destroys itself." ■

**Amber Dance** is a News Intern in *Nature's* Washington DC office.

See <http://forces.si.edu/soils/index.html> for more details.

## NEWS &amp; VIEWS

## DEVELOPMENTAL BIOLOGY

## Neither fat nor flesh

Barbara Cannon and Jan Nedergaard

**In mammals, white adipose tissue stores fat, whereas brown adipose tissue burns fat. Brown adipocytes have a common origin with muscle cells, which could help explain their unusual function.**

In 1551, when the Swiss naturalist Konrad Gessner first described<sup>1</sup> brown adipose tissue, he stated that it was “neither fat, nor flesh [*nec pin-guitudo, nec caro*] — but something in between”. Some 450 years later, Tseng *et al.*<sup>2</sup> and Seale *et al.*<sup>3</sup>, writing in this issue, provide compelling evidence that brown and white fat cells are indeed distinct and that, after all, Gessner had correctly guessed the origin of brown fat cells — they are not flesh (muscle), but they are much more flesh-like than previously suspected.

Although sometimes found intermingled, brown and white fat cells form separate tissues. The white variety tends to have a bad press, as it is associated with obesity. Brown adipose tissue, by contrast, is regarded more favourably. It contains lots of mitochondria — in which cellular combustion occurs — and uniquely expresses the UCP1 protein. Through UCP1 activity, this tissue burns off eaten or stored fat to generate heat, keeping the organism warm and slim. Until recently, it was thought that, in humans, brown fat occurred only in newborns. But accumulating evidence suggests<sup>4</sup> that adults — or at least a significant fraction of us — retain metabolically active brown fat. Determining how brown fat cells form is therefore of broad interest, because mimicking this process could have potential use as a treatment for obesity.

Young white and brown fat cells look identical. As they develop, both forms accumulate fat, which led to the idea that they are of common origin. However, Tseng *et al.*<sup>2</sup> (page 1000) show that, although a brown fat cell might look like its white counterpart, both its origin and its destiny are different.

The authors find that, depending on the tissue of origin (brown or white adipose), precursor cells respond differently to external developmental cues. Bone morphogenetic proteins (BMPs) constitute one family of such molecular cues. For example, BMP2 and BMP4 support the development of white fat cells. Tseng and colleagues find that another member of the family, BMP7, can single-handedly promote the development of precursor brown fat cells into mature cells. The distinction seems to relate to the fact that only brown precursor cells can relay external signals to intracellular signalling pathways that lead to mature brown

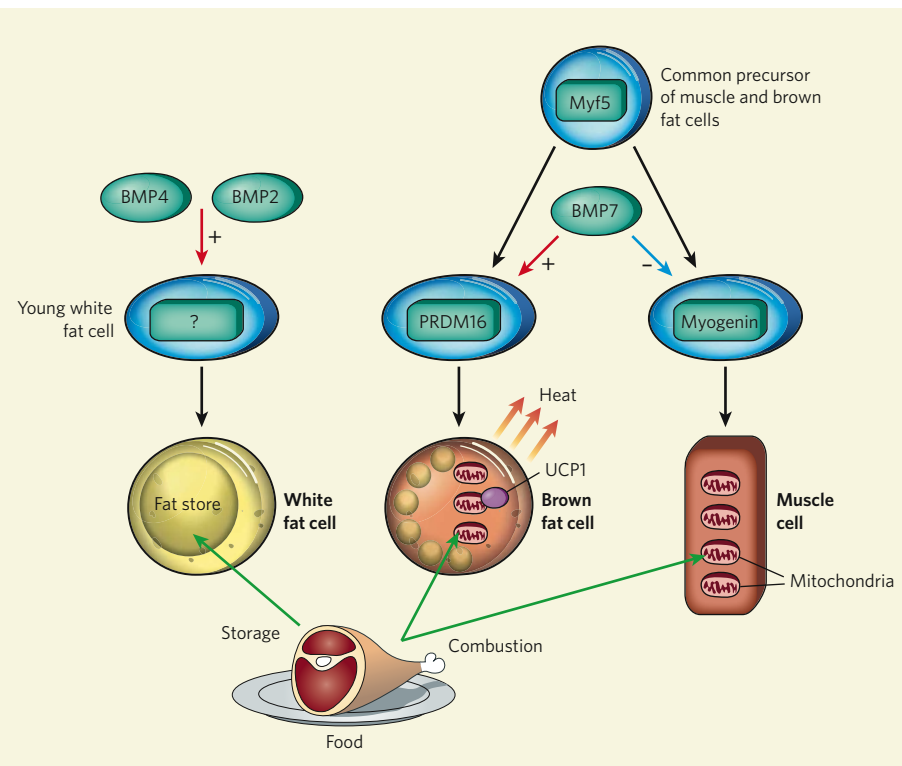


**Figure 1 | A revised model of the origins of fat cells.** White fat cells accumulate energy from food within a large fat droplet for later use (or not). Certain developmental cues, such as BMP2 and BMP4, induce young white fat cells to differentiate into mature fat cells. By contrast, brown fat cells, which also take up food energy, use it up in their mitochondria through the activity of the UCP1 protein. It emerges that brown fat cells share their predecessor cells with muscle cells. Some of these precursor cells — for example, those controlled by BMP7 (ref. 2) — can be induced to express PRDM16, a transcription factor that will direct them into the pathway to develop into brown fat cells<sup>3</sup>. In the absence of PRDM16, and possibly owing to the activity of myogenin, the precursor cells develop into muscle cells, which also contain many mitochondria and use energy, but here they use it for real work.

fat cells. Animals lacking the *Bmp7* gene fail to develop brown fat properly<sup>2</sup>.

The study by Seale *et al.*<sup>3</sup> (page 961) supports this distinction between white and brown fat cells by showing that the two cell types originate from separate precursor cells in the early embryo. Studying the expression of the muscle developmental gene *Myf5*, the authors followed the fate of all cells that at some stage had the potential to become muscle cells. As expected, they find that muscle cells arise from pre-muscle cells but, surprisingly, that brown fat cells do too — whereas white fat cells do not.

So during brown-fat-cell development, there may be a point when a cell’s fate to become muscle or brown fat is not yet sealed, but when becoming a white fat cell is not an option. Seale and colleagues find<sup>3,5</sup> that the gene transcription factor PRDM16 determines the fate of precursor cells to become brown fat cells. In the absence of this factor, precursor cells become muscle, and on its increased expression, precursor cells become brown fat cells.

Does a similar factor determine muscle-cell fate? Yes indeed. Mice deficient in the protein

myogenin lack muscle and die soon after birth<sup>6</sup>. Instead, in some areas of the animals' body, where muscle should have developed, brown fat is found. So it seems that, when the precursor of a muscle/brown-fat cell does not receive a complete muscle-promoting signal, it becomes a brown fat cell; and, when it doesn't receive a complete signal for becoming a brown fat cell, it becomes a muscle cell (Fig. 1).

In addition to the classic brown fat cells that share precursors with muscle cells, the authors find that some brown fat cells exist that seem more closely related to white fat cells. In tissues in which white adipose tissue predominates, it is possible to stimulate the formation of brown-fat-like cells. Whether a true transformation of fat cells from white to brown occurs, or whether some brown fat cells disguised as white are activated to divide and display 'brown' characteristics is unknown. But Seale *et al.*<sup>3</sup> make one point clear: these brown-fat-like cells are different from their muscle-related brown counterparts — they have never expressed *Myf5* and they do not differentiate in response to PRDM16 expression.

The unexpected discovery that brown fat and muscle cells share a common origin clarifies a series of hitherto disparate and curious observations. Very young, undifferentiated brown fat cells contain messenger RNAs for proteins that are normally found in muscle, such as *Myf5* and myosin<sup>7</sup>. As the cells begin to differentiate, however, these mRNAs gradually disappear. Another study<sup>8</sup> noted that, at an early stage of embryonic development, certain cells give rise to both muscle and brown fat. At this stage of development, however, white fat cells have not formed. The disparate origins of white and brown fat cells could therefore not be discerned — something Seale and colleagues now show with certainty.

Many proteins found in brown fat cells — especially those involved in fat uptake from the blood, intracellular fat transport and mitochondrial fat combustion — are more similar to those found in muscle than in white adipose tissue. So the more one thinks about it, the more reasonable it seems that muscle and brown fat cells are closely related. And perhaps we must now look at a brown fat cell as an 'adipomyocyte' — that is, as a muscle cell that has accumulated fat — rather than as a variety of white fat cell.

Insights into the developmental origin of brown fat cells are of particular interest because of the ability of these cells to burn fat. But, as is often the case in science, new questions follow new insights. What determines the presence of BMP7 in the vicinity of precursor brown fat cells? What is the molecular switch that determines PRDM16 expression and so the fate of the common brown-fat/muscle precursor cell to become "neither fat nor flesh — but something in between"? Answers to these questions would take us a step closer to the ultimate goal of promoting the brown fat lineage as a potential way of counteracting obesity. ■

Barbara Cannon and Jan Nedergaard are at the Wenner-Gren Institute, Arrhenius Laboratories F3, Stockholm University, SE-106 91 Stockholm, Sweden.

e-mail: barbara.cannon@wgi.su.se

1. Gessner, K. *Conradi Gesneri medici Tigurine Historiae Animalium Lib. I de Quadripedibus uiuiparis* 842 (1551).

2. Tseng, Y.-H. *et al.* *Nature* **454**, 1000–1004 (2008).
3. Seale, P. *et al.* *Nature* **454**, 961–967 (2008).
4. Nedergaard, J., Bengtsson, T. & Cannon, B. *Am. J. Physiol. Endocrinol. Metab.* **293**, E444–E452 (2007).
5. Seale, P. *et al.* *Cell Metab.* **6**, 38–54 (2007).
6. Hasty, P. *et al.* *Nature* **364**, 501–506 (1993).
7. Timmons, J. A. *et al.* *Proc. Natl. Acad. Sci. USA* **104**, 4401–4406 (2007).
8. Atit, R. *et al.* *Dev. Biol.* **296**, 164–176 (2006).

## CHEMISTRY

# Precious little catalyst

D. Wayne Goodman

**In gold catalysis, less is more. Bulk gold is an inert metal, but tiny particles containing as few as 55 gold atoms are effective at catalysing the targeted oxidation of hydrocarbons.**

Until around 20 years ago, gold was thought to be catalytically inactive. During the past two decades this view has been changed with various demonstrations that vanishingly small particles of gold, 3–5 nanometres in diameter, are highly active catalysts for a range of reactions. The origin of this size-dependent catalytic power remains poorly understood. On page 981 of this issue, Turner *et al.*<sup>1</sup> report on the ability of gold particles as small as 1.5 nanometres to catalyse the selective oxidation of alkenes by molecular oxygen alone.

The first breakthrough in catalysis by nano-sized gold came in 1987, when gold nanoparticles supported on semiconducting transition-metal oxides were found to catalyse the oxidation of carbon monoxide efficiently at low temperatures<sup>2,3</sup>. About a decade later, it was established that gold nanoparticles supported on titanium dioxide ( $TiO_2$ ) were effective for the more complex reaction of alkene epoxidation — in which an oxygen atom is inserted into the hydrocarbon's carbon–carbon double bond — when supplied with a mixture of oxygen and hydrogen<sup>4</sup>. Again and again, a new and exciting catalytic behaviour of gold was realized by decreasing the size of the gold particles. After these early successes, the field of nano-sized gold particles has developed into an area of intense research.

Despite the attention directed towards it, many questions remain about the fundamental processes underlying the properties of small gold particles and the mechanistic basis for the reactions that they catalyse. Previous investigations have been hampered by the need for molecular oxygen ( $O_2$ ; also known as dioxygen) to be supplemented with additives (such as hydrogen<sup>4</sup> or a peroxide species<sup>5</sup>) or a specific support such as titanium dioxide to achieve gold-catalysed partial oxidation reactions. This has made it difficult to assess the relative importance of the gold particles, catalyst additives and supports in activating  $O_2$ . The catalysts described by Turner *et al.*<sup>1</sup> require no

additives but are derived from 55-atom gold clusters ( $Au_{55}$ ) scattered across the surface of inert supports. These require only dioxygen to effect the selective oxidation of hydrocarbons, making them ideal environmentally friendly oxidation catalysts.

The oxidation reaction studied by Turner *et al.* is that of styrene, a derivative of benzene containing an isolated carbon–carbon double bond. In this reaction, an oxygen atom attacks the alkene's double bond to produce three major products: benzaldehyde, styrene oxide (an epoxide with a triangular arrangement of two carbon atoms and one oxygen atom) and acetophenone (Fig. 1). Oxygenated hydrocarbons, especially epoxides, are extremely valuable chemical intermediates, used in a wide range of industrial and fine chemical applications.

If atomic oxygen could be deposited on gold, partial oxidation of organic molecules such as styrene should occur readily, even on extended surfaces of solid metal<sup>6,7</sup>. However, unlike metals such as platinum or silver, extended gold surfaces do not activate oxygen; that is, they cannot adsorb dioxygen to their surface layer in such a way that the molecule is separated into individual oxygen atoms; only the adsorption of molecular oxygen is possible<sup>8</sup>. Turner *et al.*<sup>1</sup> show that, unlike larger surfaces, gold particles less than about 2 nanometres in diameter can activate dioxygen and thus promote the partial oxidation reaction. Larger gold particles, whether synthesized from 55-atom clusters or by other preparation routes, were completely inactive.

The 55-atom clusters from which Turner *et al.* make their catalysts (by carefully controlled heat treatment) are an example of 'magic-number' clusters. They contain exactly the right number of atoms to form particularly regular geometries and thus extremely stable particles. The magic-number cluster  $Au_{55}$  was first discovered by Schmid *et al.*<sup>9</sup> and has since been the subject of several characterization

myogenin lack muscle and die soon after birth<sup>6</sup>. Instead, in some areas of the animals' body, where muscle should have developed, brown fat is found. So it seems that, when the precursor of a muscle/brown-fat cell does not receive a complete muscle-promoting signal, it becomes a brown fat cell; and, when it doesn't receive a complete signal for becoming a brown fat cell, it becomes a muscle cell (Fig. 1).

In addition to the classic brown fat cells that share precursors with muscle cells, the authors find that some brown fat cells exist that seem more closely related to white fat cells. In tissues in which white adipose tissue predominates, it is possible to stimulate the formation of brown-fat-like cells. Whether a true transformation of fat cells from white to brown occurs, or whether some brown fat cells disguised as white are activated to divide and display 'brown' characteristics is unknown. But Seale *et al.*<sup>3</sup> make one point clear: these brown-fat-like cells are different from their muscle-related brown counterparts — they have never expressed *Myf5* and they do not differentiate in response to PRDM16 expression.

The unexpected discovery that brown fat and muscle cells share a common origin clarifies a series of hitherto disparate and curious observations. Very young, undifferentiated brown fat cells contain messenger RNAs for proteins that are normally found in muscle, such as *Myf5* and myosin<sup>7</sup>. As the cells begin to differentiate, however, these mRNAs gradually disappear. Another study<sup>8</sup> noted that, at an early stage of embryonic development, certain cells give rise to both muscle and brown fat. At this stage of development, however, white fat cells have not formed. The disparate origins of white and brown fat cells could therefore not be discerned — something Seale and colleagues now show with certainty.

Many proteins found in brown fat cells — especially those involved in fat uptake from the blood, intracellular fat transport and mitochondrial fat combustion — are more similar to those found in muscle than in white adipose tissue. So the more one thinks about it, the more reasonable it seems that muscle and brown fat cells are closely related. And perhaps we must now look at a brown fat cell as an 'adipomyocyte' — that is, as a muscle cell that has accumulated fat — rather than as a variety of white fat cell.

Insights into the developmental origin of brown fat cells are of particular interest because of the ability of these cells to burn fat. But, as is often the case in science, new questions follow new insights. What determines the presence of BMP7 in the vicinity of precursor brown fat cells? What is the molecular switch that determines PRDM16 expression and so the fate of the common brown-fat/muscle precursor cell to become "neither fat nor flesh — but something in between"? Answers to these questions would take us a step closer to the ultimate goal of promoting the brown fat lineage as a potential way of counteracting obesity. ■

Barbara Cannon and Jan Nedergaard are at the Wenner-Gren Institute, Arrhenius Laboratories F3, Stockholm University, SE-106 91 Stockholm, Sweden.

e-mail: barbara.cannon@wgi.su.se

1. Gessner, K. *Conradi Gesneri medici Tigurine Historiae Animalium Lib. I de Quadripedibus uiuiparis* 842 (1551).

2. Tseng, Y.-H. *et al.* *Nature* **454**, 1000–1004 (2008).
3. Seale, P. *et al.* *Nature* **454**, 961–967 (2008).
4. Nedergaard, J., Bengtsson, T. & Cannon, B. *Am. J. Physiol. Endocrinol. Metab.* **293**, E444–E452 (2007).
5. Seale, P. *et al.* *Cell Metab.* **6**, 38–54 (2007).
6. Hasty, P. *et al.* *Nature* **364**, 501–506 (1993).
7. Timmons, J. A. *et al.* *Proc. Natl. Acad. Sci. USA* **104**, 4401–4406 (2007).
8. Atit, R. *et al.* *Dev. Biol.* **296**, 164–176 (2006).

## CHEMISTRY

# Precious little catalyst

D. Wayne Goodman

**In gold catalysis, less is more. Bulk gold is an inert metal, but tiny particles containing as few as 55 gold atoms are effective at catalysing the targeted oxidation of hydrocarbons.**

Until around 20 years ago, gold was thought to be catalytically inactive. During the past two decades this view has been changed with various demonstrations that vanishingly small particles of gold, 3–5 nanometres in diameter, are highly active catalysts for a range of reactions. The origin of this size-dependent catalytic power remains poorly understood. On page 981 of this issue, Turner *et al.*<sup>1</sup> report on the ability of gold particles as small as 1.5 nanometres to catalyse the selective oxidation of alkenes by molecular oxygen alone.

The first breakthrough in catalysis by nano-sized gold came in 1987, when gold nanoparticles supported on semiconducting transition-metal oxides were found to catalyse the oxidation of carbon monoxide efficiently at low temperatures<sup>2,3</sup>. About a decade later, it was established that gold nanoparticles supported on titanium dioxide ( $TiO_2$ ) were effective for the more complex reaction of alkene epoxidation — in which an oxygen atom is inserted into the hydrocarbon's carbon–carbon double bond — when supplied with a mixture of oxygen and hydrogen<sup>4</sup>. Again and again, a new and exciting catalytic behaviour of gold was realized by decreasing the size of the gold particles. After these early successes, the field of nano-sized gold particles has developed into an area of intense research.

Despite the attention directed towards it, many questions remain about the fundamental processes underlying the properties of small gold particles and the mechanistic basis for the reactions that they catalyse. Previous investigations have been hampered by the need for molecular oxygen ( $O_2$ ; also known as dioxygen) to be supplemented with additives (such as hydrogen<sup>4</sup> or a peroxide species<sup>5</sup>) or a specific support such as titanium dioxide to achieve gold-catalysed partial oxidation reactions. This has made it difficult to assess the relative importance of the gold particles, catalyst additives and supports in activating  $O_2$ . The catalysts described by Turner *et al.*<sup>1</sup> require no

additives but are derived from 55-atom gold clusters ( $Au_{55}$ ) scattered across the surface of inert supports. These require only dioxygen to effect the selective oxidation of hydrocarbons, making them ideal environmentally friendly oxidation catalysts.

The oxidation reaction studied by Turner *et al.* is that of styrene, a derivative of benzene containing an isolated carbon–carbon double bond. In this reaction, an oxygen atom attacks the alkene's double bond to produce three major products: benzaldehyde, styrene oxide (an epoxide with a triangular arrangement of two carbon atoms and one oxygen atom) and acetophenone (Fig. 1). Oxygenated hydrocarbons, especially epoxides, are extremely valuable chemical intermediates, used in a wide range of industrial and fine chemical applications.

If atomic oxygen could be deposited on gold, partial oxidation of organic molecules such as styrene should occur readily, even on extended surfaces of solid metal<sup>6,7</sup>. However, unlike metals such as platinum or silver, extended gold surfaces do not activate oxygen; that is, they cannot adsorb dioxygen to their surface layer in such a way that the molecule is separated into individual oxygen atoms; only the adsorption of molecular oxygen is possible<sup>8</sup>. Turner *et al.*<sup>1</sup> show that, unlike larger surfaces, gold particles less than about 2 nanometres in diameter can activate dioxygen and thus promote the partial oxidation reaction. Larger gold particles, whether synthesized from 55-atom clusters or by other preparation routes, were completely inactive.

The 55-atom clusters from which Turner *et al.* make their catalysts (by carefully controlled heat treatment) are an example of 'magic-number' clusters. They contain exactly the right number of atoms to form particularly regular geometries and thus extremely stable particles. The magic-number cluster  $Au_{55}$  was first discovered by Schmid *et al.*<sup>9</sup> and has since been the subject of several characterization

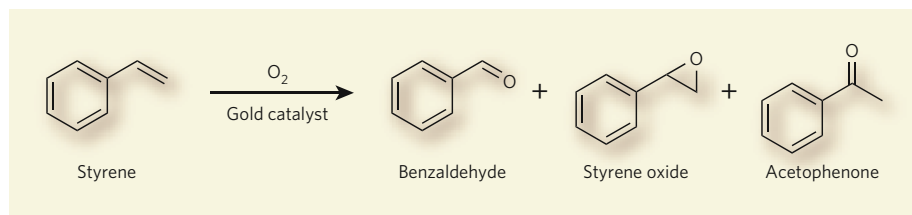


**Figure 1 | Fruits of gold.** Gold is generally considered to be an inert metal but when present as nanoparticles the situation is very different. Turner *et al.*<sup>1</sup> have used particles of gold less than 2 nanometres in diameter, derived from highly stable 55-atom clusters, to catalyse the selective oxidation of the aromatic alkene styrene. The reaction chiefly yielded benzaldehyde, with smaller amounts of styrene oxide and acetophenone.

studies. However, the study by Turner *et al.*<sup>1</sup> seems to be the first to use Au<sub>55</sub> in the synthesis of supported gold catalysts. The Au<sub>55</sub> clusters have a diameter of about 1.4 nanometres, essentially the size of the catalysts used in their work. The use of cluster chemistry would therefore seem a convenient and direct route to produce particles too small to be easily synthesized by conventional preparation methods. Furthermore, the technique yields a very narrow and reproducible size distribution for the resulting particles. Traditional catalyst preparation methods typically result in a range of particle sizes that is difficult to control, confounding attempts to relate structure to activity in gold catalysis.

What, then, makes gold particles of this size so special? The activity of nanoscale gold has been attributed to the presence of low-coordination sites<sup>6,10,11</sup>: gold atoms at the

surface, edge or corner of a particle that have fewer nearest neighbours than bulk atoms, leaving them more free to engage in chemical reactions. The smaller the particle, the larger is the density of these coordinatively unsaturated sites relative to the total number of atoms in the particle. The catalyst particles are also comparable in size to the de Broglie wavelength of an electron. This attribute can radically alter the electronic properties of the particle<sup>12</sup>. Either or both of these phenomena may be responsible for the gold clusters' catalytic dexterity.

To understand why size matters, Turner *et al.*<sup>1</sup> conducted X-ray photoelectron spectroscopic studies of their gold catalysts. The authors found that the electronic properties of the gold in their nano-sized catalyst had altered from those of a bulk gold sample. This modified electronic structure may be the source of the radically different

activity of the ~1.5-nanometre particles, but precisely how they can dissociatively adsorb oxygen remains unclear.

The studies of Turner *et al.* open numerous avenues for further exploration. An obvious next step would be to explore other reactions for which these gold particles act as catalysts. It will also be interesting to investigate whether gold nano-clusters are as effective in the gas phase as in the liquid phase. In any case, this work provides a new approach for the consistent synthesis of very small gold nano-clusters and will stimulate activity in the exciting area of gold catalysis. ■

D. Wayne Goodman is in the Department of Chemistry, Texas A&M University, College Station, Texas 77843-3255, USA.  
e-mail: goodman@mail.chem.tamu.edu

1. Turner, M. *et al.* *Nature* **454**, 981–983 (2008).
2. Haruta, M., Kobayashi, T., Sano, H. & Yamada, N. *Chem. Lett.* **16**, 405–408 (1987).
3. Haruta, M. *et al.* *Catal. Today* **36**, 153–166 (1997).
4. Hayashi, T., Tanaka, K. & Haruta, M. *J. Catal.* **178**, 566–575 (1998).
5. Hughes, M. D. *et al.* *Nature* **437**, 1132–1135 (2005).
6. Min, B. K. & Friend, C. M. *Chem. Rev.* **107**, 2709–2724 (2007).
7. Turner, M., Vaughan, O. P. H. & Lambert, R. M. *Chem. Commun.* 2316–2318 (2008).
8. Sault, A. G., Madix, R. J. & Campbell, C. T. *Surf. Sci.* **169**, 347–356 (1986).
9. Schmid, G. *et al.* *Chem. Ber. Recl.* **114**, 3634–3642 (1981).
10. Chen, M. & Goodman, D. W. *Acc. Chem. Res.* **39**, 739–746 (2006).
11. Falsig, H. *et al.* *Angew. Chem. Int. Edn* **47**, 4835–4839 (2008).
12. Valden, M., Lai, X. & Goodman, D. W. *Science* **281**, 1647–1650 (1998).

## PHYSIOLOGY

# Mutant flies lack magnetic sense

François Rouyer

**It seems that fruitflies can detect magnetic fields, but only if they are illuminated with blue light. Mutant flies reveal that a light-responsive receptor underpins this peculiar behaviour.**

Animals detect various wavelengths of light, from ultraviolet to red, using photoreceptor proteins. One reason for doing this is to synchronize their circadian clocks with the day–night cycle. In the fruitfly *Drosophila melanogaster*, a vital photoreceptor for this synchronization is cryptochrome, which uses blue light to reset circadian clocks<sup>1</sup>. Reporting on page 1014 of this issue, Geegear *et al.*<sup>2</sup> reveal a new function of this intriguing molecule. They show that both cryptochrome and blue light are required for fruitflies to sense magnetic fields.

Magnetoreception is often found in the animal kingdom, perhaps most notably in migratory species, which use Earth's magnetic field as an aid to navigation. Several mechanisms have been proposed, including electromagnetic induction, in which an electric

current is generated in a conductive organ as it passes through a magnetic field; the use of nano-sized crystals of the mineral magnetite as 'compasses'; and the modulation of magnetic-field-dependent biochemical reactions<sup>3</sup>. The biochemical mechanism might rely on the so-called radical-pair model<sup>4</sup>, in which the magnetic field modifies the electronic state of paired ions in a reacting molecule, thus altering the product of the reaction.

So which proteins could host a radical-pair mechanism for magnetoreception? Photoreceptors are strong candidates, because several examples of light-dependent magnetoreception have been described<sup>5–7</sup>. Short wavelengths of light seem to be important in these cases, so cryptochrome, which responds to blue light, has been proposed as a candidate molecule<sup>8–10</sup>. This theory is bolstered by the

finding that cryptochrome function in plants is affected by magnetic fields<sup>11</sup>. Geegear *et al.*<sup>2</sup> decided to investigate further, using fruitflies as a convenient, genetically modifiable model of other animals.

The authors first set up a simple behavioural test to assay magnetoreception in fruitflies, by making a device in which the flies could choose to enter a tube bathed in a magnetic field or one that was not. They tested several strains of wild-type flies in this way. Only flies from a few of these strains preferentially chose the tube without a magnetic field, indicating that the responses of fruitflies to magnetic fields are strongly influenced by genetic background. This is perhaps unsurprising, because such influences are a recurrent problem in behavioural experiments in general.

Geegear *et al.* therefore decided to motivate the flies to choose between the two tubes, by designing a protocol that trained them to associate magnetic fields with a reward of sugar. The authors starved their experimental subjects for a day, then placed them in a sugar-containing tube in a magnetic field. This treatment proved to be an excellent motivator: when presented with two tubes as before, all the trained flies preferentially chose the tube placed in a magnetic field, regardless of their genetic background.

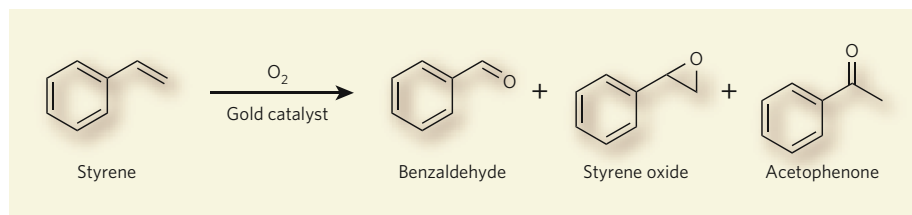


**Figure 1 | Fruits of gold.** Gold is generally considered to be an inert metal but when present as nanoparticles the situation is very different. Turner *et al.*<sup>1</sup> have used particles of gold less than 2 nanometres in diameter, derived from highly stable 55-atom clusters, to catalyse the selective oxidation of the aromatic alkene styrene. The reaction chiefly yielded benzaldehyde, with smaller amounts of styrene oxide and acetophenone.

studies. However, the study by Turner *et al.*<sup>1</sup> seems to be the first to use Au<sub>55</sub> in the synthesis of supported gold catalysts. The Au<sub>55</sub> clusters have a diameter of about 1.4 nanometres, essentially the size of the catalysts used in their work. The use of cluster chemistry would therefore seem a convenient and direct route to produce particles too small to be easily synthesized by conventional preparation methods. Furthermore, the technique yields a very narrow and reproducible size distribution for the resulting particles. Traditional catalyst preparation methods typically result in a range of particle sizes that is difficult to control, confounding attempts to relate structure to activity in gold catalysis.

What, then, makes gold particles of this size so special? The activity of nanoscale gold has been attributed to the presence of low-coordination sites<sup>6,10,11</sup>: gold atoms at the

surface, edge or corner of a particle that have fewer nearest neighbours than bulk atoms, leaving them more free to engage in chemical reactions. The smaller the particle, the larger is the density of these coordinatively unsaturated sites relative to the total number of atoms in the particle. The catalyst particles are also comparable in size to the de Broglie wavelength of an electron. This attribute can radically alter the electronic properties of the particle<sup>12</sup>. Either or both of these phenomena may be responsible for the gold clusters' catalytic dexterity.

To understand why size matters, Turner *et al.*<sup>1</sup> conducted X-ray photoelectron spectroscopic studies of their gold catalysts. The authors found that the electronic properties of the gold in their nano-sized catalyst had altered from those of a bulk gold sample. This modified electronic structure may be the source of the radically different

activity of the ~1.5-nanometre particles, but precisely how they can dissociatively adsorb oxygen remains unclear.

The studies of Turner *et al.* open numerous avenues for further exploration. An obvious next step would be to explore other reactions for which these gold particles act as catalysts. It will also be interesting to investigate whether gold nano-clusters are as effective in the gas phase as in the liquid phase. In any case, this work provides a new approach for the consistent synthesis of very small gold nano-clusters and will stimulate activity in the exciting area of gold catalysis. ■

D. Wayne Goodman is in the Department of Chemistry, Texas A&M University, College Station, Texas 77843-3255, USA.  
e-mail: goodman@mail.chem.tamu.edu

1. Turner, M. *et al.* *Nature* **454**, 981–983 (2008).
2. Haruta, M., Kobayashi, T., Sano, H. & Yamada, N. *Chem. Lett.* **16**, 405–408 (1987).
3. Haruta, M. *et al.* *Catal. Today* **36**, 153–166 (1997).
4. Hayashi, T., Tanaka, K. & Haruta, M. *J. Catal.* **178**, 566–575 (1998).
5. Hughes, M. D. *et al.* *Nature* **437**, 1132–1135 (2005).
6. Min, B. K. & Friend, C. M. *Chem. Rev.* **107**, 2709–2724 (2007).
7. Turner, M., Vaughan, O. P. H. & Lambert, R. M. *Chem. Commun.* 2316–2318 (2008).
8. Sault, A. G., Madix, R. J. & Campbell, C. T. *Surf. Sci.* **169**, 347–356 (1986).
9. Schmid, G. *et al.* *Chem. Ber. Recl.* **114**, 3634–3642 (1981).
10. Chen, M. & Goodman, D. W. *Acc. Chem. Res.* **39**, 739–746 (2006).
11. Falsig, H. *et al.* *Angew. Chem. Int. Edn* **47**, 4835–4839 (2008).
12. Valden, M., Lai, X. & Goodman, D. W. *Science* **281**, 1647–1650 (1998).

## PHYSIOLOGY

# Mutant flies lack magnetic sense

François Rouyer

**It seems that fruitflies can detect magnetic fields, but only if they are illuminated with blue light. Mutant flies reveal that a light-responsive receptor underpins this peculiar behaviour.**

Animals detect various wavelengths of light, from ultraviolet to red, using photoreceptor proteins. One reason for doing this is to synchronize their circadian clocks with the day–night cycle. In the fruitfly *Drosophila melanogaster*, a vital photoreceptor for this synchronization is cryptochrome, which uses blue light to reset circadian clocks<sup>1</sup>. Reporting on page 1014 of this issue, Geegear *et al.*<sup>2</sup> reveal a new function of this intriguing molecule. They show that both cryptochrome and blue light are required for fruitflies to sense magnetic fields.

Magnetoreception is often found in the animal kingdom, perhaps most notably in migratory species, which use Earth's magnetic field as an aid to navigation. Several mechanisms have been proposed, including electromagnetic induction, in which an electric

current is generated in a conductive organ as it passes through a magnetic field; the use of nano-sized crystals of the mineral magnetite as 'compasses'; and the modulation of magnetic-field-dependent biochemical reactions<sup>3</sup>. The biochemical mechanism might rely on the so-called radical-pair model<sup>4</sup>, in which the magnetic field modifies the electronic state of paired ions in a reacting molecule, thus altering the product of the reaction.

So which proteins could host a radical-pair mechanism for magnetoreception? Photoreceptors are strong candidates, because several examples of light-dependent magnetoreception have been described<sup>5–7</sup>. Short wavelengths of light seem to be important in these cases, so cryptochrome, which responds to blue light, has been proposed as a candidate molecule<sup>8–10</sup>. This theory is bolstered by the

finding that cryptochrome function in plants is affected by magnetic fields<sup>11</sup>. Geegear *et al.*<sup>2</sup> decided to investigate further, using fruitflies as a convenient, genetically modifiable model of other animals.

The authors first set up a simple behavioural test to assay magnetoreception in fruitflies, by making a device in which the flies could choose to enter a tube bathed in a magnetic field or one that was not. They tested several strains of wild-type flies in this way. Only flies from a few of these strains preferentially chose the tube without a magnetic field, indicating that the responses of fruitflies to magnetic fields are strongly influenced by genetic background. This is perhaps unsurprising, because such influences are a recurrent problem in behavioural experiments in general.

Geegear *et al.* therefore decided to motivate the flies to choose between the two tubes, by designing a protocol that trained them to associate magnetic fields with a reward of sugar. The authors starved their experimental subjects for a day, then placed them in a sugar-containing tube in a magnetic field. This treatment proved to be an excellent motivator: when presented with two tubes as before, all the trained flies preferentially chose the tube placed in a magnetic field, regardless of their genetic background.



## 50 YEARS AGO

It has been observed in this laboratory that when aqueous mixtures of dicarboxylic or monocarboxylic acids and certain ammonium salts are irradiated with ultra-violet light, certain amino-acids are obtained.

A cold quartz ultra-violet lamp giving 86 per cent of its output at about 2537 Å was used for irradiated mixtures of succinic, maleic, propionic and acetic acid with a number of ammonium salts ... The irradiation was continued in each case for 24 hr ...

Of all the ammonium compounds investigated only ammonia and ammonium carbonate were active, and of the acids only succinic, maleic and propionic acid gave rise to amino-acids ...

The amino-acids are aspartic acid, alanine and glycine, that is to say, amino-acids with 4, 3 and 2 carbon atoms respectively.

From *Nature* 23 August 1958

## 100 YEARS AGO

The Rev. J. W. Hayes, of West Thurrock Vicarage, Grays, has directed attention to some old underground workings for chalk at Hemel Hempstead, which in his opinion throw much light on the origin and use of dene-holes generally. It appears that in order to obtain chalk suitable for lime-making it was until recently the practice ... to work the chalk in subterranean chambers reached by deep shafts ... A vertical shaft, of circular section, about 5 feet in diameter, was sunk through superficial deposits until the hard chalk was reached, and from the bottom of the shaft three so-called "arches" were struck out. These arches were chambers, which in some cases were more than 12 feet high. The chalk was mined in these drifts for a length of twenty to twenty-five yards, and when the distance of the working face from the bottom of the shaft became inconveniently great, or when the roof proved unsound, a new pit would be sunk.

From *Nature* 20 August 1908

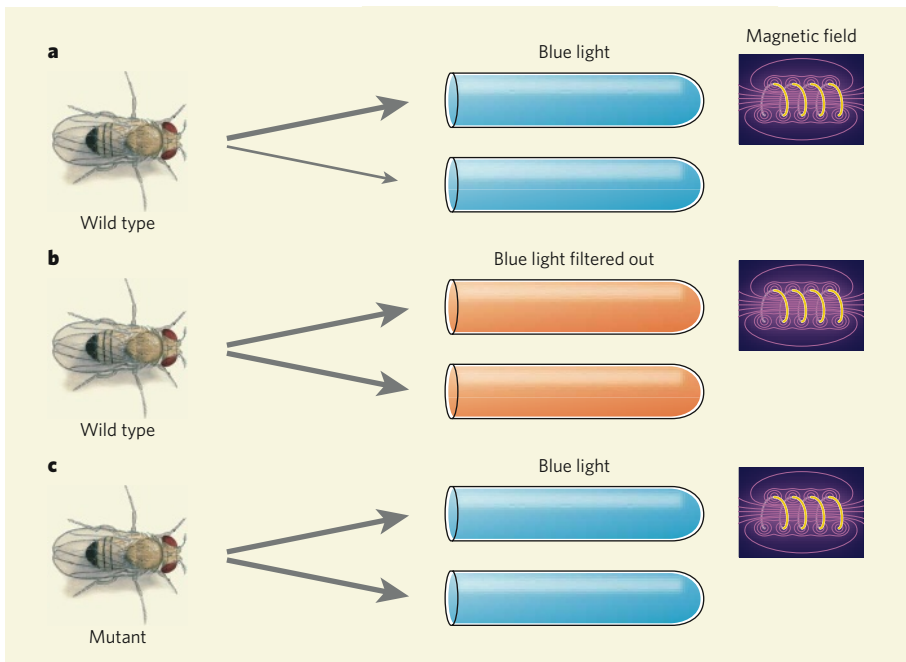


**Figure 1 | Magnetoreception in fruitflies.** Gegear *et al.*<sup>2</sup> studied the ability of fruitflies to detect a magnetic field. **a**, When trained to associate a magnetic field with a reward of sugar, wild-type flies preferentially choose to enter a tube that is bathed in a magnetic field, rather than one that is not, so long as blue light illuminates the experiment. **b**, The trained flies demonstrate no preference for the tubes if blue light is filtered out of the illumination. **c**, Genetically modified flies that lack the photoreceptor cryptochrome (which responds to blue light) do not recognize the magnetic field, even in the presence of blue light, showing that cryptochrome is essential for magnetoreception in fruitflies.

Previous studies<sup>6</sup> have shown that fruitflies respond differently to magnetic fields depending on the wavelength of light that they are exposed to. Gegear *et al.* therefore investigated the influence of different light colours on the behaviour of their trained flies, concentrating on the blue end of the spectrum for the reasons mentioned earlier. Their results indicate that light is indeed required for fruitfly magnetosensitivity — the flies were unable to detect magnetic fields in the absence of light of short wavelength (less than 420 nanometres; Fig. 1). This is close to the region of the spectrum that is absorbed by cryptochrome, suggesting that the photoreceptor might be involved in this behaviour.

To confirm the role of cryptochrome in magnetoreception, the authors tested mutant *cry<sup>0</sup>* flies, which lack the photoreceptor, in their behavioural assay. They found that untrained wild-type flies that have the same genetic background as *cry<sup>0</sup>* flies are attracted to magnetic fields. But the *cry<sup>0</sup>* mutants showed no response to the magnetic field, even if they had been through the training protocol. Moreover, flies that carried a different cryptochrome mutation — one that disrupts most of the photoreceptor's function without deleting the protein completely — were also unresponsive to the magnetic field. This strongly bolsters the idea that cryptochrome is a vital component of light-dependent magnetoreception in fruitflies.

Because cryptochrome is involved in setting the circadian clock in flies' brains, and could also have a clock-gene function in other

tissues<sup>1</sup>, Gegear *et al.* checked to see whether the flies' magnetoreceptive response depended on having a functional circadian clock. The answer was no. Even in conditions that caused the flies to be circadianly arrhythmic, wild-type flies retained their ability to detect a magnetic field, supporting the idea that magnetoreception in fruitflies is independent of their body clocks.

Clearly, cryptochrome is required for magnetoreception in fruitflies, but more sophisticated behavioural assays will be needed to understand the type of information that flies glean from magnetic fields. It also remains to be seen whether the receptor itself is the magnetosensitive molecule.

It has been proposed<sup>4</sup> that, in birds, Earth's magnetic field causes variations in signals from precisely oriented photoreceptors, thus providing a three-dimensional map of the field to the bird's brain. This raises the question of where cryptochrome localizes in the body. In fruitflies, the precisely organized compound eye seems a likely candidate. But fruitfly larvae also seem to sense magnetic fields<sup>7</sup>, yet they don't have compound eyes. The finding of cryptochrome in the nerve fibres of some circadian-clock neurons<sup>12</sup> in fruitflies suggests that sites might exist in the brain for oriented placement of these receptors. Further studies with genetically engineered fruitflies will certainly provide us with some answers to these questions.

It is not clear why fruitflies, which do not migrate and usually spend their summers flying around rotten fruit, should care about Earth's magnetic field. The magnetoreceptive function

of their cryptochrome raises the possibility that vertebrate cryptochrome does the same job, and might even explain why the light-detecting properties of the protein have been evolutionarily conserved in mammals<sup>13</sup>. In any case, Gegear and colleagues' results open a new avenue of investigation for magnetoreception — that of genetic and molecular analysis. ■

François Rouyer is at the Institut de Neurobiologie Alfred Fessard, CNRS UPR2216, 91198 Gif-sur-Yvette, France. e-mail: francois.rouyer@inaf.cnrs-gif.fr

1. Stanewsky, R. *J. Neurobiol.* **54**, 111–147 (2003).
2. Gegear, R. J., Casselman, A., Waddell, S. & Reppert, S. M. *Nature* **454**, 1014–1018 (2008).

3. Johnsen, S. & Lohmann, K. J. *Nature Rev. Neurosci.* **6**, 703–712 (2005).
4. Ritz, T., Adem, S. & Schulter, K. *Biophys. J.* **78**, 707–718 (2000).
5. Phillips, J. B. & Borland, S. C. *Nature* **359**, 142–144 (1992).
6. Phillips, J. B. & Sayeed, O. J. *Comp. Physiol. A* **172**, 303–308 (1993).
7. Dommer, D. H., Gazzolo, P. J., Painter, M. S. & Phillips, J. B. *J. Insect Physiol.* **54**, 719–726 (2008).
8. Mouritsen, H. *et al.* *Proc. Natl. Acad. Sci. USA* **101**, 14294–14299 (2004).
9. Moller, A., Sagasser, S., Wiltschko, W. & Schierwater, B. *Naturwissenschaften* **91**, 585–588 (2004).
10. Zhu, H. *et al.* *PLoS Biol.* **6**, e4 (2008).
11. Ahmad, M., Galland, P., Ritz, T., Wiltschko, R. & Wiltschko, W. *Planta* **225**, 615–624 (2007).
12. Klarsfeld, A. *et al.* *J. Neurosci.* **24**, 1468–1477 (2004).
13. Hoang, N. *et al.* *PLoS Biol.* **6**, e160 (2008).

## MATERIALS SCIENCE

# A metal left spinning

Zachary Fisk and Stephan von Molnár

**Conductors and semiconductors usually behave like conduits for fluids of electrons. But sometimes the electrons' spins conspire to produce unconventional behaviours that can be turned off and on with magnets.**

The theory of Landau–Fermi liquids is a remarkably simple but effective model to describe the behaviour of conventional metals. It views metals as consisting of a liquid of independent, mobile electrons with spin and charge, responding to applied magnetic and electric fields. That individual electrons strongly repel each other as a result of their identical electronic charges is accommodated in this picture by an adjustment to the effective electron mass. Semiconductors doped with atoms carrying either more or fewer electrons than the host atoms are also explained by this model. Instances in which this picture fails are therefore of considerable interest, and understanding how to produce such materials has both fundamental and technological potential. The possibility of a systematic method of inducing non-Landau–Fermi-liquid states is the claim in the paper by Manyala *et al.*<sup>1</sup> on page 976 of this issue.

The authors have taken the semiconductor ferrosilicon (FeSi) and replaced a few per cent of its iron atoms with manganese (Mn). This element comes just before Fe in the periodic table, having one less electron than Fe in its outer shell. Replacing an Fe atom with Mn in the semiconductor's cubic lattice introduces a 'missing electron', known as a hole. Holes act like electrons but with positive charges; a collection of holes will act exactly like a collection of electrons, apart from moving in the opposite direction in applied electric fields. As with electrons, holes have a spin of 1/2 with an associated magnetic moment.

Manganese atoms carry their own magnetic moment corresponding to a spin of 1 in the FeSi semiconductor. In metals containing

atoms from first-row transition elements (scandium to zinc, which includes Mn and Fe) that have local atomic moments, the spin of any mobile electrons or holes (collectively known as carriers) and the local moment preferentially line up anti-parallel, because the carrier attempts to compensate for the local atomic moment. When Mn substitutes for Fe, there are not enough carrier spins to balance the Mn atom's spin completely, because each spin-1 Mn atom appears in the lattice accompanied by a single spin-1/2 hole. A pair of carriers would be needed to compensate for this spin-1 moment, but then the moment of a Mn atom elsewhere would be left uncompensated.

The detailed experiments of Manyala *et al.*<sup>1</sup> show that Mn-doped FeSi does not behave in the manner expected of the standard metallic state of a doped semiconductor; for example, it has an anomalous relationship between electrical resistance and temperature. This non-Landau–Fermi behaviour arises because, even at temperatures below 2 kelvins, undercompensated atomic spins interact with the spins of the free carriers, affecting their degrees of freedom. However, Manyala and colleagues found that applying a sufficiently large magnetic field at low temperature froze the free spins in a single orientation, restoring the expected metallic behaviour.

The suggestion that undercompensated doping provides a general route to non-Landau–Fermi behaviour is a seductively simple idea. But FeSi is an unusual semiconductor whose low-temperature semiconducting state has developed out of a solid with strongly temperature-dependent magnetic properties. This may or may not be relevant.

FeSi could simply be an easily accessed venue into which a dopant carrying a local moment incompletely balanced by the net carrier moment can be introduced. It is therefore important for the studies of Manyala *et al.*<sup>1</sup> to be repeated in a more conventional semiconductor.

One might wonder whether similar effects to those occurring with Mn doping of FeSi might occur when doping with cobalt (Co). This is the element just to the right of Fe in the periodic table, and so would provide additional electrons rather than removing them. Cobalt even has a larger atomic moment (of spin 3/2). However, Manyala *et al.*<sup>1</sup> found that Co-doped FeSi becomes magnetically ordered at low temperatures, abolishing all the spin degrees of freedom associated with local moments, leaving no source for behaviour as a non-Landau–Fermi liquid. There are also atoms with local moments that couple to carrier spins in a non-compensating fashion, a process known as preferential spin alignment. Most of the rare earth metals are of this character, including gadolinium, which has a 7/2 spin moment. But no known non-Landau–Fermi liquid associated with this non-compensating situation has yet been seen.

Manyala and colleagues propose that doped semiconductors based on elements in groups III and V (for example gallium arsenide, GaAs) could be used to produce non-Landau–Fermi liquids. There is a considerable volume of literature on low-level doping with Mn in these semiconductors, especially in indium arsenide<sup>2–4</sup>. The extreme of doping, MnAs, is a ferromagnet (as is MnSi) but transition metals do not incorporate well or to high levels with group III–V elements, in contrast with the ease with which Mn dopes FeSi. Magnetic measurements indicate that with Mn replacing between 2% and 18% of the indium atoms, the sum of all spin exchange interactions produces antiferromagnetic behaviour (the moments align in a regular way, cancelling each other out and leaving the material with no overall magnetic moment), the strength of which decreases with decreasing Mn content. For materials with less than 2% Mn the exchanges result in ferromagnetic behaviour (individual moments align to reinforce each other)<sup>3,4</sup>. When Mn doping falls below 1.8%, corresponding to less than  $2.2 \times 10^{19}$  holes per cubic centimetre, the materials display long-range ferromagnetism with a transition temperature (around 7 kelvins) above which ferromagnetism breaks down<sup>3</sup>.

It seems that group III–V semiconductors with Mn doping near 2%, where the exchange between local and carrier spin is small, could provide favourable conditions in which to find systems lying between Landau–Fermi liquid and non-Landau–Fermi liquid states. In these semiconductors Mn has a spin of 5/2. In addition, the concentrations of free electrons and/or holes can be controlled independently of Mn content by the addition of impurities, which allows the preparation of materials close



## 50 YEARS AGO

It has been observed in this laboratory that when aqueous mixtures of dicarboxylic or monocarboxylic acids and certain ammonium salts are irradiated with ultra-violet light, certain amino-acids are obtained.

A cold quartz ultra-violet lamp giving 86 per cent of its output at about 2537 Å was used for irradiated mixtures of succinic, maleic, propionic and acetic acid with a number of ammonium salts ... The irradiation was continued in each case for 24 hr ...

Of all the ammonium compounds investigated only ammonia and ammonium carbonate were active, and of the acids only succinic, maleic and propionic acid gave rise to amino-acids ...

The amino-acids are aspartic acid, alanine and glycine, that is to say, amino-acids with 4, 3 and 2 carbon atoms respectively.

From *Nature* 23 August 1958

## 100 YEARS AGO

The Rev. J. W. Hayes, of West Thurrock Vicarage, Grays, has directed attention to some old underground workings for chalk at Hemel Hempstead, which in his opinion throw much light on the origin and use of dene-holes generally. It appears that in order to obtain chalk suitable for lime-making it was until recently the practice ... to work the chalk in subterranean chambers reached by deep shafts ... A vertical shaft, of circular section, about 5 feet in diameter, was sunk through superficial deposits until the hard chalk was reached, and from the bottom of the shaft three so-called "arches" were struck out. These arches were chambers, which in some cases were more than 12 feet high. The chalk was mined in these drifts for a length of twenty to twenty-five yards, and when the distance of the working face from the bottom of the shaft became inconveniently great, or when the roof proved unsound, a new pit would be sunk.

From *Nature* 20 August 1908

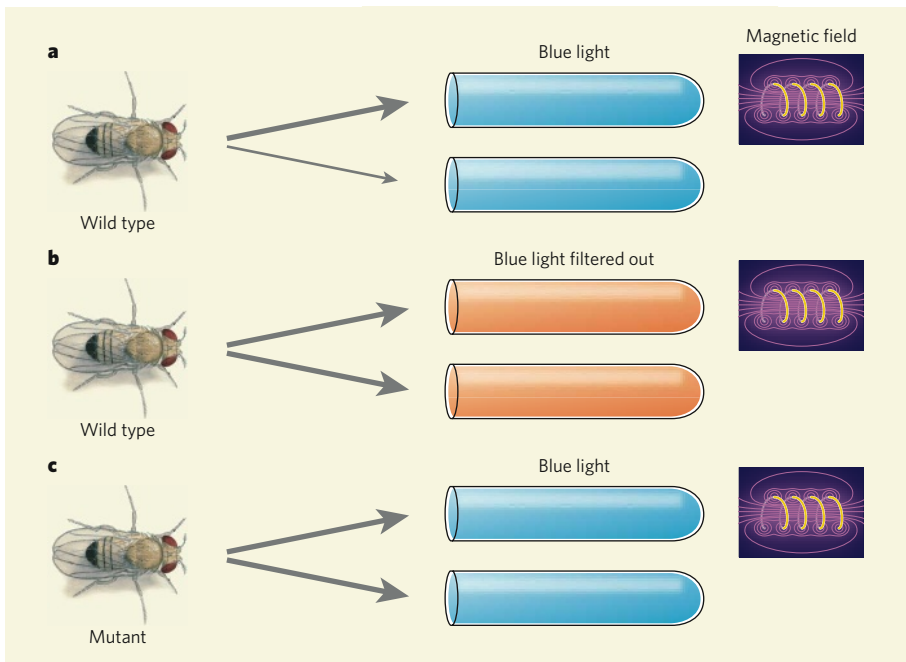


**Figure 1 | Magnetoreception in fruitflies.** Geegar *et al.*<sup>2</sup> studied the ability of fruitflies to detect a magnetic field. **a**, When trained to associate a magnetic field with a reward of sugar, wild-type flies preferentially choose to enter a tube that is bathed in a magnetic field, rather than one that is not, so long as blue light illuminates the experiment. **b**, The trained flies demonstrate no preference for the tubes if blue light is filtered out of the illumination. **c**, Genetically modified flies that lack the photoreceptor cryptochrome (which responds to blue light) do not recognize the magnetic field, even in the presence of blue light, showing that cryptochrome is essential for magnetoreception in fruitflies.

Previous studies<sup>6</sup> have shown that fruitflies respond differently to magnetic fields depending on the wavelength of light that they are exposed to. Geegar *et al.* therefore investigated the influence of different light colours on the behaviour of their trained flies, concentrating on the blue end of the spectrum for the reasons mentioned earlier. Their results indicate that light is indeed required for fruitfly magnetosensitivity — the flies were unable to detect magnetic fields in the absence of light of short wavelength (less than 420 nanometres; Fig. 1). This is close to the region of the spectrum that is absorbed by cryptochrome, suggesting that the photoreceptor might be involved in this behaviour.

To confirm the role of cryptochrome in magnetoreception, the authors tested mutant *cry*<sup>0</sup> flies, which lack the photoreceptor, in their behavioural assay. They found that untrained wild-type flies that have the same genetic background as *cry*<sup>0</sup> flies are attracted to magnetic fields. But the *cry*<sup>0</sup> mutants showed no response to the magnetic field, even if they had been through the training protocol. Moreover, flies that carried a different cryptochrome mutation — one that disrupts most of the photoreceptor's function without deleting the protein completely — were also unresponsive to the magnetic field. This strongly bolsters the idea that cryptochrome is a vital component of light-dependent magnetoreception in fruitflies.

Because cryptochrome is involved in setting the circadian clock in flies' brains, and could also have a clock-gene function in other

tissues<sup>1</sup>, Geegar *et al.* checked to see whether the flies' magnetoreceptive response depended on having a functional circadian clock. The answer was no. Even in conditions that caused the flies to be circadianly arrhythmic, wild-type flies retained their ability to detect a magnetic field, supporting the idea that magnetoreception in fruitflies is independent of their body clocks.

Clearly, cryptochrome is required for magnetoreception in fruitflies, but more sophisticated behavioural assays will be needed to understand the type of information that flies glean from magnetic fields. It also remains to be seen whether the receptor itself is the magnetosensitive molecule.

It has been proposed<sup>4</sup> that, in birds, Earth's magnetic field causes variations in signals from precisely oriented photoreceptors, thus providing a three-dimensional map of the field to the bird's brain. This raises the question of where cryptochrome localizes in the body. In fruitflies, the precisely organized compound eye seems a likely candidate. But fruitfly larvae also seem to sense magnetic fields<sup>7</sup>, yet they don't have compound eyes. The finding of cryptochrome in the nerve fibres of some circadian-clock neurons<sup>12</sup> in fruitflies suggests that sites might exist in the brain for oriented placement of these receptors. Further studies with genetically engineered fruitflies will certainly provide us with some answers to these questions.

It is not clear why fruitflies, which do not migrate and usually spend their summers flying around rotten fruit, should care about Earth's magnetic field. The magnetoreceptive function

of their cryptochrome raises the possibility that vertebrate cryptochrome does the same job, and might even explain why the light-detecting properties of the protein have been evolutionarily conserved in mammals<sup>13</sup>. In any case, Gegear and colleagues' results open a new avenue of investigation for magnetoreception — that of genetic and molecular analysis. ■

François Rouyer is at the Institut de Neurobiologie Alfred Fessard, CNRS UPR2216, 91198 Gif-sur-Yvette, France. e-mail: francois.rouyer@inaf.cnrs-gif.fr

1. Stanewsky, R. *J. Neurobiol.* **54**, 111–147 (2003).
2. Gegear, R. J., Casselman, A., Waddell, S. & Reppert, S. M. *Nature* **454**, 1014–1018 (2008).

3. Johnsen, S. & Lohmann, K. J. *Nature Rev. Neurosci.* **6**, 703–712 (2005).
4. Ritz, T., Adem, S. & Schulter, K. *Biophys. J.* **78**, 707–718 (2000).
5. Phillips, J. B. & Borland, S. C. *Nature* **359**, 142–144 (1992).
6. Phillips, J. B. & Sayeed, O. J. *Comp. Physiol. A* **172**, 303–308 (1993).
7. Dommer, D. H., Gazzolo, P. J., Painter, M. S. & Phillips, J. B. *J. Insect Physiol.* **54**, 719–726 (2008).
8. Mouritsen, H. *et al.* *Proc. Natl. Acad. Sci. USA* **101**, 14294–14299 (2004).
9. Moller, A., Sagasser, S., Wiltschko, W. & Schierwater, B. *Naturwissenschaften* **91**, 585–588 (2004).
10. Zhu, H. *et al.* *PLoS Biol.* **6**, e4 (2008).
11. Ahmad, M., Galland, P., Ritz, T., Wiltschko, R. & Wiltschko, W. *Planta* **225**, 615–624 (2007).
12. Klarsfeld, A. *et al.* *J. Neurosci.* **24**, 1468–1477 (2004).
13. Hoang, N. *et al.* *PLoS Biol.* **6**, e160 (2008).

## MATERIALS SCIENCE

# A metal left spinning

Zachary Fisk and Stephan von Molnár

**Conductors and semiconductors usually behave like conduits for fluids of electrons. But sometimes the electrons' spins conspire to produce unconventional behaviours that can be turned off and on with magnets.**

The theory of Landau–Fermi liquids is a remarkably simple but effective model to describe the behaviour of conventional metals. It views metals as consisting of a liquid of independent, mobile electrons with spin and charge, responding to applied magnetic and electric fields. That individual electrons strongly repel each other as a result of their identical electronic charges is accommodated in this picture by an adjustment to the effective electron mass. Semiconductors doped with atoms carrying either more or fewer electrons than the host atoms are also explained by this model. Instances in which this picture fails are therefore of considerable interest, and understanding how to produce such materials has both fundamental and technological potential. The possibility of a systematic method of inducing non-Landau–Fermi-liquid states is the claim in the paper by Manyala *et al.*<sup>1</sup> on page 976 of this issue.

The authors have taken the semiconductor ferrosilicon (FeSi) and replaced a few per cent of its iron atoms with manganese (Mn). This element comes just before Fe in the periodic table, having one less electron than Fe in its outer shell. Replacing an Fe atom with Mn in the semiconductor's cubic lattice introduces a 'missing electron', known as a hole. Holes act like electrons but with positive charges; a collection of holes will act exactly like a collection of electrons, apart from moving in the opposite direction in applied electric fields. As with electrons, holes have a spin of 1/2 with an associated magnetic moment.

Manganese atoms carry their own magnetic moment corresponding to a spin of 1 in the FeSi semiconductor. In metals containing

atoms from first-row transition elements (scandium to zinc, which includes Mn and Fe) that have local atomic moments, the spin of any mobile electrons or holes (collectively known as carriers) and the local moment preferentially line up anti-parallel, because the carrier attempts to compensate for the local atomic moment. When Mn substitutes for Fe, there are not enough carrier spins to balance the Mn atom's spin completely, because each spin-1 Mn atom appears in the lattice accompanied by a single spin-1/2 hole. A pair of carriers would be needed to compensate for this spin-1 moment, but then the moment of a Mn atom elsewhere would be left uncompensated.

The detailed experiments of Manyala *et al.*<sup>1</sup> show that Mn-doped FeSi does not behave in the manner expected of the standard metallic state of a doped semiconductor; for example, it has an anomalous relationship between electrical resistance and temperature. This non-Landau–Fermi behaviour arises because, even at temperatures below 2 kelvins, undercompensated atomic spins interact with the spins of the free carriers, affecting their degrees of freedom. However, Manyala and colleagues found that applying a sufficiently large magnetic field at low temperature froze the free spins in a single orientation, restoring the expected metallic behaviour.

The suggestion that undercompensated doping provides a general route to non-Landau–Fermi behaviour is a seductively simple idea. But FeSi is an unusual semiconductor whose low-temperature semiconducting state has developed out of a solid with strongly temperature-dependent magnetic properties. This may or may not be relevant.

FeSi could simply be an easily accessed venue into which a dopant carrying a local moment incompletely balanced by the net carrier moment can be introduced. It is therefore important for the studies of Manyala *et al.*<sup>1</sup> to be repeated in a more conventional semiconductor.

One might wonder whether similar effects to those occurring with Mn doping of FeSi might occur when doping with cobalt (Co). This is the element just to the right of Fe in the periodic table, and so would provide additional electrons rather than removing them. Cobalt even has a larger atomic moment (of spin 3/2). However, Manyala *et al.*<sup>1</sup> found that Co-doped FeSi becomes magnetically ordered at low temperatures, abolishing all the spin degrees of freedom associated with local moments, leaving no source for behaviour as a non-Landau–Fermi liquid. There are also atoms with local moments that couple to carrier spins in a non-compensating fashion, a process known as preferential spin alignment. Most of the rare earth metals are of this character, including gadolinium, which has a 7/2 spin moment. But no known non-Landau–Fermi liquid associated with this non-compensating situation has yet been seen.

Manyala and colleagues propose that doped semiconductors based on elements in groups III and V (for example gallium arsenide, GaAs) could be used to produce non-Landau–Fermi liquids. There is a considerable volume of literature on low-level doping with Mn in these semiconductors, especially in indium arsenide<sup>2–4</sup>. The extreme of doping, MnAs, is a ferromagnet (as is MnSi) but transition metals do not incorporate well or to high levels with group III–V elements, in contrast with the ease with which Mn dopes FeSi. Magnetic measurements indicate that with Mn replacing between 2% and 18% of the indium atoms, the sum of all spin exchange interactions produces antiferromagnetic behaviour (the moments align in a regular way, cancelling each other out and leaving the material with no overall magnetic moment), the strength of which decreases with decreasing Mn content. For materials with less than 2% Mn the exchanges result in ferromagnetic behaviour (individual moments align to reinforce each other)<sup>3,4</sup>. When Mn doping falls below 1.8%, corresponding to less than  $2.2 \times 10^{19}$  holes per cubic centimetre, the materials display long-range ferromagnetism with a transition temperature (around 7 kelvins) above which ferromagnetism breaks down<sup>3</sup>.

It seems that group III–V semiconductors with Mn doping near 2%, where the exchange between local and carrier spin is small, could provide favourable conditions in which to find systems lying between Landau–Fermi liquid and non-Landau–Fermi liquid states. In these semiconductors Mn has a spin of 5/2. In addition, the concentrations of free electrons and/or holes can be controlled independently of Mn content by the addition of impurities, which allows the preparation of materials close

to the insulator–metal transition. This would be a major advantage over the FeSi system, because the effects of the type and density of carriers could be studied in detail. In FeSi only aluminium, which substitutes for Si and introduces additional holes, can have this role.

Broader applications of the principles described by Manjala *et al.*<sup>1</sup> to wide classes of well-characterized semiconductors offer the opportunity of new approaches to the understanding of the breakdown of conventional Landau–Fermi liquid theory and with it a possible route towards the control of strong electronic correlations in solids for useful purposes. ■

Zachary Fisk is in the Physics and Astronomy Department, University of California, Irvine, Irvine, California 92697, USA. Stephan von Molnár is at the Center for Materials Research and Technology, Florida State University, Tallahassee, Florida 32306-4351, USA.  
e-mails: zfisk@uci.edu; molnar@martech.fsu.edu

1. Manjala, N., DiTusa, J. F., Aepli, G. & Ramirez, A. P. *Nature* **454**, 976–980 (2008).
2. Ohno, H., Munekata, H., Penney, T., von Molnár, S. & Chang, L. L. *Phys. Rev. Lett.* **68**, 2664–2667 (1992).
3. Ohno, H., Munekata, H., von Molnár, S. & Chang, L. L. *J. Appl. Phys.* **69**, 6103–6108 (1991).
4. von Molnár, S., Munekata, H., Ohno, H. & Chang, L. L. *J. Mag. Magn. Mater.* **93**, 356–364 (1991).

aggregate, it is ‘alive’<sup>10,11</sup>. The data almost defy imagination — on the order of a million cells in every cubic centimetre of sediment buried half a kilometre below the sea floor, or more than 50% of all microbial cells on Earth<sup>12</sup>. The overall order of magnitude is the same as the biomass of all surface plant life. In investigating what kind of cells they are, Lipp *et al.*<sup>1</sup> conclude that, deeper than 1 metre below the sea floor, it is Archaea, not Bacteria, that contribute the bulk of sedimentary microbial biomass. If true, Archaea would be the most abundant cell type in the marine system, rivalling Bacteria in total numbers globally.

Lipp *et al.*, however, are far from the first to approach the question of the phylogeny of sedimentary prokaryotes. Previous efforts generated conflicting results<sup>10,11,13</sup>, and a hung jury has been declared<sup>14</sup> over the question of the predominance of Bacteria or Archaea. But why the protracted debate? Part of the problem lies in the distinction between ‘living’ cells, total cells (including inert or dead cells), and/or cells that are in between, persisting in an undefined degree of stasis. This leads to ambiguity about what should or should not be counted. Adding to the confusion, nearly every report so far also has used a different combination of analytical techniques, and consideration of those techniques is essential to understanding the issues.

The fluorescent stains acridine orange and DAPI detect all cells — alive or dead — that contain any remnant of DNA. But they cannot reveal phylogeny or activity. So, to discriminate between Bacteria and Archaea, molecular methods have been used in various combinations. These include approaches that detect ribosomal RNA (rRNA) or intact polar lipids (IPLs) of cell membranes (both are proxies for live cells), or that quantify rRNA gene copies from extracted DNA. Of these techniques, *in situ* fluorescent tagging of ribosomes in methods known as FISH or CARD-FISH produce the most disparate (indeed, opposite) results<sup>10,11,13</sup>. Although potentially an ideal

## BIOGEOCHEMISTRY

# Who lives in the sea floor?

Ann Pearson

**The sediments that blanket the sea floor contain tremendous numbers of microorganisms. This deep marine biosphere, which is probed by deep-sea drilling, is a new frontier for microbiologists and geochemists.**

On page 991 of this issue, Lipp *et al.*<sup>1</sup> add to the debate over the nature of life in the sea floor. They report that most cells in deep-sea sediment are members of the domain Archaea and not of the other domain of the prokaryotes, the Bacteria. Although both are differentiated from the eukaryotes — which include ourselves — in lacking a nucleus, Archaea and Bacteria are fundamentally different from each other in their biochemistry, metabolism and evolutionary history. This in turn profoundly influences their role in Earth’s biogeochemical cycles.

A century ago, the suggestion that the ocean’s deep sediments had inhabitants — organisms far removed from the oxygenated, light-filled surface of Earth — would have been preposterous. Life on the sea floor was well known; such

fauna were sampled during the voyage of the HMS *Challenger* (1872–76), in an expedition that is widely recognized as marking the birth of modern oceanography (Fig. 1). The first hint of a rich microbial biosphere in the sea floor came only much later<sup>2</sup>, and it was not until the 1990s that microbial cells in deep sediments were enumerated systematically<sup>3,4</sup>. In parallel, geochemists showed that inorganic solutes in sediment pore-waters usually react in the order predicted by thermodynamic principles, but at rates exceeding expectations for abiotic processes<sup>5–7</sup>. Thus biologists and chemists agree: there must be a ‘deep biosphere’. But what populates it? And how do the organisms concerned adapt their metabolic strategies to sustain life at the limits of energetic viability<sup>8,9</sup>?

The deep biosphere is large, and, at least in

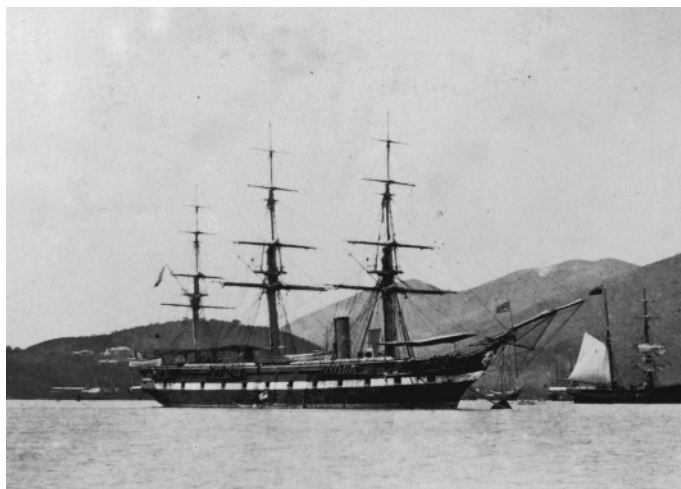


**Figure 1 | Sea change.** HMS *Challenger* (left), whose voyage in the 1870s opened eyes to the fauna living on the floor of the deep sea, and the drill ship JOIDES Resolution, mainstay of the Ocean Drilling Program and subsequent Integrated Ocean Drilling Program, which has provided the cores from which much of the information about life in deep-sea sediments has been gleaned.

to the insulator–metal transition. This would be a major advantage over the FeSi system, because the effects of the type and density of carriers could be studied in detail. In FeSi only aluminium, which substitutes for Si and introduces additional holes, can have this role.

Broader applications of the principles described by Manjala *et al.*<sup>1</sup> to wide classes of well-characterized semiconductors offer the opportunity of new approaches to the understanding of the breakdown of conventional Landau–Fermi liquid theory and with it a possible route towards the control of strong electronic correlations in solids for useful purposes. ■

Zachary Fisk is in the Physics and Astronomy Department, University of California, Irvine, Irvine, California 92697, USA. Stephan von Molnár is at the Center for Materials Research and Technology, Florida State University, Tallahassee, Florida 32306-4351, USA.  
e-mails: zfisk@uci.edu; molnar@martech.fsu.edu

1. Manjala, N., DiTusa, J. F., Aepli, G. & Ramirez, A. P. *Nature* **454**, 976–980 (2008).
2. Ohno, H., Munekata, H., Penney, T., von Molnár, S. & Chang, L. L. *Phys. Rev. Lett.* **68**, 2664–2667 (1992).
3. Ohno, H., Munekata, H., von Molnár, S. & Chang, L. L. *J. Appl. Phys.* **69**, 6103–6108 (1991).
4. von Molnár, S., Munekata, H., Ohno, H. & Chang, L. L. *J. Mag. Magn. Mater.* **93**, 356–364 (1991).

aggregate, it is ‘alive’<sup>10,11</sup>. The data almost defy imagination — on the order of a million cells in every cubic centimetre of sediment buried half a kilometre below the sea floor, or more than 50% of all microbial cells on Earth<sup>12</sup>. The overall order of magnitude is the same as the biomass of all surface plant life. In investigating what kind of cells they are, Lipp *et al.*<sup>1</sup> conclude that, deeper than 1 metre below the sea floor, it is Archaea, not Bacteria, that contribute the bulk of sedimentary microbial biomass. If true, Archaea would be the most abundant cell type in the marine system, rivalling Bacteria in total numbers globally.

Lipp *et al.*, however, are far from the first to approach the question of the phylogeny of sedimentary prokaryotes. Previous efforts generated conflicting results<sup>10,11,13</sup>, and a hung jury has been declared<sup>14</sup> over the question of the predominance of Bacteria or Archaea. But why the protracted debate? Part of the problem lies in the distinction between ‘living’ cells, total cells (including inert or dead cells), and/or cells that are in between, persisting in an undefined degree of stasis. This leads to ambiguity about what should or should not be counted. Adding to the confusion, nearly every report so far also has used a different combination of analytical techniques, and consideration of those techniques is essential to understanding the issues.

The fluorescent stains acridine orange and DAPI detect all cells — alive or dead — that contain any remnant of DNA. But they cannot reveal phylogeny or activity. So, to discriminate between Bacteria and Archaea, molecular methods have been used in various combinations. These include approaches that detect ribosomal RNA (rRNA) or intact polar lipids (IPLs) of cell membranes (both are proxies for live cells), or that quantify rRNA gene copies from extracted DNA. Of these techniques, *in situ* fluorescent tagging of ribosomes in methods known as FISH or CARD-FISH produce the most disparate (indeed, opposite) results<sup>10,11,13</sup>. Although potentially an ideal

## BIOGEOCHEMISTRY

# Who lives in the sea floor?

Ann Pearson

**The sediments that blanket the sea floor contain tremendous numbers of microorganisms. This deep marine biosphere, which is probed by deep-sea drilling, is a new frontier for microbiologists and geochemists.**

On page 991 of this issue, Lipp *et al.*<sup>1</sup> add to the debate over the nature of life in the sea floor. They report that most cells in deep-sea sediment are members of the domain Archaea and not of the other domain of the prokaryotes, the Bacteria. Although both are differentiated from the eukaryotes — which include ourselves — in lacking a nucleus, Archaea and Bacteria are fundamentally different from each other in their biochemistry, metabolism and evolutionary history. This in turn profoundly influences their role in Earth’s biogeochemical cycles.

A century ago, the suggestion that the ocean’s deep sediments had inhabitants — organisms far removed from the oxygenated, light-filled surface of Earth — would have been preposterous. Life on the sea floor was well known; such

fauna were sampled during the voyage of the HMS *Challenger* (1872–76), in an expedition that is widely recognized as marking the birth of modern oceanography (Fig. 1). The first hint of a rich microbial biosphere in the sea floor came only much later<sup>2</sup>, and it was not until the 1990s that microbial cells in deep sediments were enumerated systematically<sup>3,4</sup>. In parallel, geochemists showed that inorganic solutes in sediment pore-waters usually react in the order predicted by thermodynamic principles, but at rates exceeding expectations for abiotic processes<sup>5–7</sup>. Thus biologists and chemists agree: there must be a ‘deep biosphere’. But what populates it? And how do the organisms concerned adapt their metabolic strategies to sustain life at the limits of energetic viability<sup>8,9</sup>?

The deep biosphere is large, and, at least in

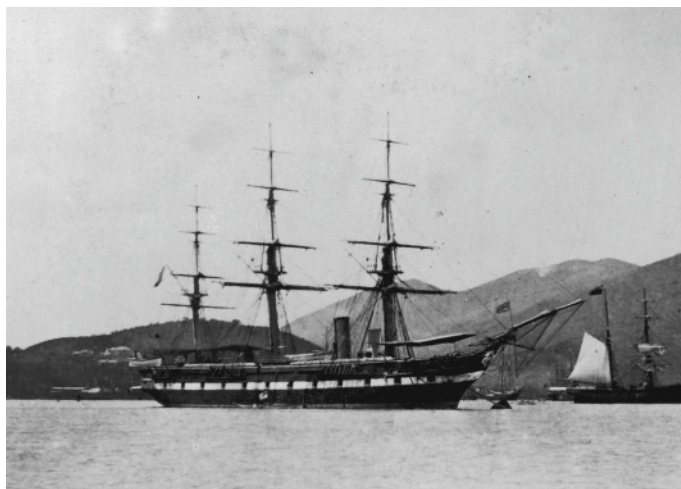


**Figure 1 | Sea change.** HMS *Challenger* (left), whose voyage in the 1870s opened eyes to the fauna living on the floor of the deep sea, and the drill ship JOIDES Resolution, mainstay of the Ocean Drilling Program and subsequent Integrated Ocean Drilling Program, which has provided the cores from which much of the information about life in deep-sea sediments has been gleaned.

## ARCHAEOLOGY

## An oasis in time

Today's Sahara is arid and inhospitable, but this was not always the case. In the early Holocene (between about 10,000 and 4,500 years ago), monsoon rains created a lush savannah rich in animal and plant life. Complex human societies settled there beside ancient lakes, as demonstrated by a recently reported archaeological site documenting nearly 5,000 years of human occupation (P. C. Sereno *et al.* *PLoS ONE* **3**, e2995; 2008).

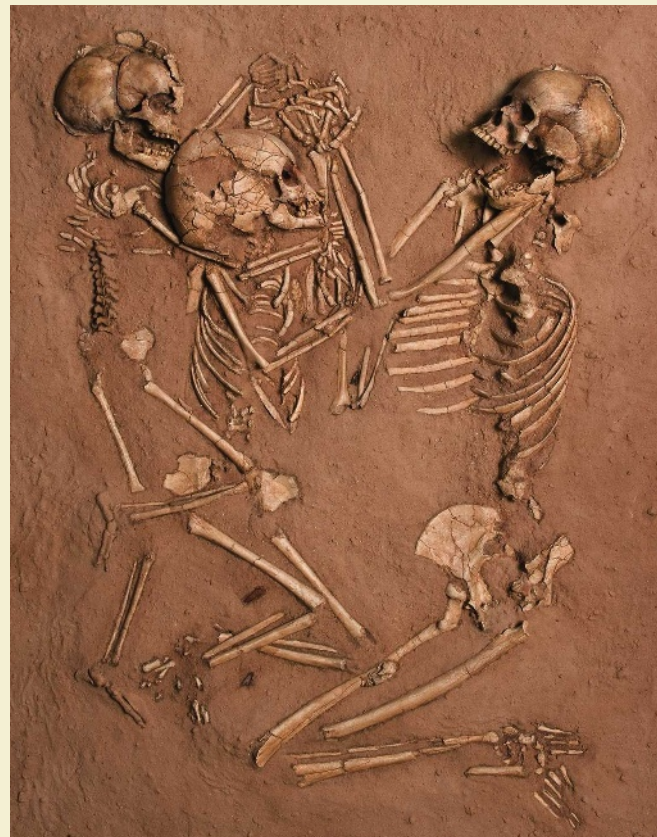
The site, named Gobero and situated in central Niger, contains about 200 burial sites, which, along with several rubbish dumps, provide a record of two distinct periods of human settlement. It was originally occupied 9,500 years ago by a tall, well-muscled people who fished the lake for Nile perch and large catfish with the use of bone harpoons and hooks. These people abandoned the site a little over 8,000 years ago when an

extended arid period dried up the lake.

Gobero was recolonized 1,000 years later by a slighter and shorter people who ate clams and small catfish from the now much shallower lake, as well as antelope and other vertebrates from the surrounding savannah. This population had sophisticated burial practices involving jewellery and grave goods, and what appear to be ritual poses. One grave, dated to be about 5,300 years old, contained a woman and two children buried together with clasped hands (pictured). Pollen found in this grave suggests that they were buried on a bed of wool flowers (*Celosia*).

Occupation of the Gobero site came to an end around 4,500 years ago, when changing climate returned this region to the arid desert conditions that persist to this day.

Christopher Surridge



MIKE HETTER/PROJECT EXPLORATION

method of identifying metabolically active cells, the data suggest that consistent application of FISH remains a challenge. To achieve a similar goal of studying only 'living' cells, direct extraction of rRNA followed by reverse transcription to DNA has been successful<sup>13</sup>, but attempts to make this approach quantitative face major hurdles.

Theoretically, there are fewer challenges when examining DNA or lipids. Quantitative amplification of extracted DNA by using the polymerase chain reaction (qPCR) allows rRNA genes to be counted, rather than seeking ribosomes directly. Even after accounting for the variable copies per cell of these genes in Bacteria and Archaea, early results from qPCR invariably declared the winner to be Bacteria<sup>11,15</sup>. How, then, is it possible that Archaea could have been underestimated?

The key word is 'extracted' — Lipp *et al.*<sup>1</sup> resolve the qPCR dilemma, showing that a more aggressive approach to obtaining total DNA is essential. It is revealing to view their Supplementary Fig. 3: depending on the method used, as many as 80% or as 'few' as 15% of cells escape lysis, the latter under optimized conditions. The implication is that DNA from these escapees would be overlooked during qPCR, and most of them would be Archaea with their more durable cell envelopes.

Improved extraction brings estimates from qPCR in line with earlier claims of archaeal abundance as derived from IPLs<sup>13</sup>. Polar lipids are presumed to reflect living biomass, because

their labile (often phosphate-containing) head groups are quickly lost after cell death. Lipp *et al.* also offer expanded IPL data covering seven different locations. Nearly 90% of IPLs below a depth of 1 metre are specific to Archaea, and the total abundance is proportional to the total organic carbon content of the sediment in which they are found. This suggests that archaeal production fundamentally scales to the available organic resources, whatever the type of metabolism involved.

In considering Archaea and Bacteria, it has been proposed that Archaea are united by a universal ecological ability to cope with energetic stress<sup>16</sup>. It is therefore reasonable that in a sub-seafloor world, where it has been estimated that cell turnover times could be centuries or longer<sup>8,9</sup>, organisms with honed strategies to conserve energy would dominate.

Nevertheless, Lipp and colleagues' results will be controversial. Much of their argument rests on the interpretation that all IPLs represent living cells — that is, that the degradation time of IPLs after cell death is infinitely fast relative to other processes in the system. Although IPLs degrade rapidly in experiments, little is known about their persistence in complex communities with extraordinarily low rates of enzymatic activity. Specifically, it is the persistence of archaeal IPLs relative to bacterial IPLs that is of particular importance. This requires further study of the turnover of both Bacteria and Archaea in sediments, especially with regard to specific rates of synthesis, alteration

and degradation of lipids. For microbes, the boundary between alive and dead is fuzzy, and the extent to which any category of biomolecule can define it remains unclear. Progress on all fronts of culture-independent and culture-dependent techniques will be necessary to tackle these uncertainties.

Ann Pearson is in the Department of Earth and Planetary Sciences, Harvard University, Cambridge, Massachusetts 02138, USA.  
e-mail: pearson@eps.harvard.edu

1. Lipp, J. S., Morono, Y., Inagaki, F. & Hinrichs, K.-U. *Nature* **454**, 991–994 (2008).
2. Zobell, C. E. & Morita, R. Y. in *Galathea Report* Vol. 1, 139–154 (Danish Science, 1959).
3. Parkes, R. J. *et al.* *Nature* **371**, 410–413 (1994).
4. Parkes, R. J., Cragg, B. A. & Wellsbury, P. *Hydrogeol. J.* **8**, 11–28 (2000).
5. Froelich, P. N. *et al.* *Geochim. Cosmochim. Acta* **43**, 1075–1090 (1979).
6. Jørgensen, B. B. *Nature* **296**, 643–645 (1982).
7. Oremland, R. S., Culbertson, C. & Simoneit, B. R. T. in *Initial Reports of the Deep Sea Drilling Project* (eds Curran, J. R. *et al.*) 759–762 (US Government Printing Office, 1982).
8. D'Honst, S., Rutherford, S. & Spivack, A. J. *Science* **295**, 2067–2070 (2002).
9. D'Honst, S. *et al.* *Science* **306**, 2216–2221 (2004).
10. Mauclaire, L., Zepp, K., Meister, P. & McKenzie, J. *Geobiology* **2**, 217–223 (2004).
11. Schippers, A. *et al.* *Nature* **433**, 861–864 (2005).
12. Whitman, W. B., Coleman, D. C. & Wiebe, W. J. *Proc. Natl. Acad. Sci. USA* **95**, 6578–6583 (1998).
13. Biddle, J. F. *et al.* *Proc. Natl. Acad. Sci. USA* **103**, 3846–3851 (2006).
14. Jørgensen, B. B. & Boetius, A. *Nature Rev. Microbiol.* **5**, 770–781 (2007).
15. Inagaki, F. *et al.* *Proc. Natl. Acad. Sci. USA* **103**, 2815–2820 (2006).
16. Valentine, D. L. *Nature Rev. Microbiol.* **5**, 316–323 (2007).

## ARCHAEOLOGY

## An oasis in time

Today's Sahara is arid and inhospitable, but this was not always the case. In the early Holocene (between about 10,000 and 4,500 years ago), monsoon rains created a lush savannah rich in animal and plant life. Complex human societies settled there beside ancient lakes, as demonstrated by a recently reported archaeological site documenting nearly 5,000 years of human occupation (P. C. Sereno *et al.* *PLoS ONE* **3**, e2995; 2008).

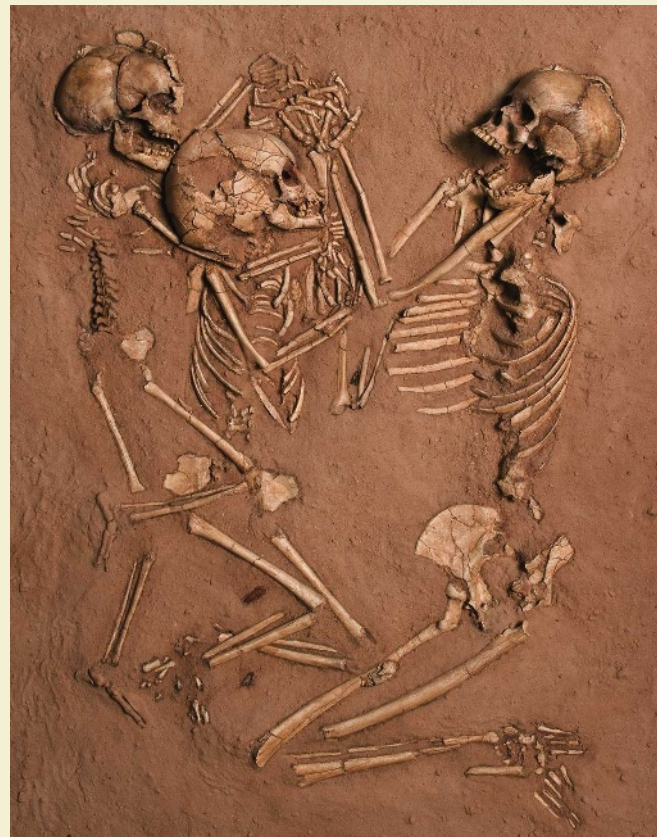
The site, named Gobero and situated in central Niger, contains about 200 burial sites, which, along with several rubbish dumps, provide a record of two distinct periods of human settlement. It was originally occupied 9,500 years ago by a tall, well-muscled people who fished the lake for Nile perch and large catfish with the use of bone harpoons and hooks. These people abandoned the site a little over 8,000 years ago when an

extended arid period dried up the lake.

Gobero was recolonized 1,000 years later by a shorter and shorter people who ate clams and small catfish from the now much shallower lake, as well as antelope and other vertebrates from the surrounding savannah. This population had sophisticated burial practices involving jewellery and grave goods, and what appear to be ritual poses. One grave, dated to be about 5,300 years old, contained a woman and two children buried together with clasped hands (pictured). Pollen found in this grave suggests that they were buried on a bed of wool flowers (*Celosia*).

Occupation of the Gobero site came to an end around 4,500 years ago, when changing climate returned this region to the arid desert conditions that persist to this day.

Christopher Surridge



MIKE HETTER/PROJECT EXPLORATION

method of identifying metabolically active cells, the data suggest that consistent application of FISH remains a challenge. To achieve a similar goal of studying only 'living' cells, direct extraction of rRNA followed by reverse transcription to DNA has been successful<sup>13</sup>, but attempts to make this approach quantitative face major hurdles.

Theoretically, there are fewer challenges when examining DNA or lipids. Quantitative amplification of extracted DNA by using the polymerase chain reaction (qPCR) allows rRNA genes to be counted, rather than seeking ribosomes directly. Even after accounting for the variable copies per cell of these genes in Bacteria and Archaea, early results from qPCR invariably declared the winner to be Bacteria<sup>11,15</sup>. How, then, is it possible that Archaea could have been underestimated?

The key word is 'extracted' — Lipp *et al.*<sup>1</sup> resolve the qPCR dilemma, showing that a more aggressive approach to obtaining total DNA is essential. It is revealing to view their Supplementary Fig. 3: depending on the method used, as many as 80% or as 'few' as 15% of cells escape lysis, the latter under optimized conditions. The implication is that DNA from these escapees would be overlooked during qPCR, and most of them would be Archaea with their more durable cell envelopes.

Improved extraction brings estimates from qPCR in line with earlier claims of archaeal abundance as derived from IPLs<sup>13</sup>. Polar lipids are presumed to reflect living biomass, because

their labile (often phosphate-containing) head groups are quickly lost after cell death. Lipp *et al.* also offer expanded IPL data covering seven different locations. Nearly 90% of IPLs below a depth of 1 metre are specific to Archaea, and the total abundance is proportional to the total organic carbon content of the sediment in which they are found. This suggests that archaeal production fundamentally scales to the available organic resources, whatever the type of metabolism involved.

In considering Archaea and Bacteria, it has been proposed that Archaea are united by a universal ecological ability to cope with energetic stress<sup>16</sup>. It is therefore reasonable that in a sub-seafloor world, where it has been estimated that cell turnover times could be centuries or longer<sup>8,9</sup>, organisms with honed strategies to conserve energy would dominate.

Nevertheless, Lipp and colleagues' results will be controversial. Much of their argument rests on the interpretation that all IPLs represent living cells — that is, that the degradation time of IPLs after cell death is infinitely fast relative to other processes in the system. Although IPLs degrade rapidly in experiments, little is known about their persistence in complex communities with extraordinarily low rates of enzymatic activity. Specifically, it is the persistence of archaeal IPLs relative to bacterial IPLs that is of particular importance. This requires further study of the turnover of both Bacteria and Archaea in sediments, especially with regard to specific rates of synthesis, alteration

and degradation of lipids. For microbes, the boundary between alive and dead is fuzzy, and the extent to which any category of biomolecule can define it remains unclear. Progress on all fronts of culture-independent and culture-dependent techniques will be necessary to tackle these uncertainties.

Ann Pearson is in the Department of Earth and Planetary Sciences, Harvard University, Cambridge, Massachusetts 02138, USA.  
e-mail: pearson@eps.harvard.edu

1. Lipp, J. S., Morono, Y., Inagaki, F. & Hinrichs, K.-U. *Nature* **454**, 991–994 (2008).
2. Zobell, C. E. & Morita, R. Y. in *Galathea Report* Vol. 1, 139–154 (Danish Science, 1959).
3. Parkes, R. J. *et al.* *Nature* **371**, 410–413 (1994).
4. Parkes, R. J., Cragg, B. A. & Wellsbury, P. *Hydrogeol. J.* **8**, 11–28 (2000).
5. Froelich, P. N. *et al.* *Geochim. Cosmochim. Acta* **43**, 1075–1090 (1979).
6. Jørgensen, B. B. *Nature* **296**, 643–645 (1982).
7. Oremland, R. S., Culbertson, C. & Simoneit, B. R. T. in *Initial Reports of the Deep Sea Drilling Project* (eds Curran, J. R. *et al.*) 759–762 (US Government Printing Office, 1982).
8. D'Honst, S., Rutherford, S. & Spivack, A. J. *Science* **295**, 2067–2070 (2002).
9. D'Honst, S. *et al.* *Science* **306**, 2216–2221 (2004).
10. Mauclaire, L., Zepp, K., Meister, P. & McKenzie, J. *Geobiology* **2**, 217–223 (2004).
11. Schippers, A. *et al.* *Nature* **433**, 861–864 (2005).
12. Whitman, W. B., Coleman, D. C. & Wiebe, W. J. *Proc. Natl. Acad. Sci. USA* **95**, 6578–6583 (1998).
13. Biddle, J. F. *et al.* *Proc. Natl. Acad. Sci. USA* **103**, 3846–3851 (2006).
14. Jørgensen, B. B. & Boetius, A. *Nature Rev. Microbiol.* **5**, 770–781 (2007).
15. Inagaki, F. *et al.* *Proc. Natl. Acad. Sci. USA* **103**, 2815–2820 (2006).
16. Valentine, D. L. *Nature Rev. Microbiol.* **5**, 316–323 (2007).

## OBITUARY

# Yoji Totsuka (1942–2008)

Leader in the discovery of neutrino oscillations.

Yoji Totsuka, a major figure in the world of particle physics, died on 10 July after a long battle with cancer. He was a leading light in the thrilling advances in the physics of neutrinos over the past 30 years, and was a notably resolute figure in seeing through the rebuilding of the Super-Kamiokande neutrino detector after a disastrous accident in 2001.

Born on 6 March 1942, in Fuji, Japan, Totsuka received his bachelor's, master's and PhD degrees from the University of Tokyo. His thesis project studied ultra-high-energy particle interactions, so kick-starting his lifelong passion for particle physics. As a research associate with the University of Tokyo, he then travelled to the Deutsches Electron Synchrotron Laboratory in Germany to investigate electron–positron collisions. He went on to accept an associate professorship at Tokyo in 1979.

Perhaps the turning point in Totsuka's career came in 1981, when he started work on the Kamiokande experiment with Masatoshi Koshiba — who was later jointly awarded the Nobel Prize in Physics with Ray Davis Jr for the detection of cosmic neutrinos. The Kamiokande project was originally designed to detect proton decays. A tank of ultra-pure water acted as a source of protons; the products of proton decay would interact with the water to produce distinctive Cherenkov radiation, which could be observed by hundreds of photomultiplier tubes arranged around the inner surface of the tank. A huge volume of water was required (3,000 tons), which was buried deep underground to block out background noise from cosmic rays.

The experiment set stringent limits on the proton-decay process and was also able to study both low-energy neutrinos from the Sun and neutrinos produced in Earth's atmosphere by cosmic rays. Solar neutrinos had previously been detected by Ray Davis Jr in the late 1960s with the use of a chlorine-based detector, but only one-third of the expected neutrino flux was observed. This discrepancy with theory became known as the solar neutrino deficit and was an early indication of a problem in understanding neutrinos.

In 1987, the Kamiokande collaboration had a stroke of luck when a supernova exploded in the Large Magellanic Cloud. Along with the Irvine–Michigan–Brookhaven consortium in the United States, the Kamiokande detector observed the resulting burst of neutrinos. This event was hailed as the birth of neutrino astronomy. More than 800 scientific papers were subsequently written that used the data to extract information about the properties

of the supernova and of the neutrinos themselves.

Shortly after the supernova, Koshiba retired and Totsuka became leader of the Kamiokande project. Two seminal results from the group were subsequently published. The first observed a deficit in atmospheric neutrinos that could not be explained by systematic experimental errors or uncertainties in the background neutrino flux. Instead, some “as-yet-unaccounted-for physics”, as the paper put it, might explain the data. The second crucially confirmed the solar neutrino deficit recorded by Davis.

In 1991, Totsuka obtained funding for a successor to Kamiokande. This was Super-Kamiokande, an underground detector that contained 50,000 tons of water. Super-Kamiokande provided the first definitive evidence for neutrino oscillations and neutrino mass. Neutrino oscillation is a process in which neutrinos convert between one of three types: electron neutrinos, muon neutrinos and tau neutrinos. Atmospheric neutrinos are predominantly muon and electron neutrinos. Because these particles can pass through the Earth without being absorbed, it was predicted that as many atmospheric neutrinos should come up from the ground as travel down from the sky. But the observations with Super-Kamiokande found that, although there were equal numbers of electron neutrinos travelling in these directions, fewer muon neutrinos were detected coming up than were going down.

We now know that, because the upward-going muon neutrinos had travelled much farther — through the planet — than those that came directly down through the atmosphere, they had more time to convert into tau neutrinos (which were essentially invisible to the detector). This evidence of neutrino oscillation suggested an explanation for the solar neutrino deficit: the ‘missing’ electron neutrinos from the Sun might simply have been converted into tau neutrinos and muon neutrinos, which could not be spotted by the earlier detectors. This was later confirmed through work at Super-Kamiokande and at the Sudbury Neutrino Observatory in Canada.

In 2003, Totsuka became the Director General of Japan's high-energy physics organization, KEK. Over the next three years, he oversaw the K2K neutrino-oscillation experiment, in which a beam of neutrinos was sent 250 km from the KEK accelerator to Super-Kamiokande. This experiment confirmed the earlier findings of atmospheric neutrino oscillation. During this period,



Totsuka also supervised the successful Belle B-factory, where particles known as B-mesons were generated to study differences between matter and antimatter.

Totsuka proved his mettle as a leader in the aftermath of the Super-Kamiokande accident in 2001, when thousands of photomultipliers in the detector imploded. The day after the accident, he announced that the detector would be reconstructed within a year. In just two months he established a road-map to achieve this, and the detector was indeed ready for action 13 months after the accident.

During the last year or so of his illness, Totsuka wrote a blog in which he aired his views on science and science policy. He also used this forum to describe his own illness, plotting the extent of his cancer as a function of time, and evaluating the effectiveness of the chemical treatment. And, revealing entirely different interests, he discussed the flowers in his garden and in the village where Super-Kamiokande is located.

Totsuka received international recognition for his work, winning many academic prizes — perhaps most notably the Order of Culture, the most prestigious prize in Japan. It is a testament to his achievements that neutrino physics continues to generate enormous interest. The efforts of the Super-Kamiokande collaboration laid the foundations for the current, detailed understanding of the atmospheric neutrino anomaly and the solar neutrino problem. Yoji Totsuka was central to those efforts, and his vision and leadership will be sorely missed.

## Henry W. Sobel & Yoichiro Suzuki

Henry W. Sobel is at the School of Physical Sciences, University of California, Irvine, Irvine, California 92697-4575, USA. Yoichiro Suzuki is at the Kamioka Observatory, Institute for Cosmic Ray Research, University of Tokyo, Higashi-Mozumi, Kamioka, Hida-City, Gifu 506-1205, Japan.  
e-mails: suzuki@suketto.icrr.u-tokyo.ac.jp; hsobel@uci.edu

## ARTICLES

# The *Trichoplax* genome and the nature of placozoans

Mansi Srivastava<sup>1</sup>, Emina Begovic<sup>1,2</sup>, Jarrod Chapman<sup>2</sup>, Nicholas H. Putnam<sup>2</sup>†, Uffe Hellsten<sup>2</sup>, Takeshi Kawashima<sup>1,3</sup>, Alan Kuo<sup>2</sup>, Therese Mitros<sup>1</sup>, Asaf Salamov<sup>2</sup>, Meredith L. Carpenter<sup>1</sup>, Ana Y. Signorovitch<sup>4,5</sup>, Maria A. Moreno<sup>4</sup>, Kai Kamm<sup>7</sup>, Jane Grimwood<sup>8</sup>, Jeremy Schmutz<sup>8</sup>, Harris Shapiro<sup>2</sup>, Igor V. Grigoriev<sup>2</sup>, Leo W. Buss<sup>5,6</sup>, Bernd Schierwater<sup>4,7</sup>, Stephen L. Dellaporta<sup>4</sup> & Daniel S. Rokhsar<sup>1,2</sup>

As arguably the simplest free-living animals, placozoans may represent a primitive metazoan form, yet their biology is poorly understood. Here we report the sequencing and analysis of the ~98 million base pair nuclear genome of the placozoan *Trichoplax adhaerens*. Whole-genome phylogenetic analysis suggests that placozoans belong to a 'eumetazoan' clade that includes cnidarians and bilaterians, with sponges as the earliest diverging animals. The compact genome shows conserved gene content, gene structure and synteny in relation to the human and other complex eumetazoan genomes. Despite the apparent cellular and organismal simplicity of *Trichoplax*, its genome encodes a rich array of transcription factor and signalling pathway genes that are typically associated with diverse cell types and developmental processes in eumetazoans, motivating further searches for cryptic cellular complexity and/or as yet unobserved life history stages.

Placozoans (literally, 'flat animals') are small (1–2 mm), disc-shaped creatures that were initially discovered<sup>1</sup> on the walls of a saltwater aquarium in the late 1800s. These unusual animals were largely neglected until they were rediscovered<sup>2</sup> in the 1970s and were subsequently found throughout tropical and subtropical oceans in near-shore habitats, particularly mangrove communities<sup>3,4</sup>. Placozoans are readily collected in the wild and can be maintained in the laboratory on diverse food sources. Although placozoans found in diverse locations are morphologically indistinguishable, they show surprising diversity at the DNA level, suggesting that cryptic species may exist<sup>5–7</sup>. The only named species in the phylum is *Trichoplax adhaerens* F. E. Schulze<sup>1</sup>.

*Trichoplax* appears as a flat disc of cells consisting of two epithelial layers, which sandwich a layer of multinucleate fibre cells (Fig. 1a). Only four cell types have been described previously<sup>8,9</sup> (Fig. 1b); nerves, sensory cells and muscle cells are apparently absent. To feed, *Trichoplax* climbs atop its food using the bottom surface as a temporary extraorganismal gastric cavity; digestion is both extracellular and phagocytic<sup>10,11</sup>. When not feeding, the animals move by cilia on the bottom surface and by the fibre cell layer<sup>10</sup>. Placozoans have no evident body axes other than top versus bottom and periphery versus interior; they show no regular directionality in their movement, although both positive and negative phototaxes have been observed (K. von der Chevallerie, T. Bergmann and B. Schierwater, unpublished observations).

In culture, *Trichoplax* reproduces by fission, whereby two (sometimes three) parts of the animal move away from each other until their connection is ruptured (Fig. 1c–e). Sexual reproduction has not been observed in culture but putative oocyte formation in degenerating animals is routinely seen<sup>12</sup>. These large cells have been observed to undergo cleavage (Fig. 1f, g) up to a 256-cell stage before degenerating (M. Eitel and B. Schierwater, unpublished observations).

Although sperm have been described previously<sup>13</sup>, this has not been seen by other investigators. Population genetic analyses, however, demonstrate allelic variation and evidence for genetic recombination in animals in the wild that is consistent with sex<sup>14</sup>.

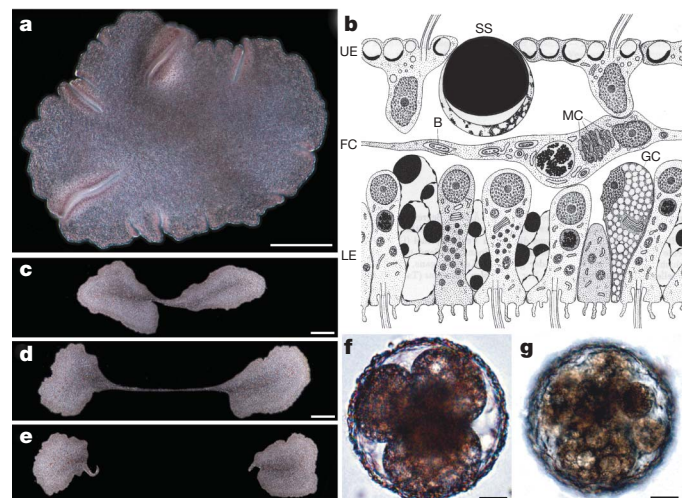


**Figure 1 | Placozoan body plan and reproduction.** **a**, *Trichoplax* in laboratory culture; scale bar, 200 µm. **b**, Schematic rendering of a transverse section through *Trichoplax*. B, bacterium in endoplasmic cisterna; FC, contractile fibre cell; GC, gland cell; LE, lower epithelium; MC, mitochondrial complex; SS, shiny sphere; UE, upper epithelium (taken with permission from ref. 45). **c–e**, *Trichoplax* progressing through asexual reproduction by fission; scale bars, 200 µm. **f**, A cleaving *Trichoplax* 'embryo' at the 4-cell stage is shown; scale bar, 20 µm. **g**, A cleaving *Trichoplax* 'embryo' at the 16-cell stage is shown; scale bar, 20 µm.

<sup>1</sup>Center for Integrative Genomics and Department of Molecular and Cell Biology, University of California, Berkeley, California 94720, USA. <sup>2</sup>Department of Energy Joint Genome Institute, Walnut Creek, California 94598, USA. <sup>3</sup>Okinawa Institute of Science and Technology, Uruma, Okinawa 904-2234, Japan. <sup>4</sup>Department of Molecular, Cellular, and Developmental Biology, <sup>5</sup>Department of Ecology and Evolutionary Biology, and <sup>6</sup>Department of Geology and Geophysics, Yale University, New Haven, Connecticut 06520, USA. <sup>7</sup>Division of Ecology and Evolution, Institut für Tierökologie und Zellbiologie, Stiftung Tierärztliche Hochschule Hannover, Bünteweg 17d, D-30559 Hannover, Germany. <sup>8</sup>Stanford Human Genome Center, Stanford University, Stanford, California 94304, USA. <sup>†</sup>Present address: Department of Ecology and Evolutionary Biology, Rice University, Houston, Texas 77005, USA.

The phylogenetic relationship of placozoans to other metazoans remains controversial. Whereas early studies on the basis of a small number of genes suggested that placozoans could be secondarily simplified cnidarians<sup>15</sup>, other analyses refuted this position<sup>16,17</sup>. Small subunit ribosomal RNA analysis suggested placozoans as eumetazoans, either as a sister group to bilaterians<sup>16</sup> or as the earliest eumetazoan branch<sup>18</sup> (although addition of the large subunit rRNA sequences reduced the resolution of the phylogenetic tree). Analyses of the complete mitochondrial genomes of *Trichoplax adhaerens*<sup>19</sup> and other placozoans<sup>20</sup>, however, led to the proposal that Placozoa could be the earliest branching basal metazoan phylum (but see ref. 21).

Here we report the draft nuclear genome sequence of *Trichoplax adhaerens* and use it to begin to address the nature of placozoans. Our phylogenetic analysis supports the identification of placozoans as a basal eumetazoan lineage that diverged before the separation of cnidarians and bilaterians but after the divergence of demosponges from other animals. The compact genome shows remarkable complexity, including conserved gene content, gene structure and synteny relative to human and other eumetazoan genomes. Despite the absence of any known developmental program and only a modest number of cell types, the *Trichoplax* genome encodes a rich array of transcription factors and signalling genes that are typically associated with embryogenesis and cell fate specification in eumetazoans, as well as other genes that are consistent with cryptic patterning of cells, unobserved life history stages and/or complex execution of biological processes such as fission and embryonic development in these enigmatic creatures.

## The *Trichoplax* genome

We produced a high-quality draft sequence of the ~98 million base pair (megabases, Mb) *Trichoplax* genome using whole-genome shotgun methods<sup>22</sup> with ~8-fold redundant sequence coverage. Because there are at present no genetic or physical maps of *Trichoplax*, we could not reconstruct entire chromosomes, but the completeness of the draft assembly (98% of the 14,571 expressed sequence tags (ESTs) align) and its long-range linkage (19 scaffolds longer than 1 Mb represent 80% of the assembly) make it an excellent substrate for annotation and comparative analysis (Supplementary Information).

As expected from genomic sequences derived from an asexually reproducing laboratory culture of diploid animals, only two alleles are observed at each locus. The single nucleotide polymorphism frequency is 1% and is distributed as expected for two haplotypes selected from a panmictic sexual population (Supplementary Information). We observed 35 extended regions of unusually low polymorphism (<0.25% over more than 40 kb), indicating recently shared ancestry of the two haplotypes by inbreeding or gene conversion and/or the influence of selective sweeps. Sampling of more than two haplotypes is required to distinguish between these two possibilities.

## Trichoplax gene complement and conserved gene structures

We estimate that the *Trichoplax* genome contains 11,514 protein coding genes, on the basis of a combination of homology-based and *ab initio* methods (Supplementary Information). Nearly 87% of these predicted genes have detectable similarity to proteins known from other animals, and most (83%) of the ~7,800 gene families that are conserved between the sea anemone and bilaterians<sup>23</sup> have homologues

in *Trichoplax* as detected by BLAST. *Trichoplax* genes have an intron density (7.6 per kb) comparable to that found in vertebrates (8.5 per kb) and the starlet sea anemone (6.7 per kb)<sup>23</sup>.

Analysis of the exon–intron structure of orthologous genes demonstrates a high degree of conservation in *Trichoplax* relative to other eumetazoans, extending the antiquity of many animal introns (Supplementary Information)<sup>23</sup>. For example, in conserved regions, 82% of human introns have orthologous counterparts with the same position and phase in *Trichoplax*. The retention of ancient introns in *Trichoplax* is in contrast to other animals with small genomes that show extensive intron loss (for example, fruitfly, soil nematode and sea squirts) that presumably accompanied their reduction in genome size<sup>23</sup>.

## Relationship of *Trichoplax* to other animals

We reassessed the phylogenetic position of placozoans relative to other metazoans using Bayesian, maximum likelihood, and parsimony analyses of a concatenation of 104 slowly evolving single-copy nuclear genes (6,783 aligned amino acid positions) drawn from nine diverse fully sequenced genomes (Fig. 2 and Supplementary Information). With 100% Bayesian support and 92% likelihood bootstrap support, placozoans are found to be a sister group to the other eumetazoans (as represented by two cnidarians and a sampling of diverse bilaterians), with demosponge sequences diverging before the *Trichoplax*–cnidian–bilaterian clade. This topology is further supported by parsimony analysis (albeit with weaker support). There is no support for *Trichoplax* as a derived or basal cnidarian or bilaterian, and these hypotheses are rejected by statistical phylogenetic tests (see Supplementary Information). Although there is strong likelihood bootstrap and Bayesian support for the topology in Fig. 2, our analysis can only reject the placement of *Trichoplax* basal to other animals at the  $P = 0.07$  level.

Although our result disagrees with results from mitochondrial trees<sup>19,20,24</sup>, these other analyses are complicated by the long branch lengths (that is, unusually high amounts of amino acid divergence) found in bilaterian mitochondrial peptides relative to their basal metazoan orthologues<sup>24,25</sup>. Figure 2 shows that peptides encoded by the nuclear genome have no notable differences in amino acid substitution levels between basal metazoans and bilaterians, suggesting that our proposed phylogeny on the basis of nuclear genes is less susceptible to long-branch attraction artefacts.

## Conserved synteny with other eumetazoans

Although the placozoan lineage diverged from that of other animal phyla in the Precambrian, we find evidence for limited conserved local gene order as well as substantial blocks of longer-range conserved linkage (synteny) in the *Trichoplax* genome relative to the larger vertebrate and the starlet sea anemone genomes (Supplementary Table 8.1). This is in sharp contrast to the relatively small genomes of flies and nematodes, which show no such conservation. Quantitative analyses of gene neighbourhoods in *Trichoplax*, human and *Nematostella* genomes show that the *Trichoplax* genome has the lowest amount of local rearrangement relative to the common placozoan–cnidarian–bilaterian ancestor (Supplementary Information).

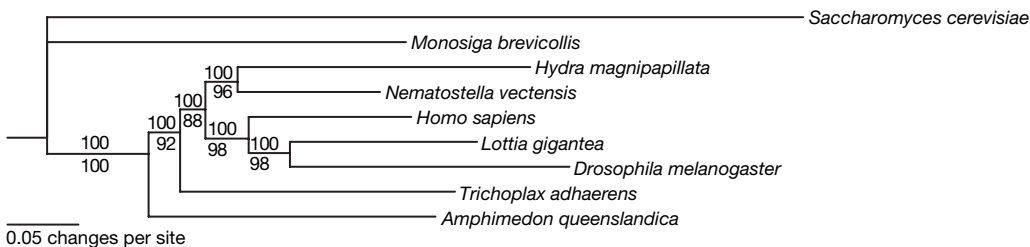


**Figure 2 | Metazoan phylogeny and *Trichoplax*.** Bayesian phylogeny of metazoans places *Trichoplax* as the sister group to cnidarians and bilaterians. Maximum parsimony applied to the same alignment results in a single tree with the same topology shown here. Posterior probabilities are reported above each branch; likelihood bootstrap support values are reported below.

The *Trichoplax* genome also shows larger blocks of conserved synteny (that is, conserved linkage without requiring colinearity<sup>26</sup>) relative to the human genome. Each of the 21 longest gene-rich *Trichoplax* scaffolds contains segments with a significant concentration of orthologues on one or more human chromosome segments (Supplementary Information). These segments are clearly visible in a dotplot of the *Trichoplax* scaffolds versus the 17 ancestral chordate linkage groups<sup>27</sup> (Fig. 3), which shows that many of these linkages have been preserved in the *Trichoplax* genome, and that most of the chordate linkage groups date back to the placozoan–vertebrate last common ancestor. Neither flies nor nematodes show such conservation. For example, chordate linkage group 10 (comprising portions of human chromosomes 1q, 6p and 9q) appears in its entirety as a relatively compact 3.2 Mb segment of *Trichoplax* scaffold 2, with substantial gene-order changes (Fig. 3 and Supplementary Fig. 8.1). The observation of blocks of conserved synteny is consistent with a relatively low rate of local rearrangement in *Trichoplax*.

### Putative developmental transcription factors

With only four (or possibly five<sup>28</sup>) morphologically identifiable somatic cell types, one might naively expect *Trichoplax* to possess few transcription factors associated with the complex regulation of cell

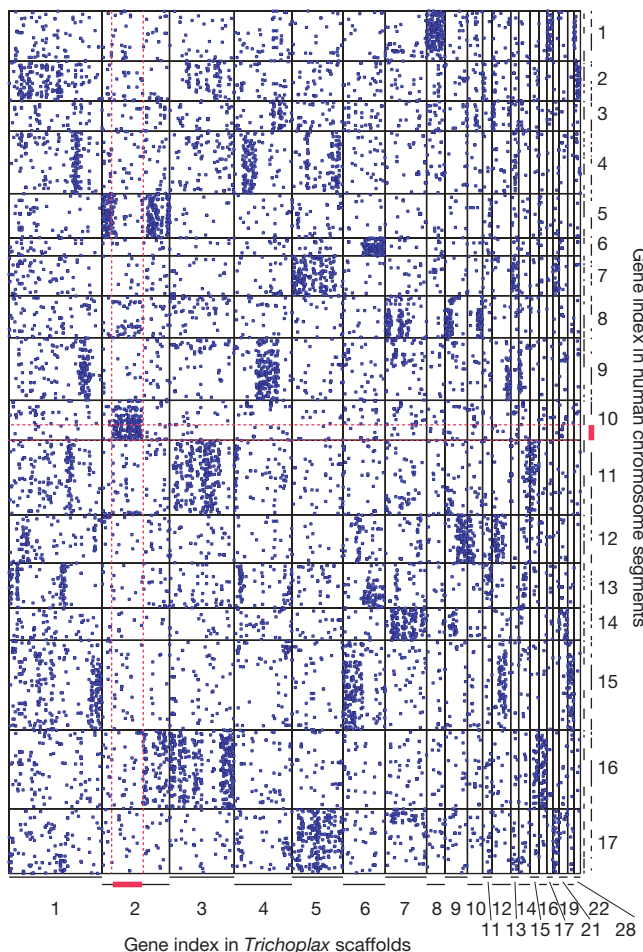


**Figure 3 | Conserved genomic features between the *Trichoplax* and human genomes.** Blue dots represent orthologues in the 21 most gene-rich *Trichoplax* scaffolds and the human genome. Human chromosomal segments have been grouped by ancestral chordate chromosome<sup>27</sup> (Supplementary Information). Horizontal lines divide groups of human segments descended from each of the 17 ancestral chordate chromosomes; vertical lines divide *Trichoplax* scaffolds; alternating bars outside the dotplot represent individual human segments (vertical) or *Trichoplax* scaffolds (horizontal). Red bars and dotted lines highlight the genomic regions compared in Supplementary Fig. 8.1.

fate, patterning and differentiation that are found in other eumetazoans (Table 1). Nevertheless, targeted studies of homeoboxes in *Trichoplax* have identified a modest complement of these essential eumetazoan patterning genes, including paired box genes<sup>29</sup> and members of the ANTP class<sup>30</sup>. Two of these (*Trox-2* and *Not*) are expressed around the rim of the animal, defining the only known molecular patterning of its body plan<sup>28,31</sup>.

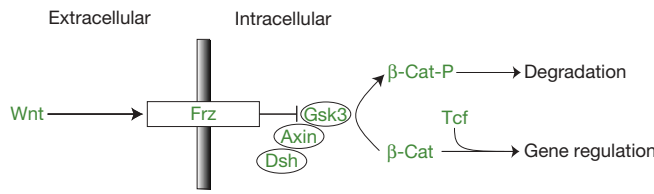
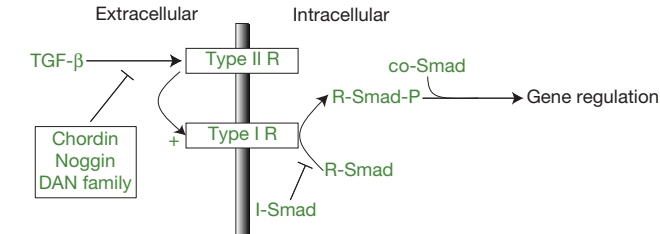
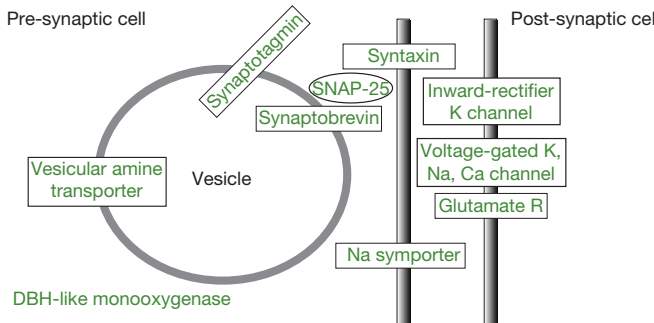
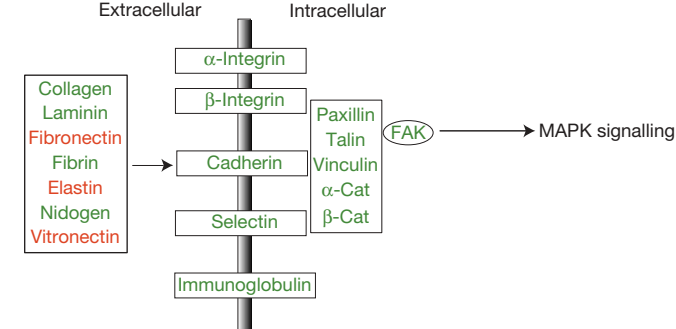
*Trichoplax* contains a rich repertoire of transcription factors (Table 1 and Supplementary Information) commonly associated with patterning and regionalization during eumetazoan development, including further homeobox-containing genes from the ANTP, Paired (PRD), POU and SIX subfamilies<sup>32</sup>. *Trichoplax* also has members of many subfamilies of the animal-specific Sox (Sry-related HMG-box) family involved in the regulation of embryonic development, the T-box family including brachury (the expression of which defines the blastopore in eumetazoan gastrulation<sup>33</sup>), and the opisthokont (animal and fungi)-specific Fox (forkhead/winged-helix) family.

Transcription factors that regulate cell type specification and differentiation in bilaterians are also abundant in *Trichoplax*, including multiple LIM-homeobox genes typically associated with subtype specification in neurons, multiple basic helix-loop-helix family genes associated with neural and muscle cell fates, a (linked) pair of POU-homeobox family genes implicated in neuroendocrine development, and a pair of GATA-family zinc-finger transcription factors that participate in the specification of endodermal, cardiac and blood cell fates. Thus, the *Trichoplax* genome encodes a variety of nominally cell-type-specific markers despite having only a few recognizable cell

**Table 1 | Developmental transcription factors in the *Trichoplax* genome**

Transcription factor family	Gene number in <i>Trichoplax</i>	Subfamilies represented
Homeobox ANTP-class	35	
	14	<i>Trox-2</i> ( <i>Hox/ParaHox-like</i> ) <sup>28</sup> , <i>Not</i> <sup>31</sup> , <i>Dlx</i> <sup>30</sup> , <i>Mnx</i> <sup>30</sup> , <i>Hmx</i> <sup>30</sup> , <i>Hex</i> , <i>Dbx</i> , seven others
PRD-class (paired box and homeobox)	9	<i>PaxB</i> <sup>29</sup> , <i>Pitx</i> , <i>Otp</i> , <i>Gsc</i> , five others
POU-class (POU domain and homeobox)	2	POU class 4 ( <i>Brn-3</i> ), one other
LIM-class (LIM domain and homeobox)	4	islet, <i>apterous</i> , <i>Lhx1/5</i> , one other
SIX-class (sine oculis homeobox)	2	<i>Six3/6</i> , one other
TALE-class	3	<i>Pbx/Exd</i> , <i>Irx</i> , <i>Meis</i>
HNF-class	1	<i>Hnf</i>
Helix-loop-helix	27	
Group A	6	<i>Ptf</i> , five others
Group B	10	<i>SrebP</i> , <i>Myc</i> , <i>Max</i> , <i>BigMax</i> , <i>Usf</i> , <i>Ap4</i> , four others
Group C	4	<i>Ahr</i> , <i>Arnt</i> , two <i>Hif/Sim</i>
Group D	2	Two <i>Hes</i> / <i>Hey</i>
Atonal group	5	Five unclassified
Zinc finger	56	
GATA	2	<i>Gata-1/2/3</i> , <i>Gata-4/5/6</i>
Nuclear receptor C2H2	4	<i>Hnf4</i> , retinoid X receptor, <i>Nr2</i> , one other
	50	<i>Zic</i> , three SP family, five <i>Klf</i> family, <i>snail</i> , <i>scratch</i> , <i>Ovo</i> , <i>Egr</i> , <i>Dpf</i> , <i>Gfi</i> , <i>MizF</i> , <i>Fez</i> , <i>Zfp277</i> , <i>Zfp143</i> , <i>Wt1</i> , AE binding protein, twenty-nine others
Sox (SRY-related HMG-box)	6	<i>Sox8/10/E</i> , <i>Sox2/3</i> , three other Sox, <i>Tcf/Lef</i>
Fox (forkhead/winged-helix)	18	<i>FoxA, B, D, F, J, K, O, Q</i> , two <i>FoxN</i> , two <i>FoxG</i> , six others
T-box	5	brachury <sup>33</sup> , <i>Tbx2/3</i> , three others
bZip	15	<i>Atf2</i> , <i>Atf6</i> , <i>Creb</i> , <i>Crem</i> , <i>Jun</i> , <i>Hlf</i> , <i>MafB</i> , <i>nfL3</i> , seven others
ETS	7	<i>Ets</i> , <i>Pea3</i> , five others

The subfamily memberships of genes listed here were determined by phylogenetic analyses using neighbour-joining and parsimony with bootstrap methods for all families of transcription factors except bZip and C2H2 zinc fingers. These two groups were characterized by BLAST.

**a Wnt signalling****b TGF-β signalling****c Neural processes****d Cell adhesion**

**Figure 4 | Metazoan signalling pathway and biological process genes in the *Trichoplax* genome. a–d,** Known signalling and biological processes in bilaterians are shown in schematic form, with the colours of the protein names indicating their presence (green) or absence (red) in the *Trichoplax* genome.

types, suggesting massive redundancy of function, alternative functions not directly analogous to those in other animals, or cryptic cellular or developmental complexity.

#### Putative developmental signalling pathways

*Trichoplax* lacks consistent directionality in its movements, and possesses upper–lower and centre–rim axes that show no evident homology to bilaterian anteroposterior or dorsoventral axes. Yet, components of a complete Wnt/β-catenin signalling pathway—used for axial patterning in bilaterians and cnidarians<sup>34</sup> and in demosponge larvae<sup>35</sup>—are present in *Trichoplax* (Fig. 4a). All essential components of the TGF-β signalling pathway are also present in the *Trichoplax* genome (Fig. 4b). In bilaterians, TGF-β signalling (mediated by BMP, one class of TGF-β superfamily ligands) is responsible for the establishment of the embryonic dorsoventral axis during bilaterian development with a similar axis-defining role proposed in cnidarian<sup>36</sup> and demosponge larvae<sup>35</sup>.

We did not find evidence for a functioning hedgehog pathway, because there is no evident hedgehog ligand, patched or smoothened receptors, or Gli-like transcription factor. Components of other signalling pathways such as the Notch and JAK/STAT pathways are present, but these pathways seem to be incomplete in that they lack molecular components critical to signal transduction (for example, a Notch-like gene with a true Notch domain in the Notch pathway, or a Janus kinase in the JAK/STAT pathway; Supplementary Table 9.1). Four nuclear receptor family transcription factors are present, suggesting that signalling by lipid-soluble ligands occurs (Table 1). Elements of the animal stress response NF-κB pathway are found in *Trichoplax*, along with a nearly complete set of orthologues of genes typically involved in eumetazoan apoptosis (except for TNFR and Fasreceptor; Supplementary Table 9.1).

The absence of components of some animal signalling pathways in *Trichoplax* relative to their completeness inferred in the cnidarian–bilaterian ancestor<sup>23</sup> suggests that *Trichoplax* branched off from an ancestor that either did not possess all animal signalling pathways or that these genes were lost in the placozoan lineage. This latter interpretation is consistent with the presence of some of these ‘missing’ components (hedgehog, EGFR, notch) in sponges<sup>37–39</sup>.

genome. Wnt/β-catenin signalling (a), TGF-β signalling (b), synapse formation and conduction of nerve impulse (c) and cell adhesion and extracellular matrix components (d) are shown.

#### Elements associated with neuroendocrine function

Although *Trichoplax* has no nervous system, it has behavioural responses to environmental stimuli, and sensitivity to the neuropeptide RFamide has been reported<sup>40</sup>. In the *Trichoplax* genome, we find various ion channels that are implicated in neural signalling in animals. For example, different members of the Kv family of voltage-dependent potassium channel α-subunits (the electrically active shaker and shaw and the electrically inactive Kv9) and β-subunits (KCNAB) are present in the *Trichoplax* genome, along with inward rectifier potassium channels and homologues of voltage-gated sodium channels and voltage-gated L-type calcium channel α1 subunits and their regulatory β-subunit (Fig. 4c).

Components of neurotransmitter biosynthesis and vesicle transport systems, as well as a putative neuroendocrine-like secretory apparatus, are also found in the genome (Fig. 4c). DOPA decarboxylase and DBH-like monooxygenase (which are involved in dopamine, noradrenaline and adrenaline synthesis in adrenergic cells), and putative vesicular amine transporters (which are used for neurotransmitter uptake) are present. The *Trichoplax* genome encodes members of the synaptic core complex (SNAP-25, synaptobrevin and syntaxin). Whereas synaptobrevin and syntaxin are found in diverse eukaryotic groups and are generally involved in vesicular trafficking, *Trichoplax* SNAP-25 has a distinct domain found only in animal versions of this protein and not in other eukaryotic members of this family (for example, Sec9 in yeast)<sup>41</sup>. The genome also contains homologues of the animal neurosecretory vesicle membrane-bound proteins synaptophysin and synaptotagmin, which aid in calcium-dependent vesicle docking and fusion by interacting with SNAP-25.

Putative neurotransmitter and neuropeptide receptors are also present, including abundant seven transmembrane G-protein-coupled receptors (GPCRs) that could be candidate sensory transducers. Four putative opsin genes, which possess a crucial lysine residue in the seventh transmembrane domain and thus are thought to function in light reception, are present. Eighty-five members of the class 3 GPCR family (unrelated to other GPCR families by sequence), including putative metabotropic glutamate receptors, are also found. Transmembrane proteins important in nerve conduction (multiple

candidate ionotropic glutamate receptors) and in neurotransmitter release and uptake (for example, sodium neurotransmitter symporter) are encoded by the genome (Fig. 4c). Synapse formation proteins (such as neurexin and neuroligin) and structural elements of the post-synaptic scaffold known to be present in sponges<sup>42</sup> (such as discs large) are also found in *Trichoplax*, including the receptors and channels missing from the sponge genome. Genes associated with neural migration and axon guidance in bilaterians (slit, netrin, NCAM, semaphorin (also known as CD100) and spondin) are also present. Although all of these nominally neural elements may be functioning in non-neural roles, the *Trichoplax* genome does encode the basic machinery required for the synthesis, release and uptake of neurotransmitters, for synapse formation, and for the conduction of electrical impulses and photoreception.

### Extracellular matrix and cell adhesion

*Trichoplax* has regular cell–cell junctions between epithelial cells but is reported to lack an underlying basal lamina, or indeed, any described extracellular matrix (ECM)<sup>2</sup>. Its genome, however, contains a diverse set of genes that code for putative ECM proteins (Fig. 4d). These include collagen IV, laminin- $\alpha$ , - $\beta$  and - $\gamma$ , and nidogen; however, fibronectin, fibrin, elastin and vitronectin are all apparently absent. Heparan sulphate proteoglycans (including two glypcans) and a matrilin-2-like gene are also found. Because many of these genes were also represented in the ESTs from cultured animals, it is possible that an ECM is present in a way that evades traditional histological stains.

The *Trichoplax* genome also encodes cell-surface adhesion proteins ( $\alpha$ - and  $\beta$ -integrins, cadherins, selectins and immunoglobulin superfamily members) that interact with each other and the ECM in bilaterians, and encodes cytoskeletal linker proteins (paxillin, vinculin, talin and  $\alpha$ - and  $\beta$ -catenin) that help organize the actin cytoskeleton and/or transduce signals in other eumetazoans (Fig. 4d). Similarly, protein components (focal adhesion kinase (FAK), paxillin and talin) that would permit dual functions of  $\beta$ -catenin and integrin receptors in adhesion and signal transduction (through Wnt and FAK signalling, respectively) are encoded by the genome. Enzyme families known to modify ECM components and/or signalling molecules in the matrix, such as lysyl oxidases, the ADAM metalloproteases (including the TACE family) and the TIMP metalloprotease inhibitor are also present.

### Sex and germ cells

Given the ancient eukaryotic origins of meiosis<sup>43</sup>, the production of putative oocytes by *Trichoplax*<sup>2</sup>, and inference of recombination in wild populations<sup>14</sup>, it is perhaps not surprising that meiosis-associated genes are found in the genome (Supplementary Table 9.1). *Trichoplax* has an orthologue of the zinc-finger protein nanos and a member of the vasa/PL10 family of DEAD-box helicases, as well as homologues of mago nashi, PAR-1, pumilio and tudor, which are all implicated in primary germ cell development in eumetazoans. Although these results indicate that *Trichoplax* has the same genetic tools that cnidarians and bilaterians use to segregate the germ line, further studies to document the expression and functions of these genes are needed to verify germ line formation in placozoans.

### Conclusions

Our whole-genome analyses are consistent with placozoans being the earliest diverging eumetazoan phylum, that is, the sister group to the cnidarian–bilaterian clade. Although we cannot formally exclude a more basal position, our analysis rejects the derivation of placozoans from within cnidarians or bilaterians. Further studies (including extra sequences, ideally from whole genomes) will be needed to test this phylogenetic hypothesis.

Although *Trichoplax* has a compact genome relative to vertebrates and many other animals, we find that it has not experienced the same degree of intron loss and genomic rearrangement as other small

(~100 Mb) metazoan genomes have (for example, the sequences of flies and soil nematodes). This suggests that many structural aspects (introns, local gene order and larger-scale linkages) of the small *Trichoplax* genome could be primitive eumetazoan characteristics.

*Trichoplax*'s apparent genomic primitiveness, however, is separate from the question of whether placozoan morphology or life history is a relict of the eumetazoan ancestor. For example, the flat form and gutless feeding could be a 'primitive' ancestral feature, with the cnidarian–bilaterian gut arising secondarily by the invention of a developmental process for producing an internal body cavity (as in Bütschli's 'plakula' theory<sup>44,45</sup>), or it could be a 'derived', uniquely placozoan feature that resulted from the loss of an ancestral eumetazoan gut. Unfortunately, the genome sequence alone cannot answer these questions, but it does provide a platform for further studies.

Although the *Trichoplax* body plan is simple, its genome encodes a rich array of transcription factors and signalling pathways that are typically associated with eumetazoan developmental patterning and cell-type specification. A question remains: what role do these genes have in placozoans? Cellular morphology may be deceptive, and complex gene expression patterns may define functionally distinct but morphologically cryptic cellular subtypes<sup>28,31,33</sup>. This would be consistent with models in which transcription factors associated with gene expression patterns for specific differentiated cell functions in the eumetazoan ancestor were co-opted in cnidarians and bilaterians for patterning roles<sup>46</sup>. We speculate that signalling and transcription factor genes may be involved in complex regulatory events required for the known processes of growth, fission and/or swarming, or the as yet undescribed processes of sexual reproduction and embryonic development (Supplementary Fig. 9.1).

It has been suggested that *Trichoplax* is a 'living fossil' relict of an early stage of animal evolution<sup>9,44</sup>. At least from a genomic perspective, *Trichoplax* retains many ancestral features of its last common ancestor with cnidarians and bilaterians, which lived in the Precambrian. The extent to which the physiology, behaviour and life history of placozoans retains primitive features remains unclear. With the genome in hand, renewed interest in this 'simple' animal with a complex genome will add to our appreciation of animal diversity and perhaps yield fundamental insights into early animal evolution.

### METHODS SUMMARY

Detailed methods are described in the Supplementary Information. The genome assembly, gene model sequences, predicted proteins and EST clusters and sequences can be downloaded from the JGI website <http://www.jgi.doe.gov/trichoplax>. Browser display of the genome sequence, including gene predictions and EST and homologous protein alignments, are also available at this site. The sequence data have been deposited in DDBJ/EMBL/GenBank as accession number ABGP00000000.

**Full Methods** and any associated references are available in the online version of the paper at [www.nature.com/nature](http://www.nature.com/nature).

Received 4 December; accepted 23 June 2008.

1. Schulze, F. E. *Trichoplax adhaerens*, nov. gen., nov. spec. *Zool. Anz.* 6, 92–97 (1883).
2. Grell, K. G. & Ruthmann, A. in *Placozoa, Porifera, Cnidaria and Ctenophora* (eds Harrison, F. W. & Westfall, J. A.) 13–27 (Wiley-Liss, 1991).
3. Pearse, V. B. Growth and behavior of *Trichoplax adhaerens*: first record for the phylum Placozoa in Hawaii. *Pacif. Sci.* 43, 117–121 (1989).
4. Maruyama, Y. K. Occurrence in the field of a long-term, year-round, stable population of placozoans. *Biol. Bull.* 206, 55–60 (2004).
5. Voigt, O. et al. Placozoa—no longer a phylum of one. *Curr. Biol.* 14, R944–R945 (2004).
6. Pearse, V. B. & Voigt, O. Field biology of placozoans (*Trichoplax*): distribution, diversity, biotic interactions. *Integr. Comp. Biol.* 47, 677–692 (2007).
7. Signorovitch, A. Y., Dellaporta, S. L. & Buss, L. W. Caribbean placozoan phylogeography. *Biol. Bull.* 211, 149–156 (2006).
8. Grell, K. G. *Trichoplax adhaerens*, F.E. Schulze und die Entstehung der Metazoen. *Naturwiss. Rundsch.* 24, 160–161 (1971).
9. Schierwater, B. My favorite animal, *Trichoplax adhaerens*. *BioEssays* 27, 1294–1302 (2005).

10. Ruthmann, A., Behrendt, G. & Wahl, R. The ventral epithelium of *Trichoplax adhaerens* (Placozoa): Cytoskeletal structures, cell contacts and endocytosis. *Zoomorphology* **106**, 115–112 (1986).
11. Wenderoth, H. Transepithelial cytophagy by *Trichoplax adhaerens* F. E. Schulze (Placozoa) feeding on yeast. *Z. Naturforsch.* **41C**, 343–347 (1986).
12. Grell, K. G. Eibildung und Furchung von *Trichoplax adhaerens* F. E. Schulze (Placozoa). *Z. Morph. Tiere* **73**, 297–314 (1972).
13. Grell, K. G. & Benwitz, G. Ergänzende untersuchungen zur ultrastruktur von *Trichoplax adhaerens* F.E. Schulze (Placozoa). *Zoomorphology* **98**, 47–67 (1981).
14. Signorovitch, A. Y., Dellaporta, S. L. & Buss, L. W. Molecular signatures for sex in the Placozoa. *Proc. Natl Acad. Sci. USA* **102**, 15518–15522 (2005).
15. Bridge, D., Cunningham, C. W., DeSalle, R. & Buss, L. W. Class-level relationships in the phylum Cnidaria: molecular and morphological evidence. *Mol. Biol. Evol.* **12**, 679–689 (1995).
16. Collins, A. G. Evaluating multiple alternative hypotheses for the origin of Bilateria: an analysis of 18S rRNA molecular evidence. *Proc. Natl Acad. Sci. USA* **95**, 15458–15463 (1998).
17. Ender, A. & Schierwater, B. Placozoa are not derived cnidarians: evidence from molecular morphology. *Mol. Biol. Evol.* **20**, 130–134 (2003).
18. da Silva, F. B., Muschner, V. C. & Bonatto, S. L. Phylogenetic position of Placozoa based on large subunit (LSU) and small subunit (SSU) rRNA genes. *Genet. Mol. Biol.* **30**, 127–132 (2007).
19. Dellaporta, S. L. et al. Mitochondrial genome of *Trichoplax adhaerens* supports placozoa as the basal lower metazoan phylum. *Proc. Natl Acad. Sci. USA* **103**, 8751–8756 (2006).
20. Signorovitch, A. Y., Buss, L. W. & Dellaporta, S. L. Comparative genomics of large mitochondria in placozoans. *PLoS Genet.* **3**, e13 (2007).
21. Ruiz-Trillo, I., Roger, A. J., Burger, G., Gray, M. W. & Lang, B. F. A phylogenomic investigation into the origin of Metazoa. *Mol. Biol. Evol.* **25**, 664–672 (2008).
22. Weber, J. L. & Myers, E. W. Human whole-genome shotgun sequencing. *Genome Res.* **7**, 401–409 (1997).
23. Putnam, N. H. et al. Sea anemone genome reveals ancestral eumetazoan gene repertoire and genomic organization. *Science* **317**, 86–94 (2007).
24. Haen, K. M., Lang, B. F., Pomponi, S. A. & Lavrov, D. V. Glass sponges and bilaterian animals share derived mitochondrial genomic features: a common ancestry or parallel evolution? *Mol. Biol. Evol.* **24**, 1518–1527 (2007).
25. Lavrov, D. V., Forget, L., Kelly, M. & Lang, B. F. Mitochondrial genomes of two demosponges provide insights into an early stage of animal evolution. *Mol. Biol. Evol.* **22**, 1231–1239 (2005).
26. Renwick, J. H. The mapping of human chromosomes. *Annu. Rev. Genet.* **5**, 81–120 (1971).
27. Putnam, N. H. et al. The amphioxus genome and the evolution of the chordate karyotype. *Nature* **453**, 1064–1071 (2008).
28. Jakob, W. et al. The *Trox-2 Hox/ParaHox* gene of *Trichoplax* (Placozoa) marks an epithelial boundary. *Dev. Genes Evol.* **214**, 170–175 (2004).
29. Hadrys, T., DeSalle, R., Sagasser, S., Fischer, N. & Schierwater, B. The *Trichoplax PaxB* gene: a putative Proto-*PaxA/B/C* gene predating the origin of nerve and sensory cells. *Mol. Biol. Evol.* **22**, 1569–1578 (2005).
30. Monteiro, A. S., Schierwater, B., Dellaporta, S. L. & Holland, P. W. A low diversity of ANTP class homeobox genes in Placozoa. *Evol. Dev.* **8**, 174–182 (2006).
31. Martinelli, C. & Spring, J. Expression pattern of the homeobox gene *Not* in the basal metazoan *Trichoplax adhaerens*. *Gene Expr. Patterns* **4**, 443–447 (2004).
32. Schierwater, B. et al. The ancestral Antp gene repertoire: Insights from the placozoan genome. *PLoS ONE* (in the press).
33. Martinelli, C. & Spring, J. Distinct expression patterns of the two T-box homologues *Brachury* and *Tbx2/3* in the placozoan *Trichoplax adhaerens*. *Dev. Genes Evol.* **213**, 492–499 (2003).
34. Lee, P. N., Kumburegama, S., Marlow, H. Q., Martindale, M. Q. & Wikramanayake, A. H. Asymmetric developmental potential along the animal–vegetal axis in the anthozoan cnidarian, *Nematostella vectensis*, is mediated by Dishevelled. *Dev. Biol.* **310**, 169–186 (2007).
35. Adamska, M. et al. Wnt and TGF- $\beta$  expression in the sponge *Amphimedon queenslandica* and the origin of metazoan embryonic patterning. *PLoS ONE* **2**, e1031 (2007).
36. Matus, D. Q., Thomsen, G. H. & Martindale, M. Q. Dorso/ventral genes are asymmetrically expressed and involved in germ-layer demarcation during cnidarian gastrulation. *Curr. Biol.* **16**, 499–505 (2006).
37. Adamska, M. et al. The evolutionary origin of Hedgehog proteins. *Curr. Biol.* **17**, R836–R837 (2007).
38. Nichols, S. A., Dirks, W., Pearse, J. S. & King, N. Early evolution of animal cell signaling and adhesion genes. *Proc. Natl Acad. Sci. USA* **103**, 12451–12456 (2006).
39. Muller, W. E. & Schacke, H. Characterization of the receptor protein-tyrosine kinase gene from the marine sponge *Geodia cydonium*. *Prog. Mol. Subcell. Biol.* **17**, 183–208 (1996).
40. Schuchert, P. *Trichoplax adhaerens* (phylum Placozoa) has cells that react with antibodies against the neuropeptide RFamide. *Acta Zool.* **74**, 115–117 (1993).
41. Risinger, C. et al. Evolutionary conservation of synaptosome-associated protein 25 kDa (SNAP-25) shown by *Drosophila* and *Torpedo* cDNA clones. *J. Biol. Chem.* **268**, 24408–24414 (1993).
42. Sakarya, O. et al. A post-synaptic scaffold at the origin of the animal kingdom. *PLoS ONE* **2**, e506 (2007).
43. Ramesh, M. A., Malik, S. B. & Logsdon, J. M. Jr. A phylogenomic inventory of meiotic genes: evidence for sex in *Giardia* and an early eukaryotic origin of meiosis. *Curr. Biol.* **15**, 185–191 (2005).
44. Büttschi, O. Bemerkungen zur Gastraeatheorie. *Morph. Jahrb.* **9**, 415–427 (1884).
45. Syed, T. & Schierwater, B. The evolution of the Placozoa: a new morphological model. *Senckenbergiana Lethaea* **82**, 259–270 (2002).
46. Erwin, D. H. & Davidson, E. H. The last common bilaterian ancestor. *Development* **129**, 3021–3032 (2002).

**Supplementary Information** is linked to the online version of the paper at [www.nature.com/nature](http://www.nature.com/nature).

**Acknowledgements** This work was performed under the auspices of the USA Department of Energy's Office of Science, Biological and Environmental Research Program and by the University of California, Lawrence Livermore National Laboratory, Lawrence Berkeley National Laboratory and Los Alamos National Laboratory. The Center for Integrative Genomics is supported by a grant from the Gordon and Betty Moore Foundation. D.S.R. acknowledges support from R. A. Melmon, L.W.B., S.L.D. and M.A.M. were supported by the National Science Foundation. B.S. acknowledges support from the German Science Foundation. S.L.D. and B.S. also acknowledge support from Human Frontiers Science Program.

**Author Information** This paper is distributed under the terms of the Creative Commons Attribution-Non-Commercial-Share Alike licence, and is freely available to all readers at [www.nature.com/nature](http://www.nature.com/nature). The sequences generated in this study are available from GenBank under the accession number ABGP00000000. Reprints and permissions information is available at [www.nature.com/reprints](http://www.nature.com/reprints). Correspondence and requests for materials should be addressed to M.S. (msrivast@berkeley.edu) or D.S.R. (dsroksar@yahoo.com).

## METHODS

A detailed description of methods used in this study can be found in the Supplementary Information.

**Genome sequencing.** Genomic DNA was sheared and cloned into plasmid and fosmid vectors for whole-genome shotgun sequencing as described<sup>47</sup>. The data were assembled using release 2.10.6 of Jazz, a WGS assembler<sup>47</sup>. The *Trichoplax* 8× assembly and the preliminary data analysis can be downloaded from <http://www.jgi.doe.gov/trichoplax> and has been deposited at DDBJ/EMBL/GenBank under accession number ABGP00000000.

**Gene prediction and annotation.** The JGI annotation pipeline took scaffolds, repeats and ESTs as inputs and produced gene models and other features that are stored in a relational database. The data can be publicly accessed through the JGI genome portal at <http://www.jgi.doe.gov/trichoplax>. Protein-coding gene predictions are deposited in DDBJ/EMBL/GenBank as accession ABGP00000000.

**Phylogenetic methods.** One hundred and four single-copy orthologous genes from nine genomes were aligned using default parameters using both CLUSTALW<sup>48</sup> and MUSCLE<sup>49</sup>, and poorly aligned regions were excluded using Gblocks, yielding 6,783 aligned amino acid positions. Phylogenetic analyses were conducted using Bayesian inference, maximum likelihood with bootstrap, and maximum parsimony with bootstrap using MrBayes<sup>50</sup>, PHYML<sup>51</sup>, and PAUP<sup>52</sup> respectively. Ribosomal sequences (18S, 5.8S and 28S) were added to the nuclear data set and analysed independently using maximum parsimony with bootstrap. Alternative likelihood topologies were tested using TREEPUZZLE<sup>53</sup> and CONSEL<sup>54</sup>.

**Identification of *Trichoplax* orthologues of specific bilaterian genes.** A list of *Trichoplax* gene models annotated with PANTHER hidden Markov models<sup>55</sup> or PFAM domains<sup>56</sup> was analysed for genes involved in various biological processes in bilaterians. In many cases, *Trichoplax* orthologues of bilaterian genes were identified by BLAST against the *Trichoplax* assembly. The resulting genes were analysed by BLAST against the database of non-redundant proteins, PFAM domain composition and phylogenetic trees to determine orthology to the vertebrate query.

47. Aparicio, S. *et al.* Whole-genome shotgun assembly and analysis of the genome of *Fugu rubripes*. *Science* **297**, 1301–1310 (2002).
48. Thompson, J. D., Higgins, D. G. & Gibson, T. J. CLUSTAL W: improving the sensitivity of progressive multiple sequence alignment through sequence weighting, position-specific gap penalties and weight matrix choice. *Nucleic Acids Res.* **22**, 4673–4680 (1994).
49. Edgar, R. C. MUSCLE: a multiple sequence alignment method with reduced time and space complexity. *BMC Bioinformatics* **5**, 113 (2004).
50. Ronquist, F. & Huelsenbeck, J. P. MrBayes 3: Bayesian phylogenetic inference under mixed models. *Bioinformatics* **19**, 1572–1574 (2003).
51. Guindon, S. & Gascuel, O. A simple, fast, and accurate algorithm to estimate large phylogenies by maximum likelihood. *Syst. Biol.* **52**, 696–704 (2003).
52. Swofford, D. L. *PAUP\**. *Phylogenetic Analysis Using Parsimony (\*and Other Methods)*, version 4.0. (Sinauer Associates, 1999).
53. Schmidt, H. A., Strimmer, K., Vingron, M. & von Haeseler, A. TREE-PUZZLE: maximum likelihood phylogenetic analysis using quartets and parallel computing. *Bioinformatics* **18**, 502–504 (2002).
54. Shimodaira, H. & Hasegawa, M. CONSEL: for assessing the confidence of phylogenetic tree selection. *Bioinformatics* **17**, 1246–1247 (2001).
55. Thomas, P. D. *et al.* PANTHER: a library of protein families and subfamilies indexed by function. *Genome Res.* **13**, 2129–2141 (2003).
56. Bateman, A. *et al.* The Pfam protein families database. *Nucleic Acids Res.* **32**, D138–D141 (2004).

## ARTICLES

# PRDM16 controls a brown fat/skeletal muscle switch

Patrick Seale<sup>1</sup>, Bryan Bjork<sup>2</sup>, Wenli Yang<sup>1</sup>, Shingo Kajimura<sup>1</sup>, Sherry Chin<sup>1</sup>, Shihuan Kuang<sup>3</sup>, Anthony Scimè<sup>3</sup>, Srikrupa Devarakonda<sup>1</sup>, Heather M. Conroe<sup>1</sup>, Hediye Erdjument-Bromage<sup>4</sup>, Paul Tempst<sup>4</sup>, Michael A. Rudnicki<sup>3</sup>, David R. Beier<sup>2</sup> & Bruce M. Spiegelman<sup>1</sup>

**Brown fat can increase energy expenditure and protect against obesity through a specialized program of uncoupled respiration. Here we show by *in vivo* fate mapping that brown, but not white, fat cells arise from precursors that express *Myf5*, a gene previously thought to be expressed only in the myogenic lineage. We also demonstrate that the transcriptional regulator PRDM16 (PRD1-BF1-RIZ1 homologous domain containing 16) controls a bidirectional cell fate switch between skeletal myoblasts and brown fat cells. Loss of PRDM16 from brown fat precursors causes a loss of brown fat characteristics and promotes muscle differentiation. Conversely, ectopic expression of PRDM16 in myoblasts induces their differentiation into brown fat cells. PRDM16 stimulates brown adipogenesis by binding to PPAR- $\gamma$  (peroxisome-proliferator-activated receptor- $\gamma$ ) and activating its transcriptional function. Finally, *Prdm16*-deficient brown fat displays an abnormal morphology, reduced thermogenic gene expression and elevated expression of muscle-specific genes. Taken together, these data indicate that PRDM16 specifies the brown fat lineage from a progenitor that expresses myoblast markers and is not involved in white adipogenesis.**

The epidemic of obesity, closely associated with increases in diabetes, hypertension, hyperlipidemia, cancer and other disorders, has propelled a major interest in adipose cells and tissues. Adipose tissues contain two distinct types of fat cell, white and brown. White fat cells are specialized for the storage of chemical energy such as triglycerides, whereas brown fat cells dissipate chemical energy in the form of heat<sup>1</sup>. Most fat depots can be characterized as either brown or white but some brown fat cells can also be found dispersed throughout white fat depots in rodents and humans<sup>2–4</sup>. Similarities in cell morphology, lipid metabolism and patterns of gene expression between the two types of fat cell has led most investigators to assume that they share a common developmental origin<sup>5–7</sup>.

Until quite recently, brown adipose tissue (BAT) was thought to be of metabolic importance only in smaller mammals and infant humans. Recent studies using positron-emission tomography scanning, however, suggest that adult humans have several discrete areas of metabolically active BAT<sup>8</sup>. BAT may thus have a much more important role in human metabolism than was previously appreciated. The manipulation of fat stores is an obvious therapeutic objective, but disruption of the normal differentiation or development of white adipose tissue (WAT) causes ectopic lipid storage and severe pathology (lipodystrophy) in both humans and experimental animals. Promotion of increased BAT development in humans, however, offers the possibility of increasing energy expenditure without necessarily causing dysfunction in other tissues. Indeed, experimental increases of BAT in animals have been associated with a lean and healthy phenotype<sup>4,9–11</sup>. In contrast, loss of BAT function is linked to obesity and metabolic disease<sup>12</sup>.

The ability to alter BAT development in a measured way depends upon a thorough understanding of the regulatory systems that control determination in this cell type. Several transcriptional suppressors of

BAT development have been identified, including pRB, p107 and RIP140 (refs 13–15). Positive transcriptional regulators include FOXC2 (ref. 9) and PRDM16 (ref. 16), but only PRDM16 has been shown to determine the fate of brown fat cells in a cell-autonomous manner. This protein, which contains several zinc fingers and a PRD1-BF1-RIZ1 homologous (PR) domain, can turn on a full set of BAT-selective genes when expressed in WAT precursors in culture or *in vivo*, while turning off the expression of several white-fat-enriched genes<sup>16,17</sup>. These actions of PRDM16 are, at least partly, mediated by its interaction with other transcriptional co-regulators, PGC-1 $\alpha$  and PGC-1 $\beta$ , and do not require DNA binding of PRDM16. Here we show that PRDM16 can powerfully control a robust, bi-directional switch in cell fate between skeletal myoblasts and brown fat cells. Furthermore, lineage tracing studies *in vivo* show that depots of BAT but not WAT arise from *Myf5*-expressing precursors that brown fat shares with skeletal muscle.

## Results

**Knockdown of PRDM16 in brown fat cells induces skeletal myogenesis.** To examine in detail the cellular and molecular consequence of PRDM16 depletion, we used adenoviral vectors to express a short hairpin (sh)SCR (scrambled) control or shRNA targeting PRDM16 in primary brown fat pre-adipocytes. PRDM16 protein was virtually undetectable in cultures expressing the shPRDM16 construct (Fig. 1a). By day 4 of adipogenic differentiation, cultures expressing the scrambled shRNA had undergone normal brown-fat cell differentiation (Fig. 1b). In striking contrast, shPRDM16-expressing cultures contained long tube-like cells interspersed among fat cells that were strongly marked by green fluorescent protein (GFP), which was co-expressed from the adenoviral vector. In fact, the cells that adopted this morphology were those that had preferentially

<sup>1</sup>Dana-Farber Cancer Institute and the Department of Cell Biology, Harvard Medical School, 1 Jimmy Fund Way, Boston, Massachusetts 02115, USA. <sup>2</sup>Genetics Division, Brigham and Women's Hospital, Harvard Medical School, New Research Building, 77 Avenue Louis Pasteur, Boston, Massachusetts 02115, USA. <sup>3</sup>The Sprott Center for Stem Cell Research, Ottawa Health Research Institute, Molecular Medicine Program, 501 Smyth Road, Ottawa, Ontario K1H 8L6, Canada. <sup>4</sup>Memorial Sloan-Kettering Cancer Center, New York, New York 10021, USA.

taken up and expressed the shPRDM16 construct (Fig. 1b). Immunohistochemistry using a pan-skeletal myosin heavy chain (MyHC) antibody unequivocally identified these cells as skeletal myocytes (Fig. 1c). The myocytes were noted here but not previously<sup>16</sup> because these studies achieved a more complete knockdown of PRDM16; and because the presence of the GFP gene in the adenoviral vector allowed a more focused examination of the transduced cells. Gene-expression analysis showed that knockdown of PRDM16 completely ablated the expression of selective genes for brown fat cells such as *Ucp1*, *Cidea* and *Elovl3* (also known as *Cig30*) (Fig. 1d). Moreover, reduction of PRDM16 was associated with a large increase in the expression of myogenic genes, including *Myod*, myogenin (*Myg*), myosin light chain (*Mlc*), muscle creatine kinase (*Mck*) and *Myhc*. Knockdown of PRDM16 induced the expression of these genes to between 5% and 25% of their levels in C2C12 myotubes, a result generally consistent with the MyHC protein expression observed immunocytochemically in approximately 10–15% of the cells in these cultures. These results strongly suggest that PRDM16 functions in brown fat precursors to restrict skeletal muscle gene expression and development.

**Brown fat and skeletal muscle but not white fat arise from *Myf5*-expressing progenitors.** The induction of skeletal muscle in cultures of brown fat pre-adipocytes suggested a surprising developmental relationship between these two cell lineages. To address this question directly, we performed lineage-tracing experiments in mice. Knock-in mice expressing cre recombinase from the regulatory elements of the skeletal muscle-specific *Myf5* gene<sup>18</sup> were crossed with indicator mice that express yellow fluorescent protein (YFP) from the *rosa26* gene locus (*R26R3-YFP*) in a cre-dependent manner. *Myf5* is a myogenic regulatory factor that is expressed in committed skeletal myogenic

precursors that were previously thought to give rise exclusively to skeletal muscle. Recombination at the *rosa26* locus induced by cre recombinase is heritable and irreversible, allowing the developmental progression of *Myf5*-expressing descendants to be traced by YFP expression<sup>19</sup> (Fig. 2a). Importantly, these *Myf5-Cre* knock-in mice have been successfully used to drive skeletal-muscle-specific cre expression in other studies<sup>20–22</sup>.

To examine the potential contribution of *Myf5*-expressing progenitors to the adipose anlagen, immunohistochemistry with anti-GFP antibodies was used to localize expression of the YFP reporter gene in skeletal muscle, BAT and WAT from the interscapular region of 2- to 3-month-old *Myf5-Cre:R26R3-YFP* mice. In *Myf5-Cre* negative (control) mice that harbour the *R26R3-YFP* reporter, YFP was not expressed in any tissues (Fig. 2b). However, in *Myf5-Cre* expressing mice, YFP was readily detected in skeletal muscle and BAT but not in WAT. YFP protein was also strongly expressed in the peri-renal BAT (Supplementary Fig. 1a) but not in any classic WAT depots (not shown). Moreover, real-time PCR showed that YFP messenger RNA (mRNA) was induced only in BAT depots and in skeletal muscle from *Myf5-Cre*-expressing mice, and at comparable levels (Fig. 2c and Supplementary Fig. 1b). YFP mRNA expression was not activated in other tissues examined, including the gluteal, inguinal and epididymal WAT depots (Fig. 2c and Supplementary Fig. 1b). These results indicate that *Myf5*-expressing cells specifically gave rise to skeletal muscle and brown fat cells. Notably, *Myf5* mRNA itself was not detected in mature BAT (Supplementary Fig. 1c), indicating that it was transiently expressed at an earlier developmental stage.

In newborn mammals, BAT is apparent at distinct anatomical sites including the interscapular, perirenal and axillary depots. It is also well established that brown fat cells emerge in WAT in response to

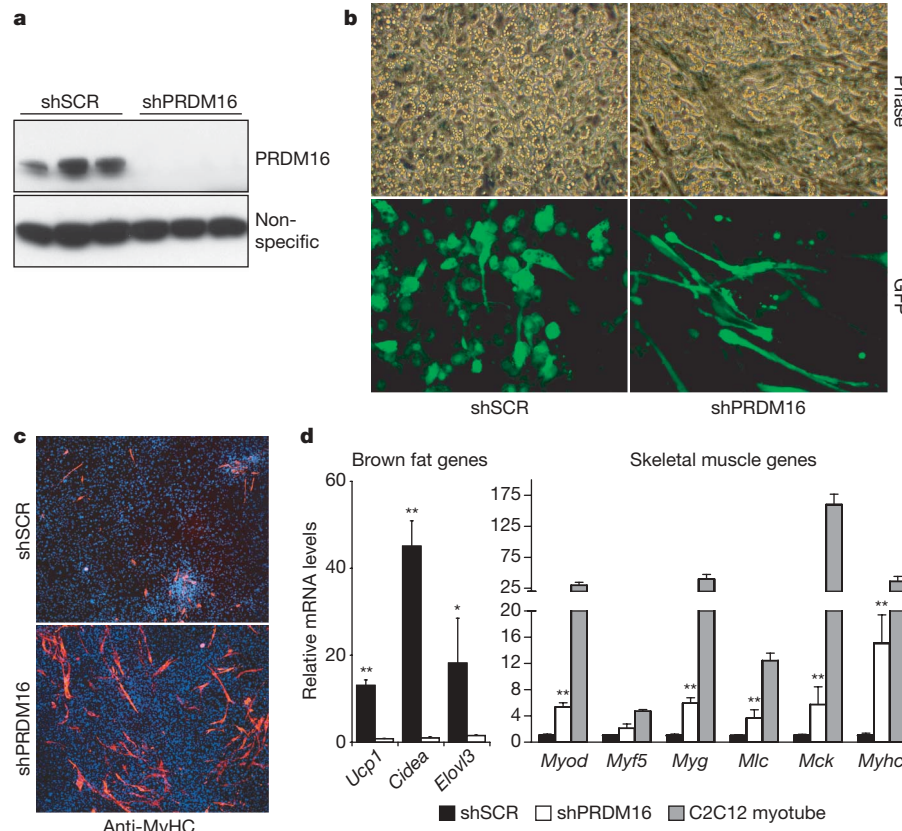


**Figure 1 | Knockdown of PRDM16 in primary brown fat cells induces skeletal myogenesis.** **a**, Western blot analysis for PRDM16 in primary brown fat cell cultures transduced with adenovirus expressing shRNA targeted to PRDM16 or a scrambled (SCR) control shRNA. **b**, These cultures were visualized by phase contrast microscopy and by GFP fluorescence.

**c**, Immunocytochemistry for skeletal myosin heavy chain (MyHC) expression. **d**, Gene expression at day 4 of adipocyte differentiation including BAT-selective and skeletal-muscle-specific genes (as indicated). C2C12 myotubes were also assayed for their expression of muscle-specific genes ( $n = 3$ , error bars are  $\pm$  s.d.; \* $P < 0.05$ , \*\* $P < 0.01$ ).

chronic cold exposure or prolonged  $\beta$ -adrenergic stimulation<sup>2,4,23</sup>. To determine whether these  $\beta$ -adrenergic-induced brown fat cells in WAT are also derived from *Myf5*-expressing precursors, we treated adult *Myf5-Cre:R26R3-YFP* mice with a selective  $\beta$ 3-adrenergic agonist, CL 316, 243, for 7 days, and examined whether the newly formed brown fat cells expressed YFP. As shown in Fig. 2d, this treatment induced the development of numerous clusters of UCP1-expressing brown fat cells in epididymal WAT. However, these brown fat cells did not express the YFP reporter gene (Fig. 2d), whereas the interscapular brown fat cells from the same mice were readily marked by YFP expression (Fig. 2d). These results suggest that the brown fat cells that develop in WAT in response to  $\beta$ -adrenergic signalling have an independent developmental origin from the distinct and classic BAT depots that develop before birth.

**PRDM16 induces brown adipogenesis in C2C12 and primary myogenic cells.** BAT depots arise from *Myf5*-expressing cells during development. To investigate whether PRDM16 is sufficient to specify the fate of brown fat in skeletal myogenic progenitors, we ectopically expressed PRDM16 in the C2C12 myoblast cell line. First, C2C12 myoblasts were transduced with control or PRDM16-expressing retroviruses, and then exposed to pro-myogenic culture conditions to induce terminal myocyte differentiation. C2C12 cells expressing the control virus differentiated efficiently into multinucleated MyHC-expressing myotubes (Supplementary Fig. 2a). PRDM16-expressing cells, however, failed to undergo myogenic differentiation (Supplementary Fig. 2a). Gene expression analysis showed that PRDM16 blocked the induction of myotube-specific genes including *Myod*, *Myg*, *Mrf4*, *Myhc* and *Mck* (Supplementary Fig. 2b). Control and PRDM16-expressing C2C12 myoblasts were also stimulated to undergo adipogenesis using adipogenic inducers. Under these conditions, the control cultures differentiated into multinucleated skeletal myotubes, whereas the PRDM16-expressing cells uniformly differentiated into lipid-filled adipocytes, as shown by Oil-Red-O staining (Fig. 3a). Gene expression studies showed that PRDM16 expression increased the mRNA levels of adipocyte-specific genes, including a 20-fold increase in the PPAR- $\gamma$  gene (*Pparg*) and a 250-fold elevation of *Ap2* (also known as *Fabp4*), with decreased levels of myogenic genes such as *Myod* and *Myg* (Fig. 3b). Importantly,

adipocytes induced by PRDM16 expression also expressed elevated levels of specific genes for brown fat cells such as *Elovl3* and *Cidea* (more than 30,000-fold; Fig. 3c), as well as the thermogenic genes *Ucp1* and *Pgc1a* (Fig. 3d). Moreover, as in real brown fat cells, *Ucp1* and *Pgc1a* were further induced in PRDM16-derived adipocytes by elevating cyclic AMP levels through forskolin treatment (Fig. 3d). These data demonstrate that PRDM16 expression alone is sufficient to drive brown adipocyte differentiation in committed and clonal skeletal myogenic cells.

To explore the adipogenic action of PRDM16 further, we ectopically expressed PRDM16 in primary mouse myoblasts isolated from postnatal skeletal muscle. As observed in C2C12 cells, control vector (ctl)-expressing cells differentiated into multinucleated myotubes in response to an adipogenic induction cocktail. In contrast, PRDM16-transduced myoblasts differentiated at near 100% efficiency into fat-storing adipocytes (Fig. 3e). Consistent with their morphological differentiation, PRDM16-transduced cultures expressed elevated mRNA levels of pan-adipocyte specific genes, such as *Pparg*, *Ap2* and adiponectin (Fig. 3f). Moreover, adipocytes derived from PRDM16-expressing myogenic precursors strongly activated the expression of brown fat cell-specific genes including *Elovl3*, *Cidea*, *Pgc1a* and a 1,000-fold increase in *Ucp1* levels (Fig. 3g). By western blot analysis, PRDM16-derived adipocytes expressed the brown fat cell selective UCP1 and CIDEA proteins to levels comparable with that in bona fide brown fat cells (Fig. 3g). Altogether, these results demonstrate that PRDM16 activates a complete brown fat differentiation program in muscle precursor cells.

**PRDM16 binds to PPAR- $\gamma$  and co-activates its transcriptional function.** To explore mechanisms that could explain the pro-adipogenic actions of PRDM16, we used an unbiased approach to identify binding partners of PRDM16. To this end, the PRDM16 protein complex was immunopurified from fat cells and analysed by mass spectrometry (Supplementary Table 1). Of particular interest was the identification of PPAR- $\gamma$  as a near-stoichiometric component of the PRDM16 complex (Fig. 4a). PPAR- $\gamma$  was the only DNA-binding transcriptional component found in the PRDM16 complex. Independent co-expression assays in COS-7 cells again showed PPAR- $\gamma$  in a complex with PRDM16 (Fig. 4b). This interaction is

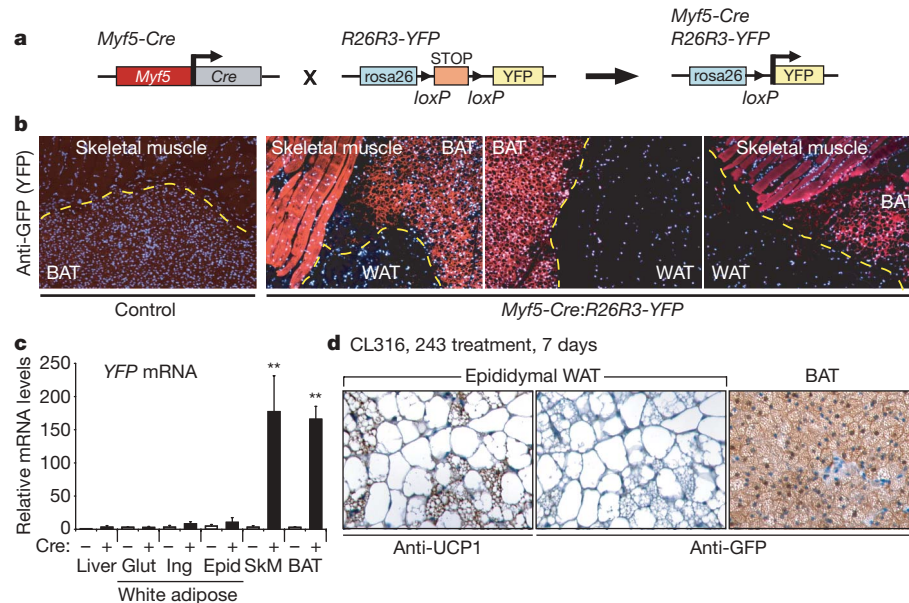


**Figure 2 | Brown fat and skeletal muscle arise from *Myf5*-expressing precursors.** **a**, *Myf5-Cre* mice were intercrossed with indicator mice that have a YFP gene integrated into the *rosa26* locus downstream of a floxed transcriptional stop sequence (*R26R3-YFP*). Expression of cre recombinase excises the stop sequence to activate YFP expression irreversibly. **b**, Immunohistochemistry to detect YFP (GFP) expression in skeletal

muscle, BAT and WAT from control (*Myf5-Cre* negative) and *Myf5-Cre:R26R3-YFP* mice. **c**, Real-time PCR of YFP mRNA levels in: liver; gluteal (Glut), inguinal (Ing) and epididymal (Epid) WAT; skeletal muscle (SkM) and BAT ( $n = 4$  per group; error bars are  $\pm$  s.e.m.; \*\* $P < 0.01$ ). **d**, UCP1 and GFP expression in WAT and BAT from CL316, 243-treated *Myf5-Cre:R26R3-YFP* mice.

likely to be direct, because a full-length glutathione S-transferase (GST)-PPAR- $\gamma$ 2 fusion protein purified from baculovirus infected insect cells bound to *in vitro* translated PRDM16 (Fig. 4c). PRDM16 and PPAR- $\gamma$ 2 interacted in a non-ligand-dependent manner, because the binding was equivalent with or without the addition of PPAR- $\gamma$  ligand, rosiglitazone, to the binding reaction. Steroid receptor co-activator-1 (SRC-1), by contrast, interacted with purified GST-PPAR- $\gamma$  only in the presence of rosiglitazone (Fig. 4c). Domain mapping experiments using GST immunoaffinity assays identified two regions in PRDM16 that bound to PPAR- $\gamma$ , corresponding to zinc-finger-1 (ZF1) and zinc-finger-2 (ZF2) (Fig. 4d).

PPAR- $\gamma$  is the master regulator of adipogenic differentiation, being both absolutely necessary and sufficient to induce adipogenesis<sup>24–26</sup>. Furthermore, overexpression and activation of PPAR- $\gamma$  was previously shown to promote adipogenic conversion of myoblasts<sup>27</sup>. We therefore investigated whether PRDM16 could enhance the transcriptional activity of PPAR- $\gamma$ . As shown in Fig. 4e, the expression of PRDM16 stimulated the activity of a luciferase reporter gene controlled by three tandem repeats of a PPAR binding site (3  $\times$  DR1-luciferase) by 15-fold. The reporter gene was further induced by PRDM16 in cells treated for 24 h with 1  $\mu$ M rosiglitazone. In *Pparg*<sup>−/−</sup> cells, PRDM16 expression induced transcription of the

reporter gene only in the presence of exogenously added PPAR- $\gamma$  (Supplementary Fig. 3). Although the binding of PRDM16 to PPAR- $\gamma$  was not ligand-dependent *in vitro*, the co-activation function of PRDM16 in cellular assays was augmented by ligand. We also examined whether PRDM16 could interact with PPAR- $\alpha$ , a related PPAR family member that is expressed at higher levels in brown versus white fat cells and has been implicated in UCP1 gene regulation<sup>28</sup>. In COS-7 cells, PRDM16 bound to PPAR- $\alpha$  with similar efficiency both in the absence and presence of the PPAR- $\alpha$  ligand, WY-14643 (Supplementary Fig. 4a). As observed with PPAR- $\gamma$ , PRDM16 also activated the transcriptional function of PPAR- $\alpha$  in a ligand-dependent manner (Supplementary Fig. 4b). These data indicate that PRDM16 can bind and co-activate the transcriptional function of both PPAR- $\alpha$  and PPAR- $\gamma$ .

The strong co-activation of PPAR- $\gamma$  transcriptional function by PRDM16 suggests that this is a key mechanism by which PRDM16 promotes adipogenesis. In this regard, PRDM16 is unable to promote adipogenesis in *Pparg*-deficient fibroblasts (data not shown). Significantly, the adipogenic conversion of C2C12 (Supplementary Fig. 5a) and primary myoblasts by PRDM16 was largely dependent on the presence of rosiglitazone, a highly specific agonist for PPAR- $\gamma$ . In C2C12 cells, PRDM16 induced the expression of adipocyte-related

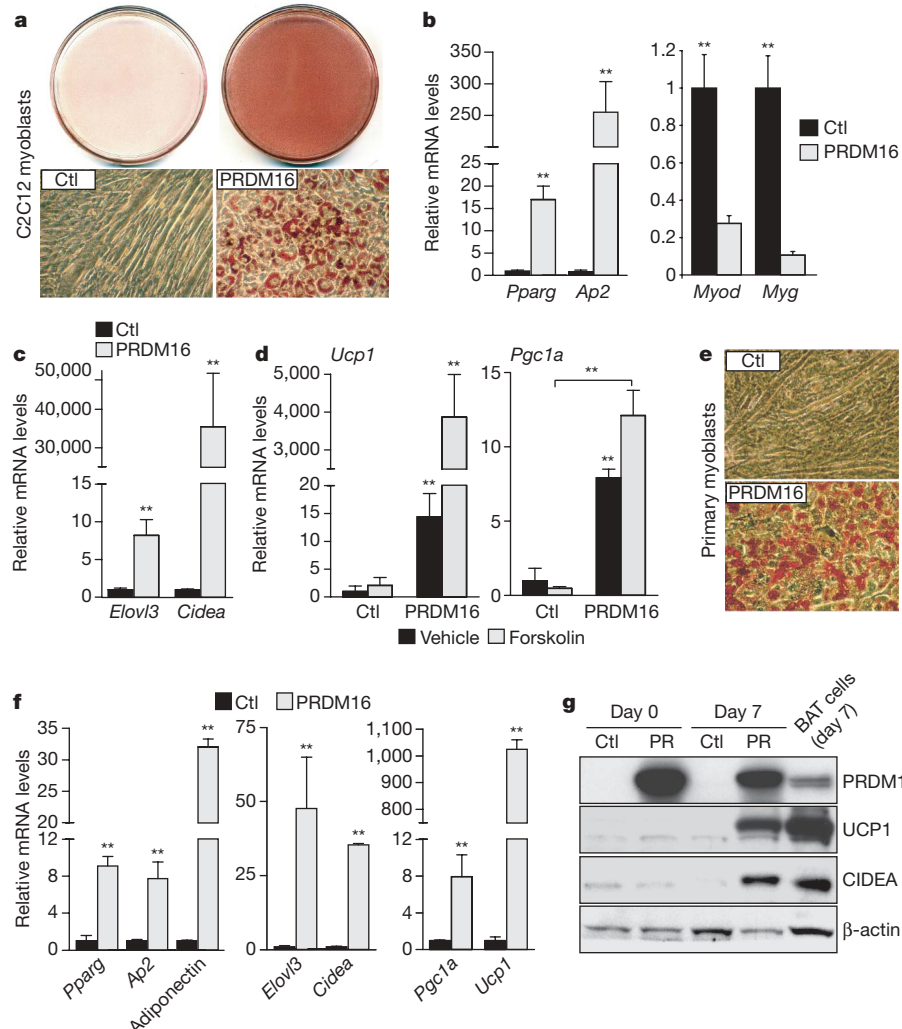


**Figure 3 | PRDM16 stimulates brown adipocyte differentiation in skeletal myoblasts.** **a–d**, C2C12 myoblasts expressing retroviral PRDM16 or vector control (Ctl) were stained with Oil-Red-O 6 days after inducing adipocyte differentiation (a); and analysed by real-time PCR for their expression of markers specific to: adipocytes (*Pparg*, *Ap2*) (b, left); skeletal muscle (*Myod*, *Myg*) (b, right); BAT (*Elov13*, *Cidea*) (c); and thermogenesis (*Ucp1*, *Pgc1a*) (d).

**e–g**, Ctl and PRDM16-expressing primary myoblasts were stained with Oil-Red-O 7 days after inducing adipocyte differentiation (e). Real-time PCR analysis of genes expressed selectively in: adipocytes (*Pparg*, *Ap2*, adiponectin) (f, left); BAT (*Elov13*, *Cidea*) (f, centre); and during thermogenesis (*Pgc1a*, *Ucp1*) (f, right). g, Western blot analysis before (day 0) and after 7 days of differentiation. (n = 4; error bars are  $\pm$  s.d.; \*\*P < 0.05).

genes like *Ap2* and adiponectin as well as *Ucp1* and *Cidea*, specific markers for brown fat cells, in a ligand-dependent manner (Supplementary Fig. 5b). These results indicate that PPAR- $\gamma$  activation is required for the adipogenic function of PRDM16.

We next examined whether expression of any potent co-activator of PPAR- $\gamma$  could induce adipogenesis in C2C12 myoblasts. Interestingly, PGC-1 $\beta$ , a strong activator of PPAR- $\alpha$  and PPAR- $\gamma$  (ref. 29 and unpublished results) had no ability to promote adipogenesis or induce adipocyte-specific genes in C2C12 myoblasts (Supplementary Fig. 6). It was, however, able to induce several mitochondrial gene targets. These data suggest that the co-activation of PPAR- $\gamma$  by PRDM16 is selectively potent in stimulating the adipocyte differentiation program in myogenic cells. Furthermore, PRDM16 was not pro-adipogenic in other non-myogenic cell types, including C3H10T1/2 cells, NIH-3T3 and several types of pre-adipocyte<sup>16</sup>. These data therefore suggest that the pro-adipogenic action of PRDM16 may be somewhat dependent on other factors present in myoblasts.

An important question arising from these studies was whether adipocytes derived from myoblasts through PPAR- $\gamma$  function per se would always display a brown fat phenotype. To address this question, we compared the adipogenic activity of ectopically expressed PRDM16 and PPAR- $\gamma$  in C2C12 myoblasts. In these experiments, PRDM16 stimulated adipocyte development with equal, if not better, efficiency compared with PPAR- $\gamma$  (Supplementary Fig. 7a). Interestingly, adipocytes formed from PRDM16-expressing cells had a uniform round shape, were smaller in size and contained numerous small lipid droplets. PPAR- $\gamma$ -driven adipocytes were larger, irregularly shaped and contained large lipid droplets. Both PRDM16 and PPAR- $\gamma$  induced the expression of pan-adipocyte genes such as *Ap2* and adiponectin (Supplementary Fig. 7b). However, only PRDM16 induced a complete brown fat differentiation program (Supplementary Fig. 7b). These data demonstrate that

PPAR- $\gamma$  can convert myogenic cells into adipocytes but PRDM16 expression additionally commits cells to the brown fat fate.

**Dysregulated gene expression in *Prdm16*-deficient brown fat.** PRDM16 belongs to a family of 16 PR domain-containing proteins, some of which display an overlapping expression pattern with PRDM16. The effect of global *Prdm16* deficiency on mouse and brown fat development has not been examined. Mice deficient for *Prdm16* were created by targeted insertion of a gene-trap cassette into intron 2 of the gene. The creation and general phenotypic characterization of this mouse model will be described elsewhere. Notably, mice homozygous for the gene-trap insertion (*Prdm16*<sup>GT/GT</sup>) die at birth. We therefore analysed the phenotype of putative BAT pads from wild-type heterozygous carriers and homozygous *Prdm16* mutant (knockout) late-stage embryos (E17). First, we established that *Prdm16* mRNA was decreased in heterozygous BAT and virtually undetectable in the putative knockout BAT (Fig. 5a). By haematoxylin and eosin (H&E) staining, the putative BAT from the knockout animals had an unusual morphology, including substantially larger lipid stores (white areas in tissue) compared with wild-type BAT (Fig. 5b). No obvious muscle tissue was observed in these fat pads. Gene expression studies showed that wild-type and knockout BAT expressed similar levels of the pan-adipocyte markers *Ap2* and adiponectin (Fig. 5c). The *Prdm16*-deficient BAT, however, expressed significantly lower levels of essentially all BAT cell-selective and thermogenic genes (Fig. 5d). This included a 50% reduction of *Ucp1* mRNA levels, 75% reduction of *Elovl3*, 50% reduction of *Cidea* and a significant reduction of *Pgc1a* and mitochondrial target genes, cytochrome c (*Cyc*) and *Cox8b*. Strikingly, the *Prdm16*-deficient BAT also exhibited large increases in the expression of skeletal myogenic genes including four- to sixfold elevated levels of *Myod*, myogenin, *Mck* and *Myf6* (Fig. 5e). These data document a genetic requirement for PRDM16 in the appropriate development and gene expression program of BAT.

## Discussion

Most models of fat development have suggested that brown and white fat cells arise from a common adipogenic precursor cell<sup>5–7</sup>. Given the ability of PRDM16 to drive a complete brown fat gene program<sup>16</sup>, we had thus expected that brown fat cells lacking PRDM16 would adopt a white phenotype. However, surprisingly, loss of PRDM16 from brown fat cells caused an increase in myogenic gene expression and bona fide skeletal muscle differentiation. Furthermore, this dependence on PRDM16 was bi-directional. Increased PRDM16 expression converted both immortalized and primary skeletal muscle myoblasts into brown fat cells.

By tracking the fate of cells that express the myoblast-specific *Myf5* gene, we provide evidence for a very close developmental relationship between skeletal muscle and BAT. Significantly, our analysis reveals that WAT and BAT depots arise from independent lineages and presumably have fundamentally distinct mechanisms of determination (Supplementary Fig. 8). Cells with the morphology and molecular phenotype of brown fat can also be induced in WAT of rodents and humans by chronic cold exposure or by  $\beta$ -adrenergic stimulation<sup>2,4,23,30</sup>. In our studies, the brown fat cells that emerged in the WAT of mice treated with a  $\beta$ 3-adrenergic agonist were not derived from *Myf5*-expressing precursors. Notably, genetic studies by Kozak and colleagues suggest that formation of brown fat cells in WAT versus BAT is controlled by distinct mechanisms<sup>31</sup>, which is consistent with the view that these two types of brown fat cell have separate developmental origins. The identity of the cells in WAT that give rise to brown adipocytes remains unknown. It is still reasonable to speculate that a common white/brown fat progenitor exists in some/all WAT depots.

The genetic tracing experiments here do not determine whether a single *Myf5*<sup>+</sup> cell gives rise to both BAT and skeletal muscle, or whether separate populations of *Myf5*<sup>+</sup> progenitors exist. However, the interconversion between muscle and BAT induced through

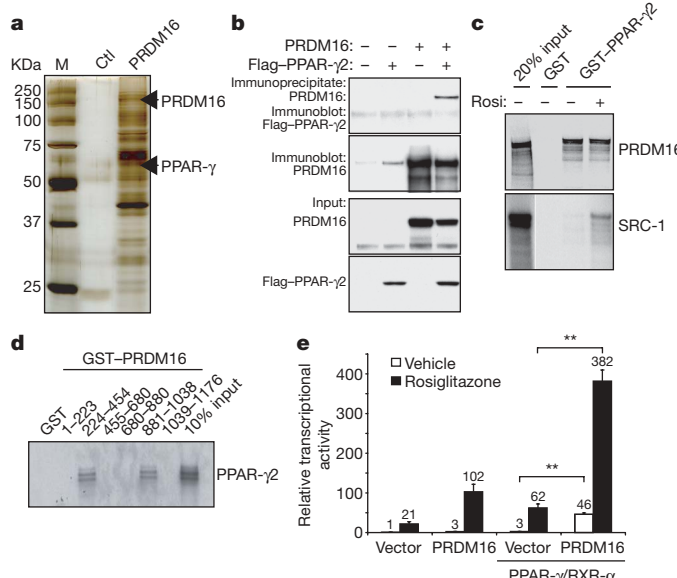


**Figure 4 | PRDM16 binds and activates the transcriptional function of PPAR- $\gamma$ .** **a**, Components in the PRDM16 complex from fat cells were separated by SDS-polyacrylamide gel electrophoresis (SDS-PAGE) and visualized by silver staining. **b**, Immunoprecipitation of PRDM16 from COS-7 cells expressing exogenous PRDM16 and/or Flag-PPAR- $\gamma$  followed by western blot analysis to detect PPAR- $\gamma$ . **c**, GST alone or a GST fusion protein containing PPAR- $\gamma$  was incubated with <sup>35</sup>S-labelled PRDM16 or SRC-1 protein ( $\pm$ 1  $\mu$ M rosiglitazone). **d**, GST fusion proteins containing different regions of PRDM16 were incubated with <sup>35</sup>S-labelled PPAR- $\gamma$ . **e**, Transcriptional activity of a PPAR-driven reporter gene in response to PPAR- $\gamma$ /RXR- $\alpha$  and PRDM16 or vector expression in COS-7 cells ( $\pm$ 1  $\mu$ M rosiglitazone) ( $n = 3$ ; error bars are  $\pm$  s.d.; \*\* $P < 0.05$ ).

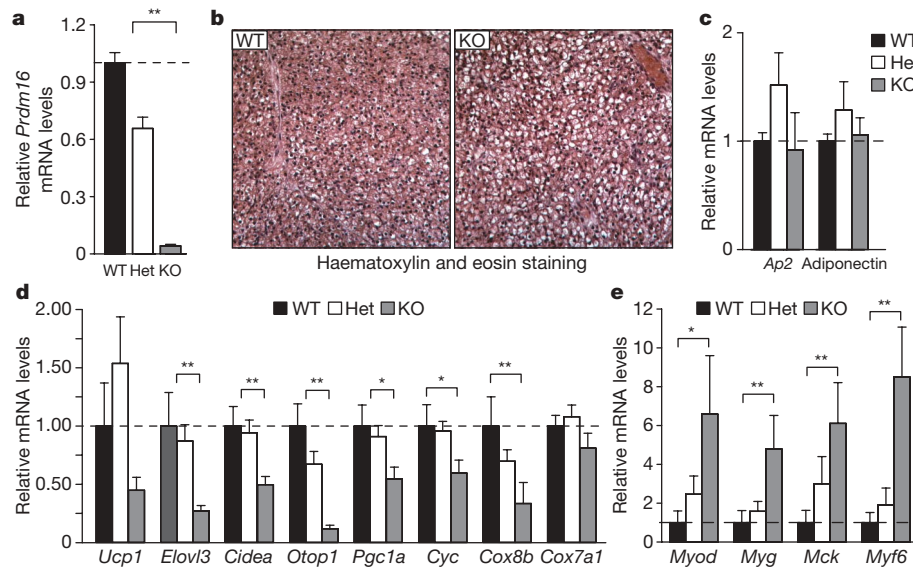


**Figure 5 | Altered morphology and dysregulated gene expression in *Prdm16*-deficient brown fat.** **a**, Real-time PCR of *Prdm16* mRNA levels in putative BAT depots from E17 wild-type (WT), heterozygous (Het) and *Prdm16* knockout (KO) mice. **b**, Haematoxylin and eosin staining of representative sections of BAT from wild-type and knockout mice.

modulation of PRDM16 levels in culture suggests that bipotent muscle–brown fat precursors may give rise to both lineages (Supplementary Fig. 8). Future studies addressing the exact nature of the muscle–brown fat precursor cell compartment(s) are needed. Interestingly, UCP1-expressing brown adipocytes have been localized in skeletal muscle and are correlated with resistance to obesity<sup>32</sup>. Our results suggest that myogenic precursor cells could be the source of these ‘ectopic’ brown fat cells. In this regard, muscle stem cells called satellite cells can undergo adipogenesis under certain experimental conditions<sup>33,34</sup>, though whether they assume a brown fat phenotype has not been examined.

Some recent experiments had hinted that BAT and muscle share important features. Timmons *et al.* showed that precursors of brown fat cells express a wide array of muscle-related genes<sup>35</sup>. Lineage-tracing experiments by Atit *et al.* revealed that embryonic BAT, along with skin and muscle, was derived from a population of engrailed-1 (*En1*)-expressing cells in the dermomyotome<sup>36</sup>. The contribution of *En1*-expressing cells to WAT depots was, however, not studied. *En1* is expressed early in mouse development and marks a variety of other cell lineages including specific neuronal pools. Thus a direct connection between muscle and BAT was not evident. The ontogenetic relationship between BAT and skeletal muscle may explain why brown fat cells are specialized for lipid catabolism rather than storage, much like oxidative muscle. Further, BAT and skeletal muscle are both highly responsive to sympathetic nerve activity and have the capacity to perform adaptive thermogenesis.

PRDM16 appears to function in brown fat cells through its ability to co-regulate the activity of other transcription factors and co-activators (Supplementary Fig. 8). The action of PRDM16 is almost certainly dependent on its interaction with PPAR- $\gamma$  because PRDM16 stimulated adipogenesis in a PPAR- $\gamma$ -ligand-dependent manner, and PPAR- $\gamma$  is known to be absolutely required for adipogenesis in cultured cells and *in vivo*<sup>24,25</sup>. Our previous study indicated that an important contribution of the ability of PRDM16 to stimulate a brown fat phenotype in white fat precursors was through its association with PGC-1 $\alpha$  and PGC-1 $\beta$ . It seems extremely likely that PRDM16 interacts with other factors, as yet undefined. At a mechanistic level, it remains to be determined how PRDM16 is able to stimulate the function of the PGC-1s and PPARs.

Although the short interfering RNA-mediated depletion of PRDM16 from cultured brown fat pre-adipocytes almost completely ablated their ability to differentiate into brown fat cells, chronic loss of PRDM16 in mice caused a significant but more modest reduction in the character of brown fat cells. Skeletal muscle gene expression was readily apparent in the knockout tissue but no overt muscle fibres were observed. It is likely that one or more of the other 15 PR domain-containing family members can partly compensate for the loss of PRDM16 from BAT *in vivo*. It will be important to examine whether any of these family members has overlapping functions with PRDM16. The *Prdm16*-deficient mice die at birth, thereby precluding functional analyses of the mutant BAT in response to cold or its effect on energy balance. Tissue-selective ablation of PRDM16 will be required to address these issues.

The role of BAT in regulating energy balance and fighting obesity in rodents is well established. Humans have BAT, and recent data suggest that it might have a more significant role in the physiology of adults than was previously recognized<sup>8</sup>. Because PRDM16 can function as a dominant regulator of the fate of brown fat cells, it will be important to investigate whether it can be used therapeutically. For example, it may be possible to use PRDM16 to drive the formation of brown fat precursor-type cells from myoblasts or white fat precursors for autologous transplantation into fat tissues. Alternatively, identifying compounds that induce the expression of PRDM16 in white fat or muscle progenitors could be powerful in fighting obesity.

## METHODS SUMMARY

**DNA constructs.** PRDM16 and PPAR- $\gamma$  expression plasmids were described before<sup>16,37</sup>. Adenoviral shRNA constructs were made in the pAdtrack vector (Stratagene), using previously validated sequences<sup>16</sup>.

**Cell culture.** Primary brown pre-adipocytes and myoblasts were prepared from P0–P4 Swiss-Webster mice as described before<sup>38,39</sup>. Adipocyte differentiation was induced by treating cells for 48 h in medium containing 10% FBS, 0.5 mM isobutylmethylxanthine, 125 nM indomethacin, 1  $\mu$ M dexamethosone, 850 nM insulin, 1 nM T3 with or without 1  $\mu$ M rosiglitazone (Alexis Biochemicals). After 48 h, cells were switched to medium containing 10% FBS, 850 nM insulin, 1 nM T3 with or without 1  $\mu$ M rosiglitazone.

**Mice.** For lineage tracing studies, heterozygous *Myf5*<sup>Cre/+</sup> mice<sup>18</sup> were intercrossed with rosa26R3 (R26R3)-YFP mice<sup>19</sup>. *Prdm16*-deficient mice were created by homologous insertion of a gene-trap cassette and will be described elsewhere.

**Immunohistochemistry.** Paraffin-embedded sections were subjected to citrate-based antigen retrieval (Vector Labs) and incubated with antibodies against GFP or UCP1 (Abcam). Secondary detection was with anti-rabbit Alexa 647 (Invitrogen) or the Dako Envision+ system.

**Binding studies.** The PRDM16 transcriptional complex was immunopurified from adipocytes stably expressing Flag-tagged PRDM16 or a control vector. Gel-resolved proteins were excised and analysed by matrix-assisted laser desorption/ionization–reflectron time of flight mass spectrometry<sup>40</sup>. Co-expression assays were performed in COS-7 cells to assess binding of PRDM16 with PPAR- $\alpha$  and PPAR- $\gamma$ . Reporter gene assays were performed in COS-7 cells or *Pparg*<sup>-/-</sup> fibroblasts using a luciferase reporter gene driven by three tandem copies of a PPAR response element (3  $\times$  DRE1-luciferase)<sup>41</sup>.

**Real-time PCR.** Complementary DNA was prepared from total RNA using the ABI reverse transcription kit. Quantitative PCR reactions contained Sybr-Green fluorescent dye (ABI). Relative mRNA expression was determined by the  $\Delta\Delta$ -Ct method using tata-binding protein levels as endogenous control.

**Full Methods** and any associated references are available in the online version of the paper at [www.nature.com/nature](http://www.nature.com/nature).

Received 22 April; accepted 19 June 2008.

1. Cannon, B. & Nedergaard, J. Brown adipose tissue: function and physiological significance. *Physiol. Rev.* **84**, 277–359 (2004).
2. Cousin, B. *et al.* Occurrence of brown adipocytes in rat white adipose tissue: molecular and morphological characterization. *J. Cell Sci.* **103**, 931–942 (1992).
3. Garruti, G. & Ricquier, D. Analysis of uncoupling protein and its mRNA in adipose tissue deposits of adult humans. *Int. J. Obes. Relat. Metab. Disord.* **16**, 383–390 (1992).
4. Guerra, C., Koza, R. A., Yamashita, H., Walsh, K. & Kozak, L. P. Emergence of brown adipocytes in white fat in mice is under genetic control. Effects on body weight and adiposity. *J. Clin. Invest.* **102**, 412–420 (1998).
5. Gesta, S., Tseng, Y. H. & Kahn, C. R. Developmental origin of fat: tracking obesity to its source. *Cell* **131**, 242–256 (2007).
6. Hansen, J. B. & Kristiansen, K. Regulatory circuits controlling white versus brown adipocyte differentiation. *Biochem. J.* **398**, 153–168 (2006).
7. Rosen, E. D. & Spiegelman, B. M. Molecular regulation of adipogenesis. *Annu. Rev. Cell Dev. Biol.* **16**, 145–171 (2000).
8. Nedergaard, J., Bengtsson, T. & Cannon, B. Unexpected evidence for active brown adipose tissue in adult humans. *Am. J. Physiol. Endocrinol. Metab.* **293**, E444–E452 (2007).
9. Cederberg, A. *et al.* FOXC2 is a winged helix gene that counteracts obesity, hypertriglyceridemia, and diet-induced insulin resistance. *Cell* **106**, 563–573 (2001).
10. Ghorbani, M., Claus, T. H. & Himms-Hagen, J. Hypertrophy of brown adipocytes in brown and white adipose tissues and reversal of diet-induced obesity in rats treated with a beta3-adrenoceptor agonist. *Biochem. Pharmacol.* **54**, 121–131 (1997).
11. Kopecky, J., Clarke, G., Enerback, S., Spiegelman, B. & Kozak, L. P. Expression of the mitochondrial uncoupling protein gene from the aP2 gene promoter prevents genetic obesity. *J. Clin. Invest.* **96**, 2914–2923 (1995).
12. Lowell, B. B. *et al.* Development of obesity in transgenic mice after genetic ablation of brown adipose tissue. *Nature* **366**, 740–742 (1993).
13. Christian, M. *et al.* RIP140-targeted repression of gene expression in adipocytes. *Mol. Cell. Biol.* **25**, 9383–9391 (2005).
14. Hansen, J. B. *et al.* Retinoblastoma protein functions as a molecular switch determining white versus brown adipocyte differentiation. *Proc. Natl. Acad. Sci. USA* **101**, 4112–4117 (2004).
15. Scime, A. *et al.* Rb and p107 regulate preadipocyte differentiation into white versus brown fat through repression of PGC-1alpha. *Cell Metab.* **2**, 283–295 (2005).
16. Seale, P. *et al.* Transcriptional control of brown fat determination by PRDM16. *Cell Metab.* **6**, 38–54 (2007).
17. Kajimura, S. *et al.* Regulation of the brown and white fat gene programs through a PRDM16/CtBP transcriptional complex. *Genes Dev.* **22**, 1397–1409 (2008).
18. Tallquist, M. D., Weismann, K. E., Hellstrom, M. & Soriano, P. Early myotome specification regulates PDGFA expression and axial skeleton development. *Development* **127**, 5059–5070 (2000).
19. Srinivas, S. *et al.* Cre reporter strains produced by targeted insertion of EYFP and ECFP into the ROSA26 locus. *BMC Dev. Biol.* **1**, 4 (2001).
20. Huh, M. S., Parker, M. H., Scime, A., Parks, R. & Rudnicki, M. A. Rb is required for progression through myogenic differentiation but not maintenance of terminal differentiation. *J. Cell Biol.* **166**, 865–876 (2004).
21. Kuang, S., Kuroda, K., Le Grand, F. & Rudnicki, M. A. Asymmetric self-renewal and commitment of satellite stem cells in muscle. *Cell* **129**, 999–1010 (2007).
22. Dong, F. *et al.* Pitx2 promotes development of splanchnic mesoderm-derived branchiomeric muscle. *Development* **133**, 4891–4899 (2006).
23. Himms-Hagen, J. *et al.* Multilocular fat cells in WAT of CL-316243-treated rats derive directly from white adipocytes. *Am. J. Physiol. Cell Physiol.* **279**, C670–C681 (2000).
24. Barak, Y. *et al.* PPAR gamma is required for placental, cardiac, and adipose tissue development. *Mol. Cell* **4**, 585–595 (1999).
25. Rosen, E. D. *et al.* PPAR gamma is required for the differentiation of adipose tissue *in vivo* and *in vitro*. *Mol. Cell* **4**, 611–617 (1999).
26. Tontonoz, P., Hu, E. & Spiegelman, B. M. Stimulation of adipogenesis in fibroblasts by PPAR gamma 2, a lipid-activated transcription factor. *Cell* **79**, 1147–1156 (1994).
27. Hu, E., Tontonoz, P. & Spiegelman, B. M. Transdifferentiation of myoblasts by the adipogenic transcription factors PPAR gamma and C/EBP alpha. *Proc. Natl. Acad. Sci. USA* **92**, 9856–9860 (1995).
28. Barbera, M. J. *et al.* Peroxisome proliferator-activated receptor alpha activates transcription of the brown fat uncoupling protein-1 gene. A link between regulation of the thermogenic and lipid oxidation pathways in the brown fat cell. *J. Biol. Chem.* **276**, 1486–1493 (2001).
29. Lin, J., Puigserver, P., Donovan, J., Tarr, P. & Spiegelman, B. M. Peroxisome proliferator-activated receptor gamma coactivator 1beta (PGC-1beta), a novel PGC-1-related transcription coactivator associated with host cell factor. *J. Biol. Chem.* **277**, 1645–1648 (2002).
30. Huttunen, P., Hirvonen, J. & Kinnula, V. The occurrence of brown adipose tissue in outdoor workers. *Eur. J. Appl. Physiol. Occup. Physiol.* **46**, 339–345 (1981).
31. Xue, B. *et al.* Genetic variability affects the development of brown adipocytes in white fat but not in interscapular brown fat. *J. Lipid Res.* **48**, 41–51 (2007).
32. Almind, K., Manieri, M., Sivitz, W. I., Cinti, S. & Kahn, C. R. Ectopic brown adipose tissue in muscle provides a mechanism for differences in risk of metabolic syndrome in mice. *Proc. Natl. Acad. Sci. USA* **104**, 2366–2371 (2007).
33. Asakura, A., Komaki, M. & Rudnicki, M. Muscle satellite cells are multipotential stem cells that exhibit myogenic, osteogenic, and adipogenic differentiation. *Differentiation* **68**, 245–253 (2001).
34. Shefer, G., Wleklinski-Lee, M. & Yablonka-Reuveni, Z. Skeletal muscle satellite cells can spontaneously enter an alternative mesenchymal pathway. *J. Cell Sci.* **117**, 5393–5404 (2004).
35. Timmons, J. A. *et al.* Myogenic gene expression signature establishes that brown and white adipocytes originate from distinct cell lineages. *Proc. Natl. Acad. Sci. USA* **104**, 4401–4406 (2007).
36. Atit, R. *et al.* Beta-catenin activation is necessary and sufficient to specify the dorsal dermal fate in the mouse. *Dev. Biol.* **296**, 164–176 (2006).
37. Mueller, E. *et al.* Genetic analysis of adipogenesis through peroxisome proliferator-activated receptor gamma isoforms. *J. Biol. Chem.* **277**, 41925–41930 (2002).
38. Megeney, L. A., Kablar, B., Garrett, K., Anderson, J. E. & Rudnicki, M. A. MyoD is required for myogenic stem cell function in adult skeletal muscle. *Genes Dev.* **10**, 1173–1183 (1996).
39. Tseng, Y. H., Kriauciunas, K. M., Kokkotou, E. & Kahn, C. R. Differential roles of insulin receptor substrates in brown adipocyte differentiation. *Mol. Cell. Biol.* **24**, 1918–1929 (2004).
40. Erdjument-Bromage, H. *et al.* Examination of micro-tip reversed-phase liquid chromatographic extraction of peptide pools for mass spectrometric analysis. *J. Chromatogr. A* **826**, 167–181 (1998).
41. Forman, B. M. *et al.* 15-Deoxy-delta 12, 14-prostaglandin J2 is a ligand for the adipocyte determination factor PPAR gamma. *Cell* **83**, 803–812 (1995).

**Supplementary Information** is linked to the online version of the paper at [www.nature.com/nature](http://www.nature.com/nature).

**Acknowledgements** We thank V. Seale and F. LeGrand for help with the lineage tracing studies and R. Gupta for discussions. We are grateful to P. Soriano for the *Myf5-Cre* mice and F. Constantini for the *R26R3-YFP* reporter mice. P.S. is supported by a fellowship from the American Heart Association. S. Kajimura is supported by a fellowship from the Japan Society for the Promotion of Science. S.D. is supported by the Susan Komen Breast Cancer Foundation. This work is funded by the Picower Foundation and a National Institutes of Health grant to B.M.S. and an National Institutes of Health/National Institute of Arthritis and Musculoskeletal and Skin Diseases grant to M.A.R.

**Author Contributions** P.S. and B.M.S. conceived and designed the experiments. P.S., W.Y., S. Kajimura, S.C. and H.M.C. performed the experiments. P.S. analysed the data. B.B., S. Kuang, A.S., S.D., H.E., P.T., M.A.R. and D.R.B. contributed reagents/materials/analysis tools. P.S. and B.M.S. wrote the paper.

**Author Information** Reprints and permissions information is available at [www.nature.com/reprints](http://www.nature.com/reprints). Correspondence and requests for materials should be addressed to B.M.S. (bruce\_spiegelman@dfci.harvard.edu).

## METHODS

**Plasmids and viral vectors.** Full-length mouse complementary DNA sequence for PGC-1 $\beta$  was cloned into pMSCV-puro retroviral vector (Stratagene). GST-PPAR- $\gamma$ 2 was cloned into pAcGHLT baculovirus expression plasmid (Pharmingen). Various fragments of PRDM16 were amplified by PCR and cloned into the EcoRI or BamHI/XbaI sites of the bacterial expression vector pGEX-4T-2 vector (GE Healthcare).

**Cell culture.** COS-7, C2C12 and C3H-10T1/2 cells were obtained from the American Type Culture Collection. Immortalized brown pre-adipocytes and PPAR- $\gamma$  $^{−/−}$  fibroblasts were described elsewhere<sup>25,42</sup>. For retrovirus production, phoenix packaging cells<sup>43</sup> were transfected by the calcium phosphate method as described<sup>16</sup>. For retroviral transduction, cells were treated overnight with viral supernatant supplemented with 8  $\mu$ g ml $^{−1}$  polybrene. For adenoviral infection of primary brown fat precursors, 70% confluent cell cultures were incubated with shPRDM16 or shSCR-expressing adenovirus (multiplicity of infection = 100) overnight in complete growth medium. The medium was then replaced and cells were maintained in complete growth medium for an additional 24 h before inducing adipogenic differentiation. Muscle differentiation was induced by culturing cells in 2% horse-serum/DMEM. To stimulate cyclic AMP-induced thermogenesis in cells, 10  $\mu$ M forskolin was added to cultures for 4 h. Oil-Red-O staining was performed as described previously<sup>26</sup>. All chemicals were obtained from Sigma unless otherwise indicated.

**Animals.** All animal experiments were performed according to procedures approved by the Dana-Farber Cancer Institute's Institutional Animal Care and Use Committee or in accordance with the University of Ottawa regulations for animal care and handling. CL316, 243, at 1 mg kg $^{−1}$ , was injected intraperitoneally into 8- to 10-week-old male mice daily for 7 days ( $n = 5$  mice per genotype).

**Immunostaining.** Paraffin-embedded sections of brown fat and white fat tissues were subjected to citrate-based antigen retrieval (Vector Labs) and incubated with anti-rabbit GFP (Abcam) or anti-UCP1 (Abcam) antibodies for 30 min at room temperature. For fluorescent detection, sections were incubated with anti-rabbit antibodies labelled with Alexa fluor 647 (Invitrogen) for 30 min and counterstained with 4',6-diamidino-2-phenylindole (DAPI). For horseradish-peroxidase-based detection, samples were processed using the Dako Envision+ system and counterstained with haematoxylin (Vector Labs). Cell cultures were fixed in 4% paraformaldehyde, followed by permeabilization in 0.3% Triton X-100. Fixed cells were incubated with anti-myosin heavy chain (MF20, Developmental Studies Hybridoma Bank (DSHB), Iowa) or anti-myogenin (F5D, DSHB) antibodies for 1 h at room temperature. Secondary detection was performed with goat anti-mouse Alexa fluor 594 (Invitrogen), and nuclei were counterstained with DAPI. Samples were visualized with a Nikon Eclipse 80i upright microscope (Nikon Imaging Center, Harvard Medical School). Digital images were acquired by a Hamamatsu Orca 100 cooled CCD (charge-coupled device) camera and Metamorph image analysis software (Molecular Devices).

**Binding studies.** For affinity purification of the PRDM16 transcriptional complexes, *Pparg*-deficient fibroblasts stably expressing PPAR- $\gamma$ 2 were infected with vectors expressing Flag-tagged PRDM16 or a control vector. These cells were grown to confluence and induced to differentiate for 4 days. Nuclei were isolated by homogenizing cells in hypotonic solution (10 mM HEPES pH 7.9, 10 mM

KCl, 1.5 mM MgCl $_{2}$ ). Nuclear proteins were extracted in hypertonic solution (20 mM HEPES pH 7.9, 400 mM NaCl, 1.5 mM MgCl $_{2}$ , 0.2 mM EDTA, 20% glycerol) and dialysed against binding buffer (20 mM HEPES pH 7.9, 150 mM KCl, 0.2 mM EDTA, 20% glycerol). The PRDM16 complex was purified using Flag M2 agarose (Sigma), washed in the binding buffer (150 mM KCl), and eluted with 3  $\times$  Flag peptide (Sigma). The eluted materials were separated by SDS-PAGE and visualized by silver staining or Coomassie blue dye. Gel-resolved proteins were excised, digested with trypsin and analysed by matrix-assisted laser desorption/ionization– reflectron time of flight mass spectrometry (UltraFlex TOF/TOF; Bruker) as described<sup>40</sup>.

To examine the interaction of PRDM16 with PPAR- $\alpha$  and PPAR- $\gamma$ 2, COS-7 cells were co-transfected with expression plasmids for PRDM16 and either Flag-PPAR- $\alpha$  or Flag-PPAR- $\gamma$ 2. Whole-cell extracts were immunoprecipitated with anti-rabbit PRDM16 or anti-Flag M2 (Sigma) overnight at 4 °C. Immunoprecipitates were washed three times with washing buffer (20 mM Tris-HCl, 200 mM NaCl, 10% glycerol, 2 mM EDTA, 0.1% NP-40, 0.1 mM PMSF), separated by SDS-PAGE, transferred to PVDF membrane and blotted with anti-Flag and anti-PRDM16 antibodies. For GST immunoaffinity assays, GST-PRDM16 fusion proteins were purified from bacteria and GST-PPAR- $\gamma$ 2 (full-length) was purified from baculovirus-infected SF9 cells on glutathione Sepharose beads as described before<sup>44</sup>.  $^{35}$ S-labelled and *in vitro* translated PRDM16, SRC1 and PPAR- $\gamma$ 2 were prepared using the TNT Coupled Transcription/Translation System (Promega). Equal amounts of GST fusion proteins (2  $\mu$ g) were incubated overnight at 4 °C with *in vitro* translated proteins in binding buffer (20 mM HEPES pH 7.7, 300 mM KCl, 2.5 mM MgCl $_{2}$ , 0.05% NP40, 1 mM DTT, 10% glycerol). The Sepharose beads were washed five times with binding buffer. Bound proteins were separated by SDS-PAGE and analysed by autoradiography.

**Reporter gene assays.** COS-7 cells or *Pparg* $^{−/−}$  fibroblasts were transfected with 50 ng PPAR- $\gamma$ 2 or PPAR- $\alpha$  and 50 ng RXR- $\alpha$  or empty vector together with 250 ng PRDM16 expression plasmid or vector control and 100 ng of 3  $\times$  DR1-luciferase reporter in 12-well plates using Lipofectamine 2000 (Invitrogen). Cells were harvested 48 h after transfection and assayed for luciferase activity using the Dual-Luciferase Reporter Assay System (Promega). Rosiglitazone or WY-14643 (1  $\mu$ M) was added to some wells for 24 h before harvesting cells. Firefly luciferase reporter gene measurements were normalized to *Renilla* luciferase activity.

**Expression analysis and western blotting.** Total RNA was isolated from cultured cells and tissue using Trizol (Invitrogen) or RNeasy columns (Qiagen) according to the manufacturer's instructions. Real-time PCR oligonucleotide sequences are provided in Supplementary Table 2. For western blot analysis, cells or tissues were lysed in RIPA buffer (0.5% NP-40, 0.1% SDS, 150 mM NaCl, 50 mM Tris-Cl (pH 7.5)). Proteins were separated by SDS-PAGE, transferred to PVDF membrane (Millipore) and probed with anti-UCP1 (Abcam), anti-PRDM16, anti-Cidea (Chemicon), and anti- $\beta$ -actin (Sigma) antibodies.

42. Uldry, M. *et al.* Complementary action of the PGC-1 coactivators in mitochondrial biogenesis and brown fat differentiation. *Cell Metab.* 3, 333–341 (2006).
43. Kinsella, T. M. & Nolan, G. P. Episomal vectors rapidly and stably produce high-titer recombinant retrovirus. *Hum. Gene Ther.* 7, 1405–1413 (1996).
44. Drori, S. *et al.* Hic-5 regulates an epithelial program mediated by PPARgamma. *Genes Dev.* 19, 362–375 (2005).

## LETTERS

# Magnetic support of the optical emission line filaments in NGC 1275

A. C. Fabian<sup>1</sup>, R. M. Johnstone<sup>1</sup>, J. S. Sanders<sup>1</sup>, C. J. Conselice<sup>2</sup>, C. S. Crawford<sup>1</sup>, J. S. Gallagher III<sup>3</sup> & E. Zweibel<sup>3,4</sup>

The giant elliptical galaxy NGC 1275, at the centre of the Perseus cluster, is surrounded by a well-known giant nebulosity of emission-line filaments<sup>1,2</sup>, which are plausibly in excess of  $10^8$  years old<sup>3</sup>. The filaments are dragged out from the centre of the galaxy by radio-emitting ‘bubbles’ rising buoyantly in the hot intracluster gas<sup>4</sup>, before later falling back. They act as markers of the feedback process by which energy is transferred from the central massive black hole to the surrounding gas. The mechanism by which the filaments are stabilized against tidal shear and dissipation into the surrounding extremely hot ( $4 \times 10^7$  K) gas has been unclear. Here we report observations that resolve thread-like structures in the filaments. Some threads extend over 6 kpc, yet are only 70 pc wide. We conclude that magnetic fields in the threads, in pressure balance with the surrounding gas, stabilize the filaments, so allowing a large mass of cold gas to accumulate and delay star formation.

The images presented here (Figs 1–4) were taken with the Advanced Camera for Surveys (ACS) on the NASA Hubble Space Telescope (HST) using three filters: F625W in the red contains the H $\alpha$  line, F550M is mostly continuum and F435W in the blue highlights young stars. In Fig. 2a we show part of the northern filament  $\sim 27$  kpc from the nucleus (we adopt a value for the Hubble constant of  $H_0 = 71 \text{ km s}^{-1} \text{ Mpc}^{-1}$ , which at a redshift of 0.0176 for NGC 1275 gives  $352 \text{ pc arcsec}^{-1}$ ). The filaments seen in the image taken with the ground-based WIYN telescope (Fig. 2b) are just resolved into narrow threads with the HST ACS (see Supplementary Information). This also occurs in many other filaments, including the northwestern ‘horseshoe’ filament (Fig. 3), which lies immediately interior to the outer ‘ghost bubble’ (in which radio emission is absent owing to synchrotron ageing) in X-ray images<sup>5</sup>. A fine thread of emission is seen in the northern filament system that extends about 16 arcsec or 5.8 kpc. Averaged over kpc strips it is about 4 pixels (0.2 arcsec) or about 70 pc wide. (This is an upper limit, as the point spread function of the ACS is about one-half this value.) The aspect ratio (length/thickness) therefore approaches 100. The top of the horseshoe, which is about 6 kpc across, is similar, as are many other relatively isolated filaments.

In order to estimate the magnetic field required to stabilize a filament, we need to know the properties of a filament and its surroundings. We shall concentrate on a thread of radius  $r = 35$  pc and length  $l = 6$  kpc at a distance of 25 kpc from the nucleus of NGC 1275 (Fig. 2) as a basic structural unit typical of what is now resolved in the filaments. To estimate the mass of such a thread, we scale from the total gas mass of  $10^8 M_\odot$  (where  $M_\odot$  is the solar mass) inferred from CO emission<sup>6</sup> observed in a 22 arcsec IRAM beam on the same northern filament complex. Assuming that the mass scales with H $\alpha$  emission, which is the case for the H<sub>2</sub> emission measured with the Spitzer telescope<sup>7</sup>, then our fiducial thread has a mass of about  $10^6 M_\odot$ . Its mean density is then  $\sim 2 \text{ cm}^{-3}$  and its perpendicular column

density  $N \approx 4 \times 10^{20} \text{ cm}^{-2}$  and surface density  $\Sigma_\perp \approx 7 \times 10^{-4} \text{ g cm}^{-2}$ . The lengthwise column density,  $\Sigma_{||}$ , is  $l/2r$  times larger.

The variation in projected radial velocity along the filaments is about  $100\text{--}200 \text{ km s}^{-1}$  (ref. 4). If we assume that after correction for projection the velocity shear is about  $300 \text{ km s}^{-1}$ , then the whole structure (out to a radius of 50 kpc) must be  $(1\text{--}2) \times 10^8$  yr old. Individual filaments may be in ballistic motion, falling back in for example, but to retain their structure over this time means that something must balance gravity or at least tidal gravitational forces.

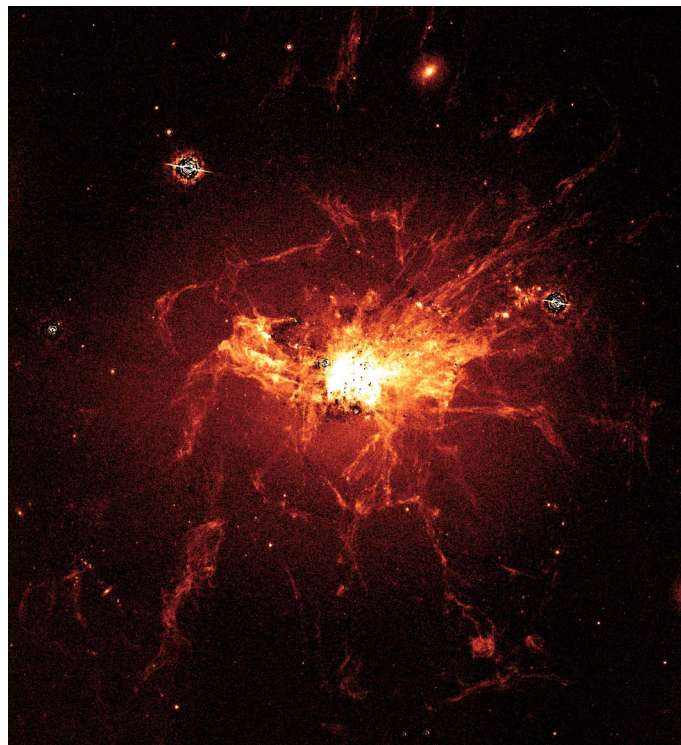


**Figure 1 | Image of the H $\alpha$  emission from the core of the cluster.** This image was created by subtracting a scaled green (F550M) image from the red image, removing the smooth galactic continuum contribution. The image measures  $140 \times 150$  arcsec in size. Multiple exposures using a three-point line dither pattern were taken at a set of three pointing positions around the centre of NGC 1275 in filters F550M and F625W, with considerable overlap between the pointings. Similar data (see Supplementary Information) were obtained in the F435W filter, but from only two pointing positions because of the failure of ACS before the completion of this programme. The data from each filter were registered relative to each other using stars, and then combined separately into large mosaic images using the latest version of the stsdas task multidrizzle<sup>18</sup>.

<sup>1</sup>Institute of Astronomy, Madingley Road, Cambridge CB3 0HA, UK. <sup>2</sup>University of Nottingham, School of Physics & Astronomy, Nottingham NG7 2RD, UK. <sup>3</sup>Department of Astronomy, <sup>4</sup>Department of Physics, University of Wisconsin, Madison, Wisconsin 53706, USA.

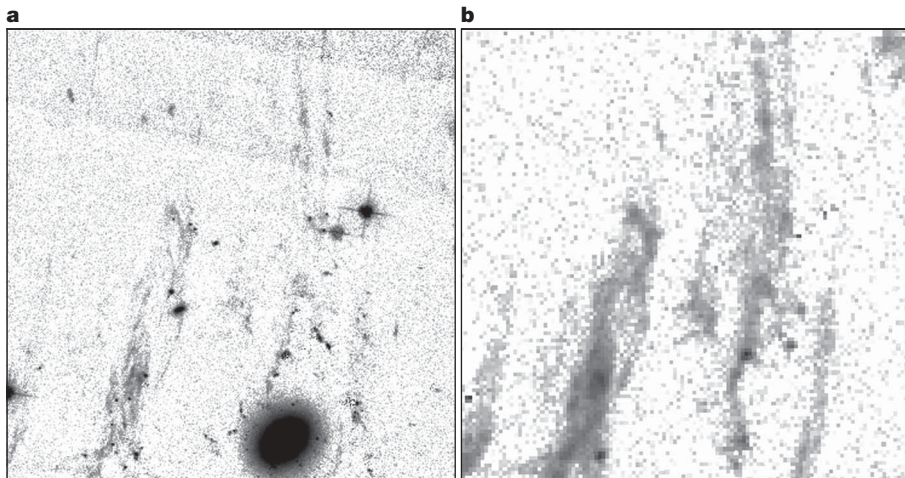


**Figure 2 | Comparison of our HST image of the northern filament system (about 25 kpc north of the nucleus) with that from the WIYN telescope<sup>2</sup>.** **a**, HST image; **b**, WIYN image. The HST image, obtained with the ACS, was produced from the red filter. The SExtractor tool<sup>19</sup> was applied to the data to identify sources and create a model for the smooth galactic light. This was

subtracted from the red filter image to enhance the filament. The SExtractor neural network was used to identify stellar sources. These sources were hidden by filling their regions with random values selected from the surrounding pixels. Each image measures  $46.6 \times 46.1$  arcsec in size. The WIYN image is narrowband and continuum subtracted.

For a filament of radial length  $l$  at galaxy radius  $R$ , the gravitational acceleration  $g \approx v^2/R$ , where  $v$  is the velocity dispersion in the potential (about  $700 \text{ km s}^{-1}$  at that radius as inferred from the X-ray measured temperature of the intracluster medium<sup>8</sup>) at radius  $R \approx 25 \text{ kpc}$ ; tidal acceleration is smaller by  $2l/R$ . The force most likely to balance a filament against gravity is that due to the tangential component of a magnetic field, as suggested by the filamentary morphology.

Consider first a horizontal thread supported against gravity; the field  $B_h$  needed for support is then  $B_h \approx (4\pi\Sigma_\perp g)^{1/2}$ . For the above values, this corresponds to  $B_h \approx 24 \mu\text{G}$ , which is less than the equipartition value of  $100 \mu\text{G}$  and so energetically possible. By equipartition, we mean that  $B^2/8\pi = nkT$ , and use the total particle density  $n = 0.06 \text{ cm}^{-3}$  and temperature  $kT = 4 \text{ keV}$  for the X-ray-emitting

surrounding gas<sup>8</sup>. For a radial filament, the value  $B_r$  is  $\Sigma_{||}^{1/2} \approx 10$  times larger than  $B_h$ , which exceeds equipartition. If the filaments are falling, then  $g$  should be replaced by the tidal acceleration, which is smaller by  $l/R$ , reducing  $B_r$  by a factor of 2, comparable with the equipartition value. Note that the required magnetic field is inversely proportional to the radius of the filamentary threads, which means that the high spatial resolution of the HST is essential for demonstrating the high magnetic field required in the NGC 1275 system.

Assuming that the total pressure in the filaments equals the outer thermal pressure means that the filaments are magnetically dominated (that is, the ratio of thermal to magnetic pressure  $\beta < 1$ ) and are essentially magnetic molecular structures, similar (but at much higher surrounding pressures) to Galactic molecular clouds<sup>9,10</sup>. Horizontal support would be by magnetic cradles, similar to what holds up solar prominences<sup>11</sup>. Vertical support, to prevent gas flowing down radial filaments, requires an unseen component of horizontal field in the filaments. Small transverse components would be compressed by vertical downflow until their pressure was adequate for vertical support. We assume of course that the magnetic field is coupled to the (low) ionized fraction of the cold gas, and that the slowness of ambipolar diffusion links the molecular, atomic and ionized components. The emission from the filaments is well reproduced by an internal heating model, possibly energized by magnetic waves and non-thermal particles powered by the kinetic energy of the clouds<sup>12</sup>. The observed velocity dispersion of  $\sim 100 \text{ km s}^{-1}$  (full-width at half-maximum) within a filament<sup>4</sup> may be direct evidence of such waves, as indeed expected for Alfvénic turbulence, where half the internal pressure is kinetic and half magnetic. A large field in filaments is also one interpretation of the high Faraday rotation measure seen against the tip of the jet at the centre of NGC 1275<sup>13</sup>.

The strong fields implied for their support can stop or delay star formation in the filaments, as matter will not be able to collect along field lines. Many massive star clusters were discovered across the face of NGC 1275 in early HST imaging<sup>14,15</sup>, most of which do not correlate in position with any filaments. However to the southeast and south there are examples of ordered chains of young star clusters (Fig. 4). They are offset from the nearest H $\alpha$  filaments by a few kpc. The ones to the southeast resemble short streamers, and are probably unbound clumps falling apart in the tidal cluster field. This gives an age for the clumps of about 20 Myr. Unless due to chance projection, their proximity to the filaments (particularly the one to the south) shows that stars sometimes do form in the filaments and that at least part of the enormous star cluster system of NGC 1275

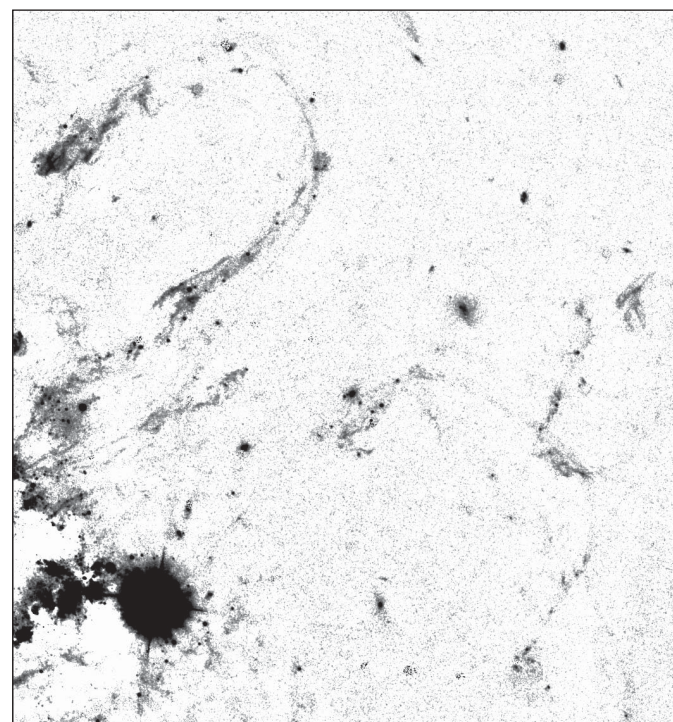


**Figure 3 | Horseshoe filament system about 25 kpc to the northwest of the nucleus.** This image has had continuum and stellar sources removed in the same way as Fig. 2. The image measures  $53.5 \times 56.5$  arcsec in size.

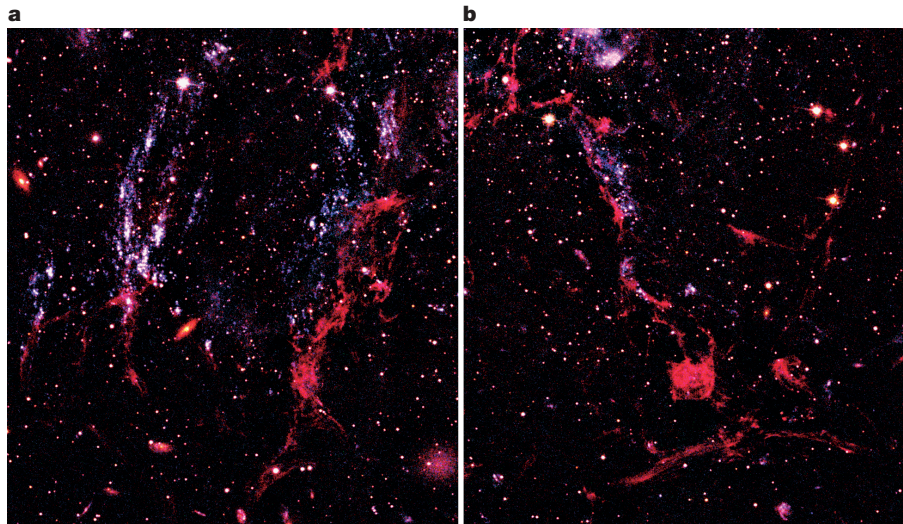


**Figure 4 | Clumps of stars and H $\alpha$  filaments to the southeast and south of the nucleus.** **a**, Southeastern image; **b**, southern image. SExtractor was used to model the smooth galactic light in the red, green and blue bands. This

originates in this way. In general, though, there are no obvious star clusters associated with the filaments, so at any given time the star formation rate in any filament must be low; cooled gas does not automatically and rapidly form stars.

The critical surface density  $\Sigma_c$  for gravitational instability corresponding to the magnetic field we infer in the filaments is given by  $\Sigma_c = B/2\pi\sqrt{G} = 0.062 B g \text{ cm}^{-2}$  (where  $B$  is in units of  $100 \mu\text{G}$ ) or a critical column density of  $N_c = 4 \times 10^{22} \text{ cm}^{-2}$  (assuming hydrogen). Given the mean density of a thread of  $\sim 2 \text{ cm}^{-3}$  and transverse column density  $\sim 2 \times 10^{20} \text{ cm}^{-2}$ , they are gravitationally stable. Instability could occur however, if either much of the molecular mass is concentrated in a much smaller thickness ( $\sim 0.1 \text{ pc}$  for  $50 \text{ K}$ , assuming thermal pressure balance) and  $\beta > 1$ , or if the field becomes well ordered parallel to a radial filament axis. Thus gravitational stability depends on the configuration of the molecular and magnetic components.

If a filament acts as a coherent unit due to the magnetic field, then it will interact dynamically with the hot, low-density, surrounding gas over a length scale corresponding to its own column density. The above mean value of  $4 \times 10^{20} \text{ cm}^{-2}$  corresponds to about  $2 \text{ kpc}$  ( $\sim 6 \text{ arcsec}$ ) in the surrounding hot gas, so the relative straightness of many filaments over scales of  $3\text{--}10 \text{ kpc}$  or more shows that motions in that gas must be reasonably ordered and not highly turbulent on those scales<sup>5</sup>. We note that the volume-filling component of a filament is probably the  $5 \times 10^6 \text{ K}$ , soft-X-ray-emitting phase seen in Chandra X-ray images<sup>16</sup>.

Filamentary emission-line structures are common in massive young galaxies<sup>17</sup>. The filament system of NGC 1275 may be a nearby example, which can be observed in unprecedented detail. The outer filaments of NGC 1275 present us with magnetically dominated molecular clouds stretched out for individual inspection, and are the only direct way (apart from X-ray imaging) of seeing the action of power from the active galactic nucleus on the surrounding intracluster gas.

Received 3 March; accepted 10 June 2008.

1. Kent, S. M. & Sargent, W. L. W. Ionization and excitation mechanisms in the filaments around NGC 1275. *Astrophys. J.* **230**, 667–680 (1979).
2. Conselice, C. J., Gallagher, J. S. III & Wyse, R. F. G. On the nature of the NGC 1275 system. *Astron. J.* **122**, 2281–2300 (2001).
3. Hatch, N. A., Crawford, C. S., Fabian, A. C. & Johnstone, R. M. Detections of molecular hydrogen in the outer filaments of NGC1275. *Mon. Not. R. Astron. Soc.* **358**, 765–773 (2005).

continuum was subtracted from each image. The images were combined as red, green and blue channels with SAOImage DS9<sup>20</sup>.

4. Hatch, N. A., Crawford, C. S., Johnstone, R. M. & Fabian, A. C. On the origin and excitation of the extended nebula surrounding NGC1275. *Mon. Not. R. Astron. Soc.* **367**, 433–448 (2006).
5. Fabian, A. C. *et al.* The relationship between the optical H $\alpha$  filaments and the X-ray emission in the core of the Perseus cluster. *Mon. Not. R. Astron. Soc.* **344**, L48–L52 (2003).
6. Salomé, P. *et al.* Cold gas in the Perseus cluster core: Excitation of molecular gas in filaments. *Astron. Astrophys.* **484**, 317–325 (2008).
7. Johnstone, R. M. *et al.* Discovery of atomic and molecular mid-infrared emission lines in offnuclear regions of NGC1275 and NGC4696 with the Spitzer Space Telescope. *Mon. Not. R. Astron. Soc.* **382**, 1246–1260 (2007).
8. Fabian, A. C. *et al.* A very deep Chandra observation of the Perseus cluster: Shocks, ripples and conduction. *Mon. Not. R. Astron. Soc.* **366**, 417–428 (2006).
9. Heiles, C. & Crutcher, R. in *Cosmic Magnetic Fields* (eds Wielebinski, R. & Beck, R.) 137–182 (Lecture Notes in Physics 664, Springer, 2005).
10. McKee, C. F., Zweibel, E. G., Goodman, A. A. & Heiles, C. in *Protostars and Planets III* (eds Levy, E. H. & Lunine, J. I.) 327–366 (Univ. Arizona Press, 1993).
11. Low, B. C. Solar activity and the corona. *Sol. Phys.* **167**, 217–265 (1996).
12. Ferland, G. J. *et al.* The origin of molecular hydrogen emission in cooling-flow filaments. *Mon. Not. R. Astron. Soc.* **368**, L72–L76 (2008).
13. Taylor, G. B. *et al.* Magnetic fields in the centre of the Perseus cluster. *Mon. Not. R. Astron. Soc.* **368**, 1500–1506 (2006).
14. Holtzman, J. A. *et al.* Planetary Camera observations of NGC 1275 — Discovery of a central population of compact massive blue star clusters. *Astron. J.* **103**, 691–702 (1992).
15. Carlson, M. N. *et al.* Deep Hubble Space Telescope observations of star clusters in NGC 1275. *Astron. J.* **115**, 1778–1790 (1998).
16. Sanders, J. S. & Fabian, A. C. A deeper X-ray study of the core of the Perseus galaxy cluster: The power of sound waves and the distribution of metals and cosmic rays. *Mon. Not. R. Astron. Soc.* **381**, 1381–1339 (2007).
17. Reuland, M. *et al.* Giant Ly $\alpha$  nebulae associated with high-redshift radio galaxies. *Astrophys. J.* **592**, 755–766 (2003).
18. Koekemoer, A. M., Fruchter, A. S., Hook, R. N. & Hack, W. in *The 2002 HST Calibration Workshop* (eds Arribas, S., Koekemoer, A. & Whitmore, B.) 337 (Space Telescope Science Institute, 2002); available at [http://www.stsci.edu/hst/HST\\_overview/documents/calworkshop/workshop2002](http://www.stsci.edu/hst/HST_overview/documents/calworkshop/workshop2002).
19. Bertin, E. & Arnouts, S. SExtractor: Software for source extraction. *Astron. Astrophys. Suppl. Ser.* **117**, 393–404 (1996).
20. Joye, W. A. & Mandel, E. in *Astronomical Data Analysis Software and Systems XIV* (eds Shopbell, P., Britton, M. & Ebert, R.) 110–113 (ASP Conference Series 347, Astronomical Society of the Pacific, 2005).

**Supplementary Information** is linked to the online version of the paper at [www.nature.com/nature](http://www.nature.com/nature).

**Acknowledgements** A.C.F. thanks the Royal Society for support. E.Z. acknowledges support from NSF AST 0507367 and J.S.G. from HST-GO-11207.07-A.

**Author Information** Reprints and permissions information is available at [www.nature.com/reprints](http://www.nature.com/reprints). Correspondence and requests for materials should be addressed to A.C.F. (acf@ast.cam.ac.uk).

# Heterogeneous chemistry in the atmosphere of Mars

Franck Lefèvre<sup>1,2</sup>, Jean-Loup Bertaux<sup>2,3</sup>, R. Todd Clancy<sup>4</sup>, Thérèse Encrenaz<sup>2,5</sup>, Kelly Fast<sup>6</sup>, François Forget<sup>2,7</sup>, Sébastien Lebonnois<sup>2,7</sup>, Franck Montmessin<sup>2,3</sup> & Séverine Perrier<sup>2,3,†</sup>

Hydrogen radicals are produced in the martian atmosphere by the photolysis of water vapour and subsequently initiate catalytic cycles that recycle carbon dioxide from its photolysis product carbon monoxide<sup>1,2</sup>. These processes provide a qualitative explanation for the stability of the atmosphere of Mars, which contains 95 per cent carbon dioxide. Balancing carbon dioxide production and loss based on our current understanding of the gas-phase chemistry in the martian atmosphere has, however, proven to be difficult<sup>3–5</sup>. Interactions between gaseous chemical species and ice cloud particles have been shown to be key factors in the loss of polar ozone observed in the Earth's stratosphere<sup>6</sup>, and may significantly perturb the chemistry of the Earth's upper troposphere<sup>7</sup>. Water-ice clouds are also commonly observed in the atmosphere of Mars<sup>8–10</sup> and it has been suggested previously that heterogeneous chemistry could have an important impact on the composition of the martian atmosphere<sup>3–5,11</sup>. Here we use a state-of-the-art general circulation model together with new observations of the martian ozone layer<sup>12–15</sup> to show that model simulations that include chemical reactions occurring on ice clouds lead

to much improved quantitative agreement with observed martian ozone levels in comparison with model simulations based on gas-phase chemistry alone. Ozone is readily destroyed by hydrogen radicals and is therefore a sensitive tracer of the chemistry that regulates the atmosphere of Mars. Our results suggest that heterogeneous chemistry on ice clouds plays an important role in controlling the stability and composition of the martian atmosphere.

One-dimensional, globally averaged models have previously explored the potential impact of heterogeneous chemical processes in the martian atmosphere<sup>3–5,11</sup> but, in the absence of sufficiently strong observational and laboratory evidence, this possibility has remained unproven. Recently, the framework for investigating this issue has improved greatly. The SPICAM ultraviolet spectrometer onboard the Mars-Express spacecraft has for the first time provided global, quasi-continuous observations of the martian ozone layer<sup>12</sup>. Ozone ( $O_3$ ) is readily destroyed by hydrogen radicals and is therefore a sensitive tracer of the chemistry that regulates the atmosphere of Mars. At the same time, the development of general circulation models (GCM) with interactive photochemistry<sup>16,17</sup> now allows

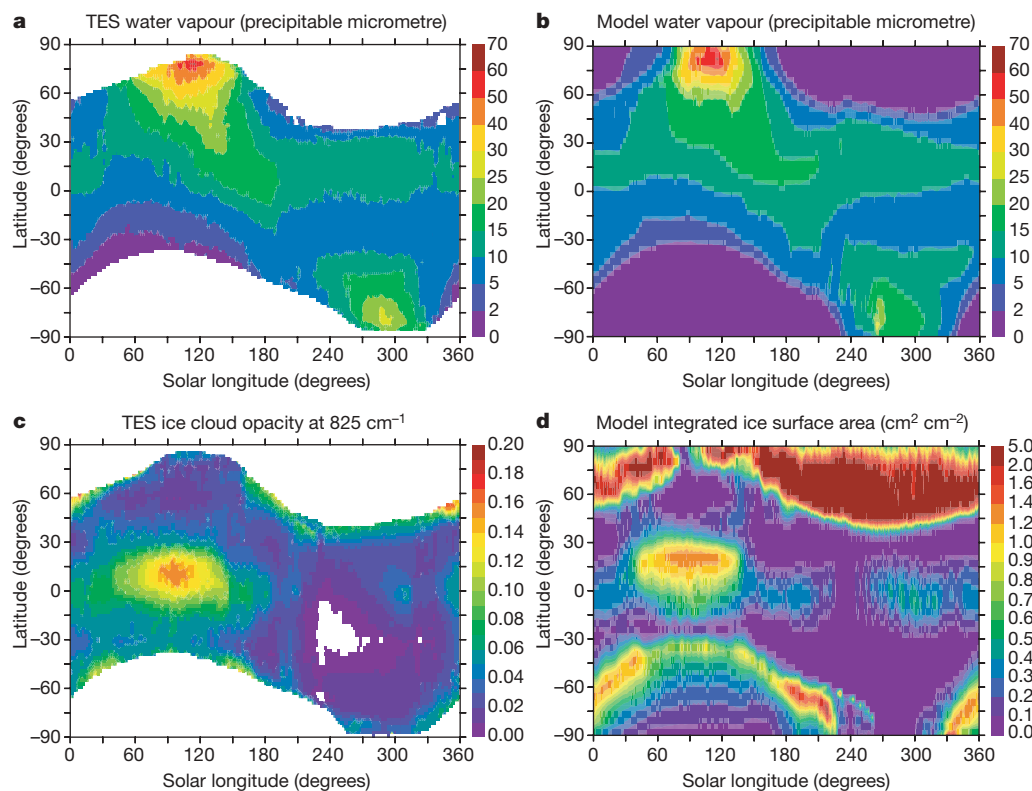


**Figure 1 | Observed and simulated seasonal evolution of water vapour and water-ice clouds.** **a**, Water vapour column observed by the thermal emission spectrometer<sup>19</sup> on the Mars Global Surveyor, in precipitable micrometres. **b**, Water vapour column calculated by the GCM. **c**, Water-ice cloud opacity at  $825\text{ cm}^{-1}$  observed by TES. **d**, Vertically integrated surface area of water-ice cloud calculated by the GCM, in  $\text{cm}^2\text{ cm}^{-2}$ . Solar longitude ( $L_s$ ) is used to specify seasons on Mars, and is  $0^\circ$  at the northern vernal equinox and  $270^\circ$  at northern winter solstice.

<sup>1</sup>UPMC Univ. Paris 06, Service d'Aéronomie, Paris F-75005, France. <sup>2</sup>CNRS/INSU, France. <sup>3</sup>Université Versailles St-Quentin, Service d'Aéronomie, Verrières-le-Buisson F-91371, France. <sup>4</sup>Space Science Institute, 4750 Walnut Street, Suite 205, Boulder, Colorado 80301, USA. <sup>5</sup>LESIA, Observatoire de Paris, F-92195 Meudon, France. <sup>6</sup>Planetary Systems Laboratory, Code 693, NASA Goddard Space Flight Center, Greenbelt, Maryland 20771, USA. <sup>7</sup>UPMC Univ. Paris 06, Laboratoire de Météorologie Dynamique, Paris F-75005, France.

†Present address: Direction Générale pour l'Armement, Bagneux F-92220, France.

observational data to be analysed at the same level of sophistication as for terrestrial studies. To re-evaluate our quantitative understanding of martian photochemistry, we carried out a stringent comparison between ozone predicted by the GCM with photochemistry developed at Laboratoire de Météorologie Dynamique<sup>16</sup> (LMD) and the SPICAM data collected during more than one martian year. Also included in our analysis are Earth-based ozone measurements made at various seasons before the Mars-Express mission, from the Hubble Space Telescope<sup>13,14</sup> (HST) and the NASA Infrared Telescope Facility (IRTF)<sup>15</sup>.

Because water vapour is the source of ozone-destroying  $\text{HO}_x$  species, it is important to ensure first that the martian water cycle is simulated correctly by the GCM. We therefore adjusted the parameters of the microphysical scheme used in the model<sup>18</sup> to obtain optimal quantitative agreement with the seasonal evolution of  $\text{H}_2\text{O}$  given by the Thermal Emission Spectrometer<sup>19</sup> (TES) onboard the Mars Global Surveyor (Fig. 1a, b; see also the Supplementary Information). The model also provides a good match to the equatorial cloud belt usually observed between solar longitudes

$L_s = 30^\circ\text{--}150^\circ$  during the colder aphelion season<sup>8,19</sup> (Fig. 1c, d). At high latitudes, the GCM predicts large ice surface areas in the polar hoods that start to form in late summer. This hypothesis is consistent with the strong opacities measured in the polar hoods at visible<sup>9</sup> and ultraviolet<sup>10</sup> wavelengths. TES data obtained at the edge of the seasonal  $\text{CO}_2$  caps also support this result.

The model ozone is compared with observations in Fig. 2. At high latitudes of both hemispheres, SPICAM indicates a marked seasonal evolution which is anti-correlated with the amount of water vapour: the largest  $\text{O}_3$  columns are found in the dry winter/spring polar vortices, whereas  $\text{O}_3$  is close to zero in summer. This behaviour is qualitatively well reproduced by our first GCM simulation, which considers only the gas-phase photochemistry. However, rigorous comparison with SPICAM shows significant quantitative differences. In the latitude band  $70^\circ\text{--}90^\circ\text{ N}$  (Fig. 2a), the model predicts ozone loss that is too fast in early spring ( $L_s = 10^\circ\text{--}40^\circ$ ) and underestimates the column by about  $10\text{ }\mu\text{m atm}$ . In late summer ( $L_s = 150^\circ\text{--}180^\circ$ ), the  $\text{O}_3$  increase is too slow in the model, which results in amounts that are lower by a factor of almost three relative to observations. This

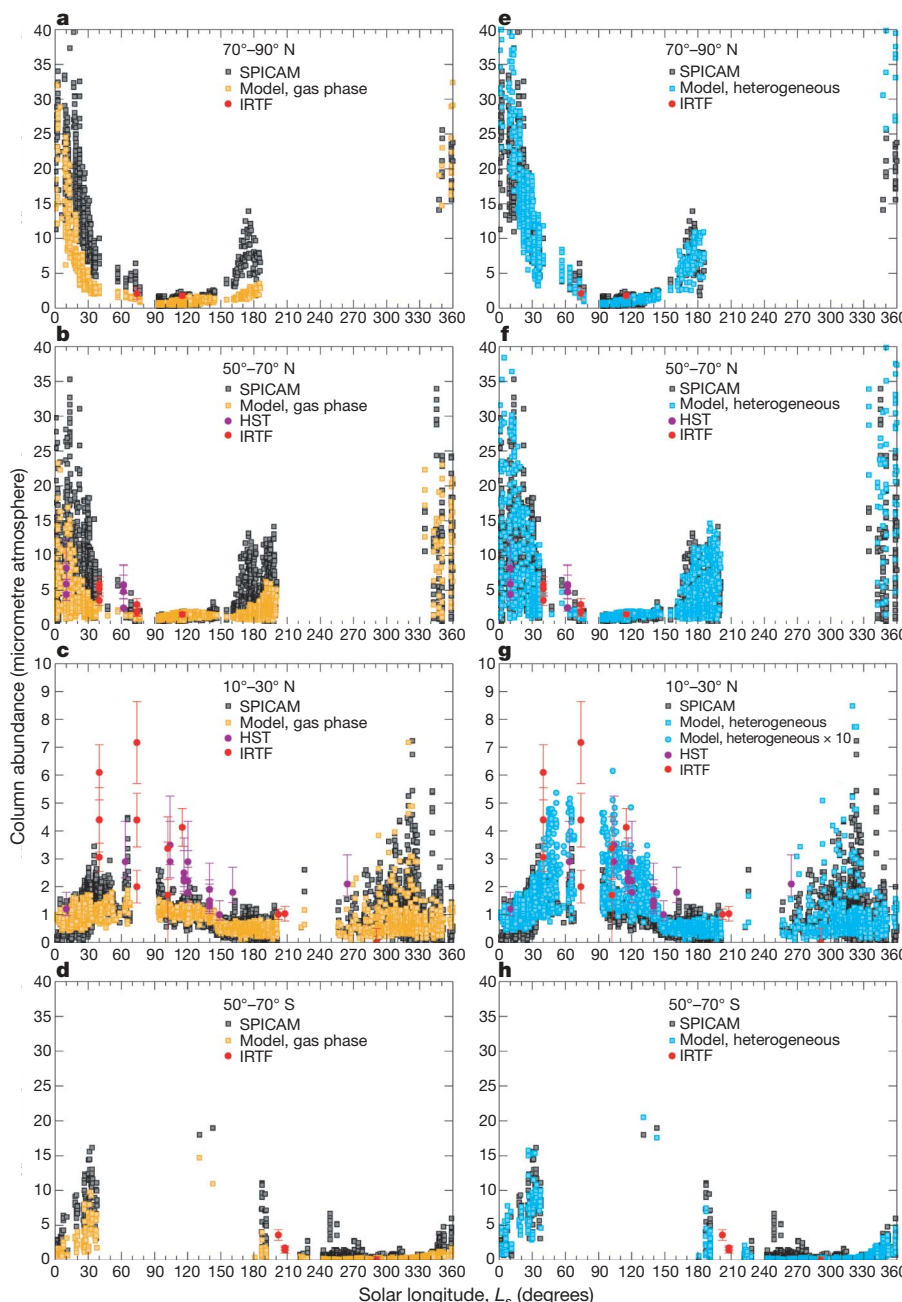


**Figure 2 | Observed and simulated seasonal evolution of martian ozone.** The GCM ozone columns are compared with those measured from SPICAM, the HST<sup>13,14</sup>, and the IRTF<sup>15</sup>. In the left column, the model only considers gas-phase photochemical reactions. The right column incorporates the heterogeneous loss of  $\text{HO}_x$  on water-ice clouds. Blue circles in g represent the  $\text{O}_3$  columns obtained when the cloud surface area is multiplied by 10 for  $L_s = 30^\circ\text{--}150^\circ$ . In all panels model values are plotted over SPICAM data points. A unit of 1 micrometre atmosphere is a column abundance of  $2.689 \times 10^{15} \text{ molecules cm}^{-2}$ , or 0.1 Dobson unit. Note the change in vertical scale at  $10^\circ\text{ N}$ – $30^\circ\text{ N}$ . Error bars indicate uncertainties in the individual measurements.

bias is confirmed at  $50^{\circ}$  N– $70^{\circ}$  N (Fig. 2b) and  $50^{\circ}$  S– $70^{\circ}$  S (Fig. 2d): although the GCM partially reproduces the strong day-to-day ozone variability related to the presence of the polar vortex edge in these latitude bands<sup>16</sup>, the peak  $O_3$  values calculated in early spring and around autumn equinox are underestimated relative to SPICAM.

The ozone annual cycle at low latitudes is of much more limited amplitude. At  $10^{\circ}$  N– $30^{\circ}$  N (Fig. 2c), it is characterized by a broad seasonal maximum centred on Mars aphelion ( $L_s = 71^{\circ}$ ), and by strong day-to-day variability in winter. The gas-phase-only GCM reproduces this behaviour qualitatively well. Near aphelion, the ozone enhancement results from the decrease in water vapour saturation altitude and the subsequent build-up of a seasonal ozone layer above 30 km altitude<sup>16,20,21</sup>. In winter, deformations of the  $O_3$ -rich polar vortex sporadically bring large quantities to mid-to-low latitudes, explaining the fast changes observed by SPICAM. However, although there is rather large scatter in the observational data, it is evident that the GCM underestimates the  $O_3$  values generally detected in the aphelion season.

The fact that the gas-phase-only model underestimates ozone amounts during opposite seasons at high and low latitudes seems to be a robust result. First, both water vapour and dust<sup>22</sup> fields are constrained by TES observation; thus we cannot invoke a possible overestimation of  $H_2O$ , or an unrealistic amount of dust that might affect the photolysis rate calculations, to explain the disagreement. Second, the GCM ozone columns are coincident with SPICAM observations; local effects induced by topography, local time or three-dimensional transport are therefore taken into account. Third, we explored the solutions offered by current uncertainties in the photochemical and gas-phase kinetics data of martian interest; changing these parameters in the limits allowed by laboratory and field evidence on Earth does not allow a significant increase in ozone<sup>16</sup>. Finally, the ozone profiles measured by SPICAM above 30 km do not indicate an underestimation by the model at high

latitudes, or at low latitudes near aphelion<sup>21</sup>. Therefore, if the discrepancy with observed ozone columns is the result of a missing process in the gas-phase model, then (1) it must be essentially confined below 30 km, (2) at high latitudes, it must be active only in or near the polar vortex, and (3) at low latitudes, it must be especially efficient in the aphelion season and no later than  $L_s = 150^{\circ}$ . Interestingly, these three conditions go against the observed climatology of atmospheric dust<sup>12,19</sup>, which tends to exclude heterogeneous reactions on dust as good candidates to explain the SPICAM data. On the other hand, these constraints are well satisfied by water-ice clouds, and we therefore introduced heterogeneous chemistry on clouds in a second GCM simulation. Heterogeneous reaction rates are proportional to the available surface area and to their surface reaction probability,  $\gamma$ . To limit the uncertainties, we made the conservative choice of considering only the reactions of martian interest for which  $\gamma$  has been identified and measured in the laboratory. This led us to implement only the uptake of  $HO_2$  and  $OH$  on water-ice, adopting  $\gamma_{HO_2} = 0.025$  and  $\gamma_{OH} = 0.03$  (ref. 23). These values are those currently recommended for terrestrial studies<sup>24</sup>.

At  $L_s = 30^{\circ}$ , the  $HO_x$  uptake on the northern polar hood multiplies the ozone abundance by a factor of about four in the polar vortex (Fig. 3). Heterogeneous chemistry brings the model into excellent quantitative agreement with SPICAM throughout the springtime period (Fig. 2e, f), does not degrade the satisfying results already obtained with the gas-phase experiment in early summer, and reproduces well the rapid growth in ozone after  $L_s = 150^{\circ}$ . As a consequence of the larger  $O_3$  latitudinal gradients, the variability observed at  $50^{\circ}$  N– $70^{\circ}$  N and  $50^{\circ}$  S– $70^{\circ}$  S is better reproduced, and the maximum values predicted in the northern hemisphere (30–40  $\mu$ m atm) are more consistent both with SPICAM and with the early observations of Mariner 9 (ref. 25).

At low latitudes, introducing heterogeneous chemistry on the aphelion cloud belt doubles the amount of ozone at  $L_s = 70^{\circ}$  (Fig. 3),

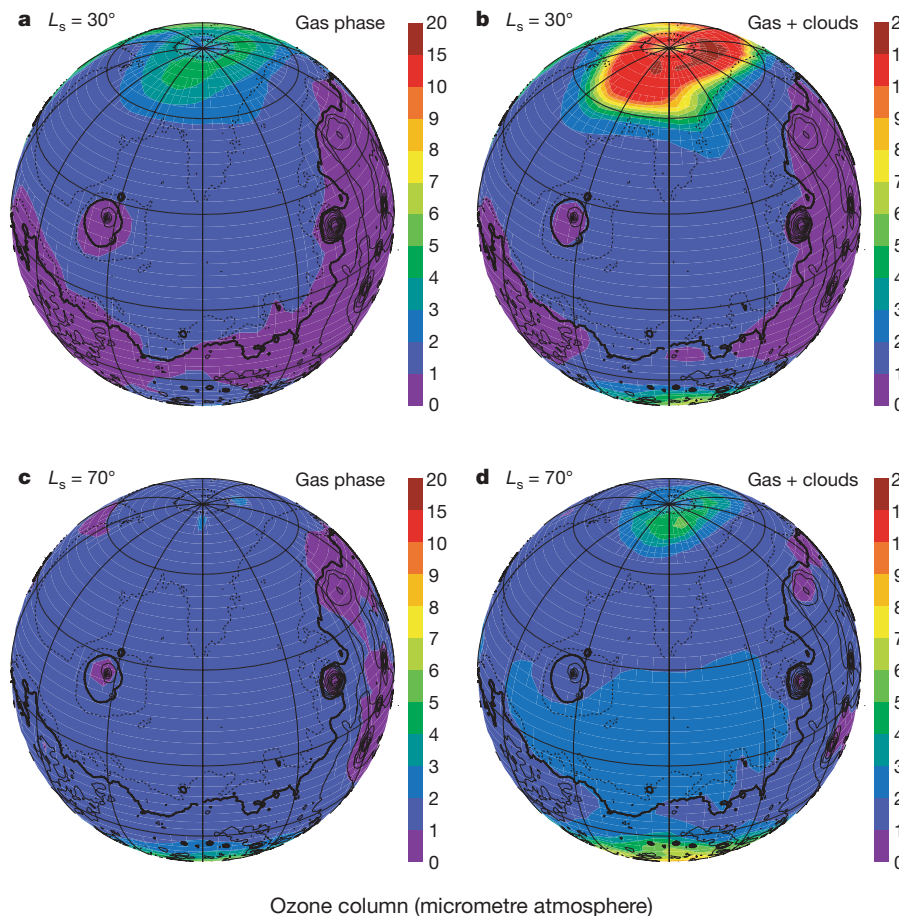


**Figure 3 | Synoptic distribution of  $O_3$  column (micrometre atmosphere) calculated in northern spring and at aphelion. a, c, Gas-phase-only photochemical scheme; b, d, with heterogeneous loss of  $HO_x$  on water-ice clouds. The observer is facing the  $180^{\circ}$  meridian at local noon, and the black contours correspond to Mars topography at 2-km intervals.**

which allows a more accurate description of the observed seasonal maximum. However, the largest values detected by SPICAM and from Earth (4 to 7  $\mu\text{m atm}$  at  $L_s = 74^\circ$ , 3 to 7  $\mu\text{m atm}$  for  $L_s = 100$ – $120^\circ$ ) still seem outstanding. We investigated this issue by multiplying the predicted cloud surface area by a factor of 10 to account for uncertainties in the modelled ice particle number density, radius, shape and sub-grid-scale inhomogeneities. This sensitivity experiment shows a further doubling in ozone which allows the model to reach virtually all the peak values measured during the aphelion season (Fig. 2g). Heterogeneous chemistry seems, therefore, to have the potential to explain the full amplitude of the  $\text{O}_3$  column variations observed in this season. Furthermore, this result is obtained with modelled CO values that also match the observations (see Supplementary Information).

A further hint of the proposed mechanism is provided by the Earth-based measurements<sup>26,28–30</sup> of Mars atmospheric  $\text{H}_2\text{O}_2$ , the temporary  $\text{HO}_x$  reservoir produced by the reaction between two  $\text{HO}_2$  radicals, also thought to be the main oxidant of the martian surface. Figure 4 shows that the seasonal variation of  $\text{H}_2\text{O}_2$  at low latitudes is reasonably well reproduced by the gas-phase GCM, except at  $L_s = 112^\circ$ , when the model prediction exceeds the observed upper limit<sup>26</sup> by a factor of three. Consistent with what is found for ozone, introducing the  $\text{HO}_x$  uptake on the aphelion cloud belt into the model largely reduces that discrepancy. We do not exclude the possibility that other unknown or poorly quantified chemical processes might diminish  $\text{H}_2\text{O}_2$  and have an impact on ozone. It must be emphasized, however, that heterogeneous chemistry as introduced in the GCM improves the agreement with measurements of both  $\text{O}_3$  and  $\text{H}_2\text{O}_2$  without violating current laboratory constraints. This result suggests that water-ice clouds play an important role in the composition and evolution of the martian atmosphere. As the same processes are believed to occur on cirrus clouds on Earth, it also sheds new light on the role of Mars as a natural laboratory for better understanding the chemistry of our own atmosphere.

## METHODS SUMMARY

The LMD GCM was integrated at a resolution of  $3.75^\circ$  latitude  $\times$   $5.625^\circ$  longitude, on 32 vertical levels from the ground up to about 120 km. In the simulations

presented here the model uses a prescribed distribution of atmospheric dust constructed from the sequential assimilation of TES data<sup>22</sup>. This dust field is three-dimensional, evolves with time and reproduces the TES observations of martian years 24 and 25 (before the global dust storm). The photochemical code implemented in the GCM is an evolution of the model extensively described previously<sup>16</sup>, with updated kinetics and photochemical data<sup>24</sup>.

In Fig. 1 the GCM is compared with water vapour data obtained from a recent re-analysis of the TES retrieval. The revised TES algorithm results in a reduction in derived  $\text{H}_2\text{O}$  abundances of about 30% when the instrument was in its lower resolution mode (M. Smith, personal communication). This correction improves the agreement with corresponding Mars-Express water vapour data<sup>27</sup>, and also reduces the year-to-year variability that was present in the original TES retrievals<sup>19</sup>.

SPICAM data were collected between January 2004 ( $L_s = 331^\circ$  of martian year 26) and June 2006 ( $L_s = 68^\circ$  of martian year 28). The uncertainty on the ozone column is estimated<sup>12</sup> to be 10–15%. When compared with SPICAM, the GCM ozone column was extracted for each observation from the closest grid point with a time difference less than 1 h. To avoid the regions where fast  $\text{O}_3$  variations may occur near the day-night terminator, we excluded from the analysis the measurements obtained at solar zenith angles larger than  $80^\circ$ . Ozone data from the HST and from the IRTF were obtained for 1995–2003 and 1988–2003, respectively.

Received 21 November 2007; accepted 27 May 2008.

- McElroy, M. B. & Donahue, T. M. Stability of the Martian atmosphere. *Science* **177**, 986–988 (1972).
- Parkinson, T. D. & Hunten, D. M. Spectroscopy and aeronomy of  $\text{O}_2$  on Mars. *J. Atmos. Sci.* **29**, 1380–1390 (1972).
- Atreya, S. K. & Blamont, J. E. Stability of the Martian atmosphere: possible role of heterogeneous chemistry. *Geophys. Res. Lett.* **17**, 287–290 (1990).
- Atreya, S. K. & Gu, Z. G. Stability of the Martian atmosphere: Is heterogeneous catalysis essential? *J. Geophys. Res.* **99**, 13133–13145 (1994).
- Krasnopolsky, V. A. Photochemistry of the Martian atmosphere: Seasonal, latitudinal, and diurnal variations. *Icarus* **185**, 153–170 (2006).
- Solomon, S. Stratospheric ozone depletion: A review of concepts and history. *Rev. Geophys.* **37**, 275–316 (1999).
- Jaegle, L. *et al.* Photochemistry of  $\text{HO}_x$  in the upper troposphere at northern midlatitudes. *J. Geophys. Res.* **105**, 3877–3892 (2000).
- Clancy, R. T. *et al.* Water vapor saturation at low altitudes around Mars aphelion: A key to Mars climate? *Icarus* **122**, 36–62 (1996).
- Akabane, T., Iwasaki, K., Saito, Y. & Narumi, Y. Martian late-northern-winter polar hood opacities and non-visibility of a surface cap: 1975 and 1990 observations. *Astron. Astrophys.* **277**, 302–308 (1993).
- Mateshvili, N. *et al.* Martian ice cloud distribution obtained from SPICAM nadir UV measurements. *J. Geophys. Res.* **112**, doi:10.1029/2006JE002827 (2007).
- Anbar, A. D., Leu, M. T., Nair, H. A. & Yung, Y. L. Adsorption of  $\text{HO}_x$  on aerosol surfaces: Implications for the atmosphere of Mars. *J. Geophys. Res.* **98**, 10933–10940 (1993).
- Perrier, S. *et al.* Global distribution of total ozone on Mars from SPICAM/MEX UV measurements. *J. Geophys. Res.* **111**, doi:10.1029/2006JE002681 (2006).
- Clancy, R. T. *et al.* Mars ozone measurements near the 1995 aphelion: Hubble space telescope ultraviolet spectroscopy with the faint object spectrograph. *J. Geophys. Res.* **101**, 12777–12783 (1996).
- Clancy, R. T., Wolff, M. J. & James, P. B. Minimal aerosol loading and global increases in atmospheric ozone during the 1996–1997 Martian northern spring season. *Icarus* **138**, 49–63 (1999).
- Fast, K. *et al.* Ozone abundances on Mars from infrared heterodyne spectra I: Acquisition, retrieval, and anticorrelation with water vapor. *Icarus* **181**, 419–431 (2006).
- Lefèvre, F., Lebonnois, S., Montmessin, F. & Forget, F. Three-dimensional modeling of ozone on Mars. *J. Geophys. Res.* **109**, doi:10.1029/2004JE002268 (2004).
- Moudden, Y. & McConnell, J. C. Three-dimensional on-line chemical modeling in a Mars general circulation model. *Icarus* **188**, 18–34 (2007).
- Montmessin, F., Forget, F., Rannou, P., Cabane, M. & Haberle, R. M. Origin and role of water ice clouds in the Martian water cycle as inferred from a general circulation model. *J. Geophys. Res.* **109**, doi:10.1029/2004JE002284 (2004).
- Smith, M. D. Interannual variability in TES atmospheric observations of Mars during 1999–2003. *Icarus* **167**, 148–165 (2004).
- Clancy, R. T. & Nair, H. Annual (perihelion–aphelion) cycles in the photochemical behavior of the global Mars atmosphere. *J. Geophys. Res.* **101**, 12785–12790 (1996).
- Lebonnois, S. *et al.* Vertical distribution of ozone on Mars as measured by SPICAM/Mars-Express using stellar occultations. *J. Geophys. Res.* **111**, doi:10.1029/2005JE002643 (2006).
- Montabone, L., Lewis, S. R. & Read, P. L. Interannual variability of Martian dust storms in assimilation of several years of Mars Global Surveyor observations. *Adv. Space Res.* **36**, 2146–2155 (2005).
- Cooper, P. L. & Abbott, J. P. Heterogeneous interactions of OH and  $\text{HO}_2$  radicals with surfaces characteristic of atmospheric particulate matter. *J. Phys. Chem.* **100**, 2249–2254 (1996).

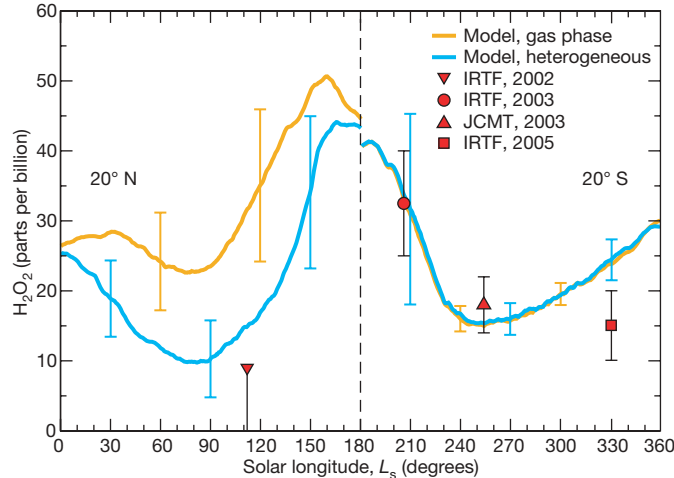


**Figure 4 | Observed and simulated seasonal evolution of martian hydrogen peroxide ( $\text{H}_2\text{O}_2$ ).** Results are plotted in parts per billion ( $10^{-9}$ ) at latitudes corresponding to the approximate subsolar point of the observations:  $20^\circ$  N between  $L_s = 0^\circ$  and  $180^\circ$ , and  $20^\circ$  S between  $L_s = 180^\circ$  and  $360^\circ$ . Measurements were obtained with the IRTF<sup>26,28,29</sup> and the James Clerk Maxwell Telescope<sup>30</sup> (JCMT). The value at  $L_s = 112^\circ$  is an upper limit in the  $10^\circ$ – $40^\circ$  N band. The orange and blue curves represent the  $\text{H}_2\text{O}_2$  abundances calculated by the model on the latitude circle, without and with consideration of heterogeneous loss of  $\text{HO}_x$  on water-ice clouds. Errors bars represent variability ( $2\sigma$ ).

24. Sander, S. P. *et al.* *Chemical Kinetics and Photochemical Data for Use in Atmospheric Studies, Evaluation Number 15*. JPL Publ. 06-2 (Jet Propulsion Lab., Pasadena, 2006).
25. Barth, C. A. *et al.* Mariner 9 ultraviolet spectrometer experiment: Seasonal variation of ozone on Mars. *Science* **179**, 795–796 (1973).
26. Encrenaz, T. *et al.* A stringent upper limit of the H<sub>2</sub>O<sub>2</sub> abundance in the Martian atmosphere. *Astron. Astrophys.* **396**, 1037–1044 (2002).
27. Fouchet, T. *et al.* Martian water vapor: Mars Express PFS/LW observations. *Icarus* **190**, 32–49 (2007).
28. Encrenaz, T. *et al.* Hydrogen peroxide on Mars: Evidence for spatial and seasonal variations. *Icarus* **170**, 424–429 (2004).
29. Encrenaz, T. *et al.* Simultaneous mapping of H<sub>2</sub>O and H<sub>2</sub>O<sub>2</sub> on Mars from infrared high-resolution imaging spectroscopy. *Icarus* **195**, 547–556 (2008).
30. Clancy, R. T., Sandor, B. J. & Moriarty-Schieven, G. H. A measurement of the 362 GHz absorption line of Mars atmospheric H<sub>2</sub>O<sub>2</sub>. *Icarus* **168**, 116–121 (2004).

**Supplementary Information** is linked to the online version of the paper at [www.nature.com/nature](http://www.nature.com/nature).

**Acknowledgements** Much of this work was done while F.L. was on leave from CNRS at the Instituto de Astrofísica de Andalucía (Granada, Spain). We thank M. Smith, who provided the TES data.

**Author Information** Reprints and permissions information is available at [www.nature.com/reprints](http://www.nature.com/reprints). Correspondence and requests for materials should be addressed to F.L. (franck.lefeuvre@aero.jussieu.fr).

## LETTERS

# Doping a semiconductor to create an unconventional metal

N. Manyala<sup>1,3</sup>, J. F. DiTusa<sup>1</sup>, G. Aeppli<sup>2</sup> & A. P. Ramirez<sup>4</sup>

Landau–Fermi liquid theory, with its pivotal assertion that electrons in metals can be simply understood as independent particles with effective masses replacing the free electron mass, has been astonishingly successful. This is true despite the Coulomb interactions an electron experiences from the host crystal lattice, lattice defects and the other  $\sim 10^{22} \text{ cm}^{-3}$  electrons. An important extension to the theory accounts for the behaviour of doped semiconductors<sup>1,2</sup>. Because little in the vast literature on materials contradicts Fermi liquid theory and its extensions, exceptions have attracted great attention, and they include the high-temperature superconductors<sup>3</sup>, silicon-based field-effect transistors that host two-dimensional metals<sup>4</sup>, and certain rare-earth compounds at the threshold of magnetism<sup>5–8</sup>. The origin of the non-Fermi liquid behaviour in all of these systems remains controversial. Here we report that an entirely different and exceedingly simple class of materials—doped small-bandgap semiconductors near a metal–insulator transition—can also display a non-Fermi liquid state. Remarkably, a modest magnetic field functions as a switch which restores the ordinary disordered Fermi liquid. Our data suggest that we have found a physical realization of the only mathematically rigorous route to a non-Fermi liquid, namely the ‘undercompensated Kondo effect’, where there are too few mobile electrons to compensate for the spins of unpaired electrons localized on impurity atoms<sup>9–12</sup>.

Combining two of the most common elements—iron and silicon—in an electric arc furnace yields FeSi, the much studied cubic semiconductor, with a narrow (15 THz) gap between filled valence and empty conduction bands<sup>13–15</sup>. In contrast to silicon, for which the solubility of substitutional impurities is highly limited, FeSi forms isostructural dilution series with metallic MnSi and CoSi, as well as accepting substitution of dopants such as aluminium for up to 30% of silicon<sup>16–21</sup>. We focus here on Mn doping onto the Fe site, which earlier work has shown to yield one missing electron (hole) per Mn atom, as predicted based on naive electron counting arguments, derived from relative valences deducible from the periodic table and applicable to the conventional doped semiconductors (see for example ref. 22) that form the bedrock of modern microelectronics. Previous work has addressed hole doping through substitution of Al onto the Si site and electron doping via replacement of Fe by Co (refs 16–21). The two alloy series are quintessential examples of the success of Landau–Fermi liquid theory with corrections for disorder<sup>1,2</sup>.

Figure 1a shows the zero-field magnetic susceptibility  $\chi = \delta M / \delta H$  of several samples where Fe has been replaced by Mn in FeSi. Despite the much studied<sup>16,20,21,23</sup> ferromagnetism of pure MnSi and  $\text{Fe}_{1-y}\text{Co}_y\text{Si}$  we find, just as in  $\text{FeSi}_{1-z}\text{Al}_z$ , no evidence of a magnetic phase transition down to 1.7 K, the base temperature of the magnetometer, for  $\text{Fe}_{1-x}\text{Mn}_x\text{Si}$  with  $x < 0.8$  (refs 17, 19). Like Al doping, Mn substitution induces both a temperature-independent Pauli

contribution  $\chi_{\text{Pauli}}$  from mobile (doping-induced) holes and a Curie–Weiss term  $(C/(T - \Theta_W))$ , where  $C$  is the Curie constant and  $\Theta_W$  is the Weiss temperature) from residual local moments (low temperature upturn)<sup>17,19,22</sup> added to the very large  $\chi$ , not accounted for by band theory, that appears for FeSi at temperatures much higher than those considered in the present experiments.

However, the contribution from residual local moments is larger than for the Al-doped material<sup>17,19</sup> as we demonstrate in Fig. 1b, c, which shows the associated Curie constant and Weiss temperature. The Weiss temperature measures the degree to which the local moments can be aligned (for  $\Theta_W > 0$ ) to eventually form a ferromagnet, or are screened (for  $\Theta_W < 0$ ) by mobile charge carriers and/or by each other on account of antiferromagnetic interactions. The solid and dashed lines in Fig. 1b represent the Curie constants  $C = g^2 S(S+1)n$  for  $g = 2$  and for moments  $S = 1/2$ ,  $S = 1$  and  $S = 3/2$  where we have fixed the number of magnetic moments,  $n$ , equal to the Mn (or Co, Al) dopant densities. For Mn,  $\Theta_W$  (Fig. 1c) is less than zero, corresponding to screening that increases with dopant density. The inset shows how  $\Theta_W$  changes sign at large  $x$ , consistent with the ferromagnetism at the MnSi end of the alloy series. For Al, the results are consistent with a picture in which each acceptor is associated with an  $S = 1/2$  impurity, and this impurity is strongly screened as  $T \rightarrow 0$ . In contrast, for Mn, the moments evolve from having values close to  $S = 1$  and only reach  $S = 1/2$  well beyond the insulator–metal transition, and these larger moments are screened much less successfully. Although the Mn dopants act as acceptors, meaning that their electronic configuration should resemble that of Fe in FeSi in having six  $d$  electrons, we find that Mn ions prefer a high spin state which appears in nominally pure FeSi only above room temperature. Cobalt dopants in FeSi are associated with an even larger spin ( $S = 3/2$ ), and an interaction  $\Theta_W(x)$  that changes sign—to ferromagnetic—very close to the insulator–metal transition. Indeed,  $\Theta_W(x)$  varies linearly with the electron count per transition metal ion (but not Al), with the pure host material, FeSi, being characterized by a very low antiferromagnetic coupling.

Mobile carriers, responsible for the temperature-independent contribution to  $\chi$ , should also induce a marked increase in the electrical conductivity ( $\sigma$ ). Figure 2a displays the expected systematic increase of  $\sigma$  with  $x$  for several of our Mn-doped samples, and Fig. 1d shows the extrapolated (see below) zero-temperature conductivities  $\sigma_0$  as a function of Mn doping,  $x$ , and for comparison, previous results<sup>17–21</sup> for Al doping,  $z$ , and Co doping,  $y$ . Although there are classic doping-induced insulator–metal transitions for all three impurities, the data show significant differences between  $\text{Fe}_{1-x}\text{Mn}_x\text{Si}$  (transition metal site, hole-doped),  $\text{Fe}_{1-y}\text{Co}_y\text{Si}$  (transition metal site, electron-doped), and  $\text{FeSi}_{1-z}\text{Al}_z$  (Si site, hole-doped). Although the carrier concentration at any particular  $x$ ,  $y$  or  $z$  is indistinguishable for the three types of substitution<sup>17,19–21</sup>, the low- $T$  conductivities of  $\text{Fe}_{1-x}\text{Mn}_x\text{Si}$  and

<sup>1</sup>Department of Physics and Astronomy, Louisiana State University, Baton Rouge, Louisiana 70803, USA. <sup>2</sup>London Centre for Nanotechnology and Department of Physics and Astronomy, UCL, London WC1E 6BT, UK. <sup>3</sup>Department of Physics and Electronics, National University of Lesotho, P.O. Roma 180, Maseru 100, Lesotho. <sup>4</sup>Bell Laboratories, Alcatel-Lucent, 600 Mountain Avenue, Murray Hill, New Jersey 07974, USA.

$\text{Fe}_{1-y}\text{Co}_y\text{Si}$  are half those of the corresponding  $\text{FeSi}_{1-z}\text{Al}_z$  samples (Figs 1d and 2a)<sup>17–21</sup>. Furthermore,  $\sigma$  for  $\text{Fe}_{1-x}\text{Mn}_x\text{Si}$  below 20 K (Fig. 2a) displays a maximum which evolves systematically to lower  $T$  as the doping is increased. This insulating-like behaviour is also apparent in  $\text{FeSi}_{1-z}\text{Al}_z$  for  $z < 0.01$  (ref. 17), but persists for  $\text{Fe}_{1-x}\text{Mn}_x\text{Si}$  up to  $x = 0.1$ . The result is a critical concentration for metallic behaviour that is three to four times as large as in  $\text{FeSi}_{1-z}\text{Al}_z$  and at least twice as large as in  $\text{Fe}_{1-y}\text{Co}_y\text{Si}$  (refs 17–21).

Magnetotransport measurements provide detail about low-energy electronic states and scattering in conducting solids, from doped semiconductors to rare-earth intermetallics<sup>1,2,5,20,24</sup>. Generically, the low-temperature conductivity in metals follows the form  $\sigma = \sigma_0 + m_\sigma T^\alpha$ . For an ordinary Fermi liquid where the dominant scattering is due to the Coulomb interaction between electrons, the asymptotic form is analytic, with a power law  $\alpha = 2$ ; this result obtains even when isolated magnetic impurities are dissolved in a conventional metal, because there are sufficient electrons to screen them<sup>22</sup>. On the other hand, near the insulator–metal transitions in carrier-doped semiconductors, nearly all previous investigations

below 1 K have observed non-analytic behaviour with  $\alpha = 1/2$ , owing to a combination of quantum interference and electron–electron interactions in disordered Fermi liquids<sup>1,2,17,19,20,24</sup>. Because our  $\text{Fe}_{1-x}\text{Mn}_x\text{Si}$  samples also span the insulator–metal transition, we expect to find the same result. As Fig. 2a reveals, our samples do have a significant  $T$ -dependent conductivity down to our lowest temperatures. A quantitative analysis of the  $T$ -dependence is shown in Fig. 2b, where we plot  $\alpha$  as a function of  $x$  and  $T$  determined by taking the logarithmic  $T$ -derivative of the  $\sigma$  data. The value of  $\alpha$  shows changes not commonly associated with an insulator–metal transition in more standard semiconductors<sup>1,2,24</sup>. Although the large values of  $\alpha$  found on the insulating side of the insulator–metal transition, and the tendency for  $\alpha$  to approach 1/2 at the lowest temperatures well into the metallic regime, are standard,  $\sigma - \sigma_0$  displays a nearly logarithmic  $T$ -dependence (that is,  $\alpha \approx 0$ ) for  $H = 0$  and  $x$  close to the critical concentration  $x_c$  for the insulator–metal transition. Although it is clear that  $\alpha$  may not vanish rigorously as  $T \rightarrow 0$ , it becomes small and passes through an obvious minimum at  $x_c$ . This is in contrast to the  $\alpha = 1/2$  behaviour found on both sides of the insulator–metal

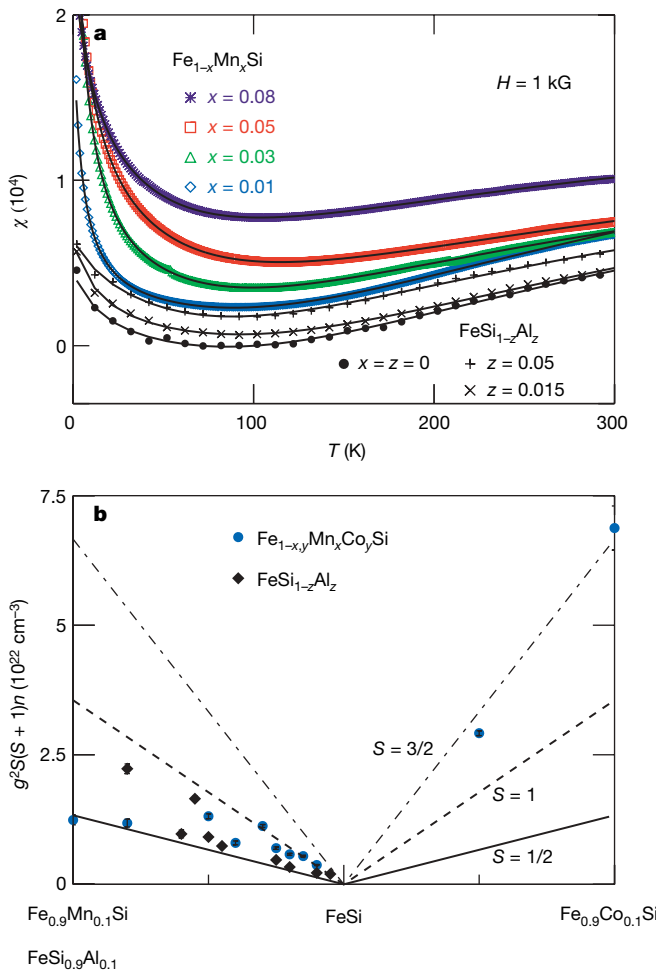
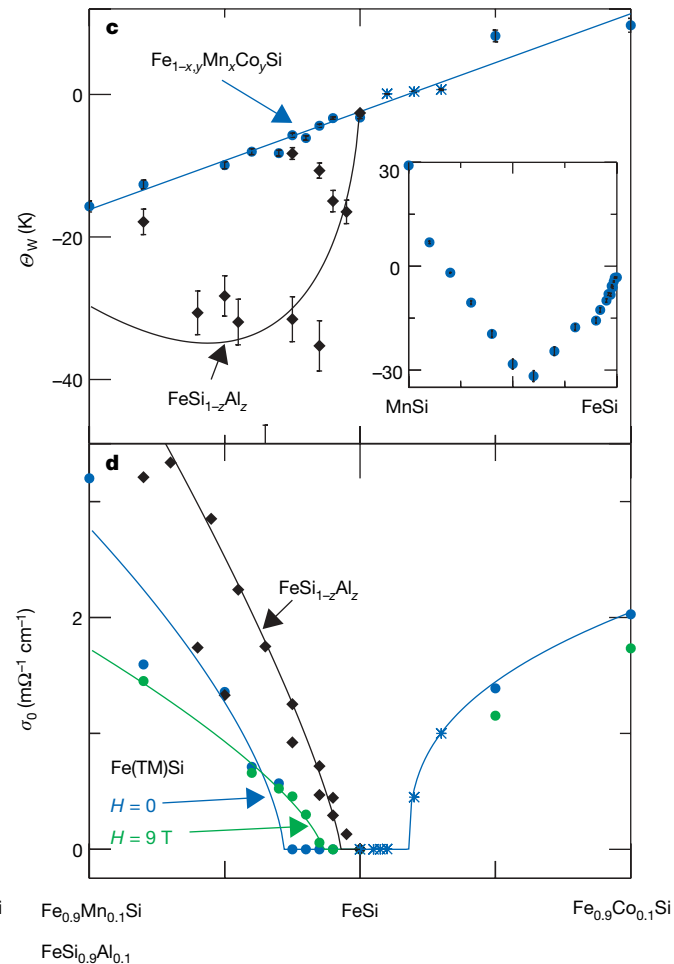


**Figure 1 | Magnetic susceptibility and phase diagram.** **a**, Magnetic susceptibility  $\chi(T)$  for a subset of our  $\text{Fe}_{1-x}\text{Mn}_x\text{Si}$  and  $\text{FeSi}_{1-z}\text{Al}_z$  samples at  $H = 1$  kG. Lines are fits to a model that includes the sum of a Pauli susceptibility, a Curie–Weiss term and a thermally activated susceptibility previously used to describe pure  $\text{FeSi}$ . **b**, Curie constant,  $C = g^2S(S+1)n$ , plotted against  $x$ ,  $y$  and  $z$  from fits of the magnetic susceptibility,  $\chi$ , data to a Curie–Weiss form,  $C/(T - \Theta_W)$ . The solid and dashed lines are the Curie constants for  $g = 2$  and  $S = 1/2$ ,  $S = 1$  and  $S = 3/2$  moments where we have fixed  $n$  equal to the dopant densities of Mn (or Co, Al). **c**, Weiss temperature ( $\Theta_W$ ). Blue line is a linear fit to the  $\Theta_W$  data for Co- and Mn-doped  $\text{FeSi}$ . Black line is a guide to the eye for the  $\text{FeSi}_{1-z}\text{Al}_z$  data. Inset,  $\Theta_W$  for  $\text{Fe}_{1-x}\text{Mn}_x\text{Si}$  over the range  $0 < x < 1$  showing the change to a positive  $\Theta_W$  at



$x > 0.8$ . **d**, Low-temperature conductivity ( $\sigma_0$ ) plotted against nominal Mn ( $x$ ), Co ( $y$ ) and Al ( $z$ ) concentrations ( $H = 0, 9$  T). The solid lines represent fits to  $\sigma_0 = \sigma_1(x/x_c - 1)^v$  with best fits corresponding to  $\sigma_1 = 1,500 \pm 200$  ( $460 \pm 100$ )  $\Omega^{-1} \text{cm}^{-1}$ ,  $x_c = 0.028 \pm 0.003$  ( $0.014 \pm 0.003$ ), and  $v = 0.66 \pm 0.15$  ( $0.7 \pm 0.1$ ) in zero field (values in parentheses for 9 T) for  $\text{Fe}_{1-x}\text{Mn}_x\text{Si}$ ;  $\sigma_1 = 600 \pm 150 \Omega^{-1} \text{cm}^{-1}$ ,  $x_c = 0.007 \pm 0.003$  and  $v = 0.85 \pm 0.1$  for  $\text{FeSi}_{1-z}\text{Al}_z$ ; and  $\sigma_1 = 1,200 \pm 100 \Omega^{-1} \text{cm}^{-1}$ ,  $x_c = 0.018 \pm 0.005$  and  $v = 0.37 \pm 0.1$  for  $\text{Fe}_{1-y}\text{Co}_y\text{Si}$ . For **c** and **d**, data are represented by asterisks taken from ref. 18. Error bars in **b** and **c** represent standard errors based on a least-squares fitting of data as in **a**. Data for  $\text{FeSi}_{1-z}\text{Al}_z$  in **a** and **d** reproduced from refs 17 and 19.

transition ( $\sigma_0 = 0$  and  $\sigma_0 > 0$ ) in  $\text{FeSi}_{1-x}\text{Al}_x$  Si:P and other common semiconductors<sup>17,20,24</sup>, although a small value for  $\alpha$  (0.22) has been reported<sup>25</sup> near the Mott–Hubbard transition in  $\text{NiS}_{2-x}\text{Se}_x$ .

Our key discoveries are shown in Fig. 2c, d, which displays how this picture changes when an external field is applied to the samples. The changes to  $\alpha$  with magnetic field  $H$  (Fig. 2c) are most marked for  $x \approx x_c$ , where  $H = 9$  T effectively replaces the black  $\alpha \approx 0$  column in the contour plot by extending the region of  $x$  described by  $\alpha \approx 0.5$ . Figure 2d shows the changes to  $\alpha$  for the  $x = 0.02$  sample as a function of magnetic field and reveals that the field scale for this change is less than 1 T. Above 1 T,  $\sigma(T)$  follows the standard form for disordered conductors with  $\alpha = 0.5$ . From Fig. 2a, it is clear that the changes in  $\alpha$  with  $H$  are accompanied by increases in  $\sigma_0$ , the  $T = 0$  intercept of our fits. Most importantly, our  $x = 0.01$  and 0.015 samples, for which  $\sigma_0(H = 0) = 0$ , display  $\sigma_0 = 12.5$  and  $70 \Omega^{-1} \text{cm}^{-1}$  respectively for  $H = 9$  T. Thus, we observe a  $T = 0$  insulator–metal transition with magnetic field in these samples. Figure 1d, where the composition-dependent insulator–metal transition is shifted to  $x_c(H) < 0.014(3)$  by the 9-T external field, provides another view of the same phenomenon. The field-induced transition observed here is a new type of insulator–metal transition, between an insulator which in zero field is the precursor of a non-Fermi liquid, and a conventional disordered metal. This is in contrast to the manganites, which are driven by external magnetic fields towards their metallic ferromagnetic states, and  $\text{Gd}_{3-x}\text{S}_4$ , where the  $x = 0$  compound is a ferromagnetic metal (unlike pure FeSi) and an external magnetic field drives an insulator–metal transition for  $x > 0$  by driving the Gd moments towards a more uniformly polarized ‘ferromagnetic’ state<sup>26</sup>.

The magnetotransport data presented in Fig. 2 and in the Supplementary Information reveal that in contrast to FeSi doped

with Al or Co, FeSi doped with Mn is a new non-Fermi liquid. A crucial clue to the origin of this state is that very modest magnetic fields convert it into a conventional disordered Fermi liquid. This suggests a magnetic origin for the state, and accordingly, the susceptibility data, along with the higher field magnetization data also presented in the Supplementary Information, reveal that FeSi:Mn contains free or weakly screened spins at low  $T$  that do not exist in FeSi:Al. If these moments were to remain truly unbound to the lowest temperatures, they should not be visible in the zero-field entropy  $S(T)$  for  $T > 0$ , but become so on application of external fields. Because of the relation  $\int_0^T C(T')/T' dT' = S(T)$ , measurements of  $C(T)/T$ , where  $C(T)$  is the specific heat, can be used to check this. The results, shown in Fig. 3a, closely resemble those for  $\text{FeSi}_{1-x}\text{Al}_x$  and standard metals. These are commonly characterized by a  $C(T)/T = \gamma + \beta T^2$  dependence where  $\gamma$  represents the electronic contribution, also responsible for the finite  $\chi_{\text{Pauli}}$ , proportional to the effective hole mass,  $m^*$ , and  $\beta T^2$  represents the lattice contribution<sup>17,19,22</sup>. The  $x = 0.015$  sample, which displays anomalous  $\sigma(T)$  at  $H = 0$  in Fig. 2a, has a non-zero  $\gamma$ , as do our  $\text{FeSi}_{1-x}\text{Al}_x$  samples at the same doping levels and Si:P just on the insulating side of the insulator–metal transition<sup>17,19,27,28</sup>. Extrapolation from  $T$  above 5 K yields a moderately heavy  $m^*$  which is increased by a factor of  $\sim 10$  above the free electron mass  $m_e$  and the carrier (hole) mass  $(1.5 \pm 0.5)m_e$  determined from band structure calculations<sup>15</sup>.

As  $T$  is reduced below 5 K,  $C(T)/T$  is further increased beyond the standard metallic form. For  $x = 0.015$ , the zero-field result is describable by a power law,  $T^{-0.27 \pm 0.02}$ , whereas just beyond the insulator–metal transition, for  $x = 0.03$ , there is a peak at 0.3 K. Increasing external magnetic fields produce peaks that move to larger temperatures,  $T_{\text{max}}$ . What is most important, though, is that the zero-field

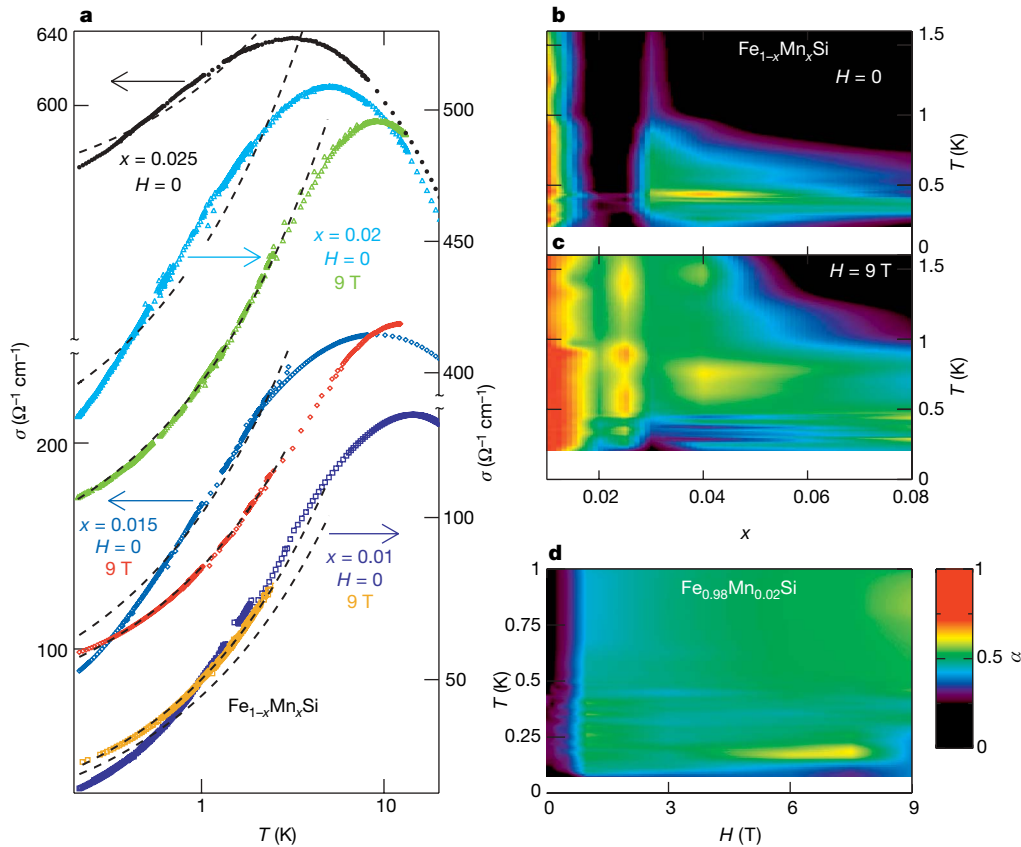


**Figure 2 | Magnetotransport.** a, Conductivity ( $\sigma$ ) versus temperature ( $T$ ) of a subset of our  $\text{Fe}_{1-x}\text{Mn}_x\text{Si}$  samples at magnetic fields ( $H$ ) identified in the figure. b, Colour contour plot of the temperature and  $x$  dependence of the conductivity of  $\text{Fe}_{1-x}\text{Mn}_x\text{Si}$  at  $H = 0$  parameterized by the logarithmic derivative of  $\sigma$  with respect to  $T$ ,  $\alpha = d \ln(\sigma - \sigma_0)/dT$ . The parameter  $\sigma_0$  is

chosen by fitting the data below 0.7 K to a power law form  $\sigma = \sigma_0 + \sigma_1 T^\alpha$ . A value of  $\alpha = 0.5$  describes classic disordered metals, such as heavily doped semiconductors. c, The exponent  $\alpha$ , as in b, with  $H = 9$  T. d, Colour contour plot of the field and temperature dependence of  $\alpha$  for the  $x = 0.02$  sample.

entropy deduced from these finite-temperature measurements is smaller than the in-field entropy. To make this clear, we present in Fig. 3b the difference between in-field and zero-field entropies, obtained by integrating the  $C(T)/T$  data. This difference begins as a negative function with a minimum at a field-dependent crossover temperature similar to  $T_{\max}(H)$ , and then eventually exceeds zero. This violation of entropy balance can only be due to very-low-temperature entropy (that is, at  $T < 50$  mK) being missed in the integration. The positive values measured for the entropy differences at  $T = 15$  K correspond to a population of moments where roughly 5% of  $S = 1$  moments associated with each Mn atom remain unbound; this number is consistent with the more complex analysis of the magnetization (see Supplementary Information), as should be the case given the Maxwell relations between  $M(H, T)$  and  $C(H, T)$ .

The conclusion from all of the thermodynamic and magnetic measurements is that there are residual, unscreened spins in FeSi:Mn that are absent for FeSi:Al. The mechanism underlying the non-Fermi liquid behaviour seen in the magnetotransport data is therefore clear: we are dealing with an undercompensated Kondo problem<sup>9–12</sup> (Fig. 4a), where there are not enough free carriers, with spin  $S = 1/2$ , to screen the remaining local moments associated with the acceptors. For this problem, down to the lowest temperatures, some impurities are always visible to the charge carriers, producing inelastic scattering of the carriers and thus destabilizing the Fermi liquid ground state. Figure 4b–d illustrates the progression from high to low

temperature. Initially (Fig. 4b), for  $T > T_K \approx T_F > \Theta_W$ , the moments are unbound, but subsequently, they first yield (Fig. 4c) the undercompensated Kondo non-Fermi liquid when  $T_K > T > \Theta_W$ . The next step (Fig. 4d) is for antiferromagnetic correlations to appear among the local moments, thus reducing the total moments that the conduction electrons need to screen. If there is no magnetic phase transition, the eventual outcome will be a collective singlet state<sup>29–31</sup> among most local moments, with some isolated, unpaired local moments of the type routinely encountered in disordered quantum spin systems with predominantly antiferromagnetic couplings. Because the latter still carry  $S = 1$  rather than  $S = 1/2$ , the undercompensated Kondo effect still applies and there will be residual entropy and the associated non-Fermi liquid behaviour as  $T \rightarrow 0$ . External magnetic fields remove the low-lying degeneracies by locking the unpaired local moments, thus always returning the system to a disordered Fermi liquid.

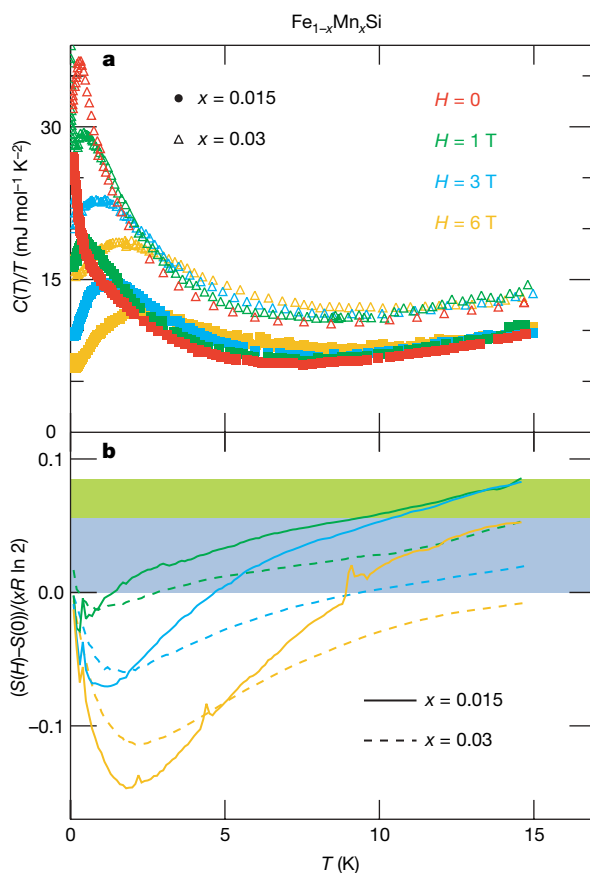


**Figure 3 | Specific heat.** **a**, Specific heat divided by temperature ( $C(T)/T$ ) against temperature for two samples of  $\text{Fe}_{1-x}\text{Mn}_x\text{Si}$  at magnetic fields indicated. **b**, The change in entropy from its zero-field value,  $(S(H) - S(0))/(x R \ln 2)$  (where  $R$  is the universal gas constant), calculated by integrating the  $C(T)/T$  data in **a** after subtraction of the phonon term in the specific heat for  $x = 0.015$  (solid lines) and  $0.03$  (dashed lines). Grey (grey and green) shaded regions emphasize the increase in entropy at 15 K over the zero-field data for the  $x = 0.03$  ( $0.015$ ) sample. This entropy must be transferred from temperatures below the lowest  $T$  of our measurements at  $H = 0$  and brought into our temperature window via the magnetic field (see text for details).

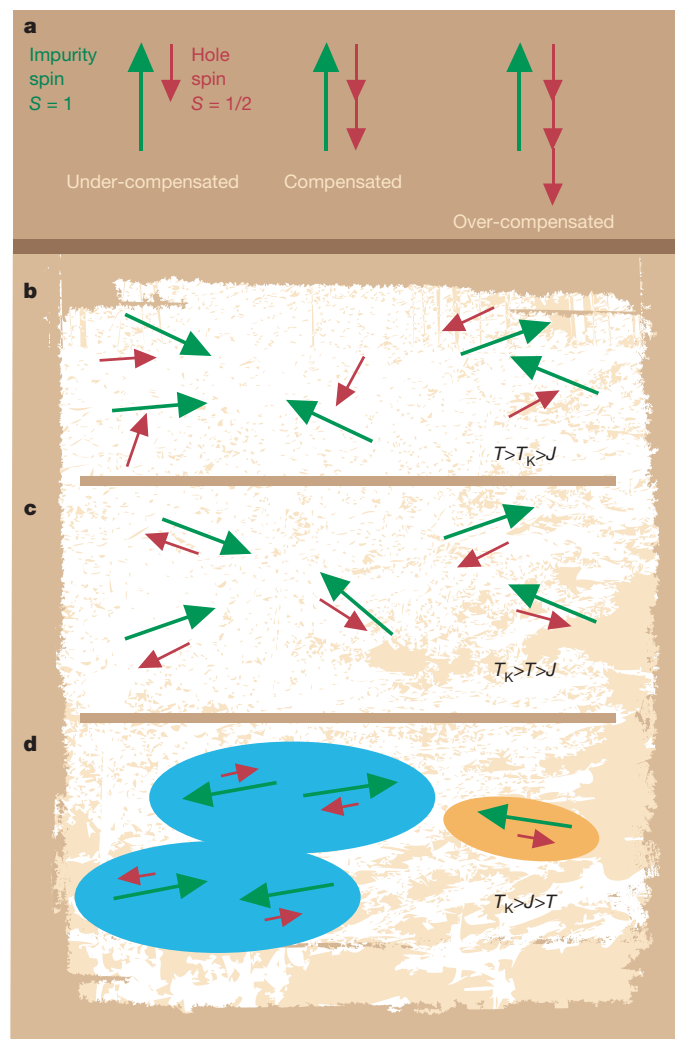


**Figure 4 | Underscreened Kondo effect.** **a**, Comparison of underscreened<sup>9–12</sup>, compensated and conventional ('overcompensated') Kondo problems. **b–d**, Spin screening mechanisms in a magnetic semiconductor such as  $\text{Fe}_{1-x}\text{Mn}_x\text{Si}$ . Green arrows represent the Mn impurity spins (1) and red arrows represent the hole spin degrees of freedom (spin-1/2). **b**, At high temperatures, there is a random distribution of rapidly fluctuating impurity and hole spins. **c**, At temperatures below the Kondo temperature ( $T_K$ ), the hole gas incompletely screens the impurity spins. **d**, At lower temperatures ( $T < J$ ), many but not all of the impurity moments have been coupled to combinations, denoted by blue groupings, with singlet ground states. A few impurity moments are incompletely screened (yellow grouping) and contribute to entropy. These are responsible for the anomalous low-temperature electrical properties.

We have discovered a new recipe for non-Fermi liquid behaviour, namely doping a narrow-gap semiconductor with impurities that each donate a single hole to the valence band while retaining a net moment larger than  $S = 1/2$  which cannot be screened down to 50 mK. An important ingredient for our recipe is that the magnetic moments associated with the acceptors are not all lost through anti-ferromagnetic exchange interactions between themselves, as indeed they are in Si:P and FeSi:Al (refs 17, 19, 27). Dilute magnetic semiconductors, which have potential in the growing area of spintronics and generally display conventional disordered metallic ferromagnetism, therefore also have a ground state of fundamental interest in the field of quantum many-body physics. For this reason, and to determine whether any of the discoveries made here depend on a Kondo insulator<sup>32</sup> as the parent compound (we think not), it will be interesting to extend the work to III–V semiconductors doped with magnetic transition metals, where it might also be possible to fabricate devices that examine, if not exploit, the unusual properties of the underscreened Kondo effect.

## METHODS SUMMARY

The  $\text{Fe}_{1-x}\text{Mn}_x\text{Si}$ ,  $\text{Fe}_{1-y}\text{Co}_y\text{Si}$  and  $\text{FeSi}_{1-z}\text{Al}_z$  samples investigated in our experiments were all polycrystalline pellets produced from high-purity (99.9985%) starting materials by arc melting in an argon atmosphere. Samples were annealed for four days at 1,000 °C in evacuated quartz ampoules to improve homogeneity. We collected (Cu-K $\alpha$ ) X-ray diffraction patterns for milled samples using a Siemens D5000 set equipped with a position sensitive detector. All patterns were consistent with the samples being single-phase with a B20 crystal structure. The lattice constant of the doped samples from the X-ray patterns depends linearly on the Mn, Co or Al concentration<sup>17,19–21</sup>, showing that Mn and Co successfully replace Fe and that Al replaces Si in the crystal structure. The stoichiometry of the samples was checked by energy-dispersive X-ray microanalysis measurements which were all within error of nominal concentrations. We made the conductivity measurements on rectangular samples cut by a string saw and polished with emery paper. Thin platinum wires were attached to four linearly arranged silver paste contacts with an average spacing between voltage probes of 2 mm. Samples had an average cross-sectional area of  $1 \times 0.5 \text{ mm}^2$ . We made the resistivity ( $\rho$ ) and magnetoconductance measurements at 19 Hz using standard lock-in techniques in a dilution refrigerator with a 9-T superconducting magnet, and at higher temperature with a gas flow cryostat in a 5-T superconducting magnet. The magnetic susceptibility and magnetization of the same samples were measured in a Quantum Design SQUID magnetometer for temperatures between 1.7 and 300 K and fields between 0 and 5 T. Specific heat measurements were made using a standard semi-adiabatic heat pulse technique.

Received 14 March; accepted 23 May 2008.

1. Al'tshuler, B. L., Aronov, A. G., Gershenson, M. E. & Sharvin, Yu. V. Quantum effects in disordered metal films. *Sov. Sci. Rev. Phys.* **9**, 223–354 (1987).
2. Lee, P. A. & Ramakrishnan, T. V. Disordered electron systems. *Rev. Mod. Phys.* **57**, 287–337 (1985).
3. Cava, R. J. *et al.* Bulk superconductivity at 91 K in a single-phase oxygen-deficient perovskite  $\text{Ba}_2\text{YC}_{1-x}\text{O}_{9-\delta}$ . *Phys. Rev. Lett.* **58**, 1676–1679 (1987).
4. Kravchenko, S. V. *et al.* Electric field scaling at a  $B = 0$  metal–insulator transition in two dimensions. *Phys. Rev. Lett.* **77**, 4938–4941 (1996).
5. Custers, J. *et al.* The break-up of heavy electrons at a quantum critical point. *Nature* **424**, 524–527 (2003).
6. Mathur, N. D. *et al.* Magnetically mediated superconductivity in heavy fermion compounds. *Nature* **394**, 39–43 (1998).

7. Si, Q. M., Rabello, S., Ingersent, K. & Smith, J. L. Locally critical quantum phase transitions in strongly correlated metals. *Nature* **413**, 804–808 (2001).
8. Schröder, A. *et al.* Onset of antiferromagnetism in heavy-fermion metals. *Nature* **407**, 351–355 (2000).
9. Coleman, P. & Pepin, C. Singular Fermi liquid behavior in the underscreened Kondo model. *Phys. Rev. B* **68**, 220405 (2003).
10. Mehta, P. *et al.* Regular and singular Fermi-liquid fixed points in quantum impurity models. *Phys. Rev. B* **72**, 104430 (2005).
11. Posazhennikova, A. & Coleman, P. Anomalous conductance of a spin-1 quantum dot. *Phys. Rev. Lett.* **94**, 036802 (2005).
12. Sacramento, P. D. & Schlottmann, P. Thermodynamics of the  $n$ -channel Kondo model for general  $n$  and impurity spin  $S$  in a magnetic field. *J. Phys. Condens. Matter* **3**, 9687–9696 (1991).
13. Wernick, J. H., Wertheim, G. K. & Sherwood, R. C. Magnetic behavior of monosilicides of 3D-transition elements. *Mater. Res. Bull.* **7**, 1431–1441 (1972).
14. Schlesinger, Z. *et al.* Unconventional charge gap formation in FeSi. *Phys. Rev. Lett.* **71**, 1748–1751 (1993).
15. Mattheiss, L. F. & Hamann, D. R. Band-structure and semiconducting properties of FeSi. *Phys. Rev. B* **47**, 13114–13119 (1993).
16. Beille, J., Voiron, J. & Roth, M. Long period helimagnetism in the cubic-B20  $\text{Fe}_{1-x}\text{Co}_x\text{Si}$  and  $\text{Co}_{1-x}\text{Mn}_x\text{Si}$  alloys. *Solid State Commun.* **47**, 399–402 (1983).
17. DiTusa, J. F. *et al.* Metal–insulator transitions in the Kondo insulator FeSi and classic semiconductors are similar. *Phys. Rev. Lett.* **78**, 2831–2834 (1997).
18. Chernikov, M. A. *et al.* Low-temperature transport, optical, magnetic, and thermodynamic properties of  $\text{Fe}_{1-x}\text{Co}_x\text{Si}$ . *Phys. Rev. B* **56**, 1366–1375 (1997).
19. DiTusa, J. F. *et al.* Heavy fermion metal–Kondo insulator transition in  $\text{FeSi}_{1-x}\text{Al}_x$ . *Phys. Rev. B* **58**, 10288–10301 (1998).
20. Manalya, N. *et al.* Magnetoresistance from quantum interference effects in ferromagnets. *Nature* **404**, 581–584 (2000).
21. Manalya, N. *et al.* Large anomalous Hall effect in a silicon-based magnetic semiconductor. *Nature Mater.* **3**, 255–262 (2004).
22. Ashcroft, N. W. & Mermin, N. D. *Solid State Physics* (Saunders College, Philadelphia, 1976).
23. Pfeifer, C., Julian, S. R. & Lonzarich, G. G. Non-Fermi-liquid nature of the normal state of itinerant-electron ferromagnets. *Nature* **414**, 427–430 (2001).
24. Rosenbaum, T. F. *et al.* Metal–insulator transition in a doped semiconductor. *Phys. Rev. B* **27**, 7509–7523 (1983).
25. Husmann, A. *et al.* Dynamical signature of the Mott–Hubbard transition in  $\text{Ni}(\text{S},\text{Se})_2$ . *Science* **274**, 1874–1876 (1996).
26. von Molnar, S., Briggs, A., Flouquet, J. & Remenyi, G. Electron localization in a magnetic semiconductor:  $\text{Gd}_{3-x}\text{V}_x\text{S}_4$ . *Phys. Rev. Lett.* **51**, 706–709 (1983).
27. Paalanen, M. A., Graebner, J. E., Bhatt, R. N. & Sachdev, S. Thermodynamic behavior near a metal–insulator transition. *Phys. Rev. Lett.* **61**, 597–600 (1988).
28. Lakner, M., von Lohneysen, H., Langenfeld, A. & Wolf, P. Localized magnetic moments in Si:P near the metal–insulator transition. *Phys. Rev. B* **50**, 17064–17073 (1994).
29. Bhatt, R. N. & Lee, P. A. Scaling studies of highly disordered spin-1/2 antiferromagnetic systems. *Phys. Rev. Lett.* **48**, 344–347 (1982).
30. Sarachik, M. P. *et al.* Scaling behavior in the magnetization of insulating Si:P. *Phys. Rev. B* **34**, 387–390 (1986).
31. Ghosh, S., Rosenbaum, T. F., Aeppli, G. & Coppersmith, S. N. Entangled quantum state of magnetic dipoles. *Nature* **425**, 48–51 (2003).
32. Aeppli, G. & Fisk, Z. Kondo insulators. *Comments Cond. Mater. Phys.* **16**, 155–165 (1992).

**Supplementary Information** is linked to the online version of the paper at [www.nature.com/nature](http://www.nature.com/nature).

**Acknowledgements** We thank Z. Fisk for discussions. J.F.D. acknowledges support from the National Science Foundation and G.A. acknowledges support from a Wolfson-Royal Society Research Merit Award and the Basic Technologies Programme of the UK Research Councils.

**Author Information** Reprints and permissions information is available at [www.nature.com/reprints](http://www.nature.com/reprints). Correspondence and requests for materials should be addressed to J.F.D. (ditusa@phys.lsu.edu).

# Selective oxidation with dioxygen by gold nanoparticle catalysts derived from 55-atom clusters

Mark Turner<sup>1</sup>, Vladimir B. Golovko<sup>1</sup>†, Owain P. H. Vaughan<sup>1</sup>, Pavel Abdulkin<sup>1</sup>, Angel Berenguer-Murcia<sup>1</sup>, Mintcho S. Tikhov<sup>1</sup>, Brian F. G. Johnson<sup>1</sup> & Richard M. Lambert<sup>1</sup>

Supported gold nanoparticles have excited much interest owing to their unusual and somewhat unexpected catalytic properties<sup>1–7</sup>, but the origin of the catalytic activity is still not fully understood. Experimental work<sup>4</sup> on gold particles supported on a titanium dioxide (110) single-crystal surface has established a striking size threshold effect associated with a metal-to-insulator transition, with gold particles catalytically active only if their diameters fall below ~3.5 nm. However, the remarkable catalytic behaviour might also in part arise from strong electronic interaction between the gold and the titanium dioxide support<sup>2,3,5</sup>. In the case of industrially important selective oxidation reactions, explanation of the effectiveness of gold nanoparticle catalysts is complicated by the need for additives to drive the reaction<sup>5,7,8</sup>, and/or the presence of strong support interactions and incomplete understanding of their possible catalytic role<sup>1–3,5</sup>. Here we show that very small gold entities (~1.4 nm) derived from 55-atom gold clusters and supported on inert materials are efficient and robust catalysts for the selective oxidation of styrene by dioxygen. We find a sharp size threshold in catalytic activity, in that particles with diameters of ~2 nm and above are completely inactive. Our observations suggest that catalytic activity arises from the altered electronic structure intrinsic to small gold nanoparticles, and that the use of 55-atom gold clusters may prove a viable route to the synthesis of robust gold catalysts suited to practical application.

We used established synthesis procedures<sup>9–13</sup> to prepare a series of catalysts based on gold (Au) nanoparticles that varied in diameter from about 1.4 nm to more than 30 nm and were supported on boron nitride (BN), silicon dioxide (SiO<sub>2</sub>) or carbon. The Au particle size distribution and electronic structure of the catalysts were probed by high-resolution transmission electron microscopy (TEM) and high-resolution X-ray photoelectron spectroscopy (XPS), respectively.

The very small Au nanoparticles (~1.5 nm) were derived from 55-atom gold (Au<sub>55</sub>) clusters when using a loading of 0.6 wt%; increasing the loading to 6 wt% yielded supported Au nanoparticle catalysts with a diameter of about 3.0 nm. Slightly larger Au nanoparticles with an average diameter of 4 nm were produced by reducing NaAuCl<sub>4</sub> in a methanol–ethylene-glycol mixture, whereas the largest nanoparticles (>30 nm) were obtained by an incipient wetness impregnation method using aqueous HAuCl<sub>4</sub>. To enable direct comparison with recently reported<sup>7</sup> styrene epoxidation by dioxygen (O<sub>2</sub>) in the presence of a peroxy initiator, catalysed by supported Au nanoparticles with a diameter of ~25 nm, we also used a microemulsion method<sup>12,13</sup> to produce Au particles (~17 nm) from an aqueous HAuCl<sub>4</sub> solution and deposit the particles on a carbon support. (For full details of the synthesis and materials characterization, see Methods and Supplementary Information.) All three support materials used are chemically inert and did not interact electronically with

the Au, in contrast to some frequently used supports such as titanium dioxide<sup>14</sup>.

Table 1 summarizes the performance of our Au catalysts at 100 °C using toluene solvent for the partial oxidation of styrene, a reactant often used to evaluate selective oxidation activity<sup>7</sup>. The results confirm that ~17-nm Au particles supported on inert materials are indeed catalytically inactive in styrene epoxidation by O<sub>2</sub> in the absence of peroxy initiators<sup>7</sup>. In contrast, Au<sub>55</sub>-derived catalysts supported on BN at low loading (0.6 wt%) achieve almost 20% conversion, with a selectivity of 14% towards the epoxide (the two other partial oxidation products were identified as benzaldehyde and acetophenone). The turnover frequencies of this catalyst were ~0.02 s<sup>-1</sup> and ~0.003 s<sup>-1</sup> with respect to styrene conversion and epoxide production, respectively. Analogous Au<sub>55</sub>-derived catalysts supported on SiO<sub>2</sub> exhibited very similar behaviour, with turnover frequencies of ~0.03 s<sup>-1</sup> for styrene conversion and ~0.003 s<sup>-1</sup> for epoxide production.

These observations show that extremely small Au nanoparticles supported on chemically and electronically inert materials can adsorb and activate O<sub>2</sub> for selective oxidation, presumably by dissociating O<sub>2</sub> to yield O adatoms that initiate the partial oxidation<sup>15,16</sup>. Larger Au particles or extended Au surfaces are incapable of this. We note that the turnover frequencies and product spectrum we observe are very similar to those obtained<sup>7</sup> with significantly larger Au particles; but the need for a peroxy compound (an initiator) to achieve any chemical conversion in this case underlines the fundamentally different chemistry induced by our Au<sub>55</sub>-derived catalysts, which are effective with O<sub>2</sub> alone. We also note that a number of catalysts (such as silver<sup>17,18</sup> and zeolites containing cobalt<sup>19,20</sup>) are well known to activate O<sub>2</sub> (ref. 18) and efficiently epoxidize styrene with O<sub>2</sub> alone, but such behaviour is unexpected in the case of Au nanoparticles on inert supports.

Table 1 shows that after recycling the 0.6-wt% Au/SiO<sub>2</sub> catalyst derived from Au<sub>55</sub>, the initial re-use resulted in decreased conversion of styrene and increased selectivity towards epoxide formation. Recycling a second time continued this trend, resulting in styrene epoxide selectivity of ~30%.

The Au<sub>55</sub> cluster synthesis (see Methods) introduces small quantities of phosphorus (P) and chlorine (Cl) during catalyst preparation, but energy-dispersive X-ray spectroscopy and XPS measurements on the Au<sub>55</sub>-derived catalysts (see Supplementary Information) showed that both elements were reduced to undetectable levels by the thermal activation step carried out before catalytic testing. To further investigate the possible influence of P and Cl, we also tested the activity of a 0.6-wt% Au<sub>55</sub>/SiO<sub>2</sub> catalyst that had not undergone thermal treatment and contained detectable quantities of P and Cl. This catalyst gave a conversion of 12.6% with a selectivity of 13.1% towards the epoxide, in comparison with a conversion of 26% and a selectivity of

<sup>1</sup>Department of Chemistry, University of Cambridge, Cambridge CB2 1EW, UK. †Present address: Department of Chemistry, University of Canterbury, Christchurch 8140, New Zealand.

**Table 1 | Catalytic results of the partial oxidation of styrene using O<sub>2</sub> alone for supported Au<sub>55</sub> and comparison catalysts prepared by various techniques.**

Catalyst	Prep.*	Exact loading† (wt%)	Mean Au size‡ (nm)	Conversion (%)	Selectivity (%)		
					Benzaldehyde	Styrene epoxide	Acetophenone
0.6-wt% Au <sub>55</sub> /BN	Au <sub>55</sub>	0.63	1.6	19.2	82.3	14.0	3.9
0.6-wt% Au <sub>55</sub> /SiO <sub>2</sub>	Au <sub>55</sub>	0.67	1.5	25.8	82.1	12.0	5.7
0.6-wt% Au <sub>55</sub> /SiO <sub>2</sub>	Au <sub>55</sub>	0.67	—	21.4	69.2	23.7	7.1
recycled 1							
0.6-wt% Au <sub>55</sub> /SiO <sub>2</sub>	Au <sub>55</sub>	0.67	—	15.9	63.7	27.1	9.2
recycled 2							
6-wt% Au/SiO <sub>2</sub>	Au <sub>55</sub>	6.35	3.0	Trace	Trace	—	—
0.6-wt% Au/SiO <sub>2</sub>	PVP	—	4.0	Trace	Trace	—	—
1-wt% Au/C	ME	—	17.0	No reaction	—	—	—
5-wt% Au/SiO <sub>2</sub>	IW	—	>30	No reaction	—	—	—

Mean Au particle size, calculated by counting particles in high-resolution TEM images of many different regions, is the crucial factor in determining activity. Results from recycled Au<sub>55</sub>-based catalysts confirm that deactivation does not occur. All reactions were carried out at 100 °C in toluene.

\* Catalyst preparation: Au<sub>55</sub>, Au<sub>55</sub> preparation; PVP, poly-*n*-vinyl pyrrolidone; ME, microemulsion; IW, incipient wetness.

† Exact loading was determined using inductively coupled plasma mass spectroscopy.

‡ For full statistical breakdown of particle size distributions, see Supplementary Information.

12% for the thermally pre-treated catalyst (Table 1). We conclude that P and Cl do not contribute to the observed catalytic activity; their role, if any, is to deactivate the catalyst.

Figure 1a shows a representative high-resolution TEM image and the associated particle size distribution of unsupported Au<sub>55</sub> taken immediately after synthesis. Fringes associated with the Au lattice appear clearly. A particle count taken from many such images, obtained from different regions of the sample, confirmed the presence of essentially monodispersed Au particles of mean diameter 1.4 nm, which is the expected size of Au<sub>55</sub> (ref. 21). Images taken after Au deposition on BN at 0.6 wt% loading and after catalytic reaction showed that the Au particle morphology was largely preserved: the modal particle diameter remained at ~1.4 nm (Fig. 1b), although the presence of a very small proportion of 2.5–3.0-nm particles resulted in a mean particle diameter of 1.6 nm.

Essentially identical TEM results were obtained for Au<sub>55</sub> supported on SiO<sub>2</sub> at 0.6 wt% loading (Fig. 1c), which was found to be an equally effective catalyst. The mean particle diameter in this system was 1.5 nm, with the size distribution weighted towards somewhat smaller sizes in comparison with the Au<sub>55</sub>/BN system. In contrast, more conventional Au catalyst systems, prepared using three different methods so as to contain somewhat larger Au particles with averages diameters of either ~4, ~17 or >30 nm (see Methods and Supplementary Information for synthesis details and TEM characterization), were all inactive in the partial oxidation of styrene using O<sub>2</sub> alone (Table 1).

To explore a possible influence of fabrication method on observed activity, an Au<sub>55</sub>/SiO<sub>2</sub> catalyst was prepared in the same way as the very active catalysts containing small particles, but with ten times the previous metal loading (6 wt%). This catalyst exhibited only very low activity, despite the presence of a much larger amount of Au (Table 1). A high-resolution TEM image and the associated particle size distribution taken from a post-reaction sample (Fig. 1d) clearly shows that the loss of activity is associated with Au agglomeration that gives rise to substantially larger particles. The mean diameter is now ~3.0 nm, with particles as large as 10 nm also present; a very few particles <2 nm in diameter remain, and it is these that are presumably responsible for the small residual activity of the system.

To examine the electronic properties of the catalytically active Au<sub>55</sub>-derived entities, a post-reaction sample of 0.6-wt% Au<sub>55</sub>/BN was studied by high-resolution XPS using monochromated Al K $\alpha$  radiation (see Methods). As shown in Fig. 2, the Au 4f<sub>7/2</sub> electron apparent binding energy was 1.1 eV higher than the value characteristic of bulk Au. This shift in binding energy is typical for very small metal particles (including Au) on a variety of support materials<sup>22–25</sup>, and is generally attributed to reduced core-hole screening in small metal particles<sup>25</sup>. It reflects the fact that the electronic properties of the very small particles are significantly different from those of the

corresponding bulk material, and suggests that the size-dependent alteration of electronic structure gives rise to unusual catalytic properties. A comprehensive X-ray absorption study of Au catalysts with different particle sizes and supports concluded that, independent of support and only for Au particles smaller than 3 nm, decreasing particle size was associated with an increase in the *d*-electron density of the Au atoms and the onset of reactivity to oxygen in air<sup>26</sup>. These conclusions fully agree with our observation that very small Au particles unmodified by support effects and in the absence of sacrificial reductants or initiators are effective selective oxidation catalysts when fed with O<sub>2</sub> alone, and that catalytic activity is quenched once the Au particle diameter is ~2 nm or more.

The principal active species in our active catalysts are Au entities ~1.4 nm in diameter, which is essentially the size of the Au<sub>55</sub> clusters

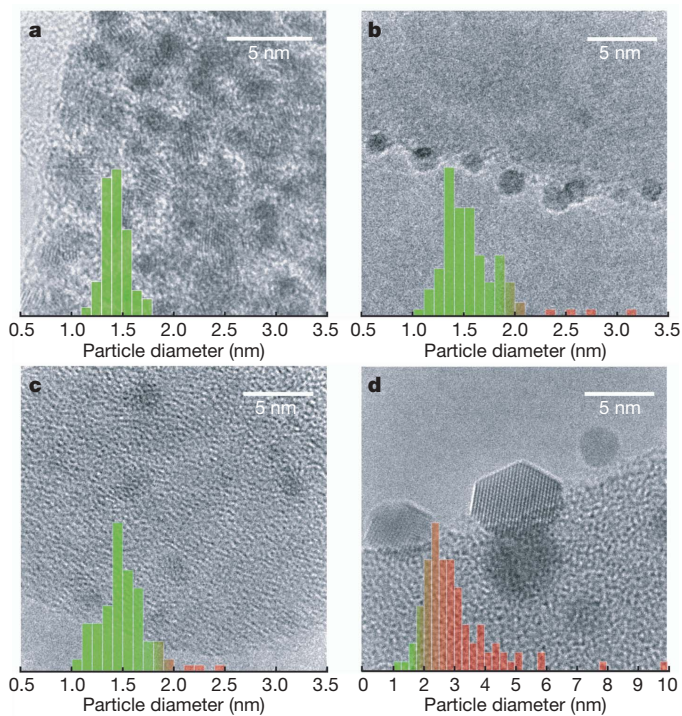


**Figure 1 | High-resolution TEM images overlaid with corresponding particle size distributions for unsupported and supported Au<sub>55</sub>. a, Freshly made, unsupported Au<sub>55</sub>; b, 0.6-wt% Au<sub>55</sub>/BN; c, 0.6-wt% Au<sub>55</sub>/SiO<sub>2</sub>; d, 6-wt% Au<sub>55</sub>/SiO<sub>2</sub>. Distributions are coloured to emphasize (green) the presence of particles of diameter <2 nm, which correlates with observed catalytic activity in the partial oxidation of styrene by O<sub>2</sub> alone.**

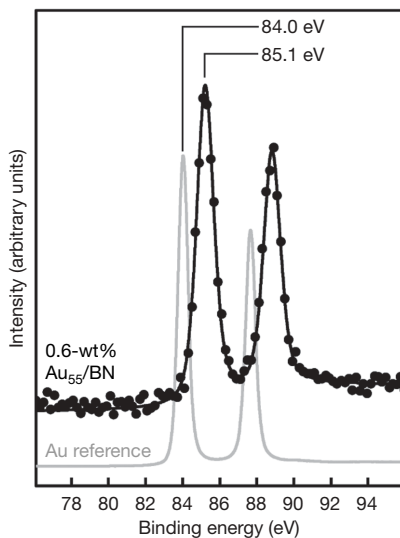


**Figure 2 | Au 4f electron region of the X-ray photoelectron spectrum of 0.6-wt%  $\text{Au}_{55}/\text{BN}$  (black curve) and the corresponding spectrum of a bulk Au reference (grey curve).** A shift to a higher binding energy of 1.1 eV is clear for the supported  $\text{Au}_{55}$ , confirming the presence and electronic effect of small particle size.

used in their preparation. Particles comprised of ‘magic number’ clusters containing 55 Au atoms were found<sup>21</sup> to exhibit unusual oxidation resistance, and this robustness might account for the stability and recyclability of our catalysts. Our observations also clearly suggest that these species can dissociatively chemisorb  $\text{O}_2$  to yield O adatoms that are necessary for triggering the subsequent catalytic chemistry, but that the organic reactant (styrene in our case) is sufficiently weakly adsorbed that its molecular electronic structure is not strongly perturbed. It is this combination of features that enables catalysis of demanding reactions that are of value in synthetic chemistry. Recall that in particles of many sizes, many of the metallic elements readily dissociatively chemisorb  $\text{O}_2$  to yield oxygen adatoms, but they usually strongly perturb the electronic structure of co-adsorbed organic molecules as well and thereby give rise to ‘burning’ of the organic to carbon dioxide and water. For this reason, the platinum metals are exceptionally effective combustion catalysts in a variety of important practical applications, yet are of less use in delicate synthetic reactions involving oxygen, such as epoxidation.

We conclude by noting that the question of exactly how the altered electronic structure of tiny Au entities enables them to dissociatively chemisorb oxygen in the first place, and thus enable selective oxidation chemistry, is one that remains and that must be addressed theoretically. It is hoped that our results will stimulate such investigations.

## METHODS SUMMARY

Very small 55-atom Au clusters stabilized by triphenylphosphane ( $\text{Au}_{55}(\text{PPh}_3)_{12}\text{Cl}_6$ ) were prepared according to the protocol described in ref. 9. Medium-sized Au nanoparticles were prepared using a recently optimized<sup>11</sup> polyol reduction method<sup>10</sup>. These were then supported on BN and silica by deposition from solution. Large supported nanoparticles were prepared by incipient wetness impregnation. To enable direct comparison with the results of ref. 7, Au particles ( $\sim 17$  nm) deposited on carbon were prepared by microemulsion<sup>12,13</sup>. High-resolution TEM studies were performed in a JEOL JEM-3011 electron microscope operating at 300 kV. High-resolution XPS was performed at the NCESS facility, Daresbury Laboratory, UK, using monochromated Al K $\alpha$  radiation.

Catalyst testing was carried out in a sealed glass reactor fitted with a water-cooled reflux head. The same procedure was followed for each run: 100 mg of catalyst was suspended in 20 ml of toluene to which 0.012 mol of styrene was added. The reactor was sealed and thrice evacuated and flushed with oxygen—reaction took place at 100 °C for 15 h, with stirring (1,100 r.p.m.), under 0.5-bar overpressure of  $\text{O}_2$ . Resulting product mixtures were analysed by gas chromatography using decane as an internal standard. Conversion of styrene was calculated

with reference to products formed. Product identification and gas chromatograph calibration were carried out using both gas chromatography–mass spectroscopy and standard solutions of each product identified.

**Full Methods** and any associated references are available in the online version of the paper at [www.nature.com/nature](http://www.nature.com/nature).

Received 31 October 2007; accepted 20 June 2008.

1. Haruta, M., Kobayashi, T., Sano, H. & Yamada, N. Novel gold catalysts for the oxidation of carbon monoxide at a temperature far below 0 °C. *Chem. Lett. (Jpn)* **16**, 405–408 (1987).
2. Haruta, M. Size- and support-dependency in the catalysis of gold. *Catal. Today* **36**, 153–166 (1997).
3. Haruta, M. et al. Low-temperature oxidation of CO over gold supported on  $\text{TiO}_2$ ,  $\alpha\text{-Fe}_2\text{O}_3$ , and  $\text{Co}_3\text{O}_4$ . *J. Catalys.* **144**, 175–192 (1993).
4. Valden, M., Lai, X. & Goodman, D. W. Onset of catalytic activity of gold clusters on titania with the appearance of nonmetallic properties. *Science* **281**, 1647–1650 (1998).
5. Hayashi, T., Tanaka, K. & Haruta, M. Selective vapor-phase epoxidation of propylene over  $\text{Au}/\text{TiO}_2$  catalysts in the presence of oxygen and hydrogen. *J. Catalys.* **178**, 566–575 (1998).
6. Haruta, M. Catalysis: Gold rush. *Nature* **437**, 1098–1099 (2005).
7. Hughes, M. D. et al. Tunable gold catalysts for selective hydrocarbon oxidation under mild conditions. *Nature* **437**, 1132–1135 (2005).
8. Sault, A. G., Madix, R. J. & Campbell, C. T. Adsorption of oxygen and hydrogen on  $\text{Au}(110)$ -(1x2). *Surf. Sci.* **169**, 347–356 (1986).
9. Hutchison, J. E. et al. In *Inorganic Syntheses* Vol. 34 (ed. Shapley, J. R.) 228–232 (Wiley, 2004).
10. Lu, P. et al. Polymer-protected Ni/Pd bimetallic nano-clusters: preparation, characterization and catalysis for hydrogenation of nitrobenzene. *J. Phys. Chem. B* **103**, 9673–9682 (1999).
11. Raja, R. et al. Highly efficient catalysts for the hydrogenation of nitro-substituted aromatics. *Chem. Commun.* 2026–2028 (2005).
12. López-Quintela, M. A. & Rivas, J. Chemical reactions in microemulsions – a powerful method to obtain ultrafine particles. *J. Colloid Interface Sci.* **158**, 446–451 (1993).
13. Vaughan, O. P. H. et al. Copper as a selective catalyst for the epoxidation of propene. *J. Catalys.* **236**, 401–404 (2005).
14. Haruta, M. Gold as a novel catalyst in the 21st century: Preparation, working mechanism and applications. *Gold Bull.* **37**, 27–36 (2004).
15. Deng, X. Y. & Friend, C. M. Selective oxidation of styrene on an oxygen-covered  $\text{Au}(111)$ . *J. Am. Chem. Soc.* **127**, 17178–17179 (2005).
16. Lambert, R. M., Williams, F. J., Cropley, R. L. & Palermo, A. Heterogeneous alkene epoxidation: past, present and future. *J. Mol. Catalys. A* **228**, 27–33 (2005).
17. Chimentao, R. J. et al. Sensitivity of styrene oxidation reaction to the catalyst structure of silver nanoparticles. *Appl. Surf. Sci.* **252**, 793–800 (2005).
18. Williams, F. J., Bird, D. P. C., Palermo, A., Santra, A. K. & Lambert, R. M. Mechanism, selectivity promotion, and new ultraselective pathways in Ag-catalyzed heterogeneous epoxidation. *J. Am. Chem. Soc.* **126**, 8509–8514 (2004).
19. Tang, Q. et al.  $\text{Co}^{2+}$ -exchanged faujasite zeolites as efficient heterogeneous catalysts for epoxidation of styrene with molecular oxygen. *Chem. Commun.* 440–441 (2004).
20. Sebastian, J., Jinka, K. M. & Jasra, R. V. Effect of alkali and alkaline earth metal ions on the catalytic epoxidation of styrene with molecular oxygen using cobalt (II)-exchanged zeolite X. *J. Catalys.* **244**, 208–218 (2006).
21. Boyen, H. G. et al. Oxidation-resistant gold-55 clusters. *Science* **297**, 1533–1536 (2002).
22. Ono, L. K., Sudfeld, D. & Cuenya, B. R. *In situ* gas-phase catalytic properties of  $\text{TiC}$ -supported size-selected gold nanoparticles synthesized by diblock copolymer encapsulation. *Surf. Sci.* **600**, 5041–5050 (2006).
23. Takahiro, K. et al. Core level and valence band photoemission spectra of Au clusters embedded in carbon. *J. Appl. Phys.* **100**, 084325 (2006).
24. Wertheim, G. K. & Dicenzo, S. B. Cluster growth and core-electron binding-energies in supported metal clusters. *Phys. Rev. B* **37**, 844–847 (1988).
25. Santra, A. K. & Goodman, D. W. Oxide-supported metal clusters: models for heterogeneous catalysts. *J. Phys. Condens. Matter* **15**, R31–R62 (2003).
26. Miller, J. T. et al. The effect of gold particle size on Au–Au bond length and reactivity toward oxygen in supported catalysts. *J. Catalys.* **240**, 222–234 (2006).

**Supplementary Information** is linked to the online version of the paper at [www.nature.com/nature](http://www.nature.com/nature).

**Acknowledgements** M.T. and O.P.H.V. acknowledge financial support from the UK Engineering and Physical Sciences Research Council and King’s College, Cambridge, respectively.

**Author Information** Reprints and permissions information is available at [www.nature.com/reprints](http://www.nature.com/reprints). Correspondence and requests for materials should be addressed to R.M.L. (rml1@cam.ac.uk).

## METHODS

**Supported Au<sub>55</sub> preparation.** 55-atom Au clusters stabilized by triphenylphosphane were prepared according to a protocol described in ref. 9. Freshly made Au nanoparticles were immobilized on appropriate supports and thermally activated *in vacuo*, following methodology reported previously<sup>11</sup>. Both 0.6-wt% and 6-wt% Au<sub>55</sub>/SiO<sub>2</sub> were obtained by stirring a solution of Au<sub>55</sub> in dichloromethane with a calculated amount of SiO<sub>2</sub> (fumed, 0.014 µm, 200 ± 25 m<sup>2</sup>g<sup>-1</sup>; Aldrich) overnight, followed by removal of solvent and thermal activation (200 °C, 2 h) *in vacuo*. In an analogous preparation of 0.6-wt% Au<sub>55</sub>/BN (98%, 1 µm; Aldrich), prolonged stirring and *in vacuo* thermal activation was found not to be required to obtain optimum catalytic activity. We note that, by controlling the Au loading (at both 0.6 wt% and 6 wt%), we used this procedure to produce both ~1.4-nm and ~3-nm Au particles, and, thus, catalysts differing in mean particle size only, eliminating the possibility that the observed particle size effect is in some way dependent on preparation method.

**PVP Au preparation.** Au nanoparticles with an average particle diameter of 4 nm were prepared following a methodology similar to that described in ref. 10. All experiments were performed in an inert atmosphere by means of a Schlenk system. Solution 1: in a two-neck round flask, 1.200 g of poly-*n*-vinyl pyrrolidone were added to 120 ml of anhydrous ethylene glycol and the mixture was heated at 80 °C for 3 h under vigorous stirring. Solution 2: in a two-neck round flask, 0.1850 g of NaAuCl<sub>4</sub> were dissolved in 50 ml of dry methanol under vigorous stirring for 1 h. Solution 1 was cooled to 0 °C by means of an ice bath and solution 2 was poured into solution 1 under stirring to ensure homogenization. The pH of the resulting mixture was adjusted to between nine and ten by addition of a 1-M NaOH solution. The resulting solution was capped and heated at 100 °C under vigorous stirring. After a few minutes the solution began to acquire a dark purple colour until it was no longer transparent, indicating that the colloid had formed. The heating was continued for 1 h, after which time the bath was removed and the colloidal suspension cooled down to room temperature (25 °C). The flask was sealed and kept for further use. We obtained 0.6-wt% Au/SiO<sub>2</sub> by adding an appropriate amount of SiO<sub>2</sub> (fumed, 0.014 µm, 200 ± 25 m<sup>2</sup>g<sup>-1</sup>; Aldrich) to the colloidal Au suspension. The catalyst was recovered by filtration, washed with excess methanol and dried at room temperature *in vacuo*.

**Microemulsion Au preparation.** Supported 1-wt% Au/C catalysts of mean particle diameter 17 nm were prepared using an established microemulsion technique<sup>12,13</sup>. Au nanoparticles were prepared in water–oil microemulsions with *n*-heptane as the continuous oil domain. An aqueous solution of the Au precursor hydrogen trichloroaurate trihydrate (0.1-M HAuCl<sub>4</sub>) was added to a mixture of the oil and 22.93-wt% surfactant, polyethyleneglycol dodecylether (Brij 30, Fluka). The volume of aqueous solution added was calculated to result

in a water-to-surfactant molar ratio of 8 ( $n_w/n_s = 8$ ). The Au complexes were reduced by adding hydrazine (Au:N<sub>2</sub>H<sub>4</sub>, 1:8) to the microemulsion. The carbon support (carbon black, 50% compressed, >99.9%, 75 m<sup>2</sup>g<sup>-1</sup>; Alfa Aesar) was added to the particle suspension under vigorous stirring, after which acetone was added slowly to break the microemulsion and allow the particles to deposit on the support material. The mixture was then stirred, filtered and washed with acetone and absolute ethanol to remove the surfactant. The resulting catalyst was dried in air at 85 °C for 24 h.

**Incipient wetness preparation.** A 5-wt% Au/SiO<sub>2</sub> catalyst was prepared by incipient wetness impregnation (a procedure known to yield Au particles of diameter >30 nm)<sup>27,28</sup> of silica (fumed, 0.014 µm, 200 ± 25 m<sup>2</sup>g<sup>-1</sup>; Aldrich) with aqueous HAuCl<sub>4</sub>, followed by drying in air (120 °C, 10 h), air calcination (300 °C, 4 h) and reduction in H<sub>2</sub> (300 °C, 2 h).

**Characterization methods.** High-resolution TEM studies were performed in a JEOL JEM-3011 electron microscope operating at 300 kV with a structural resolution of 0.16 nm. Samples were ultrasonically dispersed in acetone before deposition on carbon-coated copper grids. Particle size distributions were taken from a count of ~100 particles.

High-resolution XPS was performed out at the NCESS facility, Daresbury Laboratory, UK, using monochromated Al K $\alpha$  radiation, calibration of the binding energy scale being carried out by standard methods<sup>29</sup>.

**Catalyst testing.** Catalyst testing was carried out in a sealed glass reactor fitted with a water-cooled reflux head. The same procedure was followed for each run: 100 mg of catalyst was suspended in 20 ml of toluene (>99.9%; Chromasolv, Aldrich) to which 0.012 mol of styrene (99%; Aldrich) was added. The reactor was sealed and thrice evacuated and flushed with oxygen (99.995%, Messer)—reaction took place at 100 °C for 15 h, with stirring (1,100 r.p.m.), under 0.5-bar overpressure of O<sub>2</sub>. Resulting product mixtures were analysed by gas chromatography (Hewlett-Packard GC 5890 Series II, FID detector) using decane (99+% anhydrous; Aldrich) as an internal standard. Conversion of styrene was calculated with reference to products formed. Product identification and gas chromatograph calibration were carried out using both gas chromatography–mass spectroscopy and standard solutions of each product identified. All catalytic tests were repeated three times. Turnover frequency (the number of molecules of styrene reacting per surface Au atom per second) was estimated from the Au dispersion ( $D$ ) using  $D = 0.9/d$ , where  $d$  is the mean particle diameter in nanometres.

27. Bowker, M., Nuhu, A. & Soares, J. High activity supported gold catalysts by incipient wetness impregnation. *Catal. Today* 122, 245–247 (2007).
28. Haruta, M. Catalysis of gold nanoparticles deposited on metal oxides. *CATTECH* 6, 102–115 (2002).
29. Briggs, D. & Seah, M. P. (eds) *Practical Surface Analysis* 2nd edn (Wiley, 1990).

## LETTERS

# Effect of phase transitions on compressional-wave velocities in the Earth's mantle

Li Li<sup>1</sup> & Donald J. Weidner<sup>1</sup>

The velocities of seismic waves in the Earth are governed by the response of the constituent mineral assemblage to perturbations in pressure and stress. The effective bulk modulus is significantly lowered if the pressure of the seismic wave drives a volume-reducing phase transformation<sup>1,2</sup>. A comparison between the amount of time required by phase transitions to reach equilibrium and the sampling period thus becomes crucial in defining the softening and attenuation of compressional waves within such a two-phase zone<sup>3</sup>. These phenomena are difficult to assess experimentally, however, because data at conditions appropriate to the Earth's deep interior are required. Here we present synchrotron-based experimental data that demonstrate softening of the bulk modulus within the two-phase loop of olivine–ringwoodite on a timescale of 100 s. If the amplitude of the pressure perturbation and the grain size are scaled to those expected in the Earth, the compressional-wave velocities within the discontinuities at 410, 520 and, possibly, 660 km are likely to be significantly lower than otherwise expected. The generalization of these observations to aluminium-controlled phase transitions raises the possibility of large velocity perturbations throughout the upper 1,000 km of the mantle.

The current view of the radial seismic structure of the mantle consists of smooth velocity variations punctuated by discontinuities at 410, 520, and 660 km (ref. 4), which are thought to be caused by the olivine–wadsleyite–ringwoodite–perovskite phase transitions<sup>5,6</sup>. However, complexities arise from the possible relaxation of the bulk modulus caused by phase transitions<sup>1</sup> in regions of coexisting high- and low-pressure phases. The olivine phase transitions have finite widths owing to the partitioning of iron and magnesium between coexisting phases<sup>7,8</sup>. Some of the 'smooth' zones consist of coexisting high- and low-pressure phases of pyroxene–garnet–perovskite, which tend to have broad two-phase zones that are controlled by the partitioning of aluminium between coexisting phases<sup>9</sup>. In the regions with coexisting high- and low-pressure phases, the equilibrium bulk modulus,  $K_{eq}$ , will be considerably relaxed because a pressure change will induce a volume change that is the result of the pressure-induced phase transformation:

$$-\frac{\delta V}{V} = -\frac{\delta P}{\Delta P_{tran}} \left( \frac{\Delta V}{V} \right)_{tran} + \frac{\delta P}{K_{elas}} = \delta P \left( \frac{1}{K_{tran}} + \frac{1}{K_{elas}} \right) = \frac{\delta P}{K_{eq}}$$

where  $\Delta P_{tran}$  is the width of the two-phase zone,  $(\Delta V/V)_{tran}$  is the proportional volume change associated with the transformation and  $K_{elas}$  is the elastic unrelaxed bulk modulus of the two-phase aggregate when no phase transition occurs. Whether  $K_{eq}$  or  $K_{elas}$  defines the P-wave velocity depends on whether the kinetics of the transformation occur on a timescale respectively shorter or longer than the period of the seismic wave.

Figure 1 illustrates the effect on the P-wave velocity of transition-induced relaxation for a pyrolytic Earth<sup>10,11</sup> with an adiabatic temperature gradient<sup>12</sup>. Figure 1a illustrates the unrelaxed elastic system.

Figure 1b shows the relaxed system with only the olivine transforming. Figure 1c is similar to Fig. 1b, but both olivine and pyroxene reach equilibrium. Also illustrated in Fig. 1c is the preliminary reference Earth model<sup>3</sup>. It is noteworthy that this model lies between the relaxed and unrelaxed systems and is closest to the unrelaxed velocity in regions where no phase transitions occur. On the basis of our experimental results, we argue that the Earth most likely samples a significant fraction of the relaxed system resulting in a reduced P-wave velocity, but with little bulk attenuation.

The crucial issue is the timescale for the system undergoing phase transitions to reach equilibrium, in comparison with the period of seismic waves<sup>1</sup>. Kinetics rates are often attributed to nucleation of the new phase and growth of the new phase. As both phases coexist, nucleation is probably not important here. Growth requires that the composition of the region that is becoming the new phase change from one side of the controlling binary loop to the other, thus requiring diffusion. For the olivine system, iron and magnesium must exchange<sup>13</sup> by several per cent. The rate of this diffusion process defines one timescale ( $\tau_1$ ) of the transformation. For times longer than  $\tau_1$ , some transformation will occur. Complete transformation requires that the region furthest from the transforming zone equilibrate iron or magnesium with the transforming zone<sup>2,14</sup>, and defines a second timescale ( $\tau_2$ ). There is probably a range of characteristic

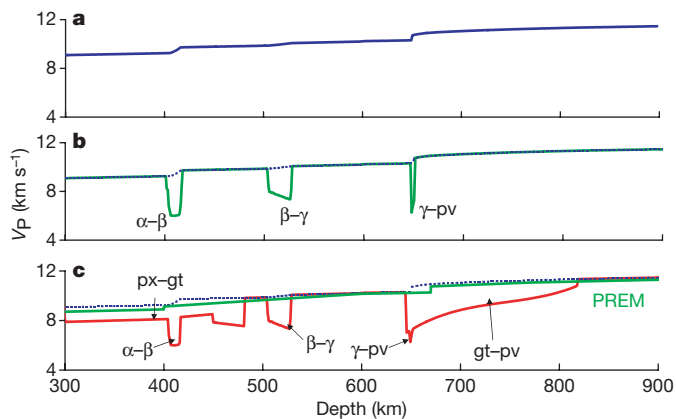


**Figure 1 | Calculated P-wave velocities ( $V_p$ ) versus depth in the Earth using pyrolite composition and adiabatic gradient<sup>8</sup>. a**, Here the measurement time is much less than the shortest characteristic time (which we estimate to be  $<10^{-2}$  s for P waves). **b**, Here we assume total phase equilibrium for olivine phases (green line; the blue line is the same as in a). **c**, Same as b except total equilibrium for pyroxene–garnet–perovskite transitions is also assumed (red line). The preliminary reference Earth model<sup>3</sup> (PREM) is included. Plots in b and c are calculated from the depth derivative of the density model. The density model is derived from the phase equilibria and equations of state for pyrolite minerals<sup>10</sup>.  $\alpha$ , olivine;  $\beta$ , wadsleyite;  $\gamma$ , ringwoodite;  $pv$ , perovskite;  $px$ , pyroxene;  $gt$ , garnet.

<sup>1</sup>Mineral Physics Institute Department of Geosciences, Stony Brook University, Stony Brook, New York 11794, USA.

times between  $\tau_1$  and  $\tau_2$  in the real system, yielding progressively more transformation for times between these bounds.

Equilibrium also requires heat diffusion. If latent heat does not diffuse from the system, the amount of relaxation of the bulk modulus is reduced by about one-half for the olivine system, but by very little for the pyroxene system. The timescale for heat flow thereby also enters the conditions for equilibrium<sup>15</sup>, but will not be discussed here. The characteristic time depends on the diffusion length,  $x$ , by  $\tau = x^2/D$  (ref. 2), where  $D$  is the appropriate diffusion coefficient. As pointed out in ref. 2,  $x \approx (d/3)\delta P/\Delta P_{\text{tran}}$ , where  $x$  is a transformed rim on a grain of size  $d$ . A smaller pressure perturbation  $\delta P$  will transform a smaller amount of material, thus reducing  $x$  and  $\tau_1$ . For seismic waves<sup>2</sup>, with  $\delta P$  of roughly  $10^{-7}$  GPa,  $\Delta P_{\text{tran}}$  of 0.3 GPa (width of the olivine–wadsleyite two-phase loop),  $d$  of 1 cm and  $D$  of  $10^{-15} \text{ m}^2 \text{ s}^{-1}$  for iron–magnesium exchange<sup>13</sup>,  $\tau_1$  is approximately  $10^{-2}$  s. Timescale  $\tau_2$ , which characterizes the longest diffusion distance for complete equilibrium, can reach values of  $10^{11}$  s if the diffusion path is as long as 1 cm. This implies that seismic waves, with periods between 1 and 1,000 s, will at least partially drive the phase transition and will exhibit partially relaxed velocities. If the seismic timescale were the same as the characteristic time, we would expect an associated attenuation. For the conditions outlined here, we conclude that the seismic velocities are partially relaxed, but with little or no attenuation.

In the laboratory, with values of  $\delta P$  at the gigapascal level and grains sizes of a few micrometres, we expect  $\tau_1$  to be of the order of 1,000 s. Furthermore, we expect that these characteristic times are reasonably appropriate for the olivine–wadsleyite–ringwoodite transformations as well as the pyroxene–garnet–perovskite transformations. Aluminium diffusion controls the two-phase region of the latter system. Although aluminium diffusion data are not available, gallium diffusion in garnets suggests characteristic times similar to those for the iron–magnesium exchange in olivine<sup>16</sup>. Thus, the characteristic times in Fig. 1c may be similar to those in Fig. 1b. However, a recent study<sup>17</sup> reported diffusion coefficients for the iron–magnesium exchange of  $10^{-21} \text{ m}^2 \text{ s}^{-1}$  for perovskite. This increases the characteristic time of the ringwoodite-to-perovskite transition by six orders of magnitude, and possibly out of the seismic band.

Testing this model by quantifying this phenomenon in the laboratory has been limited by the challenge of creating the appropriate pressure–temperature environment and simultaneously measuring elastic properties and attenuation of the bulk modulus at seismic frequencies. Use of the deformation DIA high-pressure system<sup>18</sup> on a synchrotron X-ray source has provided a new opportunity to pursue these goals<sup>19</sup>. Here we report two types of experiment on an olivine sample, of composition Fa<sub>70</sub> (Fa, fayalite), which is used to ensure a wide two-phase loop between olivine and ringwoodite. In the first set of experiments, the time-resolved transformation between olivine and ringwoodite was defined by the X-ray diffraction pattern after a change in the pressure or temperature conditions altered the equilibrium proportions of the two phases. In the other measurements, the olivine sample ( $\sim 10\text{-}\mu\text{m}$  grain size) and an aluminium oxide reference were enclosed in a silver capsule which was placed in a high-pressure cell. At high pressure and temperature (up to 15 GPa, 1,700 K), a sinusoidal uniaxial stress is applied to the sample, inducing strains of  $10^{-2}$ – $10^{-5}$ . We measured stress–strain phase and amplitude relationships, resolved using X-ray radiation, for frequencies of 1–100 mHz. Details of the experimental procedures are reported elsewhere<sup>19</sup>.

Figure 2 shows a typical evolution of the volume per cent of the phases as a function of time after a new set of equilibrium conditions has been established. The fitted curve indicates a characteristic time of about 4,000 s. This is consistent with diffusion being the controlling process, with a value for  $D$  of  $10^{-15} \text{ m}^2 \text{ s}^{-1}$  for iron–magnesium exchange<sup>13</sup> and a characteristic length of 2  $\mu\text{m}$ , which would suggest that about half of the material undergoes transformation (with 10  $\mu\text{m}$

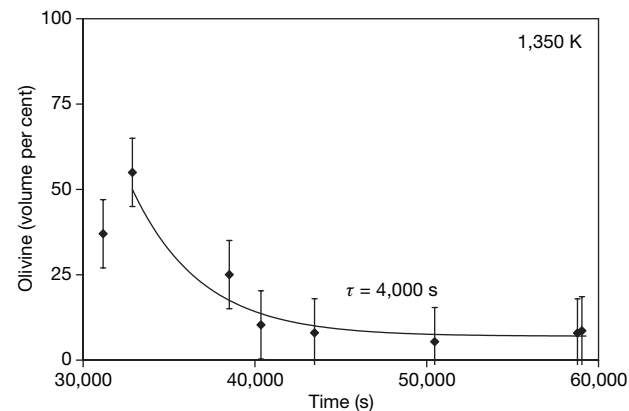


**Figure 2 | Example of the olivine content versus time, from X-ray diffraction observations.** The temperature reached 1,350 K at 33,000 s. Olivine transforms to spinel with time. The decay curve has a characteristic time of 4,000 s. These data are consistent with iron–magnesium diffusion being the dominant process, with a diffusivity of  $10^{-15} \text{ m}^2 \text{ s}^{-1}$  and a diffusion length of 2  $\mu\text{m}$ . These results support the bulk attenuation observed during loading with a period of 1,000 s (Fig. 3) and the softening observed at low amplitudes and shorter periods (Fig. 4). Run number 30; error bars, 1 s.d.

grains). This is consistent with the model described above and with previous studies on olivine phase kinetics<sup>20</sup>.

Attenuation is expected when the characteristic time is comparable to the oscillation period. Figure 3a shows one cycle of a 1,000-s oscillation, where stress (derived from the strain of the reference material) is plotted against strain of the sample. The hysteresis loop indicates energy loss in the cycle. Figure 3b shows the hysteresis loop for the same condition at a slightly lower temperature, where only the ringwoodite phase was stable as indicated by the diffraction pattern.

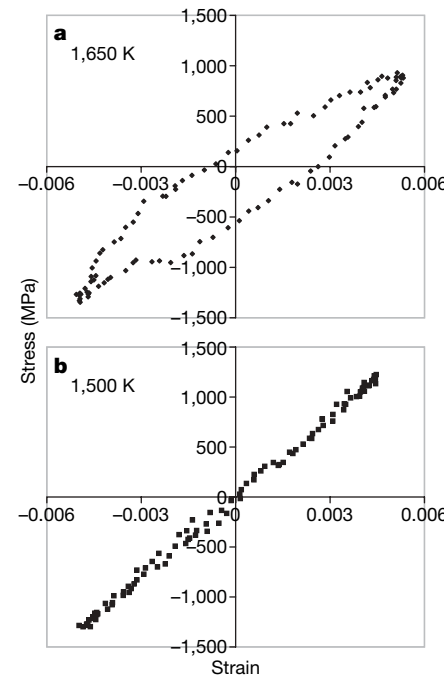


**Figure 3 | Stress versus strain for one cycle during sinusoidal loading with period of 1,000 s.** **a**, At 1,650 K both olivine and ringwoodite coexist in approximately equal amounts, as demonstrated by X-ray diffraction. The resulting  $Q$  factor is about five. **b**, At 1,500 K, X-ray diffraction indicates that ringwoodite dominates the sample. The  $Q$  factor is indistinguishable from infinity. The area inside the hysteresis loop is the energy loss during one cycle. We conclude that the phase transition is responsible for the energy dissipation.

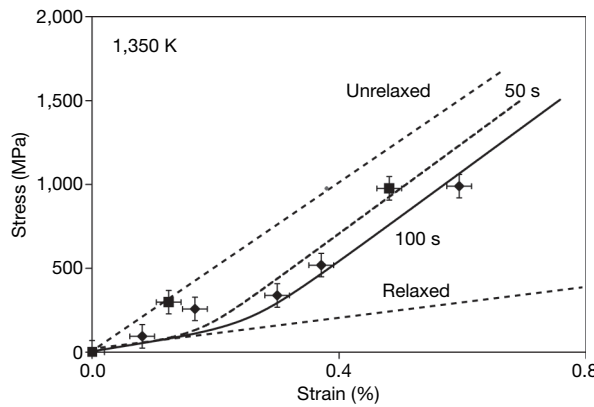


**Figure 4 | Sample stress-strain relationship at 1,350 K.** The samples contain olivine and ringwoodite in about equal proportions. The plotted curves are models for 50-s (squares), 100-s (diamonds), infinitely long (relaxed) and infinitely short (unrelaxed) sampling times. The curves are calculated using the analysis<sup>13</sup> for a two-phase mixture, with adjustments made to reflect a cycling uniaxial stress and parameters of grain size 10  $\mu\text{m}$  and diffusion coefficient  $10^{-15} \text{ m}^2 \text{ s}^{-1}$ . Run number 28; error bars, 1 s.d.

The energy loss for the mixed-phase region is considerably larger than that for the single-phase region, as expected in this model. We again emphasize that the small stress amplitude in the seismic wave may lower the characteristic time to a much smaller value and, thus, shift the attenuation peak to much higher frequencies than those sampled by seismic waves.

The observations suggest a characteristic time on the order of 1,000 s in the laboratory for gigapascal-level stresses. This phenomenon will be important in the seismic record if the characteristic time scales with stress amplitude as suggested by the model outlined above. We tested this scaling by measuring stress and strain as a function of the stress amplitude at fixed frequencies. Figure 4 compares the model predictions for stress amplitude versus strain amplitude with the results for sinusoidal oscillations with 50-s and 100-s periods. For any strain amplitude, the characteristic time  $\tau_1$  was derived in accordance with the discussion above and the stress was calculated using the relaxed modulus, the unrelaxed modulus, the characteristic time and the frequency of the oscillation, according to standard relaxation models<sup>1</sup>. The slope of the stress-strain curve for large-amplitude oscillations is equal to the unrelaxed Young's modulus, whereas the slope at small amplitude reflects the relaxed modulus. The data were constrained to go through the origin. The 50-s model curve has a smaller amount of relaxed strain than the 100-s curve because the transformed sample volume ( $\delta V$ ) is less for shorter transformation times and, hence, shorter periods. Whereas the small-amplitude data exhibit some scatter, the more robust, large-amplitude data are consistent with the model<sup>2</sup> and, therefore, support our claim that the characteristic time decreases as the amplitude of the perturbing stress decreases.

The data presented here imply that phase transitions reduce P-wave velocities in the Earth's mantle. The relaxed and unrelaxed velocities are easy to calculate, but the actual velocity will lie between these values, and the exact amount of softening is not yet known.

Whether or not associated bulk attenuation occurs requires more investigation of the timescales. This suggestion alters the information that is considered essential in creating a seismic profile from mineral physics data. More experiments and directed seismic observations are needed to define the impact of the process presented here.

Received 21 January; accepted 4 July 2008.

1. Anderson, D. L. *Theory of the Earth* 279–301 (Blackwell Scientific, 1989).
2. Jackson, I. in *Treatise on Geophysics* Vol. 2 (ed. Schubert, G.) 493–525 (Elsevier, 2007).
3. Vaisnys, J. R. Propagation of acoustic waves through a system undergoing phase transformations. *J. Geophys. Res.* 73, 7675–7683 (1968).
4. Dziewonski, A. M. & Anderson, D. L. Preliminary reference Earth model. *Phys. Earth Planet. Inter.* 25, 297–356 (1981).
5. Bina, C. R. & Helffrich, G. Phase transition Clapeyron slopes and transition zone seismic discontinuity topography. *J. Geophys. Res.* 99, 15853–15860 (1994).
6. Ringwood, A. E. Phase transformations and the constitution of the mantle. *Phys. Earth Planet. Inter.* 9, 109–155 (1970).
7. Katsura, T. & Ito, E. The system  $\text{Mg}_2\text{SiO}_4\text{-Fe}_2\text{SiO}_4$  at high pressures and temperatures – precise determination of stabilities of olivine, modified spinel, and spinel. *J. Geophys. Res.* 94, 15663–15670 (1989).
8. Irfune, T. Phase transformations in the Earth's mantle and subducting slabs: Implications for their compositions, seismic velocity and density structures and dynamics. *I. Arc 2*, 55–71 (1993).
9. Akaogi, M., Tanaka, A. & Ito, E. Garnet-ilmenite-perovskite transitions in the system  $\text{Mg}_4\text{Si}_4\text{O}_{12}\text{-Mg}_3\text{Al}_2\text{Si}_3\text{O}_{12}$  at high pressures and high temperatures: phase equilibria, calorimetry and implications for mantle structure. *Phys. Earth Planet. Inter.* 132, 303–324 (2002).
10. Weidner, D. J. & Wang, Y. in *Earth's Deep Interior: Mineral Physics and Tomography from the Atomic to the Global Scale* (eds Karato, S., Forte, A. M., Liebermann, R. C., Masters, G. & Stixrude, L.) 215–235 (American Geophysical Union, 2000).
11. Weidner, D. J. & Wang, Y. B. Chemical- and Clapeyron-induced buoyancy at the 660 km discontinuity. *J. Geophys. Res.* 103, 7431–7441 (1998).
12. Brown, J. M. & Shankland, T. J. Thermodynamic parameters in the Earth as determined from seismic profiles. *Geophys. J. R. Astron. Soc.* 66, 579–596 (1981).
13. Chakraborty, S. et al. Enhancement of cation diffusion rates across the 410-kilometer discontinuity in Earth's mantle. *Science* 283, 362–365 (1999).
14. Morris, S. J. S. Coupling of interface kinetics and transformation-induced strain during pressure-induced solid-solid phase changes. *J. Mech. Phys. Solids* 50, 1363–1395 (2002).
15. Tamisiea, M. E. & Wahr, J. M. Phase transitions and short timescale sinusoidal motions. *Earth Planet. Sci. Lett.* 198, 459–470 (2002).
16. Cherniak, D. J. Rare earth element and gallium diffusion in yttrium aluminum garnet. *Phys. Chem. Miner.* 26, 156–163 (1998).
17. Holzapfel, C., Rubie, D. C., Frost, D. J. & Langenhorst, F. Fe-Mg interdiffusion in  $(\text{Mg}, \text{Fe})\text{SiO}_3$  perovskite and lower mantle reequilibration. *Science* 309, 1707–1710 (2005).
18. Durham, W. B., Weidner, D. J., Karato, S. & Wang, Y. in *Plastic Deformation of Minerals and Rocks* Vol. 51 (eds Karato, S. & Wenk, H.-R.) 21–49 (Mineralogical Society of America, 2002).
19. Li, L. & Weidner, D. J. Energy dissipation of materials at high pressure and high temperature. *Rev. Sci. Instrum.* 78, 053902 (2007).
20. Rubie, D. C. & Ross, C. R. Kinetics of the olivine-spinel transformation in subducting lithosphere – experimental constraints and implications for deep slab processes. *Phys. Earth Planet. Inter.* 86, 223–241 (1994).

**Acknowledgements** We thank L. Wang and D. Lindsley for support for this project. We acknowledge support from the National Synchrotron Light Source and the Consortium for Materials Properties in Earth Sciences, and financial support from the US Department of Energy (contract number DE-AC02\_98CH10886) and the US National Science Foundation (awards EAR-0711365, EAR-0652887 and EAR-01-35554). This is MPI publication number 466.

**Author Information** Reprints and permissions information is available at [www.nature.com/reprints](http://www.nature.com/reprints). Correspondence and requests for materials should be addressed to L.L. (lili@ic.sunysb.edu).

# Self-destructive cooperation mediated by phenotypic noise

Martin Ackermann<sup>1</sup>, Bärbel Stecher<sup>2</sup>, Nikki E. Freed<sup>1</sup>, Pascal Songhet<sup>2</sup>, Wolf-Dietrich Hardt<sup>2</sup> & Michael Doebeli<sup>3</sup>

In many biological examples of cooperation, individuals that cooperate cannot benefit from the resulting public good. This is especially clear in cases of self-destructive cooperation, where individuals die when helping others. If self-destructive cooperation is genetically encoded, these genes can only be maintained if they are expressed by just a fraction of their carriers, whereas the other fraction benefits from the public good. One mechanism that can mediate this differentiation into two phenotypically different sub-populations is phenotypic noise<sup>1,2</sup>. Here we show that noisy expression of self-destructive cooperation can evolve if individuals that have a higher probability for self-destruction have, on average, access to larger public goods. This situation, which we refer to as assortment, can arise if the environment is spatially structured. These results provide a new perspective on the significance of phenotypic noise in bacterial pathogenesis: it might promote the formation of cooperative sub-populations that die while preparing the ground for a successful infection. We show experimentally that this model captures essential features of *Salmonella typhimurium* pathogenesis. We conclude that noisily expressed self-destructive cooperative actions can evolve under conditions of assortment, that self-destructive cooperation is a plausible biological function of phenotypic noise, and that self-destructive cooperation mediated by phenotypic noise could be important in bacterial pathogenesis.

Recent experimental work demonstrated that genetically identical organisms living in the same environment show surprisingly high levels of variation in phenotypic traits<sup>1,2</sup>, and sometimes even switch between distinct phenotypic states<sup>3</sup>. Stochastic cellular processes are one source of such phenotypic noise. The level of phenotypic noise is subject to mutational change, and can thus evolve. This raises the question whether natural selection always acts towards minimizing phenotypic noise, or whether there are cases in which genotypes that encode variable phenotypes are favoured by selection. In the existing theory<sup>4–6</sup>, the most prominent adaptive explanation for phenotypic noise is bet-hedging<sup>5</sup>, according to which the stochastic expression of alternative phenotypes allows a genotype to survive changes in external conditions and thus to persist in fluctuating environments.

Here we focus on a fundamentally different adaptive explanation for phenotypic noise: self-destructive cooperation. In this scenario, the individuals that survive and form a successful lineage all express the same phenotype. Individuals that express an alternative phenotype do exist, but they do not contribute to future generations; instead, they die while contributing to a public good that benefits others. There are many examples of cooperative acts that prevent reproduction or survival of the actor, ranging from non-reproductive workers in mammals and insects to unicellular bacteria that lyse when releasing chemical substances that benefit others. Importantly, genotypes that have the propensity to express self-destructive cooperation can only

persist if the expression is limited to a fraction of the individuals carrying the genotype, whereas another fraction does not express the cooperative behaviour and benefits from the public good produced. Sometimes, this differentiation into two fractions is mediated by signals. In other examples, notably in microorganisms, there seems to be no signal. In these cases, phenotypic noise could promote the differentiation required for self-destructive cooperation to persist.

We investigated the evolutionary dynamics of a self-destructive cooperative act that contributes to the generation of a public good and that is expressed in a stochastic manner. In general, cooperation can evolve if cooperative individuals benefit from cooperative acts of others more often than non-cooperative individuals<sup>7</sup>—a situation referred to as assortment. We used a simple model to quantify the level of assortment as a function of the external conditions, and to calculate how selection on the probability to express self-destructive cooperation depends on the level of assortment, as well as on the amount of public good generated by cooperative acts.

The model is based on the public goods game and assumes that there are two strategies: cooperate (C) and defect (D). C sacrifices itself with probability  $q$ , and only if it sacrifices itself, it contributes an amount  $b$  to the public good. The decision between sacrificing and not sacrificing is a chance outcome resulting from phenotypic bistability; every cooperator makes this decision independently of the environment or of the decisions of other individuals. D never contributes to the public good. The game is played in interaction groups of  $N$  players. In general, if there are  $k$  cooperators among the  $N$  members of an interaction group, the total amount of the public good produced in that group is  $kqb$ . The total amount of the public good is available to each surviving player in the interaction group (an alternative scenario where the public good is divided among the surviving players gives very similar results). We assume that, in addition to the public good, all players also receive a non-zero baseline payoff  $w$ .

Consider first the payoff to a focal C player in a given interaction group. Because the focal C is one of the  $k$  cooperators, its social environment consists of  $k - 1$  cooperators and  $N - k$  defectors. The focal C gets no payoff from the defectors, but if it survives it receives the benefit  $b$  with a probability  $q$  from each of the other  $k - 1$  cooperators, as well as the baseline payoff  $w$ . The probability that the focal C does not sacrifice itself is  $1 - q$ , and hence the expected payoff to C in the given interaction group is:

$$p_C(N, k) = (1 - q)((k - 1)qb + w) \quad (1)$$

The social environment of a focal D in the given interaction group consists of  $k$  cooperators and  $N - k - 1$  defectors, and its expected payoff is:

<sup>1</sup>Institute of Integrative Biology, ETH Zurich, 8092 Zürich, Switzerland. <sup>2</sup>Institute of Microbiology, ETH Zurich, 8093 Zürich, Switzerland. <sup>3</sup>Department of Zoology and Department of Mathematics, University of British Columbia, Vancouver BC V6T 1Z4, Canada.

$$p_D(N, k) = kqb + w \quad (2)$$

Because  $p_C(N, k) < p_D(N, k)$ , cooperators always do worse than defectors within a given group. Therefore, the only way in which cooperators can dominate on a population-wide scale is if cooperators have, on average, a different social environment than defectors.

The composition of the social environment of a focal C or D depends on the current frequency of cooperators in the population,  $x$ , and on how individuals come together to form interaction groups. Let  $e_C(x)$  be the average number of cooperators among the other  $N-1$  members in an interaction group containing a focal C. Similarly, let  $e_D(x)$  be the number of cooperators in an average interaction group containing a focal D. The expected population-wide payoffs to C and D are then:

$$P_C(x) = (1-q)(e_C(x)qb + w) \quad (3)$$

and

$$P_D(x) = e_D(x)qb + w \quad (4)$$

With random composition of groups, we have  $e_C(x) = e_D(x) = x(N-1)$ . In this case, the population-wide payoffs always satisfy  $P_C(x) < P_D(x)$  for all  $x$ , and hence defectors always win. Thus, for cooperation to thrive, cooperators must find themselves, on average, in interaction groups containing more cooperators than the interaction groups in which defectors find themselves on average. In other words, there must be positive assortment between cooperators.

Assortment can result from different mechanisms, for example, spatial structure, reciprocity or kin recognition<sup>7</sup>. Here we consider a simple case of spatially structured populations inhabiting an infinite number of demes. In the case of pathogenic bacteria, a deme would represent a host. Each deme is seeded by  $M$  individuals from a common pool of individuals. The number of individuals then increases to the carrying capacity of the deme, which is assumed to be  $N$ , the interaction group size. After reaching carrying capacity, cooperators sacrifice themselves with probability  $q$ ; if they do, they contribute  $b$  to the public good. Cooperators that did not sacrifice themselves and defectors then harvest the public good. The payoffs they receive determine how much they contribute to the pool of individuals from which the next generation of demes is seeded.

If the number of individuals seeding a deme,  $M$ , is small, then the degree of assortment is high, and a focal cooperator sees on average more cooperators than a focal defector. It is easy to see (see Supplementary Information) that the average social environment of a focal cooperator and a focal defector is:

$$e_C(x) = \frac{(M-1)N}{M}x + \frac{N}{M} - 1 \quad (5)$$

and

$$e_D(x) = \frac{(M-1)N}{M}x \quad (6)$$

Thus,  $e_C(x) > e_D(x)$  for all  $x$ , which enables the origin and maintenance of cooperation based on equations (3) and (4). The general picture is as follows (Fig. 1; derivation in Supplementary Information): First, there is a value  $q_1^*$  such that for any  $q < q_1^*$ , C can invade D, that is,  $P_C(0) > P_D(0)$  ( $q_1^* = [b(N-M) - Mw]/[b(N-M)]$ ; see Supplementary Information). Second, there is a value  $q_2^* < q_1^*$  such that for any  $q < q_2^*$ , C not only invades D but also goes to fixation, that is,  $P_C(1) > P_D(1)$  ( $q_2^* = [b(N-M) - Mw]/[b(NM - M)]$ ; see Supplementary Information). Third, for any  $q$  with  $q_2^* < q < q_1^*$ , there is coexistence between cooperators and defectors, that is, C can invade D and D can invade C.

These results show that the assortment generated by the deme structure changes the nature of the evolutionary game between cooperators

and defectors. In well-mixed populations without demes, D always dominates C. With demes, this remains true if C players have large probabilities  $q$  of committing cooperative suicide. However, for intermediate  $q$  (that is,  $q_2^* < q < q_1^*$ ), the structure of the game changes to a 'Snowdrift' scenario<sup>8</sup>, in which both C and D can invade when rare. For even smaller  $q$  ( $q < q_2^*$ ), assortment makes C the dominant strategy and eliminates D.

Defectors D can be viewed as cooperators with  $q = 0$ , which naturally leads to the consideration of  $q$  as a continuous trait. Evolution of such continuous traits can be studied using adaptive dynamics theory<sup>9–11</sup>. Starting with a population of defectors, the trait  $q$  evolves to a convergence stable and evolutionarily stable strategy  $q_3^*$  satisfying  $0 < q_3^* < q_2^*$  ( $q_3^* = [b(N-M) - Mw]/[b(NM + N - 2M)]$ ; see Supplementary Information). Therefore, continuous evolution by small steps results in a population consisting of a single cooperative strategy that cannot be invaded by any nearby strategies  $q$  or by pure defectors. Our model thus provides a framework for understanding the evolution of self-destructive cooperation mediated by phenotypic noise. We note that our deme-structured model of cooperative suicide can also be interpreted in the context of kin or group selection<sup>7,12</sup>. However, these perspectives are not required for understanding the evolution of cooperation; simple considerations based on assortment and interaction environments are sufficient.

This model sheds new light on the role of phenotypic noise in the biology of microbial pathogens. Phenotypic noise or bi-stability is common in unicellular pathogens, as are acts of self-destructive cooperation<sup>13</sup>. Some bacterial toxins that are instrumental in pathogenesis can only be released if the cell producing the toxin lyses<sup>14–16</sup>. Some of these toxins induce inflammation in the host, and there is now growing evidence that pathogens can decrease competition by co-inhabitants of the same niche through manipulation of the host's immune system<sup>17–20</sup>. One example is pneumolysin from *Streptococcus*

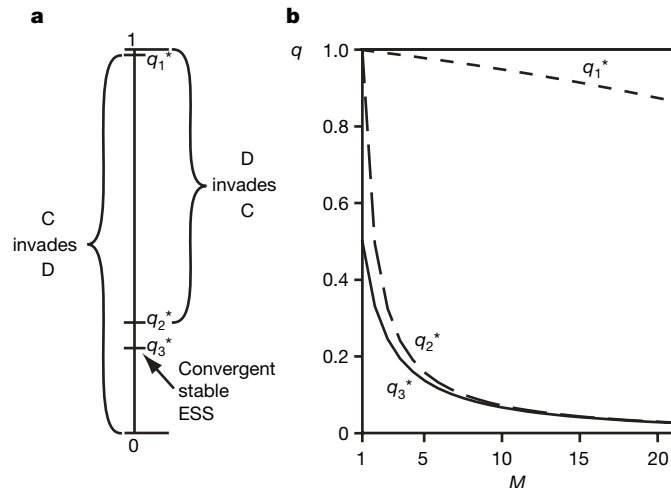


**Figure 1 | The evolutionary dynamics of stochastic self-destructive cooperation.** **a**, The dynamics are determined by three specific values for the probability  $q$  to self-sacrifice. The first value is  $q_1^*$ . A population of pure defectors can be invaded by cooperators that self-sacrifice with a probability  $q < q_1^*$ . The second value is  $q_2^*$ . A homogeneous population of cooperators can be invaded by defectors if the cooperators' probability to self-sacrifice is larger than  $q_2^*$ . Cooperators with a probability to self-sacrifice between  $q_1^*$  and  $q_2^*$  will thus stably co-exist with pure defectors. If  $q$  evolves through mutations of small effects, and the population initially consists of defectors, then  $q$  will evolve to the value  $q_3^*$ . This value is an evolutionarily stable strategy (ESS) and represents an endpoint for the evolutionary dynamics. The three values for  $q$  are determined by the parameters  $M$ ,  $N$ ,  $b$  and  $w$ , as described in the Supplementary Information. In the example shown here, the parameters are  $M = 3$ ,  $N = 100$ ,  $b = 5$  and  $w = 2$ . **b**, When the number of individuals colonizing a deme,  $M$ , increases, and assortment therefore decreases, the three values  $q_1^*$ ,  $q_2^*$  and  $q_3^*$  decrease. The parameter values are  $N = 100$ ,  $b = 5$  and  $w = 2$ .

*pneumoniae*. This toxin is released through bacterial lysis and enhances lung colonization<sup>14,21</sup>. A second example is TcdA, a key virulence factor of *Clostridium difficile*<sup>16</sup>. TcdA lacks a standard secretion signal and is released by bacterial lysis. Purified TcdA toxin alone can trigger gut inflammation<sup>22</sup>, and gut inflammation enhances intestinal *C. difficile* colonization<sup>23</sup>. In this case, TcdA released by self-destructive acts seems to provide the pathogen with a competitive advantage, presumably by decreasing competition from commensal bacteria.

We focused on *S. typhimurium* enterocolitis as a third example of bacterial pathogenesis, and tested experimentally whether central aspects of the infection process are captured by the model of self-destructive cooperation mediated by phenotypic noise. The establishment of *S. typhimurium* in the gut is hindered by the presence of the intestinal microflora. These competitors are removed by an inflammatory response in the gut triggered by *S. typhimurium* invading the gut tissue<sup>24</sup>. Gut tissue invasion and the triggering of inflammation depend on *S. typhimurium* virulence factors, namely Type III secretion systems (TTSS) and flagella. Invasion factors—that is, the invasion-mediating TTSS-1 and the flagella—are heterogeneously expressed in *S. typhimurium* populations<sup>25–27</sup>. In our experiments, gut inflammation, which alleviates competition by commensals, was regarded as the public good. We focused on TTSS-1 expression as the phenotypic trait that is expressed stochastically, and tested three main assumptions of the mathematical model (Fig. 2; see Supplementary Information for experimental methods).

Our experimental results show that: first, in a clonal population of *S. typhimurium*, in the gut lumen, only about 15% were phenotypically TTSS-1<sup>+</sup>, which is in line with *in vitro* studies<sup>26,27</sup>. In contrast, almost all bacteria in the gut tissue expressed the TTSS-1<sup>+</sup> phenotype (Fig. 2a,b). This supports the assumption that TTSS-1 expression is variable in clonal populations of *S. typhimurium*, and that the TTSS-1 phenotype of a bacterium determines whether or not it will invade the gut tissue. (Other invasion factors probably also have an important role; TTSS-1 expression is therefore required but not sufficient for invasion.) Second, the intensity of inflammation increases as the proportion of bacteria that are capable of expressing the cooperative TTSS-1<sup>+</sup> phenotype increases (Fig. 2c,d). Taking inflammation as a proxy for the public good, this supports the assumption that the public good produced increases with increasing numbers of cooperators. Third, in the *S. typhimurium* enterocolitis model, most of the bacteria that invade the gut tissue and thereby contribute to the public good seem to be killed by the intestinal innate immune defenses (Fig. 2e, f). Thus, cooperation through invasion of the gut tissue is a largely self-destructive act.

Together, these experimental results indicate that the mathematical model of self-destructive cooperation mediated by phenotypic noise captures central features of *S. typhimurium* enterocolitis. This gives a new perspective on how these and similar pathogens evolve self-destructive cooperative acts to infect their hosts. Our model predicts that this behaviour can evolve if the number of pathogens that infect a host is small. This number corresponds to the parameter  $M$ , and if  $M$  is small then bacteria that carry the genotype for stochastic cooperation without expressing this behaviour are surrounded by many cells with the same genotype that do cooperate, and hence this genotype will thrive. A first estimate for  $M$  is the number of bacteria required for an infection to establish. For *Salmonella* spp. and *Escherichia coli* infecting humans, estimates can reach levels as low as one hundred<sup>28</sup>. Mortality during the passage through the stomach, as well as spatial structure of the environment from which the inoculum originates, can lead to a small effective  $M$  even if the infective dose is substantial. Over evolutionary time, a small  $M$  leads to the evolution of larger probabilities to express the cooperative act (Fig. 1) and, as one can easily show mathematically, to larger payoffs. This is in line with previous theoretical findings that clonal infections are beneficial for pathogens, whereas coinfection tends to be detrimental<sup>29</sup>.

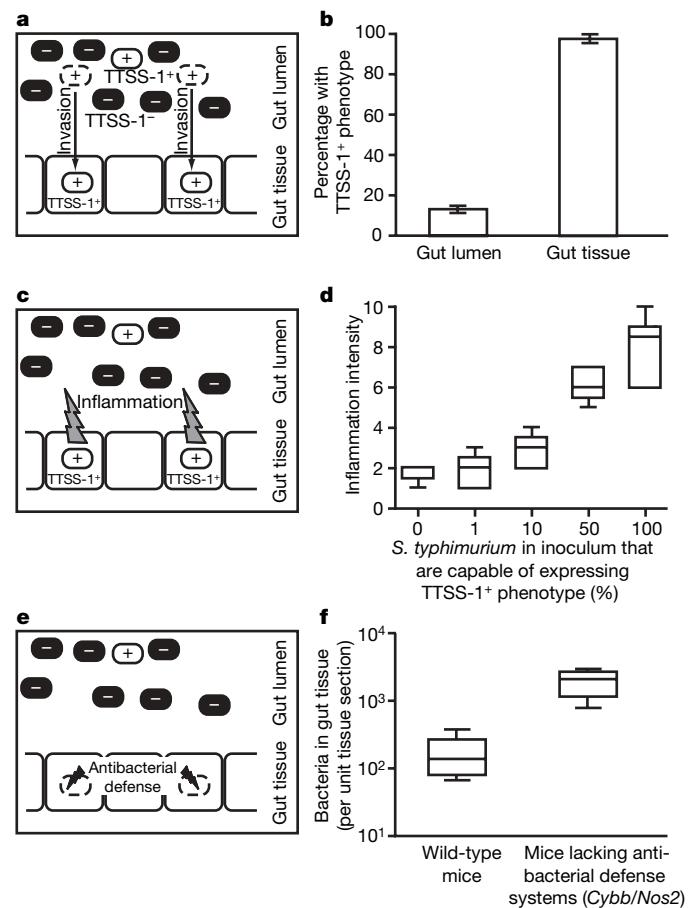


**Figure 2 | Testing biological assumptions of self-destructive cooperation mediated by phenotypic noise with a mouse model for *S. typhimurium* enterocolitis.** For experimental details, see Supplementary Information. **a**, The clonal bacterial population consists of two phenotypes; one of them (TTSS-1<sup>+</sup>; white) expresses a cooperative act consisting of gut tissue invasion. **b**, We analysed the TTSS-1 phenotype in the gut lumen and in the gut tissue. In the gut lumen, about 15% of the bacteria were TTSS-1<sup>+</sup>; in the gut tissue, almost all bacteria were TTSS-1<sup>+</sup> (Mann–Whitney U test for a difference between lumen and tissue,  $P < 0.001$ ; error bars, s.e.m.). The luminal *S. typhimurium* population differentiates into TTSS-1<sup>+</sup> and TTSS-1<sup>-</sup> phenotypes, and the TTSS-1<sup>+</sup> phenotype invades the gut tissue. **c**, The amount of public good generated in an interaction group increases with an increasing number of cooperators. In the context of *S. typhimurium* infection, the public good is gut inflammation elicited by tissue invasion. **d**, To vary the number of bacteria that commit the cooperative act, we mixed wild-type *S. typhimurium* that express both TTSS-1<sup>+</sup> and TTSS-1<sup>-</sup> phenotypes (see **b**) with an isogenic strain that is incapable of expressing the TTSS-1<sup>+</sup> phenotype ( $\Delta$ TTSS-1). The intensity of gut inflammation increased with an increasing fraction of wild-type *S. typhimurium* in the inoculum (box plots with median, quartiles and range; Spearman's rank correlation,  $P < 0.001$ ). Gut inflammation increases with an increasing number of individuals that express the cooperative act of tissue invasion. **e**, Contributing to the public good is a self-destructive act. In the context of *S. typhimurium* infection, most bacteria invading the gut tissue are expected to be killed by antimicrobial defence mechanisms, specifically by the *Cybb/Nos2*-encoded systems generating antimicrobial oxygen and nitrogen radicals. **f**, To test whether bacteria that invade the gut tissue are killed, we compared *S. typhimurium* loads in the gut tissue of wild-type mice and of mutant mice lacking the *Cybb/Nos2* systems. The bacterial loads in the gut tissue in wild-type mice were about ten times lower than in the *Cybb/Nos2*-knockout mice (box plots with median, quartiles and range; Mann–Whitney U test,  $P = 0.008$ ; in the gut lumen, bacterial loads were not significantly different; see Supplementary Information). This suggests that in wild-type mice, most bacteria that invade the gut tissue are killed. Thus, triggering of gut inflammation by tissue invasion can be regarded as a self-destructive act.

Self-destructive cooperation can be seen as an extreme form of the division of labour between two phenotypes, in which one of the phenotypes does not survive. The two phenotypes are encoded by the same genotype, which can persist because the expression of the self-destructive phenotype is stochastic. We thus conclude that self-destructive cooperation is a plausible biological explanation for certain instances of phenotypic noise. Establishing a link between phenotypic noise and cooperation gives new insights into how cooperation can persist despite its cost for the benefactor. At the same time, this link provides a new perspective into the significance of phenotypic noise in biological systems, and especially in microbial pathogens. Understanding why so many pathogens exhibit stochastic phenotypic variation is essential for developing efficient strategies for their control.

Received 13 March; accepted 6 May 2008.

1. Raser, J. M. & O'Shea, E. K. Noise in gene expression: origins, consequences, and control. *Science* **309**, 2010–2013 (2005).
2. Kaern, M., Elston, T. C., Blake, W. J. & Collins, J. J. Stochasticity in gene expression: from theories to phenotypes. *Nature Rev. Genet.* **6**, 451–464 (2005).
3. Dubnau, D. & Losick, R. Bistability in bacteria. *Mol. Microbiol.* **61**, 564–572 (2006).
4. Bull, J. J. Evolution of phenotypic variance. *Evolution* **41**, 303–315 (1987).
5. Kussell, E., Kishony, R., Balaban, N. Q. & Leibler, S. Bacterial persistence: a model of survival in changing environments. *Genetics* **169**, 1807–1814 (2005).
6. Wolf, D. M., Vazirani, V. V. & Arkin, A. P. A microbial modified prisoner's dilemma game: how frequency-dependent selection can lead to random phase variation. *J. Theor. Biol.* **234**, 255–262 (2005).
7. Nowak, M. A. Five rules for the evolution of cooperation. *Science* **314**, 1560–1563 (2006).
8. Hauert, C. & Doebeli, M. Spatial structure often inhibits the evolution of cooperation in the snowdrift game. *Nature* **428**, 643–646 (2004).
9. Nowak, M. & Sigmund, K. The evolution of stochastic strategies in the Prisoner's Dilemma. *Acta Appl. Math.* **20**, 247–265 (1990).
10. Dieckmann, U. & Law, R. The dynamical theory of coevolution: a derivation from stochastic ecological processes. *J. Math. Biol.* **34**, 579–612 (1996).
11. Metz, J. A. J., Geritz, S. A. H., Meszena, G., Jacobs, A. & van Heerwaarden, J. S. in *Stochastic and Spatial Structures of Dynamical Systems* (eds van Strien, S. J. & Verduyn, S. M.) 183–231 (North Holland, Amsterdam, 1996).
12. Charlesworth, B. Some models of the evolution of altruistic behaviour between siblings. *J. Theor. Biol.* **72**, 297–319 (1978).
13. Avery, S. V. Microbial cell individuality and the underlying sources of heterogeneity. *Nature Rev. Microbiol.* **4**, 577–587 (2006).
14. Paton, J. C. The contribution of pneumolysin to the pathogenicity of *Streptococcus pneumoniae*. *Trends Microbiol.* **4**, 103–106 (1996).
15. Wagner, P. L. et al. Bacteriophage control of Shiga toxin 1 production and release by *Escherichia coli*. *Mol. Microbiol.* **44**, 957–970 (2002).
16. Voth, D. E. & Ballard, J. D. *Clostridium difficile* toxins: mechanism of action and role in disease. *Clin. Microbiol. Rev.* **18**, 247–263 (2005).
17. Lysenko, E. S., Ratner, A. J., Nelson, A. L. & Weiser, J. N. The role of innate immune responses in the outcome of interspecies competition for colonization of mucosal surfaces. *PLoS Pathog.* **1**, e1 (2005).
18. Raberg, L. et al. The role of immune-mediated apparent competition in genetically diverse malaria infections. *Am. Nat.* **168**, 41–53 (2006).
19. Brown, S. P., Le Chat, L. & Taddei, F. Evolution of virulence: triggering host inflammation allows invading pathogens to exclude competitors. *Ecol. Lett.* **11**, 44–51 (2007).
20. Stecher, B. & Hardt, W.-D. The role of microbiota in infectious disease. *Trends Microbiol.* **16**, 107–114 (2008).
21. Ogunningyi, A. D., Grabowicz, M., Briles, D. E., Cook, J. & Paton, J. C. Development of a vaccine against invasive pneumococcal disease based on combinations of virulence proteins of *Streptococcus pneumoniae*. *Infect. Immun.* **75**, 350–357 (2007).
22. Lima, A. A. M., Lyerly, D. M., Wilkins, T. D., Innes, D. J. & Guerrant, R. L. Effects of *Clostridium difficile* toxins A and B in rabbit small and large intestine *in vivo* and on cultured cells *in vitro*. *Infect. Immun.* **56**, 582–588 (1988).
23. Rodemann, J. F., Dubberke, E. R., Reske, K. A., Seo, D. H. & Stone, C. D. Incidence of *Clostridium difficile* infection in inflammatory bowel disease. *Clin. Gastroenterol. Hepatol.* **5**, 339–344 (2007).
24. Stecher, B. et al. *Salmonella enterica* serovar Typhimurium exploits inflammation to compete with the intestinal microbiota. *PLoS Biol.* **5**, e244 (2007).
25. Cummings, L. A., Wilkerson, W. D., Bergsbaken, T. & Cookson, B. T. *In vivo*, fliC expression by *Salmonella enterica* serovar Typhimurium is heterogeneous, regulated by ClpX, and anatomically restricted. *Mol. Microbiol.* **61**, 795–809 (2006).
26. Hautefort, I., Proenca, M. J. & Hinton, J. C. D. Single-copy green fluorescent protein gene fusions allow accurate measurement of *Salmonella* gene expression *in vitro* and during infection of mammalian cells. *Appl. Environ. Microbiol.* **69**, 7480–7491 (2003).
27. Schlumberger, M. C. et al. Real-time imaging of type III secretion: *Salmonella* SipA injection into host cells. *Proc. Natl. Acad. Sci. USA* **102**, 12548–12553 (2005).
28. Kothary, M. H. & Babu, U. S. Infective dose of foodborne pathogens in volunteers: A review. *J. Food Saf.* **21**, 49–73 (2001).
29. May, R. M. & Nowak, M. A. Coinfection and the evolution of parasite virulence. *Proc. Biol. Sci.* **261**, 209–215 (1995).

**Supplementary Information** is linked to the online version of the paper at [www.nature.com/nature](http://www.nature.com/nature).

**Acknowledgements** We are grateful to Markus Schlumberger, K. Aktories, I. Just, S. Hammerschmidt and J. Fletcher for discussions, and M. Barthel and the RCHCI team for professional help with the animal experiments. M.A. and N.E.F. were supported by the Swiss National Science Foundation, and M.A. was also supported by the Roche Research Foundation and the Novartis Foundation. M.D. is supported by NSERC (Canada). B.S. and W.-D.H. were supported by the UBS foundation. *Salmonella* work in the Hardt laboratory is supported by grants from the ETH research foundation (TH-10 06-1), the Swiss National Science Foundation (310000-113623/1) and the European Union (SavinMucoPath number 032296).

**Author Contributions** M.A., W.-D.H. and M.D. formulated the question; M.A. and M.D. wrote the mathematical model; M.D. analysed the mathematical model; M.A., B.S., N.E.F. and W.-D.H. planned the experiments and interpreted the results; B.S. performed the experiments for Fig. 2b, d; P.S. performed the experiment for Fig. 2f; and M.A., W.-D.H. and M.D. wrote the manuscript.

**Author Information** Reprints and permissions information is available at [www.nature.com/reprints](http://www.nature.com/reprints). Correspondence and requests for materials should be addressed to M.A. (martin.ackermann@env.ethz.ch), W.-D.H. (hardt@micro.biol.ethz.ch) or M.D. (doebeli@zoology.ubc.ca).

# Significant contribution of Archaea to extant biomass in marine subsurface sediments

Julius S. Lipp<sup>1</sup>, Yuki Morono<sup>2</sup>, Fumio Inagaki<sup>2</sup> & Kai-Uwe Hinrichs<sup>1</sup>

Deep drilling into the marine sea floor has uncovered a vast sedimentary ecosystem of microbial cells<sup>1,2</sup>. Extrapolation of direct counts of stained microbial cells to the total volume of habitable marine subsurface sediments suggests that between 56 Pg (ref. 1) and 303 Pg (ref. 3) of cellular carbon could be stored in this largely unexplored habitat. From recent studies using various culture-independent techniques, no clear picture has yet emerged as to whether Archaea or Bacteria are more abundant in this extensive ecosystem<sup>4–7</sup>. Here we show that in subsurface sediments buried deeper than 1 m in a wide range of oceanographic settings at least 87% of intact polar membrane lipids, biomarkers for the presence of live cells<sup>7,8</sup>, are attributable to archaeal membranes, suggesting that Archaea constitute a major fraction of the biomass. Results obtained from modified quantitative polymerase chain reaction and slot-blot hybridization protocols support the lipid-based evidence and indicate that these techniques have previously underestimated archaeal biomass. The lipid concentrations are proportional to those of total organic carbon. On the basis of this relationship, we derived an independent estimate of amounts of cellular carbon in the global marine subsurface biosphere. Our estimate of 90 Pg of cellular carbon is consistent, within an order of magnitude, with previous estimates, and underscores the importance of marine subsurface habitats for global biomass budgets.

The discovery of a subsurface biosphere in deeply buried marine sediments has fundamentally influenced our view of life on Earth. Microbial life has been found down to at least 800 m below the sea floor in sediments that were deposited tens of millions of years ago<sup>1</sup>. Recent work resulting from dedicated drilling expeditions suggests a remarkable diversity of both Archaea and Bacteria and has revealed some systematic links between the abundance and structure of microbial communities and sediment geochemistry<sup>5,7,9,10</sup>. However, in intensively studied subsurface sediments at the Peru margin, culture-independent studies could not resolve whether Archaea or Bacteria are more abundant and whether they are being detected with equal efficiency<sup>4–7,9</sup>.

Phospholipid-based fatty acids (PLFAs)—molecular building blocks of cell membranes—were introduced and validated as a measure for live bacterial biomass<sup>11</sup> because they are rapidly degraded after cell death. This concept was extended to the analysis of intact phospho- and glycolipids to also detect biomass from Archaea, which were discriminated against by the PLFA approach<sup>7,8</sup>. These intact polar lipids (IPLs) have a finite lifetime after cell death that is considered to be short on geological timescales. Hence, IPLs should provide a robust basis for estimating biomass and broadly constraining the phylogenetic affiliation of the major contributors to the pool of biomass in natural ecosystems<sup>7,8,12–14</sup>.

By combining lipid- and DNA-based approaches that were specifically designed and modified to meet the analytical requirements of

the deep marine subsurface, we have obtained evidence suggesting that Archaea contribute substantially to the microbial biomass residing in this habitat (Fig. 1). In subsurface sediment samples spanning a depth range from 0.01 m to 367 m below the sea floor from sites in the Black Sea, Nankai trough, Peru margin, Hydrate ridge, Cascadia margin, Juan de Fuca, Demerara rise and Equatorial Pacific (see Supplementary Table 1), concentrations of IPLs declined with depth, exhibiting a statistically significant ( $P < 0.0001$ ) linear relationship between  $\log(\text{depth})$  and  $\log[\text{IPL}]$ , by analogy with a global data set of directly counted cells (Fig. 1a; ref. 1). The observed IPL concentrations

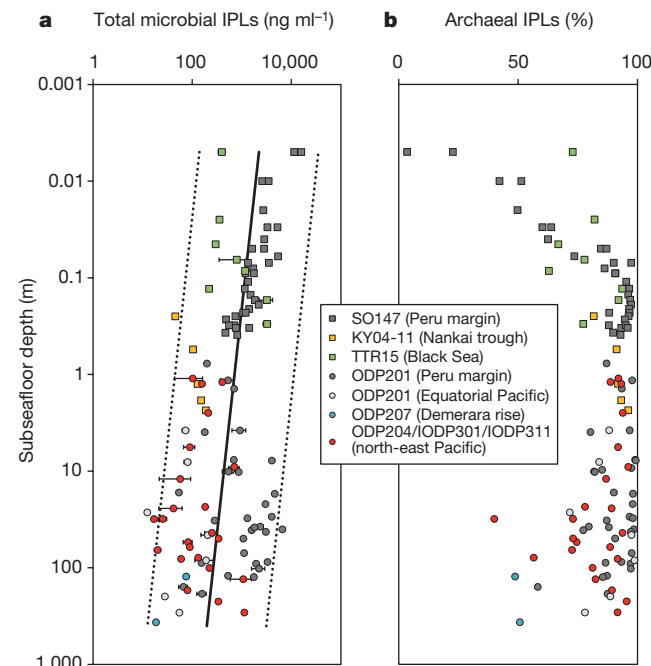


**Figure 1 | Depth profiles of IPLs in marine sediments.** **a**, Concentration of total IPLs versus depth. Error bars show the standard deviation of repeated injection of total lipid extracts. Regression lines show total microbial IPLs (solid line,  $\log[\text{IPL}]_{\text{total}} = -0.214 \times \log(\text{depth}) + 2.853$ ,  $N = 104$ ,  $R^2 = 0.20$ ,  $P < 0.0001$ ) and 95% prediction interval (dotted lines, standard error of estimate, 0.60), both of which are generated using least-squares analysis. **b**, Relative contribution of archaeal IPLs to total microbial IPLs. The limit of detection was assumed to be the bacterial proportion for samples without detectable bacterial IPLs (see Supplementary Methods). This treatment results in the artificial scatter and a seemingly increasing proportion of Bacteria at greater sediment depth owing to generally decreasing IPL concentrations and the resulting less favourable analytical conditions. Actual bacterial contributions are probably lower.

<sup>1</sup>Organic Geochemistry Group, Department of Geosciences and MARUM Center for Marine Environmental Sciences, University of Bremen, PO Box 330 440, 28334 Bremen, Germany.

<sup>2</sup>Geomicrobiology Group, Kochi Institute for Core Sample Research, Japan Agency for Marine-Earth Science and Technology (JAMSTEC), Monobe B200, Nankoku, Kochi 783-8502, Japan.

cover more than three orders of magnitude from  $12 \text{ ng ml}^{-1}$  to  $16,000 \text{ ng ml}^{-1}$  sediment. Using published conversion factors for lipid mass and cell numbers<sup>15</sup>, these values correspond to an estimated range of cell concentrations of  $9 \times 10^6 \text{ ml}^{-1}$  to  $1 \times 10^{10} \text{ ml}^{-1}$  (assuming cells of  $0.5 \mu\text{m}$  diameter, ref. 7; see Supplementary Methods). These ranges are consistent with those resulting from direct cell counts in marine subsurface environments<sup>2,4,10</sup>.

Surface sediments are dominated by bacterial IPLs with possible admixtures of eukaryotic lipids (Fig. 1b). The major bacterial IPLs identified comprise diacylglyceride derivatives of phosphatidylglycerol, phosphatidylethanolamine and phosphatidylcholine with  $C_{16}$  and  $C_{18}$  acyl groups (see Supplementary Fig. 1). The major archaeal lipids, generally dominant in sediments deeper than 0.1 m below the sea floor, are diglycosidic derivatives of archaeol and glycerol dibiphytanyl glycerol tetraether (GDGT) lipids (see Supplementary Fig. 1). The distribution of polar headgroups, the presence of glycerol dibiphytanyl nonitol tetraether (GDNT) derivatives, and a relatively high abundance of GDGT core lipids with multiple rings indicate a substantial contribution of crenarchaeota<sup>7</sup>. RNA- and DNA-based gene libraries in these environments are consistent with the lipid-based evidence and attest the widespread presence of phylogenetically diverse Archaea affiliated with the marine benthic group B (alternatively classified as deep-sea archaeal group), the South African gold mine euryarchaeotal group and the miscellaneous crenarchaeotal group<sup>5,7,9,10,16</sup>. Concentrations of bacterial IPLs decline rapidly within the first 0.1 m below the sea floor to levels significantly lower than those of their archaeal counterparts (Fig. 1b).

Does this apparent archaeal dominance result from selective preservation of fossil archaeal lipids and/or analytical discrimination of bacterial lipids, or are archaeal cells much more abundant in deeply buried sediments? Several points argue against selective preservation and discrimination.

Absence of discrimination of bacterial lipids is indicated by the consistency of results obtained from analysis of both PLFAs and IPLs in selected samples (see Supplementary Table 3) and by tests of extraction efficiencies (see Supplementary Fig. 2). Low PLFA concentrations are in agreement with the generally low concentrations found in other studies in samples deeper than 10 m below the sea floor<sup>17,18</sup>; these are too low to account for the typical range of observed cell concentrations (see Supplementary Table 3). There is no evidence that glycosidic lipids—that is, those generally dominating in subsurface sediments—preferentially accumulate. For example, glycolipids produced by marine algae and cyanobacteria<sup>19</sup> were not detected in our sample set, even in the uppermost sediment layers situated in the anoxic Black Sea and the oxygen minimum zone off Peru, thus indicating that they were degraded promptly even under anoxic conditions. This rapid removal is probably due to their exposure to extracellular enzymes that are produced by sedimentary microorganisms for catalysing the initial hydrolytic steps of substrate degradation. These enzymes hydrolyse glycosidic bonds in polymeric carbohydrates rapidly on the order of days to weeks<sup>20</sup> and are likely to catalyse the same reactions in glycosidic IPLs. Rapid turnover of glycosidic archaeal IPLs under natural conditions is also evident from a previous study<sup>21</sup> in which anaerobic methanotrophic mats from the anoxic Black Sea were analysed; it was shown elegantly that certain areas of the mat are dominated by non-intact GDGTs rather than intact, diglycosidic GDGTs, consistent with rapid hydrolysis of glycosidic bonds after cell death. Moreover, the distribution of archaeal core lipids in the pool of IPLs is clearly distinct from that of their non-intact, fossil GDGTs (data not shown), suggesting that the extant archaeal population differs from the fossil population consisting of fossil planktonic and/or fossil sedimentary species deposited during earlier stages of the sediment's history. Hypothetically, a systematic bias could result from differences in relative stabilities of archaeal and bacterial IPLs. For example, if the ratio of the turnover of archaeal IPLs relative to turnover of archaeal cells is twice as high as the analogous ratio for Bacteria, the fraction of non-cellular—that is,

fossil, archaeal IPLs—is expected to be twice as high as for bacterial IPLs. However, as long as IPL turnover is fast relative to community turnover times of up to  $100,000 \text{ yr}^{22}$ , the overall contribution of non-cellular IPLs will be small and, independent of relative differences in stability, IPLs will largely record extant biomass.

Improved protocols of DNA extraction and purification, and the quantification protocols of slot-blot hybridization and quantitative polymerase chain reaction (Q-PCR; see Supplementary Methods) of samples from the Peru margin (ODP leg 201) and the Juan de Fuca ridge flank (IODP expedition 301), indicate that previous analyses of similar and identical samples largely underestimated archaeal biomass<sup>4,5</sup> (Fig. 2 and Supplementary Table 2). Similarly high abundances of Archaea were observed at a methane-hydrate-bearing site off Japan (CK06-06; Fig. 2). Detection of archaeal DNA has improved relative to earlier studies because the efficiency of cell lysis during DNA extraction of mechanically rigid archaeal cells has increased (see Supplementary Fig. 3), and quality control of template DNA after extraction and purification using multiple displacement amplification with phi29 polymerase (see Supplementary Fig. 4) yields highly pure, inhibitor-free DNA. Also, previously applied protocols for signal detection and quantification potentially discriminated against sequences from sedimentary Archaea<sup>23</sup>, and 16S ribosomal RNA gene copy numbers are lower in archaeal relative to bacterial genomes<sup>24</sup>. Even though the DNA-based estimates of relative amounts of archaeal biomass in these environments increased by an order of magnitude relative to previous studies<sup>4,5</sup>, we note that the new data result in minimum estimates of the archaeal contribution.

What is the significance of an archaeal-dominated subsurface ecosystem? On the basis of empirical and theoretical consideration, it was recently<sup>25</sup> argued that Archaea should be better adapted than Bacteria to extreme low-energy conditions such as those found in the deep biosphere, whereas Bacteria are more successful in dynamic environments. Specifically, it was suggested that the lower membrane permeability resulting from the lipid structure lowers the demand for maintenance energy of an archaeal cell relative to a bacterial cell. Consequently, we suggest that even if the available free energy were to be evenly shared between Archaea and Bacteria, the lower energy

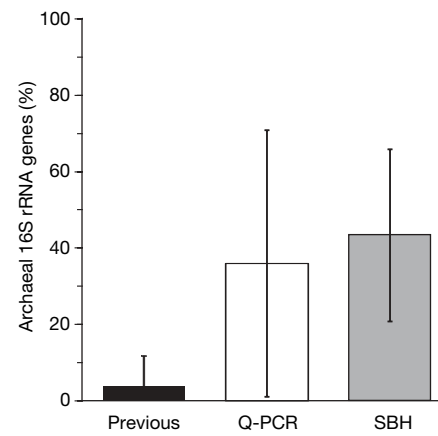


**Figure 2 | Relative abundance of archaeal 16S rRNA genes to total archaeal and bacterial 16S rRNA genes.** New results obtained by Q-PCR and slot-blot hybridization (SBH) using genomic DNA amplified with phi29 polymerase as reaction template in combination with improved DNA extraction and detection protocols are significantly greater ( $P < 0.001$ ) than previously reported data generated by Q-PCR (refs 4, 5). Bars show the averages of individual values (see Supplementary Table 2; Q-PCR,  $N = 32$ ; SBH,  $N = 33$ ; previously reported data,  $N = 93$ ) with corresponding standard deviations shown as error bars. Individual values are shown in Supplementary Table 2. The primer sets of Bac27F/EUB338R-I and ARC806F/ARC958R were used for Q-PCR amplification, and detection of 16S rRNA genes in SBH was done with EUB338-I, II, III and ARC915 probes labelled with digoxigenin (see Supplementary Methods).

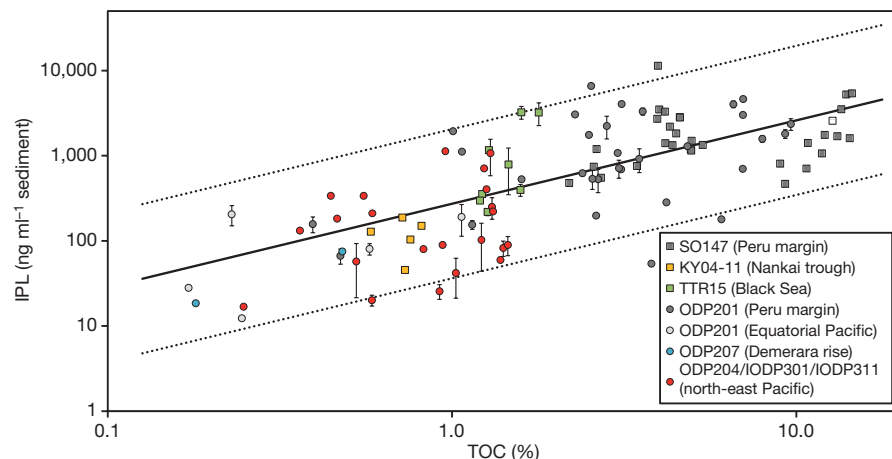


**Figure 3 | Correlation of concentrations of IPLs and TOC.** Error bars show standard deviation of repeated injection of total lipid extracts. Regression lines show  $\log[\text{IPL}]_{\text{total}}$  versus  $\log[\text{TOC}]$  (solid line;  $\log[\text{IPL}]_{\text{total}} = 0.979 \times \log[\text{TOC}] + 2.436$ ,  $N = 101$ ,  $R^2 = 0.56$ ,  $P < 0.0001$ , least squares analysis) and 95% prediction interval (dotted line, standard error of estimate: 0.44).

requirement of Archaea for maintaining cell integrity under conditions of limited energy availability would result in longer life cycles, longer community-turnover times, and thus larger standing stocks compared with Bacteria. Hence, although Archaea are more abundant than Bacteria, they do not necessarily rule the biogeochemical processes in the deep subsurface.

The sedimentary IPLs may be used as a proxy for the quantity of live microbial biomass in subsurface environments. We observed a statistically significant ( $P < 0.0001$ ) double logarithmic relationship between [IPL] and total organic carbon [TOC], extending over more than two and four orders of magnitude in [TOC] and [IPL] (Fig. 3,  $n = 101$ ,  $R^2 = 0.56$ ), respectively, and testifying to the heterotrophic nature of the subsurface ecosystem. The relationship further indicates that the quantity of fossil organic matter is an important controlling factor for the amount of microbial biomass.

This relationship can be used to derive an estimate of the global inventory of biomass in marine subsurface sediments from well constrained concentrations of TOC. Although we currently do not have representation of the most oligotrophic open-ocean sites in our sample set, we consider this approach to be less susceptible to biases in sample selection towards continental margins than previously used relationships based on cell counts versus depth<sup>1,3</sup>. We estimate that microbes inhabit a global marine sediment volume of  $193 \times 10^6 \text{ km}^3$  (see Supplementary Methods for details regarding calculations). Using a combination of regional distributions of TOC concentrations in surface sediments<sup>26</sup> and diagenetic models describing the degradation of TOC with time<sup>27</sup>, we derived an average TOC content in habitable subsurface sediments of 0.13% (see Supplementary Tables 4 and 5). This value is identical to a recent estimate of the average TOC content in subducting sediment<sup>28</sup>. It results in a quantity of TOC in habitable subsurface sediments of  $4 \times 10^5 \text{ Pg}$ —that is,  $\sim 2.5\%$  of the estimated TOC in Earth's crust<sup>29</sup>. For the amount of IPL in the respective sediment volume, we obtain 7.1 Pg IPL (Table 1, see Supplementary Methods), which can be converted into 90 Pg of microbial biomass C (assuming spherical cells with a diameter of 0.5  $\mu\text{m}$ , see Supplementary Methods for information on the influence of cell size). The inherent uncertainties resulting from the data scatter of the 95% prediction intervals in the  $\log[\text{IPL}]$ – $\log[\text{TOC}]$  relationship ( $\pm 0.9$  orders of magnitude) are comparable to those

encountered in  $\log[\text{cells}]$ – $\log(\text{depth})$  relationships previously used for estimating marine subsurface biomass ( $\pm 1$  order of magnitude)<sup>1,3</sup>.

We provide a refined and independent view on the quantity and composition of marine subsurface biomass. Our results suggest a vast ecosystem, in which Archaea contribute a major fraction of the standing stock of biomass. The environmental functions, strategies of survival and growth in extremely low-energy flux habitats, and physiologies of the key phylogenetic groups that presumably contribute largely to this biomass pool, remain to be clarified. In combination with estimates of the relative contributions of the two taxonomic domains to water column biomass<sup>3,30</sup>, our data imply that, in the marine realm, Archaea are more abundant than Bacteria.

## METHODS SUMMARY

Sub-seafloor sediment samples were collected from various cruises (see Supplementary Table 1) and were immediately frozen and stored at  $-80^\circ\text{C}$  until processing. Frozen sediment was extracted using a modified Bligh and Dyer protocol and analysed by HPLC coupled to an ion-trap mass spectrometer following details published earlier<sup>8</sup>. Concentrations of individual IPLs were calculated from mass chromatograms relative to the peak area of known quantity of internal standard and under consideration of individual response factors (see Supplementary Methods). PLFAs were analysed by gas chromatography–mass spectrometry (GC-MS) as fatty acid methyl esters after mild alkaline methanolysis of the polar fraction. DNA was extracted using ISOIL for Beads Beating Kit (Nippon Gene) after crushing frozen sediments in a mill cooled with liquid nitrogen to maximize physical cell disruption. Cell disruption efficiency was monitored by epifluorescence microscopy with SYBR Green I (see Supplementary Methods and Supplementary Fig. 4). The DNA was purified and amplified by multiple displacement amplification using phi29 polymerase before analysis with Q-PCR and slot-blot hybridization (see Supplementary Methods). Estimates of the carbon sequestered in cellular carbon of marine subsurface microbes are based on the correlation of [IPL] and [TOC] (Fig. 3). Global TOC quantities in marine sediments habitable by microbes were estimated on the basis of modern concentrations of TOC in surface sediments<sup>26</sup>, a diagenetic model describing the degradation of organic carbon with time<sup>27</sup>, and a global volume of habitable sediments resulting from the assumption that temperature is the major variable limiting microbial life at great depth<sup>3</sup>. The resulting inventory of cellular lipids was transferred into a carbon inventory of marine subsurface cells using published conversion factors<sup>15</sup> (see Supplementary Methods).

Received 12 March; accepted 17 June 2008.

Published online 20 July 2008.

**Table 1 | Estimate of TOC and biomass in habitable marine sediment**

	Open ocean	Continental margin	World ocean
TOC average; range (%)	0.099; 0.07–0.56	0.204; 0.16–0.95	0.129
Amount of TOC (Pg)	$2.0 \times 10^5$	$1.7 \times 10^5$	$3.7 \times 10^5$
Amount of IPL (Pg)	3.9	3.2	7.1
Biomass C (Pg), 500-nm cells	50	40	90

Estimates are derived from diagenetic modelling (see Supplementary Methods) of concentrations at the sediment surface<sup>26</sup>, resulting total inventories of TOC and IPL, and total inventories of microbial biomass C for a hypothetical cell diameter of 500 nm.

1. Parkes, R. J. *et al.* Deep bacterial biosphere in Pacific Ocean sediments. *Nature* 371, 410–413 (1994).
2. D'Hondt, S. *et al.* Distributions of microbial activities in deep subseafloor sediments. *Science* 306, 2216–2221 (2004).
3. Whitman, W. B., Coleman, D. C. & Wiebe, W. J. Prokaryotes: the unseen majority. *Proc. Natl. Acad. Sci. USA* 95, 6578–6583 (1998).
4. Schippers, A. *et al.* Prokaryotic cells of the deep sub-seafloor biosphere identified as living bacteria. *Nature* 433, 861–864 (2005).
5. Inagaki, F. *et al.* Biogeographical distribution and diversity of microbes in methane hydrate-bearing deep marine sediments on the Pacific Ocean Margin. *Proc. Natl. Acad. Sci. USA* 103, 2815–2820 (2006).

6. Mauclaire, L., Zepp, K., Meister, P. & McKenzie, J. Direct *in situ* detection of cells in deep-sea sediment cores from the Peru Margin (ODP Leg 201, Site 1229). *Geobiology* 2, 217–223 (2004).
7. Biddle, J. F. *et al.* Heterotrophic Archaea dominate sedimentary subsurface ecosystems off Peru. *Proc. Natl. Acad. Sci. USA* 103, 3846–3851 (2006).
8. Sturt, H. F., Summons, R. E., Smith, K. J., Elvert, M. & Hinrichs, K.-U. Intact polar membrane lipids in prokaryotes and sediments deciphered by high-performance liquid chromatography/electrospray ionization multistage mass spectrometry—new biomarkers for biogeochemistry and microbial ecology. *Rap. Comm. Mass. Spec.* 18, 617–628 (2004).
9. Inagaki, F. *et al.* Microbial communities associated with geological horizons in coastal subseafloor sediments from the Sea of Okhotsk. *Appl. Environ. Microbiol.* 69, 7224–7235 (2003).
10. Parkes, R. J. *et al.* Deep sub-seafloor prokaryotes stimulated at interfaces over geological time. *Nature* 436, 390–394 (2005).
11. White, D. C., Bobbie, R. J., King, J. D., Nickels, J. S. & Amoe, P. in *Methodology for Biomass Determination and Microbial Activities in Sediments* (eds Lichfeld, C. D. & Seyfried, P. L.) 87–103 (ASTM STP 673, 1979).
12. Rütters, H., Sass, H., Cypionka, H. & Rullkötter, J. Phospholipid analysis as a tool to study complex microbial communities in marine sediments. *J. Microbiol. Methods* 48, 149–160 (2002).
13. Zink, K. G., Wilkes, H., Disko, U., Elvert, M. & Horsfield, B. Intact phospholipids—microbial “life markers” in marine deep subsurface sediments. *Org. Geochem.* 34, 755–769 (2003).
14. Fredricks, H. F. & Hinrichs, K.-U. Data report: intact membrane lipids as indicators of subsurface life in Cretaceous and Paleogene sediments from Sites 1257 and 1258. *Proc. ODP Sci. Res.* 207, doi:10.2973/odp.proc.sr.207.112.2007 (2007).
15. Simon, M. & Azam, F. Protein content and protein synthesis rates of planktonic marine bacteria. *Mar. Ecol. Prog. Ser.* 51, 201–213 (1989).
16. Teske, A. P. Microbial communities of deep marine subsurface sediments: molecular and cultivation surveys. *Geomicrobiol. J.* 23, 357–368 (2006).
17. Summit, M., Peacock, A., Ringelberg, D., White, D. C. & Baross, J. A. Phospholipid fatty acid-derived microbial biomass and community dynamics in hot, hydrothermally influenced sediments from the Middle Valley, Juan de Fuca Ridge. *Proc. ODP Sci. Res.* 169, doi:10.2973/odp.proc.sr.169.117.2000 (2000).
18. Cardace, D., Morris, J. D., Peacock, A. D. & White, D. C. Habitability of subseafloor sediments at the Costa Rica Convergent Margin. *Proc. ODP Sci. Res.* 205, doi:10.2973/odp.proc.sr.205.213.2006 (2006).
19. Van Mooy, B. A. S., Rocap, G., Fredricks, H. F., Evans, C. T. & Devol, A. H. Sulfolipids dramatically decrease phosphorus demand by picocyanobacteria in oligotrophic marine environments. *Proc. Natl. Acad. Sci. USA* 103, 8607–8612 (2006).
20. Arnosti, C. & Jørgensen, B. B. Organic carbon degradation in arctic marine sediments, Svalbard: A comparison of initial and terminal steps. *Geomicrobiol. J.* 23, 551–563 (2006).
21. Thiel, V. *et al.* Biomarkers at the microscopic range: ToF-SIMS molecular imaging of Archaea-derived lipids in a microbial mat. *Geobiology* 5, 413–421 (2007).
22. Parkes, R. J., Cragg, B. A. & Wellsbury, P. Recent studies on bacterial populations and processes in subseafloor sediments: a review. *Hydrogeol. J.* 8, 11–28 (2000).
23. Teske, A. & Sørensen, K. B. Uncultured archaea in deep marine subsurface sediments: have we caught them all? *ISME J.* 2, 3–18 (2008).
24. Acinas, S. G., Marcelino, L., Klepac-Cera, V. & Polz, M. F. Divergence and redundancy of 16S rRNA sequences in genomes with multiple *rrn* operons. *J. Bact.* 186, 2629–2635 (2004).
25. Valentine, D. L. Adaptations to energy stress dictate the ecology and evolution of the Archaea. *Nature Rev. Microbiol.* 5, 316–323 (2007).
26. Seiter, K., Hensen, C., Schröter, J. & Zabel, M. Organic carbon content in surface sediments—defining regional provinces. *Deep-Sea Res. I* 51, 2001–2026 (2004).
27. Middelburg, J. J., Vlug, T. & van der Nat, F. J. W. A. Organic matter mineralization in marine systems. *Glob. Plan. Change* 8, 47–58 (1993).
28. Hayes, J. M. & Waldbauer, J. R. The carbon cycle and associated redox processes through time. *Phil. Trans. R. Soc. B.* 361, 931–950 (2006).
29. Sigman, D. M. & Boyle, E. A. Glacial/interglacial variations in atmospheric carbon dioxide. *Nature* 407, 859–869 (2000).
30. Karner, M. B., DeLong, E. F. & Karl, D. M. Archaeal dominance in the mesopelagic zone of the Pacific Ocean. *Nature* 409, 507–510 (2001).

**Supplementary Information** is linked to the online version of the paper at [www.nature.com/nature](http://www.nature.com/nature).

**Acknowledgements** Samples for this research were provided by the Integrated Ocean Drilling Program (IODP, expeditions 301 and 311), the Ocean Drilling Program (ODP, legs 201, 204 and 207; sponsored by the US National Science Foundation and participating countries under the Joint Oceanographic Institutions, Inc.), and cruises Sonne SO147, Kaiyo KY04-11, Professor Logatchev TTR15 and Chikyu Shakedown Expedition CK06-06. We thank the participating crews and scientists for sample recovery and data; U. Proksa and N. Buchs for assistance with lipid extraction and sample preparation; J. M. Hayes and A. Teske for comments on an earlier version of this manuscript; H. F. Fredricks and F. Schubotz for discussion of data; V. Heuer, A. Schippers and T. Toki for sample donation; B. Kockisch for TOC analysis; and T. Terada and N. Masui for DNA extraction and analyses. This work was supported by Deutsche Forschungsgemeinschaft (through MARUM Center for Marine Environmental Sciences and grant Hi616-4 from the priority program IODP/ODP) and JAMSTEC Multidisciplinary Research Promotion Award 2007 (to Y.M. and F.I.). This is MARUM publication number 0585.

**Author Contributions** J.S.L., geochemical and lipid analysis, geochemical modelling, method development and paper writing; Y.M. and F.I., DNA extraction and molecular analyses; K.-U.H., study design, paper writing and geochemical modelling. All authors participated in data analysis and interpretation and provided editorial comments on the manuscript.

**Author Information** Reprints and permissions information is available at [www.nature.com/reprints](http://www.nature.com/reprints). Correspondence and requests for materials should be addressed to K.-U.H. ([khinrichs@uni-bremen.de](mailto:khinrichs@uni-bremen.de)).

## LETTERS

# Spatio-temporal correlations and visual signalling in a complete neuronal population

Jonathan W. Pillow<sup>1</sup>, Jonathon Shlens<sup>2</sup>, Liam Paninski<sup>3</sup>, Alexander Sher<sup>4</sup>, Alan M. Litke<sup>4</sup>, E. J. Chichilnisky<sup>2</sup> & Eero P. Simoncelli<sup>5</sup>

**Statistical dependencies in the responses of sensory neurons govern both the amount of stimulus information conveyed and the means by which downstream neurons can extract it. Although a variety of measurements indicate the existence of such dependencies<sup>1–3</sup>, their origin and importance for neural coding are poorly understood. Here we analyse the functional significance of correlated firing in a complete population of macaque parasol retinal ganglion cells using a model of multi-neuron spike responses<sup>4,5</sup>.** The model, with parameters fit directly to physiological data, simultaneously captures both the stimulus dependence and detailed spatio-temporal correlations in population responses, and provides two insights into the structure of the neural code. First, neural encoding at the population level is less noisy than one would expect from the variability of individual neurons: spike times are more precise, and can be predicted more accurately when the spiking of neighbouring neurons is taken into account. Second, correlations provide additional sensory information: optimal, model-based decoding that exploits the response correlation structure extracts 20% more information about the visual scene than decoding under the assumption of independence, and preserves 40% more visual information than optimal linear decoding<sup>6</sup>. This model-based approach reveals the role of correlated activity in the retinal coding of visual stimuli, and provides a general framework for understanding the importance of correlated activity in populations of neurons.

How does the spiking activity of a neural population represent the sensory environment? The answer depends critically on the structure of neuronal correlations, or the tendency of groups of neurons to fire temporally coordinated spike patterns. The statistics of such patterns have been studied in a variety of brain areas, and their significance in the processing and representation of sensory information has been debated extensively<sup>2,3,7–13</sup>.

Previous studies have examined visual coding by pairs of neurons<sup>11</sup> and the statistics of simultaneous firing patterns in larger neural populations<sup>14,15</sup>. However, no previous approach has addressed how correlated spiking activity in complete neural populations depends on the pattern of visual stimulation, or has answered the question of how such dependencies affect the encoding of visual stimuli.

Here we introduce a model-based methodology for studying this problem. We describe the encoding of stimuli in the spike trains of a neural population with a generalized linear model (Fig. 1a), a generalization of the well-known linear–nonlinear–Poisson (LNP) cascade model<sup>4,5,16,17</sup>. In this model, each cell's input is described by a set of linear filters: a stimulus filter, or spatio-temporal receptive field; a post-spike filter, which captures dependencies on spike-train history

(for example, refractoriness, burstiness and adaptation); and a set of coupling filters, which capture dependencies on the recent spiking of other cells. For each neuron, the summed filter responses are exponentiated to obtain an instantaneous spike rate. This is equivalent to exponentiating the filter outputs and then multiplying; the exponentiated post-spike and coupling filters (as plotted in Fig. 1) may therefore be interpreted as spike-induced gain adjustments of the neuron's firing rate.

Although this model is strictly phenomenological, its components can be loosely compared to biophysical mechanisms: the stimulus filter approximates the spatio-temporal integration of light in the outer retina and passive dendritic filtering; the post-spike filter mimics voltage-activated currents following a spike; coupling filters resemble synaptic or electrical interactions between cells (and can mimic the effects of shared input noise); and the exponential non-linearity implements a 'soft threshold', converting membrane potential to instantaneous spike probability. Note that the post-spike and coupling filters, which allow stochastic spiking in one cell to affect subsequent population activity, give rise to shared, non-Poisson variability in the model response.

We fit the model to data recorded *in vitro* from a population of 27 ON and OFF parasol ganglion cells (RGCs) in a small patch of isolated macaque monkey retina, stimulated with 120-Hz spatio-temporal binary white noise. The receptive fields of each of the two cell types formed a complete mosaic covering a small region of visual space (Fig. 1b), indicating that every parasol cell in this region was recorded<sup>15,18</sup>. Such complete recordings, which have not been achieved elsewhere in the mammalian nervous system, are essential for understanding visual coding in neural populations.

The model contains many parameters that specify the shapes of all filters, but fitting by maximizing likelihood remains highly tractable<sup>5</sup>. A penalty on coupling filters was used to obtain a minimally sufficient set of coupling filters, which yields an estimate of the network's functional connectivity<sup>19,20</sup>.

Figure 1 shows the estimated filters describing input to example ON and OFF cells. The stimulus filters exhibit centre-surround receptive field organization consistent with previous characterizations of parasol cells. Post-spike filters show the time course of recovery from refractoriness after a spike, and coupling filters show the effects of spikes from nearby cells: for the ON cell (top), spikes in neighbouring ON cells elicit a large, transient excitation (increasing the instantaneous spike rate by a factor of three), whereas spikes in nearby OFF cells elicit suppression. These effects are reversed in the OFF cell, which is excited/suppressed by spikes in neighbouring OFF/ON cells. Both populations exhibit approximate nearest-neighbour connectivity, with coupling strength falling as a function of distance

<sup>1</sup>Gatsby Computational Neuroscience Unit, UCL, 17 Queen Square, London WC1N 3AR, UK. <sup>2</sup>The Salk Institute, 10010 North Torrey Pines Road, San Diego, California 92037, USA.

<sup>3</sup>Department of Statistics and Center for Theoretical Neuroscience, Columbia University, 1255 Amsterdam Avenue, New York, New York 10027, USA. <sup>4</sup>Santa Cruz Institute for Particle Physics, University of California, Santa Cruz, 1156 High Street, Santa Cruz, California 95064, USA. <sup>5</sup>Howard Hughes Medical Institute, Center for Neural Science, and Courant Institute of Mathematical Sciences, New York University, 4 Washington Place, Room 809, New York, New York 10003, USA.

between receptive field centres<sup>15</sup>. We found that fitted stimulus filters have smaller surrounds than the spike-triggered average, indicating that a portion of the classical surround can be explained by interactions between cells<sup>21</sup> (see Supplementary Information).

To assess accuracy in capturing the statistical dependencies in population responses, we compared the pairwise cross-correlation function (CCF) of RGCs and simulated model spike trains (Fig. 2). For nearby ON-ON and OFF-OFF pairs, the CCF exhibits a sharp peak at zero, indicating the prevalence of synchronous spikes; however, for ON-OFF pairs, a trough at zero indicates an absence of synchrony. For all 351 possible pairings, the model accurately reproduces the CCF (Fig. 2a-c, e, f).

To examine whether inter-neuronal coupling was necessary to capture the response correlation structure, we re-fitted the model without coupling filters (that is, so that each cell's response depends only on the stimulus and its own spike-train history). This 'uncoupled model' assumes that cells encode the stimulus independently, although correlations may still arise from the overlap of stimulus filters. However, the uncoupled model fails to reproduce the sharp CCF peaks observed in the data. These peaks are also absent from CCFs computed on trial-shuffled data, indicating that fast-timescale correlations are not stimulus-induced and therefore cannot be captured by any independent encoding model.

Higher-order statistical dependencies were considered by inspecting correlations in three-neuron groups: triplet CCFs show the spike rate of one cell as a function of the relative time to spikes in two other cells (Fig. 2e-g)<sup>15</sup>. For adjacent neurons of the same type, triplet CCFs have substantial peaks at zero ('triplet synchrony'), which are well matched by the full model.

Although the full and uncoupled models differ substantially in their statistical dependencies, the two models predict average light responses in individual cells with nearly identical accuracy, capturing 80–95% of the variance in the peri-stimulus time histogram (PSTH) in 26 out of 27 cells (Fig. 3a-c). Both models therefore accurately describe average single-cell responses to new stimuli. However, the full model achieves higher accuracy, predicting multi-neuronal spike responses on a single trial (8 ± 3% more bits per spike, Fig. 3d). This discrepancy can be explained by the fact that noise is shared across

neurons. Shared variability means that population activity carries information about a single cell's response (owing to coupling between cells) beyond that provided by the stimulus alone. Individual neurons therefore appear less noisy when conditioned on spiking activity in the rest of the population than they appear in raster plots.

We measured the effect of correlations on single-trial, single-cell spike-train prediction by using the model to draw samples of a single cell's response given both the stimulus and the spiking activity in the rest of the population on a single trial (Fig. 3e, f). Averaging the resulting raster plot gives a prediction of the cell's single-trial spike rate, or 'population-conditioned' PSTH for a single trial. We compared these predictions with the cell's true spike times (binned at 2 ms) across all trials and found that on nearly every trial, the model-based prediction is more highly correlated with the observed spikes than the neuron's full PSTH (Fig. 3g). Note that the full PSTH achieves the highest correlation possible for any trial-independent prediction. Thus, by exploiting the correlation structure, the coupled model predicts single-neuron spike times more accurately than any independent encoding model.

Although the full model accurately captures dependencies in the activity of RGCs, it is not obvious *a priori* whether these dependencies affect the amount of sensory information conveyed by RGC responses. In principle, the correlation structure could be necessary to predict the responses, but not to extract the stimulus information that the responses carry<sup>13</sup>. To examine this issue directly, we used the full and uncoupled models to perform Bayesian decoding of the population response (Fig. 4a), which optimally reconstructs stimuli given an accurate description of the encoding process. For comparison, we also performed Bayesian decoding under a Poisson (that is, LNP) model and optimal linear decoding<sup>6</sup>.

Each decoding method was used to estimate short (150-ms) segments of the stimulus given all relevant spike times from the full population (Fig. 4b). Bayesian decoding under the coupled model recovers 20% more information than Bayesian decoding under the uncoupled model, indicating that knowledge of the correlation structure is critical for extracting all sensory information contained in the population response. This improvement was invariant to enhancements of the

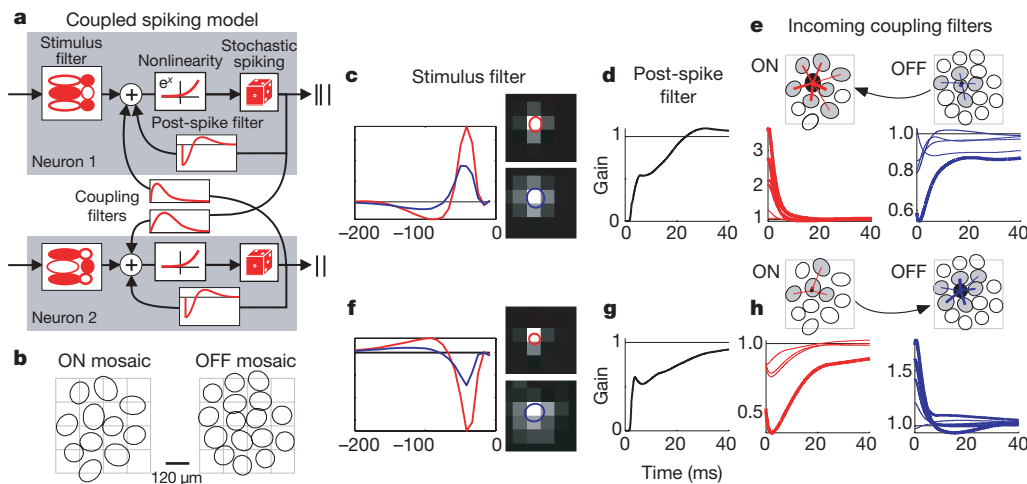


**Figure 1 | Multi-neuron encoding model and fitted parameters.** **a**, Model schematic for two coupled neurons: each neuron has a stimulus filter, a post-spike filter and coupling filters that capture dependencies on spiking in other neurons. Summed filter output passes through an exponential nonlinearity to produce the instantaneous spike rate. **b**, Mosaics of 11 ON and 16 OFF retinal ganglion cell receptive fields, tiling a small region of visual space. Ellipses represent 1 s.d. of a Gaussian fit to each receptive field centre; the square grid indicates stimulus pixels. **c–e**, Parameters for an example ON cell. **c**, Temporal and spatial components of centre (red) and surround (blue) filter components, the difference of which is the full stimulus filter.

**d**, Exponentiated post-spike filter, which may be interpreted as multiplying the spike rate after a spike at time zero. It produces a brief refractory period and gradual recovery (with a slight overshoot). **e**, Connectivity and coupling filters from other cells in the population. The black filled ellipse is this cell's RF centre, and blue and red lines show connections from neighbouring OFF and ON cells, respectively (line thickness indicates coupling strength). Below, exponentiated coupling filters show the multiplicative effect on this cell's spike rate after a spike in a neighbouring cell. **f–h**, Analogous plots for an example OFF cell.

model's stimulus filters and nonlinearities (see Supplementary Information), indicating that the difference in performance arises specifically from the coupled model's ability to incorporate the correlation structure. Our results also show that spike history is relevant for decoding (a Poisson model preserves 6% less information than the uncoupled model<sup>22</sup>) and that restricting to a linear decoder further reduces the information that can be recovered from RGC responses.

Decoding analysis can also be used to examine the coding fidelity of specific stimulus features. As a simple illustration, we examined the temporal frequency spectrum of reconstructed stimuli and found that the response correlation structure is most important for decoding those stimulus frequencies (6–20 Hz) that are encoded with highest fidelity (Fig. 4c).

These results demonstrate that the responses of a population of retinal ganglion cells are well described by a generalized linear model, and that correlations in the response can be exploited to recover 20% more visual information than if responses are regarded as independent given the stimulus. In contrast, previous studies have reported this information gain to be less than 10% for pairs of neurons<sup>9,12</sup>. However, pairwise analyses provide little evidence about the importance of correlations across an entire population. Second-order correlations between pairs of neurons could give rise to either much larger (scaling with the number of neurons  $n$ ) or much smaller (falling as  $1/n$ ) gains for a full population (see Supplementary Information). To compare more directly with previous findings,

we performed Bayesian decoding using isolated pairs of neurons from the same population; we found a  $\leq 10\%$  gain in sensory information when correlations were included (see Supplementary Information). This is consistent with previous findings, and shows that the information gain for a complete population is larger than that observed for pairs. We also compared the model to a pairwise maximum-entropy model, which has recently been shown to capture the instantaneous spiking statistics of groups of retinal ganglion cells<sup>14,15</sup>. The coupled model exhibits similar accuracy in capturing these statistics, but has the advantage that it accounts for the temporal correlation structure and stimulus dependence of responses, which are essential for assessing the effect of correlations on sensory coding.

Although it provides an accurate functional description of correlated spike responses, the generalized linear model does not reveal the biophysical mechanisms underlying the statistical dependencies between neurons: coupling does not necessarily imply anatomical connections between cells, but could (for example) reflect dependencies due to shared input noise<sup>1</sup>. The model also lacks several mechanisms known to exist in retinal ganglion cells (for example, contrast gain-control<sup>23</sup>), which may be required for characterizing responses to a wider variety of stimuli. One additional caveat is that Bayesian decoding provides a tool for measuring the sensory information available in the population response, but it does not reveal whether the brain makes use of this information.

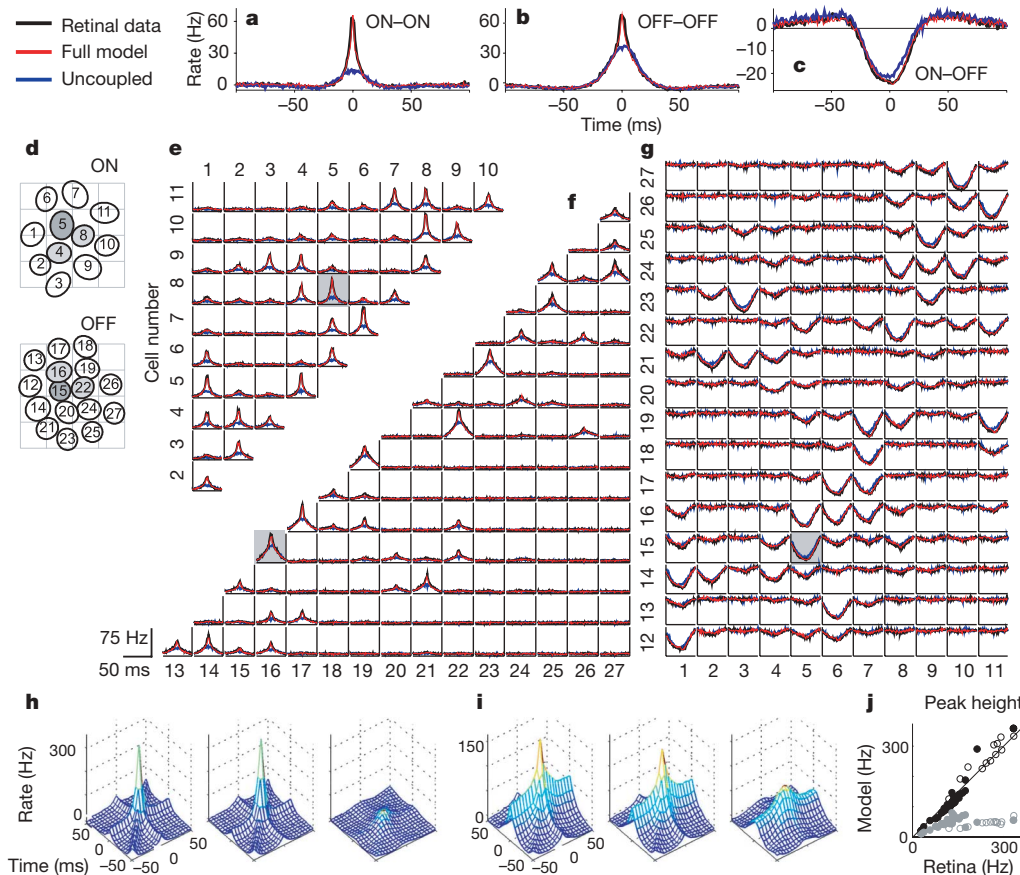


**Figure 2 | Analysis of response correlations.** **a–c**, Example CCFs of retinal responses, and simulated responses of the full and uncoupled models, for two ON cells (**a**), two OFF cells (**b**) and an ON–OFF pair (**c**). The baseline is subtracted so that units are in spikes per s above (or below) the cell's mean rate. **d**, Receptive field mosaic overlaid with arbitrary labels. Dark grey indicates cells shown in Fig. 1; light grey indicates cells used for triple correlations (**h**, **i**). **e**, CCFs between all ON pairs, where the  $i,j$ th plot shows the CCF between cell  $i$  and cell  $j$ . The grey box indicates the CCF plotted in

**a, f, g**, CCFs between all OFF–OFF pairs (**f**) and all ON–OFF pairs (**g**; abscissa height is 30 Hz). **h**, Third-order (triplet) CCF between three adjacent ON cells, showing the instantaneous spike rate of cell 5 as a function of the relative spike time in cells 4 and 8 (left, RGCs; middle, full model; right, uncoupled model). **i**, Analogous triplet CCF for OFF cells 15, 16 and 22. **j**, Comparison of the triplet CCF peak in RGC and model responses (full model, black; uncoupled, grey) for randomly selected triplets of adjacent ON (open) and OFF (filled) cells.

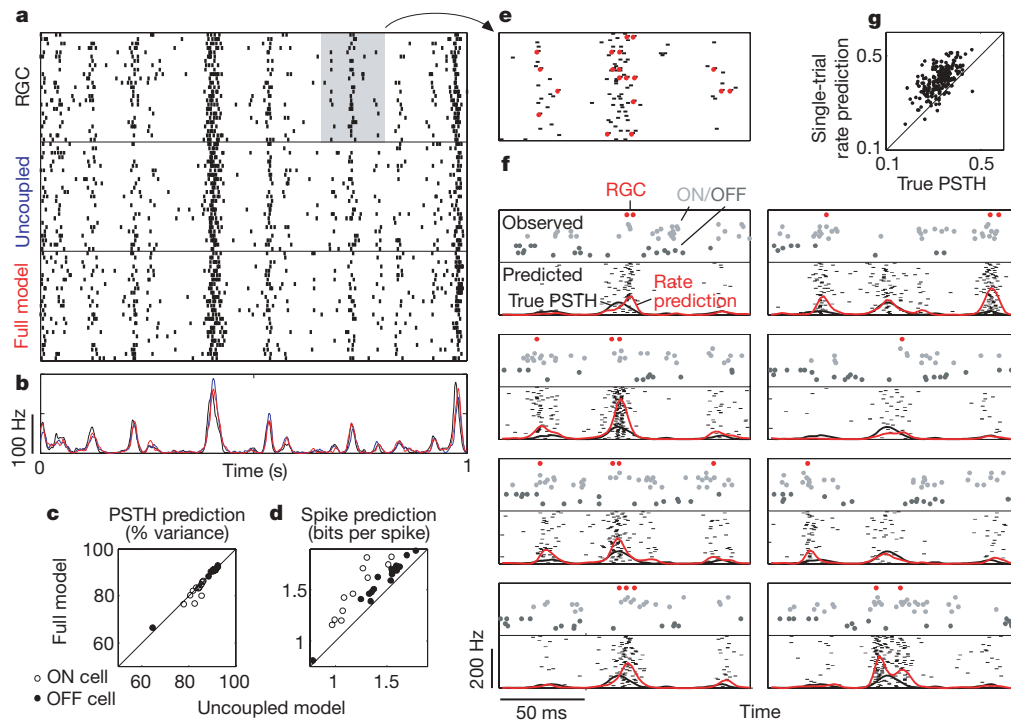


**Figure 3 | Spike-train prediction comparison.** **a**, Raster of responses of an ON RGC to 25 repeats of a novel 1-s stimulus (top), and responses of uncoupled (middle) and full (bottom) models to the same stimulus. **b**, PSTH of the RGC (black), uncoupled (blue) and coupled (red) model; both models account for  $\sim 84\%$  of the variance of the true PSTH. **c**, PSTH prediction by full and uncoupled models, showing that coupling confers no advantage in predicting average responses. **d**, Log-likelihood of novel RGC spike responses under full and uncoupled models; the full model provides 8% more information about novel spike trains. **e**, Magnified 150-ms portion of RGC raster and PSTH (grey box in **a**). Red dots highlight RGC spike times on selected individual trials, which are replotted in **f**. **f**, Single-trial spike-train prediction using the coupled model. The top half of each plot shows the

population activity on a single trial: true spike times of the cell (red dots), coupled ON cells (light grey dots) and coupled OFF cells (dark grey dots; each line in the raster shows the spike times of a different cell). The bottom half of each plot shows a raster of 50 predicted responses of the cell in question, using both the stimulus and coupled responses (shown above) to predict spike trains. The red trace shows the single-trial rate prediction (population-conditioned PSTH), compared with true PSTH of the cell (black trace, identical in all plots). **g**, Correlation coefficient of true spike trains with the PSTH (ordinate) and with population-conditioned predictions (abscissa); the full model predicts single-trial responses with higher accuracy than the true PSTH.

Physiological interpretations of the model and mechanisms for neural read-out of sensory information in higher brain areas are thus important directions for future research.

Nevertheless, the generalized linear model offers a concise, computationally tractable description of the population encoding process, and provides the first generative description of the space–time dependencies in stimulus-induced population activity. It allows us to quantify the relative contributions of stimulus, spike history and

network interactions to the encoding and decoding of visual stimuli, and clarifies the relationship between single-cell and population variability. More generally, the model can be used to assess which features of the visual environment are encoded with highest and lowest fidelity, and to determine how the structure of the neural code constrains perceptual capabilities. We expect this framework to extend to other brain areas, and to have an important role in revealing the information processing capabilities of spiking neural populations<sup>4,19,24,25</sup>.

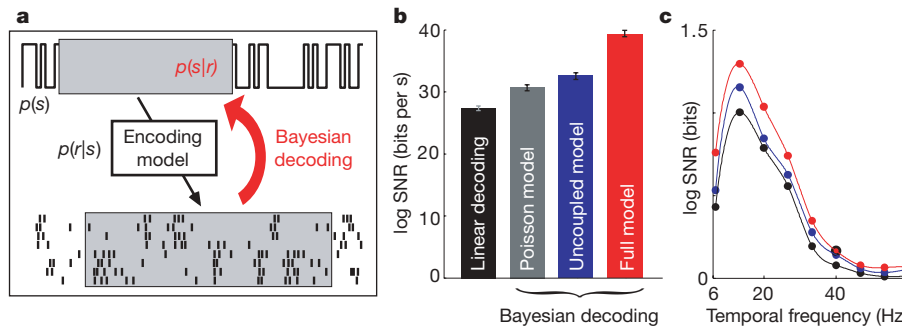


**Figure 4 | Decoding performance comparison.** **a**, Shown is a Bayesian decoding schematic: to estimate an unknown stimulus segment from a set of observed spike times (highlighted in boxes), the stimulus prior distribution  $p(s)$  is multiplied by the model-defined likelihood  $p(r|s)$  to obtain the posterior  $p(s|r)$ . The posterior mean is the Bayes' least-squares stimulus estimate. **b**, Log of the SNR for linear decoding, as well as for Bayesian decoding under the Poisson, uncoupled and full models<sup>6</sup>. The full model

preserves 20% more information than the uncoupled model, which indicates that there is additional sensory information available from the population response when correlations are taken into account. Error bars show 95% confidence intervals based on 2,000 bootstrap resamplings of 3,000 decoded stimulus segments. **c**, Log SNR decomposed as a function of temporal frequency for various decoding methods (Poisson omitted for clarity).

## METHODS SUMMARY

**Data.** Multi-electrode extracellular recordings were obtained *in vitro* from a segment of isolated, peripheral macaque monkey (*Macaca mulatta*) retina, and analysis was restricted to two cell types (ON and OFF parasol)<sup>15,26,27</sup>. A standard spike-sorting procedure, followed by a specialized statistical method for detecting simultaneous spikes, was used to sort spikes (see ref. 28). The retina was stimulated with a photopic, achromatic, optically reduced spatio-temporal binary white noise stimulus refreshing at 120 Hz, with a root-mean-square contrast of 96%.

**Fitting.** Model parameters were fitted to 7 min of spike responses to a non-repeating stimulus. Each cell's parameters consisted of a stimulus filter (parametrized as a rank-2 matrix), a spike-history filter, a set of incoming coupling filters and a constant. Temporal filters were represented in a basis of cosine 'bumps'<sup>22</sup>. Parameters for the uncoupled and Poisson (LNP) models were fitted independently. Parameters were fitted by penalized maximum likelihood<sup>4,5</sup>, with an L1 penalty on the vector length of coupling filters to eliminate unnecessary connections.

**Encoding.** Spike prediction was cross-validated using the log-likelihood of 5 min of novel spiking data (scaled to units of bits per s). Repeat rasters were obtained using 200 presentations of a novel 10-s stimulus. Population-conditional rasters were obtained from the coupled model by sampling the model-defined probability distribution over the neuron's response given the stimulus and surrounding-population activity on a single trial<sup>29</sup>.

**Decoding.** Population responses were decoded using the Bayes' least-squares estimator (posterior mean) to reconstruct 18-sample single-pixel stimulus segments (cross-validation data). Linear decoding was performed using the optimal linear estimator<sup>6</sup>. Decoding performance was quantified using the log signal-to-noise ratio (SNR) of each technique, which gives an estimate of mutual information. Breakdown by temporal frequency was obtained by computing the Fourier power spectra of the stimuli and residuals and then computing log SNR.

**Full Methods** and any associated references are available in the online version of the paper at [www.nature.com/nature](http://www.nature.com/nature).

Received 16 July 2007; accepted 5 June 2008.

Published online 23 July 2008.

1. Mastronarde, D. N. Correlated firing of retinal ganglion cells. *Trends Neurosci.* **12**, 75–80 (1989).
2. Meister, M., Lagnado, L. & Baylor, D. A. Concerted signaling by retinal ganglion cells. *Science* **270**, 1207–1210 (1995).
3. Shadlen, M. & Newsome, W. The variable discharge of cortical neurons: implications for connectivity, computation, and information coding. *J. Neurosci.* **18**, 3870–3896 (1998).
4. Truccolo, W., Eden, U. T., Fellows, M. R., Donoghue, J. P. & Brown, E. N. A point process framework for relating neural spiking activity to spiking history, neural ensemble and extrinsic covariate effects. *J. Neurophysiol.* **93**, 1074–1089 (2004).
5. Paninski, L. Maximum likelihood estimation of cascade point-process neural encoding models. *Network Comp. Neural Syst.* **15**, 243–262 (2004).
6. Warland, D., Reinagel, P. & Meister, M. Decoding visual information from a population of retinal ganglion cells. *J. Neurophysiol.* **78**, 2336–2350 (1997).
7. Dan, Y., Alonso, J. M., Usrey, W. M. & Reid, R. C. Coding of visual information by precisely correlated spikes in the lateral geniculate nucleus. *Nature Neurosci.* **1**, 501–507 (1998).
8. Panzeri, S., Golledge, H., Zheng, F., Tovee, M. P. & Young, M. J. Objective assessment of the functional role of spike train correlations using information measures. *Vis. Cogn.* **8**, 531–547 (2001).
9. Nirenberg, S., Carcieri, S., Jacobs, A. & Latham, P. Retinal ganglion cells act largely as independent encoders. *Nature* **411**, 698–701 (2001).
10. Schneidman, E., Bialek, W. & Berry, M. J. Synergy, redundancy, and independence in population codes. *J. Neurosci.* **21**, 11539–11553 (2003).

11. Nirenberg, S. & Latham, P. E. Decoding neuronal spike trains: how important are correlations? *Proc. Natl. Acad. Sci. USA* **100**, 7348–7353 (2003).
12. Averbeck, B. B. & Lee, D. Coding and transmission of information by neural ensembles. *Trends Neurosci.* **27**, 225–230 (2004).
13. Latham, P. & Nirenberg, S. Synergy, redundancy, and independence in population codes, revisited. *J. Neurosci.* **25**, 5195–5206 (2005).
14. Schneidman, E., Berry, M., Segev, R. & Bialek, W. Weak pairwise correlations imply strongly correlated network states in a neural population. *Nature* **440**, 1007–1012 (2006).
15. Shlens, J. et al. The structure of multi-neuron firing patterns in primate retina. *J. Neurosci.* **26**, 8254–8266 (2006).
16. Plessner, H. & Gerstner, W. Noise in integrate-and-fire neurons: From stochastic input to escape rates. *Neural Comput.* **12**, 367–384 (2000).
17. Simoncelli, E. P., Paninski, L., Pillow, J. & Schwartz, O. In *The Cognitive Neurosciences* 3rd edn (ed. Gazzaniga, M.) 327–338 (MIT, 2004).
18. Frechette, E. S. et al. Fidelity of the ensemble code for visual motion in primate retina. *J. Neurophysiol.* **94**, 119–135 (2005).
19. Okatan, M., Wilson, M. & Brown, E. Analyzing functional connectivity using a network likelihood model of ensemble neural spiking activity. *Neural Comput.* **17**, 1927–1961 (2005).
20. Rigat, F., de Gunst, M. & van Pelt, J. Bayesian modelling and analysis of spatio-temporal neuronal networks. *Bayes. Anal.* **1**, 733–764 (2006).
21. DeVries, S. H. Correlated firing in rabbit retinal ganglion cells. *J. Neurophysiol.* **81**, 908–920 (1999).
22. Pillow, J. W., Paninski, L., Uzzell, V. J., Simoncelli, E. P. & Chichilnisky, E. J. Prediction and decoding of retinal ganglion cell responses with a probabilistic spiking model. *J. Neurosci.* **25**, 11003–11013 (2005).
23. Shapley, R. M. & Victor, J. D. The effect of contrast on the transfer properties of cat retinal ganglion cells. *J. Physiol.* **285**, 275–298 (1978).
24. Harris, K., Csicsvari, J., Hirase, H., Dragoi, G. & Buzsaki, G. Organization of cell assemblies in the hippocampus. *Nature* **424**, 552–556 (2003).
25. Paninski, L., Fellows, M., Shoham, S., Hatsopoulos, N. & Donoghue, J. Superlinear population encoding of dynamic hand trajectory in primary motor cortex. *J. Neurosci.* **24**, 8551–8561 (2004).
26. Litke, A. M. et al. What does the eye tell the brain? Development of a system for the large scale recording of retinal output activity. *IEEE Trans. Nucl. Sci.* **51**, 1434–1440 (2004).
27. Watanabe, M. & Rodieck, R. W. Parasol and midget ganglion cells of the primate retina. *J. Comp. Neurol.* **289**, 434–454 (1989).
28. Segev, R., Goodhouse, J., Puchalla, J. & Berry, M. J. Recording spikes from a large fraction of the ganglion cells in a retinal patch. *Nature Neurosci.* **7**, 1155–1162 (2004).
29. Pillow, J. W. & Latham, P. In *Advances in Neural Information Processing Systems 20* (eds Platt, J. C., Koller, D., Singer Y. & Roweis S.) 1161–1168 (MIT, 2008).

**Supplementary Information** is linked to the online version of the paper at [www.nature.com/nature](http://www.nature.com/nature).

**Acknowledgements** We thank M. Bethge, C. Brody, D. Butts, P. Latham, M. Lengyel, S. Nirenberg and R. Sussman for comments and discussions; G. Field, M. Greschner, J. Gauthier and C. Hulse for experimental assistance; M. I. Grivich, D. Petrusca, W. Dabrowski, A. Grillo, P. Grybos, P. Hottowy and S. Kachigian for technical development; H. Fox, M. Taffe, E. Callaway and K. Osborn for providing access to retinas; and S. Barry for machining. Funding was provided a Royal Society USA/Canada Research Fellowship (J.W.P.); NSF IGERT DGE-03345 (J.S.); NEI grant EY018003 (E.J.C., L.P. and E.P.S.); Gatsby Foundation Pilot Grant (L.P.); Burroughs Wellcome Fund Career Award at the Scientific Interface (A.S.); US National Science Foundation grant PHY-0417175 (A.M.L.); McKnight Foundation (A.M.L. and E.J.C.); and HHMI (J.W.P., L.P. and E.P.S.).

**Author Information** Reprints and permissions information is available at [www.nature.com/reprints](http://www.nature.com/reprints). Correspondence and requests for materials should be addressed to J.W.P. (pillow@gatsby.ucl.ac.uk).

## METHODS

**Recording.** Multi-electrode extracellular recordings were obtained *in vitro* from a segment of isolated, peripheral macaque monkey retina, using preparation and recording methods described previously<sup>15,26</sup>. Analysis was restricted to two physiologically defined classes of cells; on the basis of light response properties and density, these were identified as ON and OFF parasol cells<sup>27</sup>. The cells shown were recorded in a square region of retina covered by 76 electrodes. A standard clustering-based spike-sorting procedure (see refs 15, 26) was used to estimate the number of units, and least-squares regression of the estimated spike times against multi-electrode voltage signal was used to estimate multi-electrode spike waveforms for each unit. Although this approach correctly and efficiently identifies isolated spikes, when two cells fire within a 1–2-ms window, the clustering approach can fail to identify the presence of both spikes. We solved this problem by using estimates of the elementary waveforms to detect the superposition of spikes. We performed maximum *a posteriori* estimation under the model that the multi-electrode voltage signal was the linear superposition of Gaussian white noise and the spike trains convolved with their associated spike waveforms, with a sparse (exponential) prior distribution on the spike trains. This corresponds to a tractable quadratic optimization problem under linear inequality constraints, which can be solved efficiently using existing methods. The real-valued solution vector was then binarized by greedily inserting spikes whenever the reduction in mean-squared error between predicted and actual voltage exceeded a threshold<sup>28</sup>. This procedure correctly identified simultaneous spikes in simulated data sets and corrected obvious cross-correlation artefacts appearing in real data sorted with standard clustering techniques.

**Stimuli.** The retina was stimulated with a photopic, achromatic image of a cathode ray tube display, refreshing at 120 Hz. The stimulus was a spatio-temporal pseudo-random binary sequence, where the intensity of each pixel was drawn independently from one of two values on each frame. The stimulus pixel size was 120 × 120  $\mu\text{m}$  on the retina, and contrast (standard deviation divided by mean) was 96%.

**Fitting.** Model parameters were fitted by maximizing likelihood<sup>5</sup> using 7 min of spiking data recorded during presentation of a non-repeating stimulus. The parameters for each cell consisted of a stimulus filter  $\mathbf{k}$ , a spike-history filter  $\mathbf{h}$ , a set of incoming coupling filters  $\{\mathbf{l}_i\}$  and a constant (specifying the log of the baseline firing rate)  $\mu$ . The filter  $\mathbf{k}$  was a 750-dimensional vector ( $5 \times 5$  spatial pixels × 30 time bins), parametrized using a lower-dimensional representation as a rank-2 matrix:  $k(x, y, \tau) = k_{s,1}(x, y)k_{t,1}(\tau) - k_{s,2}(x, y)k_{t,2}(\tau)$ , with  $k_{s,i}(x, y)$  denoting a spatial filter (25 parameters) and  $k_{t,i}(\tau)$  a temporal filter (10 parameters), giving  $2 \times 35 = 70$  parameters. A rank-3 representation did not improve performance. These filters closely resembled a time-varying difference-of-Gaussians<sup>30</sup>; spatial filters were well-approximated (in a least-squares sense) by Gaussians, which were used to plot spatial ellipses shown in Fig. 1 and to summarize receptive field properties (Supplementary Figs 2 and 3). Gaussians fit to receptive field centres and surrounds had average standard deviations of 0.25 pixels and 0.7 pixels (1.0 pixels for the uncoupled model), respectively. Temporal filters  $\mathbf{h}$  and  $\{\mathbf{l}_i\}$  and the temporal components of  $\mathbf{k}$  were represented using a basis of raised cosine ‘bumps’ of the form  $\mathbf{b}_j(t) = (1/2)\cos(a\log[t + c] - \phi_j) + (1/2)$  for  $t$  such that  $a\log(t + c) \in [\phi_j - \pi, \phi_j + \pi]$  and 0 elsewhere, with constants  $a$  and  $c$  set by hand to match the structure observed in auto- and cross-correlation functions, and  $\pi/2$  spacing between the  $\phi_j$  (see Supplementary Information). This basis allows for the representation of fine temporal structure near the time of a spike and coarser/smooth dependency at later times (see ref. 22). The  $\mathbf{h}$  filter was represented with ten such basis vectors, and the  $\mathbf{l}_i$  coupling filters were represented with four. The ‘uncoupled model’ was fitted independently without coupling filters  $\{\mathbf{l}_i\}$ , and the inhomogeneous Poisson model (Fig. 4) was fitted without  $\{\mathbf{l}_i\}$  or  $\mathbf{h}$ .

Conditional intensity (spike rate) is given by  $\lambda(t) = \exp(\mathbf{k} \cdot \mathbf{x} + \mathbf{h} \cdot \mathbf{y} + (\sum_i \mathbf{l}_i \cdot \mathbf{y}_i) + \mu)$ , where  $\mathbf{x}$  is the stimulus,  $\mathbf{y}$  the cell’s own spike-train history,  $\mu$  is the cell’s baseline log-firing rate, and  $\{\mathbf{y}_i\}$  the spike-train histories of other cells at time  $t$ . The population log-likelihood is the sum over single-cell

log-likelihoods, each given by  $L = \sum \log \lambda(t_{sp}) - \lambda(t) dt$ , where  $t_{sp}$  denotes the set of spike times and the integral is taken over the length of the experiment<sup>4,5</sup>. We added a penalty of the form  $-\alpha \int |\sum_i \mathbf{l}_i(t)|^2 dt$  to eliminate unnecessary coupling filters (using a constrained Newton–Raphson algorithm to maximize the penalized log-likelihood), which regularizes and prevents overfitting. The regularization parameter  $\alpha$  was selected by means of cross-validation on a novel 5-min data set, but results were robust with respect to both  $\alpha$  and the choice of basis. (This reduced the number of coupling filters from 702 to 243 and recovered a roughly pairwise-adjacent structure; see Supplementary Information.) **Correlations.** Spike responses of full and uncoupled models were simulated with the same 20-min stimulus (144,000 samples) presented experimentally. Pairwise cross-correlations were computed in 1-ms bins, according to  $C(\tau) = [\langle y_1(t) y_2(t + \tau) \rangle - \langle y_1(t) \rangle \langle y_2(t) \rangle] / \langle y_2(t) \rangle dt$ , where  $y_1(t)$  denotes the spike response of the first neuron in bins of width  $dt$ , and  $\langle \cdot \rangle$  denotes averaging over  $t$ . Triplet correlations were computed in 5-ms bins according to  $C(\tau_1, \tau_2) = [\langle y_1(t) y_2(t + \tau_1) y_3(t + \tau_2) \rangle - \langle y_1(t) \rangle \langle y_2(t) \rangle \langle y_3(t) \rangle] / \langle y_2(t) \rangle \langle y_3(t) \rangle dt$ . **Encoding.** Spike-train prediction was validated using the log-likelihood of novel spike trains under both models, computed on 5 min of data not used for fitting or setting  $\alpha$ . The difference of log-likelihood under the model and log-likelihood under a homogeneous Poisson process,  $\sum \log \bar{\lambda}(t_{sp}) - \int \bar{\lambda}(t) dt$  (where  $\bar{\lambda} = n_{sp}/T$  is the mean spike rate), divided by  $n_{sp}$ , gives prediction accuracy in bits per spike for each cell<sup>25</sup>. Repeat rasters were obtained using 200 presentations of a novel 10-s stimulus, and the time-varying average response (PSTH) was computed in 1-ms bins, smoothed with a Gaussian kernel of width  $\sigma = 2$  ms. Conditional rasters were obtained from the coupled model by holding the responses of all but one neuron fixed, and sampling from the model-induced probability distribution on the remaining neuron’s response. Samples were obtained by the Metropolis–Hastings algorithm, with spike ‘proposals’ drawn from a point process model as described in ref. 29. We kept only every 100th output sample of the algorithm to ensure independent samples.

**Decoding.** We decoded the population response using the Bayes’ least-squares estimator, computed under each model (fully coupled, uncoupled with spike-history terms, and inhomogeneous Poisson) using 6,000 different 18-sample single-pixel stimulus segments (validation data that were not used for fitting). Each stimulus  $\mathbf{x}_i$  (an 18-dimensional binary vector, given by the time series of light intensities for a centrally located stimulus pixel) was decoded by first extracting  $\mathbf{y}_i$ , the multi-neuronal spike response portion that was causally influenced by this stimulus. For each model, and for every one of the  $2^{18}$  possible binary  $\mathbf{x}_j$ , we then computed  $p_j = p(\mathbf{y}_j | \mathbf{x}_j)$ , the likelihood of the observed population response given that it was generated by stimulus  $\mathbf{x}_j$ . By Bayes’ rule, the posterior is  $p(\mathbf{x}_j | \mathbf{y}_i) \propto p(\mathbf{y}_i | \mathbf{x}_j) p(\mathbf{x}_j)$ , and the prior  $p(\mathbf{x}_j)$  here is constant across binary stimuli. Thus, the posterior is proportional to  $p_j$ , and the Bayes’ least-squares estimate is given by  $\hat{\mathbf{x}}_i = (\sum p_j \mathbf{x}_j) / (\sum p_j)$ . We also performed decoding on longer (30-sample) stimulus segments, where exhaustive evaluation of these sums is no longer tractable: in this case we used Gibbs sampling from  $p(\mathbf{x}_j | \mathbf{y}_i)$  to approximately evaluate the sum. The results obtained using both methods were similar.

Linear decoding was performed using the optimal linear estimator<sup>6</sup>, with the same training data as for model fitting. Decoding performance was quantified using the log SNR of each technique:  $\log(\langle |\mathbf{x}_i \mathbf{x}_i^T| \rangle / \langle |\mathbf{r}_i \mathbf{r}_i^T| \rangle)$ , where  $\mathbf{r}_i = \hat{\mathbf{x}}_i - \mathbf{x}_i$  denotes the residual error for decoding stimulus vector  $\mathbf{x}_i$ , and  $\langle \cdot \rangle$  denotes averaging over  $i$  followed by matrix determinant. Breakdown by temporal frequency was obtained by computing the Fourier power spectra of the stimuli  $\tilde{\mathbf{x}}_i(\omega)^2$  and residuals  $\tilde{\mathbf{r}}_i(\omega)^2$ , and computing log SNR according to  $\log(\langle \tilde{\mathbf{x}}_i(\omega)^2 \rangle / \langle \tilde{\mathbf{r}}_i(\omega)^2 \rangle)$ . Integrating this log SNR across frequency,  $(1/2) \int \log \text{SNR}(\omega) d\omega$ , gives a commonly used estimate of the mutual information between the stimulus and the spike-train response<sup>6</sup>, which is equivalent to the quantity shown in Fig. 4b.

30. Meister, M. & Berry, M. J. The neural code of the retina. *Neuron* 22, 435–450 (1999).

## LETTERS

# New role of bone morphogenetic protein 7 in brown adipogenesis and energy expenditure

Yu-Hua Tseng<sup>1</sup>, Efi Kokkotou<sup>3</sup>, Tim J. Schulz<sup>1</sup>, Tian Lian Huang<sup>1</sup>, Jonathon N. Winnay<sup>1</sup>, Cullen M. Taniguchi<sup>1</sup>, Thien T. Tran<sup>1</sup>, Ryo Suzuki<sup>1</sup>, Daniel O. Espinoza<sup>1</sup>, Yuji Yamamoto<sup>1</sup>, Molly J. Ahrens<sup>4</sup>, Andrew T. Dudley<sup>4</sup>, Andrew W. Norris<sup>5</sup>, Rohit N. Kulkarni<sup>2</sup> & C. Ronald Kahn<sup>1</sup>

Adipose tissue is central to the regulation of energy balance. Two functionally different types of fat are present in mammals: white adipose tissue, the primary site of triglyceride storage, and brown adipose tissue, which is specialized in energy expenditure and can counteract obesity<sup>1</sup>. Factors that specify the developmental fate and function of white and brown adipose tissue remain poorly understood<sup>2,3</sup>. Here we demonstrate that whereas some members of the family of bone morphogenetic proteins (BMPs) support white adipocyte differentiation, BMP7 singularly promotes differentiation of brown preadipocytes even in the absence of the normally required hormonal induction cocktail. BMP7 activates a full program of brown adipogenesis including induction of early regulators of brown fat fate PRDM16 (PR-domain-containing 16; ref. 4) and PGC-1 $\alpha$  (peroxisome proliferator-activated receptor- $\gamma$  (PPAR $\gamma$ ) coactivator-1 $\alpha$ ; ref. 5), increased expression of the brown-fat-defining marker uncoupling protein 1 (UCP1) and adipogenic transcription factors PPAR $\gamma$  and CCAAT/enhancer-binding proteins (C/EBPs), and induction of mitochondrial biogenesis via p38 mitogen-activated protein (MAP) kinase-(also known as Mapk14) and PGC-1-dependent pathways. Moreover, BMP7 triggers commitment of mesenchymal progenitor cells to a brown adipocyte lineage, and implantation of these cells into nude mice results in development of adipose tissue containing mostly brown adipocytes. *Bmp7* knockout embryos show a marked paucity of brown fat and an almost complete absence of UCP1. Adenoviral-mediated expression of BMP7 in mice results in a significant increase in brown, but not white, fat mass and leads to an increase in energy expenditure and a reduction in weight gain. These data reveal an important role of BMP7 in promoting brown adipocyte differentiation and thermogenesis *in vivo* and *in vitro*, and provide a potential new therapeutic approach for the treatment of obesity.

BMPs are members of the transforming growth factor- $\beta$  (TGF- $\beta$ ) superfamily and control multiple key steps of embryonic development and differentiation<sup>6</sup>. BMPs seem to have different roles in adipogenesis<sup>7</sup>. Although certain BMPs, in particular BMP2 and BMP4, enhance white adipogenesis when assisted by a hormonal induction cocktail<sup>8,9</sup>, the role of BMPs in the differentiation and function of brown adipose tissue (BAT) or the balance between white adipose tissue (WAT) and BAT is unknown. To this end, we studied the role of BMPs in the differentiation of brown preadipocytes<sup>10</sup> and 3T3-L1 white preadipocytes in the absence of other hormonal or chemical inducers. Treatment of these cells with BMP2, BMP4, BMP6 and BMP7 markedly increased lipid accumulation of brown preadipocytes in culture even in the absence of the normally required induction cocktail or thiazolidinediones (Fig. 1a). BMP5 exhibited a

weaker effect compared to other BMPs, and BMP3 had virtually no effect on brown fat differentiation. In contrast, under the same conditions, 3T3-L1 white preadipocytes exhibited little or no differentiation when treated with these BMPs.

In brown preadipocytes, whereas BMP2, BMP4, BMP6 and BMP7 induced lipid accumulation to similar extents, BMP7 was unique in that it markedly induced *Ucp1* messenger RNA expression (Fig. 1b) to a level comparable to that achieved by standard induction protocols (Supplementary Table 1). In addition, expression of several other brown-fat-selective genes was significantly induced by BMP7 (Supplementary Fig. 1). In contrast, BMP4, an adipogenic factor for white fat<sup>9</sup>, suppressed expression of *Ucp1* in these brown preadipocytes (Fig. 1b), despite its effect on lipid accumulation (Fig. 1a). Western blot analysis confirmed the specific effect of BMP7 on induction of UCP1 protein expression in brown, but not white, preadipocytes (Supplementary Fig. 2). Importantly, expression of *Pgc-1 $\alpha$*  and *Ucp1* was markedly induced by cAMP to 6- and 18-fold, respectively, in BMP7-treated cells (Fig. 1c), indicating that the differentiated lipid-containing cells induced by BMP7 are bona fide brown adipocytes with a complete capacity to initiate the thermogenic program. BMPs are known to stimulate osteogenic differentiation by inducing expression of the osteogenic runt related transcription factor 2 (RUNX2; ref. 11). In brown preadipocytes, BMP2, BMP6 and BMP7 significantly inhibited *Runx2* expression, whereas BMP4 had no effect (Fig. 1b), suggesting that these BMPs function in brown fat precursors to promote adipogenesis and inhibit osteogenic differentiation. The specific effect of BMP7 on brown preadipocyte differentiation was also verified in primary culture cells isolated from stromo-vascular fraction of interscapular BAT (Supplementary Fig 3).

Cellular responses to BMPs have been shown to be mediated by the formation of a hetero-oligomeric complex of the type 1 and type 2 BMP receptors (BMPRs). Two major signalling pathways, the SMAD (mothers against decapentaplegic *Drosophila* homologue) pathway and p38 MAP kinase pathway, confer most of the biological functions of BMPs<sup>12</sup>. We found there is only a subtle difference in expression levels of different BMPR isoforms between brown and white preadipocytes (Supplementary Fig. 4). Interestingly, whereas BMP7 increased phosphorylation of SMAD1/5/8 in both brown and white preadipocytes, robust activation of p38 MAP kinase and its downstream activating transcription factor (ATF)-2 after BMP7 stimulation was observed only in brown preadipocytes, while being blunted or almost completely absent in the 3T3-L1 white preadipocytes (Fig. 1d).

To investigate further the role of p38 MAP kinase in BMP7-induced brown adipogenesis, three pharmacological inhibitors of

<sup>1</sup>Section on Obesity and Hormone Action, and <sup>2</sup>Section on Cell and Molecular Physiology, Joslin Diabetes Center, Harvard Medical School, Boston, Massachusetts 02215, USA.

<sup>3</sup>Division of Gastroenterology, Beth Israel Deaconess Medical Center, Harvard Medical School, Boston, Massachusetts 02215, USA. <sup>4</sup>Department of Biochemistry, Northwestern University, Evanston, Illinois 60208, USA. <sup>5</sup>Division of Pediatric Endocrinology, University of Iowa Children's Hospital, Iowa City, Iowa 52242, USA.

p38 MAP kinase were added individually to the medium 7 h before and throughout BMP7 treatment. After 10 days in culture, whereas none of these inhibitors had an effect on BMP7-induced lipid accumulation (Supplementary Fig. 5), all of these drugs effectively blocked the expression of UCP1 protein induced by BMP7 (Fig. 1e). p38 MAP kinase is known to regulate thermogenesis by means of nuclear coactivator PGC-1 (refs 13, 14). Indeed, we found that BMP7-induced UCP1 expression was markedly diminished in brown preadipocytes deficient in both PGC-1 $\alpha$  and PGC-1 $\beta$  (ref. 15; Supplementary Fig. 6). Together, these data reveal an essential role for p38 MAP kinase and PGC-1 coactivators in the BMP7-induced thermogenic program in brown adipocytes, whereas they are dispensable for the effect of BMP7 on lipid accumulation.

Before entering the adipogenic program, preadipocytes must be released from suppressive factors and become committed to terminal differentiation<sup>3</sup>. Needin acts as a negative modulator of brown preadipocyte differentiation, coordinating early adipogenic events, including suppression of preadipocyte factor-1 (PREF-1; also known

as DLK1) and WNT10a expression<sup>16</sup>. Treatment of brown preadipocytes with BMP7 significantly suppressed expression of needin (Fig. 2a). In addition, BMP7 also markedly suppressed gene expression of other inhibitors of adipogenesis, including PREF-1 and WNT10a (Fig. 2a). As a consequence of release from suppression by BMP7 treatment, these brown preadipocytes initiated the full transcriptional program of adipogenesis as shown by a significant increase in gene expression of PPAR $\gamma$ , C/EBP $\alpha$  and fatty acid binding protein 4 (FABP4, also known as aP2) (Fig. 2b). Importantly, BMP7 robustly induced expression of PRDM16, a zinc-finger binding protein recently identified as an early regulator determining brown fat fate<sup>4</sup>, by 6.3-fold at day 3 (Fig. 2c). This led to increased expression of other molecular signatures of brown fat, including PGC-1 $\alpha$ , PGC-1 $\beta$  (Fig. 2c) and UCP1 (Fig. 1b).

Differentiation of brown fat is accompanied by mitochondrial biogenesis<sup>17</sup>. In the brown preadipocyte cell line, BMP7 treatment significantly increased the expression of genes involved in mitochondrial biogenesis and function (Fig. 2c, d and Supplementary Fig. 1), including *Pgc-1 $\alpha$*  and *Pgc-1 $\beta$*  as well as nuclear respiratory factor 1 (*Nrf1*), mitochondrial transcription factor A (*Tfam*) and cytochrome

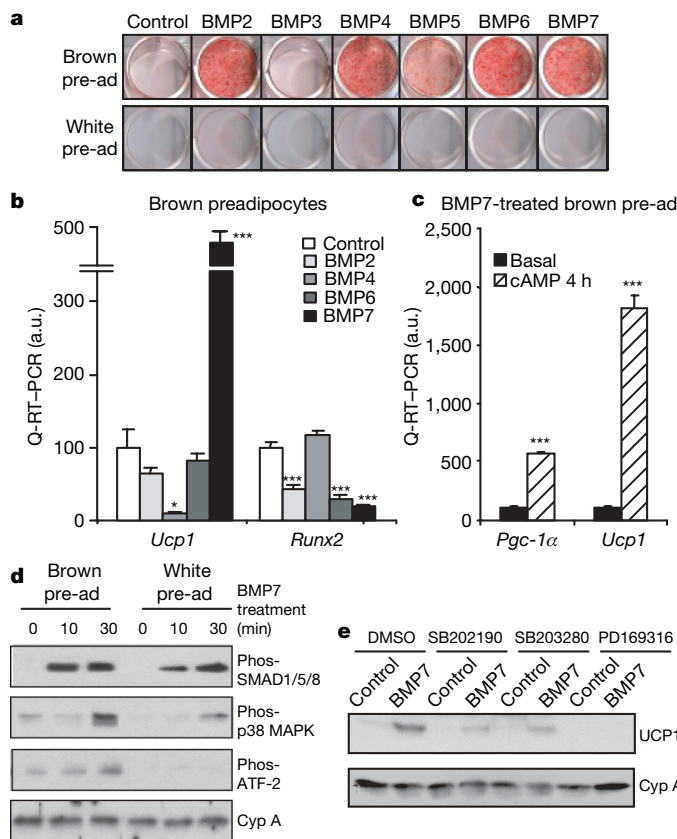


**Figure 1 | BMP7 induces brown, but not white, preadipocyte differentiation, and the essential role of p38 MAPK in BMP7-induced thermogenesis.** **a**, Oil Red O staining of brown preadipocytes and 3T3-L1 white preadipocytes (pre-ad) grown in growth medium supplemented with BMPs or vehicle (control) for 8 days. **b**, Quantitative reverse transcription polymerase chain reaction (Q-RT-PCR) analysis for *Ucp1* and *Runx2* in brown preadipocytes treated with vehicle or BMPs in a combination of insulin and T3 for 7 days. a.u., arbitrary units. **c**, Q-RT-PCR analysis for *Pgc-1 $\alpha$*  and *Ucp1* in response to 4 h of cAMP stimulation in brown preadipocytes differentiated in growth medium supplemented with BMP7. Data are presented as mean  $\pm$  s.e.m. ( $n = 3$ ). Asterisks depict statistically significant differences between control and experimental groups ( $*P < 0.05$ ,  $***P < 0.001$ ). **d**, Western blot analysis of phosphorylation of SMAD1/5/8, p38 MAP kinase and ATF-2 in response to 0, 10 and 30 min of BMP7 stimulation in brown and white preadipocytes. Cyclophilin A (Cyp A) serves as a loading control. **e**, Western blot analysis of UCP1 in brown preadipocytes cultured in growth medium supplemented with vehicle or BMP7 for 10 days. Three p38 MAP kinase inhibitors or vehicle (DMSO) were added to the cells 7 h before and throughout BMP7 treatment.

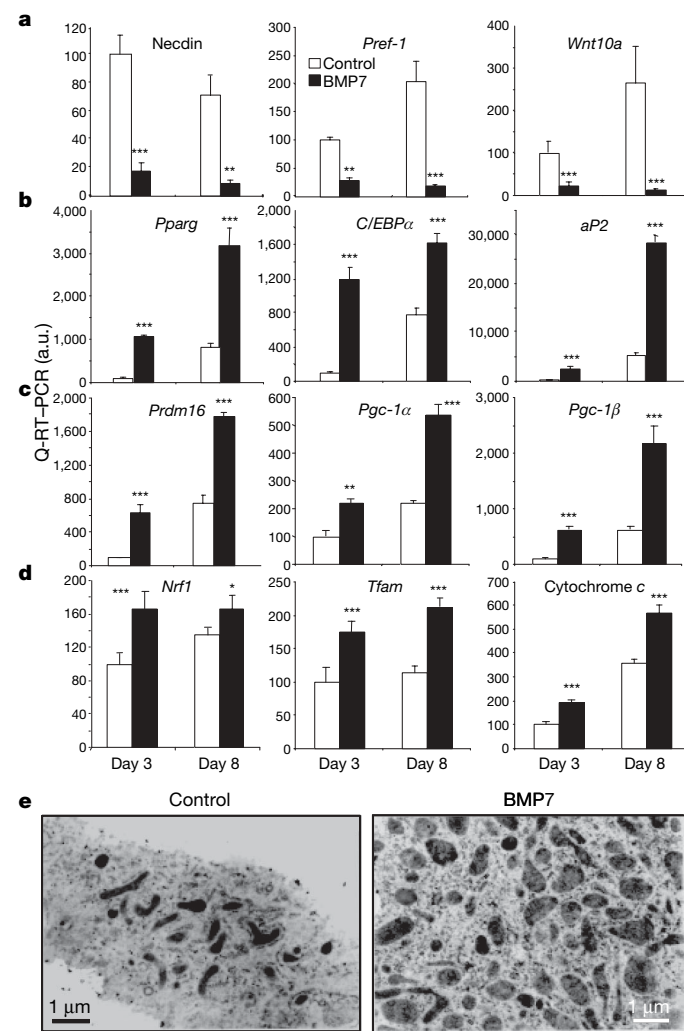


**Figure 2 | Molecular mechanisms by which BMP7 induces brown adipogenesis and mitochondrial biogenesis.** **a-d**, Q-RT-PCR analysis for genes encoding early adipogenic inhibitors (**a**), adipogenic markers common to brown and white fat (**b**), brown-fat-specific markers (**c**) and mitochondrial components (**d**) in brown preadipocytes treated with vehicle (control) or BMP7 for 3 or 8 days. Data are presented as mean  $\pm$  s.e.m. ( $n = 3$ ;  $*P < 0.05$ ,  $**P < 0.01$ ,  $***P < 0.001$ ). **e**, Transmission electron microscopy of brown preadipocytes treated with vehicle or BMP7 for 9 days. Original magnification,  $\times 24,000$ .

c. This coincided with a fivefold increase in mitochondrial density in BMP7-treated cells compared to control (Fig. 2e). Thus, BMP7 activated a full program of brown adipogenesis by suppression of early adipogenic inhibitors, induction of factors determining brown fat fate, increased expression of adipogenic transcription factors and induction of mitochondrial biogenesis.

BMPs are important in the control of stem cell commitment to various lineages<sup>18</sup>. To determine whether BMP7 could also trigger commitment of the mesenchymal progenitor/stem cells into a brown adipocyte lineage, we treated the multipotent C3H10T1/2 cells with BMP7 for 3 days before treatment with a standard adipogenic differentiation cocktail<sup>10</sup>. Cells pretreated with BMP7, but not vehicle, displayed a mature brown adipocyte phenotype with marked increases in lipid accumulation, and induction of the brown-fat-specific protein UCP1 (Fig. 3a). Expression of specific markers indicated that the C3H10T1/2 cells had become committed to the brown adipocyte lineage within 3 days of BMP7 treatment (Fig. 3b). By this time point, BMP7 pre-treatment had increased expression of *C/EBP* $\delta$  (ref. 19), followed by increased expression of *C/EBP* $\beta$ , *C/EBP* $\alpha$ , *Pparg* and *aP2* at a later stage of differentiation, consistent with the previously described gene patterns in committed white and brown pre-adipocytes<sup>20,21</sup>. Interestingly, BMP7 pretreatment also caused a transient induction of *Pgc-1* $\alpha$  expression and a significant increase in expression of *Nrf1* and *Tfam*, followed by a later increase of cytochrome *c* expression (Fig. 3c), indicating increased mitochondrial biogenesis in these BMP7-pretreated cells during the course of brown adipogenesis.

To verify the cell culture findings *in vivo*, we implanted BMP7-treated C3H10T1/2 cells subcutaneously into athymic nude mice in the sternal region. Six weeks after implantation, the BMP7-treated cells developed into a fat pad containing a large number of multilocular and UCP1-positive brown adipocytes and a small portion of uni-locular white adipocytes, whereas no additional tissue was found in mice receiving cells treated with vehicle (Fig. 3d and Supplementary Fig. 7). Additionally, BMP7, in concert with other differentiating agents, induced brown adipogenesis in two more primitive fibroblastic cell lines with no adipogenic character (Supplementary Figs 8 and 9). Thus, BMP7 triggers commitment of multipotent mesenchymal cells to the brown adipocyte lineage in both *in vitro* and *ex vivo* settings.

To determine the physiological necessity of BMP7 for BAT development, we analysed brown fat morphology and function in *Bmp7* knockout mice. Because *Bmp7* null mice die shortly after birth<sup>22,23</sup>, we focused our study in newborn mice and embryos. In rodents at these stages brown fat is already developed, whereas white fat is still not grossly visible. Notably, at birth, *Bmp7* knockout mice displayed a marked 50%–70% decrease in interscapular BAT mass compared with wild-type littermates, whereas the size of other internal organs, such as the liver, were not altered (Fig. 4a). The decrease of BAT mass in *Bmp7* knockout animals was also evident at embryonic stages. Cross-sections of 17.5 days postcoitum (d.p.c.) embryos showed a marked decrease in brown fat mass, associated with a marked decrease in the number of brown adipocytes (Fig. 4b and Supplementary Fig. 10). Most importantly, expression of UCP1 protein was markedly decreased or completely absent in brown fat from 18.5 d.p.c. *Bmp7* null embryos, whereas expression of insulin receptor, another protein involved in adipogenesis, remained unaltered (Fig. 4c). This was accompanied by a significant decrease in expression of a number of brown-fat-selective genes (Supplementary Fig. 11). These data establish an essential role of BMP7 in brown fat development *in vivo* and an almost absolute requirement for BMP7 in maintaining the brown-fat-specific thermogenic program.

Finally, to explore the potential role of BMP7 in regulation of brown adipogenesis and energy homeostasis *in vivo*, we injected adenoviruses expressing BMP3, BMP7 or LacZ (*Escherichia coli*  $\beta$ -galactosidase) as a control via the tail vein into 4-week-old C57BL/6 mice

and measured metabolic rate by indirect calorimetry. Adenoviruses are trophic for the liver, where they can drive release of secretory proteins, such as BMPs, into the blood stream (Supplementary Fig. 12a). Importantly, mice that received adenovirus expressing BMP7 showed significant increases in whole-body energy expenditure and basal body temperature, leading to a significant reduction in weight gain compared with mice that received the LacZ adenovirus (Fig. 4d). The increase in energy expenditure in BMP7-treated mice was not due to an increase in physical activity or food intake (Supplementary Fig. 12). In contrast, BMP3, which had no effect on differentiation of brown preadipocytes *in vitro* (Fig. 1a), did not induce any metabolic effects compared to control mice. Fifteen days after adenoviral injection, mice that received BMP7 treatment displayed a significant

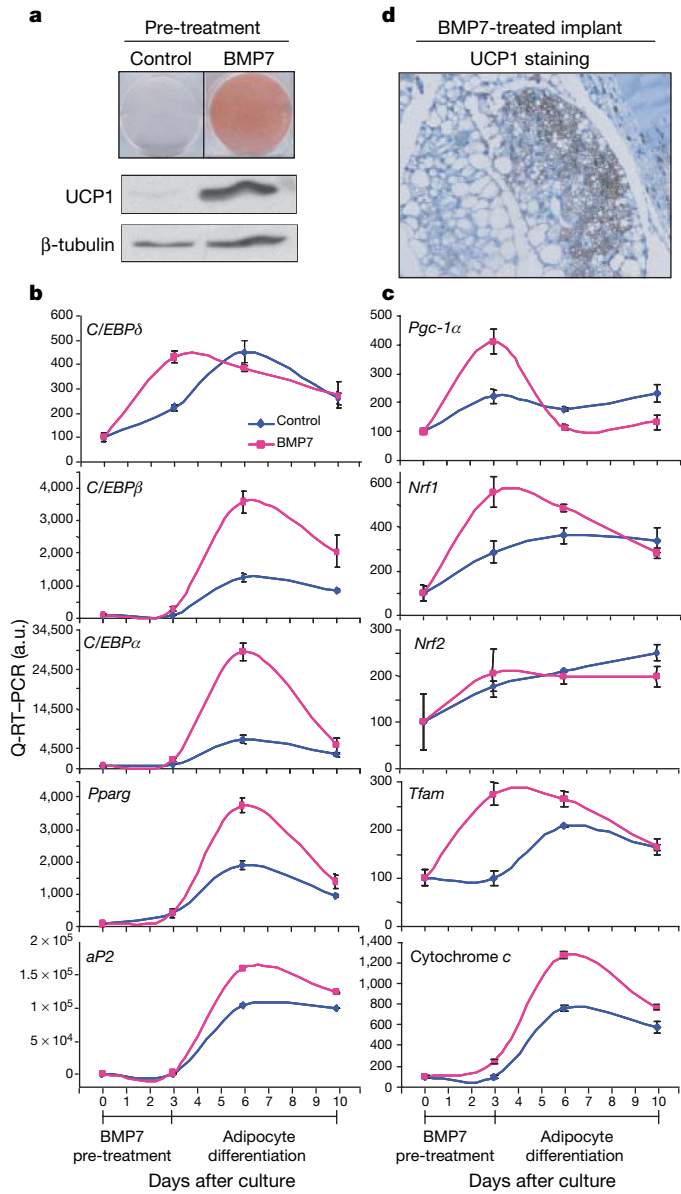


**Figure 3 | BMP7 triggers commitment of mesenchymal progenitor cells to brown adipocyte lineage *in vitro* and *in vivo*.** **a**, Oil Red O staining and western blotting analysis for UCP1 in C3H10T1/2 cells treated with BMP7 or vehicle (control) for 3 days followed by adipogenic induction for 7 days.  $\beta$ -tubulin serves as a loading control. **b, c**, Q-RT-PCR analysis for genes involved in the adipogenic program (**b**) and mitochondrial biogenesis (**c**) in cells described in **a**. Data are presented as mean  $\pm$  s.e.m. ( $n = 3$ ). **d**, UCP1 immunohistochemical staining on a tissue derived from implantation of BMP7-treated C3H10T1/2 cells into nude mice. Original magnification,  $\times 400$ .

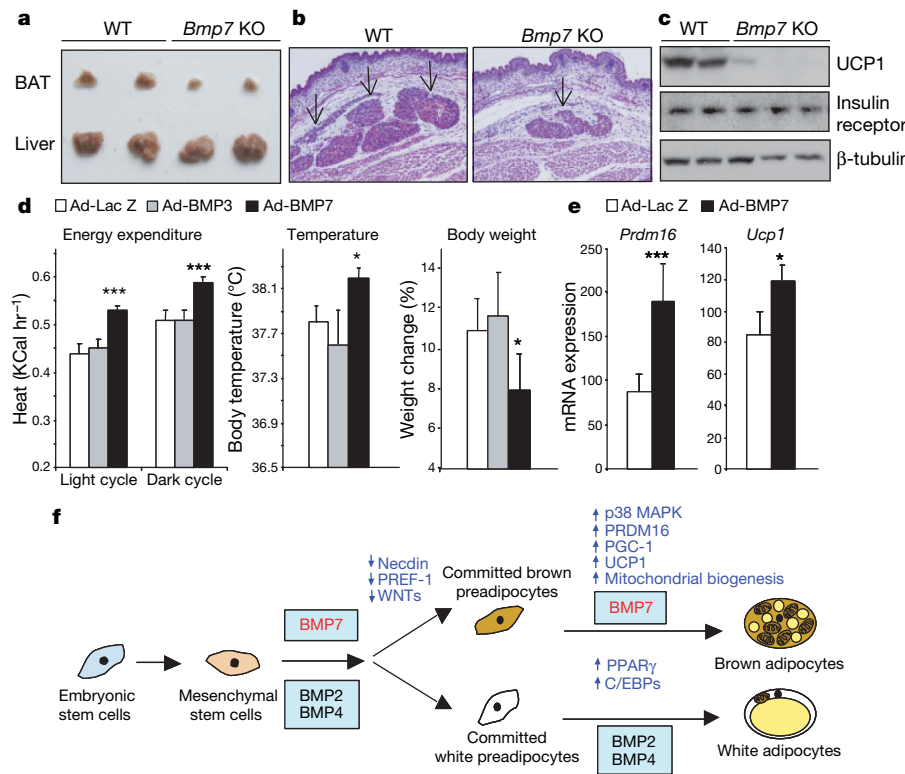


**Figure 4 | Evidence for an essential role of BMP7 in BAT development, and regulation of whole-body energy expenditure by loss-of-function and gain-of-function approaches.** **a**, Gross morphological analysis of BAT and liver from 1-day-old wild-type (WT) and *Bmp7* knockout (KO) pups. **b**, Transverse histological sections at the thoracic region from wild-type and *Bmp7* KO embryos at 17.5 d.p.c. Slides were stained by haematoxylin and eosin. Arrows indicate BAT. Original magnification is  $\times 200$ . **c**, Western blotting analysis of UCP1 and insulin receptor  $\beta$  chain in BAT from wild-type and *Bmp7* KO embryos at 18.5 d.p.c.  $\beta$ -tubulin serves as a loading control. **d**, Adenoviruses (Ad) expressing BMP7, BMP3 or LacZ control were injected into 4-week-old C57BL/6 mice by means of the tail vein ( $n = 5$ ).

increase in brown fat mass with no change in WAT mass (Supplementary Fig. 13). In a cohort of older mice, BMP7 treatment specifically induced expression of *Prdm16* and *Ucp1* in BAT. They encode two key factors determining brown fat fate and function (Fig. 4e), whereas the expression of genes involved in energy homeostasis in other tissues, including WAT, muscle and liver, remained unaltered (Supplementary Fig. 14). Together, these data not only recapitulate the brown adipogenic effect of BMP7 *in vivo*, but also reveal an important anti-obesity potential of BMP7 by increasing whole-body thermogenesis.

BAT and WAT are morphologically and functionally different tissues, and their developmental patterns are quite distinct. One of the remaining questions in adipocyte biology is how and when the developmental fate of brown versus white adipocytes is regulated and specified. On the basis of the present data and published observations from other investigators<sup>8,9,24</sup>, we propose a model for the role of BMPs in determination of brown versus white fat cell fate, as illustrated in Fig. 4f. Whereas BMP2 and BMP4 can promote differentiation of white adipocyte lineage, we demonstrate in the present study that BMP7 drives brown fat cell fate in both mesenchymal progenitor cells and committed brown preadipocytes. This is achieved by suppression of early adipogenic inhibitors, such as necdin, PREF-1 and WNTs, and by induction of key molecules that specify brown fat fate, such as PRDM16 and PGC-1 $\alpha$ , leading to a mature brown adipocyte phenotype characterized by UCP1 expression and abundant mitochondria. *Bmp7* null embryos display brown fat hypoplasia and almost complete absence of UCP1 protein, highlighting an essential

Energy expenditure was determined at 10 days after injection by indirect calorimetry. Basal body temperature was measured using a rectal thermometer after 14 days of injection. The significance of body weight change at day 5 after adenoviral injection was determined by Wilcoxon signed-rank test. **e**, Adenoviruses expressing BMP7 or LacZ control were injected into 12-week old C57BL/6 mice by means of the tail vein ( $n = 6$ ). Mice were killed 15 days after injection. Expression of *Prdm16* and *Ucp1* in BAT was measured by Q-RT-PCR. Data are presented as mean  $\pm$  s.e.m. Asterisks depict statistically significant differences between control and BMP7 groups ( $^*P < 0.05$ ,  $^{***}P < 0.001$ ). **f**, Proposed model for the role of BMPs in determination of brown versus white adipocyte development.

role of BMP7 in brown fat development. When used as a treatment *in vivo*, BMP7 is able to increase brown fat mass and thermogenic energy expenditure in mice.

Whereas BMP2, BMP4, BMP6 and BMP7 are able to induce massive lipid accumulation in brown preadipocytes, we find that only BMP7 has a specific effect on induction of the brown-fat-specific protein UCP1. Differential effects of various BMPs on other cell types have also been observed<sup>25</sup>. For example, BMP7, but not BMP4 or BMP6, is able to reverse the TGF- $\beta$ -induced epithelial-to-mesenchymal transition in distal tubular epithelial cells<sup>26</sup>. Exactly how the specificity of different BMPs is determined remains an unsolved question in the field. Our data have indicated an important role of p38 MAP kinase and PGC-1 coactivator in BMP7-induced thermogenesis. Originally identified as a bone inducer<sup>27</sup>, BMP7 is now being recognized as a multifunctional cytokine and has been implicated as a potential therapeutic agent for cardiovascular, metabolic and degenerative diseases<sup>28</sup>. In this study, our data reveal a novel function of BMP7 in the regulation of energy homeostasis by promoting brown, but not white, fat differentiation and function. Thus, we propose that treatment of humans with BMP7 or its molecular mimetic may activate brown fat differentiation, leading to an increase in energy expenditure, and thereby providing a new way to combat obesity.

## METHODS SUMMARY

**Adipocyte differentiation.** To induce adipocyte differentiation by BMPs in the absence of induction cocktails, both wild-type brown preadipocytes and 3T3-L1

white preadipocytes were grown in regular growth medium supplemented with a combination of recombinant human BMPs (rhBMPs, 3.3–8.3 nM), insulin (20 nM) and triiodothyronine (T3, 1 nM) or vehicle as indicated in the text and figure legends for 7–13 days. To stimulate the thermogenic program, differentiated cells were incubated with 500  $\mu$ M dibutyryl cAMP for 4 h. Cells were grown in growth medium without hormonal supplements for 18 h before cAMP stimulation.

C3H10T1/2 cells were grown in the presence and absence of 8.3 nM rhBMP7 for 3 days to reach confluence (day 3). These cells were then induced to adipocyte differentiation using protocols described below for an additional 7 days (day 10). Adipocyte differentiation was performed by treating confluent cells for 48 h in medium supplemented with 20 nM insulin and 1 nM T3, 0.5  $\mu$ M isobutyl-methylxanthine (IBMX), 5 mM dexamethasone, and 0.125 mM indomethacin. Cells were placed back in growth medium supplemented with insulin and T3, which was then changed every second day. After four to five more days in this medium, cells exhibited a fully differentiated phenotype with massive lipid accumulation.

**Full Methods** and any associated references are available in the online version of the paper at [www.nature.com/nature](http://www.nature.com/nature).

Received 27 February; accepted 27 June 2008.

1. Gesta, S., Tseng, Y. H. & Kahn, C. R. Developmental origin of fat: tracking obesity to its source. *Cell* **131**, 242–256 (2007).
2. Farmer, S. R. Transcriptional control of adipocyte formation. *Cell Metab.* **4**, 263–273 (2006).
3. Rosen, E. D. & MacDougald, O. A. Adipocyte differentiation from the inside out. *Nature Rev. Mol. Cell Biol.* **7**, 885–896 (2006).
4. Seale, P. *et al.* Transcriptional control of brown fat determination by PRDM16. *Cell Metab.* **6**, 38–54 (2007).
5. Puigserver, P. *et al.* A cold-inducible coactivator of nuclear receptors linked to adaptive thermogenesis. *Cell* **92**, 829–839 (1998).
6. Chen, D., Zhao, M. & Mundy, G. R. Bone morphogenetic proteins. *Growth Factors* **22**, 233–241 (2004).
7. Tseng, Y. H. & He, T. C. Bone morphogenetic proteins and adipocyte differentiation. *Cellscience Rev.* **3**, 342–360 (2007).
8. Wang, E. A., Israel, D. I., Kelly, S. & Luxenberg, D. P. Bone morphogenetic protein-2 causes commitment and differentiation in C3H10T1/2 and 3T3 cells. *Growth Factors* **9**, 57–71 (1993).
9. Tang, Q. Q., Otto, T. C. & Lane, M. D. Commitment of C3H10T1/2 pluripotent stem cells to the adipocyte lineage. *Proc. Natl. Acad. Sci. USA* **101**, 9607–9611 (2004).
10. Klein, J. *et al.*  $\beta_3$ -adrenergic stimulation differentially inhibits insulin signaling and decreases insulin induced glucose uptake in brown adipocytes. *J. Biol. Chem.* **274**, 34795–34802 (1999).
11. Ducy, P., Zhang, R., Geoffroy, V., Ridall, A. L. & Karsenty, G. Osf2/Cbfa1: a transcriptional activator of osteoblast differentiation. *Cell* **89**, 747–754 (1997).
12. Canal, E., Economides, A. N. & Gazzero, E. Bone morphogenetic proteins, their antagonists, and the skeleton. *Endocr. Rev.* **24**, 218–235 (2003).
13. Puigserver, P. *et al.* Cytokine stimulation of energy expenditure through p38 MAP kinase activation of PPAR $\gamma$  coactivator-1. *Mol. Cell* **8**, 971–982 (2001).
14. Cao, W. *et al.* p38 mitogen-activated protein kinase is the central regulator of cyclic AMP-dependent transcription of the brown fat uncoupling protein 1 gene. *Mol. Cell. Biol.* **24**, 3057–3067 (2004).
15. Uldry, M. *et al.* Complementary action of the PGC-1 coactivators in mitochondrial biogenesis and brown fat differentiation. *Cell Metab.* **3**, 333–341 (2006).
16. Tseng, Y. H. *et al.* Prediction of preadipocyte differentiation by gene expression reveals role of insulin receptor substrates and neocidin. *Nature Cell Biol.* **7**, 601–611 (2005).
17. Nedergaard, J., Connally, E. & Cannon, B. *Brown Adipose Tissue* (eds Trayhurn, P. & Nicholls, D. G.) 152–213 (Arnold, 1986).
18. Varga, A. C. & Wrana, J. L. The disparate role of BMP in stem cell biology. *Oncogene* **24**, 5713–5721 (2005).
19. Darlington, G. J., Ross, S. E. & MacDougald, O. A. The role of C/EBP genes in adipocyte differentiation. *J. Biol. Chem.* **273**, 30057–30060 (1998).
20. Wu, Z. *et al.* Cross-regulation of C/EBP $\alpha$  and PPAR $\gamma$  controls the transcriptional pathway of adipogenesis and insulin sensitivity. *Mol. Cell* **3**, 151–158 (1999).
21. Tseng, Y. H., Kriaucionas, K. M., Kokkotou, E. & Kahn, C. R. Differential roles of insulin receptor substrates in brown adipocyte differentiation. *Mol. Cell. Biol.* **24**, 1918–1929 (2004).
22. Dudley, A. T., Lyons, K. M. & Robertson, E. J. A requirement for bone morphogenetic protein-7 during development of the mammalian kidney and eye. *Genes Dev.* **9**, 2795–2807 (1995).
23. Luo, G. *et al.* BMP-7 is an inducer of nephrogenesis, and is also required for eye development and skeletal patterning. *Genes Dev.* **9**, 2808–2820 (1995).
24. Jin, W. *et al.* Schnurri-2 controls BMP-dependent adipogenesis via interaction with Smad proteins. *Dev. Cell* **10**, 461–471 (2006).
25. Cheng, H. *et al.* Osteogenic activity of the fourteen types of human bone morphogenetic proteins (BMPs). *J. Bone Joint Surg. Am.* **85-A**, 1544–1552 (2003).
26. Zeisberg, M. *et al.* BMP-7 counteracts TGF- $\beta$ 1-induced epithelial-to-mesenchymal transition and reverses chronic renal injury. *Nature Med.* **9**, 964–968 (2003).
27. Ozkaynak, E. *et al.* OP-1 cDNA encodes an osteogenic protein in the TGF- $\beta$  family. *EMBO J.* **9**, 2085–2093 (1990).
28. Tobin, J. F. & Celeste, A. J. Bone morphogenetic proteins and growth differentiation factors as drug targets in cardiovascular and metabolic disease. *Drug Discov. Today* **11**, 405–411 (2006).

**Supplementary Information** is linked to the online version of the paper at [www.nature.com/nature](http://www.nature.com/nature).

**Acknowledgements** We acknowledge T.-C. He for providing adenoviruses expressing BMPs. We thank M. Rourk and L. Mazzola for help with the animal experiments, J. Hu, C. Cahill, A. McSweeney, L. Polivy and R. Bronson for technical assistance, and P. Zhang for statistical consultation. We thank A. Butte and P. Laustsen for inputs on initiation of this project. We thank M. Uldry and B. Spiegelman for providing the PGC-1 null cells. This work was supported in part by the National Institutes of Health grants R01 DK077097, R21 DK070722, P30 DK46200 and P30 DK040561 (to Y.-H.T.), R01 DK67536 (to R.N.K.), K08 DK64906 (to A.W.N.) and R01 DK 060837 (to C.R.K.), the Tanita Healthy Weight Community, and the Eleanor and Miles Shore 50<sup>th</sup> Anniversary Scholar Program from Harvard Medical School (to Y.-H.T.).

**Author Information** Reprints and permissions information is available at [www.nature.com/reprints](http://www.nature.com/reprints). Correspondence and requests for materials should be addressed to Y.-H.T. (yu-hua.tseng@joslin.harvard.edu).

## METHODS

**Materials.** Recombinant human BMPs were purchased from R&D Systems. Antibodies used for immunoblotting included anti-UCP1, anti-PPAR $\gamma$ , anti- $\beta$ -tubulin (all purchased from Santa Cruz Biotechnology), anti-FAS (a gift from F. P. Kuhajda), anti-phospho-SMAD1/5/8, anti-phospho-p38 MAPK, anti-phospho-ATF-2, anti- $\beta$ -tubulin, anti-insulin receptor  $\beta$  subunit (Cell Signaling) and anti-cyclophilin A (Upstate Biotechnology). Immobilon-P transfer membranes were from Millipore and electrophoresis supplies were from Bio-Rad Laboratories. SB202190, SB203280 and PD169316 were purchased from Calbiochem and dissolved in DMSO. All other chemicals were purchased from Sigma Chemical Co. unless otherwise specified.

**Cell culture.** C3H10T1/2 and 3T3-L1 cells were purchased from American Type Culture Collection. Generation of wild-type brown preadipocyte cell lines derived from newborn wild-type mice was as described previously<sup>10,29–31</sup>. The PGC-1 null brown preadipocyte cell line was a gift from B. M. Spiegelman<sup>15</sup>. All cell lines used in this study were maintained in Dulbecco's modified Earle's medium (DMEM) 10% fetal clone III (HyClone) at 37 °C in 5% CO<sub>2</sub> environment unless otherwise specified.

**Q-RT-PCR analysis.** Total RNA was isolated with QIAzol lysis reagent (Qiagen) and purified by RNeasy Mini columns (Qiagen) following the manufacturer's instructions. Complementary DNA was prepared from 1  $\mu$ g of RNA using the Advantage RT-PCR kit (BD Biosciences) according to the manufacturer's instructions and diluted to a final volume of 250  $\mu$ l. Five microlitres of diluted cDNA was used in a 20  $\mu$ l PCR reaction with SYBR Green Master Mix (Applied Biosystems) and primers at a concentration of 300 nM each. PCR reactions were run in duplicate for each sample and quantified in the ABI Prism 7000 Sequence Detection System (Applied Biosystems). Data were expressed as arbitrary units after normalization to levels of expression of the internal control acidic ribosomal phosphoprotein P0 (Arbp, 36B4) for each sample. Sequences of primers used in this study are listed in Supplementary Table 2.

**Oil red O staining.** Dishes were washed twice with phosphate-buffered saline and fixed with 10% buffered formalin for 16 h at 4 °C. Cells were then stained for 2 h at room temperature with a filtered Oil red O solution (0.5% Oil red O in isopropyl alcohol), washed twice with distilled water, and visualized.

**Western blot analysis.** Cells were collected in lysis buffer (50 mM HEPES, 137 mM NaCl, 1 mM MgCl<sub>2</sub>, 1 mM CaCl<sub>2</sub>, 10 mM Na<sub>2</sub>P<sub>2</sub>O<sub>7</sub>, 10 mM NaF, 2 mM EDTA, 10% glycerol, 1% Igepal CA-630, 2 mM vanadate, 10  $\mu$ g ml<sup>−1</sup> leupeptin, 10  $\mu$ g ml<sup>−1</sup> aprotinin and 2 mM phenylmethylsulfonyl fluoride, pH 7.4). After lysis, lysates were clarified by centrifugation at 12,000g for 20 min at 4 °C; the protein amount in the supernatants was determined by the Bradford Protein Assay (Bio-Rad Laboratories). Proteins were directly solubilized in Laemmli sample buffer. Equal amounts of proteins were separated by SDS-polyacrylamide gel electrophoresis and transferred to Immobilon-P membranes. Membranes were blocked overnight at 4 °C and incubated with the indicated antibody for 2 h at room temperature. Specifically bound primary antibodies were detected with peroxidase-coupled secondary antibody and enhanced chemiluminescence (Amersham Biosciences).

**Electron microscopy.** Cells were fixed in 2.5% glutaraldehyde, and then post-fixed in 2% osmium tetroxide, dehydrated in ascending gradations of ethanol, and embedded in fresh Araldite 502 epoxy resin using BEEM capsules. Ultra-thin sections (60–80 nm) were cut and mounted on 75 mesh copper grids, and then stained with uranyl acetate and lead citrate before being examined on the Phillips 301 transmission electron microscope. Mitochondrial and total cytoplasmic areas were quantified by using the NIH Image J software (<http://rsb.info.nih.gov/ij/>). Mitochondrial density was determined by the ratio of the sum of mitochondrial area to total cytoplasmic area per cell.

**Isolation of stromo-vascular fractions and *in vitro* differentiation.** Eight 6-week-old C57BL/6 male mice were killed. Interscapular BAT and axillary subcutaneous WAT were removed, minced and digested with 1 mg ml<sup>−1</sup> collagenase for 45 min at 37 °C in DMEM/F12 medium containing 1% BSA and antibiotics. Digested tissues were filtered through sterile 150  $\mu$ m nylon mesh and centrifuged at 250g for 5 min. The floating fractions consisting of adipocytes were discarded and the pellets representing the stromo-vascular fractions were then resuspended in erythrocyte lysis buffer (154 mM NH<sub>4</sub>Cl, 10 mM KHCO<sub>3</sub>, 0.1 mM EDTA) for 10 min to remove red blood cells. The cells were further centrifuged at 500g for 5 min, plated at 8  $\times$  10<sup>5</sup> per well of a 24-well plate and grown at 37 °C in DMEM/F12 supplemented with 10% FBS at 37 °C.

*In vitro* differentiation was performed using the method described in ref. 32. After 2 days of incubation, the attached cells were washed and incubated in serum-free differentiation medium containing DMEM/F12 medium supplemented with 1  $\mu$ M dexamethasone, 66 nM insulin, 15 mM HEPES, 1 nM T3, 33  $\mu$ M biotin, 17  $\mu$ M pantothenate, 10  $\mu$ g ml<sup>−1</sup> transferrin and 100  $\mu$ g ml<sup>−1</sup> penicillin-streptomycin in the absence or presence of 1  $\mu$ g ml<sup>−1</sup> rosiglitazone or 3.3 nM rhBMP7 for 3 days.

**Implantation.** C3H10T1/2 cells were grown in the presence and absence of 3.3 nM rhBMP7 for 3 days to reach confluence. Cells were washed, trypsinized, and resuspended in growth medium. 1.5  $\times$  10<sup>7</sup> cells in 0.15 ml volume were injected into the thoracic/sternum region of 5-week-old BALB/c athymic mice (Charles River Laboratories, Inc.) using an 18-gauge needle. Mice were killed 6 weeks after injection, and adipose tissue derived from implanted cells was excised and processed for histological analysis.

**Histology and immunohistochemistry.** Tissues were fixed in 10% formalin and were paraffin-embedded. Multiple sections were prepared and stained with haematoxylin and eosin for general morphological observation. UCP1 immunohistochemistry of tissue from implanted cells was performed using polyclonal anti-mouse UCP1 antibody (Chemicon International Inc.) at 1:50 dilution and the Dako Envision Doublestain System (Dako) following the manufacturer's instruction. Slides were counterstained with haematoxylin.

**Genotyping of *Bmp7* null mice.** *Bmp7* null mice were produced by intercrosses of animals heterozygous for a null allele of *Bmp7* generated by an insertion of *lacZ* into exon 1 (ref. 33). Genotypes were initially determined by a combination of  $\beta$ -galactosidase staining and the presence or absence of a severe eye phenotype (very small eyes or no eye)<sup>22,23,33</sup>. All genotypes were confirmed by PCR as described in ref. 34. For  $\beta$ -galactosidase staining, the tips of tails were clipped, and fixed in 4% PFA plus 2 mM MgCl<sub>2</sub> in PBS for 30 min at room temperature. The tails were washed in 2 mM MgCl<sub>2</sub> in PBS 3 times for 10 min at room temperature. The tails were stained at 37 °C overnight in X-gal staining solution (5 mM potassium ferrocyanide, 5 mM potassium ferricyanide, 2 mM MgCl<sub>2</sub> and 0.5 mg ml<sup>−1</sup> 5-bromo-4-chloro-3-indolyl- $\beta$ -D-galactosidase X-gal, Denville Scientific, Inc.). The presence of  $\beta$ -galactosidase staining in the tails indicates that the *lacZ* transgene is present in *Bmp7* exon 1. A lack of  $\beta$ -galactosidase staining indicates the mouse is wild type.

**Adenoviral injection.** Adenoviruses were amplified in HEK293 cells as described previously<sup>35</sup>. Before *in vivo* use, all adenoviruses were purified on a caesium chloride gradient and dialysed into PBS plus 10% glycerol. Four- and twelve-week-old male C57BL/6 mice were injected via the tail vein with an adenoviral dose of 5  $\times$  10<sup>8</sup> viral particles per g body weight as described previously<sup>36</sup>. Mice were killed 15 days after injection. Interscapular brown fat and epididymal white fat were excised and weighed. Half of the tissue was fixed in 10% formalin and processed for histological analysis. The other half of the tissue was subjected to RNA extraction and Q-RT-PCR analysis.

**Indirect calorimetry.** Metabolic rates were measured by indirect calorimetry in mice 7–10 days after adenoviral injection by using the Comprehensive Lab Animal Monitoring System (CLAMS, Columbus Instruments). Mice were maintained at 24 °C under a 12-h light/dark cycle. Food and water were available *ad libitum*. Mice were acclimatized to individual cages for 24 h before recording, and then underwent 24 h of monitoring.

Heat production (energy expenditure) was calculated using the following equation:

$$\text{Heat} = [3.815 + 1.232(V_{\text{CO}_2}/V_{\text{O}_2})] \times V_{\text{O}_2} \times \text{body weight}$$

where heat is measured in kcal h<sup>−1</sup>, V<sub>O<sub>2</sub></sub> is measured in litres kg<sup>−1</sup> h<sup>−1</sup> and body weight is measured in kg.

**Measurement of plasma BMP7 concentrations.** Blood was collected at day 1 and day 3 after adenoviral injection and at the time the mouse was killed. Plasma BMP7 levels were determined by ELISA using the DuoSet ELISA Development kit purchased from R&D Systems following the manufacturer's instructions. Concentrations were calculated using a standard curve generated by rhBMP7 standards included in the kit.

**Statistical analysis.** Statistical significance in gene expression between the control and the BMP-treated group was determined by analysis of variance (ANOVA) test or Student's *t* test unless otherwise specified. To evaluate if there was a significant change in body weight between BMP7 and control groups, we performed a multivariate ANOVA (MANOVA) test. Based on multivariate normal assumption on the data, Hotelling's *T*<sup>2</sup> statistics was calculated and yielded *T*<sup>2</sup> = 3.9613 and a significant *P*-value of 0.0191. The *T*<sup>2</sup> test of Harold Hotelling compares means of two or more continuous measures simultaneously for the two groups. Considering the small size of samples and the validity of multivariate normal assumption, we also performed the sign- and rank-based MANOVA analyses. The sign-based MANOVA gave a *P*-value of 0.0581 and the rank-based MANOVA yielded a *P*-value of 0.0612. Both are marginally statistically significant. Comparison was also conducted at different time points individually. We found that at day 5 after adenoviral injection, the percentage of body weight changes relative to the initial body weight was significant between the control and the BMP7 groups (*P*-value = 0.0469 by Wilcoxon signed-rank test).

29. Fasshauer, M. et al. Essential role of insulin receptor substrate-2 in insulin stimulation of GLUT4 translocation and glucose uptake in brown adipocytes. *J. Biol. Chem.* 275, 25494–25501 (2000).

30. Fasshauer, M. *et al.* Essential role of insulin receptor substrate 1 in differentiation of brown adipocytes. *Mol. Cell. Biol.* **21**, 319–329 (2001).
31. Tseng, Y. H., Ueki, K., Kriauciunas, K. M. & Kahn, C. R. Differential roles of insulin receptor substrates in the anti-apoptotic function of insulin-like growth factor-1 and insulin. *J. Biol. Chem.* **277**, 31601–31611 (2002).
32. Hauner, H. *et al.* Promoting effect of glucocorticoids on the differentiation of human adipocyte precursor cells cultured in a chemically defined medium. *J. Clin. Invest.* **84**, 1663–1670 (1989).
33. Godin, R. E., Takaesu, N. T., Robertson, E. J. & Dudley, A. T. Regulation of BMP7 expression during kidney development. *Development* **125**, 3473–3482 (1998).
34. Bandyopadhyay, A. *et al.* Genetic analysis of the roles of BMP2, BMP4, and BMP7 in limb patterning and skeletogenesis. *PLoS Genet.* **2**, e216 (2006).
35. Ueki, K., Kondo, T., Tseng, Y. H. & Kahn, C. R. Central role of suppressors of cytokine signaling proteins in hepatic steatosis, insulin resistance, and the metabolic syndrome in the mouse. *Proc. Natl Acad. Sci. USA* **101**, 10422–10427 (2004).
36. Laustsen, P. G. *et al.* Lipoatrophic diabetes in *Irs1*<sup>−/−</sup>/*Irs3*<sup>−/−</sup> double knockout mice. *Genes Dev.* **16**, 3213–3222 (2002).

# The pathogen protein EspF<sub>U</sub> hijacks actin polymerization using mimicry and multivalency

Nathan A. Sallee<sup>1,2</sup>, Gonzalo M. Rivera<sup>3</sup>, John E. Dueber<sup>2</sup>†, Dan Vasilescu<sup>3</sup>, R. Dyche Mullins<sup>2</sup>, Bruce J. Mayer<sup>3</sup> & Wendell A. Lim<sup>2</sup>

Enterohaemorrhagic *Escherichia coli* attaches to the intestine through actin pedestals that are formed when the bacterium injects its protein EspF<sub>U</sub> (also known as TccP) into host cells<sup>1</sup>. EspF<sub>U</sub> potently activates the host WASP (Wiskott–Aldrich syndrome protein) family of actin-nucleating factors, which are normally activated by the GTPase CDC42, among other signalling molecules. Apart from its amino-terminal type III secretion signal, EspF<sub>U</sub> consists of five-and-a-half 47-amino-acid repeats. Here we show that a 17-residue motif within this EspF<sub>U</sub> repeat is sufficient for interaction with N-WASP (also known as WASL). Unlike most pathogen proteins that interface with the cytoskeletal machinery, this motif does not mimic natural upstream activators: instead of mimicking an activated state of CDC42, EspF<sub>U</sub> mimics an autoinhibited element found within N-WASP. Thus, EspF<sub>U</sub> activates N-WASP by competitively disrupting the autoinhibited state. By mimicking an internal regulatory element and not the natural activator, EspF<sub>U</sub> selectively activates only a precise subset of CDC42-activated processes. Although one repeat is able to stimulate actin polymerization, we show that multiple-repeat fragments have notably increased potency. The activities of these EspF<sub>U</sub> fragments correlate with their ability to coordinate activation of at least two N-WASP proteins. Thus, this pathogen has used a simple autoinhibitory fragment as a component to build a highly effective actin polymerization machine.

Many pathogens target the cytoskeletal machinery of their host to facilitate attachment, entry or cell-to-cell spreading<sup>2,3</sup>. Enterohaemorrhagic *E. coli* (EHEC, O157:H7) causes severe gastrointestinal disease, and infection is dependent on attachment of the bacterium to intestinal epithelial cells by means of actin pedestals<sup>1</sup>. Pedestal formation is mediated by the pathogenic protein EspF<sub>U</sub> (*E. coli*-secreted protein F-like protein from prophage U; refs 4, 5), which is injected through a type III secretion system<sup>6</sup> into host cells where it stimulates actin polymerization by activating host WASP family proteins (Fig. 1a). WASPs are activators of the actin-related protein (ARP)2/3 complex, but under basal conditions this function is regulated by an autoinhibitory interaction between the GTPase-binding domain (GBD) and the 'C-helix' in the catalytic WCA region (named for its WASP-homology 2 (WH2) motif(s), C-helix, and acidic motif)<sup>7</sup>. Normal activation of N-WASP requires disruption of autoinhibition (Fig. 1b), involving the coordinated action of multiple endogenous activators, including CDC42, the phospholipid PtdIns(4,5)P<sub>2</sub>, and SH3-domain-containing proteins such as NCK (refs 8, 9; Fig. 1c). EspF<sub>U</sub> can independently activate N-WASP with a potency that is orders of magnitude higher than single endogenous activators<sup>8</sup> (Fig. 1c, d and Supplementary Fig. 1).

A common strategy exploited by pathogens in targeting host cell processes is to produce a protein that mimics an endogenous activator of that process<sup>6,10,11</sup>. This mimic will generally be constitutively active compared to the endogenous protein, which shows regulated activity<sup>12,13</sup>. Among pathogens that target actin polymerization, there

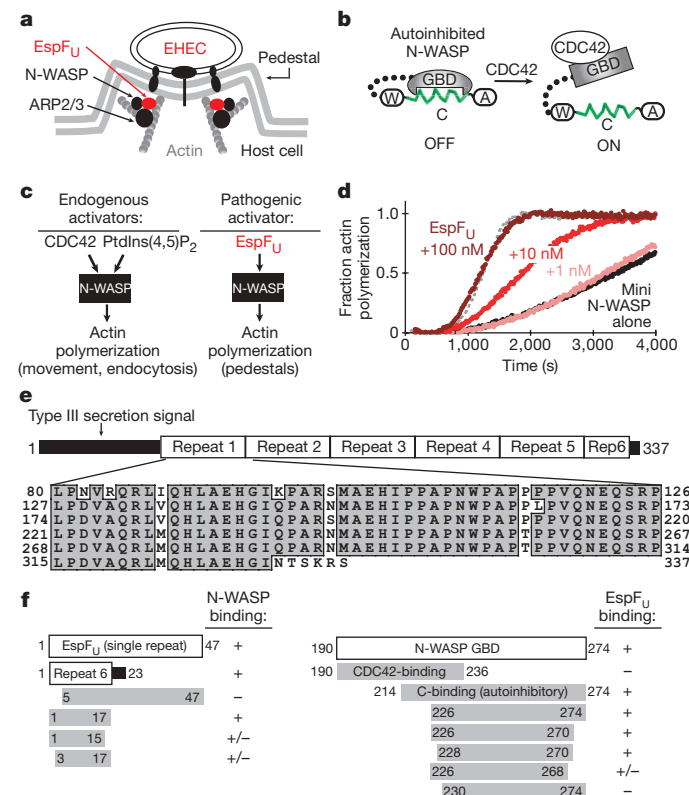


**Figure 1 | EspF<sub>U</sub> is a potent activator of N-WASP.** **a**, EspF<sub>U</sub> is secreted from EHEC into a host cell where it stimulates actin polymerization through endogenous N-WASP and ARP2/3, leading to pedestal formation. **b**, N-WASP is basally autoinhibited, but can be activated by inputs such as CDC42. **c**, Multiple endogenous activators are necessary to potently activate N-WASP. EspF<sub>U</sub> accomplishes this with a single input. **d**, EspF<sub>U</sub> potently activates N-WASP in an *in vitro* pyrene-actin-polymerization assay. Maximal rate (50 nM unregulated N-WASP WCA) is shown by the grey dotted line. All other reactions contain 50 nM mini N-WASP (GBD-linker-WCA). **e**, Sequence of EspF<sub>U</sub>. **f**, Mapping minimal binding fragments of EspF<sub>U</sub> and N-WASP with a GST-pull-down assay.

<sup>1</sup>Graduate Program in Chemistry and Chemical Biology and <sup>2</sup>Department of Cellular and Molecular Pharmacology and the Cell Propulsion Laboratory (an NIH Nanomedicine Development Center), University of California, San Francisco, 600 16th Street, San Francisco, California 94158, USA. <sup>3</sup>Raymond and Beverly Sackler Laboratory of Genetics and Molecular Medicine, Department of Genetics and Developmental Biology and Center for Cell Analysis and Modeling (CCAM), University of Connecticut Health Center, Farmington, Connecticut 06030, USA. <sup>†</sup>Present address: Department of Synthetic Biology, California Institute of Quantitative Biomedical Research (QB3), University of California, Berkeley, 327 Stanley Hall, Berkeley, California 94720, USA.

are examples of effector proteins that mimic the active states of N-WASP (ref. 14) or N-WASP activators such as CDC42 (ref. 15). Previous studies have shown that EspF<sub>U</sub> interacts with the GBD (refs 16, 17), the regulatory domain in N-WASP that participates in autoinhibition and binds to activated CDC42 (ref. 7). Thus, we set out to test the hypothesis that EspF<sub>U</sub> may mimic an activated state of CDC42.

EspF<sub>U</sub> has a type III secretion signal followed by five-and-a-half 47-amino-acid repeats (Fig. 1e; a six-and-a-half-repeat isoform of EspF<sub>U</sub> has also been reported<sup>5</sup>). The repeats are nearly identical and share little sequence homology with other proteins, except for the related EHEC protein EspF. EspF also activates N-WASP (ref. 18) but does not participate in pedestal formation<sup>4,19</sup> (EspF contributes to the disruption of epithelial tight junctions).

We first mapped the minimal interacting fragments of both EspF<sub>U</sub> and N-WASP using pull-down-binding assays. We found that the N-WASP GBD could bind to a single EspF<sub>U</sub> repeat. We tested other truncations and found that the first 17 amino acids of each repeat constitute the minimal fragment with high affinity for the GBD (Fig. 1f and Supplementary Fig. 2). This sequence corresponds to a predicted  $\alpha$ -helix<sup>20</sup> and it is repeated six times in the full-length protein. There are minor sequence differences among the six copies of this motif, but the repeats seem to be equivalent in binding and functional assays (data not shown).

The N-WASP GBD is a composite regulatory domain made up of two overlapping elements—a CDC42-binding element and an autoinhibitory element that binds to the C-helix<sup>1</sup>. Detailed mapping of the N-WASP side of the interaction showed that the carboxy-terminal, autoinhibitory portion of the GBD interacts with EspF<sub>U</sub> and that the amino-terminal, CDC42-binding portion does not. The minimal EspF<sub>U</sub>-binding fragment of N-WASP is residues 228–270 (Fig. 1f and Supplementary Fig. 2), which form the core of the interaction with the C-helix in the autoinhibited structure (Fig. 2a)<sup>7</sup>.

Because a small peptide from EspF<sub>U</sub> interacts with the autoinhibitory portion of the GBD, it seemed unlikely that EspF<sub>U</sub> was activating N-WASP by mimicking CDC42. Instead, we postulated that this EspF<sub>U</sub> fragment might be mimicking the C-helix and disrupting N-WASP autoinhibition by competitively binding to the GBD. We found that EspF<sub>U</sub> does indeed competitively disrupt the N-WASP autoinhibitory interaction in a pull-down-binding assay (Fig. 2b). Sequence alignment of the C-helix and the first 17 amino acids of the EspF<sub>U</sub> repeat revealed sequence homology at three positions at which hydrophobic amino acids are known to be critical for interaction with the GBD (Fig. 2a, c)<sup>21</sup>. We carried out a systematic alanine scan of both the N-WASP and the EspF<sub>U</sub> fragments and tested binding of the mutants to the GBD. The results showed that mutation of any of the conserved hydrophobic positions to alanine on either the C-helix or the EspF<sub>U</sub> fragment completely disrupted interaction with the GBD (Fig. 2c).

Previous work has shown that the isolated WASP GBD is only partially folded and unstable, but that fusion of the C-helix to the GBD leads to a stably folded, helical structure that approximates the autoinhibited state<sup>7</sup>. We made a fusion of the GBD to the minimal 17-amino-acid interacting fragment from EspF<sub>U</sub> found that this protein had very similar helical content and thermal stability to the GBD–C-helix fusion (Supplementary Fig. 3).

These results show that the N-terminal 17 amino acids of the EspF<sub>U</sub> repeat are mimicking the C-helix (an autoinhibitory element) and this motif competitively disrupts autoinhibition of WASPs (Fig. 2d). A similar sequence motif is present in EspF and probably activates N-WASP using the same mechanism. We found that one EspF<sub>U</sub> repeat binds to the N-WASP GBD (amino acids 214–274) with a dissociation constant ( $K_d$ ) of 18 nM (Supplementary Fig. 4). This affinity is about 100-fold tighter than previously measured values for the corresponding WASP GBD–C-helix interaction (*in trans*)<sup>7</sup>, and this higher affinity explains how an intermolecular interaction can competitively disrupt an intramolecular interaction. The C-helix also

contributes to the interactions of N-WASP with actin monomers and the ARP2/3 complex<sup>22</sup>. We found that EspF<sub>U</sub> can bind to these molecules as well (Supplementary Fig. 4). In spite of this, EspF<sub>U</sub> cannot stimulate actin polymerization without N-WASP (data not shown).

Utilization of a competitive autoinhibitory fragment represents a previously unknown strategy for a pathogen to use in hijacking host cell signalling. One possible advantage of this strategy is increased specificity: a constitutively active signalling mimic will activate all downstream endogenous signalling pathways, whereas a mimic of a regulatory element should only activate a small subset. To test this idea, we investigated whether EspF<sub>U</sub> could activate the p21-activated kinases (PAKs)—another group of CDC42-responsive proteins, the regulation of which is most closely related to that of WASPs. CDC42 activates PAKs by disrupting an autoinhibitory interaction (which is structurally homologous to that of WASP)<sup>23</sup>. However, the PAK homologue of the WASP C-helix lacks the consensus sequence of three conserved hydrophobic amino acids. EspF<sub>U</sub> was unable to activate PAKs (Fig. 2e and Supplementary Fig. 5), indicating specificity of EspF<sub>U</sub> towards WASP family proteins (Fig. 2d). This more targeted activation may be advantageous for the pathogen, given the broad range of downstream effects mediated by WASP activators such as CDC42.

We also investigated the functional significance of this autoinhibitory mimic being repeated six times in one EspF<sub>U</sub> molecule. We tested the relative abilities of EspF<sub>U</sub> fragments of different lengths to stimulate actin assembly using an *in vitro* pyrene-actin-polymerization assay. One repeat from EspF<sub>U</sub> can disrupt the N-WASP autoinhibitory interaction in a binding assay (Supplementary Fig. 6), but has low ability to stimulate actin polymerization (comparable to that of a single endogenous activator; Fig. 3a). A fragment of two repeats

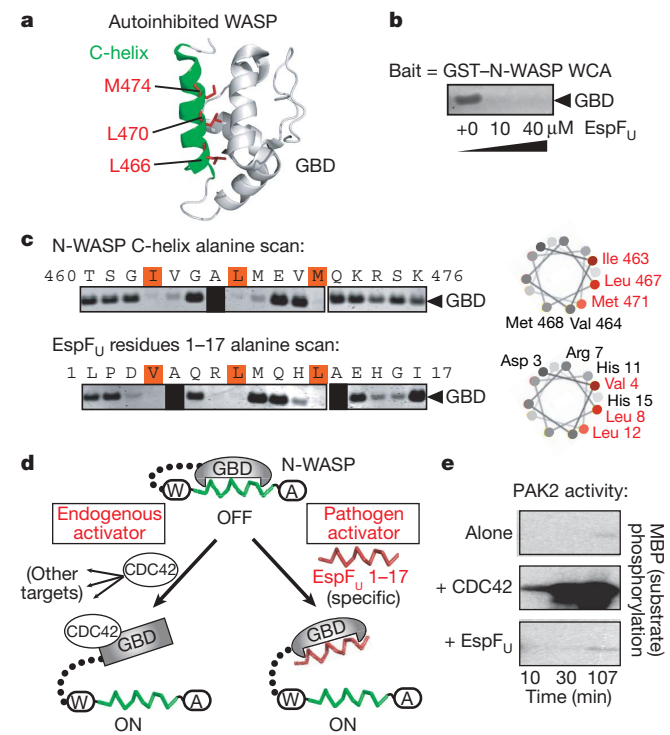


**Figure 2 | EspF<sub>U</sub> mimics the N-WASP autoinhibitory C-helix.** **a**, The structure of an autoinhibited fragment of WASP<sup>7</sup>, highlighting the C-helix (green) and three critical side chains (red). **b**, EspF<sub>U</sub> can competitively disrupt the N-WASP autoinhibitory interaction (*in trans*) in a GST-pull-down assay. **c**, Alanine scanning mutagenesis shows a similar pattern of critical residues in the N-WASP C-helix and in EspF<sub>U</sub> (repeat 4, residues 1–17; assayed by binding to GBD in a GST-pull-down assay). **d**, Model comparing N-WASP activation by CDC42 and EspF<sub>U</sub>. **e**, PAK kinase assay showing phosphorylation of myelin basic protein (MBP). PAK2 alone is autoinhibited; CDC42 activates it, but EspF<sub>U</sub> does not.

shows intermediate activity in the actin assay, but at least three repeats are necessary for high potency. Each additional repeat gives higher activity until full-length EspFU (residues 80–337, lacking the secretion signal), which has a maximal activity at the same level as unregulated N-WASP (Fig. 3a and Supplementary Fig. 7). To see whether this trend continued, we made an EspFU protein that has eight-and-a-half repeats and found that it reaches the same maximal activity as the wild-type protein, but is even more potent at low concentrations (Fig. 3a). At very high concentrations, EspFU proteins had a partial inhibitory effect on actin polymerization (data not shown), probably owing to EspFU sequestering actin monomers and/or ARP2/3.

We constructed a minimized EspFU protein in which six copies of the 17-residue C-helix mimic are separated by glycine–serine linkers. This construct was still able to stimulate actin polymerization (albeit with lower potency than wild-type EspFU), showing that the C-terminal portion of each EspFU repeat is not essential for activity (Supplementary Fig. 8).

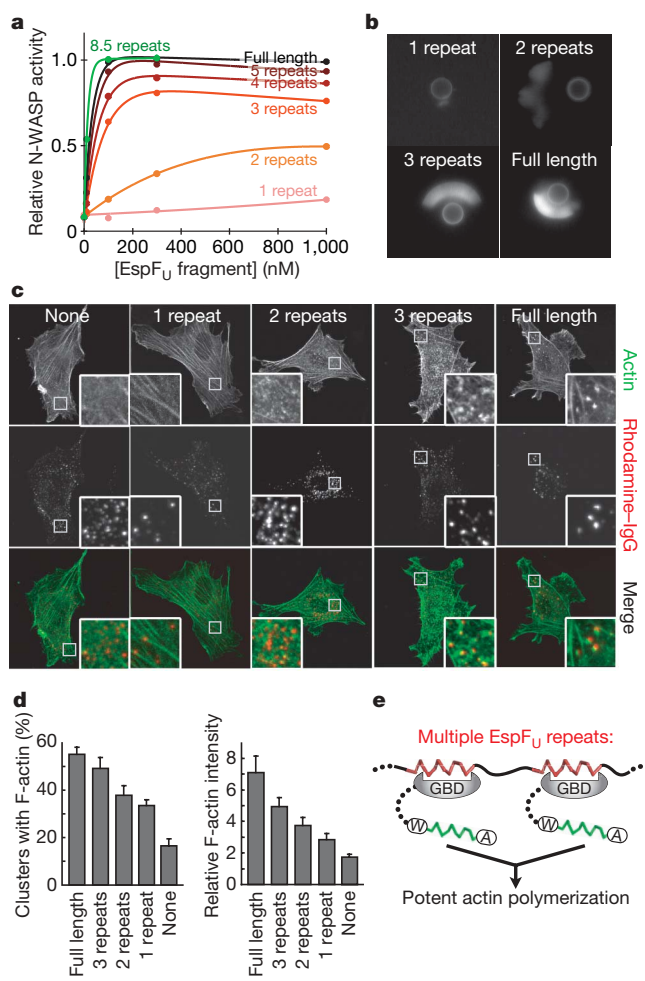


**Figure 3 | Multiple repeats of EspFU are required for potent activation of actin polymerization.** **a**, Activities of EspFU fragments in a pyrene-actin-polymerization assay. Data are fit to single exponential curves using Matlab (MathWorks), with a small linear term subtracted to account for EspFU sequestration of actin and/or ARP2/3. **b**, Visualization of fluorescently labelled actin around beads coated with EspFU fragments. Images were acquired four minutes after initiation. **c**, NIH 3T3 cells expressing GFP-actin and EspFU fused to a transmembrane protein (CD16/7), which is clustered with a rhodamine-tagged antibody<sup>26</sup>. Inset in each image is a portion of that cell (white box) shown at higher magnification. **d**, Results from quantification of clustered cells, shown in two metrics. Bars represent mean  $\pm$  s.e.m. of 10 cell images. **e**, Activity correlates with ability of EspFU fragments to bind at least two N-WASP proteins simultaneously.

Next, we tested whether multiple repeats were also required in more complex assays of actin assembly—namely a reconstituted bead motility assay and an *in vivo* clustering assay. In the first assay, EspFU fragments are chemically coupled to polystyrene beads; these beads are incubated with a mixture of actin and actin-regulatory proteins and are examined by microscopy for the ability to stimulate actin assembly and motility<sup>24</sup>. Beads coated with full-length EspFU triggered formation of an F-actin shell that breaks symmetry and induces transient polarized bead movement (Fig. 3b). Beads coated with three EspFU repeats showed similar behaviour (albeit with a slightly more diffuse actin shell), whereas two-repeat beads formed shells that were very diffuse, showed significantly reduced actin fluorescence, and disassembled within minutes. Beads coated with a single repeat showed minimal ability to polymerize actin (Fig. 3b). We varied the surface density of EspFU protein on the beads and found that this had little effect on the relative activities of the different fragments (data not shown). In particular, one-repeat beads had weak activity, even at maximal density. This shows that a high local concentration of a single repeat has minimal effect—multiple repeats in the same polypeptide chain are required for potent activation of actin polymerization.

To test the ability of EspFU fragments to form actin structures in cells, we used an antibody-induced clustering assay. Previous work has shown that N-WASP or N-WASP activators can form actin structures when clustered at the plasma membrane<sup>25</sup>. In our assay, the EspFU fragment was expressed as a fusion to the cytoplasmic tail of a transmembrane protein and then clustered using an antibody that recognizes the extracellular portion of the protein<sup>26</sup>. On clustering of full-length EspFU, we observed co-localization of N-WASP and bright actin foci to the clusters, showing that clustering of EspFU is sufficient to trigger localized actin assembly (Fig. 3c and Supplementary Figs 9 and 10). Furthermore, we tested three-, two- and one-repeat fragments and observed the same trend: three repeats showed similar activity to full-length EspFU, two repeats had intermediate activity and one repeat had lower activity (Fig. 3c). We used a computational image analysis tool (D.V., unpublished) to detect and correlate antibody and actin clusters (Supplementary Fig. 11). These quantitative results show that clustering of EspFU fragments with more repeats causes formation of actin clusters with higher frequency and intensity (Fig. 3d).

The requirement of multiple repeats for activation of actin polymerization suggests that EspFU needs to simultaneously bind and activate multiple N-WASP proteins to be highly active. To address this, we investigated the stoichiometry of the EspFU–N-WASP complex using analytical ultracentrifugation (AUC). By AUC (data not shown) and binding assays (Supplementary Fig. 12), we found that each repeat in an EspFU fragment could simultaneously bind an isolated N-WASP GBD (for example, a three-repeat fragment bound to three GBDs). However, the model in which EspFU has high potency because it can activate multiple N-WASPs does not explain why a two-repeat fragment has lowered activity in our actin assays. We found a likely answer to this question through stoichiometric analyses of complexes of a two-repeat protein with a larger, auto-inhibited N-WASP construct. These AUC data showed that whereas the two-repeat fragment can bind one N-WASP easily, binding of a second is less favourable (possibly owing to steric effects) and only happens in large excess of N-WASP (Supplementary Fig. 13). Larger fragments of EspFU, in contrast, readily formed complexes with two or more N-WASP proteins (Supplementary Fig. 13). Taken with our activation data, this suggests that activity of EspFU fragments correlates with their ability to coordinate the activation of at least two N-WASP proteins (Fig. 3e). There are a number of other cases in which oligomerization of WASPs or WASP activators leads to similarly increased activity—including the potent actin polymerization induced by glutathione S-transferase (GST)-tagged N-WASP WCA<sup>27</sup> (presumably owing to GST dimerization) and by oligomerized SNX9 in endocytosis<sup>28</sup>.

We have shown here that the EHEC protein EspF<sub>U</sub> has evolved a unique mechanism to potently and specifically activate N-WASP-mediated actin polymerization through a repeated autoinhibitory mimic. This co-opting of a small internal regulatory unit for activation of a target protein represents a previously unknown pathogenic strategy. Furthermore, multiple repeated copies of this motif are essential for potent activity, apparently because a single EspF<sub>U</sub> protein must coordinate simultaneous activation of multiple N-WASPs.

## METHODS SUMMARY

**EspF<sub>U</sub> expression and purification.** EspF<sub>U</sub> fragments were amplified by PCR from EHEC genomic DNA (ATCC). All cloning and expression was done in *E. coli* BLR(DE3) strains lacking recombinase A. Unless explicitly stated, EspF<sub>U</sub> fragments consist of the most N-terminal repeats.

**Pyrene-actin-polymerization assay.** ARP2/3 was purified from bovine brain, and actin was purified from rabbit muscle and pyrene-labelled, as described previously<sup>29</sup>. Actin polymerization was monitored as an increase in pyrene-actin fluorescence. Raw fluorescence data were normalized to the lower and upper baselines of each curve. Relative activities of EspF<sub>U</sub> fragments were determined through calculation of the time required to reach half-maximal fluorescence ( $t_{1/2}$ ).

**Bead motility assay.** Actin and ARP2/3 were purified from *Acanthamoeba castellanii*, as described previously<sup>30</sup>. EspF<sub>U</sub> proteins were coupled to polystyrene beads and mixed with actin, ARP2/3, N-WASP, capping protein and profilin. The assay was adapted from a protocol developed in ref. 24. Images were acquired with a Nikon TE300 Eclipse inverted epifluorescence microscope with constant imaging settings between experiments.

**In vivo clustering experiments.** NIH 3T3 fibroblasts were co-transfected with actin-GFP (green fluorescent protein) and the corresponding CD16/7 fusion construct. Cells were treated with clustering antibodies, as described previously<sup>26</sup>. Fixed cells were imaged with an oil-immersion  $\times 60$  NA 1.4 objective on a Zeiss LSM 510 Meta microscope. Imaging settings were constant between experiments, except for minor adjustments of detector gain to accommodate variation in expression level.

Quantitative detection of clusters was performed with a computational tool developed by D. Vasilescu. Ten cell images from three independent experiments were quantified for each construct. Data were presented in two metrics: the percentage of antibody clusters that have associated actin clusters and the intensities of these associated actin clusters. The relative intensity value is the ratio of the sum of intensities of associated actin clusters to the sum of intensities of all antibody clusters.

**Full Methods** and any associated references are available in the online version of the paper at [www.nature.com/nature](http://www.nature.com/nature).

Received 24 December 2007; accepted 12 June 2008.

Published online 23 July 2008.

1. Caron, E. et al. Subversion of actin dynamics by EPEC and EHEC. *Curr. Opin. Microbiol.* **9**, 40–45 (2006).
2. Gruenheid, S. & Finlay, B. B. Microbial pathogenesis and cytoskeletal function. *Nature* **422**, 775–781 (2003).
3. Rottner, K., Lommel, S., Wehland, J. & Stradal, T. E. Pathogen-induced actin filament rearrangement in infectious diseases. *J. Pathol.* **204**, 396–406 (2004).
4. Campellone, K. G., Robbins, D. & Leong, J. M. EspF<sub>U</sub> is a translocated EHEC effector that interacts with Tir and N-WASP and promotes Nck-independent actin assembly. *Dev. Cell* **7**, 217–228 (2004).
5. Garmendia, J. et al. TccP is an enterohaemorrhagic *Escherichia coli* O157:H7 type III effector protein that couples Tir to the actin-cytoskeleton. *Cell. Microbiol.* **6**, 1167–1183 (2004).
6. Galan, J. E. & Wolf-Watz, H. Protein delivery into eukaryotic cells by type III secretion machines. *Nature* **444**, 567–573 (2006).
7. Kim, A. S., Kakalis, L. T., Abdul-Manan, N., Liu, G. A. & Rosen, M. K. Autoinhibition and activation mechanisms of the Wiskott–Aldrich syndrome protein. *Nature* **404**, 151–158 (2000).
8. Prehoda, K. E., Scott, J. A., Mullins, R. D. & Lim, W. A. Integration of multiple signals through cooperative regulation of the N-WASP-Arp2/3 complex. *Science* **290**, 801–806 (2000).

9. Rohatgi, R., Nollau, P., Ho, H. Y., Kirschner, M. W. & Mayer, B. J. Nck and phosphatidylinositol 4,5-bisphosphate synergistically activate actin polymerization through the N-WASP-Arp2/3 pathway. *J. Biol. Chem.* **276**, 26448–26452 (2001).
10. Mattoo, S., Lee, Y. M. & Dixon, J. E. Interactions of bacterial effector proteins with host proteins. *Curr. Opin. Immunol.* **19**, 392–401 (2007).
11. Stebbins, C. E. Structural insights into bacterial modulation of the host cytoskeleton. *Curr. Opin. Struct. Biol.* **14**, 731–740 (2004).
12. Mukherjee, S., Hao, Y. H. & Orth, K. A newly discovered post-translational modification — the acetylation of serine and threonine residues. *Trends Biochem. Sci.* **32**, 210–216 (2007).
13. Aktories, K. & Barbier, J. T. Bacterial cytotoxins: targeting eukaryotic switches. *Nature Rev. Microbiol.* **3**, 397–410 (2005).
14. Zalevsky, J., Grigorova, I. & Mullins, R. D. Activation of the Arp2/3 complex by the *Listeria* acta protein. Acta binds two actin monomers and three subunits of the Arp2/3 complex. *J. Biol. Chem.* **276**, 3468–3475 (2001).
15. Alto, N. M. et al. Identification of a bacterial type III effector family with G protein mimicry functions. *Cell* **124**, 133–145 (2006).
16. Lommel, S., Benesch, S., Rohde, M., Wehland, J. & Rottner, K. Enterohaemorrhagic and enteropathogenic *Escherichia coli* use different mechanisms for actin pedestal formation that converge on N-WASP. *Cell. Microbiol.* **6**, 243–254 (2004).
17. Garmendia, J., Carlier, M. F., Egile, C., Didry, D. & Frankel, G. Characterization of TccP-mediated N-WASP activation during enterohaemorrhagic *Escherichia coli* infection. *Cell. Microbiol.* **8**, 1444–1455 (2006).
18. Alto, N. M. et al. The type III effector EspF coordinates membrane trafficking by the spatiotemporal activation of two eukaryotic signaling pathways. *J. Cell Biol.* **178**, 1265–1278 (2007).
19. McNamara, B. P. et al. Translocated EspF protein from enteropathogenic *Escherichia coli* disrupts host intestinal barrier function. *J. Clin. Invest.* **107**, 621–629 (2001).
20. Rost, B., Yachdav, G. & Liu, J. The PredictProtein server. *Nucleic Acids Res.* **32**, W321–W326 (2004).
21. Panchal, S. C., Kaiser, D. A., Torres, E., Pollard, T. D. & Rosen, M. K. A conserved amphipathic helix in WASP/Scar proteins is essential for activation of Arp2/3 complex. *Nature Struct. Biol.* **10**, 591–598 (2003).
22. Marchand, J. B., Kaiser, D. A., Pollard, T. D. & Higgs, H. N. Interaction of WASP/Scar proteins with actin and vertebrate Arp2/3 complex. *Nature Cell Biol.* **3**, 76–82 (2001).
23. Lei, M. et al. Structure of PAK1 in an autoinhibited conformation reveals a multistage activation switch. *Cell* **102**, 387–397 (2000).
24. Akin, O. & Mullins, R. D. Capping protein increases the rate of actin-based motility by promoting filament nucleation by the Arp2/3 complex. *Cell* **133**, 841–851 (2008).
25. Castellano, F. et al. Inducible recruitment of Cdc42 or WASP to a cell-surface receptor triggers actin polymerization and filopodium formation. *Curr. Biol.* **9**, 351–360 (1999).
26. Rivera, G. M., Briceno, C. A., Takeshima, F., Snapper, S. B. & Mayer, B. J. Inducible clustering of membrane-targeted SH3 domains of the adaptor protein Nck triggers localized actin polymerization. *Curr. Biol.* **14**, 11–22 (2004).
27. Higgs, H. N. & Pollard, T. D. Activation by Cdc42 and PIP(2) of Wiskott–Aldrich syndrome protein (WASp) stimulates actin nucleation by Arp2/3 complex. *J. Cell Biol.* **150**, 1311–1320 (2000).
28. Yarar, D., Waterman-Storer, C. M. & Schmid, S. L. SNX9 couples actin assembly to phosphoinositide signals and is required for membrane remodeling during endocytosis. *Dev. Cell* **13**, 43–56 (2007).
29. Sallee, N. A., Yeh, B. J. & Lim, W. A. Engineering modular protein interaction switches by sequence overlap. *J. Am. Chem. Soc.* **129**, 4606–4611 (2007).
30. Dayel, M. J., Holleran, E. A. & Mullins, R. D. Arp2/3 complex requires hydrolyzable ATP for nucleation of new actin filaments. *Proc. Natl. Acad. Sci. USA* **98**, 14871–14876 (2001).

**Supplementary Information** is linked to the online version of the paper at [www.nature.com/nature](http://www.nature.com/nature).

**Acknowledgements** We thank O. Akin for reagents and assistance with the bead motility experiments; J. C. Anderson, A. Chau, R. Howard, M. Lohse, A. Remenyi and L. Weaver for assistance; and members of the Lim laboratory for discussion. This work was supported by grants from the NIH (NIGMS and Nanomedicine Development Centers, NIH Roadmap), the NSF and the Packard Foundation. G.M.R. was supported by the American Heart Association.

**Author Information** Reprints and permissions information is available at [www.nature.com/reprints](http://www.nature.com/reprints). Correspondence and requests for materials should be addressed to W.A.L. (lim@cmp.ucsf.edu).

## METHODS

**Protein construction and purification.** Because of the high DNA sequence conservation between EspFU repeats, PCR reactions would result in a ladder of bands on a gel that corresponded to 1 repeat, 2 repeats, and so on. We made repeat fragments by cutting out the bands that corresponded to 1 repeat up to 5 repeats. EspFU proteins were expressed as N-terminal hexahistidine (pET19-derived vector) or GST (pGEX4T-1 vector) fusions and purified on Ni-NTA resin (Qiagen) or glutathione agarose (Sigma), respectively. Proteins were further purified by ion exchange chromatography on a Source Q column (Pharmacia).

The synthetic eight-and-a-half-repeat EspFU protein was assembled through introduction of a silent AatII restriction site near the N terminus of the repeat. By PCR, we made one three-repeat fragment starting at the N terminus of EspFU and ending with the AatII site, and a second five-and-a-half-repeat fragment starting with the AatII site and ending at the C terminus of EspFU. These two fragments were cut with AatII (NEB) and ligated to form the eight-and-a-half-repeat protein.

The two WASP family proteins used in this study are human WASP (referred to as 'WASP') and rat neuronal WASP (referred to as 'N-WASP'). Mini N-WASP consists of residues 178–274 fused to residues 392–501 through a 9-amino-acid glycine–serine linker.

Single alanine mutations of the N-WASP C-helix (residues 452–487) and EspFU C-mimic (repeat 4, residues 1–17) sequences were made using QuikChange mutagenesis<sup>31</sup>. Mutants were expressed as GST fusions.

**GST-pull-down binding assays.** GST-tagged bait protein was bound to glutathione agarose. Sufficient resin was added to bring the bait protein concentration to 1  $\mu$ M. Hexahistidine-tagged prey protein was added at 10  $\mu$ M. For competitions, a series of pull-downs were performed with increasing concentration of the competitor. Binding was performed in 20 mM Tris, pH 8.0, 50 mM NaCl and 1 mM DTT. Bound prey protein was detected by western blotting with a mouse His-probe primary antibody (Santa Cruz Biotech), followed by a fluorescent goat anti-mouse IRDye 800CW secondary antibody (Li-Cor Biosciences). Bands were visualized on a Li-Cor Odyssey infrared fluorescence scanner.

**PAK kinase assays.** Assays were performed as described previously<sup>32</sup>. Human PAK1 and PAK2 proteins were purchased from Cell Signaling Technology. MBP (Invitrogen) from bovine brain was used as the phosphorylation substrate. The CDC42 used is a soluble fragment of the human protein (residues 1–179) bearing a G12V constitutively active mutation. Each reaction was performed with 0.5  $\mu$ g PAK and 15  $\mu$ g MBP substrate in 35  $\mu$ l volume, with or without 2.5  $\mu$ g of CDC42 G12V or full-length EspFU. The assay buffer consisted of 50 mM HEPES, pH 7.5, 10 mM MgCl<sub>2</sub>, 10 mM NaF, 2 mM MnCl<sub>2</sub>, 1 mM DTT and 0.05% Triton X-100. The reaction was initiated by addition of 10  $\mu$ Ci [ $\gamma$ -<sup>33</sup>P]ATP. Aliquots were removed at three time points. Samples were analysed by SDS-PAGE, vacuum dried and exposed to film.

**Pyrene-actin-polymerization assays.** Assays were performed essentially as described previously<sup>33</sup>. Exact assay conditions were 1.3  $\mu$ M actin (10% pyrene-labelled), 20 nM ARP2/3, 50 nM mini N-WASP, 50 mM KCl, 1 mM MgSO<sub>4</sub>, 1 mM EGTA, 0.2 mM ATP, 1 mM DTT, 3  $\mu$ M MgCl<sub>2</sub> and 11.5 mM imidazole, pH 7.0, in a total volume of 100  $\mu$ l. Actin polymerization was monitored as an increase in pyrene-actin fluorescence (excitation: 365 nm; emission: 407 nm) with a SpectraMax Gemini XS fluorescence plate reader (Molecular Devices). Raw fluorescence data were normalized to the lower and upper baselines of each

curve using the equation  $(F_{\text{data}} - F_{\text{lower}})/(F_{\text{upper}} - F_{\text{lower}})$ . To determine the minimal (min) rate of actin polymerization, mini N-WASP was omitted from the assay (ARP2/3 alone) and to determine the maximal (max) rate, mini N-WASP was replaced by 50 nM unregulated N-WASP WCA. Relative activities of EspFU fragments were determined with the equation  $[t_{1/2}(\text{min}) - t_{1/2}(\text{data})]/[t_{1/2}(\text{min}) - t_{1/2}(\text{max})]$ .

**Bead motility assays.** Actin was labelled with rhodamine. Human profilin I (ref. 34) and mouse capping protein CP  $\alpha 1\beta 2$  (ref. 35) were grown recombinantly and purified as described previously. GST fusions of EspFU fragments were covalently crosslinked to 5  $\mu$ m carboxylated polystyrene beads (Bangs Labs). In brief, 1% (w/v) solutions of beads were charged with EDC and stabilizing SulfoNHS (Pierce) and then reacted with 4  $\mu$ M of the GST-fused EspFU fragment. We also coupled EspFU fragments diluted in GST alone. Coupling reactions were quenched with Tris and the beads were washed to remove non-covalently attached protein. EspFU-coupled bead solutions were diluted 1:30 into a motility mixture consisting of 62.5 nM ARP2/3, 300 nM capping protein, 3  $\mu$ M profilin and 100 nM  $\Delta$ EVH1 N-WASP (residues 136–501) in 0.5 mM ATP, 1 mM MgCl<sub>2</sub>, 1 mM EGTA, 15 mM TCEP, 50 mM KOH, 20 mM HEPES, pH 7.0, 2.5 mg ml<sup>-1</sup> BSA and 0.2% methylcellulose. Motility was initiated by addition of 7.5  $\mu$ M actin (5% labelled). Samples were mounted between silanized glass slides and coverslips. Images in the paper are of beads coated with EspFU fragments diluted 1:4 in GST alone. We also tested beads with maximal surface density of EspFU fragments (no GST added) and observed the same trends in activity (data not shown).

**In vivo clustering assays and quantification.** Details of the CD16/7 chimaeric construct were described previously<sup>26</sup>. Aggregation of membrane-targeted EspFU fragments was performed by antibody-mediated cross-linking of CD16/7 (ref. 26). In brief, 24 h after transfection, cells were incubated with a mouse CD16 antibody (Calbiochem) at 1  $\mu$ g ml<sup>-1</sup> in complete medium for 1 h at 37 °C. After washing, cells were incubated with rhodamine-conjugated goat anti-mouse IgG (Pierce) at 0.5  $\mu$ g ml<sup>-1</sup> for an additional hour. Fluorescent images were collected on a Zeiss LSM 510 Meta confocal microscope using a  $\times 63$  NA 1.4 Plan-NEOFLUAR oil immersion objective. Specimens were illuminated with an argon laser with emission at 488 nm and a HeNe laser with emission at 543 nm.

Quantitative data were derived using the Comet Detector, a newly developed computational tool (D.V., unpublished). For details, see the Supplementary Information.

31. Wang, W. & Malcolm, B. A. Two-stage PCR protocol allowing introduction of multiple mutations, deletions and insertions using QuikChange Site-Directed Mutagenesis. *Biotechniques* **26**, 680–682 (1999).
32. Chong, C., Tan, L., Lim, L. & Manser, E. The mechanism of PAK activation. Autophosphorylation events in both regulatory and kinase domains control activity. *J. Biol. Chem.* **276**, 17347–17353 (2001).
33. Machesky, L. M. et al. Scar, a WASp-related protein, activates nucleation of actin filaments by the Arp2/3 complex. *Proc. Natl. Acad. Sci. USA* **96**, 3739–3744 (1999).
34. Kaiser, D. A., Goldschmidt-Clermont, P. J., Levine, B. A. & Pollard, T. D. Characterization of renatured profilin purified by urea elution from poly-L-proline agarose columns. *Cell Motil. Cytoskeleton* **14**, 251–262 (1989).
35. Palmgren, S., Ojala, P. J., Wear, M. A., Cooper, J. A. & Lappalainen, P. Interactions with PIP2, ADP-actin monomers, and capping protein regulate the activity and localization of yeast twinfilin. *J. Cell Biol.* **155**, 251–260 (2001).

## LETTERS

# Structural mechanism of WASP activation by the enterohaemorrhagic *E. coli* effector EspF<sub>U</sub>

Hui-Chun Cheng<sup>1</sup>, Brian M. Skehan<sup>2</sup>, Kenneth G. Campellone<sup>2</sup>, John M. Leong<sup>2</sup> & Michael K. Rosen<sup>1</sup>

During infection, enterohaemorrhagic *Escherichia coli* (EHEC) takes over the actin cytoskeleton of eukaryotic cells by injecting the EspF<sub>U</sub> protein into the host cytoplasm<sup>1,2</sup>. EspF<sub>U</sub> controls actin by activating members of the Wiskott–Aldrich syndrome protein (WASP) family<sup>1–5</sup>. Here we show that EspF<sub>U</sub> binds to the autoinhibitory GTPase binding domain (GBD) in WASP proteins and displaces it from the activity-bearing VCA domain (for verprolin homology, central hydrophobic and acidic regions). This interaction potently activates WASP and neural (N)-WASP *in vitro* and induces localized actin assembly in cells. In the solution structure of the GBD–EspF<sub>U</sub> complex, EspF<sub>U</sub> forms an amphipathic helix that binds the GBD, mimicking interactions of the VCA domain in autoinhibited WASP. Thus, EspF<sub>U</sub> activates WASP by competing directly for the VCA binding site on the GBD. This mechanism is distinct from that used by the eukaryotic activators Cdc42 and SH2 domains, which globally destabilize the GBD fold to release the VCA<sup>6–8</sup>. Such diversity of mechanism in WASP proteins is distinct from other multimodular systems, and may result from the intrinsically unstructured nature of the isolated GBD and VCA elements. The structural incompatibility of the GBD complexes with EspF<sub>U</sub> and Cdc42/SH2, plus high-affinity EspF<sub>U</sub> binding, enable EHEC to hijack the eukaryotic cytoskeletal machinery effectively.

Pathogenic bacteria often target the host actin cytoskeleton during infection to assist entry, cell-to-cell spreading and intimate attachment to host membranes<sup>9–13</sup>. EHEC (serotype O157:H7) is a food-borne human pathogen that causes severe diarrhoea and haemolytic uraemic syndrome<sup>14</sup>. During infection, EHEC binds eukaryotic host intestinal epithelial cells and secretes translocated intimin receptor (Tir) and EspF<sub>U</sub> (also known as TccP) into the host cell<sup>1,2</sup>. The secreted Tir localizes in the host plasma membrane and, on clustering by binding to the bacterial outer surface protein intimin, recruits EspF<sub>U</sub> by means of its carboxy-terminal cytoplasmic domain<sup>3</sup>. EspF<sub>U</sub> in turn then hijacks members of the WASP family, which locally stimulate the actin nucleation factor, the Arp2/3 complex<sup>1–5</sup>. Together, these interactions induce the formation of an actin-rich membrane protrusion beneath the site of EHEC attachment, termed an actin pedestal<sup>1,2,15</sup>.

WASP proteins activate the Arp2/3 complex through a C-terminal VCA domain<sup>16</sup>. In free WASP, this activity is blocked by intramolecular interactions with a central GTPase binding domain (GBD). Structural and biochemical studies have shown that the GBD sequesters an amphipathic helix in the C region of the VCA that is necessary for activation of the Arp2/3 complex, resulting in autoinhibition<sup>7,17,18</sup>. WASP can be allosterically activated by several intracellular ligands, including Cdc42 and (for phosphorylated WASP) SH2 domains<sup>8,19</sup>. These ligands bind to WASP and N-WASP in a manner that is structurally incompatible with the autoinhibited fold of the

GBD. Thus, they activate WASP by globally destabilizing the GBD, consequently releasing the VCA<sup>6,8,20,21</sup>.

EspF<sub>U</sub> is composed of an amino-terminal signal sequence which is necessary for translocation into the eukaryotic host, followed by 2–7 nearly identical 47-residue repeats (Fig. 1a)<sup>22</sup>. Each full repeat consists of an N-terminal 27-residue hydrophobic segment and a C-terminal 20-residue proline-rich segment. Previous studies have shown that EspF<sub>U</sub> can bind to the N-WASP GBD and activate N-WASP towards the Arp2/3 complex in actin assembly assays *in vitro*<sup>1,2,4</sup>. A similar sequence is found in the related bacterial effector EspF, which also can activate N-WASP (Supplementary Fig. 1)<sup>23</sup>.

To understand EspF<sub>U</sub>-mediated activation, we examined fragments containing the full 47-residue fifth repeat (R47; Fig. 1 and Supplementary Fig. 1) and an N-terminal 33-residue fragment lacking most of the proline-rich sequence (R33). In Arp2/3-mediated pyrene-actin assembly assays, R47 and R33 appreciably and similarly enhanced the activities of autoinhibited N-WASP and WASP proteins (N-WASP<sub>C</sub> and GBD–VCA, respectively; Fig. 1b and Supplementary Fig. 2). Titration of R47 into N-WASP<sub>C</sub> (C-terminal residues 193–501, containing the GBD, proline-rich segment and VCA) produced a monotonic increase in actin assembly rate (Fig. 1c and Supplementary Fig. 3), which reached a plateau value similar to that of the N-WASP VCA. Thus, the endpoint of the titration produces a state that biochemically resembles free N-WASP VCA. Fitting the data to a single-site binding isotherm yields a  $K_{\text{Act}}$  (the concentration of EspF<sub>U</sub> R47 required for half-maximal activation in actin assembly assays) of 24 nM, approximating the dissociation constant ( $K_d$ ) of R47 for N-WASP<sub>C</sub> as 35 nM (Supplementary Fig. 4). EspF<sub>U</sub> binds to N-WASP more than 100-fold more strongly than Cdc42 does (ref. 21), resulting in much greater potency in actin assembly assays (Fig. 1c). This higher affinity should enable EspF<sub>U</sub> to hijack N-WASP away from its endogenous regulators *in vivo*<sup>21</sup>.

Cdc42 and SH2 domains activate WASP by physically displacing the VCA from the GBD<sup>7,8</sup>. EspF<sub>U</sub> R33 disrupted GBD–VCA interactions similarly (Supplementary Fig. 5), indicating that it also binds the GBD in a manner that is incompatible with the autoinhibitory interactions. The combined data show that EspF<sub>U</sub> R33 is functionally equivalent to Cdc42 and SH2 domains: all three ligands activate WASP and N-WASP by releasing the VCA from the GBD.

The WASP GBD is largely unstructured on its own, but folds to a well-defined conformation on binding VCA<sup>7</sup>.  $^1\text{H}$ – $^{15}\text{N}$  and  $^1\text{H}$ – $^{13}\text{C}$  amide and methyl transverse relaxation-optimized spectroscopy (TROSY) NMR spectra showed that EspF<sub>U</sub> R33, or a five-repeat fragment, R47<sub>5</sub>, also induced folding of the GBD (Supplementary Fig. 6). Reciprocally, the GBD induces folding of the unstructured R33 (Supplementary Figs 6B and 7). Titrations of R33 and R47<sub>5</sub> into GBD saturated at 1:1 and 0.2:1 EspF<sub>U</sub>:GBD stoichiometry, respectively, showing that each repeat can bind N-WASP. The endpoint

<sup>1</sup>Department of Biochemistry and Howard Hughes Medical Institute, University of Texas Southwestern Medical Center, Dallas, Texas 75390, USA. <sup>2</sup>Department of Molecular Genetics and Microbiology, University of Massachusetts Medical School, Worcester, Massachusetts 01655, USA.

spectra are similar, indicating that the GBD folds to the same structure on each repeat, and that the molecular nature of allosteric activation can be understood through analysis of the R33 complex.

We determined the solution structure of the WASP GBD in complex with EspF<sub>U</sub> R33 (GBD–R33) using NMR spectroscopy (Fig. 2, Supplementary Fig. 8 and Supplementary Table 1). The complex can be considered in three stacked structural layers<sup>7</sup>. The first layer is composed of a short N-terminal i+4  $\beta$  hairpin ( $\beta$ 1, 252–253;  $\beta$ 2, 257–258; two backbone hydrogen bonds between D253 and G257) and  $\alpha$ 1 helix (265–274) from the GBD. The second layer lies behind the first and consists of GBD helices  $\alpha$ 2– $\alpha$ 4 ( $\alpha$ 2, 278–281;  $\alpha$ 3, 284–296;  $\alpha$ 4, 300–306), which have a roughly planar C-shaped arrangement. The third layer is an amphipathic  $\alpha$ 5 helix (3–14) and an extended arm (16–20) from EspF<sub>U</sub>. These elements contact the back of the GBD and are roughly antiparallel to  $\alpha$ 3 and  $\alpha$ 2, respectively (Fig. 2a, structural details in Supplementary Fig. 9). On the basis of the absence of long-range  $^1\text{H}$ – $^1\text{H}$  nuclear Overhauser effects (NOEs) and low heteronuclear  $^1\text{H}$ – $^{15}\text{N}$  NOEs, WASP residues 242–249 and EspF<sub>U</sub> residues 21–33 seem to be largely disordered in solution (Supplementary Fig. 10). The EspF<sub>U</sub> relative, EspF, is expected to bind to the GBD through an analogous amphipathic  $\alpha$ 5 helix, but may not use an extended arm as these C-terminal residues are not conserved (Supplementary Fig. 1).

To understand the physical basis of EspF<sub>U</sub> activity better, we examined a series of single repeat mutants on the basis of the structure. First, we C-terminally fused these proteins to the WASP GBD through a short linker. Because the GBD and R33 are only folded

when bound to each other, the thermodynamic stability of the fusions reports on the relative strengths of interaction between the two elements. We mutated three conserved hydrophobic residues (V4, L8 and L12) which lie at the centre of the interface between  $\alpha$ 5 and the GBD (Supplementary Fig. 9). The L12A (R33<sup>VL\*</sup>) and V4A/L8A (R33<sup>\*\*L</sup>) mutants have substantially reduced stability relative to wild type in the GBD–R33 fusions (Fig. 1d and Supplementary Fig. 11), demonstrating the importance of  $\alpha$ 5 in the interaction of N-WASP with EspF<sub>U</sub>. Truncations from R33 to R30 or R27 decrease stability by  $\sim 2$  kcal mol<sup>−1</sup>. Thus, residues beyond Ala 30 contribute thermodynamically to the GBD–R33 interaction, despite the absence of discrete structure in these regions. Similar contributions to affinity through disordered regions have also been observed in other systems<sup>24</sup>. Truncation of all (R14) or part (R18) of the EspF<sub>U</sub> C-terminal arm decreases the stability further, indicating that the arm contributes appreciably to binding of the GBD to EspF<sub>U</sub>. These unfolding studies mirror direct binding measurements. R33 and R18 bind N-WASP<sub>C</sub> with  $K_d$  values of 35 and 4,000 nM, respectively (Fig. 1d), corresponding to a difference in free energy of 2.9 kcal mol<sup>−1</sup>. This value agrees closely with the stability difference between the two GBD fusions (2.6 kcal mol<sup>−1</sup>; Fig. 1d). Furthermore, these differences in binding correspond well to the activities of the EspF<sub>U</sub> mutants in N-WASP-mediated actin assembly assays, in which activity decreases together with the strength of interaction (Fig. 1b, d).

To test how the biophysical properties of the EspF<sub>U</sub>–N-WASP interaction relate to biological function, we examined the ability of

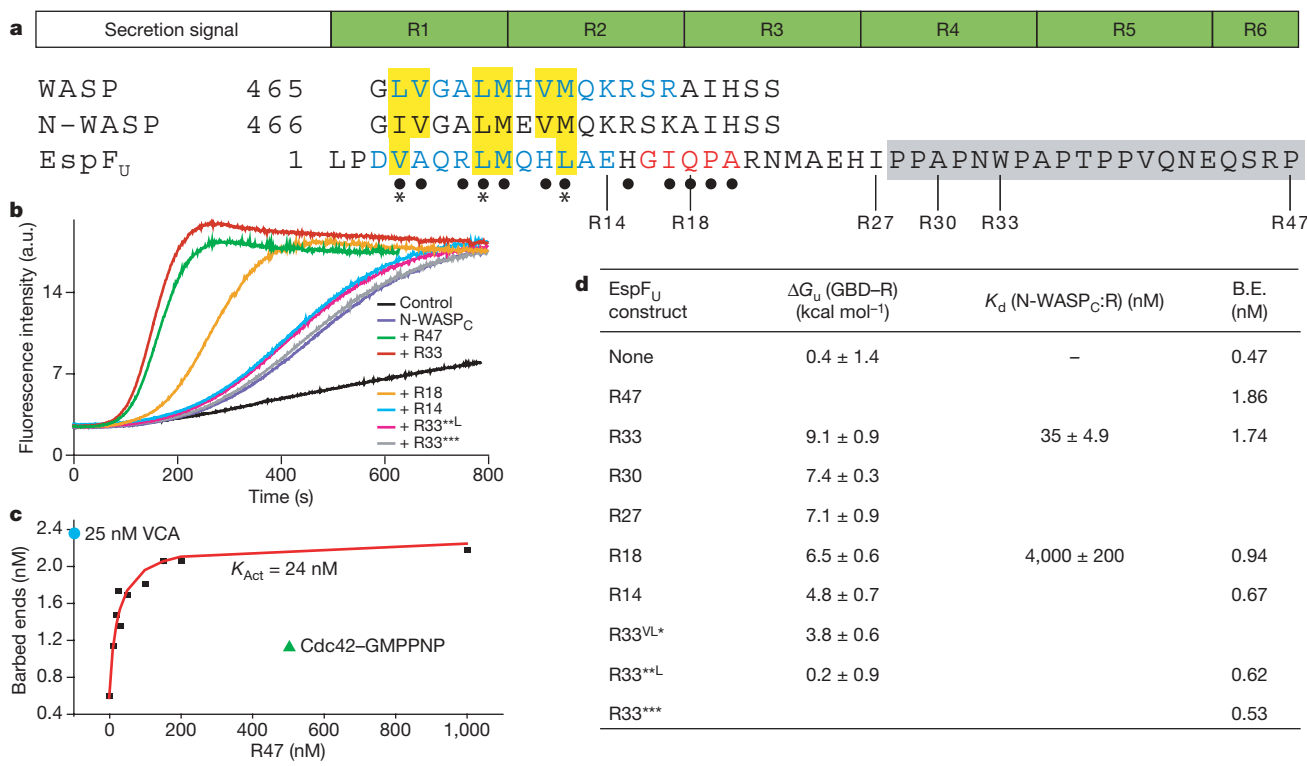


**Figure 1 | A single repeat of EspF<sub>U</sub> activates WASP/N-WASP with high potency.** **a**, Sequence alignment of WASP and N-WASP VCA C regions and the fifth repeat element of EspF<sub>U</sub>. Helix residues in the autoinhibited GBD–C structure and GBD–R33 complex are blue; residues in the extended EspF<sub>U</sub> arm are red; aligned hydrophobic residues are boxed in yellow. EspF<sub>U</sub> residues that contact the GBD are indicated by black circles. Asterisks indicate sites of EspF<sub>U</sub> mutations used in **b** and **d**. The proline-rich motif is boxed in grey. The C termini of EspF<sub>U</sub> single repeat constructs used throughout this work are indicated below the sequence. **b**, Pyrene-actin fluorescence measured during assembly of 4  $\mu\text{M}$  actin (5% pyrene-labelled) plus 10 nM Arp2/3 complex (black) and 25 nM N-WASP<sub>C</sub> (blue) and 500 nM of: R47 (green), R33 (red), R18 (orange), R14 (cyan), R33<sup>\*\*L</sup> (pink) or

R33<sup>\*\*\*</sup> (V4A/L8A/L12A, grey). **c**, Concentration of filament barbed ends produced during assembly of 4  $\mu\text{M}$  actin by 10 nM Arp2/3 complex, 25 nM N-WASP<sub>C</sub> and increasing concentrations of R47 (black squares; red curve shows fit to single-site binding isotherm) or 500 nM Cdc42–GMPPNP (green triangle). The blue circle shows barbed ends produced by actin plus Arp2/3 plus 25 nM N-WASP VCA. **d**, For the EspF<sub>U</sub> proteins listed, the table shows the free energy of unfolding of GBD–EspF<sub>U</sub> fusion ( $G_u$ ), the dissociation constant for binding to N-WASP<sub>C</sub> and actin filament barbed ends (B.E.) produced by assays in **b**. In the ‘none’ row,  $\Delta G_u$  represents melting of the isolated GBD and B.E. represents assays performed with only N-WASP<sub>C</sub> and Arp2/3 complex.

$\text{EspF}_U$  derivatives to induce localized actin assembly in mammalian cells. To uncouple Tir-mediated recruitment of  $\text{EspF}_U$  from  $\text{EspF}_U$  function in pedestal generation after recruitment, we replaced the C-terminal cytoplasmic domain of Tir with two repeats of  $\text{EspF}_U$  (giving rise to  $\text{Tir}\Delta\text{C}-\text{R47}_2$ ). We expressed  $\text{Tir}\Delta\text{C}-\text{R47}_2$  in mouse fibroblast-like cells, where it inserted into the plasma membrane, and then clustered it by adding *E. coli* expressing intimin. Immunostaining showed that foci of clustered Tir and N-WASP coincided with bound bacteria (Fig. 3a). Similarly, F-actin strongly colocalized with Tir. In contrast, a control Tir derivative ( $\text{Tir}\Delta\text{C}$ ) lacking cytoplasmic elements did not recruit N-WASP or produce actin pedestals (Fig. 3a). Mutation of Leu 12 to Ala in both  $\text{EspF}_U$  repeats (giving  $\text{Tir}\Delta\text{C}-\text{R47}_2^{\text{VL}*}$ ) also abolished both actin assembly and N-WASP recruitment (Fig. 3a), consistent with the decreased binding of this mutant to N-WASP *in vitro* (Fig. 1). To examine the activity of  $\text{EspF}_U$  truncation mutants, we modified this assay to analyse derivatives of one  $\text{EspF}_U$  repeat unit. As predicted by *in vitro* data (Fig. 1), the triple V4A/L8A/L12A mutant,  $\text{Tir}\Delta\text{C}-\text{R47}^{***}$ , was also unable to assemble actin (Supplementary Fig. 12). Truncation of R47 to R33 decreased activity, probably owing to the loss of most of the proline-rich region, which in EspF is known to bind SH3-containing proteins to promote actin assembly<sup>23</sup> (Fig. 3b). R30 and R27 showed even lower actin assembly levels, consistent with the diminished N-WASP<sub>C</sub> binding by these proteins compared to R33 (Fig. 1). Furthermore, R14, which bound N-WASP<sub>C</sub> only very weakly (Fig. 1), did not promote actin assembly above background amounts. Together, these data show that the ability of  $\text{EspF}_U$  derivatives to promote actin assembly *in vivo* reflects the physical interactions between  $\text{EspF}_U$  and WASP *in vitro*.

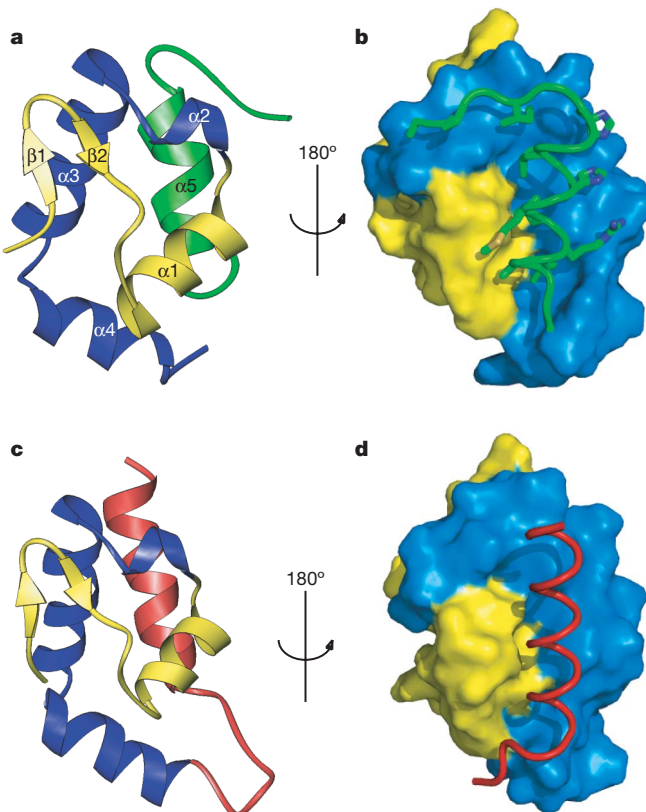


**Figure 2 | Structures of the WASP GBD in complex with different ligands.** **a, b**, The complex of WASP GBD and  $\text{EspF}_U$  R33 is shown. Layer 1 (WASP 250–276) is shown in yellow, layer 2 (WASP 277–310) in blue and layer 3 ( $\text{EspF}_U$  2–20) in green. In **b**, GBD is shown as a surface representation; R33 is shown as a ribbon with sticks for side chains that contact the GBD. Views are related by a  $180^\circ$  rotation about a vertical axis. **c, d**, Autoinhibited WASP (GBD–C'). GBD is coloured as in **a**; the C region of WASP VCA is coloured red. Representation and views are as in **a** and **b**.

The complexes of the GBD with R33 and with the C region of the VCA (GBD–C) are highly similar (Fig. 2). In both cases, ligand binding causes the GBD to fold into a  $\beta$ -hairpin and four helices. The backbone root mean squared deviation (r.m.s.d.) between the

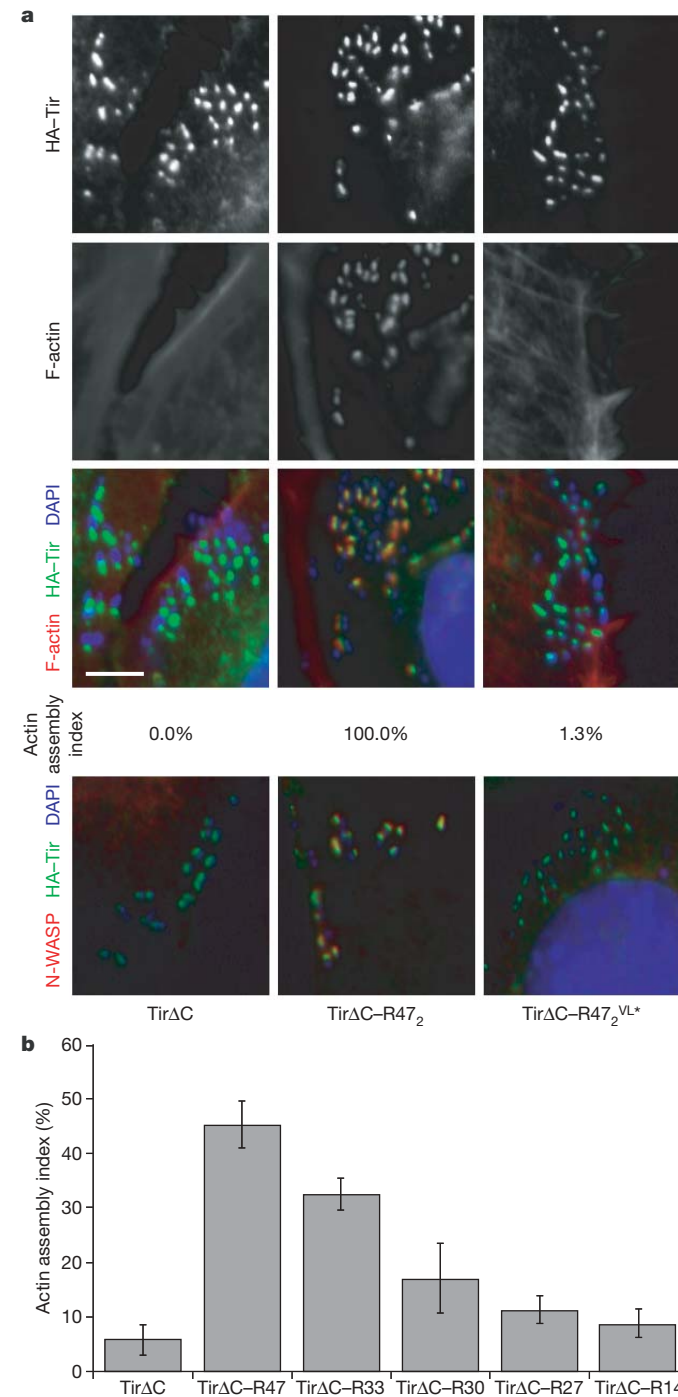


**Figure 3 |  $\text{EspF}_U$  induces actin pedestal formation.** **a**, Cells expressing the  $\text{Tir}\Delta\text{C}$ ,  $\text{Tir}\Delta\text{C}-\text{R47}_2$  or  $\text{Tir}\Delta\text{C}-\text{R47}_2^{\text{VL}*}$  (with N-terminal HA-tags) were challenged with *E. coli* expressing intimin and stained with anti-HA antibody (green) and Alexa568-phalloidin (red, top panels) or anti-N-WASP antibody (red, bottom panels). Colocalization is shown in yellow in the merged images. The percentage of transfected cells harbouring at least five F-actin foci was quantified (actin assembly index). Bacteria were visualized by 4,6-diamidino-2-phenylindole (DAPI) staining. Scale bar, 10  $\mu\text{m}$ . **b**, Cells expressing Tir-repeat proteins were challenged with anti-Tir antibody and *S. aureus* particles and the actin assembly index was determined. In **b** data represent mean  $\pm$  s.d. from at least two samples with 20–50 cells examined per sample.

average GBD coordinates in the two structures is only 0.95 Å (residues 247–310). This structural similarity is reflected in high chemical shift similarity: the average GBD chemical-shift differences are 0.015 parts per million (p.p.m.) for HN, 0.062 p.p.m. for H $\alpha$ , 0.043 p.p.m. for H $\beta$ , 0.21 p.p.m. for C $\alpha$  and 0.30 p.p.m. for C $\beta$ . The largest chemical shift differences between the two complexes occur in  $\alpha$ 2, which contacts the extended arm of EspF<sub>U</sub> in the GBD–R33 complex, but is solvent exposed in the GBD–C complex. The WASP C helix and the EspF<sub>U</sub> helix bind the GBD at the same site and orientation through analogous hydrophobic contacts involving similar sequences (Fig. 1a and Supplementary Fig. 9). EspF<sub>U</sub> makes further contacts to the GBD through its C-terminal arm, which are not seen in the bound C region helix in autoinhibited WASP. These contacts contribute to the much higher WASP affinity of EspF<sub>U</sub> compared to its eukaryotic counterparts<sup>21</sup>. The combined structural and biochemical data lead to a clear and simple mechanism for WASP and N-WASP activation by a single repeat element of EspF<sub>U</sub>: displacement of the VCA through competitive binding to a common site on the folded GBD.

We have described the autoinhibited GBD–VCA structure as composed of three layers, analogous to the three layers of the GBD–R33 structure, with the C region of the VCA substituting for R33 (ref. 7). Three structurally distinct mechanisms for relieving autoinhibition of WASP and N-WASP are now known that involve attacks on distinct regions of this fold (Supplementary Fig. 13). Cdc42 globally destabilizes the GBD by binding to the first layer of structure. Similarly, following phosphorylation of the conserved Tyr 291 and Tyr 256 in WASP and N-WASP respectively, SH2 domains can also destabilize the GBD by binding to this site in the second layer. EHEC has evolved the simplest and structurally most direct means of releasing the VCA: EspF<sub>U</sub> binds to the GBD–VCA interface, displacing the VCA from the folded GBD by structural competition. Of the three known allosteric mechanisms, only this latter one is akin to those found in most other autoinhibited multidomain systems, in which activation is driven by rearrangements of intact functional modules. The diversity of WASP regulation probably originates from the intrinsically unstructured nature of the GBD, which enables its broad binding specificity. Because the folded GBD is structurally incompatible with Cdc42/S2 binding, EspF<sub>U</sub> can displace the VCA while simultaneously preventing interactions with eukaryotic activators, thus sequestering WASP proteins away from their normal signalling pathways. This, coupled with very high affinity binding, allows EHEC to subvert the host actin cytoskeleton to its own ends.

## METHODS SUMMARY

**Protein expression and purification.** EspF<sub>U</sub> and WASP proteins were expressed in bacteria as either His<sub>6</sub>- or glutathione S-transferase (GST)-fusions, and purified by affinity and conventional chromatographies. The bovine Arp2/3 complex and rabbit skeletal muscle actin were purified as described<sup>25,26</sup>.

**Biochemical assays.** All biochemical assays were performed in KMEI buffer (10 mM imidazole pH 7.0, 50 mM KCl, 1 mM MgCl<sub>2</sub> and 1 mM EGTA), or KMEI plus 5 mM  $\beta$ -mercaptoethanol at 25 °C. Actin assembly assays were performed as described<sup>25</sup>, with 4  $\mu$ M actin (5% pyrene labelled) and 10 nM Arp2/3 complex. Filament barbed end concentrations were calculated as described<sup>27</sup>. GBD–EspF<sub>U</sub> fusion proteins (10  $\mu$ M) were denatured using guanidine hydrochloride. Tryptophan fluorescence emission ( $\lambda_{\text{ex}} = 295$  nm,  $\lambda_{\text{em}} = 320$  nm and 355 nm) was fitted to a six parameter equation<sup>28</sup> to yield  $\Delta G_{\text{unfolding}}$ . EspF<sub>U</sub> proteins were titrated into N-WASP<sub>C</sub> in a Microcal VP-ITC microcalorimeter. Baseline was corrected for EspF<sub>U</sub> addition to buffer. Data were fit to a single-site binding model.

**Mammalian cell culture.** Mouse fibroblast-like cells were transfected with HA-Tir–EspF<sub>U</sub> fusions as described<sup>1</sup>. Transfected cells were treated with *E. coli* expressing intimin for 3.5 h (for Tir–R47<sub>2</sub> fusions) or antibodies recognizing the extracellular domain of EHEC Tir (gift from A. Donohue-Rolfe), followed by *Staphylococcus aureus* particles (Pansorbin; Calbiochem) (for Tir fusions with a single EspF<sub>U</sub> repeat).

**Immunofluorescence microscopy.** Monolayers were fixed and permeabilized as described<sup>29</sup>. Cells were treated with HA.11 or anti-N-WASP (gift from S. Snapper), washed and treated with Alexa488 goat anti-mouse antibody (1:200;

Molecular Probes) or Alexa568 goat anti-rabbit antibody (1:150; Molecular Probes), respectively. F-actin was stained with Alexa568-phalloidin (1:100; Molecular Probes).

**NMR spectroscopy and structure calculation.** The structure of the complex of GBD (residues 242–310) and R33 (residues 1–33 in Fig. 1, corresponding to residues 268–300 in EspF<sub>U</sub>; Supplementary Fig. 1) was determined in iterative fashion on the basis of NOE, dihedral and hydrogen bond restraints using ARIA 2.1 (ref. 30).

**Full Methods** and any associated references are available in the online version of the paper at [www.nature.com/nature](http://www.nature.com/nature).

Received 24 December 2007; accepted 10 June 2008.

Published online 23 July 2008.

1. Campellone, K. G., Robbins, D. & Leong, J. M. EspF<sub>U</sub> is a translocated EHEC effector that interacts with Tir and N-WASP and promotes Nck-independent actin assembly. *Dev. Cell* **7**, 217–228 (2004).
2. Garmendia, J. *et al.* TccP is an enterohaemorrhagic *Escherichia coli* O157:H7 type III effector protein that couples Tir to the actin-cytoskeleton. *Cell. Microbiol.* **6**, 1167–1183 (2004).
3. Campellone, K. G. *et al.* Enterohaemorrhagic *Escherichia coli* Tir requires a C-terminal 12-residue peptide to initiate EspFu-mediated actin assembly and harbours N-terminal sequences that influence pedestal length. *Cell. Microbiol.* **8**, 1488–1503 (2006).
4. Garmendia, J., Carlier, M. F., Egile, C., Didry, D. & Frankel, G. Characterization of TccP-mediated N-WASP activation during enterohaemorrhagic *Escherichia coli* infection. *Cell. Microbiol.* **8**, 1444–1455 (2006).
5. Lommel, S., Benesch, S., Rohde, M., Wehland, J. & Rottner, K. Enterohaemorrhagic and enteropathogenic *Escherichia coli* use different mechanisms for actin pedestal formation that converge on N-WASP. *Cell. Microbiol.* **6**, 243–254 (2004).
6. Buck, M., Xu, W. & Rosen, M. K. A two-state allosteric model for autoinhibition rationalizes WASP signal integration and targeting. *J. Mol. Biol.* **338**, 271–285 (2004).
7. Kim, A. S., Kakalis, L. T., Abdul-Manan, N., Liu, G. A. & Rosen, M. K. Autoinhibition and activation mechanisms of the Wiskott–Aldrich syndrome protein. *Nature* **404**, 151–158 (2000).
8. Torres, E. & Rosen, M. K. Contingent phosphorylation/dephosphorylation provides a mechanism of molecular memory in WASP. *Mol. Cell* **11**, 1215–1227 (2003).
9. Munter, S., Way, M. & Frischknecht, F. Signaling during pathogen infection. *Sci. STKE* **2006**, re5 (2006).
10. Caron, E. *et al.* Subversion of actin dynamics by EPEC and EHEC. *Curr. Opin. Microbiol.* **9**, 40–45 (2006).
11. Hayward, R. D., Leong, J. M., Koronakis, V. & Campellone, K. G. Exploiting pathogenic *Escherichia coli* to model transmembrane receptor signalling. *Nature Rev. Microbiol.* **4**, 358–370 (2006).
12. Gruenheid, S. & Finlay, B. B. Microbial pathogenesis and cytoskeletal function. *Nature* **422**, 775–781 (2003).
13. Galán, J. E. & Cossart, P. Host-pathogen interactions: a diversity of themes, a variety of molecular machines. *Curr. Opin. Microbiol.* **8**, 1–3 (2005).
14. Rangel, J. M., Sparling, P. H., Crowe, C., Griffin, P. M. & Swerdlow, D. L. Epidemiology of *Escherichia coli* O157:H7 outbreaks, United States, 1982–2002. *Emerg. Infect. Dis.* **11**, 603–609 (2005).
15. DeVinney, R. *et al.* Enterohaemorrhagic *Escherichia coli* O157:H7 produces Tir, which is translocated to the host cell membrane but is not tyrosine phosphorylated. *Infect. Immun.* **67**, 2389–2398 (1999).
16. Higgs, H. N. & Pollard, T. D. Regulation of actin filament network formation through Arp2/3 complex: Activation by a diverse array of proteins. *Annu. Rev. Biochem.* **70**, 649–676 (2001).
17. Kelly, A. E., Kranitz, H., Dotsch, V. & Mullins, R. D. Actin binding to the central domain of WASP/Scar proteins plays a critical role in the activation of the Arp2/3 complex. *J. Biol. Chem.* **281**, 10589–10597 (2006).
18. Panchal, S. C., Kaiser, D. A., Torres, E., Pollard, T. D. & Rosen, M. K. A conserved amphipathic helix in WASP/Scar proteins is essential for activation of Arp2/3 complex. *Nature Struct. Biol.* **10**, 591–598 (2003).
19. Rohatgi, R. *et al.* The interaction between N-WASP and the Arp2/3 complex links Cdc42-dependent signals to actin assembly. *Cell* **97**, 221–231 (1999).
20. Buck, M., Xu, W. & Rosen, M. K. Global disruption of the WASP autoinhibited structure on Cdc42 binding. Ligand displacement as a novel method for monitoring amide hydrogen exchange. *Biochemistry* **40**, 14115–14122 (2001).
21. Leung, D. W. & Rosen, M. K. The nucleotide switch in Cdc42 modulates coupling between the GTPase-binding and allosteric equilibria of Wiskott–Aldrich syndrome protein. *Proc. Natl. Acad. Sci. USA* **102**, 5685–5690 (2005).
22. Garmendia, J. *et al.* Distribution of tccP in clinical enterohaemorrhagic and enteropathogenic *Escherichia coli* isolates. *J. Clin. Microbiol.* **43**, 5715–5720 (2005).
23. Alto, N. M. *et al.* The type III effector EspF coordinates membrane trafficking by the spatiotemporal activation of two eukaryotic signalling pathways. *J. Cell Biol.* **178**, 1265–1278 (2007).
24. Volkman, B. F., Prehoda, K. E., Scott, J. A., Peterson, F. C. & Lim, W. A. Structure of the N-WASP EVH1 domain–WIP complex: insight into the molecular basis of Wiskott–Aldrich Syndrome. *Cell* **111**, 565–576 (2002).

25. Higgs, H. N., Blanchoin, L. & Pollard, T. D. Influence of the C terminus of Wiskott-Aldrich syndrome protein (WASp) and the Arp2/3 complex on actin polymerization. *Biochemistry* **38**, 15212–15222 (1999).
26. Cooper, J. A. & Pollard, T. D. Methods to measure actin polymerization. *Methods Enzymol.* **85**, 182–210 (1982).
27. Leung, D. W., Morgan, D. M. & Rosen, M. K. Biochemical properties and inhibitors of (N-)WASP. *Methods Enzymol.* **406**, 281–296 (2006).
28. Pace, C. N. Measuring and increasing protein stability. *Trends Biotechnol.* **8**, 93–98 (1990).
29. Campellone, K. G., Giese, A., Tipper, D. J. & Leong, J. M. A tyrosine-phosphorylated 12-amino-acid sequence of enteropathogenic *Escherichia coli* Tir binds the host adaptor protein Nck and is required for Nck localization to actin pedestals. *Mol. Microbiol.* **43**, 1227–1241 (2002).
30. Rieping, W. *et al.* ARIA2: automated NOE assignment and data integration in NMR structure calculation. *Bioinformatics* **23**, 381–382 (2007).

**Acknowledgements** We thank T. Otomo for discussion and assistance on biochemical assays and NMR spectroscopy; P. Li, I. Martins, C. A. Amezcuia, K. H. Gardner and Q. Wu for assistance with NMR spectroscopy and structure calculations; G. K. Amarasinghe and D. W. Leung for sharing reagents; D. Trobaugh, J. Rennie and D. Robbins for technical assistance; S. B. Padrick for help with Mathematica and X. Yao and S. B. Padrick for assistance in writing and for critical reading of the manuscript. This work was supported by grants from the National Institute of Health (NIH-R01-GM56322 to M.K.R.; NIH-R01-AI46454 to J.M.L.), Welch Foundation (I-1544 to M.K.R.) and a Chilton Foundation Fellowship to H.-C.C.

**Author Information** The atomic coordinates of the 20 final lowest energy conformers have been deposited in the Protein Data Bank under accession number 2K42. Reprints and permissions information is available at [www.nature.com/reprints](http://www.nature.com/reprints). Correspondence and requests for materials should be addressed to M.K.R. (michael.rosen@utsouthwestern.edu).

## METHODS

**Protein expression and purification.** To simplify nomenclature, EspF<sub>U</sub> residues are numbered 1–47 below and throughout the text (see Fig. 1), corresponding to residues 268–314 of the full-length protein (Supplementary Fig. 1). WASP GBD (residues 242–310), EspF<sub>U</sub> R33 (residues 1–33), R33 mutants, GBD–R33 (WASP 242–310 GGSGGSHM EspF<sub>U</sub> 1–33) and other GBD-repeat fusions were cloned into a modified pGEX-2T vector with a Tev protease cleavage site at the C terminus of GST. EspF<sub>U</sub> R47<sub>5</sub> (residues 80–314) was cloned into a pET15b vector. EspF<sub>U</sub> R47 (residues 1–47) was cloned into a modified pET19b vector with a His<sub>10</sub>-ubiquitin–Tev protease site at the N terminus. All proteins were expressed in *E. coli* strain BL21(DE3). Uniform <sup>15</sup>N/<sup>13</sup>C labelling of proteins was carried out in M9 minimum media supplemented with <sup>15</sup>NH<sub>4</sub>Cl and <sup>13</sup>C-glucose as the sole nitrogen and carbon sources. Samples of U-[<sup>15</sup>N,<sup>2</sup>H], Ile-[<sup>13</sup>C<sup>8</sup>H<sub>3</sub>], Leu-[<sup>13</sup>CH<sub>3</sub>,<sup>12</sup>CD<sub>3</sub>] and Val-[<sup>13</sup>CH<sub>3</sub>,<sup>12</sup>CD<sub>3</sub>] labelled proteins were obtained from bacterial growth in M9 D<sub>2</sub>O media containing 3 g l<sup>-1</sup> of U-[<sup>2</sup>H]-glucose, 1 g l<sup>-1</sup> of <sup>15</sup>NH<sub>4</sub>Cl, and 50 mg l<sup>-1</sup> of 2-keto-3-methyl-d<sub>3</sub>-d<sub>1</sub>-4-<sup>13</sup>C-butyratate and 50 mg l<sup>-1</sup> 4-[<sup>13</sup>C,<sup>1</sup>H]-3,3-<sup>2</sup>H- $\alpha$ -ketobutyrate (the last two were added 1 h before induction)<sup>31</sup>. The 3,3-[<sup>1</sup>H] or the 3-[<sup>1</sup>H] positions of commercially available  $\alpha$ -ketobutyrate or 2-keto-3-methyl-butyratate were exchanged to <sup>2</sup>H before use, according to the procedure previously described<sup>32</sup>. EspF<sub>U</sub> R14 and R18 peptides were synthesized at the University of Texas Southwestern Protein Chemistry Technology Center and quantified by amino acid analysis.

Cells expressing GBD and GBD–EspF<sub>U</sub> fusions were lysed by sonication in GST buffer (20 mM Tris pH 8.0, 100 mM NaCl, 1 mM dithiothreitol (DTT) and 1 mM EDTA) with protease inhibitors. Cleared lysates were applied to glutathione sepharose 4B (GE Healthcare). After washing, GST-tagged proteins were eluted in GST buffer containing 10 mM reduced glutathione. Proteins were concentrated, cleaved with Tev protease to separate the GST tag, diluted three-fold into QA buffer (20 mM Tris pH 8.0, 1 mM DTT and 1 mM EDTA) and loaded onto an anion exchange column (Mono Q, GE Healthcare) equilibrated in QA buffer. The column was developed with a linear gradient from 0% to 50% QB buffer (buffer A plus 1 M NaCl) in 10-bed volumes. Protein-containing fractions were further purified by size exclusion chromatography (Superdex 75 column, GE Healthcare). GST–GBD was purified similarly, except that the Tev protease cleavage was omitted. EspF<sub>U</sub> R33 and its mutants were purified similarly, except that in the anion-exchange step the protein was collected in the flow through. His<sub>10</sub>-ubiquitin tagged EspF<sub>U</sub> R47 was retained from cleared bacterial lysate on a Ni-NTA column (Qiagen), eluted with an imidazole gradient, desalts into QA buffer and cleaved with Tev protease to remove the His<sub>10</sub>-ubiquitin tag. Subsequent anion exchange and size exclusion chromatographies were the same as described for EspF<sub>U</sub> R33. His<sub>6</sub>–EspF<sub>U</sub> R47<sub>5</sub> was purified by Ni affinity chromatography and buffer exchanged into SA buffer (50 mM sodium phosphate pH 6.0, 1 mM DTT and 1 mM EDTA). Thrombin (GE Healthcare) cleaved EspF<sub>U</sub> R47<sub>5</sub> was purified by cation exchange (Mono S, GE Healthcare) in a gradient from 300 mM to 600 mM NaCl over 10 column volumes. Fractions containing EspF<sub>U</sub> R47<sub>5</sub> were pooled and further purified by gel filtration chromatography (Superdex 200, GE Healthcare). WASP GBD–VCA, N-WASP<sub>C</sub> (residues 193–501), bovine Arp2/3 complex and rabbit skeletal muscle actin were purified as described previously<sup>25–27</sup>.

**Pull-down assays.** GST–GBD was immobilized on glutathione–sepharose 4B beads ( $\sim$ 75 nmol ml<sup>-1</sup> beads, GE Healthcare). Beads (60  $\mu$ l) were incubated with 30  $\mu$ M EspF<sub>U</sub> R33 and 15  $\mu$ M WASP VCA separately in a final volume of 230  $\mu$ l and washed three times. The same volume of beads containing VCA-bound GST–GBD was further incubated with 200  $\mu$ M R33 and washed four times. Flow through and beads were analysed by SDS-PAGE stained with Coomassie blue.

**Mammalian cell culture and immunofluorescence microscopy.** To create transfection plasmids expressing Tir–EspF<sub>U</sub> fusions (all N-terminally HA-tagged), DNA fragments encoding EspF<sub>U</sub> R14, R30, R33, R47, R47<sub>2</sub> (repeats 4–5) and point mutants were cloned into the KpnI and BamHI sites of pHN-Tir $\Delta$ C (ref. 1). Mouse fibroblast-like cells were cultured in six-well plates in DMEM plus 10% fetal bovine serum and transfected with 1  $\mu$ g of plasmid per well for 12–16 h using Lipofectamine Plus reagent (Invitrogen)<sup>1</sup>. Cells were reseeded onto 12-mm glass coverslips to achieve 50%–75% confluence after an extra 24 h of growth. Transfected cells expressing Tir $\Delta$ C-R47<sub>2</sub> proteins were treated with an *E. coli* expressing intimin for 3.5 h. Cells expressing Tir $\Delta$ C fused

to a single EspF<sub>U</sub> repeat were treated with a 1:200 dilution of antibodies raised against the extracellular domain of EHEC Tir (anti-TirM) for 30 min, washed to remove excess antibody and then treated with *S. aureus* particles (Pansorbin; Calbiochem) for a further 2.5 h. In all cases, monolayers were fixed in PBS plus 4% paraformaldehyde for 30 min and permeabilized with 0.1% Triton X-100 as described<sup>29</sup>. Cells were then treated with HA.11 (diluted 1:500 in PBS plus 1% BSA) or HA.11 and anti-N-WASP (1:500) for 30 min before washing and addition of Alexa488 goat anti-mouse antibody (1:200; Molecular Probes) or Alexa568 goat anti-rabbit antibody (1:150). F-actin was identified by staining with Alexa568-phalloidin (1:100; Molecular Probes).

**NMR spectroscopy and structure calculation.** The complex between GBD and R33 was isolated by gel filtration chromatography (in 50 mM sodium phosphate pH 6.8, 100 mM NaCl, 1 mM DTT and 1 mM EDTA), and concentrated to 1–1.5 mM for all NMR experiments. Backbone and side-chain chemical shift assignments were obtained using standard triple-resonance methods in <sup>15</sup>N/<sup>13</sup>C-labelled samples<sup>33,34</sup>. A total of 1,552 distance restraints were obtained from two-dimensional <sup>1</sup>H-NOESY, 3D <sup>15</sup>N-edited NOESY ( $\tau_{\text{mix}} = 100$  ms) and 4D <sup>13</sup>C-<sup>13</sup>C-edited NOESY ( $\tau_{\text{mix}} = 75$  ms)<sup>35</sup> spectra. One hundred intermolecular NOEs were identified in a <sup>13</sup>C-filtered NOESY spectrum ( $\tau_{\text{mix}} = 100$  ms) of <sup>15</sup>N/<sup>13</sup>C-GBD in complex with unlabelled R33 recorded in D<sub>2</sub>O (ref. 36). A total of 165 unambiguously assigned NOEs define the GBD–R33 interface. Backbone dihedral angles were restrained on the basis of chemical shift analyses in the program TALOS<sup>37</sup> (maximum of 30° or the standard deviation observed in the TALOS database matches). Hydrogen bond restraints (HN–O distance, 1.5–2.8  $\text{\AA}$ ; N–O distance, 2.4–3.5  $\text{\AA}$ ) were applied to amide groups that were protected for  $>1$  h in a sample of a <sup>15</sup>N-GBD–R33 fusion protein freshly dissolved in D<sub>2</sub>O NMR buffer. Structures were calculated and iteratively refined using the program ARIA 2.1 (ref. 30). Intermolecular NOEs were assigned manually, in iterative fashion, from the <sup>13</sup>C-filtered NOESY spectrum, and assigned distance restraints in ARIA 2.1. Other NOEs were assigned automatically in ARIA 2.1. In the final iteration, structures were refined in explicit water to improve side-chain packing and hydrogen bonding<sup>38</sup>. All spectra were processed and analysed using NMRPipe<sup>39</sup> and NMRView<sup>40</sup>. The 20 final lowest energy conformers were analysed with ProCheckNMR<sup>41</sup>. Structure figures were generated with Ribbons<sup>42</sup> and PyMOL<sup>43</sup>.

31. Goto, N. K., Gardner, K. H., Mueller, G. A., Willis, R. C. & Kay, L. E. A robust and cost-effective method for the production of Val, Leu, Ile ( $\delta$ 1) methyl-protonated <sup>15</sup>N-, <sup>13</sup>C-, <sup>2</sup>H-labeled proteins. *J. Biomol. NMR* 13, 369–374 (1999).
32. Gardner, K. H. & Kay, L. E. Production and incorporation of <sup>15</sup>N, <sup>13</sup>C, <sup>2</sup>H (<sup>1</sup>H-<sup>1</sup>D methyl) isoleucine into proteins for multidimensional NMR studies. *J. Am. Chem. Soc.* 119, 7599–7600 (1997).
33. Clore, G. M. & Gronenborn, A. M. Multidimensional heteronuclear nuclear magnetic resonance of proteins. *Methods Enzymol.* 239, 349–363 (1994).
34. Muhandiram, D. R. & Kay, L. E. Gradient-enhanced triple-resonance three-dimensional NMR experiments with improved sensitivity. *J. Magn. Reson. B* 103, 203–216 (1994).
35. Clore, G. M., Kay, L. E., Bax, A. & Gronenborn, A. M. Four-dimensional <sup>13</sup>C/<sup>13</sup>C-edited nuclear Overhauser enhancement spectroscopy of a protein in solution: application to interleukin 1 $\beta$ . *Biochemistry* 30, 12–18 (1991).
36. Zwahlen, C. et al. Methods for measurement of intermolecular NOEs by multinuclear NMR spectroscopy: application to a bacteriophage  $\lambda$  N-peptide/ $\lambda$  boxB RNA complex. *J. Am. Chem. Soc.* 119, 6711–6721 (1997).
37. Cornilescu, G., Delaglio, F. & Bax, A. Protein backbone angle restraints from searching a database for chemical shift and sequence homology. *J. Biomol. NMR* 13, 289–302 (1999).
38. Linge, J. P., Williams, M. A., Spronk, C. A., Bonvin, A. M. & Nilges, M. Refinement of protein structures in explicit solvent. *Proteins* 50, 496–506 (2003).
39. Delaglio, F. et al. NMRPipe: a multidimensional spectral processing system based on UNIX pipes. *J. Biomol. NMR* 6, 277–293 (1995).
40. Johnson, B. A. & Blevins, R. A. NMR View: A computer program for the visualization and analysis of NMR data. *J. Biomol. NMR* 4, 603–614 (1994).
41. Laskowski, R. A., Rullmann, J. A., MacArthur, M. W., Kaptein, R. & Thornton, J. M. AQUA and PROCHECK-NMR: programs for checking the quality of protein structures solved by NMR. *J. Biomol. NMR* 8, 477–486 (1996).
42. Carson, M., Charles, W. C. Jr & Robert, M. S. *Methods in Enzymology* 493–502 (Academic, 1997).
43. DeLano, W. L. *The PyMOL User's Manual* (DeLano Scientific, 2002).

## LETTERS

# Cryptochrome mediates light-dependent magnetosensitivity in *Drosophila*

Robert J. Geegar<sup>1</sup>, Amy Casselman<sup>1</sup>, Scott Waddell<sup>1</sup> & Steven M. Reppert<sup>1</sup>

Although many animals use the Earth's magnetic field for orientation and navigation<sup>1,2</sup>, the precise biophysical mechanisms underlying magnetic sensing have been elusive. One theoretical model proposes that geomagnetic fields are perceived by chemical reactions involving specialized photoreceptors<sup>3</sup>. However, the specific photoreceptor involved in such magnetoreception has not been demonstrated conclusively in any animal. Here we show that the ultraviolet-A/blue-light photoreceptor cryptochrome (Cry) is necessary for light-dependent magnetosensitive responses in *Drosophila melanogaster*. In a binary-choice behavioural assay for magnetosensitivity, wild-type flies show significant naive and trained responses to a magnetic field under full-spectrum light (~300–700 nm) but do not respond to the field when wavelengths in the Cry-sensitive, ultraviolet-A/blue-light part of the spectrum (<420 nm) are blocked. Notably, Cry-deficient *cry<sup>0</sup>* and *cry<sup>b</sup>* flies do not show either naive or trained responses to a magnetic field under full-spectrum light. Moreover, Cry-dependent magnetosensitivity does not require a functioning circadian clock. Our work provides, to our knowledge, the first genetic evidence for a Cry-based magnetosensitive system in any animal.

The ability of an animal to detect geomagnetic fields has substantial biological relevance as it is used by many invertebrate and vertebrate species for orientation and navigation purposes, including homing, building activity and long-distance migration<sup>2,4</sup>. Three general modes of magnetoreception have been proposed<sup>5</sup>. One mode is electromagnetic induction by the Earth's magnetic field, which may occur in electrosensitive marine fish, although there is little evidence to support such sensing. The two other modes, for which experimental evidence does exist, are a magnetite-based process<sup>6–8</sup> and chemical-based reactions<sup>9,10</sup> that are modulated by magnetic fields. One chemical model of magnetoreception proposes that magnetic information is transmitted to the nervous system through the light-induced product of magnetically sensitive radical-pair reactions in specialized photoreceptors<sup>3</sup>.

Cry proteins are flavoproteins that have been postulated to generate magnetosensitive radical pairs that could provide a photoinduced electron transfer reaction for the detection of magnetic fields<sup>3</sup>. Cry proteins are best known for their roles in the regulation of circadian clocks<sup>11,12</sup> and can be categorized into two groups on the basis of current phylogenetic and functional relationships<sup>13,14</sup>. *Drosophila*-like Cry proteins are sensitive to light in the ultraviolet-A/blue range<sup>15</sup> and function primarily as photoreceptors that synchronize (entrain) circadian clocks. Vertebrate-like Cry proteins, which have also been found in every non-drosophilid insect so far examined<sup>14</sup>, do not seem to be directly light-sensitive. Instead, vertebrate-like Cry proteins are potent repressors of the Clock and Bmal1 (known as Cycle in insects) transcription factors which, as heterodimers, drive the intracellular transcriptional feedback loop of the circadian clock mechanism in all animals studied.

Although there is good behavioural evidence for the involvement of short-wavelength photoreceptors in the detection of a geomagnetic field<sup>5,16–18</sup>, an essential link between Cry and magnetoreception has not been established in any animal. *Drosophila* are ideally suited to investigate a role for Cry as a magnetoreceptor, because they only have the light-sensitive Cry<sup>14</sup> in which the action spectrum peaks in the ultraviolet-A range (350–400 nm) with a plateau in the near blue range (430–450 nm)<sup>19,20</sup>. Notably, flies that lack Cry (*cry<sup>0</sup>*)<sup>21</sup> or harbour the chemically induced missense *cry<sup>b</sup>* mutation<sup>22,23</sup> can be used to evaluate the role of Cry in magnetosensitive responses.

We initiated our studies by developing a behavioural assay for magnetosensitivity in *Drosophila* (Fig. 1a). In this illuminated apparatus, flies experience a magnetic field generated by an electric coil system and display their magnetosensitivity in a binary-choice T-maze. The two-coil system is ideal for behavioural studies of magnetosensitivity, because it produces a magnetic field on one side of the T-maze, while producing no field on the opposite side. This design eliminates non-magnetic differences such as heat generated by the electric coils between sides during test sessions<sup>24</sup>. Flies were tested either for their response to the magnetic field in the naive state (naive group) or after a training session pairing the field with sucrose reward (trained group).

Wild-type Canton-S, white-eyed *w*;Canton-S, Oregon-R and Berlin-K strains all developed a learned preference for a magnetic field (Fig. 1b). The trained groups in the two Canton-S lines showed the greatest response to the field ( $P = 0.002$ , one-way analysis of variance (ANOVA)) and were the only ones to show a naive avoidance of the field ( $P < 0.0001$ , one-sample *t*-test). Thus, *Drosophila* consistently show magnetosensitivity that varies in magnitude in a strain-dependent manner. The similarity of behavioural responses between red-eyed, wild-type Canton-S flies and white-eyed *w*;Canton-S flies shows that eye colour does not substantially alter behavioural responses to the magnetic field.

Because wild-type Canton-S flies showed the most robust trained and naive responses of the strains tested, we used them to determine whether the magnetic responses we observed were light-dependent. We assayed naive and trained Canton-S flies under different long-wavelength pass filters that transmitted wavelengths of light at  $>500$  nm,  $>420$  nm or  $>400$  nm (Fig. 2a). In contrast to flies assayed under full-spectrum light (Fig. 1b and Fig. 2a), flies did not show either naive or trained responses to the field when wavelengths  $<420$  nm were blocked (Fig. 2b). Because the filter that blocked light  $<420$  nm also caused a 13% decrease in total irradiance (Fig. 2c, red line), we examined whether the filter-induced lack of behavioural responses to the magnetic field was secondary to the decrement in irradiance. When Canton-S flies were studied under full-spectrum light, with a total irradiance level lower than that imposed by the filter (Fig. 2c, blue line), the flies still showed significant naive ( $P = 0.0005$ , one-sample *t*-test) and trained responses to

<sup>1</sup>Department of Neurobiology, University of Massachusetts Medical School, Worcester, Massachusetts 01605, USA.

the magnetic field (Fig. 2d). Thus, the filter-induced loss of behavioural responses to the magnetic field is due to the loss of short-wavelength light.

Behavioural responses to the magnet were partially restored when 400–420 nm light was included (Fig. 2b), which is consistent with the action spectrum of *Drosophila* Cry tailing into the near blue<sup>19</sup>, and, as expected, the trained response was weaker than that under full-spectrum light (full spectrum versus  $>400$  nm,  $P < 0.001$ , Student's *t*-test). This wavelength-dependent effect of the magnetic field on behaviour suggests that *Drosophila* has a photoreceptor-based magnetosensitive system. Moreover, because the response to the magnetic field requires ultraviolet-A/blue light ( $<420$  nm; Fig. 2e), these

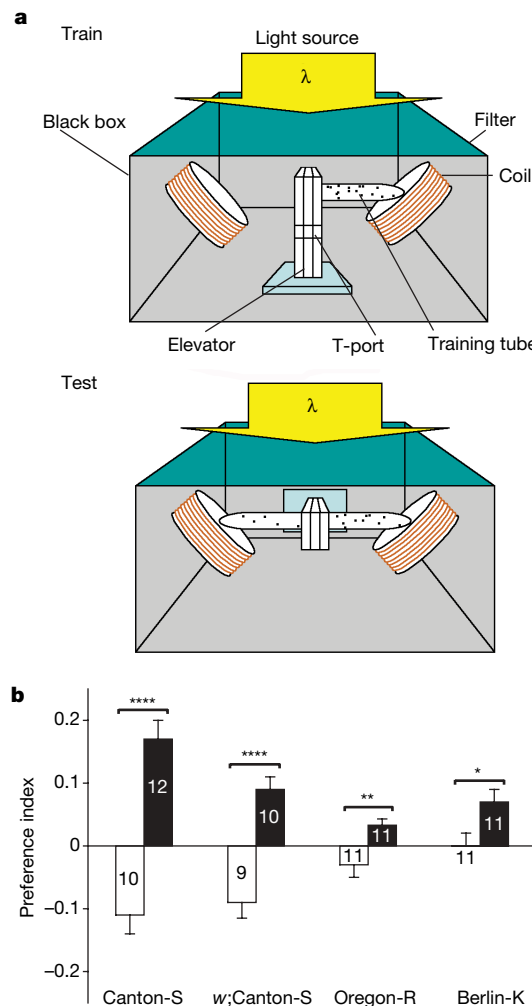


**Figure 1 | Behavioural apparatus for magnetosensitivity and behavioural responses in different *Drosophila* strains.** **a**, Behavioural apparatus for magnetosensitivity. The top diagram (Train) shows the frontal view of the choice chamber apparatus positioned for training. The chamber apparatus consisted of a training tube, an elevator to transfer flies, and a duel-choice point (T-port). For training, the apparatus, with training tube only, was placed upright in an illuminated black box containing a two-coil system. A population of flies (dots) was loaded into the training tube with or without sucrose reinforcement and a magnetic field. The bottom diagram (Test) shows the frontal view of the choice chamber apparatus positioned for testing. For testing, the apparatus, with tubes attached to the T-port (T-maze), was rotated to the horizontal and flies were transferred from the elevator section to the T-port. Wavelength dependence was examined using long-wavelength pass filters. **b**, *Drosophila* strains vary in their behavioural response to a magnetic field under full-spectrum light (Fig. 2a). Bars show the preference index of the naive (white) or trained (black) groups. Numbers represent the groups tested and values are mean  $\pm$  s.e.m. \*,  $P < 0.05$ ; \*\*,  $P < 0.01$ ; \*\*\*,  $P < 0.0001$ .

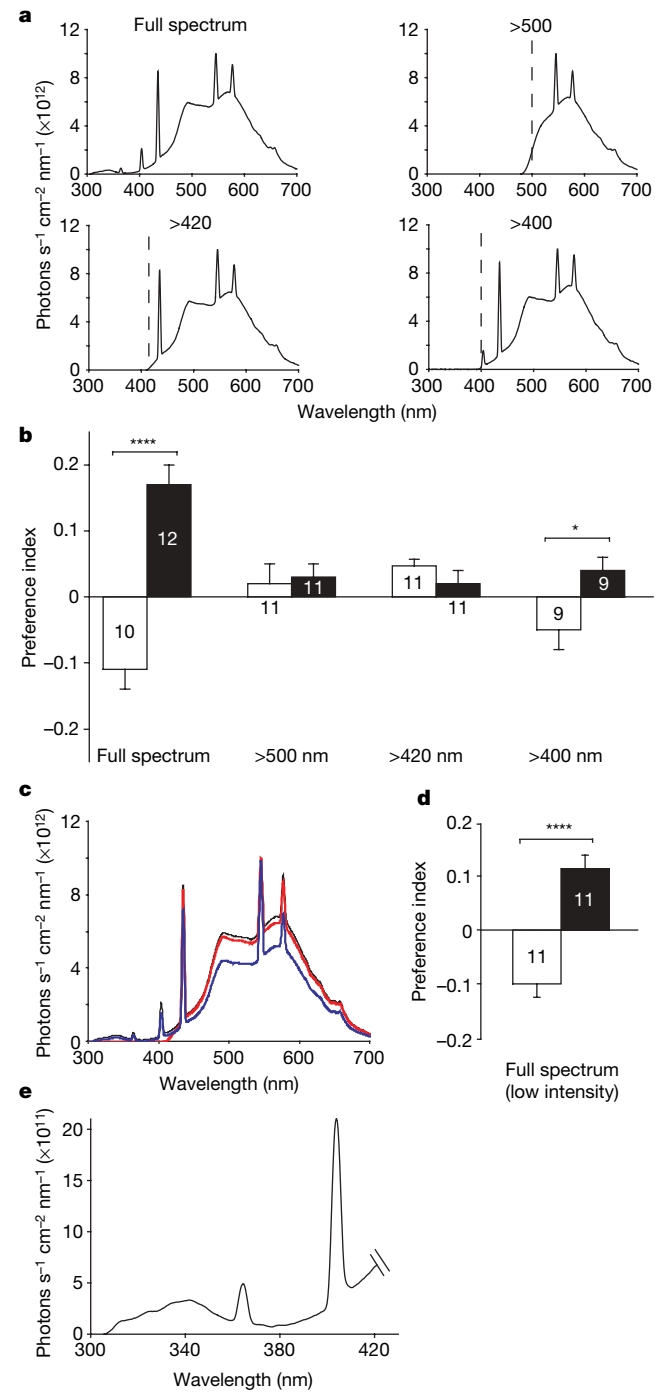


**Figure 2 | Short-wavelength light is required for magnetosensitivity in Canton-S flies.** **a**, Irradiance curves for different light conditions. Light measurements were taken inside the training and test tube. Dashed lines denote cutoff points of the blocking filters. **b**, Wavelength-dependence of the magnetic response. Bars show the preference index of the naive (white) or trained (black) groups. Full-spectrum data are from Fig. 1b. Numbers represent the groups tested. \*,  $P < 0.05$ ; \*\*\*,  $P < 0.0001$ . **c**, Irradiance curves depicting full-spectrum light (black line), light  $>420$  nm (red line) and full-spectrum light with reduced total irradiance (full spectrum, low intensity; blue line). **d**, Canton-S flies still elicited significant responses to the magnetic field under full-spectrum, low intensity light. \*\*\*,  $P < 0.0001$ . **e**, Irradiance values from 300–420 nm. Data are expanded scale from full-spectrum pattern in **a**. The irradiance values in ultraviolet-A/blue light in our studies (300–420 nm) are in line with those reported for *Drosophila* Cry function using other biological responses<sup>19,20</sup>; that is, a range of  $10^{11}$  to  $10^{12}$  photons  $s^{-1} \text{cm}^{-2} \text{nm}^{-1}$ . Values from **b** and **d** are mean  $\pm$  s.e.m.

data are consistent with the hypothesis that Cry can function as a magnetoreceptor in *Drosophila*.

We next used Cry-deficient *cry<sup>0</sup>* mutant flies to examine directly whether Cry is required for magnetosensitive behaviour. We tested two of the newly generated *cry<sup>0</sup>* fly lines, because, in *cry<sup>0</sup>* flies, the entire *cry* coding sequence has been replaced with mini-white<sup>+</sup> by homologous recombination, ensuring that, unlike in the more commonly used point-mutant *cry<sup>b</sup>* flies, there is no possibility of residual Cry activity<sup>21</sup>. In addition, the three *cry<sup>0</sup>* fly lines (from *cry<sup>01</sup>* to *cry<sup>03</sup>*) were backcrossed independently into a *w<sup>1118</sup>* background<sup>21</sup>. Thus, we were able to use the appropriate *w<sup>1118</sup>* control flies to test the contribution of the *cry* gene in magnetosensitive behaviour.

Control *w<sup>1118</sup>* flies showed a clear naive preference for, rather than avoidance of, the magnetic field (Fig. 3a). The difference in the direction of the naive response to the magnetic field between Canton-S flies and the *w<sup>1118</sup>* line re-emphasizes the importance of controlling for genetic background in studies of magnetosensitivity in flies. Nonetheless, like Canton-S flies, the naive response of *w<sup>1118</sup>* flies to the magnetic field was light dependent; the naive preference for the magnetic field was abolished in the absence of ultraviolet-A/blue light (<420 nm; Fig. 3a).

Homozygous *cry<sup>02</sup>* flies lacking Cry did not show a naive response to the magnet under full-spectrum light, in contrast to the significant naive responses manifested by both *w<sup>1118</sup>* and heterozygous *cry<sup>02</sup>/+* flies (Fig. 3b). Training control *w<sup>1118</sup>* flies to prefer the magnetic field under full-spectrum light significantly enhanced their naive preference for the field (Fig. 3c). In contrast, homozygous *cry<sup>01</sup>* flies did not show either a naive preference for the field (like *cry<sup>02</sup>* flies) or an enhanced preference for the field after training (Fig. 3c). The loss of the response to the magnetic field in the Cry-deficient flies resembled the behaviour when *w<sup>1118</sup>* flies were deprived of ultraviolet-A/blue light (Fig. 3a), which is consistent with Cry being the relevant light sensor. These data using two *cry* null strains strongly suggest that both naive and trained responses to the magnetic field in *Drosophila* require Cry function.

The Cry-defective *cry<sup>b</sup>* mutant flies are also unable to respond to the magnetic field; the *cry<sup>b</sup>* mutation renders Cry<sup>B</sup> essentially non-functional<sup>22,23</sup>. Because the genetic background of *cry<sup>b</sup>* mutant flies is not well defined, we compared behavioural responses to the magnetic field between homozygous *cry<sup>b</sup>* flies and heterozygous *cry<sup>b</sup>*/Canton-S flies. Whereas homozygous *cry<sup>b</sup>* flies did not show either naive or trained responses to the magnetic field under full-spectrum light, heterozygous *cry<sup>b</sup>*/Canton-S flies showed significant naive ( $P = 0.0004$ , one-sample *t*-test) and trained responses (Fig. 3d); the trained response in the heterozygotes was less than that of wild-type Canton-S flies (Fig. 1b) and probably results from differences in genetic background.

To rule out non-*cry* mutations as the reason for the lack of magnetic responses in *cry<sup>b</sup>* mutants, we showed that the *cry<sup>b</sup>* mutation fails to complement the *cry<sup>01</sup>* null mutation. Transheterozygous *cry<sup>b</sup>*/*cry<sup>01</sup>* flies did not show significant naive or trained responses to the magnet, whereas heterozygous *cry<sup>01</sup>*/Canton-S and *cry<sup>b</sup>*/Canton-S flies did (naive response,  $P = 0.006$ , one-sample *t*-test; Fig. 3d). Taken together, these data indicate that the *cry* locus is necessary for light-dependent magnetosensitivity in *Drosophila*. Furthermore, the lack of a trained response in both *cry<sup>01</sup>* and *cry<sup>b</sup>* mutant flies is consistent with Cry being an essential component of the magnetosensitive sensory input pathway and perhaps the magnetoreceptor itself.

Because light-activated Cry interacts with the critical circadian clock protein Timeless to reset the circadian clock mechanism<sup>25</sup>, we examined whether an intact circadian system is necessary for the Cry-dependent magnetosensitive responses in wild-type Canton-S flies. Circadian arrhythmicity was induced by constant light, which disrupts circadian clock function in Cry-containing cells by causing the constant degradation of not only Cry but also Timeless and then Period<sup>25</sup>. We subsequently tested behavioural responses to the

magnetic field after at least 5 days in constant light when the flies were shown to express arrhythmic locomotor behaviour (Fig. 4a), to have disrupted Period abundance rhythms (Fig. 4b), and to express constantly low levels of Cry (Fig. 4c). Notably, these arrhythmic flies continued to show significant naive ( $P = 0.004$ , one-sample *t*-test)

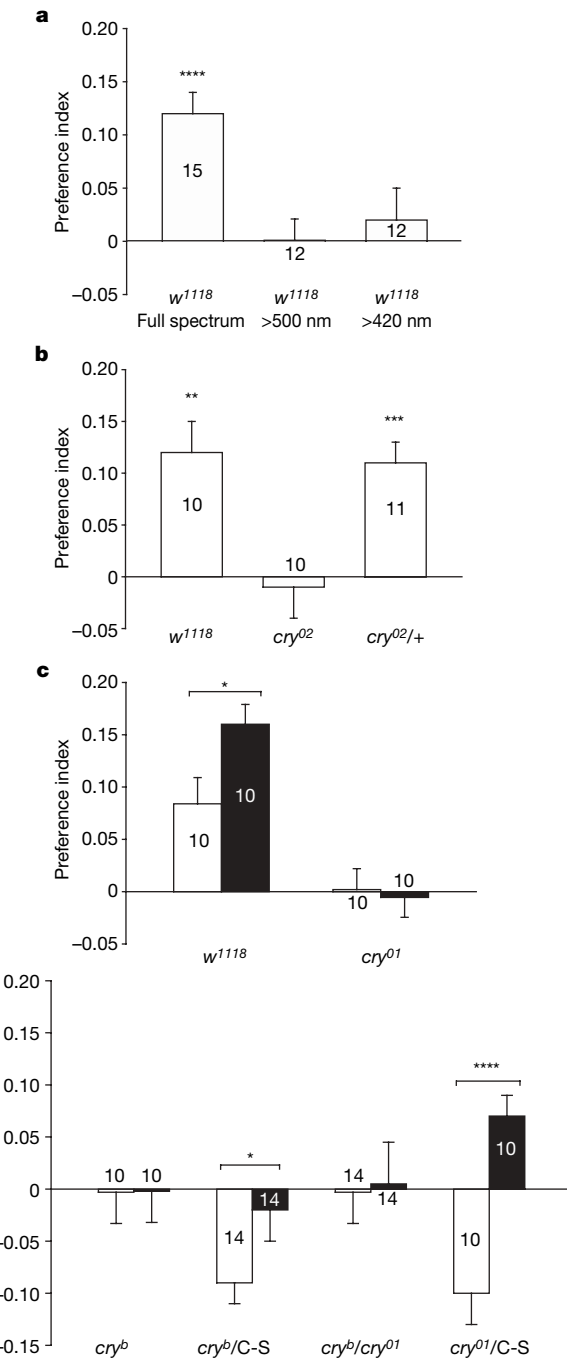


**Figure 3 | Drosophila Cry mediates magnetosensitivity.** **a**, Magnetosensitivity in *w<sup>1118</sup>* flies depends on ultraviolet-A/blue light. Bars show preference index values for naive responses under full-spectrum light and light >500 nm and >420 nm. Numbers represent the groups tested. **b**, **c**, **d**, Naive response to a magnetic field is impaired in Cry-deficient *cry<sup>02</sup>* flies, but not in *cry<sup>02</sup>/+* flies. Bars show preference index values for naive responses. **c**, **d**, Naive and trained responses to a magnetic field are impaired in Cry-deficient *cry<sup>01</sup>* flies. Bars are preference index values for naive (white) and trained (black) groups. **c**, **d**, Naive and trained responses to a magnetic field are impaired in homozygous *cry<sup>b</sup>* and transheterozygous *cry<sup>b</sup>*/*cry<sup>01</sup>* flies. Bars show preference index values for naive (white) or trained (black) groups. C-S, Canton-S. **a**, **b**, **c**, **d**,  $P < 0.05$ ; **a**, **b**, **c**, **d**,  $P < 0.0001$ . Values from **a**–**d** are mean  $\pm$  s.e.m.

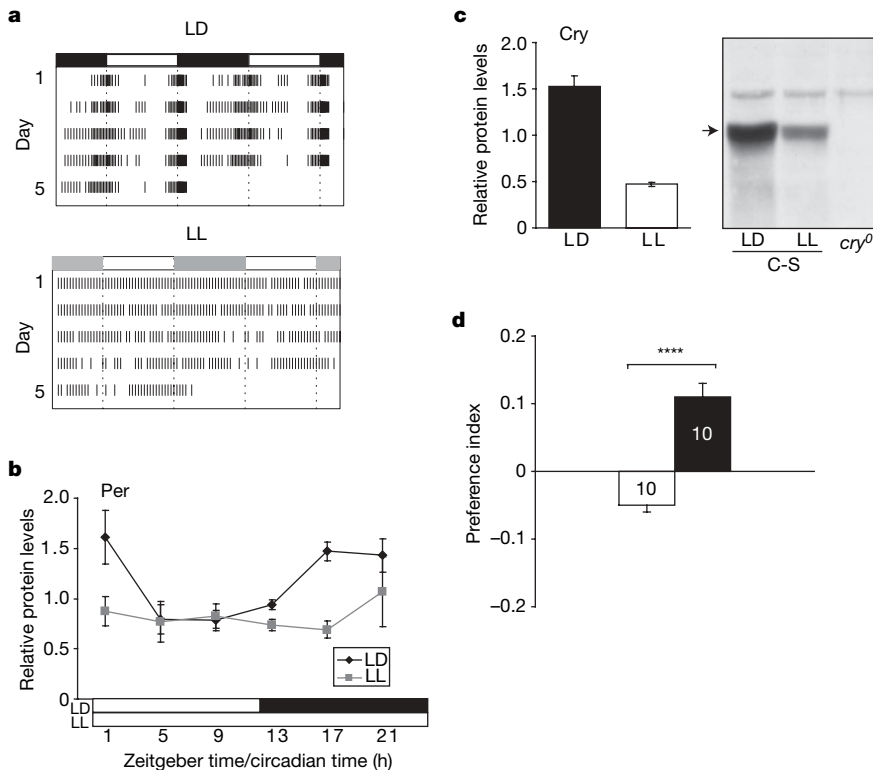


**Figure 4 | Constant light disrupts circadian function but not Cry-mediated magnetosensitivity in Canton-S flies.** **a**, Mean activity records in 12 h light:12 h dark lighting cycle (LD; top) or constant light (LL; bottom) in double-plotted format ( $n = 62$  for each group). The lighting conditions were identical to those used for housing flies tested for responses to magnet; light irradiance,  $1.5 \times 10^{15}$  photons  $s^{-1} \text{ cm}^{-2} \text{ nm}^{-1}$ . For the light-dark cycle, 94% expressed circadian rhythms when released in constant darkness (period,  $24.6 \pm 0.03$  h). All the constant-light flies were arrhythmic. **b**, Temporal profiles of Period (Per) in heads. Protein abundance was rhythmic in the

light-dark cycle ( $P < 0.01$ , one-way ANOVA), but not in constant light. Head extracts were analysed by western blot<sup>30</sup> and normalized against  $\alpha$ -tubulin. Values are mean  $\pm$  s.e.m. from three sets of heads. **c**, Cry abundance is decreased in LL. Values are mean  $\pm$  s.e.m. from three sets of heads collected over 24 h in the light-dark cycle or in constant light. Right, western blot probed for Cry<sup>30</sup> showing presence (arrow) in the light-dark cycle or in constant light in Canton-S (C-S) heads, and absence in  $cry^{01}$  heads. **d**, Flies in constant light elicit behavioural responses to the magnetic field. Values are mean  $\pm$  s.e.m. \*\*\*\* $P < 0.0001$ .

and trained responses to the magnetic field (Fig. 4d). Thus, the continuous activation of Cry by light does not disrupt its ability to sense the magnet, and an intact circadian system is not required for the magnetoreception mechanism to operate.

There are two other published reports of magnetosensitivity in adult *Drosophila*<sup>26,27</sup>. One describes behavioural evidence that male wild-type Oregon-R flies show a light-dependent magnetic compass response in a radial maze whereas female flies did not respond to the magnet<sup>27</sup>. Additionally, male flies responded in opposite directions when tested under either 365 nm or 500 nm light. In our studies, both male and female flies showed a magnetic response. Regardless of experimental differences, both the previous study<sup>27</sup> and ours demonstrate that fruitflies can respond to a magnetic field in a wavelength-dependent manner.

Our results extend substantially the presence of a light-dependent magnetic sense in *Drosophila* by showing the necessity of Cry. We cannot distinguish unequivocally whether fly Cry functions as the actual magnetoreceptor or whether it is an essential component downstream of the receptor. Cry is necessary for both the naive and trained responses to the magnetic field, consistent with the notion that Cry is in the input pathway of magnetic sensing. In addition, the continued behavioural responses to the magnet in constant light, in which the known Cry signalling components are being constantly degraded and the circadian clock is rendered non-functional, is also consistent with an input function. The most compelling evidence supporting a magnetoreceptor role for Cry is that the Cry-dependent behavioural responses to the magnetic field require ultraviolet-A/blue light, which matches the action spectrum of *Drosophila* Cry<sup>19,20</sup>.

Our behavioural assay for magnetosensitivity does not at present have a pure directional component, and therefore it is difficult to relate our findings directly to the use of geomagnetic fields for animal orientation and navigation. Nevertheless, it is probable that the response we have identified is the prototype for the involvement of Cry in chemical-based magnetic sensing. Thus, our findings open new avenues of investigation into the cellular and molecular basis of chemical-based magnetic sensing in animals. The powerful genetics of *Drosophila* will facilitate an understanding of the precise mechanism of action of Cry in magnetosensitivity, such as the actual involvement of magnetosensitive radical pairs produced by photo-induced electron transfer reactions<sup>28</sup>. Our data further show that the biological functions of *Drosophila* Cry extend beyond those in circadian clocks.

## METHODS SUMMARY

Fly stocks were raised on standard cornmeal/agar medium at 25 °C and 60% relative humidity under a 12 h light:12 h dark lighting cycle. The  $w^{1118};cry^0$  flies (from  $cry^{01}$  to  $cry^{03}$ ) were a gift from J. C. Hall and are described in ref. 21. The  $w^{1118}$  stock used in our experiments was the same stock used to create  $w^{1118};cry^0$  flies<sup>21</sup>. The  $cry^b$  line was a gift from P. Emery<sup>22</sup>. Our choice apparatus was based on the olfactory conditioning apparatus as described<sup>29</sup>. Our two-coil system was based on the double-wrapped coil system described previously<sup>24</sup>. We adjusted the current flowing through the coils so that the magnetic field intensity was no more than 5 G in any area along the tube. Coils were positioned 45° to the horizontal for experiments involving Canton-S,  $w$ ;Canton-S, Berlin-K and Oregon-R flies. Coils were positioned parallel to the horizontal for all other experiments, because it produced a more robust response and eliminated a polar gradient; that is, there was no horizontal magnetic gradient, as the field was perpendicular to the T-port tubes. To assess the magnetoresponse of flies, we used a simple choice paradigm. Flies were placed in a glass vial containing

moistened Whatman paper and starved for 22 h before training. All experiments were performed between 8:00 and 12:00 EST. For each population of flies tested (100–150 flies per group), we calculated a preference index value on the basis of the equation:  $(P_M - 0.5)/[(P_M + 0.5) - (2P_M \times 0.5)]$ , in which  $P_M$  is the proportion of flies on the magnetic field side of the T-port. To test whether flies responded to the experimental magnetic field, we used either a Student's *t*-test to compare preference index values between trained and naive groups or a one-sample *t*-test to compare preference index values to zero (that is, preference index values expected with no response to the magnetic field).

**Full Methods** and any associated references are available in the online version of the paper at [www.nature.com/nature](http://www.nature.com/nature).

Received 25 February; accepted 19 June 2008.

Published online 20 July 2008.

1. Lohmann, K. J., Lohmann, C. M. F. & Putman, N. F. Magnetic maps in animals: nature's GPS. *J. Exp. Biol.* **210**, 3697–3705 (2007).
2. Wiltschko, W. & Wiltschko, R. Magnetic orientation and magnetoreception in birds and other animals. *J. Comp. Physiol. A Neuroethol. Sens. Neural Behav. Physiol.* **191**, 675–693 (2005).
3. Ritz, T., Adem, S. & Schulten, K. A model for photoreceptor-based magnetoreception in birds. *Biophys. J.* **78**, 707–718 (2000).
4. Luschi, P. *et al.* Marine turtles use geomagnetic cues during open-sea homing. *Curr. Biol.* **17**, 126–133 (2007).
5. Johnsen, S. & Lohmann, K. J. The physics and neurobiology of magnetoreception. *Nature Rev. Neurosci.* **6**, 703–712 (2005).
6. Kirschvink, J. L. & Gould, J. L. Biogenic magnetite as a basis for magnetic-field detection in animals. *Biosystems* **13**, 181–201 (1981).
7. Walker, M. M. A model for encoding of magnetic field intensity by magnetite-based magnetoreceptor cells. *J. Theor. Biol.* **250**, 85–91 (2008).
8. Kirschvink, J. L., Walker, M. M. & Diebel, C. E. Magnetite-based magnetoreception. *Curr. Opin. Neurobiol.* **11**, 462–467 (2001).
9. Leask, M. J. M. Physicochemical mechanism for magnetic-field detection by migratory birds and homing pigeons. *Nature* **267**, 144–145 (1977).
10. Schulten, K., Swenberg, C. E. & Weller, A. Biomagnetic sensory mechanism based on magnetic-field modulated coherent electron-spin motion. *Z. Phys. Chem. (Frankfurt)* **111**, 1–5 (1978).
11. Cashmore, A. R. Cryptochromes: Enabling plants and animals to determine circadian time. *Cell* **114**, 537–543 (2003).
12. Partch, C. L. & Sancar, A. Photochemistry and photobiology of cryptochrome blue-light photopigments: The search for a photocycle. *Photochem. Photobiol.* **81**, 1291–1304 (2005).
13. Zhu, H. *et al.* The two CRYs of the butterfly. *Curr. Biol.* **15**, R953–R954 (2005).
14. Yuan, Q., Metterville, D., Briscoe, A. D. & Reppert, S. M. Insect cryptochromes: Gene duplication and loss define diverse ways to construct insect circadian clocks. *Mol. Biol. Evol.* **24**, 948–955 (2007).
15. Öztürk, N., Song, S. H., Selby, C. P. & Sancar, A. Animal type 1 cryptochromes—analysis of the redox state of the flavin cofactor by site-directed mutagenesis. *J. Biol. Chem.* **283**, 3256–3263 (2008).
16. Phillips, J. B. & Borland, S. C. Behavioral evidence for use of a light-dependent magnetoreception mechanism by a vertebrate. *Nature* **359**, 142–144 (1992).
17. Ritz, T., Dommer, D. H. & Phillips, J. B. Shedding light on vertebrate magnetoreception. *Neuron* **34**, 503–506 (2002).
18. Wiltschko, R. & Wiltschko, W. Magnetoreception. *Bioessays* **28**, 157–168 (2006).
19. VanVickle-Chavez, S. J. & Van Gelder, R. N. Action spectrum of *Drosophila* cryptochrome. *J. Biol. Chem.* **282**, 10561–10566 (2007).
20. Helfrich-Forster, C. *et al.* The extraretinal eyelet of *Drosophila*: Development, ultrastructure, and putative circadian function. *J. Neurosci.* **22**, 9255–9266 (2002).
21. Dolezelova, E., Dolezel, D. & Hall, J. C. Rhythm defects caused by newly engineered null mutations in *Drosophila*'s cryptochrome gene. *Genetics* **177**, 329–345 (2007).
22. Emery, P. *et al.* CRY, a *Drosophila* clock and light-regulated cryptochrome, is a major contributor to circadian rhythm resetting and photosensitivity. *Cell* **95**, 669–679 (1998).
23. Stanewsky, R. *et al.* The *cry<sup>b</sup>* mutation identifies cryptochrome as a circadian photoreceptor in *Drosophila*. *Cell* **95**, 681–692 (1998).
24. Kirschvink, J. L. Uniform magnetic-fields and double-wrapped coil systems—improved techniques for the design of bioelectromagnetic experiments. *Bioelectromagnetics* **13**, 401–411 (1992).
25. Stanewsky, R. Genetic analysis of the circadian system in *Drosophila melanogaster* and mammals. *J. Neurobiol.* **54**, 111–147 (2003).
26. Wehner, R. & Labhart, T. Perception of geomagnetic field in fly *Drosophila melanogaster*. *Experientia* **26**, 967–968 (1970).
27. Phillips, J. B. & Sayeed, O. Wavelength-dependent effects of light on magnetic compass orientation in *Drosophila melanogaster*. *J. Comp. Physiol. A Sens. Neural Behav. Physiol.* **172**, 303–308 (1993).
28. Maeda, K. *et al.* Chemical compass model of avian magnetoreception. *Nature* **453**, 387–390 (2008).
29. Tully, T. & Quinn, W. G. Classical-conditioning and retention in normal and mutant *Drosophila melanogaster*. *J. Comp. Physiol. A Sens. Neural Behav. Physiol.* **157**, 263–277 (1985).
30. Rush, B. L., Murad, A., Emery, P. & Giebultowicz, J. M. Ectopic CRYPTOCHROME renders TIM light sensitive in the *Drosophila* ovary. *J. Biol. Rhythms* **21**, 272–278 (2006).

**Supplementary Information** is linked to the online version of the paper at [www.nature.com/nature](http://www.nature.com/nature).

**Acknowledgements** We thank H. Zhu for the protein work in Fig. 4b, c; L. Foley for assistance; J. C. Hall for the *cry<sup>b</sup>* flies; P. Emery for the Per and Cry antibodies; and P. Emery, P. Perrat, B. Leung, S. DasGupta, M. Krashes and H. Zhu for discussions. This work was supported by grants from the NIH.

**Author Contributions** S.M.R. and R.J.G. conceived the idea of using *Drosophila* to study magnetosensitivity; S.W. and R.J.G. conceived the idea of using appetitive conditioning to study magnetoresponses; R.J.G. designed the experimental apparatus; R.J.G., S.W., A.C. and S.M.R. designed the experiments and analysed the data; R.J.G. performed the experiments with help from A.C.; R.J.G., S.M.R., S.W. and A.C. wrote the paper.

**Author Information** Reprints and permissions information is available at [www.nature.com/reprints](http://www.nature.com/reprints). Correspondence and requests for materials should be addressed to S.M.R. (steven.reppert@umassmed.edu).

## METHODS

**Fly strains.** Oregon-R, Berlin-K and  $w^{1118}$  stocks were provided by the Bloomington *Drosophila* Stock Center (product number 6326, 4269 and 8522, respectively).

**Behavioural apparatus.** The main chamber consisted of a training tube, a centre elevator section to transfer flies, and a two-tube choice point or T-port for testing the relative response of flies to a magnetic field (Fig. 1a). The training and T-port tubes were round-bottom polystyrene tubes and could be removed from the main section of the apparatus. The magnetic stimulus was delivered to the training and T-port tubes by placing the choice chamber apparatus inside an opaque housing box that contained the magnetic coil system. The box was constructed such that the main chamber could be placed between the two coils in either an upright position (as shown in Fig. 1a, top panel) or a horizontal position (as shown in Fig. 1a, bottom panel). The upright position of the chamber apparatus was used for training so that the tube could be placed in the centre of one coil, and the horizontal position of the apparatus was used to suspend the two tubes of the T-maze in the same area of the coil during test sessions. In this way, flies were subjected to the same light conditions and intensity of magnetic field during training and test sessions.

Each of the two coils was wrapped with two wires; the wires were wrapped in one direction on one coil and in the opposite direction on the other. Current flow through the coils produced a magnetic field in one coil (parallel current flow) but not in the other (opposite current flow). A double-pole, double-throw switch reversed the current flow in one wire loop but not the other, which allowed us to move the magnetic field easily from the right to the left side of the T-maze. A DC power supply with current and voltage controls was used so that we could change the intensity of the magnetic field produced by the coils. Each coil was mounted on a plastic track so that it could be positioned directly under the tubes (field perpendicular to the tubes), at the end of the tubes at a 45° angle (as shown in Fig. 1a), or at the end of the tubes (field parallel to the tubes). We used a magnetic field intensity of 5 G for our experiments, because it gave the most consistent naive response; decreasing to 1 G increased variability to the point that responses were no longer significant.

The housing box for the test or choice chamber was open on the top so that the chamber, regardless of position, could be illuminated by one ZooMed Reptisun 10.0 UVB fluorescent tube (F20T12) and one Agrobrite full spectrum fluorescent grow tube. Wavelengths entering the box were restricted by covering the top of the box with a long-wavelength filter that transmitted wavelengths of light  $>500$  nm (Edmund Optics) or  $>420$  nm or  $>400$  nm (E400 and E420 from Gentex). Irradiance measurements (from an Ocean Optics USB 2000 fibre optic spectrometer) were taken from inside one arm of the T-maze portion of the choice chamber apparatus; thus, lighting conditions represent those experienced by flies while being either trained or assayed for sensitivity to a magnetic field.

**Experimental procedure.** For the training group, a population of 100–150 flies was loaded into the elevator section of the choice apparatus with an empty training tube facing one of the coils (Fig. 1a, top panel). Flies were transferred to the training tube for 2 min and then transferred back to the elevator and held for a 1-min rest period. The empty training tube was next replaced with a tube containing sucrose reinforcement and flies were allowed to feed for 2 min in the presence of a magnetic field. Flies were then transferred back to the elevator and held for 1 min while the coil system was turned off. During this time, the training tube was also removed, and two empty tubes were added to form the two arms of the T-port. The choice chamber was then positioned horizontally in the box (Fig. 1a, bottom panel). The coil system was turned on, and flies were transferred to the T-port, in which they were allowed to choose between the sides with or without a magnetic field. After 2 min, the two arms of the T-port were blocked and flies from each side were collected into separate empty vials and counted.

For the naive group, a second population of 100–150 flies was immediately loaded into the elevator section of the horizontally placed choice chamber and the coil system was turned on. After 1 min, flies were transferred directly to the T-port for 2 min.

Trained and naive groups were tested consecutively and with the magnetic field on the same side. This was done to control for the possibility that the choice behaviour of flies reflected a preference for one arm of the T-port and not a response to the magnetic field. As an extra control for side preferences independent of magnetic stimuli, we alternated the side of the T-port containing the field after each consecutive set of trained and naive flies (that is, trained and naive with magnet on the left side and then trained and naive with magnet on the right).

# Molecular basis of the copulatory plug polymorphism in *Caenorhabditis elegans*

Michael F. Palopoli<sup>1</sup>\*, Matthew V. Rockman<sup>2</sup>\*, Aye TinMaung<sup>1</sup>, Camden Ramsay<sup>1</sup>, Stephen Curwen<sup>1</sup>, Andrea Aduna<sup>1</sup>, Jason Laurita<sup>1</sup> & Leonid Kruglyak<sup>2</sup>

Heritable variation is the raw material for evolutionary change, and understanding its genetic basis is one of the central problems in modern biology. We investigated the genetic basis of a classic phenotypic dimorphism in the nematode *Caenorhabditis elegans*. Males from many natural isolates deposit a copulatory plug after mating, whereas males from other natural isolates—including the standard wild-type strain (N2 Bristol) that is used in most research laboratories—do not deposit plugs<sup>1</sup>. The copulatory plug is a gelatinous mass that covers the hermaphrodite vulva, and its deposition decreases the mating success of subsequent males<sup>2</sup>. We show that the plugging polymorphism results from the insertion of a retrotransposon into an exon of a novel mucin-like gene, *plg-1*, whose product is a major structural component of the copulatory plug. The gene is expressed in a subset of secretory cells of the male somatic gonad, and its loss has no evident effects beyond the loss of male mate-guarding. Although *C. elegans* descends from an obligate-outcrossing, male–female ancestor<sup>3,4</sup>, it occurs primarily as self-fertilizing hermaphrodites<sup>5–7</sup>. The reduced selection on male–male competition associated with the origin of hermaphroditism may have permitted the global spread of a loss-of-function mutation with restricted pleiotropy.

The synthesis of evolutionary and developmental genetics demands empirical data on the structure of heritable variation in populations. The required data include the identities of the genes that underlie variation, the mutations that affect those genes, and the positions of the genes within the networks of molecular interactions that shape phenotypes. *C. elegans* is a promising system for the discovery of the molecular basis of variation. Although most studies of *C. elegans* have employed a single genetic background, natural isolates exhibit a wide range of phenotypes<sup>1,8</sup>. Some of this phenotypic variation may result from the change in selective environment associated with the recent origin of hermaphroditism in *C. elegans*. Males arise through rare non-disjunction events and contribute at a low rate to outcrossing<sup>5–7</sup>. Because their relatives in the *Caenorhabditis* clade produce copulatory plugs, the plugging strains of *C. elegans* probably retain an ancestral trait that confers significant advantages in male–male competition for matings (Supplementary Information and Supplementary Fig. 1). The failure of some strains of *C. elegans* to produce plugs may represent a loss-of-function mutation with minimal impact on fitness due to the diminished competition among males. Hodgkin and Doniach<sup>1</sup> showed that plugging exhibits Mendelian inheritance attributable to a single locus, *plg-1*. The plugging phenotype is dominant, consistent with a model of evolutionary and molecular loss of function in the N2 strain. We tested this model and characterized the molecular basis for heritable variation in copulatory plugging by identifying the gene and molecular lesion underlying *plg-1*.

Hodgkin and Doniach localized *plg-1* to a large region of chromosome III. We employed genetic mapping in crosses between the non-plugging strain N2 and a plugging natural isolate from Palo Alto, CB4855, to refine the location of *plg-1* to a 74-kilobase (kb) interval (Supplementary Methods and Supplementary Figs 2 and 3). Independently, we mapped *plg-1* to a coincident interval in a panel of recombinant inbred lines between N2 and a plugging natural isolate from Hawaii, CB4856 (Supplementary Fig. 4). A search for PCR-product length polymorphism showed that a retrotransposon present in the interval in the non-plugging strain N2 is absent in the plugging strains. Sequence analysis revealed that the retrotransposon and its long terminal repeats (LTRs) interrupt a novel, unannotated protein-coding gene whose predicted product has similarity to canonical mucins (Fig. 1a). Mucins are large glycoproteins that are often secreted to form gelatinous substances, including mucus, in diverse metazoans<sup>9</sup>; a mucin is therefore a natural candidate for a major structural component of the plug. The protein is predicted to contain proline-, threonine- and serine-rich (PTS) repeats, characteristic of highly O-glycosylated mucoproteins<sup>10,11</sup> (Fig. 1b); each PTS repeat contains 15 predicted O-glycosylation sites<sup>12</sup>. The non-repetitive amino and carboxy termini of the predicted protein are evolutionarily conserved among *Caenorhabditis* species, and the N terminus includes a predicted 21-amino-acid secretory signal peptide<sup>13</sup> (Fig. 1c). Each class of PTS repeats is much more similar within species than between species, consistent with standard models of concerted evolution of repetitive sequences<sup>14</sup> (Fig. 1d).

We used RT-PCR (PCR with reverse transcription) to show that the stable transcript of the putative mucin is absent in non-plugging strains. A spliced transcript from the gene is present in RNA from adult males of plugging strains, but is undetectable in adult males of non-plugging strains (Supplementary Fig. 5). The transcript is also undetectable in adult hermaphrodites from plugging strains, consistent with a male-specific function.

To confirm that the disruption of the putative mucin is responsible for the loss of plugging, we used two functional tests. First, we knocked down the expression of the gene with RNAi (RNA interference) in a plugging strain. The resulting males failed to produce copulatory plugs, confirming that the gene is necessary for copulatory plug formation (Fig. 2a). Second, we introduced a transgene carrying the putative mucin into a non-plugging strain. This was sufficient to transform the strain into one that produced plugs (Fig. 2b). We conclude that the putative mucin is the gene underlying the *plg-1* locus, and the absence of the disruptive retrotransposon is the plugging allele *e2001* defined by Hodgkin and Doniach<sup>1</sup>.

We next confirmed that the copulatory plug consists of an O-glycosylated mucin. We isolated hermaphrodites immediately

<sup>1</sup>Department of Biology, Bowdoin College, 6500 College Station, Brunswick, Maine 04011, USA. <sup>2</sup>Lewis-Sigler Institute for Integrative Genomics and Department of Ecology and Evolutionary Biology, Carl Icahn Laboratory, Princeton University, Princeton, New Jersey 08544, USA.

\*These authors contributed equally to this work.

after mating, and stained the resulting copulatory plugs with a fluorescently tagged peanut agglutinin lectin that recognizes Gal $\beta$ 1,3GalNAc-S/T, a carbohydrate modification characteristic of mucins<sup>15,16</sup>. The lectin stained the plugs specifically (Fig. 3a, b), indicating that an important constituent of each plug contains a carbohydrate structure that is typical of mucin glycoproteins.

In order to examine expression of *plg-1*, we introduced a transgenic construct with the evolutionarily conserved 5' upstream region of *plg-1* driving green fluorescent protein (GFP). We observed strong expression of GFP in 12 cells of the vas deferens (Fig. 3c–f), a tube of 30 secretory cells connecting the seminal vesicle to the cloaca<sup>17</sup>. Expression commences during the fourth larval stage, before the adult moult. In adult males, the cuboidal GFP-expressing cells are arranged in two rows (Fig. 3c). There is left-right asymmetry in the location of the GFP-expressing cells and in the intensity of their expression. Although there seems to be variation among individuals, typically five of the cells are on the right-hand side of the midline, whereas seven are on the left-hand side of the midline; furthermore, three posterior cells express a lower level of GFP, and two of these low-level cells are on the left-hand side (Supplementary Movie 1).

Expression of *plg-1*:GFP provides the first marker for this suite of vas deferens cells, a previously uncharacterized feature of male anatomy, and reveals their dynamic role in mating. Unmated males have a single large vacuole that occupies most of the cell volume in each of the 12 cells (Fig. 3d, e); in contrast, males examined immediately after mating lack these large vacuoles, and the 12 cells exhibit instead multiple smaller vacuoles (Fig. 3f). The vacuoles are present in both plugging and non-plugging genotypes and are probably storage compartments for seminal fluid.

We next assessed the geographic distribution of *plg-1* alleles. We tested 153 natural isolates from around the globe for the ability to complement the N2 loss-of-function allele. Strains (48) from Europe,

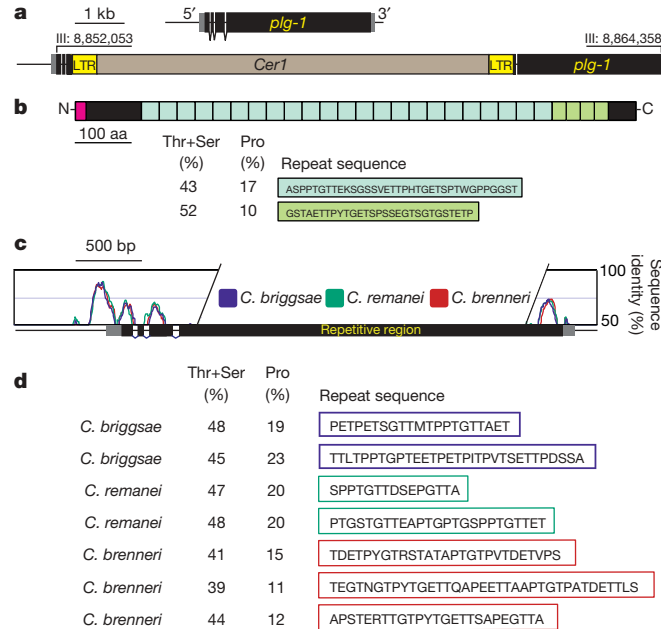


**Figure 1 | The *plg-1* gene.** **a**, Genomic structure of the *plg-1* gene, showing the exons (black) and UTRs (grey) determined by RACE. *Cer1* (brown) and its LTRs (yellow) disrupt exon 3 in N2, whose genomic organization is shown below. **b**, The PLG-1 protein contains a secretory signal (pink) and unique sequences at the N and C termini (black). The remainder consists of PTS repeats, shown in the coloured boxes. **c**, The non-repetitive regions of the gene and 5' upstream region are conserved among species. The PTS repeats are not conserved at the sequence level in *C. briggsae* (blue), *C. remanei* (green) and *C. brenneri* (red). Percentage identity to the *C. elegans* sequence is plotted for 100 bp windows of a multiple alignment<sup>30</sup>. **d**, The PTS repeats (boxes coloured as in **c**) exhibit concerted evolution<sup>14</sup>.

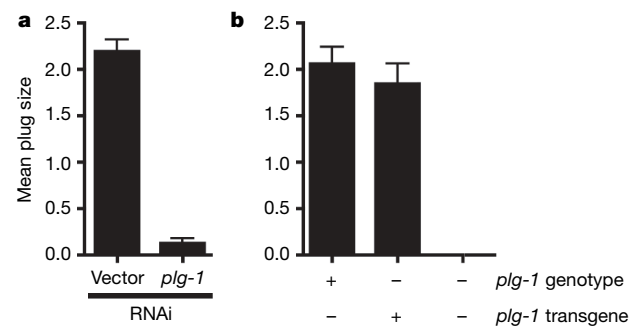


**Figure 2 | The mucin gene is *plg-1*.** **a**, CB4856 males in which *plg-1* has been knocked down by RNAi produced fewer and smaller plugs than control males (Mann–Whitney *U*-test,  $P < 0.0001$ ;  $n = 24$  and 23, respectively). **b**, Transgenic *plg-1* males deposited plugs similar in size and frequency to those produced by males with endogenous *plg-1* and larger than those produced by a strain lacking a functional *plg-1* gene (Mann–Whitney *U*-test,  $P < 0.0001$ ). The genotypes from left to right are CB4856 ( $n = 17$ ), F1 ( $n = 19$ ) from cross of N2 and QX1015 (*plg-1*(N2) *unc-119(ed3)* III), CB4856 background (−), and F1 ( $n = 18$ ) from cross of N2 and QX1015 without the array. Plug size was assessed in arbitrary units (0: none, 1: small, 2: medium, 3: large) by an observer blind to treatment. Error bars, s.e.m.

North America, and Australia failed to complement N2, and all carried the retrotransposon insertion in *plg-1*. All 105 strains that complemented N2 lacked the insertion (Fig. 4). As our PCR assay confirms that the location of the insertion and its orientation are shared among the non-plugging strains (Supplementary Information), we infer that the common loss-of-function allele of *plg-1* represents a single mutation that has spread across the globe.

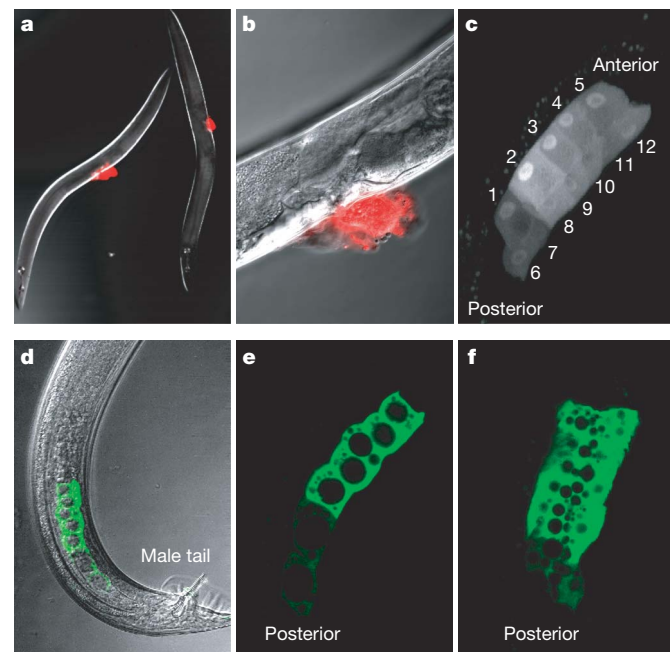


**Figure 3 | The copulatory plug contains carbohydrate structures typical of mucins and *plg-1* is expressed in only a small number of male cells.** **a, b**, Fluorescently labelled lectin that recognizes a carbohydrate modification characteristic of mucins specifically stains copulatory plugs. **c**, The *plg-1* promoter drives GFP expression in 12 vas deferens cells; this image is taken from Supplementary Movie 1. **d**, The GFP-expressing cells are in the central region of the vas deferens, anterior to the mating structures. **e**, In unmated males, each cell contains a large vacuole. **f**, After mating, the large vacuole is replaced by many smaller vacuoles. In **e** and **f**, an optical slice was taken from just left of the midline, so each image includes 5 bright cells anterior and 2 faint cells posterior. Approximate panel sizes: **a, b**,  $0.8 \times 1.1$  mm; **c, d**,  $0.13 \times 0.19$  mm; **c, e, f**,  $0.08 \times 0.11$  mm.

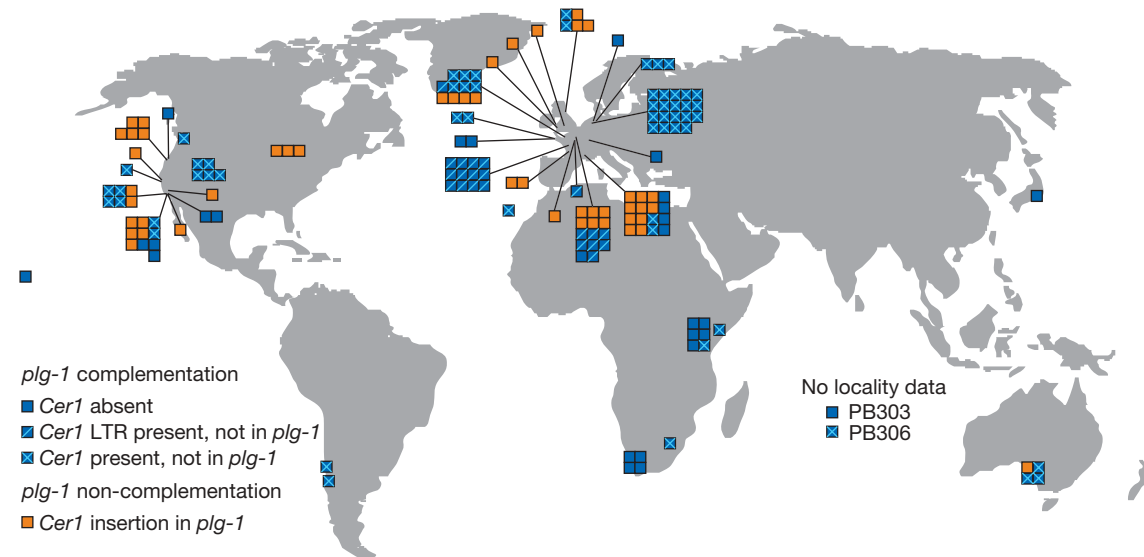


**Figure 4 | The *plg-1* loss-of-function allele is globally distributed and *Cer1* has been recently active.** Strains that complement the N2 loss-of-function allele of *plg-1* (F1 males produce plugs) are shown as blue boxes, and those

Plugging and non-plugging strains co-occur within localities, and the non-plugging genotype persists across years<sup>5,6</sup>, suggesting that the loss of plugging incurs little fitness cost in nature.

In the complete genome sequence of N2, the insertion of *Cer1* into *plg-1* is the sole intact copy of the retrotransposon<sup>18</sup>. We assayed natural isolates of *C. elegans* with uninterrupted *plg-1* sequences by PCR for the presence of *Cer1* elsewhere in the genome (Supplementary Table 1). While 25 strains had no evidence of *Cer1* or its LTRs, 59 strains carry the retrotransposon and its LTRs and another 21 carry the LTRs alone, evidence of having had and later lost the retrotransposon. We found by sequence analysis that *Cer1*, a *gypsy/Ty3* type retrotransposon<sup>19</sup>, is similar to retrotransposons in the genome sequences of *Caenorhabditis briggsae*, *Caenorhabditis brenneri* and *Caenorhabditis remanei*, and these mobile genetic elements may be a common source of new mutations in populations of *Caenorhabditis*.

Induced mutations in a large number of genes disrupt male mating and copulatory plug production<sup>20–22</sup>, but the naturally occurring allele of *plg-1* pinpoints the terminal gene in the plug-production network, a structural component of the plug itself. Genes upstream of *plg-1* in the male mating network, including genes required for cilium development, neurotransmitter biosynthesis and transmission, and male tail morphogenesis, have extensive pleiotropic roles in *C. elegans* biology<sup>22</sup>. In contrast, the *plg-1* gene has no apparent roles outside plugging. We found that the gene is expressed exclusively in males in a subset of cells with no other known function. Males with the loss-of-function allele of *plg-1* suffer no evident consequences apart from the loss of plugging. This result is consistent with a role for pleiotropy in filtering the mutations that actually contribute to evolutionary change from the much larger set of mutations that possibly could, a principle laid out by Fisher nearly 80 years ago<sup>23</sup>. Mutations with the fewest effects are those least likely to change some traits for the worse and hence are those most likely to contribute to evolutionary divergence<sup>24</sup>.

The only other naturally occurring allele known to disrupt male mating is a loss-of-function allele of *mab-23*, a gene required for development of the male copulatory organs, and this allele is known only from a single natural isolate<sup>1</sup>. Although *mab-23* is expressed in both males and hermaphrodites, it exhibits an obvious mutant phenotype only in males<sup>25</sup>, consistent with restricted pleiotropy; at the same time, the rarity of the *mab-23* allele suggests that complete loss of male function might be deleterious. Although *C. elegans* reproduces primarily by self-fertilization in hermaphrodites, selection probably acts to preserve male function<sup>26–28</sup>, eliminating mutations that disrupt male development, morphology or behaviour. The high frequency

that fail to complement (F1 males fail to plug) are shown orange. The distribution of *Cer1* and its LTR in the genomes of plugging strains is indicated with diagonals across the boxes.

of the *plg-1* loss-of-function allele, its co-occurrence with the functional *plg-1* allele, and its temporal persistence all suggest that the frequency of males in typical populations is insufficient to select for mate guarding, which requires not just functional males but competition among males. The evolution of hermaphroditism in *C. elegans* appears to have altered the selective regime of genes required for male–male competitive function. Although it is possible that the loss of *plg-1* is selectively favoured, it may also represent a neutral change drifting to high frequency in the absence of selection against it.

## METHODS SUMMARY

**Nematode stocks.** Nematodes were cultured using standard protocols<sup>29</sup>.

**Sequence analysis.** We merged partial gene predictions across *Cer1* in the N2 genome ([www.wormbase.org](http://www.wormbase.org)) and then refined the gene model using RACE with RNA from CB4855 males (Clontech SMART RACE kit). Sequences from other species were collected using synteny tracks ([www.ucsc.genome.org](http://www.ucsc.genome.org)); we identified N- and C-terminal *plg-1* sequences based on sequence conservation and generated alignments of flanking and intervening sequence using LAGAN<sup>30</sup>.

**Expression analyses.** RT–PCR primers flank intron three of *plg-1* and fall downstream of the *Cer1* insertion site; chimaeric *Cer1:plg-1* transcript should be detected if present. We generated integrated *plg-1::GFP* transgene (allele *qq1s1*) by cloning 311 bp of 5' upstream sequence into pSM\_GFP and co-bombardment with *unc-119(+)* plasmid pMM016b into QX1015, which carries *unc-119(ed3)* and *plg-1(N2)* introgressed into CB4856. We imaged the GFP using a Zeiss 510 META confocal microscope.

**Functional confirmation experiments.** We cloned 3 kb of CB4856 *plg-1* exon 4 into RNAi feeding vector L4440 and fed worms *Escherichia coli* HT115(DE3) carrying the vector or L4440 with no insert. Transgenic rescue of plugging employed a construct derived from CB4856 spanning from 686 bp 5' of the RACE-defined start of transcription to 178 bp 3' of the RACE-defined 3' UTR.

**Mucin staining.** Virgin adults were cleaned of bacteria in PBS, allowed to mate for 30 min on clean agarose plates, then fixed and stained with fluorescently labelled lectin. A labelled antibody that fluoresces at a different wavelength but does not bind to nematodes was included to control for the possibility that the gelatinous plug absorbs probe indiscriminately.

**Natural isolates.** Each isolate was mated to N2 males and the F1 males tested individually in overnight assays with single N2 hermaphrodites for the ability to produce plugs.

**Full Methods** and any associated references are available in the online version of the paper at [www.nature.com/nature](http://www.nature.com/nature).

Received 28 March; accepted 13 June 2008.

Published online 16 July 2008.

- Hodgkin, J. & Doniach, T. Natural variation and copulatory plug formation in *Caenorhabditis elegans*. *Genetics* 146, 149–164 (1997).

2. Barker, D. M. Copulatory plugs and paternity assurance in the nematode *Caenorhabditis elegans*. *Anim. Behav.* **48**, 147–156 (1994).
3. Kiontke, K. *et al.* *Caenorhabditis* phylogeny predicts convergence of hermaphroditism and extensive intron loss. *Proc. Natl Acad. Sci. USA* **101**, 9003–9008 (2004).
4. Cho, S., Jin, S. W., Cohen, A. & Ellis, R. E. A phylogeny of *Caenorhabditis* reveals frequent loss of introns during nematode evolution. *Genome Res.* **14**, 1207–1220 (2004).
5. Barrière, A. & Félix, M. A. High local genetic diversity and low outcrossing rate in *Caenorhabditis elegans* natural populations. *Curr. Biol.* **15**, 1176–1184 (2005).
6. Barrière, A. & Félix, M. A. Temporal dynamics and linkage disequilibrium in natural *Caenorhabditis elegans* populations. *Genetics* **176**, 999–1011 (2007).
7. Sivasundar, A. & Hey, J. Sampling from natural populations with RNAi reveals high outcrossing and population structure in *Caenorhabditis elegans*. *Curr. Biol.* **15**, 1598–1602 (2005).
8. Barrière, A. & Félix, M. A. Natural variation and population genetics of *Caenorhabditis elegans*. *WormBook* doi:10.1895/wormbook.1.43.1 (2005); (<http://www.wormbook.org>).
9. Desseyen, J. L., Aubert, J. P., Porchet, N. & Laine, A. Evolution of the large secreted gel-forming mucins. *Mol. Biol. Evol.* **17**, 1175–1184 (2000).
10. Perez-Vilar, J. & Hill, R. L. The structure and assembly of secreted mucins. *J. Biol. Chem.* **274**, 31751–31754 (1999).
11. Lang, T., Alexandersson, M., Hansson, G. C. & Samuelsson, T. Bioinformatic identification of polymerizing and transmembrane mucins in the puffer fish *Fugu rubripes*. *Glycobiology* **14**, 521–527 (2004).
12. Julenius, K., Molgaard, A., Gupta, R. & Brunak, S. Prediction, conservation analysis, and structural characterization of mammalian mucin-type O-glycosylation sites. *Glycobiology* **15**, 153–164 (2005).
13. Bendtsen, J. D., Nielsen, H., von Heijne, G. & Brunak, S. Improved prediction of signal peptides: SignalP 3.0. *J. Mol. Biol.* **340**, 783–795 (2004).
14. Dover, G. Molecular drive: A cohesive mode of species evolution. *Nature* **299**, 111–117 (1982).
15. Lotan, R., Skutelsky, E., Danon, D. & Sharon, N. The purification, composition, and specificity of the anti-T lectin from peanut (*Arachis hypogaea*). *J. Biol. Chem.* **250**, 8518–8523 (1975).
16. Carlson, D. M. Structures and immunochemical properties of oligosaccharides isolated from pig submaxillary mucins. *J. Biol. Chem.* **243**, 616–626 (1968).
17. Lints, R. & Hall, D. H. Handbook of *C. elegans* male anatomy. *WormAtlas* (<http://www.wormatlas.org/handbook/contents.htm>) (2005).
18. Ganko, E. W., Fielman, K. T. & McDonald, J. F. Evolutionary history of Cer elements and their impact on the *C. elegans* genome. *Genome Res.* **11**, 2066–2074 (2001).
19. Britten, R. J. Active *gypsy/Ty3* retrotransposons or retroviruses in *Caenorhabditis elegans*. *Proc. Natl Acad. Sci. USA* **92**, 599–601 (1995).
20. Barr, M. M. & Sternberg, P. W. A polycystic kidney-disease gene homologue required for male mating behaviour in *C. elegans*. *Nature* **401**, 386–389 (1999).
21. Peden, E. M. & Barr, M. M. The KLP-6 kinesin is required for male mating behaviors and polycystin localization in *Caenorhabditis elegans*. *Curr. Biol.* **15**, 394–404 (2005).
22. Barr, M. M. & Garcia, L. R. Male mating behavior. *WormBook* doi:10.1895/wormbook.1.78.1 (2006); (<http://www.wormbook.org>).
23. Fisher, R. A. *The Genetical Theory of Natural Selection* (Oxford Univ. Press, 1930).
24. Stern, D. L. Evolutionary developmental biology and the problem of variation. *Evolution* **54**, 1079–1091 (2000).
25. Lints, R. & Emmons, S. W. Regulation of sex-specific differentiation and mating behavior in *C. elegans* by a new member of the DM domain transcription factor family. *Genes Dev.* **16**, 2390–2402 (2002).
26. Chasnov, J. R. & Chow, K. L. Why are there males in the hermaphroditic species *Caenorhabditis elegans*? *Genetics* **160**, 983–994 (2002).
27. Cutter, A. D. & Ward, S. Sexual and temporal dynamics of molecular evolution in *C. elegans* development. *Mol. Biol. Evol.* **22**, 178–188 (2005).
28. Stewart, A. D. & Phillips, P. C. Selection and maintenance of andro dioecy in *Caenorhabditis elegans*. *Genetics* **160**, 975–982 (2002).
29. Sulston, J. E. & Hodgkin, J. in *The Nematode Caenorhabditis elegans* (Cold Spring Harbor Press, 1988).
30. Brudno, M. *et al.* LAGAN and Multi-LAGAN: Efficient tools for large-scale multiple alignment of genomic DNA. *Genome Res.* **13**, 721–731 (2003).

**Supplementary Information** is linked to the online version of the paper at [www.nature.com/nature](http://www.nature.com/nature).

**Acknowledgements** We thank the *Caenorhabditis* Genetics Center, M. Ailion, E. Dolgin, A. Barrière, M.-A. Félix and P. McGrath for strains and reagents. Work at Bowdoin College was supported by college funds, by the NIH (grant P20 RR-016463 from the INBRE Program of the National Center for Research Resources), the NSF (grant 0110994), and by an award to Bowdoin College by the Howard Hughes Medical Institute under the Undergraduate Science Education Program. Work at Princeton University was supported by grants from the NIH (R01 HG004321 to L.K. and P50 GM071508 to the Lewis-Sigler Institute), a James S. McDonnell Foundation Centennial Fellowship (L.K.), and a Jane Coffin Childs Fellowship (M.V.R.). We thank S. Civillico for assistance in the laboratory, F. Hagen for experimental advice, and E. Anderson, H. Coller, L. Gordon and H. Seidel for comments on the manuscript.

**Author Information** Reprints and permissions information is available at [www.nature.com/reprints](http://www.nature.com/reprints). Correspondence and requests for materials should be addressed to M.F.P. (mpalopol@bowdoin.edu).

## METHODS

**RT-PCR assays.** RNA was isolated using the RNeasy Mini Kit (Qiagen) and amplified using the OneStep RT-PCR Kit (Qiagen) with primers specific for *plg-1* (plgRT125F and plgRT259R, flanking intron 3) and for the male-expressed gene *lov-1* (lovRT497F and lovRT993R), a positive control for male mRNA. Primer sequences for all experiments are provided in Supplementary Information.

**RNAi construct and assay.** A fragment of the *plg-1* locus was amplified using primers e2.2F1 and plgR12BglII and the product cut with BglII and cloned into the RNAi feeding vector L4440 (Andy Fire Vector Kit, Addgene). The insert is approximately 3 kb and contains almost the entirety of the large repetitive last exon of *plg-1*. The plasmid was then transformed into HT115(DE3) RNase III-deficient bacteria for RNAi feeding experiments, which were conducted using the protocol described in ref. 31. Insertless vector L4440 in HT115 cells served as a negative control. Individual virgin N2 hermaphrodites were allowed to mate overnight with 3–5 CB4856 virgin males that were either exposed to bacteria containing insertless vector (these males should generate normal plugs), or exposed to bacteria producing *plg-1* dsRNA (these males should generate fewer/smaller plugs). The hermaphrodites were scored for plugs the next morning, using an arbitrary plug size rating scale (0: none, 1: small, 2: medium, 3: large), and the observer was blind to treatment. CB4856 exhibits germline RNAi resistance, but it retains sensitivity to systemic RNAi in somatic tissues<sup>32</sup>, permitting us to use RNAi to assay gene function in the somatic gonad.

**Transgenic complementation construct and transformation.** We constructed the *plg-1* rescue transgene pMR5.3 by sequentially cloning the 5' and 3' fragments. We cloned the 5' part of the gene, amplified from CB4856 with primers plgF3 and plgR1 and cut with ApaI and BglII, into pPD34\_110 (Andy Fire Vector Kit, Addgene), cut with the same enzymes. The 5' insert is 1,469 bp and includes 686 bp upstream of the 5' end of the transcript as determined by RACE. We cloned the 3' part of the gene, amplified with plgF1 and plgR1 and cut with XbaI and BglII, separately into pPD34\_110 cut with those enzymes. This 3' fragment from CB4856 is ~3.9 kb, versus 2.9 kb in the WormBase N2 genome sequence. We next excised the ApaI–BglII fragment from the first vector and ligated it into the second. We sequenced the resulting construct to the extent possible given the repetitive nature of the last *plg-1* exon and found no differences from the sequence derived from CB4856 genomic DNA.

We introduced pMR5.3 and an *unc-119* rescue plasmid, pMM016B, into strain QX1015, which carries *unc-119(ed3)* in a CB4856 background. Because *unc-119* maps close to *plg-1*, QX1015 retains the N2 allele of *plg-1* and other genes in this region, and N2/QX1015 F1 males fail to plug. We co-bombarded 3 µg of each plasmid into QX1015 using a BioRad gene gun. We recovered several independent transformed lines and selected one with high transmission of the extrachromosomal array, as judged by the scarcity of Unc worms in its progeny. This transformed line was assayed quantitatively for plug formation. Males of three genotypes were compared: CB4856, which is a natural plugging strain; F1

from a cross of N2 to QX1015 (*plg-1(N2) unc-119(ed3)* III, CB4856 background) carrying the extrachromosomal array [*plg-1(CB4856) unc-119(+)*], which are expected to produce plugs; and F1 from a cross of N2 to QX1015 without the array, which are expected to be unable to produce plugs. We allowed 3–5 males to mate overnight with a single N2 virgin hermaphrodite, and plug size was assessed the next morning in arbitrary units (0: none, 1: small, 2: medium, 3: large), with the observer blind to male genotype.

**Promoter::GFP construct and transformation.** We cloned a CB4856 PCR fragment encompassing the 311 bp 5' of the start of translation, amplified using primers NotIplgprom471F and NplgproR1, into vector pSM\_GFP using a NotI cut site. The plasmid, pMR18K, was introduced into QX1015 by biolistic transformation. We recovered a line with an integrated transgene, assigned allele name *qq1s1*. The transgene maps near the centre of chromosome III, near *plg-1* and *unc-119*, based on linkage mapping with strains MT3751 (*dpn-5* I; *rol-6* II; *unc-32* III), EG1020 (*bli-6* IV; *dpn-11* V; *lon-2* X) and CB1562 (*vab-7* III). We recovered 0/13 Vab GFP worms and 0/50 Unc-32 GFP worms. Several additional lines, in which the transgene is not integrated into the genome, show qualitatively identical GFP expression. Nematodes expressing GFP were imaged with a Zeiss 510 META confocal microscope using a Plan-NEOFLUAR 40X/1.3 oil objective. Nematodes were anesthetized in 10 mM sodium azide and mounted on 5% agar pads for examination. Unmated males (for example, Fig. 3d, e) were collected as L4 larvae and held overnight without access to hermaphrodites. To obtain males soon after mating (for example, Fig. 3f), individual virgin males were placed in the presence of several virgin hermaphrodites and watched until matings were completed, then examined under the microscope immediately afterwards. We corroborated the relationship between mating and vacuole morphology by examining *qq1s1; mab-23* homozygotes, which are incapable of mating. These males exhibited the large vacuole morphology.

**Lectin staining.** Plugged and unplugged hermaphrodites were fixed in 4% paraformaldehyde in PBS. Fixed hermaphrodites were stained in 1:100 dilutions of the two molecules mentioned below (Invitrogen Molecular Probes), in PBS + 0.1% TritonX, then washed several times in PBS + 0.1% TritonX, and then several times in PBS. (1) Alexa Fluor 488 donkey anti-mouse IgG (A21202); (2) lectin PNA from *Arachis hypogaea* (peanut), Alexa Fluor 594 conjugate (L32459).

Worms were mounted on 5% agar pads and examined under the confocal microscope. Strong lectin signal was observed; negligible signal was observed from the donkey anti-mouse antibody, suggesting that the plug was not simply absorbing probe.

31. Kamath, R. S. & Ahringer, J. Genome-wide RNAi screening in *Caenorhabditis elegans*. *Methods* **30**, 313–321 (2003).
32. Tijsterman, M., Okihara, K. L., Thijssen, K. & Plasterk, R. H. PPW-1, a PAZ/PIWI protein required for efficient germline RNAi, is defective in a natural isolate of *C. elegans*. *Curr. Biol.* **12**, 1535–1540 (2002).

# naturejobs

THE CAREERS  
MAGAZINE FOR  
SCIENTISTS

**P**ublished rankings and top tens of all sorts seem to be increasingly common — and many now go beyond best films or books to look at all aspects of people's lives. *Forbes* magazine, for example, runs rankings that range from the best places to get ahead, to the best cities for recent college graduates or the best places for businesses and careers.

Higher education is one of the major areas ranked. Numerous organizations draw up tables on universities and graduate programmes, although they tend to use varying criteria in their assessments. On page 1024 we analyse some popular rankings schemes for graduate programmes, examine their methodology and reveal some of the suggestions being made for improvement.

Rankings can suffer from biases and data limitations. But they have become big business for publications such as *US News & World Report* — to the displeasure of some observers. Last year for example, the Annapolis Group, an organization of US liberal arts colleges, objected to rankings that asked college presidents to gauge the reputations of other schools (see *Nature* **447**, 1139; 2007). The Education Conservancy, a nonprofit organization based in Portland, Oregon, and another critic of current rankings, has ambitious plans to replace undergraduate rankings systems. It is planning a college 'information system' to assist prospective students. Colleges will be suggested based on students' priorities and a set of diagnostic exercises that help students determine the sort of college experience they are seeking. If the conservancy can raise the funds to develop the system and update it regularly, this could be an invaluable tool.

If all goes well, hopefully the feat can be repeated for graduate schools and, even more ambitiously, on an international level so that prospective graduate students can judge schools across borders — a key capability for a scientific enterprise and educational system that is increasingly global. Ideally, graduate students would have a better chance of finding the right fit, and institutions would worry more about education than about reputation.

**Gene Russo is editor of *Naturejobs*.**

## CONTACTS

**Editor:** Gene Russo

**European Head Office, London**  
The Macmillan Building,  
4 Crinan Street, London N1 9WX, UK  
Tel: +44 (0) 20 7843 4961  
Fax: +44 (0) 20 7843 4996  
e-mail: [naturejobs@nature.com](mailto:naturejobs@nature.com)

**European Sales Manager:**

Andy Douglas (4975)  
e-mail: [a.douglas@nature.com](mailto:a.douglas@nature.com)

**Business Development Manager:**

Amelie Pequignot (4974)  
e-mail: [a.pequignot@nature.com](mailto:a.pequignot@nature.com)

**Naturevents:**

Claudia Paulsen Young (+44 (0) 20 7014 4015)  
e-mail: [c.paulsenyoung@nature.com](mailto:c.paulsenyoung@nature.com)

**France/Switzerland/Belgium:**

Muriel Lestranguez (4994)

**Southwest UK/RoW:** Nils Moeller (4953)

**Scandinavia/Spain/Portugal/Italy:**

Evelina Rubio-Hakansson (4973)

**Northeast UK/Ireland:**

Matthew Ward (+44 (0) 20 7014 4059)

**North Germany/The Netherlands:**

Reya Silao (4970)

**South Germany/Austria:**

Hildi Rowland (+44 (0) 20 7014 4084)

**Advertising Production Manager:**

Stephen Russell  
To send materials use London address above.

Tel: +44 (0) 20 7843 4816

Fax: +44 (0) 20 7843 4996

e-mail: [naturejobs@nature.com](mailto:naturejobs@nature.com)

**Naturejobs web development:** Tom Hancock

**Naturejobs online production:** Dennis Chu

**US Head Office, New York**

75 Varick Street, 9th Floor,  
New York, NY 10013-1917

Tel: +1 800 989 7718

Fax: +1 800 989 7103

e-mail: [naturejobs@natureny.com](mailto:naturejobs@natureny.com)

**US Sales Manager:** Peter Bless

**India**

Vikas Chawla (+91 1242881057)

e-mail: [v.chawla@nature.com](mailto:v.chawla@nature.com)

**Japan Head Office, Tokyo**

Chiyoda Building, 2-37 Ichigayatamachi,  
Shinjuku-ku, Tokyo 162-0843

Tel: +81 3 3267 8751

Fax: +81 3 3267 8746

**Asia-Pacific Sales Manager:**

Ayako Watanabe (+81 3 3267 8765)

e-mail: [a.watanabe@natureasia.com](mailto:a.watanabe@natureasia.com)

**Business Development Manager, Greater**

**China/Singapore:**

Gloria To (+852 2811 7191)

e-mail: [g.to@natureasia.com](mailto:g.to@natureasia.com)

# Dissension in the ranks

Graduate programmes are rated by various organizations using different criteria. How much use are these rankings? **Genevieve Bjorn** surveys the options.



**B**efore deciding which doctoral astrophysics programme to apply for, Nick Lee perused the published rankings. He found a grab bag of results. The *US News & World Report*'s numbers offered little substantive insight about the institutions he was interested in. The statistics from the US National Research Council (NRC) were updated too infrequently to help him. And the *Times Higher Education* World University Rankings offered data about the best universities for natural sciences, but not specifically PhD programmes in astronomy. Lee was left confused.

Despite their flaws, prospective graduate students frequently use such ranking schemes to assess doctoral programmes. But the various criteria in use make it hard to know which scheme to rely on. Students need to identify the most desirable programme, where they will not only invest the next several years of their lives but also start their research careers. For universities trying to attract top talent, the stakes are just as high.

Competition for a place in a top graduate school is fierce, and the number of applicants continues to

swell. According to the US National Science Foundation (NSF), more than 150,000 science and engineering doctoral degrees were awarded worldwide in 2005, compared with 125,000 in 2002. In Britain, for example, the number of final-year PhD students at universities grew by 31% between 1999 and 2003.

Despite the limitations of ranking schemes, many professors and administrators admit to using them to plan recruiting strategies and gauge where their institutions stand. "It is easier to attract higher-quality faculty members to a highly ranked institution," says Brian Maple, chair of the department of physics at the University of California, San Diego.

And the tables can play a major part in applicants' decision processes. One tenure-track faculty member in physics at a highly ranked university says he is worried about accepting a faculty job offer from a lower-ranked institution. (He asked to remain anonymous, as he is still negotiating.) Despite the department's positive attributes, including access to top research facilities, he worries that this early-career move could hurt his prospects later on. "Once faculty step down the rankings ladder, it's often difficult to climb back up," he says. "I have concerns about the loss of prestige, possibly leading to less funding and less competitive students."

## Playing the system

With so much at stake for faculty members and students, it's no wonder that some universities attempt to manipulate the system.

Geoff Davis, mathematician and founder of the online resource PhDs.org, says he was once hired as a consultant to a university disappointed with the fall in its rankings. "My job was to figure out strategies they could use to regain their standing," says Davis.

One of those strategies is to manipulate 'admissions yield', the ratio of students offered a place to those who actually take up the offer. A higher yield boosts the rankings. To keep yields high and avoid being perceived as a safety net, upper-tier institutions may, for example, decide not to offer a spot to students with perfect test scores if they are considered likely to go to a higher-ranked institution. According to Davis, most rankings are vulnerable to this kind of manipulation. But it creates difficulties for a student trying to make the best choice.

Disparities among rankings criteria add to the confusion. Consider, for example, how the physics department at the Massachusetts Institute of Technology (MIT) fared in various schemes. *US News & World Report*'s 2008 rankings of best US graduate schools in physics place MIT firmly at the top with a perfect 5.0 score. Bob Morse, data research director at *US News & World Report*, explains that the science rankings are based solely on a peer survey of deans and department heads. Small changes in the ranks are the norm because people's opinions tend to change slowly.

*The Times Higher Education* table of the top 50 natural-sciences universities (it does not offer a ranking for physics alone) places MIT second to the University of California, Berkeley, scoring 97.6 out of 100. *The Times Higher Education* combines six criteria to produce an overall table. Peer review accounts for 40% of the possible score. It also factors in citations and



**Brian Maple:** high ranking attracts top-quality faculty members.

staff-to-student ratios, and asks employers at which institutions they seek future employees.

In the category of natural sciences and mathematics, rankings drawn up by China's Shanghai Jiao Tong University rank MIT in sixth place, with a score of 90.4 out of 100, behind four other US institutions and the University of Cambridge, UK. This scheme does not use peer-review surveys but ranks according to academic or research performance. It uses criteria such as whether staff have won Nobel prizes or Fields medals, and the percentage of articles published in top journals. Clearly, varying criteria mean varying results.

Most of these schemes have multiple caveats. For example, basing scores on opinions could confer serious bias. "Assessing programmes this way comes down to measurement of the views in the field by peer review," says Jerry Ostriker, chair of the NRC's committee to examine the methodology for the assessment of research-doctorate programmes. This means that an institution with a good reputation is likely to keep it, Ostriker notes, whereas up-and-coming programmes are overlooked.

Ostriker calls this the 'halo effect'. The reputation of a highly ranked university such as MIT could buoy the ratings of an otherwise weak programme in one particular field. The halo effect also works in reverse. A university's overall low ranking could mask one stellar department.

Davis cites research done by the US National Bureau of Economic Research, showing that student decisions are a more reliable source of preference rankings than expert opinion, citation rates or admission yields. The bureau used students' choices of university as the measure of competitiveness, while controlling for biasing factors such as free tuition, alumni parents and distance from home. This scheme, according to the rationale, is more telling and less subject to manipulation by the universities.

In 2004, an initiative by the European Centre for Higher Education and the US Institute for Higher Education Policy attempted to address rankings inequities. The International Rankings Expert Group (IREG) sought a broad international standard. It published the Berlin Principles on Ranking of Higher Education Institutions in 2006, urging that rankings systems use rigorous data and transparent data collection and analysis methods. Some have heeded this recommendation.

### Tailor-made rankings

Part of the solution, as the IREG report asserts, may be league tables tailor-made for the user. At the PhDs.org site, which Lee eventually turned to for help, users seek the US doctoral programme of their dreams by sorting through dozens of attributes and choosing only the ones that matter most, such as sub-field, size, cost and prestige. Users input their priorities and assign a value from one to five, leaving fields blank if they are not important. Users can further customize the search by weighing and adjusting specific details, such as faculty citations and job placement rate. The site returns a list of ranked matches. Data come from numerous US sources including the NRC, NSF and the National Center for Education Statistics.

"We don't declare any programme 'the best,'" says Davis. "Rather, we provide a tool to help people find the



**"We asked faculty which metrics are important for their field, and are using those metrics to determine the new rankings."**

— Jerry Ostriker

programmes that are the best for them."

Ostriker and others at the NRC recognize the need for better data. "We've asked faculty, in all the different fields, which metrics are important for that field," says Ostriker. "Now we're using those metrics to determine the new rankings."

In the past, the NRC relied on survey questions and statistics published by the universities. Its new rankings, to be released in September, seek to remedy flaws. The new metrics include citation counts for science programme rankings as well as data about the other graduate students, the mix of faculty members and student funding opportunities. Ostriker anticipates that some institutions will be upset, although he declines to name names.

Using the 'random halves' method to analyse the data, the NRC plans to provide a more honest assessment of the uncertainty involved. This requires comparing the results of one half of the data to the other half and then repeating that step using different sets of halves multiple times. It's a way of estimating how much the answers to questions depend on who is asked.

"We're hoping that once we have all the methodology in place we can update it every two years," says Ostriker. The NRC is also planning a website that allows users to rate institutions on the basis of variables that they consider important. Following the Berlin Principles, users will be able to disagree with the NRC committee's assigned weights.

### See for yourself

Of course, looking at tables is no substitute for visiting a place in person. Dagney Looper, a third-year doctoral student in astrophysics at the University of Hawaii, recalls hosting a clutch of undecided prospective doctoral students this spring. She showed off everything from the school's world-class observing facilities to its local surf spots. Looper says that many of the students used rankings to decide where to apply. They were torn between offers from higher-ranked schools and from the University of Hawaii, which has a strong astronomy programme but less overall prestige.

"I told the prospective graduate students that getting into a good doctoral programme is important," says Looper. "But it's what you do there that really matters."

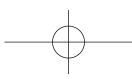
**Genevieve Bjorn is a freelance science writer based in Maui, Hawaii.**

### Web links

- Zeit Center for Higher Education ranking  
► [www.excellenceranking.org/eusid/EUSID?module=FAQ](http://www.excellenceranking.org/eusid/EUSID?module=FAQ)
- PhDs.org  
► [www.phds.org](http://www.phds.org)
- Shanghai Jiao Tong University  
► [ed.sjtu.edu.cn/ARWU-FIELD2008.htm](http://ed.sjtu.edu.cn/ARWU-FIELD2008.htm)
- The Times Higher Education  
► [www.timeshighereducation.co.uk/hybrid.asp?typeCode=146](http://www.timeshighereducation.co.uk/hybrid.asp?typeCode=146)
- US News & World Report  
► [grad-schools.usnews.rankingsandreviews.com/grad](http://grad-schools.usnews.rankingsandreviews.com/grad)
- National Research Council, 1995 report on doctoral programmes in the United States  
► [www.nap.edu/catalog.php?record\\_id=4915](http://www.nap.edu/catalog.php?record_id=4915)
- National Research Council, ratings and rankings  
► [www7.nationalacademies.org/resdoc/ranking\\_and\\_ratings.html](http://www7.nationalacademies.org/resdoc/ranking_and_ratings.html)



**Dagney Looper: it's what you do at the institution that really matters.**



MONTCLAIR  
STATE  
UNIVERSITY  
1908-2008

The Margaret and Herman

**Sokol Institute**

for Pharmaceutical Life Sciences

Department of Chemistry and Biochemistry

Montclair State University is a comprehensive state-assisted institution founded in 1908. Montclair State University offers a rich array of programs to more than 16,000 undergraduate and graduate students. Montclair State University awards the following degrees: Bachelor of Arts, Bachelor of Fine Arts, Bachelor of Music, Bachelor of Science, Master of Arts, Master of Arts in Teaching, Master of Science, Master of Business Administration, Master of Education, Master of Fine Arts, Doctor of Education, and Doctor of Environmental Management and Doctor of Philosophy..

The Department of Chemistry and Biochemistry is certified by the American Chemical Society Committee on Professional Training and offers programs leading to undergraduate degrees Chemistry and Biochemistry. Additionally, there are a number of Graduate Programs offered in the Department. Aside from a Master of Science in Chemistry and a Master of Science in Chemistry with a concentration in Biochemistry, the Department offers is a combined BS/MS, a combined MS/MBA as well as other graduate programs.

The **Margaret and Herman Sokol Institute for Pharmaceutical Life Sciences** (<http://www.montclair.edu/sokolinstitute/>) supports trans-disciplinary research among College of Science and Mathematics faculty, students, and academic and industry collaborators in the broad area of pharmaceutical science. The Sokol Institute promotes a diversity of research programs in the Pharmaceutical Life Sciences that impact human health in general and also strives to bring a global view to some of its research with programs in AIDS, malaria, and other important global issues. The Institute will be creating advanced analytical and discovery technologies as well as entering into partnerships with various business partners to establish business incubators for the development of new technologies and products. The Institute is also helping develop advanced graduate and post-doctoral programs in pharmaceutical disciplines such as medicinal chemistry, biochemistry and pharmacology with the College of Science and Mathematics.

In September, Montclair State University plans to initiate a search for a Chair of the Department of Chemistry and Biochemistry. It is expected that the chair will develop new programs, take a lead in attracting new faculty, build and enhance research programs, expand and update curricula, develop outreach to expand enrollments and provide innovative and enthusiastic leadership. The candidate should have a record of distinction in research, teaching and leadership.

The Department and the Sokol Institute will be seeking applications for the Margaret and Herman Sokol Chair in Chemistry from outstanding scientists whose research is focused on pharmaceutical chemistry and/or medicinal chemistry. The Sokol Chair is a tenure track appointment at a rank appropriate for the experience and accomplishments of the candidate.

For additional information contact Department Chair, Dr. Marc L. Kasner at [kasnerm@mail.montclair.edu](mailto:kasnerm@mail.montclair.edu) or Sokol Institute, Dr. John Siekierka at [siekierkaj@mail.montclair.edu](mailto:siekierkaj@mail.montclair.edu)

NW168575R

HIGHLIGHT: NEW JERSEY

**Is your work-life  
out of balance?**



Keep up-to-date with all  
the latest issues affecting  
scientists and their  
working environment on  
**naturejobs.com**

nature publishing group npg

1|NATUREJOBS|21 August 2008

## MICROCHIPS

**PharmaSeq, Inc.**, a well-funded biotech start-up company, is developing rapid, light-powered microchip-based fluorometric technologies and needs talented people for our Engineering and Microarray Genomics and Proteomics Teams. Benefit from cutting-edge technology & a dynamic work environment in a company with great potential! We have started clinical trials of our technology, received a substantial grant support from NIH, and our company is growing!

We currently seek **engineers, scientists, research associates and team leaders (B.S., M.S. and Ph.D. level)** in the following areas:

### Molecular Biology and Immunoassay Electrical Engineering

(RFID, Systems and Instrumentation Design)

### Software Engineering (C++, FPGA)

### Flow Fluorometry

People with managerial experience are also encouraged to contact us. For more information about these job opportunities, go to our web site, [www.pharmaseq.com](http://www.pharmaseq.com).

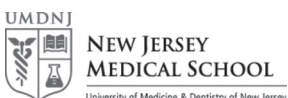
**PharmaSeq** is located on U.S. Route 1 in the NJ high-tech corridor **near Princeton**, minutes from Princeton University and Rutgers. We offer a competitive compensation package, including benefits and stock options. Become a part of the recent dramatic growth in the tools business!

Send your resume with cover letter in strict confidence to:

**Job Code T1,**  
**PharmaSeq, Inc., 11 Deer Park Dr., Suite 104,**  
**Monmouth Junction, NJ 08852. Fax: (732) 355-0102**  
**Email: [mandecki@pharmaseq.com](mailto:mandecki@pharmaseq.com)**



PHARMASEQ



## (Senior) Bioinformatics Specialist

We are seeking an enthusiastic bioinformatics specialist for our new Bioinformatics Core Facility at UMDNJ - New Jersey Medical School (<http://njms.umdnj.edu/>). The successful candidate will have a key role in initiating and executing collaborative projects with investigators in a range of research fields. Qualified applicants should have a Ph.D. degree in bioinformatics/computational biology or a related field, with working knowledge of genome informatics and DNA microarray data analysis. Experience with next-generation sequencing data is a strong advantage. Title and rank will be commensurate with experience. Interested individuals should contact Dr. Bin Tian by e-mail ([btian@umdnj.edu](mailto:btian@umdnj.edu)) with a CV including a summary of previous research and contact information of 2-3 referees.

New Jersey Medical School is a dynamic scientific community, part of UMDNJ, with research excellence in several basic and clinical areas. It is located in Newark, New Jersey, in close proximity to New York City. Many scientific and educational opportunities are available in the NY/NJ metropolitan area, as well as cultural, entertainment and sports activities

NW168499R



RUTGERS  
NEWARK

The Center for Molecular & Behavioral Neuroscience, Rutgers-Newark invites applications from outstanding candidates for a state-funded, tenure-track, assistant professorship. Applicants must have a Ph.D or equivalent in neuroscience or a related field, a strong publication record and expertise in cellular and/or systems neurophysiology and multiphoton laser scanning imaging. Participation in graduate teaching in the *Integrative Neuroscience Graduate Program* administered jointly by Rutgers and the University of Medicine and Dentistry of New Jersey- New Jersey Medical School (UMDNJ) and in the *Quantitative Neuroscience Graduate Program*, a consortium comprising Rutgers, The New Jersey Institute of Technology and UMDNJ, will be expected. Please send a curriculum vita, research program and three letters of recommendation to Dr. Gyorgy Buzsaki, Rutgers University, 197 University Avenue, Newark, NJ 07102.

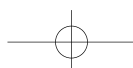
Rutgers University is an equal opportunity employer.

NW167627R

**Corrosive,  
uncompromising  
opinions and views  
on workplace issues  
affecting YOU.**



naturejobs



## NATUREJOBS presents a HIGHLIGHT ON MINNESOTA

**NATURE ISSUE: SEPTEMBER 4, 2008**

**DEADLINE FOR ADVERTISERS:**  
AUGUST 28, 2008

This Highlight is a dedicated section for promoting Minnesota's strong scientific environment. It is an excellent opportunity for the R&D community, research institutes and companies within Minnesota to gain international exposure in *Nature*. If you are looking to recruit top-tier scientific talent for your organization and raise your profile in front of this audience, you won't want to miss this issue.

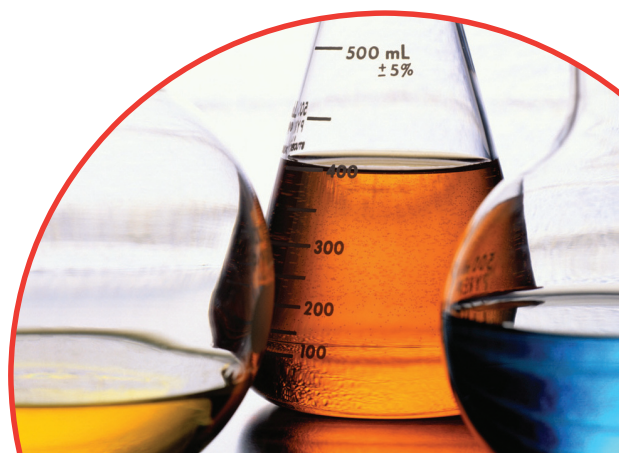
Whether you are recruiting, creating awareness, or positioning your organization, this feature provides you with a unique opportunity to deliver your message to the global scientific community.

**TO PROFILE YOUR ORGANIZATION AND EVENTS TO POTENTIAL EMPLOYEES,  
PARTNERS AND INVESTORS, PLEASE CONTACT:**

**Helen Wu**  
T: 212-726-9347  
F: 800-989-7103  
E: [h.wu@natureny.com](mailto:h.wu@natureny.com)

[WWW.NATUREJOBS.COM](http://WWW.NATUREJOBS.COM)

IN167096R



**naturejobs**

nature publishing group 

# All of me

A man walks into a bar ...

**Ed Rybicki**

You know, I have the cover of an issue of *Nature* on the wall in my bar. There's very few of my regulars who actually notice it. It's not even very special, in a scientific way: more a spoof, commemorating a semi-centenary. But it's a good in-joke — for those of us who know.

Anyway, tonight was a night like pretty much any other at the Cat-in-the-Box: reasonable crowd, the usual three-to-one man-to-woman ratio. The guitarist seemed pretty good — but I suppose I'm biased.

I stood for a while in my usual inspection place just inside the door, scanning the customers. Once you know what to look for, it's easy to spot: about half and half, then; insiders and civilians. I found my gaze lingering on the cover. More a visual cue than anything particular — hell, I could hardly see the thing — but it got me to thinking, again, of the might-have-beens. If I hadn't tried out on a whim for the rugby team; if I'd carried on down the physics post-grad trail my father so wanted me to follow; if I'd swung one way rather than the other.

If I'd never met Eileen.

I noticed someone loitering in the entrance, then; more as a darkening of the ambient light than anything else, but it got me looking at him. My height, pretty much; a bit shabby, running shoes and jeans, hair overlong — typical student, I couldn't help thinking, casting a glance down at my own understatedly elegant rig. He came in a bit farther, so I was now behind him and to his right. Just let him look to the far side of the circular bar, I thought; then we'll know.

His double-take was almost comical: he started so hard he almost hit me. OK, so he'd recognized the Eileen — and now for the intervention, I thought, as I gently took his arm, just as he set off to sprint around the bar.

"Hey, sport!" I gave him, as he whipped round, wild-eyed. "Just got in?" That got to him: I could almost see the wheels turning as he wondered how I could possibly know. I noticed a couple of folk watching

me as I smiled at him, and gestured to my left. "Come sit and have a beer," I said. His eyes went back to the Eileen. I could feel him tensing to pull away, so I leaned in to his ear. "She won't know you, whatever you might want," I said. "She's with a bunch that she does know" — and I indicated his get-up — "who do a whole lot better than you."

He looked over to her, yearningly. Sure enough, the crew around her was pretty well-dressed; about half gay, the rest straight. Nice to see the talents being used for profit, I thought. He looked back to me. I could see his eyes flicker over me,



then he decided to follow. Good idea, that: we were of a height, but I massed easily a third as much again as he did. Professional rugby leaves you with more than just aches and scars: if you keep up the exercise, the bulk stays pretty firm too. Not to mention impressive, if you're the under-exercised lab rat I knew he was.

He came along pretty meekly as I ushered him into a seat — I made sure he could still see the object of his affection over my shoulder. I put up a hand without looking round, and Thomas was at my shoulder just about instantly.

"Pint of draught for John here — and a sparkling water for me." He nodded and was off, as the new boy gaped at me.

"What ... how did you ...?" I noticed he had a faint accent: off to one side of the bell curve, then. That made what I had to say quite a bit easier. I leaned onto the table, clasped my hands together and smiled as winningly as I could.

"You want to know how I know your name, how I knew what you were looking for ..." I flapped my hand at him to shut him up "... how I knew what you'd drink?" I sat back, and raised my eyebrows at him.

As he started to babble, I leaned in and chopped him off. "Let me tell you the things I know" — counting on the fingers. "One, you work in a high-energy physics lab." Gobsmacked would be a good term for it; he looked as though I'd punched him. "Two, you've had this recurring dream of Eileen over there for years, but you've never met her." Eyes wide enough

to be twin moons now.

"Three, you've come a long and devious way to get here; you can never go back." He gulped, and nodded. "And four, you've got a pocket full of funny-looking money you can't spend here, so you're going to need some help." He could have doubled for my labrador right about then: eyes wide, fixed on me, mouth open ... except with the dog, it's always about food. "So, fortunately, you've come to the right place," I finished, sitting back and gesturing out to the bar.

He followed the wave, to see a rather large cross-section of the clientele looking at us. Some were amused; some — generally the outsiders — frankly curious; some looked sympathetic. I think he got it, right about then: pretty bright, but again, I'm biased.

That *Nature* cover? It's the one with a parody cover of a pulp SF magazine with 'Many Worlds' blazoned on it, marking 50 years of quantum strangeness — and the much-repeated young woman on the cover bears a remarkable resemblance to Eileen. Which is ironic, because there's only a few of her. On the other hand, as the only non-physicist among the insiders, I have the best proof of anyone of the many worlds theory: *all of me*. ■

**Ed Rybicki** is a Cape Town virologist who works on expressing vaccine proteins in plants and insect cells. He has been writing science fiction since 1968, but nobody has ever paid him for it before now.